CHALMERS
UNIVERSITY OF TECHNOLOGY

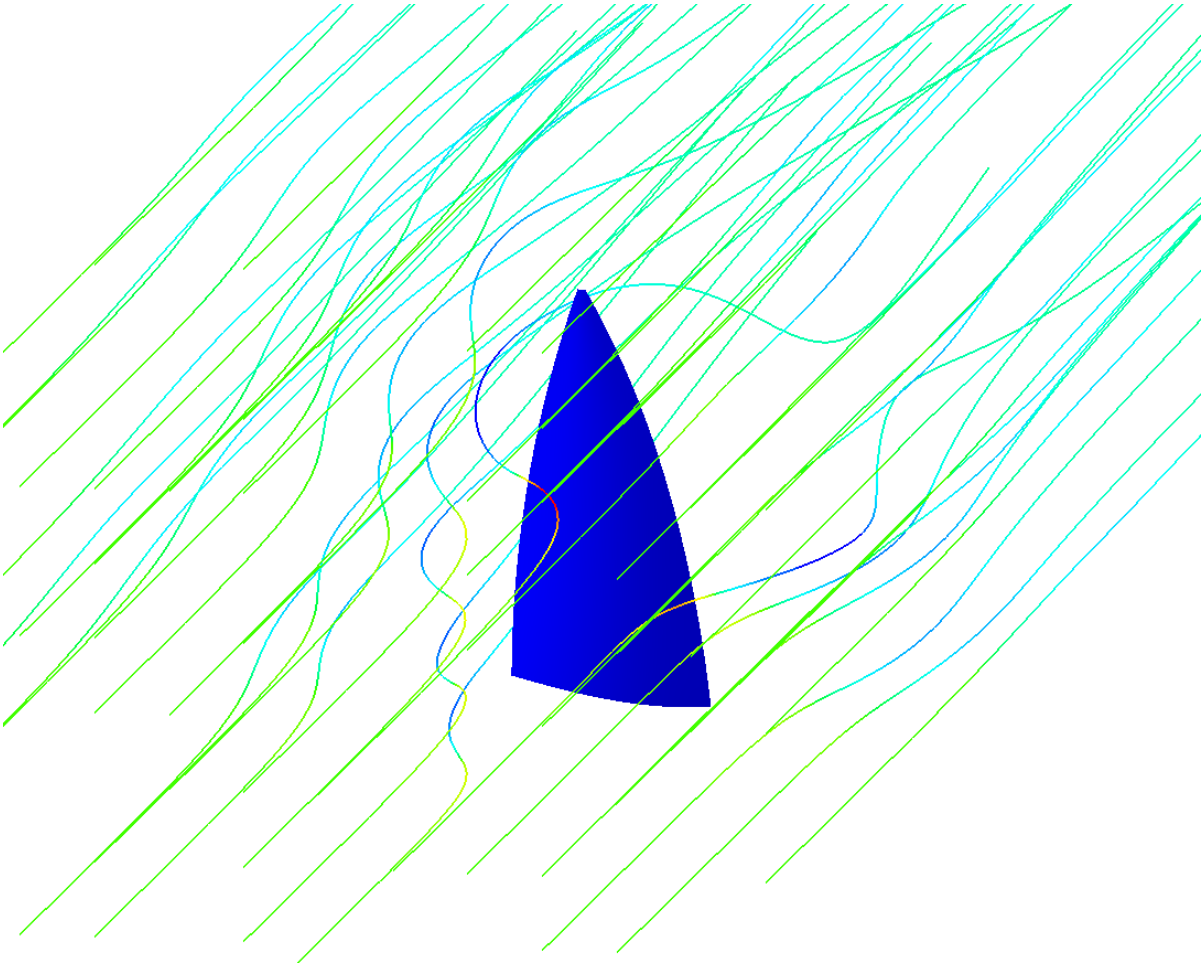

Aerodynamic Analysis of the Bi-Radial MKII Sail for the Olympic Sailing Class Dinghy ILCA 7

Master's of Science Thesis in Naval Architecture and Ocean Engineering

Gustaf Magnander

Department of Mechanics and Maritime Sciences
CHALMERS UNIVERSITY OF TECHNOLOGY
Gothenburg, Sweden 2022

Master's thesis 2022:X-22/396

Aerodynamic Analysis of the Bi-Radial MKII Sail for the Olympic Sailing Class Dinghy ILCA 7

GUSTAF MAGNANDER

CHALMERS
UNIVERSITY OF TECHNOLOGY

Department of Mechanics and Maritime Sciences
Division of Marine Technology
Chalmers University of Technology
Gothenburg, Sweden 2022

Aerodynamic Analysis of the Bi-Radial
MKII Sail for the Olympic Sailing Class Dinghy ILCA 7
GUSTAF MAGNANDER

Supervisor: Professor Lars Larsson
Examiner: Professor Rickard Bensow

Master's Thesis 2022/396
Department of Mechanics and Maritime Sciences
Division of Marine Technology
Chalmers University of Technology
SE-412 96 Gothenburg
Telephone +46 31 772 1000

Cover: The Cambered Sail Model with Computed 3D Streamlines

Typeset in LaTeX
Printed by [Chalmers Reproservice]
Gothenburg, Sweden 2022

Master's Thesis in the International Master's Program Naval Architecture and Ocean Engineering

GUSTAF MAGNANDER
Department of Mechanics and Maritime Sciences
Chalmers University of Technology

Abstract

The most widely used model for sail force coefficients is probably *Hazen's* model. The model, which is presented in [18], offers great flexibility and can be used for a wide range of different sail plans. However, even if it has been extensively used since Hazen presented the model in 1980 and is still used today 4 decades later, it has shown not to be fully satisfying for downwind analysis of sails. To properly analyze the Olympic sailing class dinghy ILCA 7 sailing downwind, the aerodynamic sail coefficients of the new bi-radial MKII sail first has to be retrieved from experimental wind tunnel tests.

The sail coefficients can then be used in a *Velocity Prediction Program (VPP)*, where they are balanced against the corresponding hydrodynamic coefficients, obtained from experimental towing-tank tests of a full-scale ILCA dinghy in 2014 at SSPA, a Swedish Maritime Consulting Company, situated at the main campus of Chalmers University of Technology in Gothenburg Sweden. With the output from the VPP, in the form of a *polar plot*, the optimal way to sail the ILCA 7 dinghy can be established, which is of great value for the Swedish elite ILCA 7 dinghy sailor, who will have the honor of representing Sweden at the Summer Olympics 2024.

A 1:7 scale model of the new bi-radial MKII sail, released in 2016, was manufactured by North Sails and tested for downwind sailing in flat water conditions, in the low turbulence subsonic wind tunnel, at Chalmers University of Technology. The sail model was tested for two different apparent wind speeds that represented light and strong wind conditions. The Reynolds numbers for these two conditions were 1.8×10^5 and 3.0×10^5, respectively. Even though the flow at these Reynolds numbers presumably is turbulent, a grid, that induced turbulence with an intensity of 2 % was used and the sail model was therefore with certainty tested in turbulent flow. For the light wind condition, the sail model was tested for five different headings, three different heel angles (upright condition included), seven different sheet angles and for each configuration of these, three different settings with the kicker were tested. For the strong wind condition, only the heading corresponding to when the ILCA 7 dinghy is sailed dead downwind in a planing mode was of interest; for that heading, the sail model was tested for the upright sailing condition, i.e. with a heel angle of 0°, for four different sheet angles and three different settings with the kicker. For each configuration of these variables, for both wind conditions, the other two trim controls, the outhaul and the cunningham were continuously trimmed. Altogether 327 different configurations of the above mentioned variables were tested.

This Master's Thesis describes how the aerodynamic sail coefficients were retrieved from experimental tests in Chalmers low-turbulence subsonic wind tunnel and how the measurements were corrected for blockage effects, after performing a numerical analysis with Reynolds Averaged Navier-Stokes (RANS) simulations, using the commercial CFD-code STAR-CCM+. The final results is a full set of sail coefficients needed for optimizing downwind sailing of the ILCA 7 dinghy, using a VPP.

Keywords: *ILCA 7, MKII Sail, Scaling, Chalmers Subsonic Wind Tunnel, Blockage Effects, Sail Coefficients, STAR-CCM+, RANS, DES, Verification & Validation*

Acknowledgments

I would like to pay my sincere gratitude to the persons below, who all made it possible for me to carry out this Master's of Science Thesis in Naval Architecture and Ocean Engineering.

Professor Lars Larsson, my supervisor, for his tolerance and continuous support, during the whole project.

Professor Rickard Bensow, my examiner.

Richard Lindstrand Levin, a former Ph.D. student at Chalmers, for his support in the initial phase of the project.

Arash Eslamdoost, Associate Professor at Mechanics and Maritime Sciences, Division of Marine Technology, for continuously providing me with a valid academic power of demand (PoD) license to the commercial CFD-code STAR-CCM$^+$.

Adam Persson, Ph.D. student, at Chalmers University/SSPA Sweden AB, for letting me borrow his CAD model of the old MKI sail for the ILCA 7 dinghy.

Valery Chernoray, Research Professor and Director of Chalmers Laboratory of Fluid and Thermal Science, and Isac Johnsson, Research Engineer, at Applied Mechanics for their help and support, when performing the experimental tests in Chalmers low turbulence subsonic wind tunnel.

The personnel at North Sails in Gothenburg, who did a fantastic job manufacturing the sail model.

The personnel in the mechanical workshop, at SSPA Sweden AB for manufacturing the nice mast model.

Daniel Birgmark, Swedish Olympic Finn class sailor and head trainer at *The Royal Gothenburg Yacht Club (GKSS)*; the elite ILCA 7 dinghy sailors at GKSS, for their expertise and help in the prephase, when analyzing how the ILCA 7 dinghy should be sailed and in the initial phase of the experimental tests, evaluating the manufactured sail model; assisting the author with trimming the sail model.

The computations were performed on resources at the National Supercomputer Centre (NSC) and Chalmers Centre for Computational Science and Engineering (C3SE), provided by the Swedish National Infrastructure for Computing (SNIC); I want to thank the personnel at C3SE for their support.

Gustaf Magnander, Gothenburg, October 2022

Contents

List of Figures

List of Tables

Nomenclature

α	Angle of attack/incidence, [°]
α_E	Elastic scale factor, [-]
$\alpha_E I$	Flexural Rigidity scale factor, [-]
α_F	Force scale factor, [-]
α_L	Linear length scale factor, [-]
α_t	Thickness scale factor, [-]
α_V	Velocity scale factor, [-]
β	Angle of drift or side-slip, [°]
β_L	Leeway angle, [°]
β_{AW}	Apparent wind angle, [°]
β_{TW}	True wind angle, [°]
δ	Boom sheet angle, [°]
δ	Deflection, [m]
δ_R	Rudder angle, [°]
μ	Dynamic Viscosity, [Pa-s]
ν	Kinematic viscosity (μ/ρ), [m^2/s]
ω	Balance rotation or balance angle, [°]
ϕ	Angle of heel, [°]
ψ	Angle of yaw, heading or course, [°]
ρ	Mass density (m/V), [kg/m^3]
σ	Tensile stress, [Pa]
τ_w	Wall shear stress or local skin friction $\left(\mu \left(\frac{\partial U}{\partial y}\right)_{y=0}\right)$, [Pa]
θ	Angle of pitch, [°]
θ_W	Wind direction, [°]
ε	Strain, [m]
A	Projected area, [m^2]
A_{cross}	Cross sectional area, [m^2]
AR	Aspect ratio (b^2/A), [-]
b	Width of wing span or length of appendage, [m]

BAD	Boom above deck, [m]
C	Chord length, [m]
C_{F_D}	Drag force coefficient, [-]
C_{F_L}	Lift force coefficient, [-]
C_{F_M}	Drive force coefficient, [-]
C_{F_S}	Side force coefficient, [-]
C_{M_P}	Pitch moment coefficient, [-]
C_{M_R}	Roll moment coefficient, [-]
C_{M_Y}	Yaw moment coefficient, [-]
E	Modulus of elasticity or Young's modulus, [N/m^2]
E_m	Model-scale base of sail, [m]
E_p	Full-scale/Prototype base of sail, [m]
E_{kin}	Kinetic energy, [J]
E_{mec}	Mechanical energy, [J]
E_{pot}	Potential energy, [J]
f	Frequency, [Hz]
F_D	Drag force, [N]
F_L	Lift force, [N]
F_M	Drive force, [N]
F_S	Side force, [N]
f_s	Frequency of sampling, [Hz]
F_x	Force in direction of body axis x, [N]
F_y	Force in direction of body axis y, [N]
F_z	Force in direction of body axis z, [N]
g	Acceleration due to gravity, [m/s^2]
h	Height above ground level, [m]
L_c	Characteristic length, [m]
L_m	Model-scale length, [m]
L_p	Full-scale/Prototype length, [m]
m	Mass, [kg]
M_P	Pitch moment, [Nm]
M_R	Roll moment, [Nm]
M_x	Moment around body axis x, [Nm]
M_Y	Yaw moment, [Nm]
M_y	Moment around body axis y, [Nm]
M_z	Moment around body axis z, [Nm]
Ma	Mach number (V/a), [-]

p	Local pressure, [Pa]
p_0	Undisturbed or ambient pressure, [Pa]
P_A	Ambient pressure, [Pa]
P_m	Model-scale height of sail, [m]
P_p	Full-scale/Prototype height of sail, [m]
P_{dyn}	Dynamic pressure, [Pa]
P_{stat}	Static pressure, [Pa]
P_{tot}	Total pressure, [Pa]
q	Dynamic pressure, density of kinetic flow energy $(\rho V^2/2)$, [Pa]
Re	Reynolds number $(V\,L/\nu)$, [-]
Re_m	Model-scale Reynolds number $(V_m\,L_m/\nu)$, [-]
Re_p	Full-scale/Prototype Reynolds number $(V_p\,L_p/\nu)$, [-]
SA_m	Model-scale sail area, [m^2]
SA_p	Full-scale/Prototype sail area, [m^2]
t	Time, [s]
T_A	Temperature air, [°]
T_s	Sample interval $(1/f_s)$, [s]
U	Undisturbed velocity of a fluid, [m/s]
u^+	Non-dimensional distance from surface (U/u_τ), [-]
V	Volume, [m^3]
V_p	Full-scale wind speed, [m/s]
V_S	Boat speed, [m/s]
V_{AW}	Apparent wind velocity or wind tunnel velocity, [m/s]
V_{TW}	True wind velocity, [m/s]
x, y, z	Cartesian coordinates, [m]
y^+	Non-dimensional distance from wall $(y\,u_\tau/\nu)$, [-]

1
Introduction

1.1 Background

The ILCA is a cat-rigged one-design Olympic sailing class dinghy, designed by Bruce Kirby 1970, with strict regulations preventing any changes that can increase its performance. What distinguishes one ILCA sailor from another are therefore their physical endurance and strength, their technical skill of sailing the dinghy, their tactical skill to read the game and use the wind, currents, and waves to their favor. Knowing how to sail the ILCA dinghy for optimal *Velocity Made Good (VMG)* is therefore of huge value for the ILCA sailor.

A *velocity prediction program (VPP)* is a software tool, commonly used in sail and yacht design, where aerodynamic and hydrodynamic coefficients and boat data are inputs and the most common output is a so-called polar plot, which contains information of how to sail the particular boat for optimal VMG, in different wind conditions.

Chalmers Sports and Technology [5] is a multi-disciplinary initiative, established in 2012 at Chalmers University of Technology, that undertake advanced sports-related research and sailing is one of the disciplines. The analysis of the Olympic sailing class ILCA 7 dinghy started at Chalmers University in 2014 by the Naval Architecture students Richard Lindstrand Levin and Jeremy Peters, who in a Master's Thesis analyzed the effect of heel and trim on the hydrodynamic resistance, when sailing the ILCA 7 dinghy upwind [21]. Since the ILCA is a relatively small dinghy, it was possible to perform the experimental towing-tank tests with a full-scale ILCA dinghy and therefore avoid scaling effects. The tests were carried out in the towing tank at SSPA, a Swedish Maritime Consulting Company, situated at the main campus of Chalmers University of Technology. The hydrodynamic coefficients, received from the towing-tank tests were first used by Richard Lindstrand Levin and Jeremy Peters and then by Mikka Pennanen, another student of Naval Architecture, in 2016. Pennanen continued the analysis of the ILCA 7 dinghy in upwind sailing, searching for the optimal position of the sailor [29], and validated the method with the experimental hydrodynamic data. This work was presented at the 11th conference of the International Sports Engineering Association, (ISEA) at Delft, The Netherlands [15].

The Olympic race track consists of both an *upwind leg* and an *downwind leg*, and since the ILCA 7 dinghy, up until this point, only had been analyzed sailing upwind, a downwind analysis of the ILCA 7 dinghy remained. However, the aerodynamic sail model Pennanen used in his upwind analysis, i.e. Hazen's model, is not optimal for downwind sailing analysis; in order to properly analyze the ILCA 7 dinghy sailing downwind, the aerodynamic coefficients first has to be retrieved from experimental tests in a wind tunnel.

In the following text, when a *sailboat* is being referred to in general terms, it is assumed that it only has one sail, like the ILCA dinghy.

For a sailboat, the sail and the wind corresponds respectively to as what the engine and the fuel does for a motorboat, but in contrast to a motorboat the crew on a sailboat always must consider the direction of the true wind. This because it is not possible to sail straight against the true wind. Sailing *upwind* and sailing *downwind* was mentioned in the text above as well as the *upwind leg* and the *downwind leg*, but what does sailing upwind and sailing downwind mean; what is a leg? For the non-sailing reader, these concepts might be confusing and will therefore briefly be explained.

Even though there are variations, a traditional race track consists of a so-called upwind leg and a downwind leg; a leg is simply the part of the race track that stretches from either the leeward mark, which is the rounding buoy farthest from the origin of the true wind, to the windward mark, which is the rounding buoy closest to the origin of the true wind, or the other way around; depending on the origin of the true wind, the leg is therefore either called the upwind leg or the downwind leg. Sailing upwind is thus when one sail the upwind leg, towards the origin of the true wind and sailing downwind is when sailing the downwind leg, away from the origin of the true wind. One lap on a traditional race track that only has a windward mark and a leeward mark thus consists of one upwind leg and one downwind leg; different races has different amount of laps. Without going to deep into the technical details about a race track, it must be mentioned that the description of a traditional race track above, with only one buoy at windward and one buoy at leeward is simplified, because in reality there are usually two buoys, both at windward and at leeward, which in pair is called a *gate*. When rounding a gate, it is allowed to choose either one of the two buoys.

As previously mentioned, it is not possible to sail straight against the true wind when sailing upwind and a sailboat therefore has to be sailed in a zigzag pattern with approximately $\pm 45°$ to the true wind; even though it is possible to sail straight downwind in the same direction as the true wind, this is usually not the fastest way, unless the wind is strong and there is power enough in the sails. In light to medium wind strengths it is instead faster to sail downwind in a zigzag pattern, with a certain angle to the true wind. Whenever a sailboat not is aligned with the true wind, it is tilted (heeled), to either left (port) or right (starboard) and thus has a certain *heel angle*. The crew on a sailboat can choose to either increase or reduce the heel angle with their own body weight, by positioning it consciously, in order to balance the boat and increase the speed when sailing downwind.

A sailboat is partly submerged in water and partly surrounded by air; is therefore respectively subjected to both hydrodynamic and aerodynamic forces. The hydrodynamic forces works on the hull and the appendages, i.e. the keel and rudder and the aerodynamic forces works on the sail. When these forces are balanced, equilibrium is achieved and the sailboat can sail on a straight course. As explained later in the text, sailing downwind in light to medium wind strengths, the sailor purposely heels the ILCA dinghy in order to find equilibrium and for higher speed, because the less wet surface, i.e. the less area of the hull and appendages that is in contact with the water, the lower frictional resistance.

While the crew on a motorboat more or less can sit back, relax and enjoy the ride, the crew on a sailboat constantly has to adjust (trim) the sail, so that it is used optimally on

the particular course that the helmsman has decided; different conditions require different sail trim. A sail is trimmed by either pulling or releasing different ropes, so-called trim controls, which makes it possible to alter and optimize the shape of the sail. The different trim controls that the ILCA dinghy is equipped with as well as the description of how the ILCA 7 dinghy should be sailed in various conditions are described in detail in Chapter 3 where the ILCA dinghy is presented. However, since the usage of the trim controls as well as the particular parameters that defines the position of the dinghy are so important for the outcome in a race, these were the natural choice of variables in the experimental wind tunnel tests; the most important ones will therefore be mentioned here briefly. The trim control, the *sheet*, for example, controls the angle between the sail and the true wind direction; by pulling the sheet, the *sheet angle* decreases and the sail becomes more centralized in the boat and by releasing it, the sheet angle increases. Theoretically, the more sail area that is exposed to the wind when sailing downwind, the more speed. It is however not that simple in reality, because other parameters influences and the optimal way of sailing the dinghy is a combination of the different variables; can only be found by using a VPP.
When sailing downwind in light and medium wind conditions there are two alternative techniques, i.e. either sailing *positive* or sailing *negative*. These techniques are defined by a certain range of sheet angles. The different sheet angles that were chosen to be tested, were therefore chosen so that it would be possible to analyze both these sailing techniques on the downwind leg. Another trim control of huge importance is the so-called *kicker*, which controls both the depth in the sail as well as the twist, together with the sheet. Two other very important variables was the *heading*, i.e. the course sailed, and the heel angle.

1.2 Objective

The objective of this project was to retrieve the aerodynamic coefficients with the bi-radial MKII sail for the ILCA 7 dinghy sailing downwind in flat water conditions, from experimental tests with a scale model, so that the ILCA 7 dinghy can be properly analyzed in a VPP on the downwind leg.

Chalmers low-turbulence subsonic wind tunnel, has a closed test section and the airflow around the sail model was therefore affected by the presence of the lateral boundaries, causing so-called *blockage effects*. These effects affected the measurements, which had to be corrected. To quantify the blockage effects and get the correction factors for the experimental test data, a numerical analysis had to be carried out with two computational domains of different sizes. One of the domains had an identical cross-sectional area, of the inlet of the test section, and the other domain, had an enlarged cross-sectional area, simulating an open test section. The numerical analysis included both Reynolds Averaged Navier-Stokes (RANS) simulations, a turbulence model investigation with RANS and detached-eddy simulations (DES), which is a hybrid of large-eddy simulation (LES) and RANS.

1.3 Delimitation's

For the experimental part of this project, the apparent wind speeds that were tested were limited to two. These include a light wind case and a strong wind case, which respectively correspond to a full-scale apparent wind speed of 4 m/s and 7 m/s. For both these wind

speeds, only downwind sailing in flat water conditions have been tested, which represents a sea state of grade zero, with no waves.

For the light wind case, the amount of headings the sail model was tested for were limited to five, which ranged between 150° - 190°, with 10° increments. The different heel angles, for each heading, were limited to three, i.e. 0°, 10° and 20°. For each configuration of heading and heel angle, the different sheet angles were limited to seven, ranging from 60° - 120°, with 10° increments. For each configuration of heading, heel angle, and sheet angle, the sail model was only tested for three different settings corresponding to *light, medium & hard*, with the trim control, the kicker. For each configuration of these variables, the other two trim controls that the ILCA dinghy is equipped with, the *outhaul* and the *cunningham* were continuously adjusted, so that the desired sail shape was received. This sums up to a test matrix of 315 configurations for the light wind condition. The corresponding test matrix for the strong wind case was limited to only cover one heading and one heel angle, which respectively was 180° and 0°. For this case, when sailing dead downwind in upright planing mode, the sail model was tested for only four sheet angles, i.e. 60°, 70°, 80° & 90°; for each sheet angle, the sail model was tested for the same three settings with the kicker. The test matrix for the strong wind condition was thus limited to 12 configurations.

For the numerical part of this project, only the light wind case was simulated and the test matrix for the simulations was limited to cover the heading of 180°, the heel angle of 0°, all seven sheet angles, i.e 60° - 120°, with 10°, increments but only the hard setting with the kicker. However, the numerical investigation required two computational domains of different sizes; both a flat sail model and a cambered sail model were tested, for each computational domain. The test matrix for the numerical part was thus limited to only seven basic cases, but since these were performed with both computational domains and both sail models, 28 configurations were simulated.

2
Theory

2.1 Governing Flow Equations

2.1.1 The Navier-Stokes Equation

Navier-Stokes equations express the conservation of mass and momentum and are widely used when describing viscous fluid flows.

The Continuity Equation

The first equation is the transport equation for mass, i.e. the continuity equation, which expresses the conservation of mass in a system:

$$\frac{d\rho}{dt} + \frac{\partial \rho\, v_i}{\partial x_i} = 0 \tag{2.1}$$

where ρ is the density of mass and v is the velocity. The variations of the subscript $i = 1, 2, 3$ respectively represent the coordinate direction (x_1, x_2, x_3), which corresponds to (x, y, z).

The Momentum Equation

The second equation is the transport equation for momentum, i.e. the *momentum equation*, which expresses the conservation of momentum. In Eq. (2.2), the balance equation for linear momentum is presented:

$$\rho \frac{dv_i}{dt} = \frac{\partial \sigma_{ji}}{\partial x_j} + \rho\, f_i \tag{2.2}$$

where the first term on the right-hand side, with the stress tensor σ_{ij}, represent the net force of the surface forces, and $f_i = (0, 0, -g)$ in the second term, represents the net force of the volume forces, acting on a fluid element, where g is the acceleration due to gravity.

$$\begin{aligned} \sigma_{ij} &= -P\delta_{ij} + \tau_{ij} \\ \tau_{ij} &= 2\mu S_{ij} - \frac{2}{3}\mu S_{kk}\,\delta_{ij} \end{aligned} \tag{2.3}$$

The first expression in Eq. (2.3), show that the stress tensor σ_{ij} equals the sum of the pressure P and the viscous stress tensor, τ_{ij}. The negative sign in front of the pressure term, simply means that the normal forces, acting on the fluid element, point inwards

towards the center of the fluid element. The pressure on a fluid element is therefore defined as the negative sum of the normal stress: $P = -\sigma_{kk}/3$. Further, in the pressure term, we see δ_{ij}, which is the *identity tensor* or the so-called *Kronecker's delta* and is a function with two variables and ensures that the Reynolds stresses where $i = j$ are correct. It is defined as:

$$\delta_{ij} = \begin{cases} 1 & \text{if } i = j \\ 0 & \text{if } i \neq j \end{cases}$$

The second expression in Eq. (2.3) show that the viscous stress tensor, τ_{ij}, includes the dynamic viscosity, μ and the strain-rate tensor, S_{ij}, which is the symmetric part of the velocity gradients that deforms the fluid element [8]. The velocity gradient tensor can be split into two parts, where one of the parts is the aforementioned symmetric strain-rate tensor, S_{ij} and the other part is an anti-symmetric vorticity tensor Ω_{ij}:

$$\begin{aligned} \frac{\partial v_i}{\partial x_j} &= \frac{1}{2}\left(\underbrace{\frac{\partial v_i}{\partial x_j} + \frac{\partial v_i}{\partial x_j}}_{2\partial v_i/\partial x_j} + \underbrace{\frac{\partial v_j}{\partial x_i} - \frac{\partial v_j}{\partial x_i}}_{=0} \right) \\ &= \frac{1}{2}\left(\frac{\partial v_i}{\partial x_j} + \frac{\partial v_j}{\partial x_i} \right) + \frac{1}{2}\left(\frac{\partial v_i}{\partial x_j} - \frac{\partial v_j}{\partial x_i} \right) \\ &= S_{ij} + \Omega_{ij} \end{aligned} \tag{2.4}$$

The vorticity tensor, Ω_{ij}, which represents the rotation of the fluid element, is related to the vorticity vector, which is the curl of the velocity vector [8], i.e.

$$\omega_i = \varepsilon_{ijk} \frac{\partial v_k}{\partial x_j} \tag{2.5}$$

where ε_{ijk} is the so-called *permutation tensor*.

Inserting Eq. (2.3) into Eq. (2.2) leads to the Navier-Stokes equation, which also can be called the *transport equation for momentum*:

$$\rho \frac{dv_i}{dt} = -\frac{\partial P}{\partial x_i} + \frac{\partial \tau_{ji}}{\partial x_j} + \rho f_i = -\frac{\partial P}{\partial x_i} + \frac{\partial}{\partial x_j}\left(2\mu S_{ij} - \frac{2}{3}\mu \frac{\partial v_k}{\partial x_k}\delta_{ij} \right) + \rho f_i \tag{2.6}$$

For incompressible flow, i.e. when the changes of the density of the fluid is negligible ($\rho = constant$) the continuity equation, Eq. (2.1) reads:

$$\frac{\partial v_i}{\partial x_i} = 0 \tag{2.7}$$

with the result that last term in the diffusion term in Eq. (2.6) is zero and Eq. (2.6) can be written:

$$\rho \frac{dv_i}{dt} = -\frac{\partial P}{\partial x_i} + \frac{\partial}{\partial x_j}\left[\mu\left(\frac{\partial v_i}{\partial x_j} + \frac{\partial v_j}{\partial x_i}\right)\right] + \rho f_i \tag{2.8}$$

Further, if the dynamic viscosity μ is constant, it can be moved outside the derivative [8] and the second term on the right hand side of Eq. (2.8) becomes:

$$\frac{\partial}{\partial x_j}\left[\mu\left(\frac{\partial v_i}{\partial x_j} + \frac{\partial v_j}{\partial x_i}\right)\right] = \mu\frac{\partial}{\partial x_j}\left(\frac{\partial v_i}{\partial x_j} + \frac{\partial v_j}{\partial x_i}\right) = \mu\frac{\partial^2 v_i}{\partial x_j\,\partial x_j} \tag{2.9}$$

because the second term in Eq. (2.9) is zero due to the continuity equation, Eq. (2.7), i.e.

$$\mu\frac{\partial}{\partial x_j}\left(\frac{\partial v_j}{\partial x_i}\right) = \mu\frac{\partial}{\partial x_i}\left(\frac{\partial v_j}{\partial x_j}\right) = 0 \tag{2.10}$$

The Navier-Stokes equation, Eq. (2.6) can then with constant viscosity μ and for incompressible flow be written:

$$\rho \frac{dv_i}{dt} = -\frac{\partial P}{\partial x_i} + \mu\frac{\partial^2 v_i}{\partial x_j\,\partial x_j} + \rho f_i \tag{2.11}$$

and the viscous stress tensor:

$$\tau_{ij} = 2\,\mu\,S_{ij} = \mu\left(\frac{\partial v_i}{\partial x_j} + \frac{\partial v_j}{\partial x_i}\right) \tag{2.12}$$

2.2 Turbulence

Most flow in nature are turbulent, which in contrast to laminar, smooth, and parallel flow, are characterized by highly irregular and chaotic eddies. The wake behind bluff bodies such as cars, buildings and sails, trimmed for downwind sailing, with huge separation of the flow, are dominated by these 3D irregular and chaotic eddies of different velocity and length scales. Turbulent flows are despite of this governed by Navier-Stokes equation Eq. (2.6) [8]. Beyond being irregular, chaotic, and 3D to its structure, turbulent flow increases the diffusivity and is dissipative. Meaning respectively, that turbulent flow increases the exchange of momentum and that the kinetic energy of the smallest eddies is transformed into thermal energy [8]. Even though it is possible to solve the Navier-Stokes equation directly, it can be quite costly and it requires a grid with a very fine spatial resolution to capture the smallest turbulent scales, i.e. the so-called *Kolmogorov micro scales* and a fine temporal resolution, since turbulent flow is unsteady [8]. For many engineering purposes, it is however usually of interest to calculating the mean flow quantities rather than the

instantaneous values, and by averaging the Navier-Stokes equation one receive the so-called Reynolds Averaged Navier-Stokes (RANS) equation. By using RANS simulations, it is possible to keep the numerical cost at a reasonable level.

2.2.1 Turbulent Mean Flow

Time Averaged Navier-Stokes

If one studies the time history of a particle in motion one can decompose its instantaneous value of for example the velocity v_i in one time-averaged part $\bar{v}_i$ and one fluctuating part v_i', i.e:

$$v_i = \bar{v}_i + v_i' \tag{2.13}$$

where the time averaged value is defined as:

$$\bar{v} = \frac{1}{2\,T} \int_{-T}^{T} v dt \tag{2.14}$$

When time averaging Eq. (2.13), it is averaged into a steady state condition and we get:

$$\bar{v}_i = \overline{\bar{v}_i + v_i'} = \overline{\bar{v}_i} + \overline{v_i'} = \bar{v}_i + \overline{v_i'} = \bar{v}_i \tag{2.15}$$

because:

$$\overline{\bar{v}_i} = \bar{v}_i \quad \& \quad \overline{v_i'} = 0 \tag{2.16}$$

The continuity equation and Navier-Stokes equation for incompressible flow were presented in Eq. (2.7) & Eq. (2.11), respectively and with the left hand side of Eq. (2.11) expressed with partial derivatives and with the gravitational term $\rho f_i = \rho(0, 0, -g)$ omitted, which means that the pressure, p represent the hydrodynamic pressure, we have:

$$\rho \frac{\partial v_i}{\partial t} + \rho \frac{\partial v_i\, v_j}{\partial x_j} = -\frac{\partial p}{\partial x_i} + \mu \frac{\partial^2 v_i}{\partial x_i\, \partial x_i} \tag{2.17}$$

Inserting Eq. (2.13) in the continuity equation Eq. (2.7) we get:

$$\frac{\partial \overline{\bar{v}_i + v_i'}}{\partial x_i} = \frac{\partial \overline{\bar{v}_i}}{\partial x_i} + \frac{\partial \overline{v_i'}}{\partial x_i} = \frac{\partial \overline{\bar{v}_i}}{\partial x_i} + 0 = \frac{\partial \bar{v}_i}{\partial x_i} \tag{2.18}$$

since $\partial \overline{\bar{v}_i} = \partial \bar{v}_i$ and $\partial \overline{v_i'} = 0$.

Performing the decomposition of the pressure, which was done with the velocity in Eq. (2.13) and using these in Navier-Stokes equation for incompressible flow Eq. (2.17), we get:

$$\underbrace{\rho \frac{\partial(\overline{\bar{v}_i + v_i'})}{\partial t}}_{1} + \underbrace{\rho \frac{\partial(\overline{\bar{v}_i + v_i')\,(\bar{v}_j + v_j')})}{\partial x_j}}_{2} = \underbrace{- \frac{\partial(\overline{\bar{p}_i + p_i'})}{\partial x_i}}_{3} + \underbrace{\mu \frac{\partial^2(\overline{\bar{v}_i + v_i'})}{\partial x_j\, \partial x_j}}_{4} \tag{2.19}$$

Analyzing each of the four terms of the time averaged Navier-Stokes equation in Eq. (2.19), starting with the first term:

Term 1:

$$\frac{\partial(\overline{\bar{v}_i + v_i'})}{\partial t} = \frac{\partial \overline{\bar{v}_i}}{\partial t} + \frac{\partial \overline{v_i'}}{\partial t} = \frac{\partial \overline{\bar{v}_i}}{\partial t} + 0 = \frac{\partial \bar{v}_i}{\partial t}$$

With the assumption that the mean flow v_i is steady, this term becomes zero.
The second term reads:

Term 2:

$$\begin{aligned}
\frac{\partial(\overline{\bar{v}_i + v_i')\,(\bar{v}_j + v_j')})}{\partial x_j} &= \frac{\partial \overline{\bar{v}_i\,\bar{v}_j + \bar{v}_i\,v_j' + v_i'\,\bar{v}_j + v_i'\,v_j'}}{\partial x_j} \\
&= \frac{\partial \overline{\bar{v}_i\,\bar{v}_j}}{\partial x_j} + \frac{\partial \overline{\bar{v}_i\,v_j'}}{\partial x_j} + \frac{\partial \overline{v_i'\,\bar{v}_j}}{\partial x_j} + \frac{\partial \overline{v_i'\,v_j'}}{\partial x_j} \\
&= \frac{\partial \bar{v}_i\,\bar{v}_j}{\partial x_j} + \frac{\partial \overline{v_i'\,v_j'}}{\partial x_j}
\end{aligned}$$

because: $\overline{\bar{v}_i\,v_j'} = \bar{v}_i\,\overline{v_j'} = 0 \quad \& \quad \overline{v_j'\,\bar{v}_i} = \overline{v_j'}\,\bar{v}_i = 0.$

Term 3:

$$- \frac{\partial(\overline{\bar{p}_i + p_i'})}{\partial x_i} = \frac{\partial \overline{\bar{p}_i}}{\partial x_i} + \frac{\partial \overline{p_i'}}{\partial x_i} = \frac{\partial \bar{p}_i}{\partial x_i}$$

Term 4:

$$\frac{\partial^2(\overline{\bar{v}_i + v_i'})}{\partial x_j\, \partial x_j} = \frac{\partial^2 \overline{\bar{v}_i}}{\partial x_j\, \partial x_j} + \frac{\partial^2(\overline{v_i'})}{\partial x_j\, \partial x_j} = \frac{\partial^2 \bar{v}_i}{\partial x_j\, \partial x_j}$$

Summing up the analyzed terms, the *time averaged* continuity equation and Navier-Stokes equation for steady flow reads respectively:

$$\frac{\partial \bar{v}_i}{\partial x_i} = 0 \tag{2.20}$$

$$\rho \frac{\partial \bar{v}_i\,\bar{v}_j}{\partial x_j} = - \frac{\partial \bar{p}_i}{\partial x_i} + \frac{\partial}{\partial x_j}\left(\mu \frac{\partial \bar{v}_i}{\partial x_j} - \rho \overline{v_i'\,v_j'}\right) \tag{2.21}$$

The time averaged Navier-Stokes equation is, as aforementioned, called the *Reynolds Averaged Navier-Stokes (RANS)* equation, which control the transport of the mean flow quantities. The last term in Eq. (2.19) $\rho\overline{v_i' v_j'}$ is called the *Reynolds Stress Tensor*, which is symmetric and represents turbulence. Due to the symmetry, Reynolds stress tensor $\rho\overline{v_i' v_j'}$ has only six unknowns of the nine terms in Eq. (2.22):

$$\rho\overline{v_i' v_j'} = \rho \begin{pmatrix} \overline{v_{1,1}'} & \overline{v_{1,2}'} & \overline{v_{1,3}'} \\ \overline{v_{2,1}'} & \overline{v_{2,2}'} & \overline{v_{2,3}'} \\ \overline{v_{3,1}'} & \overline{v_{3,2}'} & \overline{v_{3,3}'} \end{pmatrix} \tag{2.22}$$

since $\overline{v_{2,1}'} = \overline{v_{1,2}'}$, $\overline{v_{3,1}'} = \overline{v_{1,3}'}$ and $\overline{v_{3,2}'} = \overline{v_{2,3}'}$. These six unknowns, together with the four other unknowns from the three velocity components and the pressure, i.e, $\bar{v}_i$ and $\bar{p}$, gives in total 10 unknowns. In order to close the equation system and be able to calculate the time averaged continuity equation and the three momentum equations in Eq. (2.20) & Eq. (2.21), respectively, it is necessary to find some equations for the turbulent stresses. This circumstance has come to be known as the *closure problem*. There are basically two ways to approach the closure problem. One is to solve for $\overline{v_i' v_j'}$, i.e. as exact as Navier-Stokes equation can be solved, which can be done with *Reynolds Stress Transport (RST) Models*; the other is to use an approximated approach, with eddy-viscosity models, which are based on the *Boussinesq assumption*. The two-equation models $k-\varepsilon$ and $k-\omega$ and the one-equation model *Spalart-Allmaras (S-A)* are examples of popular eddy-viscosity models.

If the dynamic viscosity, μ is constant, we saw in Eq. (2.9) that it can be lifted out from the derivative and if the temperature, θ is included; the density of mass, ρ is represented as a constant reference density, ρ_0; the time averaged Navier-Stokes equation, Eq. (2.21) can be written:

$$\frac{\partial \rho_0 \bar{v}_i}{\partial t} + \frac{\partial}{\partial x_j}\left(\rho_0 \bar{v}_i \bar{v}_j\right) = -\frac{\partial \bar{p}}{\partial x_i} + \mu \frac{\partial^2 \bar{v}_i}{\partial x_j \partial x_j} - \frac{\partial \tau_{ij}}{\partial x_j} - \beta \rho_0 \left(\bar{\theta} - \theta_0\right) g_i \tag{2.23}$$

where the volume force is expressed as $\beta\rho_0(\bar{\theta}-\theta_0)g_i$; β is the volumetric thermal expansion, a physical property; Reynolds stress tensor are expressed as:

$$\tau_{ij} = \rho_0 \overline{v_i' v_j'} \tag{2.24}$$

The interested reader can read about the exact $\overline{v_i' v_j'}$ equation, the k equation, the ε equation, the *Boussinesq Assumption* and the $k-\varepsilon$ model in Appendix.

2.3 Discretization

Simcenter STAR-CCM+ is a commercial Computational Fluid Dynamics (CFD) code that solves the conservation equations for mass, momentum, and energy, for both incompressible and compressible fluids flows. When observing, and simulating, fluid flow, the *Eulerian* approach is more or less always used, except when simulating the motion of certain particles, within a fluid. Then the *Lagrangian* approach is useful [8]. With the Eulerian approach, one observes the fluid particle as it flows through a certain volume in space; with the Lagrangian approach, one instead keeps track of the original position of the fluid particle and then follows its path through space and time. STAR-CCM+ offers both these approaches in its code.

For the discretization of the governing equations in space and time, where the system of partial differential equations are transformed into a set of linear algebraic equations, which then are solved numerically with an algebraic multigrid-solver, Simcenter STAR-CCM+ offers two methods, which are the *Finite Volume Method (FVM)* and *Finite Element Method (FEM)*. In this project, the FVM was used. When discretizing with the FVM the control volume, which is a certain volume of space where the simulation is taking place, is subdivided into a finite number of smaller control volumes, so-called *cells* or *element*; the unknown quantities are stored at the center of each cell/element of the generated mesh/grid. Then, either an integral or *weak form* of the differential equations are used for the spatial discretization. When simulating unsteady flow cases, a specified amount of time, that is assigned for the flow case to be observed, is subdivided into so-called time-steps; discretizing in time generally results in a coupled system of algebraic equations, that are solved at each time-step.

When the RANS equations, presented in Eq. (2.20) & Eq. (2.19), are discretized with the FVM, they are rewritten in a general transport equation:

$$\frac{\partial \phi}{\partial t} + \frac{\partial}{\partial x_i}\left(u_i\,\phi\right) = \frac{\partial}{\partial x_i}\left(\Gamma\,\frac{\partial \phi}{\partial x_i}\right) + S \tag{2.25}$$

where ϕ represent a scalar property that is transported, Γ is a diffusion coefficient and S is a source term. Integrating Eq. (2.25) over a control volume V and applying *Gauss's divergence theorem*, the following integral form of Eq. (2.25) is received:

$$\underbrace{\frac{d}{dt}\int_V \rho\,\phi\,dV}_{Transient\ Term} + \underbrace{\int_A \rho\,\mathbf{v}\phi\cdot d\mathbf{a}}_{Convective\ Flux} = \underbrace{\int_A \Gamma\,\nabla\,\phi\,d\mathbf{a}}_{Diffusive\ Flux} + \underbrace{\int_V S_\phi\,dV}_{Source\ Term} \tag{2.26}$$

where A is the surface area of the control volume and $d\mathbf{a}$ represent the surface vector.

- The transient term represent the time rate of change of the scalar fluid property ϕ
- The convective flux expresses the net rate of decrease of the scalar fluid property ϕ across the control volume boundaries, due to convection
- The diffusive flux represent the net rate of increase of the scalar fluid property ϕ across the control volume boundaries, due to diffusion

- The source term expresses the generation/destruction of the scalar fluid property ϕ inside the control volume

2.3.1 Meshing

When the computational domain is discretized, it is, as previously mentioned, subdivided into smaller cells/elements, which can be arranged either in a *structured* way or in an *unstructured* way. The meshing tool in Simcenter STAR-CCM+ can create both mesh-types and also support the import of meshes, created with other meshing tools.

2.3.2 Boundary Conditions

Imagine that the case to be observed, that takes place within this certain volume of space, is external airflow around a single sail for downwind sailing, which is the actual case in this project. In reality, this volume of space does not have any lateral boundaries that restrict the airflow in any way, beyond the natural boundary of the water surface. However, in the computational world, when simulating a real event and not use a *panel method*, one has to define lateral boundaries that enclose a certain volume of space; since the lateral boundaries only exist in the simulation, one has to define certain rules of how the airflow is affected at the boundaries. These rules are called *boundary conditions* and there exist different boundary conditions for the different types of lateral boundaries, that encloses the computational domain. For external flow cases, the computational domain often has the shape of a 3D rectangle, with six sides and for internal flows in tube-shaped geometries, such as pipelines or veins, the computational domain is naturally enclosed by the inner wall of the tube-shaped geometry. Regardless of whether the flow is external or internal, common boundary types are *inlet, outlet, symmetry-plane* & *wall*. The inlet is a boundary where the fluid is defined to enter the computational domain and the outlet is a boundary where the fluid is defined to exit the computational domain. The symmetry-plane is very useful if the geometry of the model is symmetric because then only half of the model is required and the computational costs can be heavily reduced. If the geometry of the model is symmetric and the computational domain has the shape of a 3D rectangle with one inlet and one outlet, the boundary type *wall* is then generally used for the remaining three sides of the computational domain, i.e. the top, bottom and one of the vertical sides, positioned opposite of the symmetry-plane. If the geometry of the model, on the other hand, not is symmetric, the whole model is required and the boundary type, the wall is instead commonly used for the remaining four sides, of the computational domain, beyond the inlet and the outlet. It should also be mentioned that the inlet and the outlet are the only boundaries that are defined as permeable and therefore allows fluid flow across their boundaries. The symmetry-plane and the wall are thus defined to be impermeable and restrict fluid flows across their boundaries. The boundary conditions on the different boundaries are described below.

Inlet

In Simcenter STAR-CCM+, different types of boundary conditions for the inlet are available, i.e. *Stagnation Inlet*, *velocity inlet* and *Mass Flow Inlet*. The velocity and other fluid properties, at the inlet boundary, are defined in the settings.

Outlet

For the outlet, Simcenter STAR-CCM+ has two main boundary conditions, i.e. *Outlet* and *Pressure outlet*. As with the inlet, the pressure at the outlet is defined in the settings.

Wall

The boundary condition for a wall can either be *no-slip* or *slip* and which condition that is chosen, depends upon whether it is desired to account for viscous effects on the lateral boundaries that exist in reality, or not. With the *no-slip* condition, the fluid velocity next to the wall has the same velocity as the wall itself and for non-moving domains, the velocity at the wall is therefore zero. When a fluid flow is surrounded by one or several boundaries such as inside a pipeline or a 3D rectangular-shaped test section of a wind tunnel, viscous effects generate the growth of a *boundary layer* on each of the surrounding walls, which successively reduces the cross-sectional area of the *free stream flow*. In the case of external flows when no boundaries exist in reality, the appropriate boundary condition on the lateral boundaries is the *slip* condition, because, with this condition, the shear stresses at the walls are zero; hence, no growth of any boundary layers occur at the walls.
For turbulent flow, Simcenter STAR-CCM+ has different approaches to calculate the shear stresses near the wall; the different turbulence models in STAR-CCM+ use different approaches, which are: *Algebraic Wall Functions, Two-Layer Models* and *Low Reynolds Number Models*.

Courant Number

The *Courant number*, named after the mathematician Richard Courant, is a non-dimensional number that can be used when calculating the required time-step when performing transient simulations, such as detached-eddy simulations (DES). The Courant number is linked to the Courant–Friedrichs–Lewy (CFL) stability condition of numerical schemes [12] and is defined as:

$$C = \frac{U\,\Delta t}{\Delta h} \tag{2.27}$$

where U is the flow velocity, Δt represent the time step and Δh represent the characteristic cell-size.

2.4 Aerodynamics

2.4.1 The Airflow Around a Sail

Traditional sails, made of a relatively soft Dacron cloth have a sectional profile of an asymmetric airfoil, with almost zero thickness, which is illustrated in Fig. 2.1. The relative softness in this type of sails makes them highly ductile and with a set of trim controls, the sail and the mast can be trimmed, so that the sail always has the optimal sail shape.

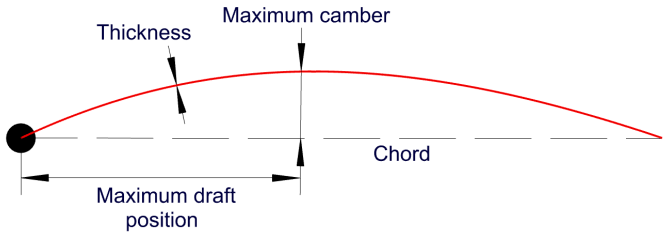

Figure 2.1: Top view of a 2D sail profile, where the theoretically zero sail thickness is shown as well as the *chord*, which is the imaginary straight line from the luff to the leech. The maximum *camber* and its position along the chord are also illustrated.

In Fig. 2.2 we see a top view image of the ILCA 7 dinghy and its single sail, in an airflow, represented by *streamlines*, which per definition are curves where the velocity vector is tangential in every point along the curve [36]. When the airflow approaches the sail, the streamlines are forced to deviate from their initial flow path and an outward normal force component arises in each point on the surface of the sail as well as a tangential friction force component. The air particles that deviate and flow around the sail on the leeward side of the sail will accelerate, which creates a low-pressure zone on the leeward side that therefore also is called the *suction side*. On the windward side of the sail, a high-pressure zone is instead created and this side is called the *pressure side*. The size of the pressure difference that is created between the windward side of the sail and the leeward side of the sail thus depends upon how much the sail forces the streamlines to deviate.

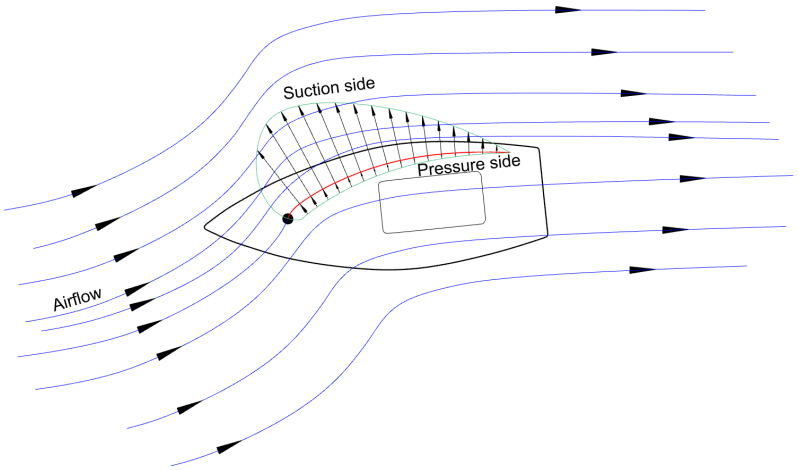

Figure 2.2: Laminar airflow around the ILCA 7 dinghy sail, showing the pressure side and the suction side. The closer streamlines, the higher the velocity magnitude, and vice versa.

The total aerodynamic force on a surface, which can be decomposed into a pressure force, normal to the surface and a tangential friction force, are often represented by a resultant. This is illustrated in Fig. 2.3 which shows the ILCA 7 dinghy in a 2D top view, beating upwind. Here the total aerodynamic force is decomposed into a drag force *Drag*, that is aligned with the *apparent wind*, and a lift force *Lift*, which is orthogonal to the drag force. The theoretical point at which the total aerodynamic force "works" is called the *Center of Effort (CoE)*.

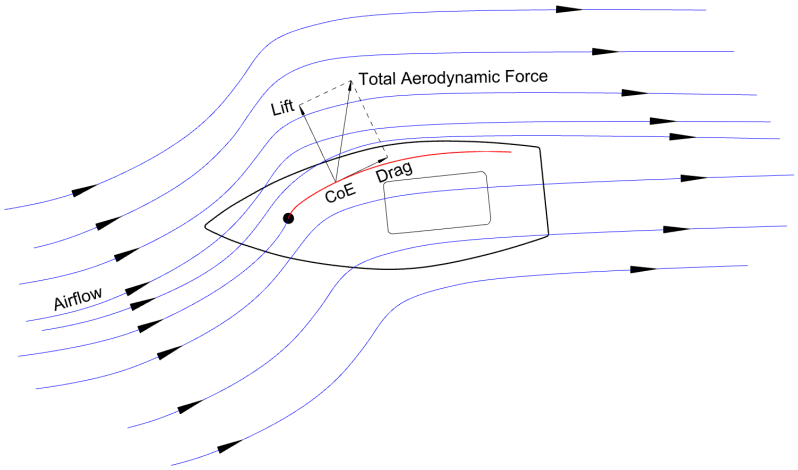

Figure 2.3: The normal pressure force and the tangential friction force, in every point on the 2D sail profile, have been replaced by a resultant force, i.e. the total aerodynamic force, which here is decomposed into a lift force and a drag force. The Center of Effort (CoE), where the resultant total aerodynamic force "works" is also illustrated.

The normal force on the sails is caused by the static pressure. There is also a dynamic pressure in the flow, defined as:

$$P_{dyn} = \frac{1}{2}\rho V^2 \tag{2.28}$$

The streamline that divides the flow at the mast is called the *stagnation streamline* and the point on the mast where the velocity decreases to zero and the pressure reaches its highest value is called the *stagnation point*. At this point the pressure is often referred to as the *stagnation pressure* or the *total pressure*. According to Bernoulli´s theorem the total pressure is the sum of the static pressure and the dynamic pressure and is defined as:

$$P_{tot} = P_{stat} + \frac{1}{2}\rho V^2 \tag{2.29}$$

In a simplified perspective in 2D of the mainsail, only two stagnation points exist, and the first appears where the stagnation streamline ends at the mast and the second appears on the sail further aft towards the leech, where the airflow separates from the sail. How the total pressure is calculated with wind tunnel equipment, is explained in the next section where the wind tunnel facility, used in this project, is presented.
In Fig. 2.2 & Fig. 2.3 we saw a 2D profile of a single mainsail and the forces, that arose when the sail was subjected to airflow. The sail was depicted as if it was trimmed for

upwind sailing and in Fig. 2.4 we see the ILCA 7 dinghy in a 2D top view, now sailing downwind. Again we have the total aerodynamic force and its decomposed components, but instead of the drag force we now have the drive force, which is defined as the force in direction of motion and for the lift force we now see the side force which, in this coordinate system, is orthogonal to the drive force. The image illustrates how the airflow separates at the luff and the leach and how a huge wake, behind the sail, with a highly turbulent flow, is created.

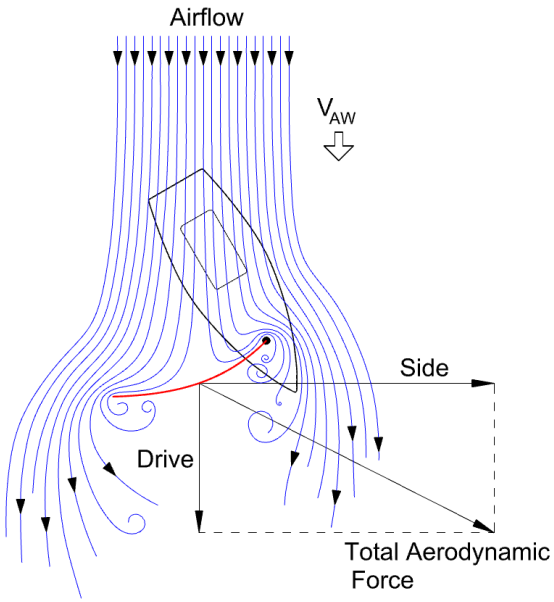

Figure 2.4: The image shows a 2D case of the ILCA 7 dinghy sailing downwind. The apparent wind speed, the total aerodynamic force and its components, i.e. the drive force, which is aligned with the apparent wind, and the side force are illustrated.

Fig. 2.4 above illustrates a 2D case with the force components in a top view, showing the ILCA 7 dinghy sailing downwind. In reality the case is tree dimensional and a lift force, normal to the horizontal plane, is present as well. Eq. (2.30) shows how the three forces coefficients C_{F_i} are defined, where the subscript $i = 1, 2, 3$, for the forces F_i, stand for the *drag/drive* force, *side* force and $lift$ force, respectively. Eq. (2.31) shows the definition of the corresponding three coefficients for the moments C_{M_i} around the y, x, z principal axes, where the subscript $i = 1, 2, 3$, stand for *pitch*, *roll* and *yaw*, respectively.

$$C_{F_i} = \frac{2\,F_i}{\rho\,V_{AW}^2\,A_{sail}} \tag{2.30}$$

$$C_{M_i} = \frac{2\,M_i}{\rho\,V_{AW}^2\,A_{sail}\,L_c} \tag{2.31}$$

where the coefficient C is a dimensionless quantity that varies with the shape of the object. ρ is the air density, V_{AW} is the apparent wind speed, A_{sail} is the sail area, and L_c, is the *characteristic length* that depends upon the distance from the center of effort (CE) to each principal axis.

2.4.2 The Velocity Triangle & Velocity Made Good (VMG)

With a known true wind angle β_{TW}, a known true wind speed V_{TW} and an assumption of the boat-to-true-wind-speed-ratio of $V_S \,/\, V_{TW}$, the *apparent wind speed* V_{AW} can be calculated from the so-called *velocity triangle*, which is illustrated in Fig. 2.5 below:

$$V_{AW} \;=\; \left(V_{TW}^2 \;+\; V_S^2 \;+\; 2\,V_{TW}\,V_S \cos\left(\beta_{TW}\right)\right)^{1/2} \tag{2.32}$$

Eq. (2.32) is the *Law of cosines* but with $\cos\left(180° - \beta_{TW}\right) \;=\; -\cos\left(\beta_{TW}\right)$, thereof the plus-sign in front of the third term in Eq. (2.32). Further, with the apparent wind speed calculated, the apparent wind angle β_{AW} can be calculated as:

$$\beta_{AW} \;=\; \sin^{-1}\left(\frac{V_{TW}}{V_{AW}}\,\sin\left(\beta_{TW}\right)\right) \tag{2.33}$$

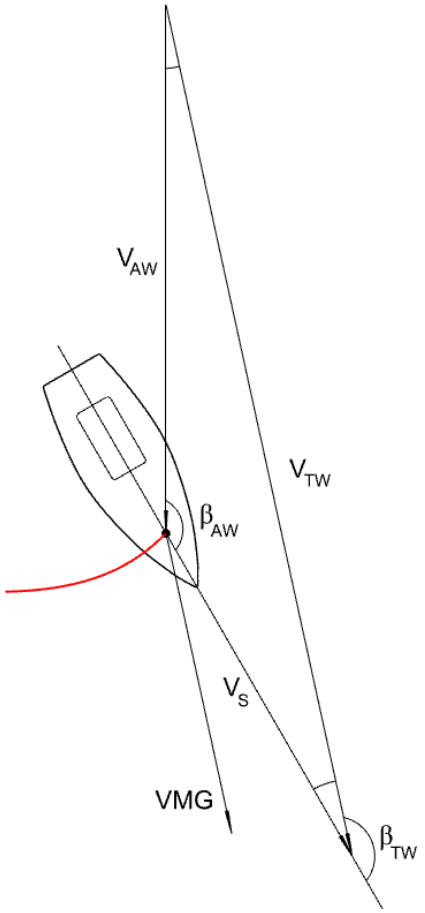

Figure 2.5: The velocity triangle for the ILCA 7 dinghy, sailing downwind. Note that it is assumed that no leeway exists. The Velocity Made Good (VMG), which is the component of the boat speed V_S that is aligned with the direction of the true wind, is also illustrated.

The *Velocity Made Good (VMG)* is the component of the boat speed V_S that is aligned with the direction of the true wind TW, which in Fig. 2.5 is illustrated with the true wind speed V_{TW}.

2.5 Chalmers Low Turbulence Subsonic Wind Tunnel

In this project, Chalmers large-scale low turbulence subsonic wind tunnel was used. It was built in 1964 and is situated at *Chalmers Laboratory of Fluids and Thermal Sciences*, at the head campus of Chalmers University of Technology, in Gothenburg Sweden. The wind tunnel is a classic semi-closed loop tunnel that operates at atmospheric pressure and can be seen in Fig. 2.6 & Fig.2.9. It is Chalmers most versatile wind tunnel and can be used for many different types of experiments. It can for instance be equipped with an external balance for force measurements on bodies or used for detailed flow field studies using hot-wire anemometry, optical measurement techniques, and advanced pressure measurements [6].

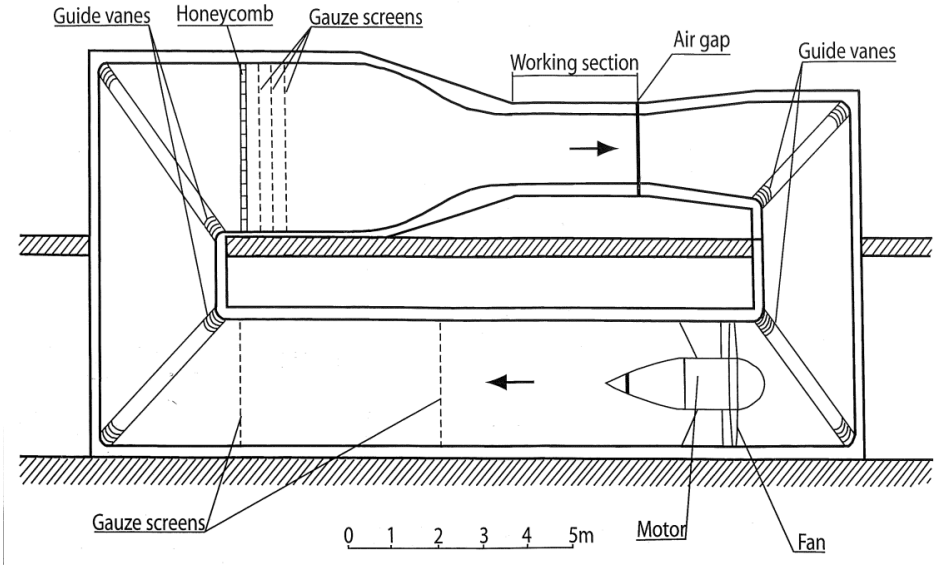

Figure 2.6: Profile view of Chalmers subsonic semi-closed loop tunnel.

Data for Chalmers subsonic wind tunnel are presented in Table 2.1 and Table 2.2.

Table 2.1: Geometrical data for Chalmers subsonic wind tunnel L2.

Geometrical data	
General	
Contraction ratio of the nozzle [-]	5.68 : 1
Center line circumference [m]	37.1
Total length of WT plane [m]	16.6
Test section	
Length [m]	3.0
Width [m]	1.8
Height [m]	1.25
Area (at the inlet) [m^2]	2.07
Fillet (at the inlet) [m]	0.2

Table 2.2: Data of the airflow generation & control of Chalmers low-turbulence subsonic wind tunnel L2.

Airflow generation & control	
General	
Power (total) [kW]	220
Maximum velocity [m/s]	60
Main fan	
No. Blades	6
Diameter [m]	2.0
No. Revolutions [rpm]	0 - 1000
Power [kW]	170
Cooling air fan	
Power [kW]	80

2.5.1 Airflow in the Wind Tunnel

The wind tunnel is equipped with an air-cooled electric motor that drives the 6-bladed fan, which creates the circulating airflow. Downstream the motor, stators are used as motor support and for cooling the main motor by ventilating the hot air through channels in the stators. Fresh air is injected by the cooling air fan and the inlet temperature is regulated by an inter-cooler before injected into the mainstream [17].

The Acceleration of the Airflow in the Wind Tunnel

In a closed-circuit wind tunnel, such as Chalmers wind tunnel, the air is kept in motion with the 6-bladed fan and as the airflow circulates, it accelerates when it enters the *nozzle*, which is positioned just before the inlet of the test section and the airflow decelerates as it leaves the test section and enters the *diffuser*. The reason for the acceleration is the design of the nozzle, that contracts the airflow. The nozzle is therefore also commonly called the *contraction cone*; the deceleration occurs because the diffuser is designed so that the air is allowed to expand, which can be seen in Fig. 2.6. This acceleration and deceleration thus always occur, even though no model is mounted in the test section, but when a sail or any other object is mounted, the airflow has to flow around the test object; the airflow has to accelerate a second time. How much the airflow accelerates the second time in the test section depends on the size of the object, whether or not the object is symmetrical and how streamlined it is in shape.

The physical explanation of the acceleration of the airflow can be understood if Fig. 2.7 is studied, which shows the *settling chamber, the nozzle and the test-section* in a top view. The *law of continuity* explains that the airflow has to accelerate in the nozzle.
Bernoulli's theorem, defined in Eq. (2.29), and the law of continuity can be applied to analyze the airflow passing through the nozzle in a wind tunnel (see Fig. 2.7). If for instance the velocity field in the nozzle is known, Bernoulli's theorem can be used to find the pressure field:

$$P_1 + \frac{1}{2}\rho V_1^2 = P_2 + \frac{1}{2}\rho V_2^2 \equiv P_{tot} \tag{2.34}$$

where the subscript 1 and 2 respectively represent the local condition at cross-section 1 and 2, in Fig. 2.7.

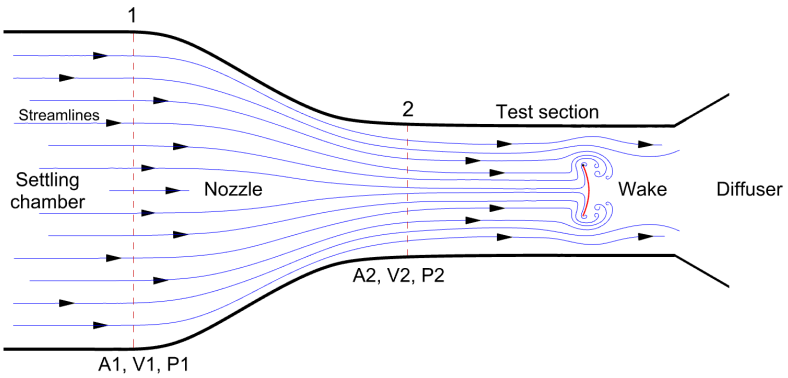

Figure 2.7: The acceleration of the airflow in the nozzle, in Chalmers low turbulence subsonic wind tunnel.

The law of continuity applied over the nozzle in Fig. 2.7 is written:

$$A_1 V_1 = A_2 V_2 \tag{2.35}$$

Where A_1 and V_1 represent the cross-sectional area and velocity, respectively, at cross-section 1; A_2 and V_2 thus represent the cross-sectional area and the velocity at cross-section 2. It can be seen that the cross-sectional area at cross-section 1 is much larger than the cross-sectional area at cross-section 2. Law of continuity in Eq. (2.35) say that the velocity at cross-section 2, therefore, must be higher than the velocity at cross-section 1, which means that the airflow must accelerate in the nozzle. This is indicated by the smaller distance between the streamlines.

Flow Quality in the Test Section

To receive accurate test results in a wind tunnel experiment, it is very important that the flow quality in the test section is good, which is synonymous with low turbulence and mean velocity vectors that are equal in magnitude and parallel to the lateral boundaries in all positions in the test section. In Fig. 2.6 it can be seen that each corner of the tunnel is equipped with guide vanes, which are section-shaped foils to guide the circulating airflow so that a uniform flow in the test section can be attained. The last time the flow quality in the test section was investigated was 1997 and is described in detail in [16]. Further, keeping a stable temperature in the test section is also very important for the flow quality. The turbulence intensity in the test section was investigated in 2015 by *Applied Mechanics Internal Resources* and was measured to be approximately 0.125 %. The measurement was carried out with a centrally positioned probe that successively was moved from the inlet of the test section 1.5 m downstream, to the middle of the test section. The results from the turbulence measurements can be seen in Fig. A.1, in Appendix. Since test objects often are positioned approximately in the middle of the test section, which is 1.5 m downstream of the inlet in Chalmers subsonic wind tunnel it is sufficient to only measure the turbulence intensity in the first half of the test section.

Since sailing boats operate in the boundary layer of the earth, which is highly turbulent

most of the time, it can be of interest to induce turbulent flow in the test section, so that the flow around the model becomes more realistic. For this purpose, grids, with vertical and horizontal bars of various sizes, shapes, and materials are designed to generate a certain desired level of turbulence in the test section, are commonly used. The material of the grid, used for all tests in this project, was aluminum and the size of each bar, i.e. the width times the height, times the depth; the distance between them are $W \times H \times D = 15 \times 15 \times 15\ mm$ and 65 mm, respectively. A close-up image of one cell the grid can be seen in Fig. 2.8 below. Further, this grid should produce a turbulence intensity of 2 % according to Valery Chernoray, Director of Chalmers Laboratory of Fluid and Thermal Science. In Fig. 2.9, taken downstream the model sail in the test section, the grid can be seen in the background.

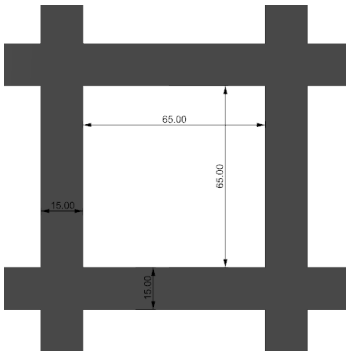

Figure 2.8: A close-up image of one cell in the grid used for generating turbulent flow in the test section.

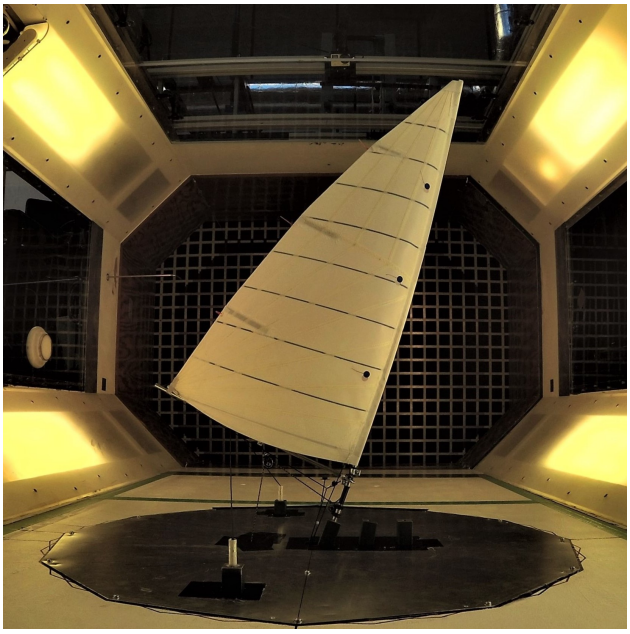

Figure 2.9: Picture of the octagonal test-section, where the grid can be seen behind the sail model, which in the picture is tested for a heel angle of 20°, a sheet angle of 90° and with the light trim with the kicker.

In Fig. 2.9 the full size grid, which is mounted after the *settling chamber* and before the *nozzle*, can be seen. The picture, which is taken downstream of the model, shows the cross-section of the test section. The purpose of the fillets, which is mounted at a 45° and give the rectangular test section an octagonal shape, is to avoid stagnating flow in the corners. Behind the corner fillets, several lights are mounted allowing the model to be

properly illuminated. Further, to compensate for the gradual growth of the boundary-layer along the test section walls in the stream-wise direction, the octagonal cross-sectional area increases as the corner fillets successively decrease. Further downstream, 200 mm before the end of the test section and before the diffuser, there is a 20 mm pressure recovery slot in the wind tunnel, which equalizes the pressure and decreases the pressure gradient between the test section and the surroundings. Furthermore, the pressure recovery slot creates a boundary layer suction, preventing separation in the diffuser [16].

Chalmers wind tunnel is, as previously mentioned, a classic semi-closed and versatile loop tunnel which means that it unfortunately therefore not is optimal for sail analysis. Wind tunnels specialized for sail analysis and sail optimization, usually have an open test section to avoid *blockage effects* and are equipped with large vertical turning vanes, which can be seen in Fig. 2.10 that can be twisted to create a twisted flow. This makes it possible to simulate the effect of the vertical velocity gradient and to trim the sail more realistic with a suitable twist.

Figure 2.10: Picture of the Twisted Flow Wind Tunnel (TFWT), at the University of Auckland SW, in New Zeeland, which is an open circuit wind tunnel; equipped with vertical turning vanes that can be twisted and generate twisted flow. The picture is published with the approval of Professor Richard GJ Flay, at The University of Auckland, New Zeeland.

The Boundary Layer in the Test Section

As the airflow enters the test section a thin *boundary layer* is created along the lateral boundaries, where each surface boundary can be said to be a thin flat plate, which is illustrated in Fig. 2.11. Boundary layer theory is therefore applicable and the formulas for *flat-plate flow* in Eq. (2.36) for both laminar flow and turbulent flow can be used for the determination of the boundary thickness δ at the x-position where the test object is mounted in the test section. The border of the boundary layer is per definition each point in the flow where the local velocity reaches 99 % of the *free-stream velocity* [36].
The test object should preferably be outside the boundary layer and be tested in the *free-stream flow*; according to the wind tunnel personnel who had performed a flow-quality investigation, the height of the boundary layer (δ) along the test section floor was measured to be only a couple of centimeters high, which meant that the sail model was mounted above the boundary layer.

$$\frac{\delta}{x} \approx \begin{cases} \frac{5.0}{Re_x^{1/2}} & \text{laminar} \quad 10^3 < Re_x < 10^6 \\ \frac{0.16}{Re_x^{1/7}} & \text{turbulent} \quad 10^6 < Re_x \end{cases} \tag{2.36}$$

where the $Re_x = Ux/\nu$ is the *local Reynolds number* of the flow along with the plate (surface boundary). In Eq. (2.36) it can be seen that the laminar flow formula applies for a local Reynolds number between 10^3 - 10^6 and that the turbulent flow formula applies for local Reynolds number, higher than 10^6.

Table 2.3: Some calculated values from Eq. (2.36), from [36]

Re_x	10^4	10^5	10^6	10^7	10^8
$(\delta/x)_{lam}$	0.050	0.016	0.005	–	–
$(\delta/x)_{turb}$	–	–	0.022	0.016	0.011

The fields without a value in Table 2.3 have a local Reynolds number that is outside the range where the formulas in Eq. (2.36) are valid.

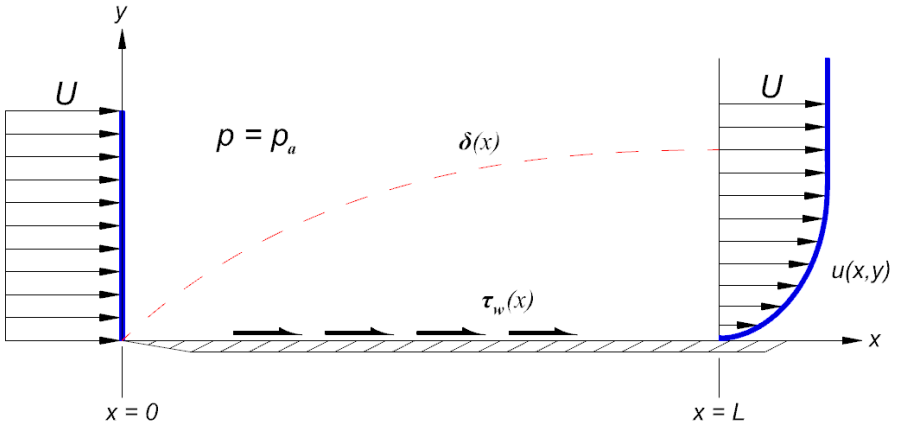

Figure 2.11: Growth of a boundary layer on a flat plate. The image is modeled from Fig. 7.3 in [36].

In Fig. 2.11 U represent the free-stream velocity and outside the boundary layer, where the dashed red curve marks the border, the pressure is the atmospheric pressure $p = p_a$. Further, the height of the boundary layer increases downstream and is thus a function of the position x, i.e. $\delta(x)$; $\tau_w(x)$ is the wall shear stress, which also is a function of x. A quote from [36] "A shear layer of unknown thickness grows along with the flat plate and the *no-slip* wall condition retards the flow, making it into a rounded profile $u(x, y)$, which merges with the free-stream velocity U, which is constant at a certain "thickness" $y = \delta(x)$", [36].

Blockage Effects

When a wind tunnel facility has a closed working section, the presence of the lateral boundaries, i.e. the walls and the ceiling, give rise to a flow phenomenon that is called *blockage effects*. There are several different types of these blockage effects, where a few of these are listed and presented further down in the text. The interested reader can read more about these effects in [4]. For this reason, working sections of modern wind tunnels used for sail design and sail analysis, are preferably designed without lateral boundaries to minimize these unwanted effects.
Test objects are usually positioned in the center, at a certain distance downstream the inlet of the test section; blocking effects can be explained by that the presence of the test object forces the airflow to deviate from its initial straight path when it approaches the test object. When the airflow then deviates from its original path, it also starts to accelerate and if the test section has lateral boundaries, these restrict the airflow to expand laterally and vertically, respectively, on the new deviated path around the test object. The airflow thus cannot expand freely which causes the airflow to accelerate even further and it reaches its maximum speed when it passes the test object [36]. If the test section on the other hand are open and do not have any lateral boundaries, the airflow is free to expand and the second acceleration of the airflow would be smaller and the contribution of blockage effects would therefore also be smaller. The consequence of the lateral boundaries is that the test object is subjected to airflow with higher velocity and since the forces on the test object depend upon the velocity squared, the measured data becomes higher than it would be if the test object were tested in a wind tunnel with a test section without lateral boundaries. The usual formulas for calculating the blockage effects postulates that the test object is streamlined, like an airplane wing and since the test object in this project more or less resembles a flat surface that is perpendicular to the airflow, these formulas could not be used. This is the reason why the numerical analysis was necessary to perform.

Different types of blockage effects exist, as mentioned, and a few of these that are presented below:

- **Horizontal Buoyancy**
  This effect occurs when there exists a variation of the static pressure along the test section when no model is present [4] and is nonzero in most wind tunnels. This effect can be dealt with by adding fillets to an rectangular cross-section, creating an octagonal cross-section and since Chalmers subsonic wind tunnel that was used in this project has these fillets, horizontal buoyancy was not one of the effects that had to be considered.

- **Solid Blockage**
  Optimally, the ratio of the cross-sectional area, i.e. the frontal area of a test object and the stream-wise cross-sectional area is zero, which is the case when a wind tunnel has no lateral boundaries, such as in an *open jet*. In those cases when a wind tunnel facility has lateral boundaries, solid blockage gives rise to larger surface stresses due to the acceleration of the airflow. However, it can be corrected by choosing the right scale of the test object. The ratio thus reflects the relative size of the test object and the test section; are usually somewhere between $1\,\% - 10\,\%$ [4].

- **Wake Blockage**
  Wake blockage occurs since the wake displaces the streamlines laterally, which means that the cross-sectional area available for the airflow becomes smaller. The airspeed, therefore, becomes higher behind the body, which means lower pressure and the presence of a horizontal buoyancy force.

2.5.2 Wind Tunnel Equipment

The Balance

In Fig. 2.3 we could see that the airflow generates forces and moments on the sail and these can be measured with an external 6-component strain-gauge wind tunnel balance that is mounted below the test section of Chalmers wind tunnel, which can be seen in Fig. 2.12.

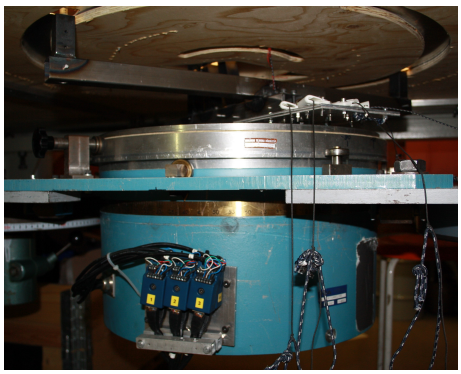

Figure 2.12: The picture shows the external 6-comp. strain-gauge wind tunnel balance, mounted under the test section, that was used in this project.

The wind tunnel balance has different load capacity for the *Drag force* D, the *Side force* S and the *Lift force* L, which can be seen in Table 2.4.

Table 2.4: Capacity of the load cells, mounted inside the wind tunnel balance.

Force component	**Drag**	**Side**	**Lift**
No. Load cells, a 30 kg	1	2	3
Total weight [kg]	30	60	90

Coordinate Systems

Fig. 2.13 illustrates the coordinate system in Chalmers wind tunnel, where the drag force D has positive sign in the opposite direction of the airflow and correspond to the $+X$ in Fig. 2.14 which illustrates the coordinate system for the 6-component wind tunnel balance. Fig. 2.14 thus show how the 3 forces, the *Drag force* $D, +X$, the *Side force* $S, +Y$ and the *Lift force* $S, +Z$; the 3 moments, the *pitch moment* $m, +M_y$, the *roll moment* $l, +M_x$ and the *yaw moment* $n, -M_z$ are measured. Note that the yaw moment n in Fig. 2.13 measure negative.

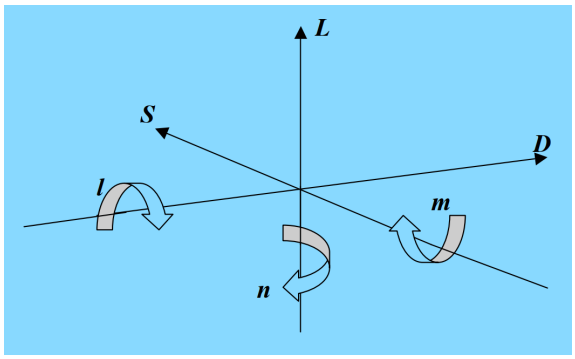

Figure 2.13: Illustration of the coordinate system in Chalmers wind tunnel, where the drag force D points in the opposite direction of the airflow.

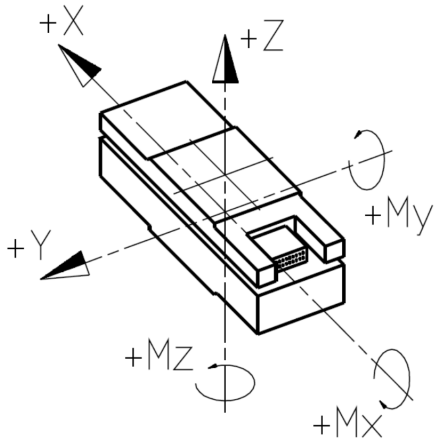

Figure 2.14: Illustration of the coordinate system of the 6-component wind tunnel balance, where $+X$ points in the opposite direction of the airflow

LabVIEW

The airflow in the wind tunnel is controlled by the standard laboratory software LabVIEW [37], which processes the input-data from the different measurement instruments, presented in the following text, that commonly are used in experimental tests.

Pitot-Static Tube

The Pitot-static tube Fig. 2.15 is an L-shaped standard pressure measurement instrument, positioned so that the *nose* is exactly at the inlet of the test section, at a height of 770 mm, from the wind tunnel floor and at a distance of 355 mm, from the wind tunnel wall. The Pitot-static tube is used for measurement of the total pressure P_{tot} and the static pressure P_{stat} in the test section, so that the airflow velocity in the test section can be calculated with the Precision Micro-Manometer [40].

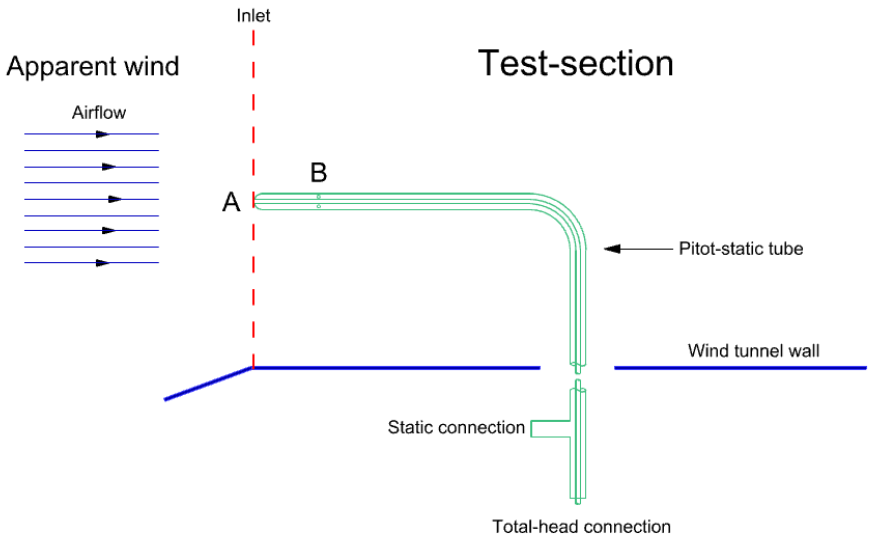

Figure 2.15: Top-view illustration of the round-nosed Pitot-static tube that was used for measurement of the total pressure P_{tot} and the static pressure P_{stat} in the test section.

The Precision Micro-Manometer

The precision Micro-Manometer (FCO510), which is positioned outside the wind tunnel, is connected to the Pitot-static tube through the *total-head connection* and the *static connection*, illustrated in Fig. 2.15; measures the total pressure at the opening at the nose (A); the static pressure at the 6 orifices, equally spaced around the tube and positioned 20 mm downstream the nose at (B).

Table 2.5: Front panels settings of the Precision Micro-Manometer FC0510.

Mode	Differential Pressure (D.P)
Range	200.00 AUTO
Average	Activated
State	Read

By subtracting the static pressure from the total pressure, the dynamic pressure is received, which can be seen in Eq. (2.37) & (2.38). From the dynamic pressure, LabVIEW then calculates the airflow velocity Eq. (2.38).

$$P_{dyn} = P_{tot} - P_{stat} \tag{2.37}$$

$$P_{dyn} = \frac{1}{2}\rho V^2 \quad \Longrightarrow \quad V = \sqrt{\frac{2\,P_{dyn}}{\rho}} \tag{2.38}$$

It can be seen in Fig. 2.15 above, which shows the Pitot-static tube in a top view, that the long part of the L-shaped Pitot-static tube is mounted orthogonal to the airflow direction, and that the short part is aligned with the airflow. Depending on the shape of the nose,

the Pitot-tube is more or less sensitive to the inclination of the short tube axis to the airflow direction. There exist many different shapes of the nose, which can be round, flat, chamfered, hemispherical, sharp filleted, etc. The Pitot-tube used in this project was, as previously mentioned, a round-nosed tube and this particular nose shall not be inclined more than approximately 9° to the airflow, to avoid errors in the measurement of the total pressure [4].

2.6 Scaling

Because of spatial restrictions of the test section in most wind tunnels it is often necessary to scale the prototype, so that the test object fits inside the test section;.

2.6.1 Dimensional Analysis & Similarity

Two other important reasons for scaling a prototype and perform tests on a model are usually *time* and *money*. This because performing experimental tests on a full-scale prototype usually requires a very large test facility that probably is more expensive to run and maintain than a smaller facility. A large prototype is usually also more difficult to handle, which makes it more time-consuming to perform tests on a full-scale prototype than on a small test model. Taken these aspects into account, performing wind tunnel tests with a large full-scale prototype easily becomes much more expensive.
Without going too deep into *dimensional analysis*, which the interested reader can read more about in [36], dimensional analysis is a very useful tool that provides certain rules, so-called *scaling law's* that has to be satisfied for similarity to exist between a model and a full-scale prototype. However, usually and unfortunately it is practically impossible to satisfy all requirements for complete similarity between a model and a prototype. In wind tunnel tests, for example, the dimensionless *Reynolds number* (Re), which is the only similitude parameter of interest in low-speed wind tunnel tests, when the *Mach number* (Ma) is below the *critical Mach number* (Ma_{crit}), hardly ever can be satisfied. The reason for that and the consequences it has will be described further down in the subsection *Scale effects*. Complete similarity can be decomposed into four different types of similarity which cover the dimensions *force*, or *mass*, *length*, *time* and *temperature*, or the so-called $FLT\Theta$-system, which it commonly is called. The four different kinds of similarity are:

- Geometric similarity
- Kinematic similarity
- Dynamic similarity
- Thermal similarity

Geometric, kinematic, and dynamic similarity are described more in-depth below, but the thermal similarity is not addressed any further in this project.

Geometric Similarity

A formal definition of geometric similarity from [36] is:

"A model and prototype are geometrically similar if and only if all body dimensions in all three coordinates have the same linear scale ratio."

In other words, geometric similarity between a model and a full-scale prototype only exist if all lengths of the prototype L_p are scaled with the same linear length scale factor α_L:

$$L_m = \alpha_L L_p \tag{2.39}$$

where the subscript m and p stand for model and prototype, respectively. Areas are therefore scaled with the linear length scale factor squared and volumes with the linear length scale factor cubed. The prototype sail thus has to be scaled as:

$$A_m = \alpha_L^2 A_p \tag{2.40}$$

Kinematic Similarity

The flow around the model and prototype are kinematically similar if and only if the velocity at all points in the flow, in all three directions have the same scale ratio. The *velocity scale factor* α_V is defined as:

$$V_m = \alpha_V V_p \tag{2.41}$$

Dynamic Similarity

The flow around the model and prototype are dynamically similar if and only if the forces at all points in the flow, in all three directions have the same scale ratio. The *force scale factor* α_F is defined as:

$$F_m = \alpha_F F_p \tag{2.42}$$

2.6.2 Scale Law

In wind tunnel testing with air as medium and with no free water surface present, the *Reynolds number* Re and the *Mach number* Ma are two important similitude parameters. The Reynolds number describes the relation between inertial and viscous forces in a fluid and is defined as:

$$Re = \frac{\rho V L}{\mu} = \frac{V L}{\nu} \tag{2.43}$$

where ρ is the fluid density, V is the flow velocity, L is the length of the object, but is changed for the diameter $\varnothing$ if the object has a cylindrical 2D geometry, μ is the *dynamic viscosity* and ν is the *kinematic viscosity*. The Mach number is defined as:

$$Ma = \frac{V}{a} \tag{2.44}$$

where V is the flow velocity and a is the *local speed of sound*. In lower speeds (sub-sonic) air can be regarded as incompressible and the Mach number can be neglected when the value is lower than 0.3. Since the Mach numbers were calculated as approximately 0.05 for the strong wind case and as 0.03, for the light wind case, the Mach number was neglected in this project, leaving the Reynolds number Re, as the only important similitude parameter. To satisfy the requirements for kinematic- and dynamic similarity the Reynolds number has to be same in both scales, which the interested reader can read more about in [19].

If the aerodynamic forces F on, for example, a sail model that is subjected to a circulating airflow in a wind tunnel are assumed to be a function of the *fluid density* ρ, the *fluid velocity* V, the *fluids dynamic viscosity* μ and the *characteristic length* L_c, then we have:

$$F = f(L_c\, V \rho\, \mu) \tag{2.45}$$

The subscript c in the expression for the characteristic length is omitted in the remaining equations. The characteristic length is defined differently depending on the geometry of the object; when sails are involved, the characteristic length is usually defined as the horizontal distance between the luff and the leech of the sail, at the height of the geometrical center of effort (CoE).

With dimensional analysis, Eq. (2.45) can be written:

$$\frac{F}{\rho\, V^2\, L^2} = g\left(\frac{\rho\, V\, L}{\mu}\right) \tag{2.46}$$

where the left-hand side represents the dimensionless force coefficient C_F and as can be seen, therefore is a function of the dimensionless Reynolds number, i.e.

$$C_F = g(Re) \tag{2.47}$$

This means that if the dimensionless Reynolds number are same in both scales, then the dimensionless force coefficients are also same in both scales:

$$Re_m = Re_p \quad \Longrightarrow \quad C_{F_m} = C_{F_p} \tag{2.48}$$

Using the left-hand side of Eq. (2.46) and the equality between the force coefficients in both scales in Eq. (2.48), then the law of similitude can be used to analyze the forces in the model scale F_m, i.e.

$$\frac{F_p}{F_m} = \frac{\rho_p}{\rho_m}\left(\frac{V_p}{V_m}\right)^2\left(\frac{L_p}{L_m}\right)^2 \tag{2.49}$$

which is a *scale law*, where F_p/F_m represents the force ratio, ρ_p/ρ_m the density ratio, V_p/V_m the velocity ratio and L_p/L_m the length ratio, between the prototype and the model.

Scale Effects

When one speaks of scale effects it is commonly the dimensionless Reynolds number Re, that cannot be scaled properly. The reason for not being able to scale the Reynolds number perfectly usually is that the required wind tunnel speed must be so high that the sail model and the other equipment could be at risk and suffer from structural damage, which then could jeopardize the whole test project with large financial losses as consequence. One usually therefore has to compromise and use as high tunnel speed as the model and the wind tunnel balance can handle.

If the force coefficients not are equal in both scales, means that the dimensionless Reynolds number not are equal in both scales and that Eq. (2.48) instead has to be written:

$$Re_m \neq Re_p \quad \Longrightarrow \quad C_{F_m} \neq C_{F_p} \tag{2.50}$$

2.6.3 Hooke's Law

A materials deformation properties can be determined experimentally in a so-called tensile test with a rod of the material of interest. In the tensile test, the elongation of the material and the applied force are measured from time zero to fracture; with the collected data a *stress-strain diagram* can be created [22]. The so-called *Hooke's law* for tensile stress is defined as:

$$\sigma = E\,\varepsilon \tag{2.51}$$

where σ is the tensile stress, E is the modulus of elasticity or *Young's modulus* and ε is the strain. Hooke's law is a constitutive relationship and materials that are described with it are linearly elastic [22].

The strain ε describes the non-dimensional deformation a material suffer when subjected to a load:

$$\varepsilon = \frac{\delta}{L_0} \tag{2.52}$$

where δ is the elongation of the material and L_0 is the original length, before the load was applied. Eq. (2.52) thus gives rise to another expression where the elongation in model-scale can be coupled to the elongation in full-scale, with the linear length scale factor, α_L, i.e.

$$\delta_m = \alpha_L\,\delta_p \tag{2.53}$$

2.6.4 Elemental Case for a Cantilever Beam

Fig. 2.16 illustrates an elemental case for a cantilever beam and can be found in table 32.1 in [14] as well as Eq. (2.56) - (2.67), which are expressions for the calculation of the angle change, θ and the displacement, δ.

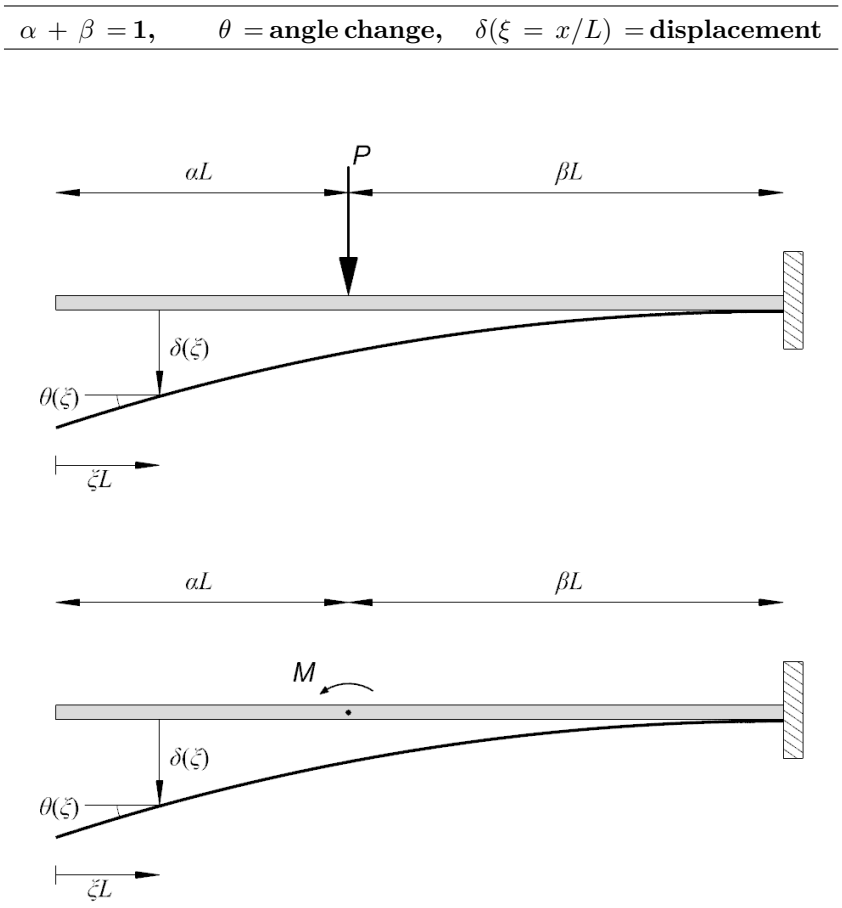

Figure 2.16: Elemental case for a cantilever beam, Table 32.1 in [14].

In Fig. 2.16 it can be seen that the angle change and the displacement are defined as functions of ξ, i.e. $\theta(\xi)$ & $\delta(\xi)$ where ξ, which is defined as:

$$\xi = \frac{x}{L} \tag{2.54}$$

is dimensionless and is used only to define the position where it is desired to calculate the angle change and the displacement. Further, in Fig. 2.16 α and β were defined as:

$$\alpha + \beta = 1 \tag{2.55}$$

where $0 < \alpha, \beta < 1$. α is the relative length $\alpha\, L/L$ between the point where the load is applied and the free end of the beam and β is the relative length $\beta\, L/L$ between the point

where the load is applied and the fix end of the beam. Depending on whether it is desired to calculate the angle change and the displacement at exactly the position where the load is applied or on either side of it, different expressions should be used. These are presented in Eq. (2.56) - (2.62) for the point load P and Eq. (2.63) - (2.67) for the moment M.

$$\theta\left(\xi < \alpha\right) = \frac{P\,L^2}{2\,E\,I}\,\beta^2 \tag{2.56}$$

$$\delta\left(\xi < \alpha\right) = \frac{P\,L^3}{6\,E\,I}\left(-\beta^3 + 3\,\beta^2\left(1 - \xi\right)\right) \tag{2.57}$$

$$\theta\left(\xi > \alpha\right) = \frac{P\,L^2}{2\,E\,I}\left(\beta^2 - \left(\xi - \alpha\right)^2\right) \tag{2.58}$$

$$\delta\left(\xi > \alpha\right) = \frac{P\,L^3}{6\,E\,I}\left(\left(\xi - \alpha\right)^3 - 3\,\beta^2\left(\xi - \alpha\right) + 2\,\beta^3\right) \tag{2.59}$$

$$\theta\left(\alpha\right) = \frac{P\,L^2}{2\,E\,I}\,\beta^2 \tag{2.60}$$

$$\delta\left(\alpha\right) = \frac{P\,L^3}{3\,E\,I}\,\beta^3 \tag{2.61}$$

$$\theta\left(\xi < \alpha\right) = \frac{M\,L}{E\,I}\,\beta \tag{2.62}$$

$$\delta\left(\xi < \alpha\right) = \frac{M\,L^2}{E\,I}\,\beta\left(1 - \xi - \beta/2\right) \tag{2.63}$$

$$\theta\left(\xi > \alpha\right) = \frac{M\,L}{E\,I}\left(1 - \xi\right) \tag{2.64}$$

$$\delta\left(\xi > \alpha\right) = \frac{M\,L^2}{2\,E\,I}\left(\left(\xi - \alpha\right)^2 - 2\,\beta\left(\xi - \alpha\right) + 2\,\beta^2\right) \tag{2.65}$$

$$\theta(\alpha) = \frac{M\,L}{E\,I}\,\beta \tag{2.66}$$

$$\delta(\alpha) = \frac{M\,L^2}{2\,E\,I}\,\beta^2 \tag{2.67}$$

2.6.5 Area Moment of Inertia

Circular Tube

Fig. 2.17 illustrates section-cuts of the mast bottom section and the mast top section of the aluminum ILCA 7 mast.

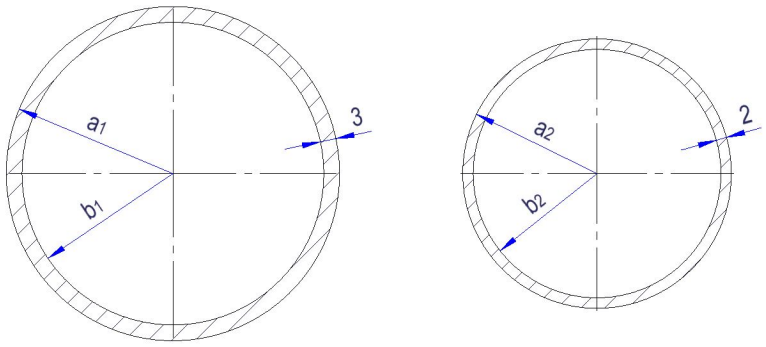

Figure 2.17: Cross sections of the aluminum mast bottom section and the aluminum mast top section, where a_1 and b_1 are the outer and inner radius of the mast bottom section; a_2 and b_2 are the outer and inner radius of the mast top section, respectively.

The area moment of inertia, I for two circular tubes, with different outer and inner radius, that shall be combined by inserting one of the tubes into the other with an overlap, can be calculated with:

$$I_1 = \frac{\pi\,a_1^4}{4} - \frac{\pi\,b_1^4}{4} \tag{2.68}$$

$$I_2 = \frac{\pi\,a_2^4}{4} - \frac{\pi\,b_2^4}{4} \tag{2.69}$$

$$I_{tot} = I_1 + I_2 \tag{2.70}$$

where a and b are the outer and inner radius, respectively and the subscripts 1, 2, *tot* respectively represent the bottom tube, the top tube, and the total combined tube.

Circular Solid Beam

The area moment of inertia I for a circular beam with a solid cross-section can be calculated with Eq. (2.71), which can be found in Table 31.1 "Cross-sectional data for solid cross sections" in [14],

$$I = \frac{\pi\, a^4}{4} \tag{2.71}$$

where a is the radius of the solid cross-section.

2.6.6 Flexural Rigidity

The flexural rigidity of a beam is defined as the product of the Young's modulus, E and the area moment of inertia I, for the beam:

$$E\, I \tag{2.72}$$

2.7 Sail Area Measurement with the ORC Method

ORC (Offshore Racing Congress) Rating systems use the IMS (International Measurement System) when measuring sails [28] and the method for measurement of the mainsail is described as,

$$Area = \frac{P}{8}\,(E + 2\,MQW + 2\,MHW + 1.5\,MTW + MUW + 0.5\,MHB) \tag{2.73}$$

where,

P - is the length [m] of the luff
E - is the length [m] of the foot
MQW - is the chord length [m] between the luff and the leech, $1/4\,P$ vertically up from the tack
MHW - is the chord length [m] between the luff and the leech, $1/2\,P$ vertically up from the tack
MTW - is the chord length [m] between the luff and the leech, $3/4\,P$ vertically up from the tack
MUW - is the chord length [m] between the luff and the leech, $7/8\,P$ vertically up from the tack
MHB - is the distance [m] between the luff and the leech at the head

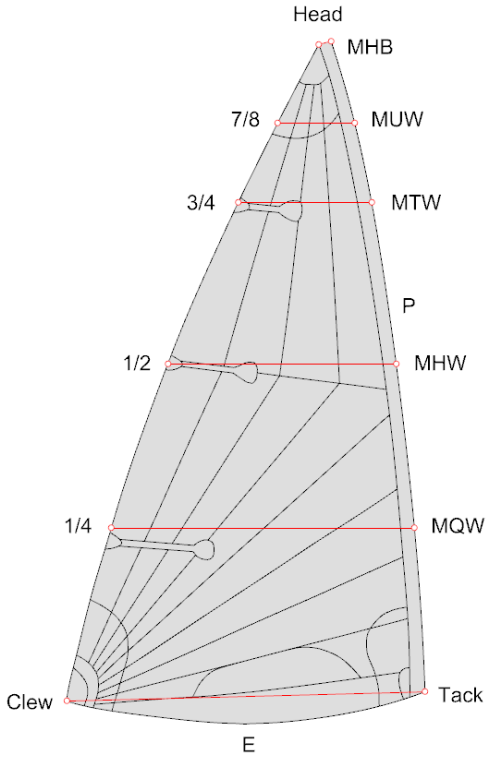

Figure 2.18: The image illustrates how the measures are taken in a main sail with the ORC-method.

2.8 Grid Dependence Study

A grid dependence study, aimed at generating as geometric similar grids as possible, will make it possible to estimate the quality and the uncertainty of the data. A method used by Crepier [7] and Eça & Hoekstra [9] for a grid dependence study and an estimation of the uncertainty, respectively, are briefly presented in this section.

2.8.1 Isotropic Volume Grid Generation

The domain is initially divided into a coarse grid with large cells, which successively are sub-divided into smaller cells that finally enclose the prism-cell layers around the model. Each cell-size is referred to as a *refinement level* or *surface refinement degree* and the transition zone between two refinement-levels is called the *diffusion depth* (d). The user thus has to decide the cell size of the initial coarse grid, the appropriate refinement degree for the model, and the diffusion depth. Once the user is satisfied with the isotropic volume grid generation an *anisotropic sub-layer grid generation* can be used to increase the resolution of the boundary-layer on the walls. In [7], 8 refinement levels are used and the grid refinement study is based on a coarse grid where the resolution is gradually refined, resulting in 5 grids. Further, in the section "2.2 Isotropic volume grid generation" in [7], Crepier lists 4 steps as a guide to ensure that the grids become as geometrically similar as possible:

1. The initial cell size should be decreased by a factor of 2, 3, 4, and 5 in each direction by using 2, 3, 4, 5 cells in each direction.
2. The surface refinement degree should be kept constant throughout the sets.

3. The size of the transition region between 2 neighboring cells, the so-called diffusion depth, should be adjusted so that it matches the global size of the grid.
4. The anisotropic sub-layer settings should be adapted to the refinement.

2.8.2 Anisotropic Sub-Layer Grid Generation

Eq. (2.74) & Eq. (2.75) below are used for the *anisotrophic sub-layer grid generation*. The total thickness of all prism layers should be less than the turbulent boundary-layer thickness, which has to be calculated first.

$$S_n = S_0 \frac{1 - r_1^{1/n}}{1 - r_1} \tag{2.74}$$

where S_0 is the *thickness of near wall prism layer* for the initial coarse grid and the output S_n represents the thickness of the n^{th} prism cell-layer for the refined grid. The level of refinement is represented by (n), where n=1 is the coarsest grid.

$$r_n = r_1^{1/n} \tag{2.75}$$

where r_1 is the *prism layer stretch factor* or *growth ratio* of the initial coarse grid and the output r_n represent the growth ratio of the n^{th} refined grid.

2.9 Verification & Validation

Verification and validation are two methods used to quantify numerical and modeling errors in CFD and thus a way to establish the credibility of the results.

2.9.1 Verification

There are two verification aims, i.e. *Code Verification* and *Solution Verification*. Code Verification is all about if the software is properly coded or if there are any "bugs" present in the code, causing a numerical error. Solution Verification, on the other hand, quantifies the uncertainty of the numerical solution. Following Roache [32], "as an error requires the knowledge of the "truth/exact solution" and has a sign; an uncertainty defines an interval that should contain the "truth/exact solution" with a certain degree of confidence and is defined with a plus-minus sign". In this project, it was Solution Verification that was of interest, and the numerical uncertainty was estimated with the method suggested by Eça and Hoekstra [9] who estimate the uncertainties as "the absolute value of an error estimator multiplied by a factor of safety". Below, the suggested procedure in [9] is described.

2.9.2 Validation

Validation quantifies the modeling errors, but a formal validation according to, for example ITTC (*International Towing Tank Conference*) will not be carried out. Instead, an informal validation will be performed, where modeled data will be compared to measured data.

2.9.3 Error Estimation

Numerical Errors

In [9] the authors lists three components of numerical errors that exists in CFD predictions:

- Round-off error
- Iteration error
- Discretization error

where the first component, the round-off error, is a consequence of the finite precision of computers; the second component, the iteration error, is unavoidable due to the non-linearity of the mathematical equations and finally, the third component, the discretization error, is a consequence of the approximation made when transforming the partial differential equations of the continuum formulation into a system of algebraic equations.

Power Series Representation of the Discretization Error

In [9] the authors assumes that both the round-off error and the iteration error are negligible compared to the discretisation error; they estimates the discretization error with (truncated) power series expansions. The basic equation to estimate the discretization error ϵ_ϕ is:

$$\delta_{RE} = \phi_i - \phi_0 = \alpha h_i^p \tag{2.76}$$

where ϕ_i is any integral or other functions of a local flow quantity, ϕ_0 is the estimate of the exact solution, α is a constant to be determined, h_i is the typical cell size and p is the *observed order of grid convergence*. If $0.5 \leq p \leq 2$, $\epsilon_\phi = \delta_{RE}$. To estimate the discretization error, ϵ_ϕ, the estimate of the exact solution, ϕ_0, α and the observed order of grid convergence, p has to be determined. The procedure for the determination of these unknowns are described in detail in Appendix A and Appendix B in [9].

The assumptions with the use of Eq. (2.76) are:

1. The grids has to be in the "asymptotic range".
2. The density of the grids is represented by a single parameter, the typical cell size of the grids, h_i, which requires that the grids are *geometrically similar*, i.e. the grid refinement ratio must be constant in the entire domain.

With equal grid refinement ratios between the medium/finest and coarsest/medium, i.e. $h_2/h_1 = h_3/h_2$, three grids is the only that is required to estimate the apparent grid convergence behavior, based on the discriminating ratio:

$$R = \frac{\phi_1 - \phi_2}{\phi_2 - \phi_3} \tag{2.77}$$

where the subscripts 1, 2 and 3 represent *fine, medium* and *coarse* grid, respectively.

- Monotonic convergence for $0 < R < 1$
- Monotonic divergence for $R > 1$
- Oscillatory convergence for $R < 0$ and $|R| < 1$
- Oscillatory divergence for $R < 0$ and $|R| > 1$

The discriminating ratio R is related to the observed order of grid convergence p and the grid refinement ratios h_2/h_1 and h_3/h_2 by

$$R = \left(\frac{h_1}{h_2}\right)^p \left(\frac{(\frac{h_2}{h_1})^p - 1}{(\frac{h_3}{h_2})^p - 1}\right), \tag{2.78}$$

which for h_2/h_1 reduces to

$$\log(R) = p \log\left(\frac{h_1}{h_2}\right). \tag{2.79}$$

Thus, when $p > 0$ is equivalent to *monotonic convergence* $0 < R < 1$ and when $p < 0$ is equivalent to monotonic divergence $R > 1$, $\frac{h_1}{h_2} < 1$.
It is therefore only possible to estimate ϵ_ϕ when there exists monotonic convergence when the three grids are in the "asymptotic range" and the data do not have any scatter. For easy geometries and "simple equations" these requirements are relatively easy to satisfy according to [9], but harder, if not impossible for complex geometries and complex equations. The main reason for "noisy data" [9] is the lack of geometrical similarity of the grids, which is harder to get for unstructured grids than it is for structured grids. In cases with complex geometries and complex equations, i.e. when the estimation with Eq. (2.76) is impossible or unreliable, three other "error estimators" can and should be used [9]:

$$\delta_1 = \phi_i - \phi_o = \alpha \tag{2.80}$$

$$\delta_2 = \phi_i - \phi_o = \alpha \tag{2.81}$$

and

$$\delta_{12} = \phi_i - \phi_o = \alpha_1 h_i + \alpha_2 h_i^2. \tag{2.82}$$

Eq. (2.80) & Eq. (2.81) are only suitable for monotonically converging solutions but Eq. (2.82) can be used also for non-monotonic convergence [9].

Least-Squares Error Estimation

If is is expected that scatter might occur in the data, it is recommended to use at least four grids, i.e. $n_g \geq 4$ [9], because it is then possible to perform a least-squares error estimation and determine ϕ_0 from the minimum of functions:

$$S_{RE}(\phi_0,\, \alpha,\, p) \,=\, \sqrt{\sum_{i=1}^{n_g} (\phi_i \,-\, (\phi_0 \,+\, \alpha\, h_i^p))^2}, \tag{2.83}$$

$$S_1(\phi_0,\, \alpha) \,=\, \sqrt{\sum_{i=1}^{n_g} (\phi_i \,-\, (\phi_0 \,+\, \alpha\, h_i))^2}, \tag{2.84}$$

$$S_2(\phi_0,\, \alpha) \,=\, \sqrt{\sum_{i=1}^{n_g} (\phi_i \,-\, (\phi_0 \,+\, \alpha\, h_i^2))^2}, \tag{2.85}$$

and

$$S_{12}(\phi_0,\, \alpha_1,\, \alpha_2) \,=\, \sqrt{\sum_{i=1}^{n_g} (\phi_i \,-\, (\phi_0 \,+\, \alpha_1\, h_i \,+\, \alpha_2\, h_i^2))^2}. \tag{2.86}$$

The least-squares minimization of the non-weighted approach in Eq. (2.83) - (2.86) and the weighted approach is presented in Appendix B in [9], where also the definition of the standard deviation of the fits σ that is used as a measure can be found.

Uncertainty Estimation

With the estimated discretization error ϵ_ϕ determined it is possible to estimate the uncertainty U_ϕ, i.e. the interval where the exact solution can be found with 95% certainty,

$$\phi_i \,-\, U_\phi \,\leq\, \phi_{exact} \,\leq\, \phi_i \,+\, U_\phi \tag{2.87}$$

"First a judgment is made of the quality of the data fit". After that a data range parameter is defined:

$$\Delta_\phi \,=\, \frac{(\phi_i)_{max} \,-\, (\phi_i)_{min}}{n_g \,-\, 1} \tag{2.88}$$

If the solution is monotonically convergent with $0.5 \,\leq\, p \,<\, 2.1$[4] and if $\sigma \,<\, \Delta_\phi$, the error estimation is considered reliable and receive a safety factor, $F_s \,=\, 1.25$ after the Grid Convergence Index (GCI). In every other case, the error estimation is not considered reliable and receives instead a safety factor, $F_s \,=\, 3$. The determination of U_ϕ and weather the estimation is good or bad do not only depend on the safety factor, there exist other expressions that classify an error estimation as "good" or "bad", i.e. for $\sigma \,\leq\, \Delta_\phi$ or $\sigma \,>\, \Delta_\phi$.

- For $\sigma < \Delta_\phi$:

$$U_\phi(\phi_i) = F_s\,\epsilon_\phi(\phi_i) + \sigma + |\phi_i - \phi_{fit}\,| \tag{2.89}$$

- For $\sigma \geq \Delta_\phi$:

$$U_\phi(\phi_i) = 3\,\frac{\sigma}{\Delta_\phi}(\epsilon_\phi(\phi_i) + \sigma + |\phi_i - \phi_{fit}\,|) \tag{2.90}$$

The estimated uncertainty thus has 3 components, i.e. the absolute value of the estimated discretization error multiplied with a safety factor, the standard deviation of the fit, and "the difference between the real data point and the value obtained from the fit for the dame grid density" [9]. The quantity of the two last components is a result of scatter in the data [9] and that for a grid refinement study with monotonically convergent data, the method should reduce to the Grid Convergence Index.
The asymptotic range is defined as: $p = 1.99$ for $h_i/h_1 = 1$ and $p = 1.95$ for $h_i/h_1 = 2$.

Grid Refinement Ratio

The grid refinement ratio (*relative step size*) is used to generate as geometrical similar grids as possible and is defined as:

$$\frac{h_i}{h_1} = \frac{NX_1}{NX_i} = \frac{NY_1}{NY_i} = \frac{NZ_1}{NZ_i} = \sqrt[3]{n_1/n_i} \tag{2.91}$$

where $NX_i, NY_i \, and \, NZ_i$ are the number of cells in the X, Y, and Z-directions in the i:th grid, respectively, and n_i is the number of cells in the i:th 3D grid.

2.10 Chalmers Compute Cluster

Chalmers Center for Computational Science and Engineering (C3SE) has a compute cluster system, which runs on the stable Linux Distribution centOS and uses the SLURM queuing system for higher efficiency.

3
Test Object

3.1 The ILCA Dinghy

The ILCA dinghy, designed by Bruce Kirby, is a strict one-design class which means that very few adjustments and improvements are allowed. In this section, the new bi-radial MKII sail and the old cross-cut MKI sail are presented as well as the ILCA 7 mast and the ILCA boom. The trim controls that are used to trim the sail are also presented as well as how the ILCA 7 should be sailed on the downwind leg.

3.1.1 The Old MKI Sail and the New MKII Sail

The new class approved MKII sail for the ILCA 7 (men's Olympic sailing class dinghy) is manufactured of 4.5 ounce Dacron cloth with a bi-radial design, which better matches the load paths and therefore offer better durability than the old MKI sail, manufactured of 3.8 ounces Dacron of the cross-cut design with diagonally placed panels. Images of MKI and MKII can be seen in Fig. 3.1 & Fig. 3.2, respectively and the corresponding data are presented in Table 3.1.

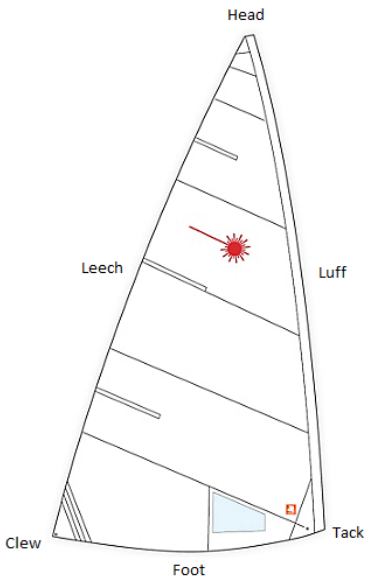

Figure 3.1: ILCA 7 MKI Sail.

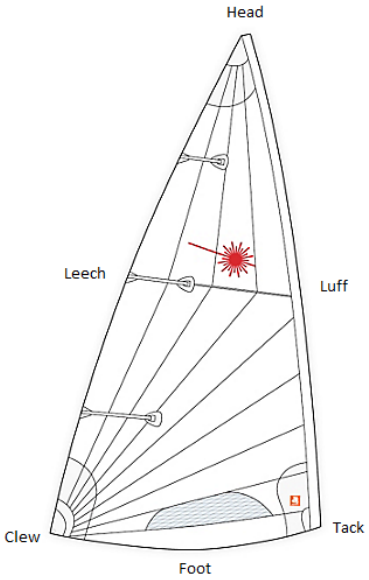

Figure 3.2: ILCA 7 MKII Sail.

Table 3.1: The corresponding full-scale data for each sail.

Luff length (max) [m]	5.130	**Luff length (max)** [m]	5.120
Leech length (max) [m]	5.570	**Leech length (max)** [m]	5.555
Foot length (max) [m]	2.740	**Foot length (max)** [m]	2.750
Sail area [m^2]	7.06	**Sail area** [m^2]	7.06

3.1.2 The Mast & the Boom

The mast for the ILCA dinghy consists of two sections of tubes, one *bottom section* and one *top section*, which are combined by inserting the top section into the bottom section, with an overlap. At the time of carrying out this project, a new version of the mast top section in carbon composite was about to be introduced on the market. However, it was decided that the traditional mast top section in aluminum and the mast bottom section, also that in aluminum, should be used as reference in this project. Three classes of the ILCA dinghy exists, i.e. *ILCA 4, ILCA 6* and *ILCA 7*. They all have the same hull and fittings as well as the boom and the mast top section, but the mast bottom section for the ILCA 7 is thicker; the sail area also differs between the three classes. The required effort to bend the mast, to get the desired curvature, therefore differs, which has been the idea from the beginning. ILCA 7 (Standard) is as previously mentioned the men's Olympic sailing class, ILCA 6 (Radial) is the women's Olympic sailing class and ILCA 4 is the class for children and youths. The equipment that is class specific has therefore been designed with this in mind. The boom for the ILCA dinghy is also a circular tube made out of aluminum.

Images of the mast bottom section and the mast top section can be seen in Fig. 3.3 & Fig. 3.4, respectively; an image of the boom can be seen in Fig. 3.5. These three images are taken from the class rules of the International Laser Class Association (ILCA) [13] and contain some geometrical data in millimeter.

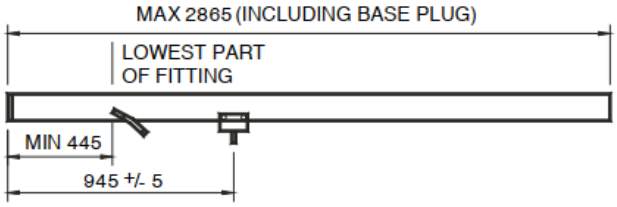

Figure 3.3: The bottom section for the ILCA 7 dinghy (from ILCA).

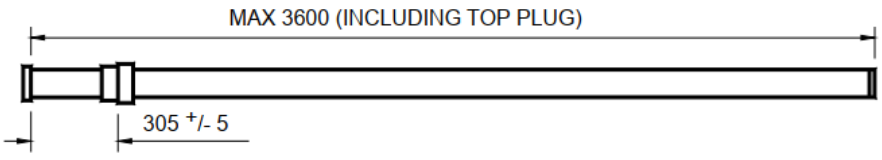

Figure 3.4: The top section (aluminum) for the ILCA dinghy (from ILCA).

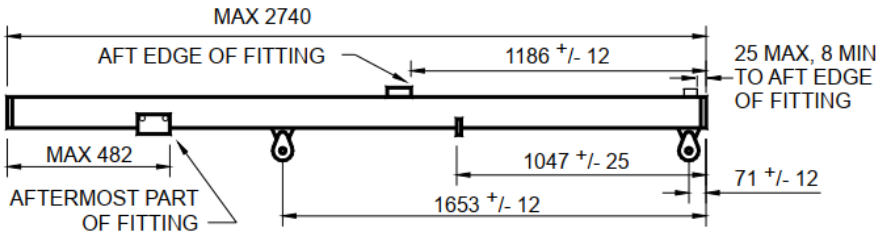

Figure 3.5: The boom for the ILCA dinghy (from ILCA).

The corresponding data for the two full-scale mast sections and the full-scale boom are presented in Table 3.2.

Table 3.2: Full-scale data for the two mast sections & the boom.

	Bottom section	**Top section**	**Boom**
Length (max) [m]	2.8650	3.6000	2.7400
Inner radius [m]	0.0288	0.0236	-
Outer radius [m]	0.0318	0.0256	0.0250

3.1.3 Trim Controls on the Full-Scale ILCA Dinghy

As described above, both the old MKI sail and the new MKII sail are manufactured of relatively thin Dacron cloth, which makes it possible to alter the shape of the sail with a set of different trim controls. The possibility of trimming the sail model as identically as possible during the wind tunnel tests is generally of utmost importance for the wind tunnel tests to be meaningful. However, Chalmers wind tunnel is of general design with a semi-closed test section and is not equipped with vertical guiding vanes that can create twisted flow and simulate the natural *aerodynamic twist* that is present in reality due to the vertical velocity gradient. It was therefore not possible to create a twisted airflow in the test section and the requirement of being able to trim the sail model with a twist during the tests was therefore not crucial. The kicker and the sheet, which are those two trim controls that control the curvature of the mast and are used when twisting the sail, were mounted slightly differently on the sail model. Exactly how they were mounted to control the sail model are described in Chapter 4, where they are compared with the positions of the trim controls on a full-scale sail.
The ILCA dinghy has four trim controls, i.e. *sheet, kicker, cunningham* and *outhaul*; they can all be seen in Fig. 3.6, as well as the nautical names of the edges and corners of a sail. Each trim control is described more in-depth, further down in the text.

Even though all trim controls are important, the importance of each trim control varies, depending on whether the sail is trimmed for the upwind leg or the downwind leg. The sea state and the wind properties, i.e. the wind speed and the amount of turbulence, also influence the importance of each trim control. However, they are all continuously used together, in order to always have the optimal sail shape. How the trim controls were used during the wind tunnel tests is described in chapter 4, when the testing procedures are presented. As with many other cat-rigged dinghies, the ILCA sail has a separate sleeve along the *luff*, where the mast is inserted. Further, the ILCA sail is *loose-feetened*, which

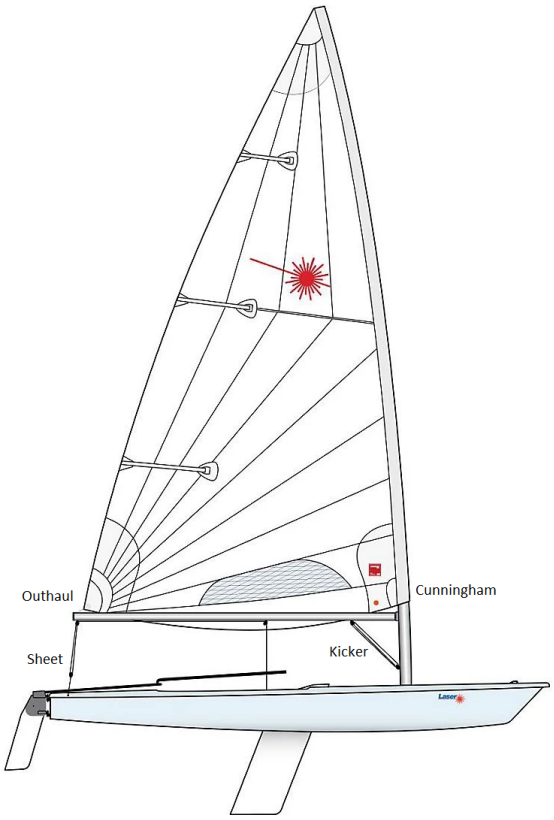

Figure 3.6: The trim controls on the full-scale ILCA dinghy, i.e. the *sheet, kicker, cunningham & outhaul.*

means that only the aft-most positioned corner of the *foot* of the sail, i.e. the *clew*, is attached to the boom at the free end. Here the foot of the sail meets the *leech* of the sail, which is the "hypotenuse" of a right-angled triangle. The other corner of the foot of the sail, i.e. the *tack* is integrated with the sleeve of the sail. Bending the mast, with the usage of a couple of the trim controls presented above, is one of the main trim techniques with a cat-rigged dinghy and it was therefore very important to scale the mast properly so that the curvature of the mast model would be identical to the full-scale mast when the sail was trimmed in the wind tunnel. How the mast and the sail were scaled are described in Chapter 4. Now, an in-depth description of the different trim controls, presented above will follow.

Sheet

The sheet is the most important trim control on the ILCA dinghy and has a dual function as it controls the sail in two degrees of freedom, i.e. by horizontal rotation of the boom and the sail around the z-axis; vertically by pulling the free end of the boom downwards. The sheet, therefore, controls the *angle of attack* α and the *flatness* in the sail, respectively. However, the sheet also has an important function together with the trim control, the kicker, to adjust the twist in the sail, which was mentioned in the text above, and will be described more further down. By pulling the sheet, the boom and the sail rotate around the z-axis and become more centered in the boat. The sheet angle δ thus decreases, and the angle between the boom and the apparent wind β_{aw}, i.e. the *angle of attack* increases. At the same time, the sail is flattened because the free end of the boom, which is attached to the sail at the clew, is pulled downwards. The leech is thus stretched up and the top

of the mast is bent backward. Further, the design of the sail with a sleeve gives the mast a so-called pre-bend, which is a small initial curvature the mast receives as it is inserted into the sleeve in the sail. When the sheet then is pulled maximum as it many times is, especially when beating upwind, the mast receives the highest curvature and resembles somewhat a quarter of an ellipse. Maximum flexion is naturally received at the top of the mast and successively decreases vertically towards the boom. At the height, where the boom is attached to the mast, the flexion of the mast is positive along the x-axis, where positive x-direction is with the *"right-hand-rule"* in the forward direction, which increases the overall curvature of the mast. This is the reason why the sail is flattened when the main sheet and the kicker both are pulled. It is easy to understand that the opposite naturally occur if the sheet instead is eased, i.e. the sheet angle increases and the angle of attack decreases, as the boom and the sail rotate around the mast and becomes less centered in the boat. Further, when the sheet is eased, the free end of the boom consequently rises, because the sheet no longer pulls it down, provided that the kicker also has been eased, if it has been used, since this trim control also pulls the boom down and bends the mast. If no trim control holds the boom down, the leech becomes less loaded and the curvature of the mast decreases.

As described in the text above, the sheet controls the angle of attack, which preferable shall be constant along the luff of the sail, if it is desired to use as much sail area as possible. However, the sheet does not control this angle alone. The kicker helps the sheet to control the angle of attack along the luff and the twist is thus the angle between the chord-line at the foot of the sail and the chord-line at the top of the sail. It is a well-known fact that the wind speed increases with height due to the friction against the water surface, where the air molecules interact with water molecules in a thin stratum. The twist of the sail should therefore follow the rotation of the apparent wind which is governed by the vertical velocity gradient $\partial V_{AW_p}/\partial z$. The apparent wind thus becomes more aligned with the true wind β_{TW} with height. Unfortunately, Chalmers wind tunnel could not create a twisted flow in the working section, as mentioned previously. Wind tunnels that are designed for sail design usually have an open test section and are often equipped with these guiding vanes that can create a twisted flow in the test section for the model sail to "operate in". The tunnels that have these vertical guiding vanes are called *Twisted Flow Wind Tunnels*. As previously mentioned, the sheet also controls the flatness, i.e. the depth in the sail, of approximately 2/3 of the sail, from the top down; the lower 1/3 are controlled by the outhaul and the kicker.

Kicker

As mentioned above, the kicker flattens approximately 1/3 of the lower part of the sail by flexing the mast backward, but it also controls the *twist* in the sail together with the sheet. To increase the twist in the sail, the kicker is pulled and the sheet is eased. This allows the leech to be opened, and the local chord in the sail to be aligned with the apparent wind. To decrease the twist, i.e. "close the sail", the sheet is instead pulled.

Cunningham

The cunningham controls the tension in the *luff* of the sail, i.e. the leading edge; control the horizontal position of the camber in the sail.

Outhaul

The outhaul controls the tension of the *foot* of the sail, i.e. the side of the sail that is aligned to the boom; thus the vertical position of the camber in the sail. When the outhaul is pulled, the "belly" moves upwards and the lower part of the sail is flattened, and vice versa.

3.1.4 Sailing the ILCA 7 Dinghy Downwind

To understand how the sail model of the new MKII sail should be trimmed during the tests in the wind tunnel, the recommendations, from the Swedish Sailing Federation (SSF), in the *ILCA Guide* [34] were studied. The ILCA Guide is written in Swedish, so the relevant sections for this project, which concerns the ILCA 7 on the downwind leg were translated and are presented in Fig. 3.9, as well as pictures from the corresponding sections. However, these recommendations are associated with the old MKI sail, and since the design of the MKII sail is slightly different, these recommendations had to be viewed with this fact in mind.

Light and Strong Wind Conditions

When sailing downwind in light wind conditions, the ILCA 7 dinghy should not be sailed dead downwind as it can be in stronger wind conditions, when the power in the sails often is enough and the ILCA 7 is planing. In light wind conditions, it is usually instead faster to prioritize a higher speed, even if it means sailing a longer distance; the recommended choice is, therefore, to head up slightly and sail with a higher speed and larger angle towards the downwind rounding mark; if there are waves present, catch them and ride them. In stronger wind conditions when the power in the sails generates a sufficiently high speed, the sailor can instead go for a higher VMG (Velocity Made Good) and sail more or less straight dead downwind towards the leeward mark.

Figure 3.7: Downwind sailing in light wind conditions. The picture is taken from the ILCA guide [34] and published with the approval of SSF.

Figure 3.8: Downwind sailing in strong wind conditions. The picture is taken from the ILCA guide [34] and published with the approval of SSF.

Downwind			
Trim control	**Light wind**	**Medium wind**	**Strong wind**
Kicker	Released, so that the sail can move up to 30 cm back and forth, from neutral	So, that the sail can twist 30°, in the top	Up to 30° twist
Cunningham	Loose	Loose	Loose
Outhaul	Approximately 25 cm depth at the boom	Approximately 20 cm depth at the boom	Approximately 15 cm depth at the boom
Sheet	Release the sheet, so that the sheet angle is somewhere between 90° - 110°	Do not release the sheet, so that the sheet angle exceeds 90°	Release the sheet, so that the sheet angle is somewhere between 75° - 85°
Centerboard	Up 15 - 20 cm	Up 15 - 20 cm	Up 15 - 20 cm
Body position	Forward, close to the centerboard	Move backwards as the dinghy accelerates and starts planing; move forward again when it decelerates	Move as far aft as possible, in order to raise the bow
Heel	10° - 20° heel to windward	Neutral	Neutral
General advice	Calm body movements	Move much back and forth and fall off, when the speed decreases	Highest stability is to sail slightly negative and not exceed the recommended sheet angle

Figure 3.9: Trim recommendations on the downwind leg, from the Laser Guide [34], compiled by SSF.

Because of these different recommendations on the downwind leg in different wind conditions, the interest of testing the sail model with different headings, therefore, varied from the light wind case and the strong wind case.

Sailing Positive and Sailing Negative

Two fundamental sailing techniques, when sailing downwind are sailing *positive* and sailing *negative*. Sailing positive means that the wind reaches the luff of the sail first and sailing negative is simply the opposite, i.e. the wind reaches the leech first. Sailing negative thus allows sailing with a higher VMG, since it is possible to point higher. The Laser Guide [34] recommend sailing negative with a small windward heel in light wind conditions because it should be faster than sailing positive. Further, in gustier wind conditions sailing negative should offer higher stability and prevent the dinghy to head up, away from the leeward mark in a hard gust and capsize at lee, which easily can happen when sailing positive. This because when sailing negative the dinghy instead bears away on a higher running course, towards the leeward mark when subjected to a hard gust. However, the course on the downwind leg is hardly ever completely straight, especially if waves are present and the wind direction switches back and forth. The sailor therefore usually sail both positive and negative during the downwind leg. How much or how little the sailor sail either technique depends on which alternative the sailor prefers, this according to elite ILCA 7 sailors from GKSS that were consulted about these matters in the prephase of the project. In Fig. 3.9, it can be seen that the recommended range for the sheet angle in light wind conditions is between $90° \leq \delta \leq 110°$ and in strong wind conditions $75° \leq \delta \leq 85°$. To investigate the technique of sailing negative in light wind, the range of the sheet angles was extended down to 60°, with a step size of 10°; up, to also include 120°. Looking at the range of the sheet angles for the strong wind case, it can be seen that negative sailing always occur, if the heading is within the range $175° < \psi$ for a sheet angle of 75° and $185° < \psi$ for a sheet angle of 85°. The range of the sheet angles for the strong wind case was also extended to include both a higher value and a couple of lower values. The actual ranges of the sheet angles, for both wind conditions, for which the sail model was investigated for during the tests are presented in Chapter 4. Remembering the definition of sailing positive/negative, explained above, makes it easier identifying which sheet angles that represented positive and negative for the actual test case. The sheet angle 90° when sailing with the heading 180° is, therefore, neither positive nor negative.

Body Position - Finding Equilibrium

As with most dinghies, the ILCA sailor constantly has to use his/her body weight and position it to balance the heeling moment. When sailing downwind in light wind conditions, the sailor should heel the ILCA dinghy 10° - 20° to windward to find a neutral position, i.e. equilibrium, where the aerodynamic forces balance the hydrodynamic forces. Further, to minimize the usage of the rudder and thus keep the drag as low as possible when changing the course, the sailor frequently uses his/her body weight to initiate a change of the course. Depending on the reader's previous knowledge in dinghy sailing, it will at this point be clear that sailing the ILCA is an extremely physical activity and the need for a good physique is crucial to be competitive at the highest level of racing.

Trim Controls - Analysis of Recommendations

In Fig. 3.9 it can also be seen that the cunningham should be loose in all wind conditions; that the outhaul should be used so that the depth in the sail is 15 cm in strong wind and 25 cm in light wind. The reason for the different depths in the sail is because, in strong wind, there is no need for the extra power a deeper camber provide, but in the light wind this is desired. Further, according to Fig. 3.9, the trim with the kicker should allow the sail to "move up to 30 cm back and forth from neutral" in light wind and twist up to

30° in strong wind. As mentioned in the text above where the kicker was presented, the bending of the mast, i.e. the curvature of the mast, is controlled with both the sheet and the kicker on the full-scale ILCA, but in the wind tunnel tests, the bending of the mast was done only with the kicker, that were mounted slightly different. This is explained more in detail in Chapter 4.

Translation of Kicker Trim Recommendations for Wind Tunnel Tests

Since it was not possible to re-create the natural velocity gradient in Chalmers wind tunnel, it was not possible to analyze the effect of different twist in the sail, which is controlled by the sheet and the kicker in combination. The trim recommendations for the kicker were therefore translated to be represented by three different settings with the kicker, i.e. *light, medium* and *hard*, to find which setting that maximized the force in the direction of motion F_M. How much light, medium, and hard the trim with the kicker represents will now be explained.

First of all, the elite ILCA 7 sailors from GKSS, who had gained experience from sailing with the new MKII sail during one season said that the kicker had to be pulled much harder on the new MKII sail, compared with the old MKI sail. These sailors were also involved as consultants in the initial phase of the wind tunnel tests and provided the author with invaluable information regarding the proper sail shape and trim of the sail for downwind sailing. The light setting with the kicker more or less simply corresponded to a trim where the kicker was tightened up and given a slight pull. The hard setting with the kicker corresponded, on the contrary, to a very hard pull that gave a deep and prominent wrinkle in the sail from the clew to a point approximately halfway up on the luff. The medium setting with the kicker was simply chosen as an intermediate setting between the light and the hard setting.

4
Methods

4.1 Experimental Setup

In the prephase to the experimental wind tunnel tests many questions had to be answered and preparations carried out. A thorough analysis of how the ILCA 7 dinghy should be sailed and the sail trimmed had, for example, to be performed in order to select the relevant parameters that should be chosen to vary during the wind tunnel tests. The most fundamental questions, beyond choosing the range of variables for the test matrix, were those of scaling the sail and the mast, choosing the cloth for the sail model and choosing the material for the mast model. Two other very important questions were those of how the mast model should be mounted and connected to the wind tunnel balance; how the sail model, the mast model, and the boom model should be controlled in the test section.

In this section, all the necessary preparations that were carried out in the prephase, and how the wind tunnel tests and the numerical analysis were performed, will be described.

4.1.1 Downwind Sailing and Sail Trim Analysis

The Swedish Sailing Federation (SSF) has, as previously mentioned, compiled a guide [34] with recommendations for how the three different classes of the ILCA dinghy, i.e. *ILCA 4 (4.7), ILCA 6 (Radial)* and *ILCA 7 (Standard)* should be sailed; how the sail should be trimmed in varying sea states and wind conditions. The guide thus contained very valuable information of the variables that were of interest for the wind tunnel tests. However, the recommendations in the guide were compiled from experiences with the old cross-cut MKI sail, presented in Chapter 3; since the old design differed in some aspects from the new bi-radial MKII sail, the recommendations in the guide could not be assumed to be completely valid for the new MKII sail. Anyhow, the guide functioned very well as a valuable source of reference.

To find out more about how the bi-radial MKII sail should be trimmed and which apparent wind speeds to analyze, a meeting was held with a couple of Swedish elite ILCA 7 dinghy sailors and the head-trainer from the *Royal Gothenburg Sailing Society* (*GKSS*). The sailors, who had sailed with the MKII sail during one season had during this relatively short period at least learned that the new MKII sail should be trimmed slightly different than the old MKI sail. This was not a surprise, because the MKII sail is designed with a larger and more prominent camber along the luff and has a thicker sailcloth.

Documentation of a ILCA 7 Training Session

The author and a couple of Ph.D. students, involved in *Sailing Dynamics* at Chalmers, were invited to spend a day on the water in a tender boat with the head-trainer, at GKSS

in Långedrag during a ILCA 7 training session. This made it possible to investigate and gather first-hand information of how the sailors sailed the ILCA 7 and how they trimmed the new MKII sail. This was documented with both Go-Pro cameras, mounted at the top of a couple of masts, and with a hand-held video camera from the tender boat. The go-pro cameras gave valuable information of, for example, how much the sailors sheeted the sail as they sailed both upwind and downwind on a race track between two buoys. The top view also gave valuable information about the size of the camber in the sail and its position, and the rudder angle. Further, filming with the hand-held video camera from the tender boat gave information of how much the sailors heeled the ILCA 7 to windward, on the downwind leg, as they strived to find equilibrium between the aerodynamic and hydrodynamic forces. The gathered film material together with the Laser Guide [34] were very valuable when choosing the ranges for the different variables that were chosen for the wind tunnel tests.

The GKSS elite ILCA 7 sailors suggested several interesting apparent wind speeds that they believed would be of great interest for them. Unfortunately, all these wind speeds could not be tested, due to the restriction of the wind tunnel time, that was allotted for the project. However, it was decided that the model sail at least should be tested for two of the suggested apparent wind speeds, which should represent a light wind case and a strong wind case. Before it could be determined which two speeds that should be chosen, the wind tunnel personnel at Chalmers had to be consulted and the limitations of the wind tunnel balance established. According to the wind tunnel personnel, the accuracy, i.e. the resolution, of the balance was better than 3 %; the balance should therefore not give any measurement errors larger than 3 %, regardless of the magnitude of forces measured. When choosing the speed for the light wind case it was decided that 4 m/s had to be the lowest full-scale apparent wind speed, to avoid too small forces. Regarding the speed for the strong wind case, it was desired that this was at least that high that is required for the ILCA 7 to sail in a planing mode. Research, performed by the former Chalmers Ph.D. student Richard Lindstrand Levin, who was involved in full-scale towing-tank tests of the ILCA dinghy at SSPA Sweden AB in 2014 [21], provided the necessary information regarding at which full-scale apparent wind speed the ILCA 7 starts to plane. The full-scale apparent wind speed for the strong wind case was, therefore, preliminary chosen to 7 m/s. However, before this speed could be chosen definitely, a *speed test* had to be carried out to ensure that there would be no risk of structural damage to neither the mast model nor to the sail model, with this strong wind speed. Furthermore, with the acquired information regarding the limitations of the load-cells, inside the wind tunnel balance, which was presented in Table 2.4, a quick calculation of the estimated forces with the preliminary apparent wind speed for the strong wind case, showed that none of the load cells inside the wind tunnel balance would be at any risk during the strong wind tests.

Variables

The variables that were chosen for the downwind analysis of the MKII sail in the wind tunnel tests, except for the trim controls, the outhaul and the cunningham, are illustrated in Fig. 4.1 & Fig. 4.2; in Table 4.1 & Table 4.2, all variables, including the outhaul and the cunningham, are presented for the light wind condition and the strong wind condition, respectively. The outhaul and the cunningham are defined as "floating", which means that they were adjusted continuously for each separate configuration of the other variables. It should also be mentioned that the sheet angle is defined as the angle between the centerline of the hull and the boom.

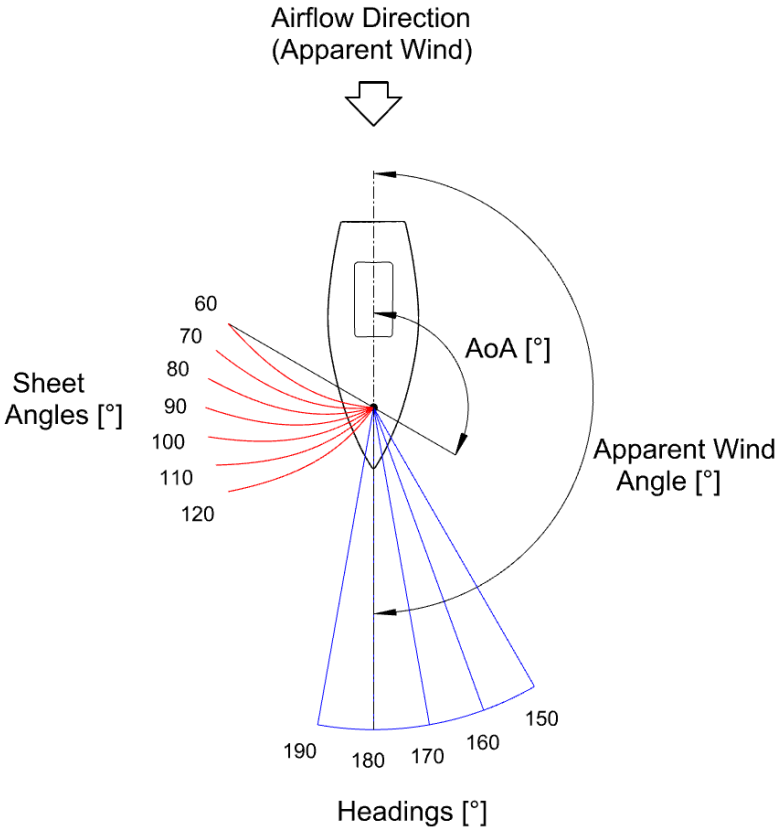

Figure 4.1: The figure shows a top view of the ILCA 7 dinghy and the five different headings ψ and the seven different sheet angles δ for the downwind analysis of the MKII sail, as well as the direction of the airflow in the wind tunnel, i.e. the apparent wind, the apparent wind angle and the angle of attack.

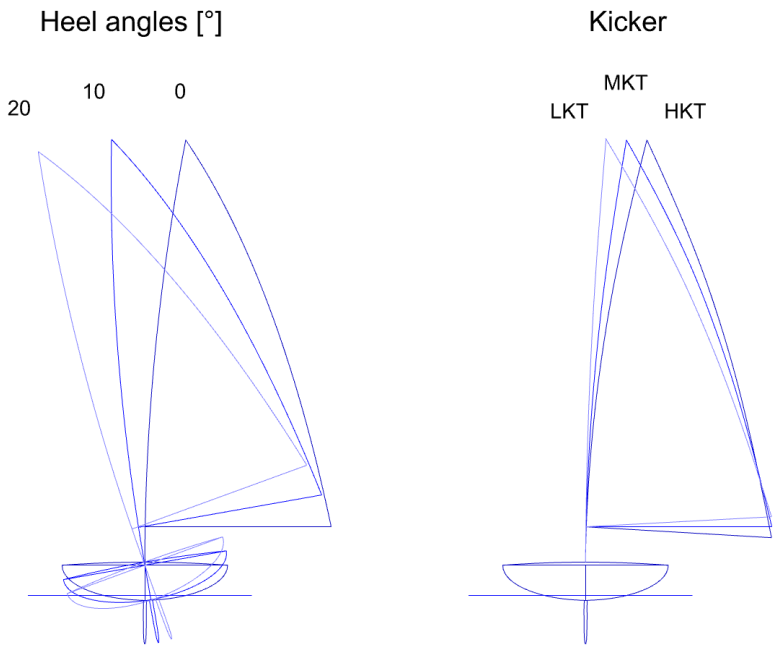

Figure 4.2: The illustrations show the three different heel angles ϕ and three different settings with the kicker that the sail model was tested for in the wind tunnel tests, where LKT, MKT and HKT, stands for Light Kicker Trim, Medium Kicker Trim and Hard Kicker Trim, respectively.

Table 4.1: Variables for the downwind analysis of the MKII sail, for the light wind condition, where LKT, MKT and HKT, stands for Light Kicker Trim, Medium Kicker Trim and Hard Kicker Trim, respectively.

Apparent wind speed [m/s]				10.6			
Heading (ψ) [°]		150	160	170	180	190	
Heel angle (ϕ) [°]			0	10	20		
Sheet angle (δ) [°]	60	70	80	90	100	110	120
Kicker			LKT	MKT	HKT		
Outhaul				Floating			
Cunningham				Floating			

Table 4.2: Variables for the downwind analysis of the MKII sail, for the strong wind condition, where LKT, MKT and HKT, stands for Light Kicker Trim, Medium Kicker Trim and Hard Kicker Trim, respectively.

Apparent wind speed [m/s]		18.5		
Heading (ψ) [°]		180		
Heel angle (ϕ) [°]		0		
Sheet angle (δ) [°]	60	70	80	90
Kicker	LKT	MKT		HKT
Outhaul		Floating		
Cunningham		Floating		

4.1.2 The Sail Prototype

The sail prototype is presented in Chapter 3.

4.1.3 The Mast Prototype

When trimming the sail, the sailor frequently flexes the mast by pulling the trim controls, the sheet, and the kicker; having a mast model with the same properties as the full-scale (prototype) mast when performing the wind tunnel tests was therefore very important.

4.1.4 Elemental Case for a Cantilever Beam

The full-scale ILCA 7 mast, as described in Chapter 3, consists of a *bottom section* and a *top section* that are connected by inserting the top section into the bottom section, with an overlap. Further, the *mast foot* of the full-scale mast bottom section is inserted into a cylinder-shaped cavity in the deck and is free to rotate but "fixed" vertically by a security line. The mast is thus kept in place even though the dinghy capsizes and is turned upside-down. Theoretically, the mast therefore only has one degree of freedom, i.e. horizontal rotation around the principal z-axis. The suitable elemental case for the ILCA 7 mast, being subjected to flexing, was that of a cantilever beam in straight flexing.
When the sailor uses the trim controls, the *sheet* and the *kicker*, the leech of the sail is stretched and the mast is flexed backward. Since these trim controls are the ones that mainly causes the strains in the sail, the load on the mast can therefore be approximated with a point load at the top of the mast top section where the leech ends. The appropriate

elemental cases of cantilever beams for calculation of the *angle change* θ and the *displacement* δ, are case 1 and case 2 in Table 32.1, in [14]. These elemental cases were illustrated in Fig. 2.16 and the expressions for calculating the angle change θ and the displacement δ were defined in Eq. (2.56) - (2.67). Small deformations were assumed and the ILCA 7 dinghy mast was regarded as a circular tube-shaped cantilever beam, with a fixed end at the deck surface and a free end to deflect, at the top of the mast.

Fig.4.3 below shows four illustrations of the ILCA 7 mast. The first illustration shows the combined mast, the deck surface, and the point load P. The second illustration, shows a section cut, along the whole length of the combined mast, and exposes the overlap. In the same illustration the mast foot, the overlap, the bottom section, and the top section are defined, as well as three cuts, i.e. *cut 1, cut 2* and *cut 3* and the point load P. In the third illustration, the individual lengths of the mast foot, the overlap, the bottom section, and the top section are defined as: $L_{mast\,foot}$, $L_{overlap}$, $L_{bottom\,section}$ and $L_{top\,section}$, respectively. Finally, the fourth illustration shows the free body diagram, with the three separate parts *1, 3* and *2*; their individual lengths L_1, L_3 and L_2, which respectively are defined in Eq. (4.1) - (4.3). The free-body diagram also shows the forces P, R and Q, on the left edge of each part and the moments M_1 *and* M_3.

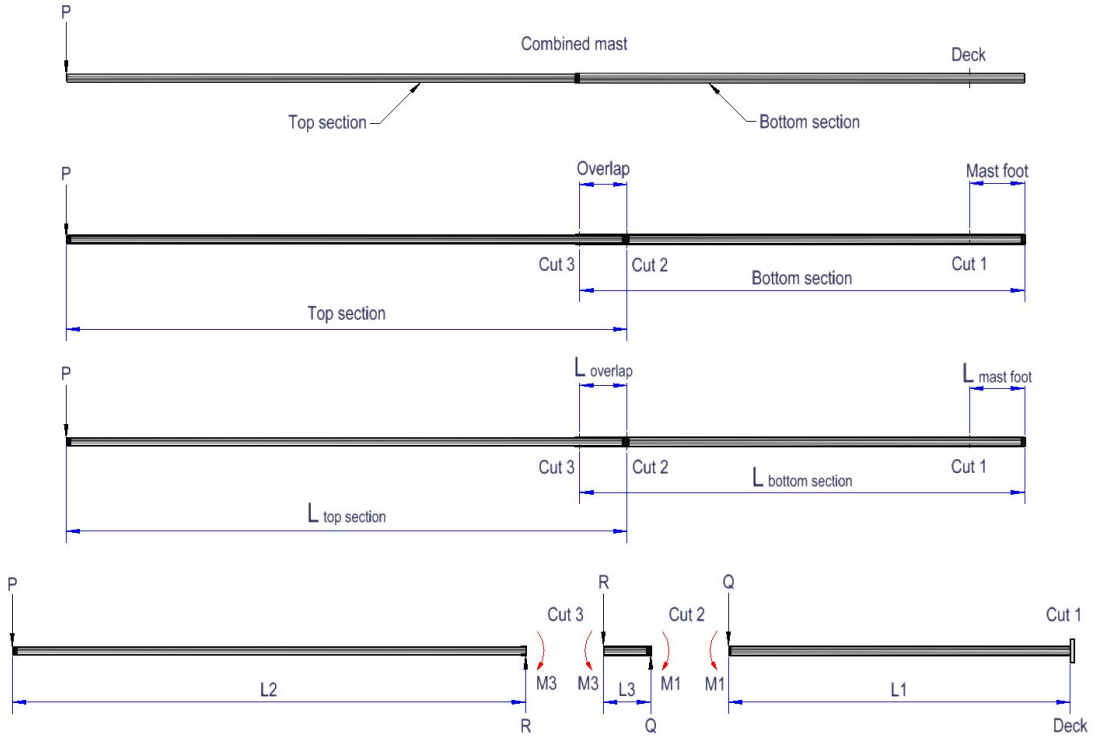

Figure 4.3: The free body diagram illustrates the combined mast and the different defined lengths of the mast foot, the overlap and the two sections, the point load P, the internal reaction forces and moments over the cuts.

The lengths of the different parts of the mast in Fig. 4.3 are defined as:

$$L_1 = L_{bottom\,section} - L_{mast\,foot} - L_{overlap} \tag{4.1}$$

$$L_3 = L_{overlap} \tag{4.2}$$

$$L_2 = L_{top\,section} - L_{overlap} \tag{4.3}$$

To calculate the angle change θ and the displacement δ of the three lengths of the mast, i.e. L_1, L_3 and L_2, defined in Eq. (4.1) - (4.3), the forces and moments first have to be defined. By analyzing the equilibrium of the forces and moments over cut 2 and cut 3, in the free body diagram, in Fig. 4.3, the appropriate formulas for the angle change and displacement with elemental cases could be found. Starting from left, at the free end of the mast, the equilibrium of forces and moments over cut 3 require that:

$$\uparrow: R - P = 0 \tag{4.4}$$

$$\circlearrowleft: M_3 - P\,L_2 = 0 \tag{4.5}$$

and equilibrium of forces and moments over cut 2 require that:

$$\uparrow: Q - R = 0 \tag{4.6}$$

$$\circlearrowleft: M_1 - M_3 - R\,L_3 = 0 \tag{4.7}$$

Eq. (4.4) & Eq. (4.6) define the forces:

$$R = P = Q \tag{4.8}$$

Inserting Eq. (4.5) & Eq. (4.8) in Eq. (4.7) define the moment over cut 2:

$$M_1 = P\,(L_3 + L_2) \tag{4.9}$$

and rewriting Eq. (4.5) we define the moment over cut 3:

$$M_3 = P\,L_2 \tag{4.10}$$

Where P is the point load N, at the top of the mast.

The section cuts of the full-scale tube-shaped mast sections were illustrated in Fig. 2.17, in Chapter 2, where a_1 and b_1 are the outer and inner radius of the mast bottom section; a_2 and b_2 are the outer and inner radius of the mast top section, respectively.
In Eq. (4.11) - (4.13), expressions for the calculation of the *area moment of inertia* of the mast bottom section, the mast top sections and the combined area moment of inertia for the whole mast are presented:

$$I_1 = \frac{\pi\, a_1^4}{4} - \frac{\pi\, b_1^4}{4} \tag{4.11}$$

$$I_2 = \frac{\pi\, a_2^4}{4} - \frac{\pi\, b_2^4}{4} \tag{4.12}$$

$$I_3 = I_1 + I_2 \tag{4.13}$$

where a and b are the outer and inner radius, respectively and the subscripts 1, 2, 3 represents the bottom section, the top section, and the sum of the area moment of inertia for the bottom section and the top section (the combined mast), respectively.

With the Young's modulus E and the calculated area moments of inertia I in Eq. (4.11) - (4.13) the *flexural rigidity* EI were calculated for the bottom section, the top section and the whole mast, respectively:

$$E\, I_1 \tag{4.14}$$

$$E\, I_2 \tag{4.15}$$

$$E\, I_3 \tag{4.16}$$

With the defined lengths in Eq. (4.1) - (4.3), the calculated moments in Eq. 4.9 & 4.10 and the calculated flexural rigidity for the bottom section, the whole mast and the top section, in Eq. (4.14) - (4.16), respectively, the angle change θ and the displacement δ of each part could be calculated with the two elemental cases Eq. (2.60) & Eq. (2.61) for the point load P and Eq. (2.66) & Eq. (2.67) for the contribution of the moments, due to the inner reactions, i.e.

$$\theta\,(\alpha) = \frac{P\, L^2}{2\, E\, I}\,\beta^2 \tag{4.17}$$

$$\delta\,(\alpha) = \frac{P\, L^3}{3\, E\, I}\,\beta^3 \tag{4.18}$$

$$\theta(\alpha) = \frac{M\,L}{E\,I}\,\beta \tag{4.19}$$

$$\delta(\alpha) = \frac{M\,L^2}{2\,E\,I}\,\beta^2 \tag{4.20}$$

This because, with the point load P on the free end of the top section, the relative distance from the point load P to the free end therefore was zero, i.e. $\alpha = 0$ and the relative distance, from the point load P to the fix end was one, i.e. $\beta = 1$. See Fig. 2.16 for the definition of the relative lengths α and β. Since the angle change and the displacement were searched for at the left edge of each separate part, the dimensionless position parameter $\xi = \alpha = 0$. With the numerical values inserted in Eq. (4.17) - (4.20), these can be rewritten as:

$$\theta(\alpha) = \frac{P\,L^2}{2\,E\,I} \tag{4.21}$$

$$\delta(\alpha) = \frac{P\,L^3}{3\,E\,I} \tag{4.22}$$

$$\theta(\alpha) = \frac{M\,L}{E\,I} \tag{4.23}$$

$$\delta(\alpha) = \frac{M\,L^2}{2\,E\,I} \tag{4.24}$$

Combining Eq. (4.21) - Eq. (4.24) and inserting the appropriate lengths and area moment of inertia for each part and the moments, resulted in Eq. (4.25) - Eq. (4.31), that were used for the calculations of the angle changes and the displacements:

$$\theta_1 = \frac{P\,L_1^2}{2\,E\,I_1} + \frac{M_1\,L_1}{E\,I_1} \tag{4.25}$$

$$\delta_1 = \frac{P\,L_1^3}{3\,E\,I_1} + \frac{M_1\,L_1^2}{2\,E\,I_1} \tag{4.26}$$

$$\theta_3 = \frac{P\,L_3^2}{2\,E\,I_3} + \frac{M_3\,L_3}{E\,I_3} + \theta_1 \tag{4.27}$$

$$\delta_3 = \frac{P\,L_3^3}{3\,E\,I_3} + \frac{M_3\,L_3^2}{2\,E\,I_3} \tag{4.28}$$

$$\delta_2 = \frac{P\,L_2^3}{3\,E\,I_2} \tag{4.29}$$

$$\delta_{joint} = \delta_1 + \delta_3 + L_3 \sin(\theta_1) \tag{4.30}$$

$$\delta_{top} = \delta_1 + \delta_3 + \delta_2 + L_2 \sin(\theta_3) \tag{4.31}$$

θ_1 and δ_1 is the angle change and the displacement of the joint at cut 2; θ_3 and δ_3 is the angle change and the displacement of the overlap; δ_2 is the displacement of the top section; δ_{joint} is the displacement of the joint at cut 3; δ_{top} is the total displacement at the top of the mast. The displacement contributions $L3\sin(\theta_1)$ & $L2\sin(\theta_3)$ is added due to the rotation of the overlap and the top section at cut 2 and cut 3, respectively.

4.1.5 Scaling

Dynamic similarity require that kinematic similarity exist, which in its turn, require that geometric similarity exist. Dynamic similarity therefore require that the force coefficients are equal in both scales, which they are if the dimensionless Reynolds number are same in both scales. This is showed in Eq. (2.48).

Assumptions: All three similarities presented in Chapter 2 are satisfied, i.e.

1. Geometric similarity
   (a) Sail cloth stretching
   (b) Mast bend
2. Kinematic similarity
3. Dynamic similarity

The sailcloth is considered as a thin membrane and its thickness is therefore not scaled with the linear length scale factor. Further, the Reynolds number Re is assumed constant for both the kinematic similarity and the dynamic similarity.

Sail Cloth Stretching

The requirements for having the same sail shape in both scales are that the strain in both scales are equal, in other words, the deformation of the sail under load has to be dimensionless.

Assumption: Equal strain

$$\varepsilon_m = \varepsilon_p \tag{4.32}$$

In Chapter 2, *Hooke's Law* was defined as:

$$\sigma = E\,\varepsilon \tag{4.33}$$

which can be rearranged to define the strain ε:

$$\varepsilon = \frac{\sigma}{E} \tag{4.34}$$

The stress σ at any cut of length Δc through the sail:

$$\sigma = \frac{F}{\Delta c\, t} \tag{4.35}$$

where F is the force on the cut and t is the thickness. Inserting Eq. (4.35) in Eq. (4.34), we get:

$$\varepsilon = \frac{F}{E\,\Delta c\, t} \tag{4.36}$$

Combining Eq. (4.32) & Eq. (4.36) and inserting the appropriate scale factors for the force F, the flexural rigidity E, the length L and the thickness t, we get:

$$\varepsilon_m = \frac{F_m}{E_m\,\Delta c_m\, t_m} = \frac{\alpha_F\, F_p}{\alpha_E\, E_p\, \alpha_L\, \Delta c_p\, \alpha_t\, t_p} \tag{4.37}$$

where α_F is the force scale factor, α_E is the elastic scale factor for the flexural rigidity, α_L is the linear length scale factor, defined in Eq. (2.39) and α_t is the thickness scale factor.

Accepting the small difference between the Reynolds number in both scales, the density ratio in Eq. (2.49) can be approximated with $\rho_p/\rho_m \approx 1$; the scale law be re-written as:

$$\frac{F_p}{F_m} = \left(\frac{V_p}{V_m}\right)^2 \left(\frac{L_p}{L_m}\right)^2 \tag{4.38}$$

and by replacing each term in Eq. (4.38) with its corresponding scale factor we get:

$$\frac{1}{\alpha_F} = \left(\frac{1}{\alpha_V}\right)^2 \left(\frac{1}{\alpha_L}\right)^2 \tag{4.39}$$

which can be simplified to:

$$\alpha_F = \alpha_V^2 \, \alpha_L^2 \tag{4.40}$$

where α_V is the velocity scale factor, defined earlier in Eq. (2.41).

Inserting Eq. (4.40) in Eq. (4.37) we get:

$$\varepsilon_m = \frac{\alpha_V^2 \, \alpha_L^2}{\alpha_E \, \alpha_L \, \alpha_t} \, \varepsilon_p \tag{4.41}$$

Performing some cancellation, Eq. (4.41) can be simplified:

$$\varepsilon_m = \frac{\alpha_V^2 \, \alpha_L}{\alpha_E \, \alpha_t} \, \varepsilon_p \tag{4.42}$$

and for equal strain:

$$\frac{\alpha_V^2 \, \alpha_L}{\alpha_E \, \alpha_t} = 1 \tag{4.43}$$

The condition of equal strain in both scales are satisfied for: $\alpha_E = 1$, $\alpha_t = 1$, $\alpha_V = \sqrt{7}$ and $\alpha_L = 1/7$.

Mast Bend

In Fig. 2.16 it could be seen that the angle change θ and the displacement δ are defined as functions of ξ, i.e. $\theta(\xi)$ and $\delta(\xi)$ where ξ is a dimensionless position indicator used solely to define the position where it is desired to calculate the angle change and the displacement. In Eq. (4.25) & Eq. (4.26), respectively, the appropriate expressions for the calculation of the angle change and the displacement of the joint at cut 2 were presented; below it will be shown how these are scaled. The angle change and the displacement at the other cuts are scaled similarly and are therefore not presented.

Angle Change θ

By inserting Eq. (4.9) in Eq. (4.25), we get the simplified general expression for the angle change θ at cut 2, due to the point load P:

$$\theta_1 = \frac{P \, L_1^2}{2 \, E \, I_1} + \frac{P \, (L_3 + L_2) \, L_1}{E \, I_1} \tag{4.44}$$

Defining the angle change θ at cut 2 in both scales:

$$\theta_{1_m} = \theta_{1_p} \tag{4.45}$$

Inserting Eq. (4.44) in Eq. (4.45), for both scales:

$$\left[\frac{P\,L_1^2}{2\,E\,I_1} + \frac{P(L_3 + L_2)L_1}{E\,I_1}\right]_m = \left[\frac{P\,L_1^2}{2\,E\,I_1} + \frac{P(L_3 + L_2)L_1}{E\,I_1}\right]_p \tag{4.46}$$

Simplifying the terms within the square brackets in Eq. (4.46):

$$\left[\frac{P\,L_1^2}{E\,I_1}\left(\frac{1}{2} + \frac{L_3 + L_2}{L_1}\right)\right]_m = \left[\frac{P\,L_1^2}{E\,I_1}\left(\frac{1}{2} + \frac{L_3 + L_2}{L_1}\right)\right]_p \tag{4.47}$$

and since:

$$\left(\frac{L_3 + L_2}{L_1}\right)_m = \left(\frac{L_3 + L_2}{L_1}\right)_p$$

Eq. (4.47) can be simplified:

$$\left(\frac{P\,L_1^2}{E\,I}\right)_m = \left(\frac{P\,L_1^2}{E\,I}\right)_p \tag{4.48}$$

The force scale factor α_F was defined in Eq. (4.39) and since P in Eq. (4.48) represent force, the corresponding scale factor to each parameter in the term on the left side of the equal sign in Eq. (4.48) are inserted, which gives:

$$\frac{\alpha_L^2\,\alpha_V^2\,P_p\,\alpha_L^2\,L_{1_p}^2}{\alpha_{EI}\,E\,I_p} = \frac{P_p\,L_{1_p}^2}{E\,I_p} \tag{4.49}$$

Performing some cancellation, Eq. (4.49) can be simplified:

$$\frac{\alpha_L^4\,\alpha_V^2}{\alpha_{EI}} = 1 \tag{4.50}$$

Deflection δ

By inserting Eq. (4.9) in Eq. (4.26), we get the simplified general expression for the displacement δ at cut 2, due to the point load P:

$$\delta_1 = \frac{P\,L_1^3}{3\,E\,I_1} + \frac{P\,(L_3 + L_2)\,L_1^2}{2\,E\,I_1} \tag{4.51}$$

Defining the displacement δ at cut 2 in both scales:

$$\frac{1}{\alpha_L}\,\delta_{1_m} \;=\; \delta_{1_p} \tag{4.52}$$

Inserting Eq. (4.51) in Eq. (4.52), for both scales:

$$\frac{1}{\alpha_L}\left[\frac{P\,L_1^3}{3\,E\,I_1} + \frac{P(L_3 + L_2)L_1^2}{2\,E\,I_1}\right]_m = \left[\frac{P\,L_1^3}{3\,E\,I_1} + \frac{P(L_3 + L_2)L_1^2}{2\,E\,I_1}\right]_p \tag{4.53}$$

where the subscript 1 in L_1 and EI_1 represent the bottom section for the length L and the flexural rigidity EI, respectively. Simplifying the terms within the square brackets in Eq. (4.53), we get:

$$\frac{1}{\alpha_L}\left[\frac{P\,L_1^3}{E\,I_1}\left(\frac{1}{3} + \frac{\frac{L_3+L_2}{L_1}}{2}\right)\right]_m = \left[\frac{P\,L_1^3}{E\,I_1}\left(\frac{1}{3} + \frac{\frac{L_3+L_2}{L_1}}{2}\right)\right]_p \tag{4.54}$$

and since:

$$\left(\frac{L_3 + L_2}{L_1}\right)_m = \left(\frac{L_3 + L_2}{L_1}\right)_p$$

Eq. (4.54) can be simplified:

$$\frac{1}{\alpha_L}\left(\frac{P\,L_1^3}{E\,I_1}\right)_m = \left(\frac{P\,L_1^3}{E\,I_1}\right)_p \tag{4.55}$$

The force scale factor α_F was defined in Eq. (4.39) and since P in Eq. (4.55) represent force, the corresponding scale factors to each parameter in the term on the left side of the equal sign in Eq. (4.55) are inserted, which gives:

$$\frac{1}{\alpha_L}\,\frac{\alpha_L^2\,\alpha_V^2\,P_p\,\alpha_L^3\,L_{1_p}^3}{\alpha_{EI}\,E\,I_p} \;=\; \frac{P_p\,L_{1_p}^3}{E\,I_p} \tag{4.56}$$

where α_{EI} is the scale factor for the flexural rigidity. Performing some cancellation, Eq. (4.56) can be simplified:

$$\frac{\alpha_L^4\,\alpha_V^2}{\alpha_{EI}} \;=\; 1 \tag{4.57}$$

which is, and should be, the same result that was received for the angle change θ in Eq. (4.50).

4.1.6 The Sail Model

By choosing the linear length scale factor $\alpha_L = 1/7$ and the velocity scale factor $\alpha_V = \sqrt{7}$, Eq. (4.50) showed that it was possible to receive equal strain in both scales with a full-scale thickness for the sail model cloth. A new MKII sail was therefore purchased and delivered to North Sails in Gothenburg who manufactured the sail model.

4.1.7 The Mast Model

Scaling the Flexural Rigidity

It was decided that a solid circular rod of stainless steel, should be used for the mast model and that it should be manufactured in one single piece. However, since the mast prototype has two separate sections, the mast model should have two sections with different radii, that represented the mast bottom section and the mast top section.

The flexural rigidity should be scaled as:

$$(E\,I_i)_m \;=\; \alpha_{EI}\;(E\,I_i)_p \tag{4.58}$$

where the subscript $i = 1,\ 2,\ 3$ respectively represent the bottom section, the top section and the combined mast.

Rearranging either Eq. (4.50) or Eq. (4.57), which both expresses the ratio between the product of the linear length scale factor, with the power of four and the velocity scale factor, with the power of two and the scale factor for the flexural rigidity; inserting numerical values for the chosen linear length scale factor α_L and velocity scale factor α_V, a numerical value of the scale factor for the flexural rigidity is received:

$$\alpha_{EI} \;=\; \alpha_L^4\,\alpha_V^2 \;=\; \left(\frac{1}{7}\right)^4 \left(\sqrt{7}\right)^2 \;=\; 0.002915 \tag{4.59}$$

The flexural rigidity for the mast model should thus only constitute approximately 0.3 % of the flexural rigidity of the mast prototype.

Combining Eq. (4.58) & Eq. (4.59) we get:

$$(E\,I_i)_m \;=\; 0.002915\;(E\,I_i)_p \tag{4.60}$$

which was used for calculating the flexural rigidity for the two mast model sections.

The Radii of the Mast Model

To calculate the two different radii of the mast model sections, the LHS of Eq. (4.60) is developed and divided with the Young's Modulus of the mast model E_m; then combined with Eq. (2.71), which is the expression for the area moment of inertia, of a beam with a solid cross-section and radius a:

$$\frac{E_m\, I_{m_i}}{E_m} \;=\; \frac{\pi\, a_{m_i}^4}{4} \tag{4.61}$$

Rearranging Eq. (4.61) we get:

$$a_{m_i} \;=\; \left(\frac{4\, E_m\, I_{m_i}}{\pi\, E_m}\right)^{(1/4)} \tag{4.62}$$

where a_{m_i} is the radius for the two different sections of the mast model and the subscript $i = 1,\, 2$ represent the bottom section and the top section, respectively.

The stainless steel, that was chosen for the mast model, that would give a properly scaled mast bend, had a Young's modulus of $E_m \;=\; 196$ GPa. Material was purchased and the mast model was manufactured by personnel in the mechanical workshop at SSPA. The data for the mast model can be seen in Table 5.10.

Flexural Tests

In the prephase, it was decided that experimental flexing tests should be carried out to analyze and compare the displacement curve of the mast prototype, i.e. the full-scale ILCA 7 mast with a theoretical approach, with a elemental case for a cantilever beam, that was described in the text above. To receive the displacement curve of the full-scale ILCA 7 mast under load, 5 separate flexural tests were carried out. For the tests, 4 complete aluminum masts (4 bottom sections and 4 top sections) were borrowed from one of the Swedish elite ILCA 7 dinghy sailors at GKSS, in Gothenburg. Officially all bottom sections and top sections should have the same weight, but since it was known that some variations existed, each section was control weighted before choosing one of the bottom sections and one of the top sections that should be used for the 5 separate tests. In the flexural tests, which is illustrated in Fig. 4.4, the combined mast was subjected to a point load on 4 different positions along the length of the mast. A rigid mounting bracket in wood, with the same length as the mast foot, was manufactured for the tests. The combined mast was inserted in the mounting bracket, and the distance between the unloaded mast and the floor was measured, at the four x-positions, which were marked on the floor. Then a second measurement was carried out when the mast was under load. The difference between the two test series, i.e. the unloaded test series and the loaded test series gave the displacement curve. The procedure was repeated 5 times which resulted in a matrix, which is presented in Table 5.8, where also the 4 loading points can be seen, and the calculated average value of the displacements at the loading points, from the 5 tests. The displacement curve from the experimental flexural tests is presented in Fig. 5.37, in Chapter 5 where they are compared to the theoretical approach. Note that in this project the theoretical method, with a single point load in the top of the mast was used for the scaling and the calculation of the radius for the mast model.

Figure 4.4: Flexural tests of the ILCA 7 mast, for the analysis of the displacement curve.

4.1.8 The Boom Model

An image of the boom and the corresponding data for the full-scale ILCA boom, was presented in Fig. 3.5 and Table 3.2, respectively. The boom model was not scaled exactly, because its influence on the shape of the sail model was negligible compared to a properly scaled mast model. However, the radius that was chosen was very close to what a properly scaled radius for the boom model would have been. Further, the length of the boom model was slightly longer; the reason for this was completely practical and necessary to be able to mount the trim control, the outhaul, at the free end of the boom model.

4.1.9 Scale Effects

As mentioned in Chapter 2, when one speaks of scale effects it is commonly the dimensionless Reynolds number Re, defined in Eq. (2.43), that not has been scaled properly, which means that the dimensionless force coefficient C_F not is same in both scales.

Analyzing the Reynolds number in both scales, we have:

$$Re_m = \frac{\rho_m V_m L_m}{\mu_m} = \frac{\rho_p \alpha_V V_p \alpha_L L_p}{\mu_p} = \alpha_V \alpha_L Re_p \tag{4.63}$$

because $\rho_m \approx \rho_p$ and $\mu_m \approx \mu_p$. Eq. (4.63) can be rewritten:

$$Re_m \approx \alpha_V \alpha_L Re_p \tag{4.64}$$

Inserting numerical values for the velocity scale factor and the linear length scale factor, we get:

$$Re_m = \sqrt{7}\,\frac{1}{7} \approx 0.38\,Re_p \tag{4.65}$$

The fact that the model scale Reynolds number only is 38% of that at full scale means that the boundary layer will be relatively thicker at model scale, but since the thickness (and friction) depends on the Reynolds number to the 1/5th power [19], the effect is very small. It will cause a slightly larger frictional drag coefficient and a very small difference in lift due to different displacement thicknesses. However, friction contributes very little to the drag in this investigation, because of the large fix separation at the sail edges. The total effect of the difference in Reynolds number is therefore so small that it is neglected in the following. In Eq. (4.68) the turbulent boundary thickness dependence of the Reynolds number is even smaller than in [19], i.e. to the 1/7th power.

Geometrical Differences

Even though the sail model was properly scaled and manufactured by sail makers at North Sails in Gothenburg, some geometrical differences could not be avoided. The cloth for the sail model was, as previously mentioned, cut from a brand-new full-scale MKII sail and the sailmakers strived to scale most of the small details that are mounted on a full-scale MKII sail. An example of geometrical differences is when it is practically impossible to scale all these small details, which gives a too high surface roughness. Examples of details that are hard to scale properly are:

- The fiber structure of the cloth
- Tell-tails
- Eyelets
- Overlapping panels
- Stitches from the sail thread

Since the new MKII sail is of bi-radial design, which has a larger amount of overlapping panels and therefore also more stitches than the old cross-cut MKI sail, the surface roughness in the new MKII sail is consequently larger. To get the sail model as accurate as possible, the width of the overlapping panels was also scaled and because of this straight stitches had to be used instead of the usual zigzag stitches. The window in the full-scaled sail was also deselected, since it should not influence the performance, according to the sailmakers at North Sails. Further, instead of a traditional eyelet, which the full-scale sail has, the sail model was equipped with thin U-shaped sailcloth where the trim control, the cunningham could be mounted.

4.2 Wind Tunnel Equipment

In this section, the design, manufacturing, and installation of the necessary wind tunnel equipment are presented.

4.2.1 Design and Manufacture of the Mounting Bracket

The ILCA mast is inserted in a sleeve along the luff of the sail and the boom is attached to the mast. To hold the mast model, the boom model, and the sail model in the desired position during the tests, a mounting bracket was necessary to have. Even though the wind tunnel facility had several different mounting brackets, all of them were designed so that the mast model and the sail model only could have been tested for an upright sailing condition; since two heel angles were of great interest, beyond the upright sailing condition, it was necessary to design and manufacture a custom made mounting bracket that could be used for both the upright sailing condition and the two heeled sailing conditions. Further, the mounting bracket had to be rigid enough to transfer the correct forces and moments to the balance and not flex or deform during the tests.

In wind tunnel tests with symmetrical test objects, where the test section is of the semi-closed design, such as Chalmers wind tunnel, the test object is preferably positioned centrally, somewhere on the vertical xz-plane in the test section. This for the flow to be symmetric around the model and to avoid blockage effects, which otherwise can arise if the model is positioned closer to one of the lateral boundaries, causing an asymmetric flow around the model. The ILCA 7 sail has an asymmetric triangular geometry and the sail model, which should be tested for several sheet angles in downwind conditions, would expose more or less the whole sail area to the airflow, depending on the sheet angle. For the 90° sheet angle the ratio of the sail area to the cross-sectional area of the test section would be largest. The position of the model in the y-direction (orthogonal to the airflow) for the upright condition and for the two heeled conditions, would therefore differ and it was not obvious how to solve it at first. The natural solution was that the *aerodynamic center of effort CoE* should be in the center of the test section when testing the sail for both the upright sailing condition and for the two heeled conditions, with the 90° sheet angle, because, this was the sheet angle with the largest projected sail area. The mounting bracket was therefore designed so that the center of effort only would vary slightly in the z-direction when the sail model was tested for the different heel angles, which can be seen in Fig. 4.5.

A CAD model of the mounting bracket, which was modeled and manufactured by the author, can be seen in Fig. 4.6 below, where it is mounted on the wind tunnel balance. For the base structure of the mounting bracket, square steel tubes were welded together and for the three mast feet, solid square pieces of steel were chosen. The mast feet were cut with the angle that corresponded to each heel angle that should be investigated and were then welded to the base structure. The so-called "keyboard" is the position on board a sailboat where the majority of trim controls strategically are positioned, so they are easily accessible. The mounting bracket thus needed some sort of keyboard and this was manufactured in aluminum and mounted to the base structure of the mounting bracket with a screw joint. Fig. 4.6 also illustrates how the trim controls were connected to the mast model and the boom model and run from where they were attached, through blocks, mounted inside the base structure and out to the keyboard, where they could be controlled.

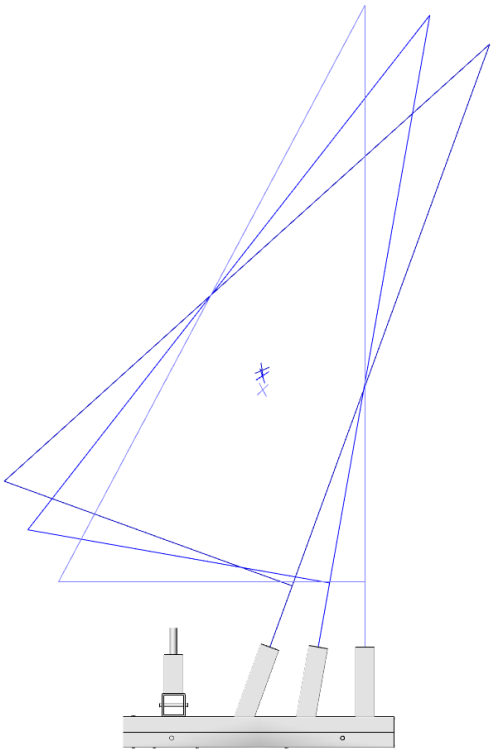

Figure 4.5: The image shows how the geometrical center of effort *CoE* in the sail model, only varies slightly in the z-direction, for the three heel angles, i.e. 0°, 10° and 20°.

When a new heel angle should be investigated, only a couple of the trim controls had to be untied and the mast model moved to the new mast foot, which made the testing procedure relatively smooth.

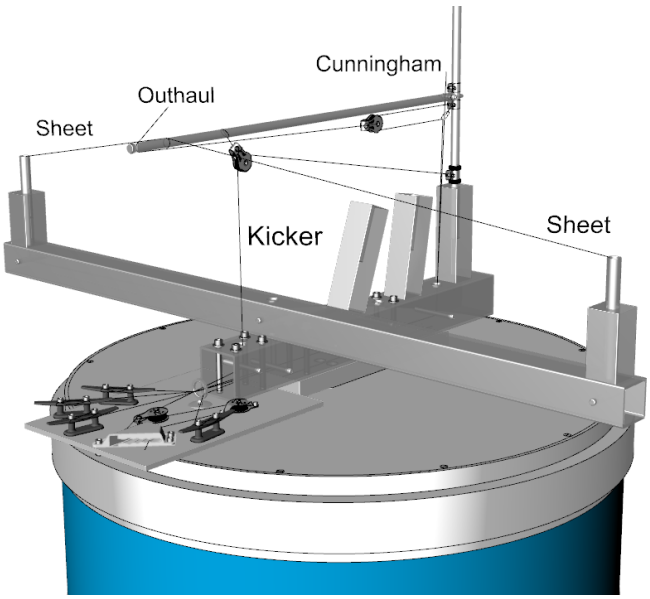

Figure 4.6: A CAD model of the manufactured mounting bracket, positioned on the wind tunnel balance. The trim controls and the other small equipment such as blocks and cleats are also shown.

4.2.2 Design and Manufacture of the Test Section Floor and the Aluminum Cover Plate

Analyzing model sails in Chalmers wind tunnel is not very common and as previously mentioned, the standard equipment for mounting the mast model, the boom model, and the sail model could not be used and had to be designed and manufactured for this project. This was also the case with the test section floor in plywood and an aluminum cover plate, mounted on top of the floor. The test section floor is positioned between the wind tunnel balance and the test objects in the test section. Because of this the mounting bracket, which is fixed to the balance and keeps the mast model and the sail model in position inside the test section during the tests, had to penetrate the wind tunnel floor. Since the mounting bracket also should be able to rotate freely when different headings ψ, which are presented in Table 4.1, should be investigated, a certain rotation pattern, which can be seen in Fig. 4.7 below, had to be plotted on the floor and milled. The rotation pattern had to be designed so that the mounting bracket also could be adjusted vertically, without touching the floor, to have the correct distance between the boom model and the test section floor, which represented the water surface during the tests. Having the correct distance between the test section floor (the water surface) and the boom model would ensure that the scale of the vortices created when the airflow on the pressure side of the sail model passed under the boom model to the suction side of the sail model was correct. Having as accurately scaled trailing vortices as possible would ensure that the contribution from the induced resistance was as accurate as possible.

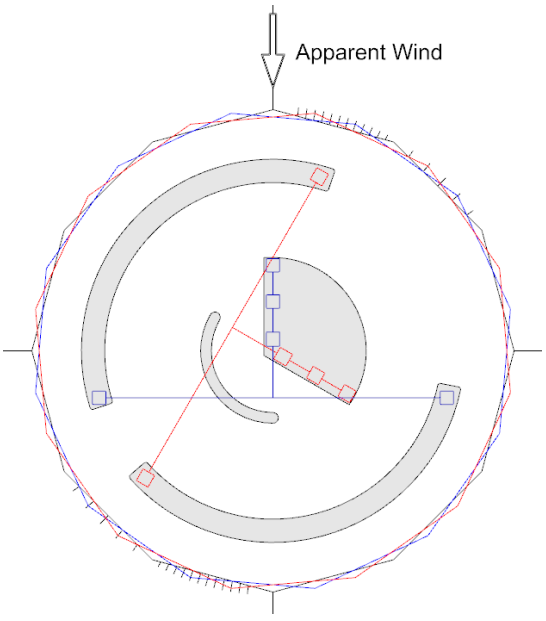

Figure 4.7: Top view of the rotation pattern that was milled in the test section floor for the align--ment of the sail model.

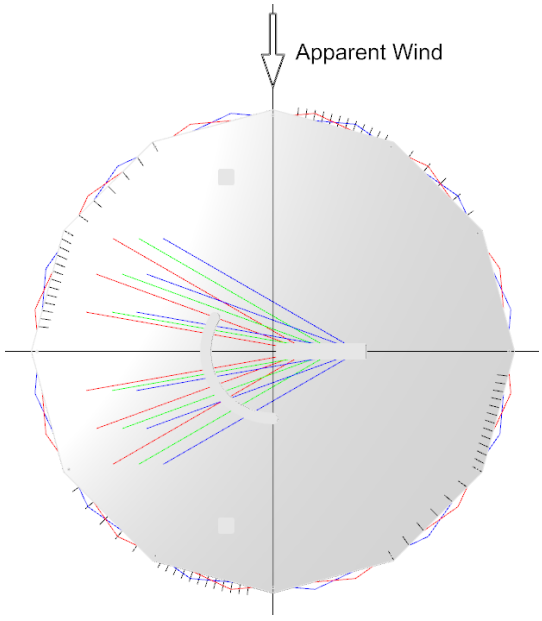

Figure 4.8: Top view of the aluminum plate that covered the rotation pattern in the floor and prevented leakage.

In Fig. 4.7 two colorized extreme positions of the mounting bracket can be seen, where the blue mounting bracket pattern, is aligned with the x-axis and the direction of the apparent wind; the red mounting bracket pattern is rotated 120° and represent a heading of 190° downwind. When the heading of 180° was tested, the red mounting bracket pattern was orthogonal to the apparent wind, and when the 150° heading was tested the red mounting

bracket pattern was rotated 60° anti-clockwise from the current heading in the figure. Further, the wavy pattern that surrounds the rotation pattern marks the edges of the 12-sided polygon aluminum plate, shown in Fig. 4.8, that was designed and manufactured to primarily cover the milled rotation cavities in the floor and prevent excessive leakage; secondarily to function as a scale for the different headings.

The centerline of the test section, and all balance angles and sheet angles, were plotted on the aluminum plate as well so that the aluminum plate correctly could be aligned with the headings as the balance was rotated and the boom correctly positioned at the desired sheet angle. The blue marks on the aluminum plate correspond to the sheet angles for the upright sailing condition and the green and the red marks correspond to the heel angles 10° and 20°, respectively. The aluminum plate, which was fixed to the floor with screws thus followed every rotation of the balance.

4.2.3 Installation of the Balance and the Mounting Bracket

As described earlier, Chalmers wind tunnel uses external balances for the measurement of forces and moments; in this project a 6-components wind tunnel balance with serial number: Y-603 from the *Aeronautical Defense Research Institution FFA* in Bromma, Sweden was used, Fig. 2.12. This balance allows a rotation of 360°, and has a circumferential scale for ocular reading. On the wind tunnel facility floor, under the test section, long rails that run parallel with the test section are fixed. On these rails two horizontal mounting plates for the balance are mounted (see Fig. 4.9) below. These can be raised and lowered, which makes it possible for the balance and the test object to be adjusted vertically in the test section. The rails also allow the balance and the model to be adjusted in the x-direction, along the test section. The balance was centered and fixed 1.5 meters downstream of the inlet of the test section. Fig. 4.9 also shows the mounting bracket, mounted on top of the balance.

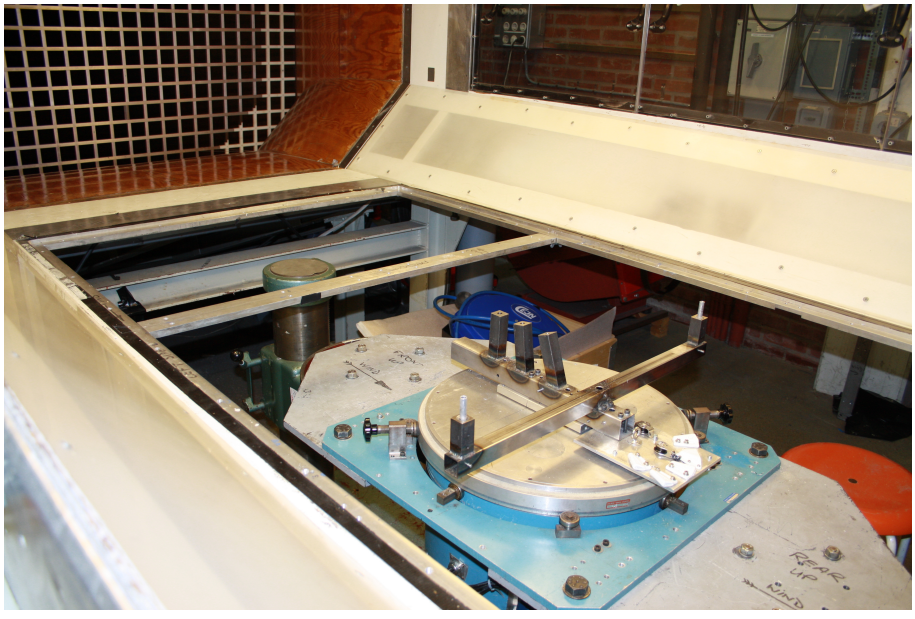

Figure 4.9: Installation of the wind tunnel balance and the mounting bracket in the test section.

4.2.4 Installation of the Pitot-Static Tube

As described earlier in Chapter 2, the Pitot-static tube is used for measurement of the total pressure and the static pressure, at the inlet of the test section. Fig. 4.10 below shows the round-nosed Pitot-static tube that was used in the project. Since a deviation of more than 9° against the airflow, could result in measurement error of the total pressure, the Pitot-static tube was carefully adjusted, so that the short part of the L-shaped tube was parallel to the airflow by aligning it with the horizontal metal frame around the wind tunnel floor, which should be reliable as reference, according to the wind tunnel personnel.

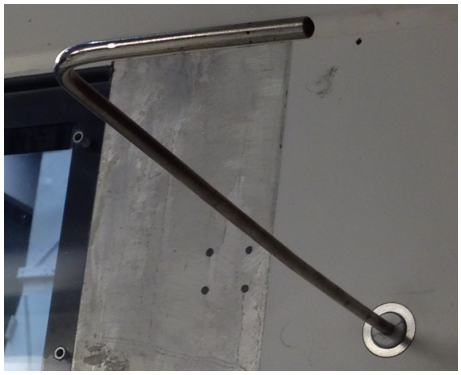

Figure 4.10: A picture of the round-nosed Pitot-static tube that was used for the measurements of the total and static pressure in the wind tunnel tests.

4.2.5 Installation of the Mast Model and the Sail Model

Fig. 4.11 below, illustrates how the mast model and the sail model were mounted in the mounting bracket, in the test section. In the particular picture, the upright sailing condition is shown.

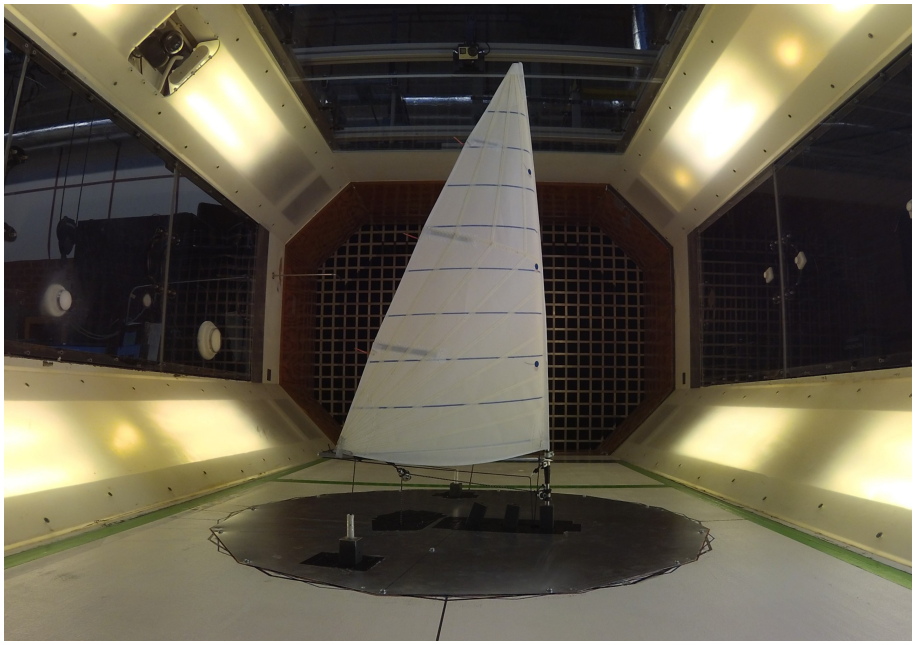

Figure 4.11: The mast model and the sail model mounted in the mounting bracket, inside the test section.

4.3 Experimental Tests

4.3.1 Trimming The Sail Model

The sail model was trimmed manually by pulling thin, static, and strong ropes from the "keyboard", which was described earlier and shown in Fig. 4.6. The manual trimming procedure made it however necessary to investigate the repeatability; repeatability tests were therefore performed after the actual tests, in order to investigate how much the sampled data deviated. How the repeatability tests were performed are described in the subsection "Repeatability Tests". An alternative to trim the sail manually would have been to make the trimming procedure more or less automatic. One could for instance have used small servo-engines, one for each trim control, but this would have required more allotted tunnel-time to prepare and fine-tune all instruments properly so that they pulled the particular trim control with high precision. Larger wind tunnels involved in professional sail design have more or less a fully automatic system, with servos connected to each trim control and an engine that rotates the floor under the model, which allows the lab engineers and sail designers to comfortably monitor and trim the sail from a separate control room.

The function of each trim control, *sheet, kicker, cunningham* and *outhaul* and their position, on the full-scale sail, were described, in Chapter 3. The importance of the possibility to alter the shape of the sail model exactly as on the full-scale sail has also been mentioned. Even though the positions of a couple of the trim controls on the full-scale sail were mounted slightly differently on the sail model, the possibility to alter the shape and trim the sail model more or less the same, was possible to achieve, except twisting the sail. How the trim controls are mounted on the full-scale sail could be seen in Fig. 3.6 and the same image is presented in Fig. 4.12 below, to easily view the difference of how the trim controls were mounted on the sail model and the mast model, which are shown in Fig. 4.13.

In Fig. 4.12 & Fig. 4.13 it can be seen that both the cunningham and the outhaul on the sail model are mounted exactly as on the prototype sail. The kicker, however, was moved further back and took over one of the sheets two major functions, namely that of pulling the boom downwards, which bends the mast, flattens the sail and "closes" the sail. The dual function of the full-scale sheet were thus separated and the model sheet was mounted so that it only rotated the boom and the sail around the z-axis; therefore only controlled the *angle of incidence* α. However, since the setting with the kicker was one of the variables that should be varied in three steps for each heading ψ and heel angle ϕ, it was not possible to practically position the sheet so that it rotated the boom perfectly and horizontally around the mast for all three settings with the kicker. For the first trim with the kicker, i.e. *light*, the free end of the boom model was positioned slightly higher than the position on the mounting bracket, where the sheet left the mounting bracket and therefore the sheet had a small angle at the first kicker trim. This angle decreased however when the other two kicker trims *medium* and *hard* were investigated, but the consequence was that some "slack" in the *leeward* sheet had to be tightened up and adjusted for each new setting with the kicker.

The reason for mounting the kicker further aft on the boom model was that it would require much less manual force when pulling it during the tests. It was previously mentioned that it was not possible to twist the sail model exactly as in full-scale since the sheet and kicker were mounted slightly differently on the model sail. However, since Chalmers wind tunnel does not have vertical turning vanes, that otherwise could have been used for creating

twisted flow, it was therefore not possible to create a twisted flow in the test section anyway and the importance of trimming the sail so that it received a proper twist was therefore not crucial.

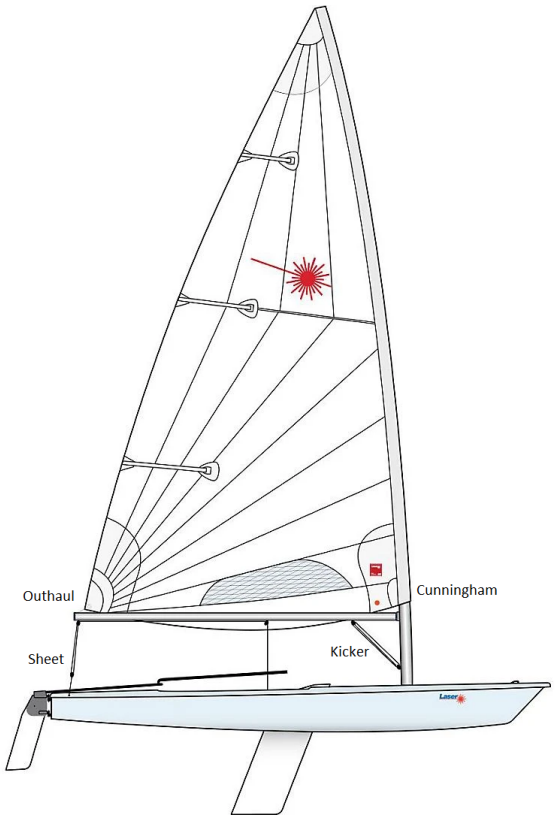

Figure 4.12: Trim controls on the full-scale sail.

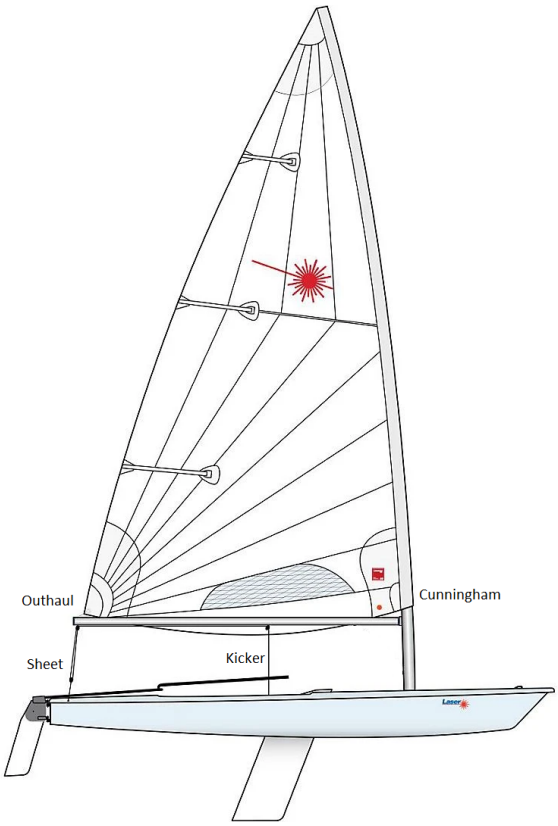

Figure 4.13: Trim controls on the sail model.

4.3.2 Test Procedure and Data Acquisition

The test procedure and data acquisition, for both the strong wind tests and the light wind tests, was carefully and methodically carried out, as illustrated in the flowchart in Fig. 4.14; the repeatability tests as illustrated in the flowchart, in Fig. 4.15.

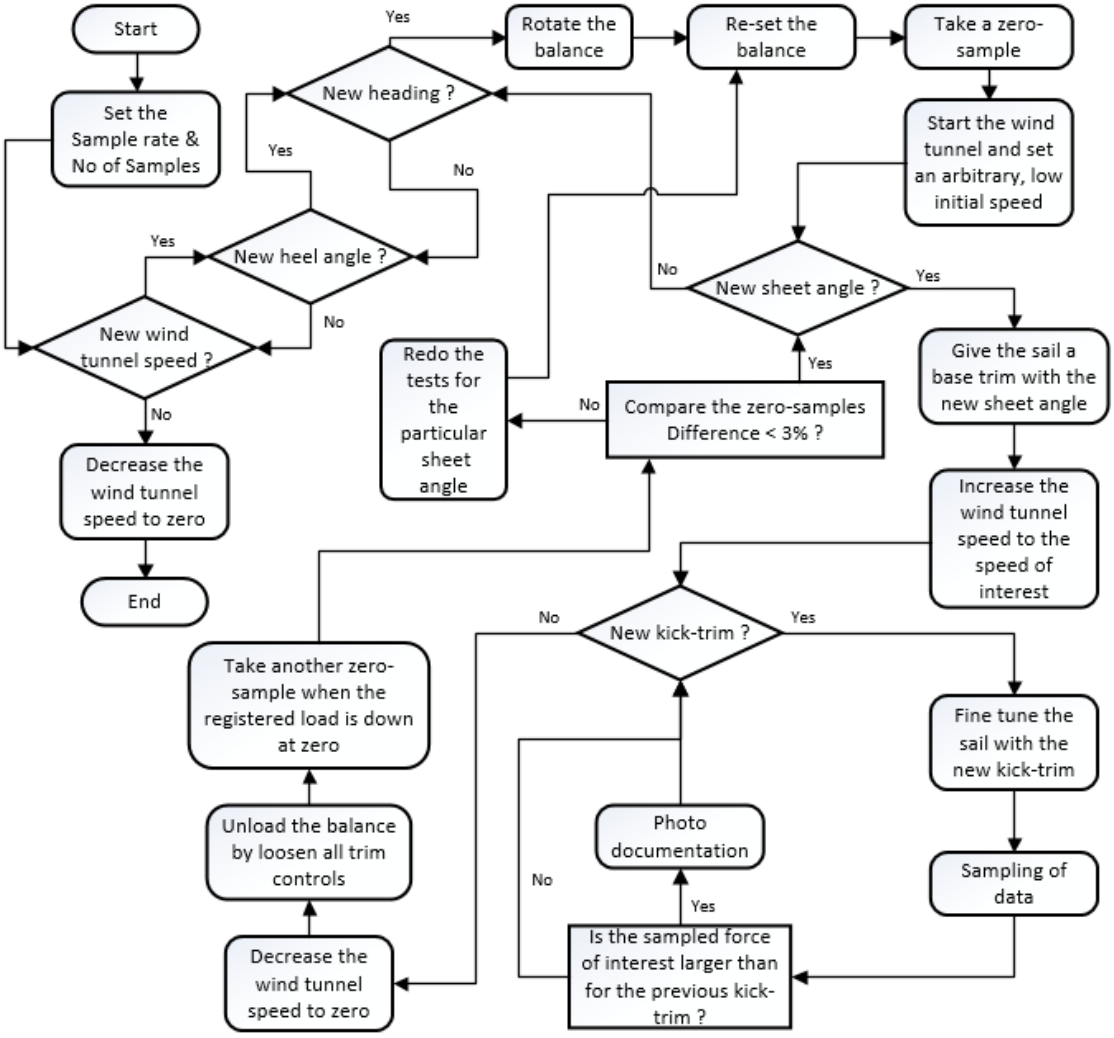

Figure 4.14: The flowchart shows the test procedure and data acquisition, when performing the wind tunnel tests, for both wind speeds.

Data Acquisition

In the flowchart, Fig. 4.14 it can be seen that the first step was to set the *sample rate* and *number of samples*. The sample rate, which is the rate in seconds at which measurements are taken, was set to 1000 HZ and the number of samples was set to 1000. Thus 1000 measurements were taken automatically by LabView during one second and then LabView calculate an average value. The calculated average value is presented as the *filtered data* in the LabVIEW sampling window, which can be seen in Fig. A.2, in Appendix. This particular setting of the sample rate and the number of samples was used for all tests.

The time window for measurements was 30 seconds and during this time 30 measurements

were taken manually. From these 30 average values, the largest, the smallest, and a third approximate average value were chosen for the calculation of an overall average value.

Table 4.3: Data acquisition settings for the wind tunnel tests.

No of Samples	Sample Rate [Hz]
1000	1000

4.3.3 Tunnel Tests

All wind tunnel tests that were carried out are listed below in the order they were executed; how they were executed are described more in detail in the following text.

- Speed test
- Zero test
- Strong wind tests
- Light wind tests
- Repeatability tests
- Drag Tare tests
- Balance tests

Speed Test

The speed test was only a control test to check whether or not it would be possible to use the full-scale apparent wind speed of 7 m/s for the strong wind tests. The balance and all equipment were prepared as if it was the actual strong wind test that should be carried out, i.e. the mast foot that corresponded to the upright sailing condition was chosen for the mast, the balance was rotated so that the heading of $\psi = 180°$ was set; since it was anticipated that max projected sail area would give the highest force in the direction of motion, i.e. the drive force F_M, the sheet angle $\delta = 90°$ was chosen. During the speed test, the tunnel speed was slowly increased until it was believed that a further increase of the tunnel speed could result in material damage. The performed speed test was successful and it was believed that both the sail model and the mast model and the other equipment would be able to handle the scaled apparent wind speed for all the strong wind tests.

The two full-scale apparent wind speeds, together with their scaled wind tunnel speeds can be seen in Table 4.4. The scaled tunnel speeds were as previously mentioned, calculated as the product of the full-scale apparent wind speed with the velocity scale factor $\alpha_V = \sqrt{7}$. The control panel speeds (LabVIEW speeds) for both the light wind case and the strong wind case are also presented in Table 4.4 and the safety velocity V_{Safety}. The so-called LabVIEW speed, $V_{LabVIEW}$ was the speed the software had to be set at, to test the sail for the desired apparent wind tunnel speeds.

Table 4.4: The full-scale apparent speeds V_{AW_p}, the scaled apparent wind speeds V_{AW_m}, the LabVIEW speeds $V_{LabVIEW}$ and the safety velocity V_{Safety}.

	Light wind	**Strong wind**
V_{AW_p} **[m/s]**	4	7
V_{AW_m} **[m/s]**	10.6	18.5
$V_{LabVIEW}$ **[m/s]**	13.7	23.9
V_{Safety} **[m/s]**	25	25

Zero Test

To investigate how often it was required to re-set the balance to zero, a *zero test* was performed for each new sheet angle that should be tested. Before the balance was loaded, i.e. before any of the trim controls had been tightened and the wind tunnel still was turned off, the balance was re-set to zero, and a *zero sample* was taken. When the sail model had been tested for the three different settings with the kicker, i.e. light kicker trim (LKT), medium kicker trim (MKT), and hard kicker trim (HKT), the wind tunnel was switched off and all trim controls were loosened. The balance was now unloaded and when the airflow had calmed down, a second zero-sample was taken. Then the drive forces were compared with the two zero-samples and if the difference was below 3 % it was regarded as sufficiently good. The difference between the two zero-samplings was more or less always kept below 3 % and on the few occasions when the difference was higher, the tests were repeated.

Strong Wind Tests

The test series for the strong wind tests are presented in Table 4.5 below and it can be seen that the sail model was only tested for one single heading, i.e. $\psi = 180°$, which simulate sailing the ILCA 7 dinghy dead down before the wind towards the lee mark. It can also be seen that the sail model was only tested for the upright sailing condition, i.e. with a heel angle of 0°, and for sheet angles between 60° and 90°. The reason for limiting the strong wind tests of the sail, to only cover the upright condition, was because when running in strong wind, it was anticipated that the ILCA 7 is sailing in a planing mode; in this mode, the sailor tries to balance the ILCA 7 dinghy and sail it as upright as possible, so the average heel angle could therefore be approximated as being zero. Furthermore, when running in strong wind the sail should never be sheeted more than 90°, which was the reason for only testing the sail with sheet angles up to 90°. Both the Laser Guide [34] and the elite ILCA 7 sailors from GKSS that were consulted in this project verified this. The trim controls, the outhaul, and the cunningham are defined as "floating" in Table 4.5, meaning that they were continuously adjusted for each configuration of the other variables.

Table 4.5: Strong wind test series, for the heel angle 0° & the heading of 180°, where LKT, MKT and HKT stands for Light Kicker Trim, Medium Kicker Trim and Hard Kicker Trim, respectively.

Balance rotation (ω) [°]	90
Heading (ψ) [°]	180
Heel angle (ϕ) [°]	0
Sheet angle (δ) [°]	60 70 80 90
Kicker	LKT MKT HKT
Outhaul	Floating
Cunningham	Floating

Light Wind Tests

The testing procedure for the light wind tests was slightly different than the testing procedure for the strong wind tests and the reason for this was that the sail model now was tested for five different headings instead of only one; two heeled conditions, beyond the upright sailing condition. Further, three more sheet angles were also tested. The differences, between the two wind speed conditions, are summoned in the list below:

- The amount of headings were increased to also include the headings of 150°, 160°, 170° and 190°, beyond the heading of 180°.
- The amount of sheet angles δ investigated for each heading ψ and heel angle ϕ were increased to also include 100°, 110° and 120°.
- Beyond the 0° heel angle, the two heel angles 10° and 20° were also tested.

The test series for the light wind tests are presented in Table 4.6 - Table 4.10 below. The reason for expanding the test series for the light wind case and analyze five different headings, was because in light to medium wind conditions, the ILCA 7 dinghy shall not be sailed dead down before the wind, as it can in stronger wind conditions. In light to medium wind conditions it is instead faster to luff slightly and if waves are present, catch them and ride them. Further, when sailing downwind in light to medium wind conditions the ILCA 7 dinghy sailor heels the dinghy to windward, to find equilibrium, which was the reason for also include the heel angles 10° and 20°. Furthermore, when sailing downwind in light to medium wind conditions, some ILCA 7 sailors prefer to *sail positive* and others prefer to *sail negative*. Sailing positive and negative has already been explained, but is briefly explained again. Sailing positive means letting out the sheet, so that the airflow reaches the luff of the sail first and sailing negative is simply the opposite, i.e. pulling in the sheet, so that the airflow reaches the leech first. This meant that, by increasing the amount of sheet angles to also include the 100°, 110° and 120° sheet angles, it was possible to analyze the sailing technique of sailing positive in light wind conditions.

Table 4.6: Light wind test series 1, 2 & 3 shows the test series for the three heel angles 0°, 10° & 20°, respectively, for the heading of 150°, where LKT, MKT and HKT stands for Light Kicker Trim, Medium Kicker Trim and Hard Kicker Trim, respectively.

Balance rotation (ω) [°]	60						
Heading (ψ) [°]	150						
Heel angle (ϕ) [°]	0	10	20				
Sheet angle (δ) [°]	60	70	80	90	100	110	120
Kicker		LKT	MKT	HKT			
Outhaul	Floating						
Cunningham	Floating						

Table 4.7: Light wind test series 4, 5 & 6 shows the test series for the three heel angles 0°, 10° & 20°, respectively, for the heading of 160°, where LKT, MKT and HKT stands for Light Kicker Trim, Medium Kicker Trim and Hard Kicker Trim, respectively.

Balance rotation (ω) [°]	70						
Heading (ψ) [°]	160						
Heel angle (ϕ) [°]	0	10	20				
Sheet angle (δ) [°]	60	70	80	90	100	110	120
Kicker		LKT	MKT	HKT			
Outhaul	Floating						
Cunningham	Floating						

Table 4.8: Light wind test series 7, 8 & 9 shows the test series for the three heel angles 0°, 10° & 20°, respectively, for the heading of 170°, where LKT, MKT and HKT stands for Light Kicker Trim, Medium Kicker Trim and Hard Kicker Trim, respectively.

Balance rotation (ω) [°]	80						
Heading (ψ) [°]	170						
Heel angle (ϕ) [°]	0	10	20				
Sheet angle (δ) [°]	60	70	80	90	100	110	120
Kicker		LKT	MKT	HKT			
Outhaul	Floating						
Cunningham	Floating						

Table 4.9: Light wind test series 10, 11 & 12 shows the test series for the three heel angles 0°, 10° & 20°, respectively, for the heading of 180°, where LKT, MKT and HKT stands for Light Kicker Trim, Medium Kicker Trim and Hard Kicker Trim, respectively.

Balance rotation (ω) [°]	90						
Heading (ψ) [°]	180						
Heel angle (ϕ) [°]	0	10	20				
Sheet angle (δ) [°]	60	70	80	90	100	110	120
Kicker	LKT	MKT	HKT				
Outhaul	Floating						
Cunningham	Floating						

Table 4.10: Light wind test series 13, 14 & 15 shows the test series for the three heel angles 0°, 10° & 20°, respectively, for the heading of 190°, where LKT, MKT and HKT stands for Light Kicker Trim, Medium Kicker Trim and Hard Kicker Trim, respectively.

Balance rotation (ω) [°]	100						
Heading (ψ) [°]	190						
Heel angle (ϕ) [°]	0	10	20				
Sheet angle (δ) [°]	60	70	80	90	100	110	120
Kicker	LKT	MKT	HKT				
Outhaul	Floating						
Cunningham	Floating						

Repeatability Tests

Due to the manual testing procedure, it was necessary to quantify the variation of the measured data and calculate the *standard deviation* σ. To do this, repeatability tests were carried out. For the tests, it was regarded sufficient to only perform the repeatability tests for one of the apparent wind tunnel speeds and one heading; since the repeatability tests were carried out directly after the light wind tests with the heading of 190°, same wind speed, and same heading were chosen for all repeatability tests. For this heading, 5 identical and separate repeatability tests were carried out for all three heel angles, with the sheet angle 90°; for these fifteen tests, all three settings with the kicker: LKT, MKT, and HKT, representing Light Kicker Trim, Medium Kicker Trim and Hard Kicker Trim, respectively, were tested.

The test procedure and data acquisition for the repeatability tests was carefully and methodically carried out, as illustrated in the flowchart, in Fig. 4.15. The test series for the repeatability tests can be seen in Table 4.11 further down.

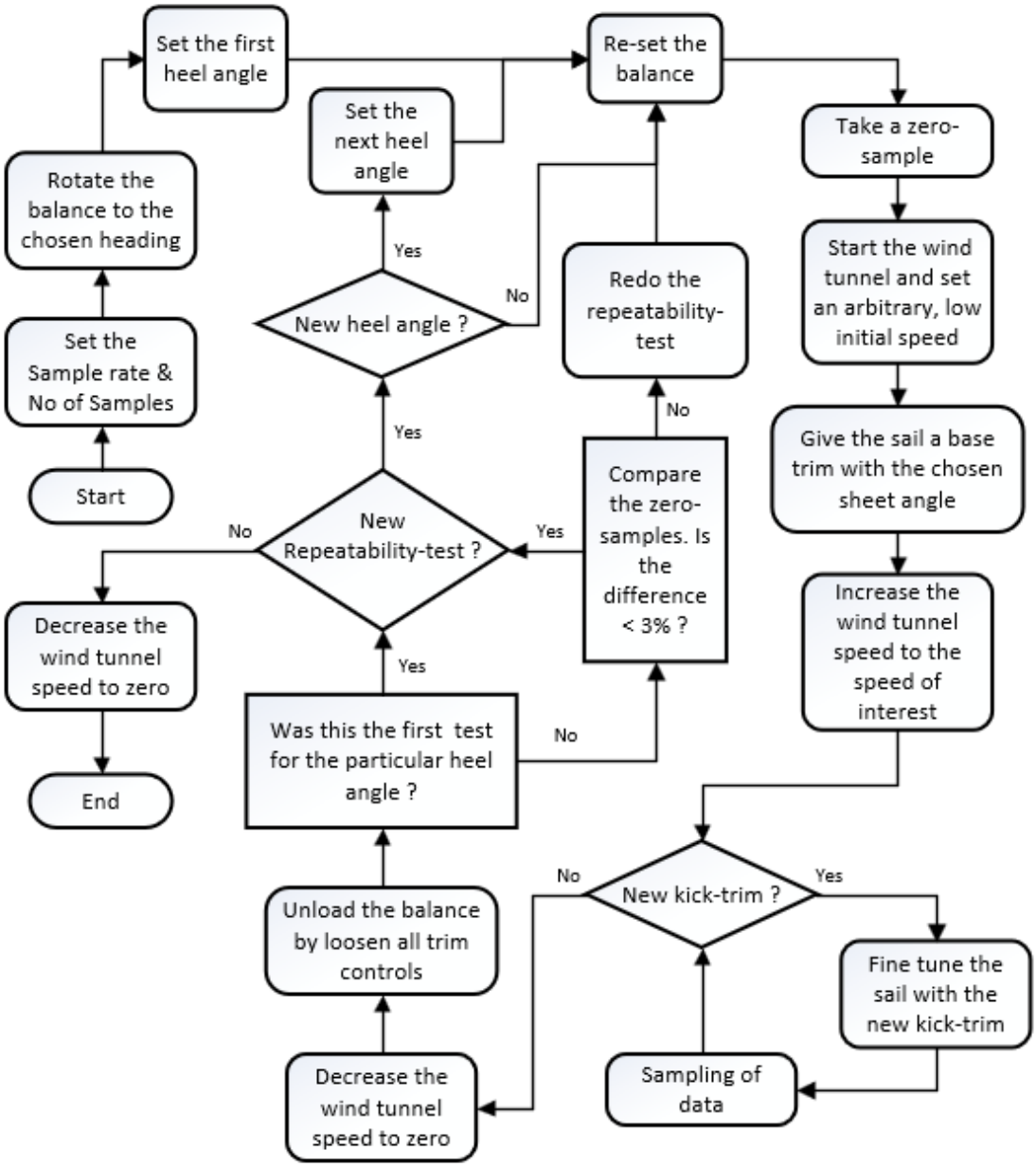

Figure 4.15: The flowchart for the repeatability tests.

The procedure when sampling the data and trimming the sail during the repeatability tests should for obvious reasons be identical to how the real tests had been carried out and they were, with the only exception that the balance only had to be re-set to zero before every new repeatability test. This because the balance was kept at a heading of 190°, the sheet angle was fixed at 90° and the balance had shown to not drift much, way below 3 %, for the vast majority of all the tests. The zero tests for the repeatability tests were therefore conducted between the zero samples for every test.

In Table 4.11 below, the test series for the 5 separate repeatability tests are presented, where LKT, MKT, and HKT stands for Light Kicker Trim, Medium Kicker Trim, and Hard Kicker Trim, respectively.

Table 4.11: The repeatability tests series shows the constants and variables for the 5 separate repeatability tests, where LKT, MKT and HKT stands for Light Kicker Trim, Medium Kicker Trim and Hard Kicker Trim, respectively.

Rep. tests [No.]	5
Balance rotation (ω) [°]	100
Heading (ψ) [°]	190
Heel angle (ϕ) [°]	0 10 20
Sheet angle (δ) [°]	90
Kicker	LKT MKT HKT
Outhaul	Floating
Cunningham	Floating

Drag Tare Tests

The wind tunnel floor represented, as previously mentioned, the water surface during all wind tunnel tests and the mounting bracket, that was manufactured to keep the mast model and the sail model in the desired position in the test section and connect the wind tunnel balance with the mast model, perforated the wind tunnel floor. The part of the mounting bracket that was above the wind tunnel floor was therefore exposed to the airflow and drag tare, which had to be subtracted from the sampled test data. The drag tare tests were performed in two separate tests. In the first test, nothing but the mounting bracket was present in the test section, which is illustrated in Fig. 4.16. This allowed the wind tunnel balance to register the contribution of the drag tare, from the parts of the mounting bracket that perforated the wind tunnel floor. In test 2, the mounting bracket was lowered under the wind tunnel floor, which can be seen in Fig. 4.17. For the second test, a short mast with the same diameter as the full-length model mast, but with a length that corresponded to the part of the mast between the foot of the sail and the wind tunnel floor. To the short mast, the boom and all other small equipment, such as the blocks and control ropes were mounted. In this way, it was possible to filter out the drag tare that everything under the sail model contributed with. These two tests were carried out for both apparent tunnel speeds.

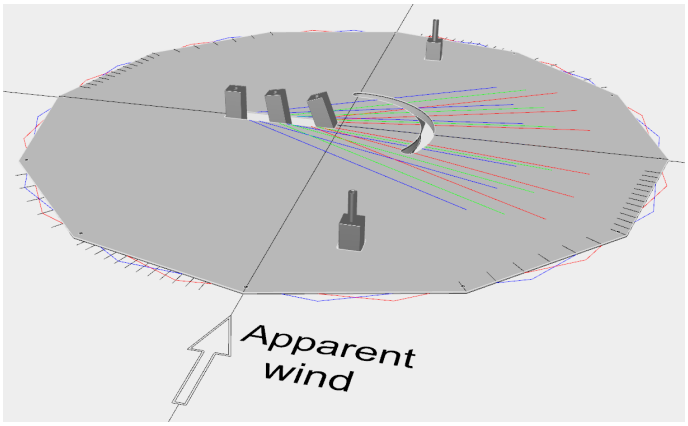

Figure 4.16: Drag tare test 1. Only the mounting bracket is present in the test section, in order to isolate and register its contribution of the drag tare.

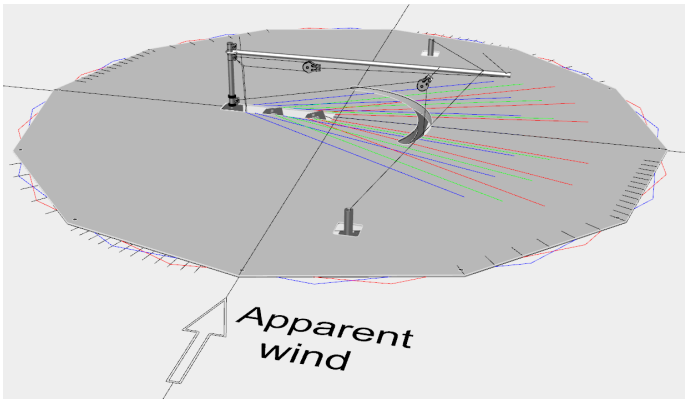

Figure 4.17: Drag tare test 2. The mounting bracket is lowered under the wind tunnel floor and the contribution of the drag tare from everything under the sail is registered.

The attentive reader can see that in Fig. 4.16 & Fig. 4.17 there are relatively big holes in the aluminum cover plate, which allows the mounting bracket to penetrate the wind tunnel floor. These holes were carefully sealed with thin adhesive tape, and continuously adjusted in every single test case, in order to minimize leakage and for the pressure to equalize at the test object.

Balance Tests

When the wind tunnel tests of the sail model were completed, the wind tunnel personnel carefully removed the balance from the test section and mounted it in a calibration frame, which can be seen in Fig. 4.18. The purpose of the balance tests was to quantify the balance measurement error, in order to correct the measurements from this error source.

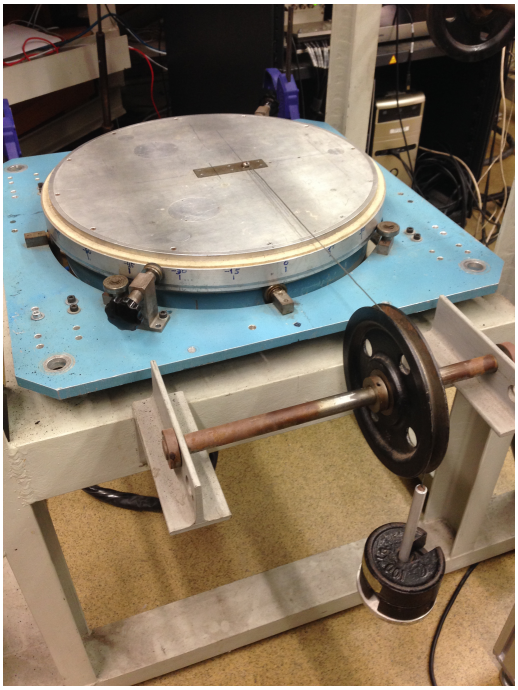

Figure 4.18: A close-up picture of the balance, mounted in the calibration frame, and the weight carrier, with the calibrated control weights.

The balance is, as previously mentioned, a 6-component wind tunnel balance and measures the 3 force components, i.e. the drag force F_D, the side force F_S and the lift force F_L; the 3 moments, the pitch moment M_P, the roll moment M_R and the yaw moment M_Y.
All these components, except the yaw moment, were measured directly in the *balance resolving center* (BRC), but to measure the yaw moment, an aluminum adapter, that was borrowed from the wind tunnel facility, was mounted at a certain horizontal distance from the balance resolving center where this component was measured.

To know how much weight that should be used for the tests, the measurements from the downwind tests were studied. The data showed that the forces in the direction of motion F_M were of the magnitude of 20 N, so two calibrated weights of each 1001 g were chosen for the tests. The balance, which still was connected to the wind tunnel software, was loaded with these two calibrated weights and the forces and moments were registered. Three separate balance tests were carried out and an average balance-measurement error was calculated in the post-processing and a correction factor for each load component.

4.4 Numerical Setup

The objective with the numerical investigation was to analyze the *blockage effects*, in order to correct the experimental data, retrieved from the wind tunnel tests. For the analysis, two computational domains of different sizes were required. The computational domain that had the same cross-sectional area as the inlet of the test section of Chalmers wind tunnel, is referred to as the *normal computational domain*, or NCD; the other domain, with an enlarged cross-sectional area of the inlet of the test section, is referred to as the *large computational domain*, or LCD. The aim when deciding the size for the large domain was that it should be large enough for the airflow to be unaffected by the lateral boundaries, i.e. simulating an open test section. Images of the two computational domains can be seen in Fig. 4.19 & Fig. 4.20. For the simulations, Siemens CFD-code STAR-CCM+ was used and Reynolds Averaged Navier-Stokes (RANS) simulations were performed as well as detached-eddy simulations (DES).

4.4.1 Sail Model

Even though the physical sail model had a natural camber, because of the relatively soft and ductile sailcloth, it was initially considered sufficient to model a simplified flat sail model of the MKII sail, that could be used for the analysis of the blockage effects. This flat sail model was modeled with the surface modeling software Rhinoceros 3D [25], with the help of pictures taken with a Go-Pro camera, positioned downstream the sail model, in the test section just before the diffuser. The flat sail model was modeled so that it captured a certain sail trim, received from the combination of variables, that had generated the highest drive force coefficients overall when analyzing the uncorrected experimental test data. The hard setting with the kicker and the trim with the cunningham was for example modeled into the flat sail model for the numerical investigation. The outhaul could, however, for natural reasons, not be captured in a flat object. The other variables, more of a positional nature, for the sail model are presented in Table 4.13.

4.4.2 Computational Domains

The computational domains were created with the CAD-software Autodesk Inventor [3]. The dimensions were taken from a CAD model of the test section that the lab personnel

in the wind tunnel facility were kind to share with the author. The two computational domains, that were created can be seen in Fig. 4.19 & Fig. 4.20 below, where also the flat sail model can be seen. The geometrical data for each domain, are presented in Table 4.12. When deciding the length of the domains, the *characteristic length* $L_c = 250\ mm$ of the flat sail model was used. The length for both domains was chosen to $30 \times L_c$ and the position of the sail, downstream the inlet of the domain to $10 \times L_c$, which resulted in a wake distance of $20 \times L_c$, downstream the sail model to the outlet of the domain. Which boundary conditions that were chosen for each boundary of both computational domains are presented further down in the text.

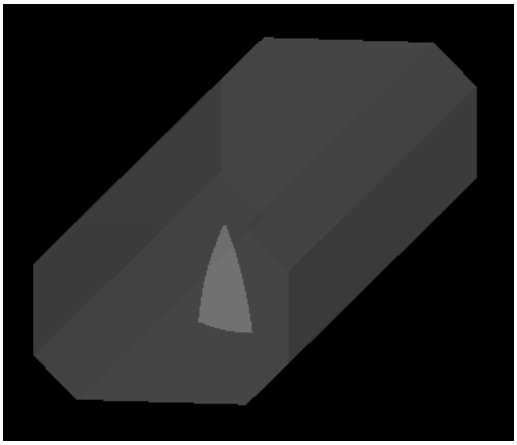

Figure 4.19: An oblique view of the flat sail model positioned in the normal computational domain.

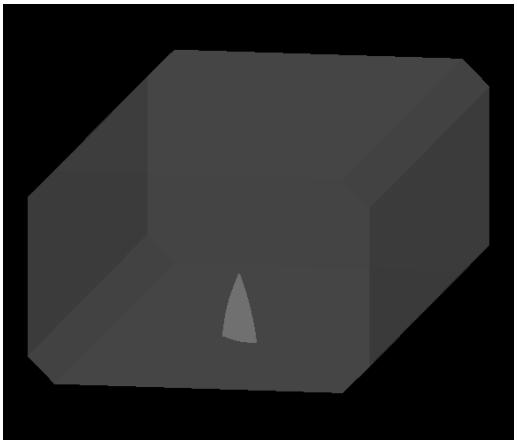

Figure 4.20: An oblique view of the flat sail model positioned in the large computational domain.

A front view, of the cross-sections, of the inlet to the test section, of both computational domains can be seen in Fig. 4.21 & 4.22; the corresponding dimensions are presented in Table 4.12. The size of the large domain, was as previously mentioned, chosen to simulate an open test section, where no lateral boundaries should affect the airflow. The walls and the ceiling of the normal domain were thus simply translated outward until the cross-sectional area of the inlet of the large domain was four times larger than the cross-sectional area of the inlet of the normal domain. The ratio of the cross-sectional areas were calculated with Eq. (4.66):

$$A_{ratio} = \frac{A_{cross_{LCD}}}{A_{cross_{NCD}}} \tag{4.66}$$

Which also was used when calculating the ratio of the front surface area of the flat sail model to the cross-sectional area of the inlet of the test section, for both domains.

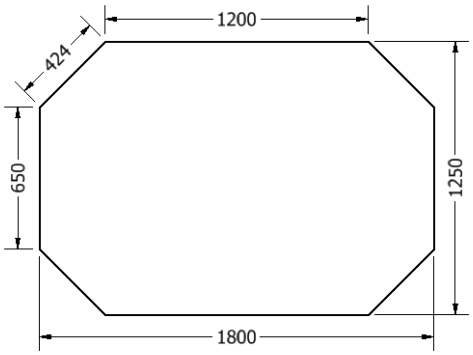

Figure 4.21: Cross sectional dimensions [mm] of the inlet, of the normal computational domain.

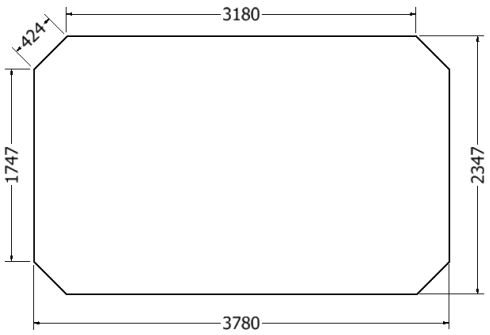

Figure 4.22: Cross sectional dimensions [mm] of the inlet, of the large computational domain.

Table 4.12: Geometrical data for both computational domains and the ratio of the front-surface area of the flat sail model and the cross-sectional area of the test section.

Domain	$\mathbf{L \times W \times H}$ [m]	$\mathbf{L}_{oblique}$ [m]	$\mathbf{A}_{cross}$ [$\mathbf{m^2}$]	$\mathbf{A}_{ratio}$ [-]
Normal	$7.500 \times 1.800 \times 1.250$	0.424	2.07	7
Large	$7.500 \times 3.780 \times 2.347$	0.424	8.7	1.66

Boundary Conditions

In Chapter 2, where the CFD-code STAR-CCM+ was presented, the different boundary conditions available in the software were mentioned. In this project the *velocity inlet* and *pressure outlet*, were chosen for the inlet and the outlet, respectively; for the remaining sides of the octagonal-shaped computational domain, i.e. the top, the bottom, the two sides, and the fillets, and the surface of the sail model, the boundary type, *wall* was used. The boundary condition for walls can as mentioned in Chapter 2, either be *no-slip* or *slip* and for the sail model, the *no-slip* condition was chosen, since it was desired to capture the shear stresses at the surface of the sail model. For the top, bottom, the two sides, and the fillets of the computational domain, the *slip* condition was chosen, even though boundary layers were generated on the lateral boundaries in the test section of Chalmers wind tunnel. The reason for this is that the lateral boundaries in the test section widen downstream the inlet, in order to account for the growth of the boundary layer; by modeling a simplified computational domain, with a constant cross-sectional area, corresponding to the cross-sectional area of the inlet of the test section, the *slip* condition was appropriate.

4.4.3 Grid Dependence Study

Isotropic Volume Grid Generation

A grid dependence study, following the method used by Crepier in [7] generated 5 relatively geometrically similar Cartesian grids of unstructured mesh, with different resolution. Relatively geometrically similar, because it was, unfortunately, not possible to follow the method completely for the isotropic volume grid generation, due to differences in the meshing tools. In [7] Crepier used NUMECAS/FINE MARINE'S meshing tool HEXPRESS [27]; the meshing-tool in Siemens STAR-CCM+ [33] that was used in this project, unfortunately had restrictions when discretizing uneven numbers, which meant that step 1 in

the List 2.8.1 could not be completely satisfied.

Anisotropic Sub-Layer Grid Generation

For the anisotrophic sub-layer grid generation, the non-dimensional y^+ first had to be calculated for each grid, which was done in the steps presented below:

1. Calculation of the Reynolds number Re:

$$Re = \frac{U\,L_c}{\nu} \tag{4.67}$$

   where U is the apparent wind tunnel speed for the light wind case, L_c is the *characteristic length* of the sail and ν is the kinematic viscosity, which was retrieved from the text file that LabVIEW compiled during the wind tunnel tests.

2. Calculation of the thickness of the turbulent boundary layer at the sail, from [36]:

$$\delta_{turb} = \frac{0.16\,L_c}{Re^{1/7}} \tag{4.68}$$

   The total thickness of all prism layers should be less than the turbulent boundary layer thickness δ_{turb}, which was kept for all grids, but the amount of prism-cell layers varied. For the coarsest grid nr. 5, 10 prism-cell layers were chosen; the amount of prism-cell layers for the other grids were increased with the factor that corresponded to the grid number in reversed order, which meant that the amount of prism-cell layers for the finest grid nr. 1 was 50.

3. Calculation of the turbulent wall shear stress:

$$\tau_w = \frac{0.0135\,\mu^{1/7}\,\rho^{6/7}\,U^{13/7}}{L_c} \tag{4.69}$$

   where μ and ρ are respectively the dynamic viscosity and density, retrieved from the text file that LabVIEW compiled, for the particular case from the wind tunnel tests that was chosen to analyze numerically.

4. Calculation of the non-dimensional u*:

$$u^* = \left(\frac{\tau_w}{\rho}\right)^{1/2} \tag{4.70}$$

5. Calculation of the non-dimensional y^+:

$$y^+ = y_1\,\frac{u^*}{\nu} \tag{4.71}$$

It was desired to have a low y^+ wall treatment, so the y^+ for the coarsest grid was chosen as 1. Left side of Eq. (4.71) was thus set to 1 and Eq. (4.71) rearranged, so that y_1, the thickness of the near wall prism layer could be calculated:

$$1 = y_1 \frac{u^*}{\nu} \quad \longrightarrow \quad y_1 = \frac{\nu}{u^*} \tag{4.72}$$

6. Calculation of y^+ for each grid, which is the non-dimensional distance, from the surface of the sail to the center of the first prism-cell layer. Since the thickness of the first prism-cell layer varied for each grid, y^+ for each grid was calculated using half of the thickness of the first prism-cell layer:

$$y^+ = y_1 \frac{u^*}{2\,\nu} \tag{4.73}$$

where y_1 represents, as above mentioned, the thickness of near wall prism layer and is denoted as S_0 by [7]. Note that the denominator now is twice as large compared to Eq. (4.71) above, this in order to get the distance to the center of the first prism-cell.

7. Calculation of the thickness of the n^{th} prism cell-layer for the refined grid with Eq. (2.74):

$$S_n = S_0 \frac{1 - r_1^{1/n}}{1 - r_1} \tag{4.74}$$

where $S_0 = 10.4\,e^{-5}$ is the *Thickness of Near Wall Prism Layer* for the initial coarse grid and the output S_n represent the thickness of the n^{th} prism cell-layer for the refined grid. The level of refinement is represented by (n), where $n = 1$ is the coarsest grid.

8. Calculation of the growth ratio of the n^{th} refined grid, with Eq. (2.75):

$$r_n = r_1^{1/n} \tag{4.75}$$

where $r_1 = 1.4$ is the *Prism layer stretch factor* or *growth ratio* of the initial coarse grid and the output r_n represent the growth ratio of the n^{th} refined grid.

The results from the calculation of y^+, S_n and r_n in step 6-8 are presented in Table. 5.1 where also the base size, the amount of prism-cell layers, the refinement degree, the diffusion depth, the cell count and the grid refinement ratio for each of the 5 generated grids, for both domains, are presented.

Reynolds Averaged Navier-Stokes (RANS) Simulations

As previously mentioned, an analysis of the uncorrected experimental test results, filtered out a case, with a certain combination of variables, that overall generated the highest drive force coefficients C_{F_M} [-]. This case was chosen for the RANS simulations, that were performed for the grid dependence study. The set of parameters for the study are presented in Table 4.13 below. It can be seen that the flat sail model should be tested for a heel angle of 0° and with a sheet angle of 90°, for both domains. Further, it was considered sufficient to perform the numerical investigation with only one of the two apparent wind tunnel speeds and since a more thorough analysis had been carried out with the speed, for the light wind conditions, the apparent wind speed for the light wind case, was chosen for the numerical investigation.

Table 4.13: The set of parameters for the RANS simulations, carried out for the grid dependence study.

Domain	Both
Grid	1 2 3 4 5
Sail model	Flat
Air speed [m/s]	10.6
Heading (ψ) [°]	180
Heel angle (ϕ) [°]	0
Sheet angle (δ) [°]	90
Kicker	HKT

The models for the mesh generation are presented in Table 4.14 below.

Table 4.14: Models for the mesh generation.

Mesh generation
Models
Prism Layer Mesher
Surface Remesher
Trimmer

Table 4.15: A few of the models for the physics, for the RANS simulations, with the $k-\varepsilon$ turbulence model.

Physics
Models
All y^+ Wall Treatment
K-Epsilon
Realizable K-Epsilon Two-Layer
Convection: 2nd-order
Segregated Flow
Convection: 2nd-order

4.4.4 Verification Analysis of Discretization Uncertainty

The results from the RANS simulations, for both domains, were used for an estimation of the uncertainty, following the method suggested by Eça & Hoekstra in [9]. The software tools for the analysis of the numerical uncertainty and error estimation are provided by MARIN [24] and are available on ReFRESCO's homepage [31]. The tool for the analysis was very user-friendly and consisted of a software file and two additional input files, i.e. one *ini*-file which the software reads upon execution, and the other input file is an *dat*-file, with the results from the CFD-simulations. The user of the software tool only has to modify the *ini*-file slightly, to the users' desire and insert the results from the CFD simulations in the *dat*-file.

The *ini*-file and the *dat*-file used for the analysis of the normal domain and the command for the execution on GNU/Linux systems can be seen in Fig. A.106 & A.107, respectively, in Appendix.

4.4.5 Sail Camber & Sheet Angle Analysis

Even though it was initially considered sufficient to use a flat sail model, which had been used for the grid dependence study, the thoughts of the potential difference in the size of the wake between a simplified flat sail model and the physical sail model lingered. It could differ relatively much between a flat sail model and a cambered sail model and the contribution to the blockage effects could therefore differ relatively much. Due to this, it was decided that a cambered sail model of the old cross-cut MKI sail for the ILCA 7 dinghy, should be borrowed from Ph.D. student Adam Persson, at SSPA/Chalmers, who had modeled and used this sail model in his work. When analyzing the shape of the two sail models, a comparison of the curvature of the luff showed a very large resemblance between the two sail models, and the depth of the cambered sail model was more or less identical to the depth, which the physical sail model had for the case that had been filtered out. The cambered sail model could therefore be considered to have a hard kicker trim and the same trim with the outhaul as the physical sail model had for the chosen case. Further, in the grid dependence study only the sheet angle of 90° was analyzed and in order to also investigate the other sheet angles that had been tested experimentally, it was decided that a more thorough sail camber and sheet angle analysis should be carried out. The analysis was performed by defining a reference case and then run two sets of identical simulations, where one set of the simulations were conducted with the flat sail model and the other set of simulations with the cambered sail model. The parameters, for the sail camber and sheet angle analysis, can be seen in Table 4.16 and were basically the same set of parameters that were used for the grid dependence study, with the exception that all seven sheet angles, that had been tested experimentally, were now included and all simulations for the sail camber and sheet angle analysis were performed with only grid 3.

Table 4.16: The set of parameters, for the sail camber and sheet angle analysis.

Domain	Both						
Grid	3						
Sail model	Both						
Air speed [m/s]	10.6						
Heading (ψ)	180						
Heel angle (ϕ)	0						
Sheet angle (δ)	60	70	80	90	100	110	120
Kicker	HKT						

The turbulence model used in the grid dependence study was the two-equation model K-Epsilon, but since it would be interesting to analyze some other turbulence models as well, before deciding which one to use for the sail camber and sheet angle analysis, it was decided that the sail camber and sheet angle analysis should start with a turbulence model investigation.

Turbulence Model Investigation

The different turbulence models chosen for the turbulence model investigation are listed below:

- K-Epsilon two-equation model
- Shear-Stress Transport (SST) (Menter) K-Omega two-equation model
- Reynolds Stress Transport (RST) model
- Spalart-Allmaras (S-A) one-equation model

The set of parameters, for the turbulence model investigation, which was performed with RANS simulations, can be seen in Table 4.17 below:

Table 4.17: The set of parameters for the turbulence model investigation.

Domain	Both
Grid	3
Sail model	Both
Air speed [m/s]	10.6
Heading (ψ) [°]	180
Heel angle (ϕ) [°]	0
Sheet angle (δ) [°]	90
Kicker	HKT

Some of the models for the physics, with the $k-\varepsilon$ turbulence model were presented in Table 4.15 above, and the corresponding models, for the physics, for the other three turbulence models can be seen in Table 4.18 - 4.20, below.

Table 4.18: Some of the models for the physics, with the SST $k-\omega$ turbulence model.

Physics
Models
All y^+ Wall Treatment
K-Omega Turbulence
SST (Menter) K-Omega
Convection: 2nd-order
Segregated Flow
Convection: 2nd-order

Table 4.19: Some of the models for the physics, with the *RST* turbulence model.

Physics
Models
All y^+ Wall Treatment
Reynolds Stress Turbulence
Elliptic Blending
Convection: 2nd-order
Segregated Flow
Convection: 2nd-order

Table 4.20: Some of the models for the physics, with $Spalart-Allmaras$ $(S-A)$ turbulence model.

Physics
Models
All y^+ Wall Treatment
Spalart-Allmaras Turbulence
Elliptic Blending
Convection: 2nd-order
Segregated Flow
Convection: 2nd-order

Detached-Eddy Simulation (DES)

When the results from all the RANS simulations had been analyzed, no prominent signs of *vortex shedding* could be seen and since a comparison with the drive force coefficients from the experimental test results showed a quite large difference, it was decided that an unsteady approach with detached-eddy simulation (DES) should be performed. It should however be limited to only a sheet angle analysis with the cambered sail model.

Table 4.21: The set of parameters for DES.

Domain	Both						
Grid	3						
Sail model	Cambered						
Air speed [m/s]	10.6						
Heading (ψ)	180						
Heel angle (ϕ)	0						
Sheet angle (δ)	60	70	80	90	100	110	120
Kicker	HKT						

Table 4.22: Some of the models for the physics, for DES with *Spalart − Allmaras* turbulence model.

Physics
Models
All y^+ Wall Treatment
Coupled Energy
Coupled Flow
Discretization: Hybrid-BCD
Detached-Eddy Simulation
Implicit Unsteady
Spalart-Allmaras Detached Eddy
Constitutive Relation: QCR
Convection: 2nd-order
Formulation: IDDES

When setting up the simulations for DES, the Courant–Friedrichs–Lewy (CFL) number was calculated using Eq. 2.27:

$$C = \frac{U\,\Delta t}{\Delta h} = \frac{10.6 \quad 2.0\,e^{-4}}{4.0\,e^{-3}} = 0.53\,[-] \tag{4.76}$$

where the velocity $U = 10.6$ m/s, the time step $\Delta t = 2.0e^{-4}$ s and the characteristic cell size $\Delta h = 4.0e^{-3}$ m. The characteristic cell-size Δh was received by measuring the cell-size in the x-direction, of the cells directly after the prism-cell layers in the wake of the sail model, from grid nr 3.

Chalmers Compute Cluster

Every DES was initialized with a RANS simulation, that ran locally for a while, then the settings were changed and adapted for unsteady DES; submitted to Chalmers Compute Cluster. The same turbulence model was used for both the initializing RANS simulation and for DES, which was Spalart-Allmaras turbulence model ($S-A$).

4.4.6 Blockage Effects

A few blockage effects were presented in Chapter 2 and those considered in this project are *Solid Blockage* and *Wake Blockage*. A calculation with Eq. (4.66) revealed that the ratio of the surface area of the sail model to the cross-sectional area of the test-section was 7 % and according to [4] this ratio usually are between $1-10$ %, so the sampled data were most certainly affected by the presence of the lateral boundaries in the test-section. In order to correct the experimental data from blockage effects, a numerical investigation was carried out. For the calculation of the correction factors, the results from the steady RANS simulations with the K-Epsilon turbulence model were used. The correction factors for the drive force coefficients, pitch moment coefficients and yaw moment coefficients were calculated with Eq. (4.77); the correction factors for the side force coefficients and the roll moment coefficients were calculated with Eq. (4.78).

$$F_{C_{C_{FM}}} = \frac{C_{F_{M_{LCD}}}}{C_{F_{M_{NCD}}}} \tag{4.77}$$

$$F_{C_{C_{FS}}} = \frac{C_{F_{S_{LCD}}}}{C_{F_{S_{NCD}}}} \tag{4.78}$$

where LCD and NCD stands for large computational domain and normal computational domain, respectively.

However, the vectors with correction factors from Eq. (4.77) & Eq. (4.78) only contained the correction factors for the sheet angles 60° - 120°; since correction factors for the sheet angels 50°, 130°, 140° and 150°, also were needed, these were received with "Least-Square Approximation by Natural Cubic Splines", with Matlab's "Curve Fitting Toolbox".

4.4.7 Sail Area Measurement with the ORC Method

The local North Sails loft in Gothenburg, who manufactured the sail model for the wind tunnel tests, uses the ORC-method [28] when they measure their sails in the manufacturing process, and in order to check the sail area of the sail model, a control measurement with the ORC-method was carried out, i.e. with Eq. (2.73).

4.5 Post-Processing

The wind tunnel software LabVIEW compiled a text file with all the sampled data from the experimental tests, which can be seen in Table 4.23. This was read by a Matlab script, where all the post-processing of the data was performed.

Table 4.23: The variables printed on the text-file that LabVIEW compiled.

Name	Details of the test case, written in the "identifier"
DP	Dynamic pressure [Pa]
U	Airflow velocity, at the test-section inlet [m/s]
T	Temperature, at the test-section inlet [°C]
Pa	Atmospheric pressure [Pa]
Rho	Density of the air [kg/m^3]
Nu	Kinematic viscosity [m^2/s]
Tb	Balance temperature [°C] (not in use and NaN was received)
D	Drag force [N]
S	Side force [N]
L	Lift force [N]
l	Roll moment [Nm]
m	Pitch moment [Nm]
n	Yaw moment [Nm]
Scaled Voltages	E0-E8 [V]

4.5.1 Correction of the Sampled Test Data

Once the numerical investigation was completed and the blockage effects calculated, the following corrections of the sampled test data were performed:

- Balance Error Correction
- Non-Zero Correction
- Drag Tare Correction
- Blockage Effects Correction

Balance Error Correction

It turned out that the balance measured too low for all forces and moments; the error in % and the correction factor, for each component can be seen in Table 5.11, in Chapter 5.

Non-Zero Correction

The non-zero correction was performed after the data had been corrected for the balance measurement error and before the mounting bracket drag tare corrections. This error occurs because the starting value of the registered forces and moments not exactly is zero when a new sampling interval starts. The magnitude of the starting value was generally very low and could be either negative or positive.

Drag Tare Correction

As previously described, two drag tare tests were carried out, where each test isolated and registered contributions to the drag tare from the mounting bracket and the small mounting equipment, respectively. The drag tare from both tests was then subtracted from

the measurements of the strong wind tests, the light wind tests, and the repeatability tests.

Blockage Effects Correction

To be able to correct the measurements from the wind tunnel tests, from blockage effects, a numerical investigation had to be carried out and the final correction of the measurements could then be performed.

4.6 Validation

With the experimental wind tunnel data corrected for all error sources except for blockage, an informal validation was performed by comparing the numerical results with the partly corrected experimental test data.

5
Results

The two main parts of this project are the experimental tests and the numerical investigation. Even though the experimental tests were carried out before the numerical investigation, the results from the numerical investigation were used for the correction of the experimental measurements, for blockage. The results from the numerical investigation are therefore presented first and then the corrected results from the wind tunnel tests are presented.

5.1 Numerical Investigation

The results from the different parts of the numerical investigation are presented in the order, in which they are specified in the list below.

- **Grid Dependence Study**
  - Isotropic Volume Grid Generation & Anisotropic Sub-Layer Grid Generation
  - RANS Simulations *(flat sail model)*
  - Verification Analysis of Discretization Uncertainty
- **Sail Camber & Sheet Angle Analysis**
  - Turbulence Model Investigation *(both sail models)*
  - RANS Simulations *(both sail models)*
  - DES *(cambered sail model)*
  - Blockage Effects

5.1.1 Grid Dependence Study

Isotropic Volume Grid Generation & Anisotropic Sub-Layer Grid Generation

The output from the isotropic volume grid generation and the anisotropic sub-layer grid generation are presented in Table 5.1 together with additional data for the generation of the 5 unstructured grids, with hexahedral cells, of different resolution for both computational domains.

Table 5.1: Results from the isotropic volume grid generation and the anisotropic sub-layer grid generation of the grid set of 5 unstructured grids, with hexahedral cells, with different resolution as well as the refinement degree, the diffusion depth and the grid refinement ratio (relative step size) $h_i \,/\, h_1 = \sqrt[3]{n_1 \,/\, n_i}$, for both computational domains.

Grid	**1**	**2**	**3**	**4**	**5**
Base size [m]	0.0125	0.025	0.05	0.1	0.2
Refinement degree	6	6	6	6	6
Diffusion depth (d)	5	4	3	2	1
Prism-cell layers	50	40	30	20	10
S_n (10^{-5}) [m]	1.81	2.28	3.09	4.76	10.40
r_n [-]	1.0696	1.0878	1.1187	1.1832	1.4
y^+ [-]	0.17	0.22	0.30	0.46	1.00
Cell count (10^6)					
Normal Domain	43.71	7.37	1.29	0.21	0.03
Large Domain	45.35	7.58	1.31	0.21	0.03
Grid refinement ratio [%]					
Normal Domain	1.00	1.81	3.24	5.92	11.17
Large Domain	1.00	1.82	3.26	5.96	11.24

In Table 5.1 above, it can be seen that the base size of a refined grid is received by dividing the base size of the previous coarser grid with a factor of 2. The surface refinement degree is 6 for all grids, i.e. the coarsest cell size, of each grid, is successively and evenly divided into 4 smaller sub-cells, five times, before the prism-cell layers and the sail model surface. The diffusion depth corresponds to the number of grids, in reverse order. The height of the turbulent boundary layer is kept for all refinement levels when calculating the amount of prism-cell layers for each grid refinement. Further, the thickness of the nth prism cell-layer for the refined grid S_n, the growth ratio r_n, and the calculated y^+, for each grid are presented as well.

Grid Images

2D images of the five generated unstructured grids from the grid dependence study, of both computational domains, can be seen in Fig. A.4 - A.35, in Appendix.

5.1.2 RANS Simulations

Drive Force Coefficients

Fig. 5.1 - 5.3 below, shows plots of the drive force coefficients from the RANS simulations with K-Epsilon turbulence model, performed for the grid dependence study. In Fig. 5.1, the drive force coefficients C_{F_M} are plotted against grid 1-5, for both computational domains; in Fig. 5.2 & Fig. 5.3, the drive force coefficients are plotted against the step size $1/\sqrt[3]{No.\ Cells}$, for the normal computational domain (NCD) and the large computational domain (LCD), respectively.

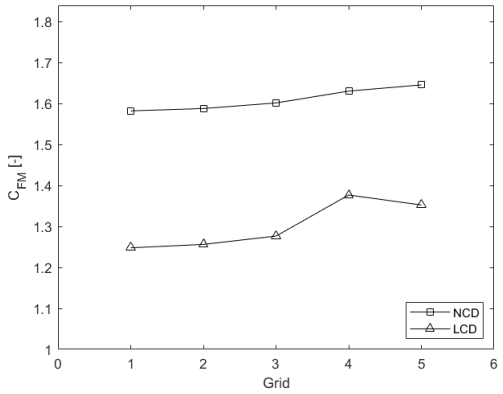

Figure 5.1: Calculated drive force coefficients C_{F_M} [-] vs grid, for both computational domains with the flat sail model.

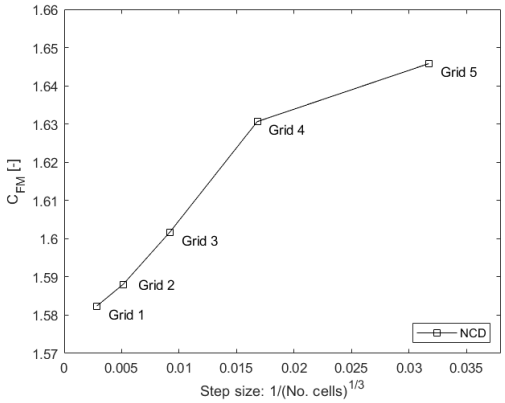

Figure 5.2: Calculated drive force coefficients C_{F_M} [-] vs step size $1/\sqrt[3]{No.\ Cells}$, for the flat sail model in the normal computational domain.

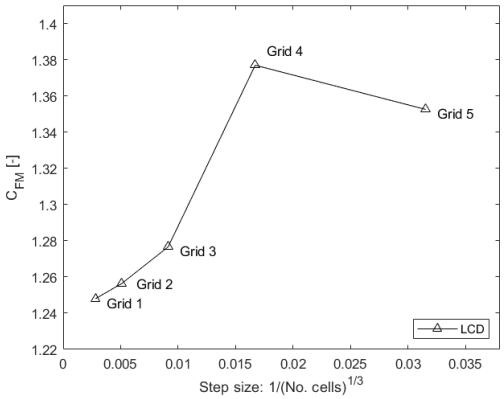

Figure 5.3: Calculated drive force coefficients C_{F_M} [-] vs step size $1/\sqrt[3]{No.\ Cells}$, for the flat sail model in the large computational domain.

The corresponding data from Fig. 5.1 - 5.3 as well as the difference in % of both the drive force coefficients and the step size for each grid and domain, with grid 1 as reference, are presented in Table A.1 & Table A.2, in Appendix.

In Fig. 5.2 & Fig. 5.3, it can be seen that the drive force coefficients decrease almost linearly, for decreasing step size, from the coarsest grid (5) to the finest grid (1), with the exception of grid 4, for both computational domains.

Flow Field Visualization & Residuals

Top view images of the pressure distribution, velocity distribution, and constrained streamlines, from the RANS simulations performed in the grid dependence study, show the scalar quantities at a horizontal xy-plane, at the height of the center of effort (CoE) and can be seen in Fig. A.36 - A.65, in Appendix. The corresponding side view images, that shows the scalar quantities at a centered xz-plane can be seen in Fig. A.66 - A.95, also that in Appendix. Further, images of the residuals, from all RANS simulations, performed in the grid dependence study, can be seen in Fig. A.96 - A.105, in Appendix.

5.1.3 Verification Analysis of Discretization Uncertainty

The relative step size and drive force coefficient, for each grid and both computational domains from the grid dependence study, are used in the discretization verification where an estimation of the uncertainty U is received for each domain. The uncertainty tool that was used for the discretization analysis generated two plots which are presented in Fig. 5.4 & 5.5.

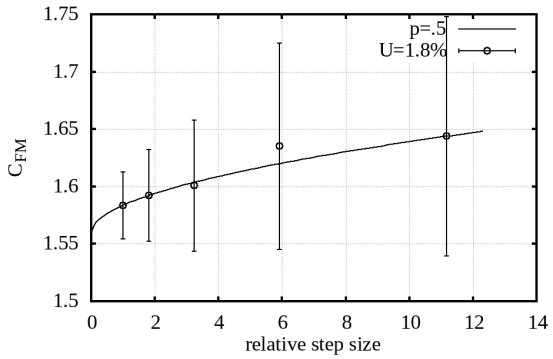

Figure 5.4: Drive force coefficients C_{F_M} [-] vs the relative step size $h_i \,/\, h_1 = \sqrt[3]{n_1 \,/\, n_i}$, for the flat sail model in the normal domain, showing the observed order of convergence $p = 0.5$ and the estimation of the uncertainty $U_\phi = 1.8\,\%$.

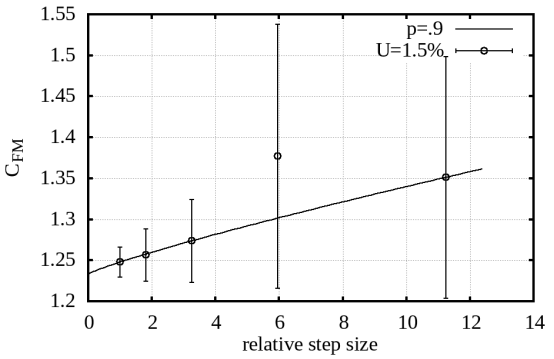

Figure 5.5: Drive force coefficients C_{F_M} [-] vs the relative step size $h_i \,/\, h_1 = \sqrt[3]{n_1 \,/\, n_i}$, for the flat sail model in the large domain, showing the observed order of convergence $p = 0.9$ and the estimation of the uncertainty $U_\phi = 1.5\,\%$.

The corresponding data from Fig. 5.4 & 5.5, are presented in Table A.3, in Appendix.

In Fig. 5.4 & 5.5 the calculated drive force coefficients from the grid dependence study are plotted against the relative step size, for each grid. The estimated uncertainty U_ϕ and the observed order of convergence p can be seen as well. If the error estimation is regarded as reliable, a safety factor F_s of 1.25 is received, and 3 if not. Even though step 1 in the isotropic volume grid generation not could be satisfied completely, the error estimation, which requires geometrically similar grids to be regarded as reliable, indeed was regarded as reliable, this because a safety factor of 1.25 was received for both computational domains. This means that the generated grids at least are geometrically similar enough. Note that the subscript ϕ is missing after U in Fig. 5.4 & 5.5 and that it should be U_ϕ. Note also that the values of the estimated uncertainty U_ϕ are for the finest grid, i.e. for grid 1.

5.1.4 Sail Camber & Sheet Angle Analysis

RANS Simulations

From the grid dependence study, grid number 3 was chosen for the sail camber and sheet angle analysis, because it was regarded as the most reasonable choice, considering the difference in % of the calculated drive force coefficients and the step size, for each grid and computational domain, which can be seen in Table A.2, in Appendix. Further, since the hard setting with the kicker overall gave the highest drive force coefficients in the grid dependence study, the hard setting with the kicker was chosen for the sail camber and sheet angle analysis. The only variable, for each sail model, in the sail camber and sheet angle analysis was therefore the sheet angle, which varies between 60° - 120°, with increments of 10°.

Turbulence Model Investigation

In the initial stage of the sail camber and sheet angle analysis, a turbulence model investigation was performed. The objective with the investigation was to perform RANS simulations for both sail models and both computational domains, with four different turbulence models, analyze the difference and select one for all RANS simulations for the sail camber and sheet angle analysis. The turbulence models are the K-Epsilon two-equation, Menter Shear-Stress Transport (SST) K-Omega two-equation model, Reynolds Stress Transport (RST) model, and Spalart-Allmaras (S-A) one-equation model. The calculated drive force coefficients vs turbulence model, for both sail models in the normal computational domain, are presented in Fig. 5.6 and the corresponding results for both sail models in the large computational domain are presented in Fig. 5.7. In Fig. 5.8 the calculated drive force coefficients for the cambered sail model in the normal computational domain vs turbulence model and the corrected measured drive force coefficients from the experimental tests are plotted together in overlay bars; in Fig. 5.9 the ratio of the Numerical/Experimental results, for each turbulence model, from Fig. 5.8 are presented.

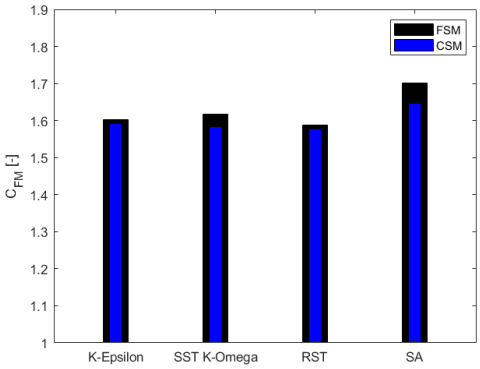

Figure 5.6: Calculated drive force coefficients C_{F_M} [-] vs turbulence model, for the flat sail model (FSM) and the cambered sail model (CSM) in the normal computational domain (NCD).

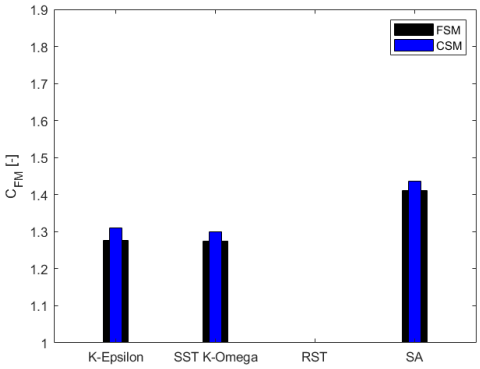

Figure 5.7: Calculated drive force coefficients C_{F_M} [-] vs turbulence model, for the flat sail model (FSM) and the cambered sail model (CSM) in the large computational domain (LCD).

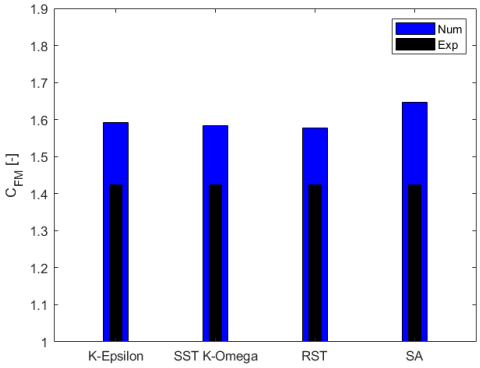

Figure 5.8: Calculated drive force coefficients C_{F_M} [-] vs turbulence model, for the cambered sail model (CSM), in the normal computational domain (NCD) are compared with measured drive force coeff--icients from the wind tunnel tests.

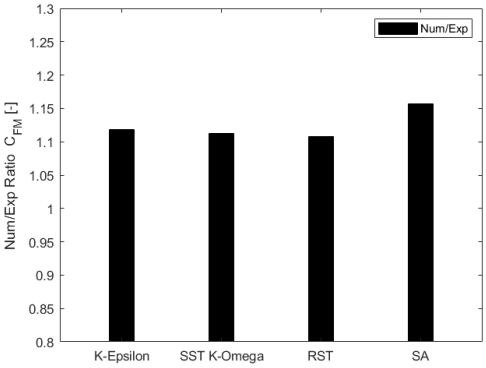

Figure 5.9: Numerical/Experimental ratio of the calculated drive force coefficients C_{F_M} [-] vs turbulence model for the cambered sail model (CSM), in the normal computational domain (NCD) and the measured drive force coefficients from the wind tunnel tests.

The tabulated results from the turbulence model investigation are presented in Table A.4 & Table A.5, in Appendix.

In Fig. 5.6 it can be seen that the difference of the calculated drive force coefficients between K-Epsilon, Menter SST K-Omega and RST, for both sail models in the normal domain is very small. The same trend between K-Epsilon and SST K-Omega in the large domain, where RST diverged can be seen in Fig. 5.7. Since the drive force coefficients with Spalart-Allmaras one-equation model (S-A) are much higher than the drive force coefficients for the other turbulence models, for both sail models and both domains, Spalart-Allmaras turbulence model was deselected and so was the RST model, due to that it diverged with the large computational domain. The final choice therefore stood between K-Epsilon and Menter SST K-Omega. The K-Omega model is, according to [26], dependent of the free stream value of the turbulence frequency ω in external flows with air as medium; since large separation was anticipated and K-Epsilon turbulence model is more suited for wake regions of boundary layers, the latter was chosen for the sail camber & sheet angle analysis. Studying the bar graphs in Fig. 5.8 & 5.9 it becomes evident that the numerical calculations overpredicts the corrected, measured drive force coefficients from the wind tunnel tests.

Sail Coefficients

Fig. 5.10 - 5.15 below, shows the calculated sail coefficients from the RANS simulations with K-Epsilon turbulence model performed for the sail camber and sheet angle analysis. The corresponding data from Fig. 5.10 - 5.15 are presented in Table A.6 - A.9, in Appendix. All forces and moments are measured from the position, downstream the inlet and vertically below the floor, that corresponds to the *balance resolving center*, i.e. the origin of the coordinate system for the wind tunnel balance.

The drive force coefficients and the side force coefficients, for the cambered sail model in the normal domain are used for the calculation of the blockage effects.

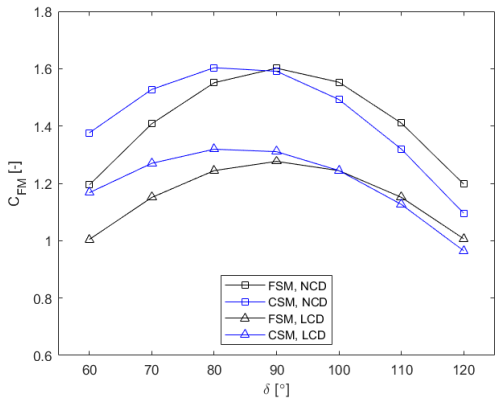

Figure 5.10: Calculated drive force coefficients C_{F_M} [-] vs sheet angle δ [°], for both sail models and both computational domains.

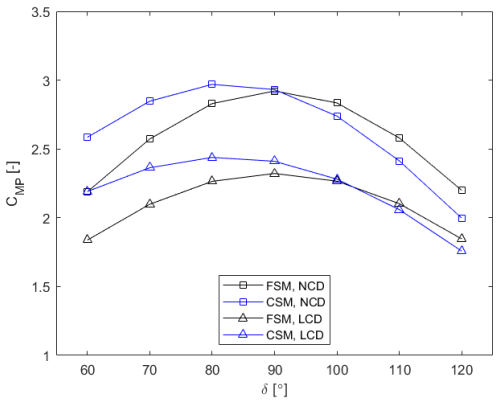

Figure 5.11: Calculated pitch moment coefficients C_{M_P} [-] vs sheet angle δ [°], for both sail models and both computational domains.

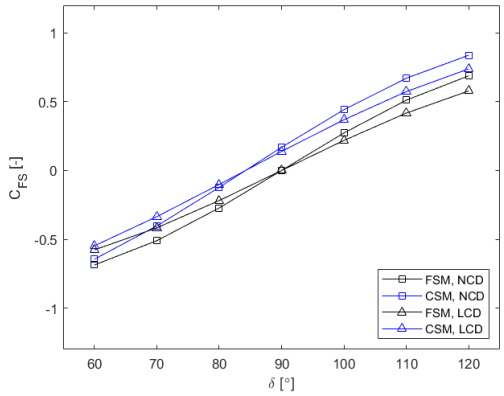

Figure 5.12: Calculated side force coefficients C_{F_S} [-] vs sheet angle δ [°], for both sail models and both computational domains.

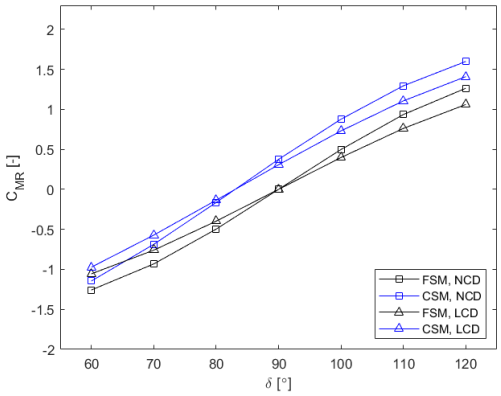

Figure 5.13: Calculated roll moment coefficients C_{M_R} [-] vs sheet angle δ [°], for both sail models and both computational domains.

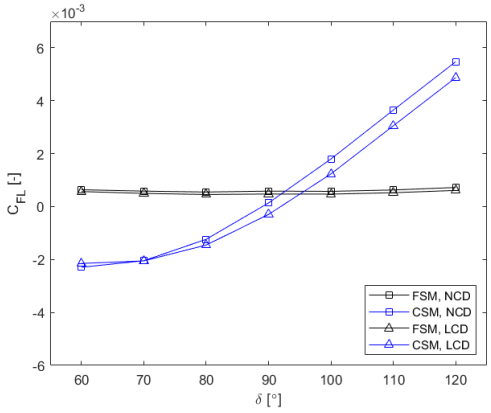

Figure 5.14: Calculated lift force coefficients C_{F_L} [-] vs sheet angle δ [°], for both sail models and both computational domains.

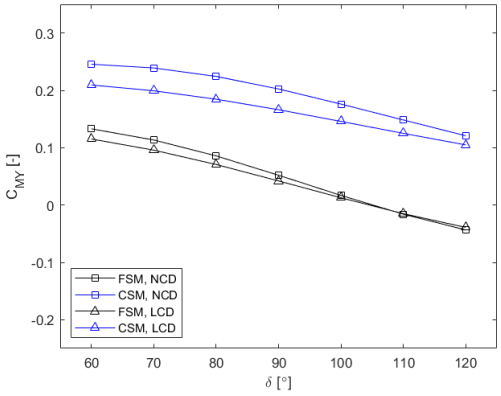

Figure 5.15: Calculated yaw moment coefficients C_{M_Y} [-] vs sheet angle δ [°], for both sail models and both computational domains.

Studying the curves of the drive force coefficients in Fig. 5.10 it can first of all be concluded that the overall appearance of the curves looks reasonable. This because the highest drive force coefficients should be received for the largest projected sail area, which theoretically corresponds to a sheet angle around 90°, and the lowest drive force coefficients should, by the same reasoning, be received with 60° and 120° sheet angles. Since the highest coefficients indeed are received with a sheet angle in the range between 90° - 100°, for both sail models and both domains, and the lowest drive force coefficients also are received for the 60° and 120° sheet angles, this conclusion can be drawn. Continuing the analysis with the curves for both sail models in the normal domain, it can be seen that the curves looks somewhat rotated around the 90° sheet angle, for which the flat sail model only has a slightly larger drive force coefficient. In the lower sheet angle range, 60° - 80°, the cambered sail model has the highest drive force coefficients and in the higher sheet angle range, 100° - 120°, the flat sail model instead has higher drive force coefficients. Looking at the curves for the large domain the trends are similar, except that here the two sail models has almost same drive force coefficients for a sheet angle of 100°. The curve for the flat sail model, for both domains, is more or less completely symmetric around the 90° sheet angle, which is reasonable. The small difference can be explained by that its shape

not is a perfect triangle. The cambered sail model has, as mentioned above, higher drive force coefficients in the lower sheet angle range, 60° - 80°, for both domains, and the main explanation for this is that the projected sail area simply is larger for these sheet angles than the projected sail area for the higher sheet angle range, 100° - 120°. The fact that the shape of the cambered sail model not is symmetric around the 90° sheet angle most probably also influence. The sail model actually has a slightly larger curvature closer to the mast and a flatter aft part, which can be seen in Fig. A.109, in Appendix.
Moving on to study the pitch moment coefficients for both sail models and both domains in Fig. 5.11, the trends are, and should be, similar to the drive force coefficients in Fig. 5.10. This because the pitch moment coefficients simply are the drive force coefficients, multiplied with a factor that corresponds to the vertical lever arm, for each sheet angle.
In Fig. 5.12, it can be seen that the curves of the side force coefficients, for both sail models and both domains, are almost linear. For the lower sheet angle range, 60° - 80°, the curves are however slightly concave with negative coefficients. For $C_{F_S} \approx 0$ we have inflection points. For the higher sheet angle range, 100° - 120°, the curves are slightly convex with positive coefficients. It must be stressed that positive and negative coefficients only indicates the direction of the side force. Further, it can be seen that in the lower sheet angle range, 60° - 80°, for the normal domain, the side force coefficients for the cambered sail model are lower than the coefficients for the flat sail model; in the higher sheet angle range, 100° - 120°, the side force coefficients for the cambered sail model are higher than the side force coefficients for the flat sail model. For the sheet angle 90°, the side force coefficients, for the two different sail models have different sign, but are almost equal in size. The trends are more or less identical for both sail models in the large domain.
In Fig. 5.13 it can be seen that the curves for the roll moment coefficients, for both sail models and both domains, looks almost identical to the corresponding curves for the side force coefficients in Fig. 5.12, with the difference that the values are larger negative and larger positive, which is correct. This because the roll moment coefficients are the side force coefficients, multiplied with a factor that corresponds to the vertical lever arm, for each sheet angle.
In Fig. 5.14 the curves for the lift force coefficients are presented and it can be seen that the coefficients for the flat sail model, in both domains, are almost of the same magnitude for all sheet angles, which is reasonable. The coefficients for the normal domain are however slightly larger positive than the coefficients for the large domain, which is less reasonable. Moving forward to the curves for the cambered sail model, the coefficients increase almost exponentially in the sheet angle range 60° - 90°, and linearly between 90° - 120°. For 60° sheet angle, the cambered sail model is larger negative for the normal domain and for the sheet angle range 70° - 90°, the cambered sail model in the large domain are larger negative and finally for the sheet angle range 100° - 120°, the coefficients for the cambered sail model in the normal domain are larger positive.
In Fig. 5.15, the yaw moment coefficients for the cambered sail model are, for both domains, larger than all coefficients for the flat sail model, which has positive values for the sheet angles 60° and 100°. Comparing the coefficients for the cambered sail model, it can be seen that the coefficients are larger for the normal domain, for all sheet angles. For the flat sail model in the normal domain, the coefficients are slightly larger in the sheet angle range 60° - 100° and more or less the same as the coefficients for the large domain for the sheet angles 100° and 120°.

Flow Field Visualization

Fig. 5.16 - 5.21 below, shows 2D top view images of the pressure distribution, velocity dis-

tribution and constrained streamlines, at a horizontal xy-plane, at the height of the center of effort (CoE) for the cambered sail model, with a sheet angle of 90° in both computational domains. Only these will be presented in this Chapter. The remaining 2D top view images; the corresponding 2D side view images that shows the scalar quantities at a vertical xz-plane in the center of the domain, from all RANS simulations, performed for the sail camber and sheet angle analysis, can be seen in Fig. A.110 - A.277, in Appendix.

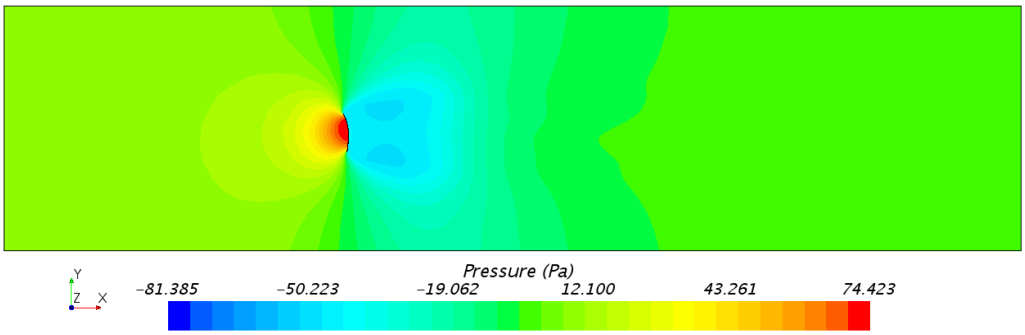

Figure 5.16: Top view of the normal computational domain, showing the pressure distribution, at the height of the center of effort (CoE); the cambered sail model, with a sheet angle of 90°.

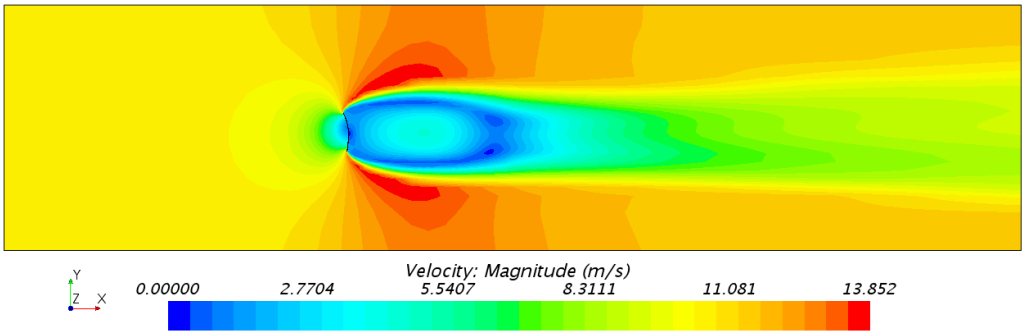

Figure 5.17: Top view of the normal computational domain, showing the velocity distribution, at the height of the center of effort (CoE); the cambered sail model, with a sheet angle of 90°.

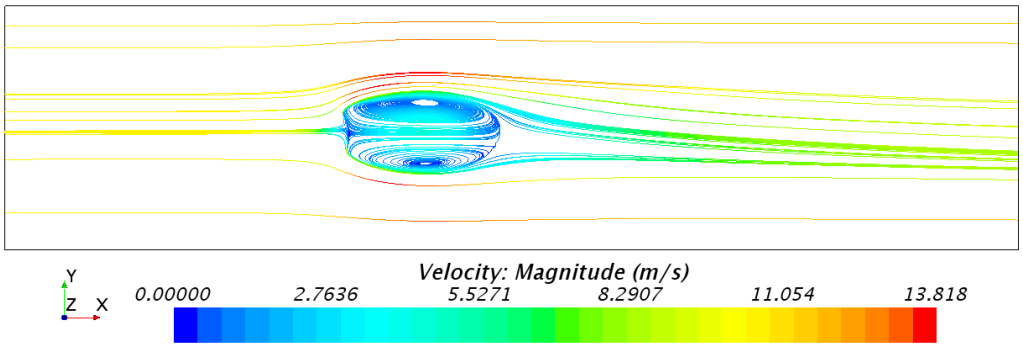

Figure 5.18: Top view of the normal computational domain, showing constrained streamlines, at the height of the center of effort (CoE); the cambered sail model, with a sheet angle of 90°.

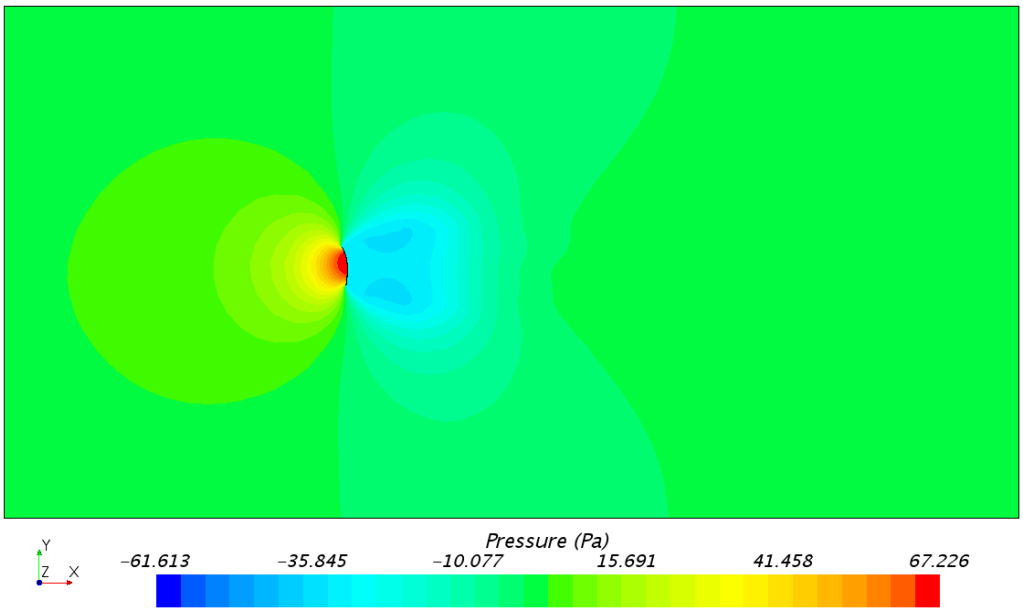

Figure 5.19: Top view of the large computational domain, showing the pressure distribution, at the height of the center of effort (CoE); the cambered sail model, with a sheet angle of 90°.

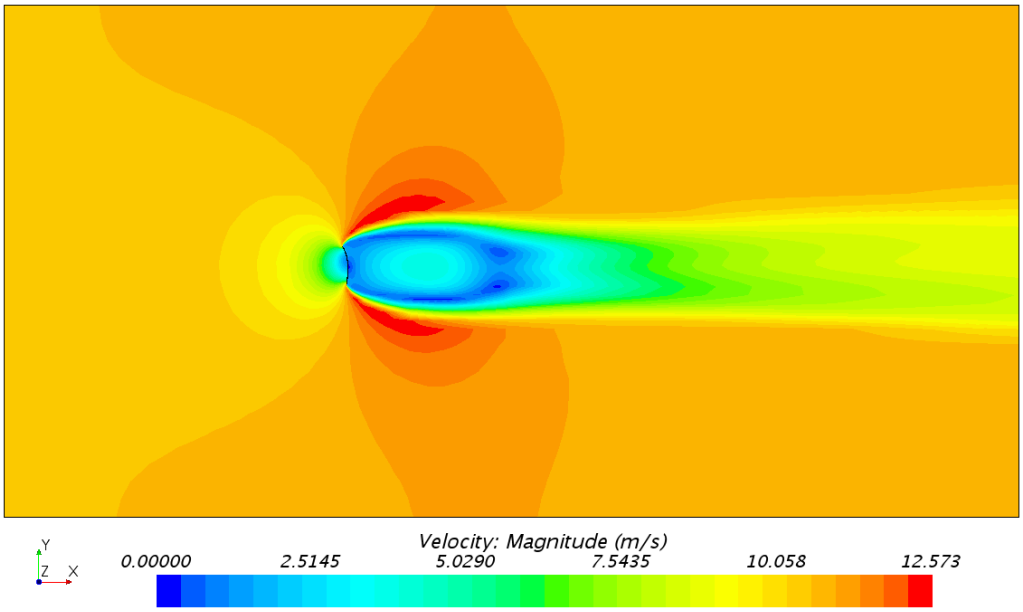

Figure 5.20: Top view of the large computational domain, showing the velocity distribution, at the height of the center of effort (CoE); the cambered sail model, with a sheet angle of 90°.

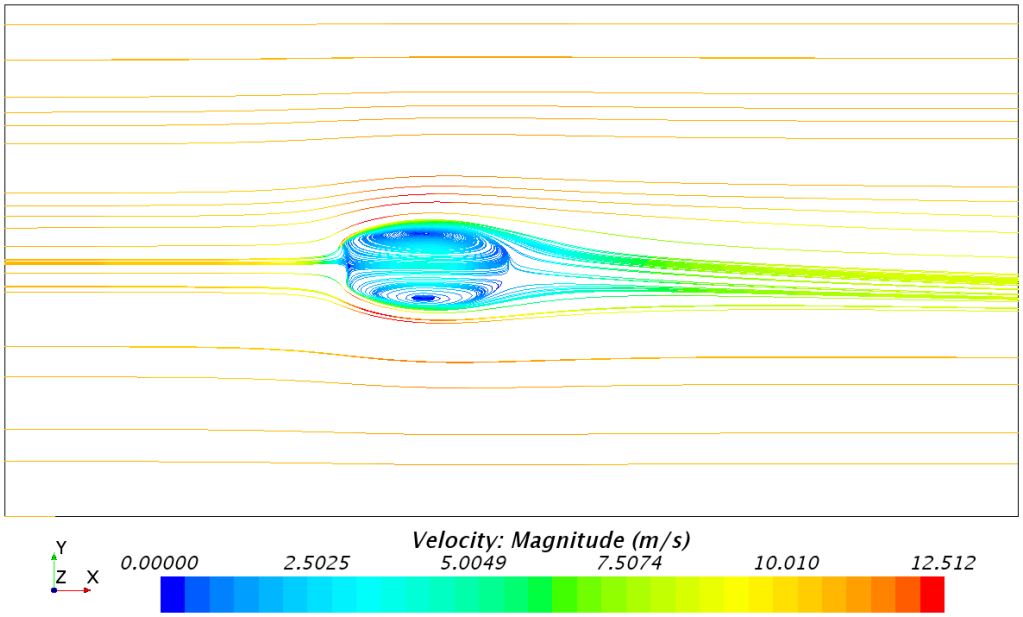

Figure 5.21: Top view of the large computational domain, showing constrained streamlines, at the height of the center of effort (CoE); the cambered sail model, with a sheet angle of 90°.

In Fig. 5.16 - 5.21 a high degree of symmetry can be seen in the wake behind the sail model for both the pressure field and the velocity field, for both computational domains, but no clear oscillations, which are characteristic for von Karman's vortex street, can be seen. A 10.7 % higher pressure and 10.1 % higher velocity magnitude are received with the normal computational domain. The separation bubbles and the recirculation region can easily be distinguished in Fig. 5.18 and Fig. 5.21, for the normal and large computational domain, respectively.

Sail Camber and Wake Analysis of the Normal Computational Domain

Fig. 5.22 & 5.23 show close-up images of the top half of the two sail models; Fig. 5.24 & 5.25 are close-up images of the wakes, showing two huge separation bubbles behind each sail model, as well as the length and the width of the wakes.

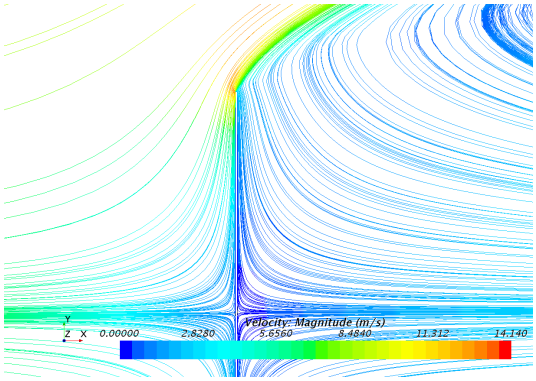

Figure 5.22: Top view, of constrained streamlin--es around the flat sail model, at the height of CoE, in the normal computational domain, showing the angle by which the airflow separates from the sail.

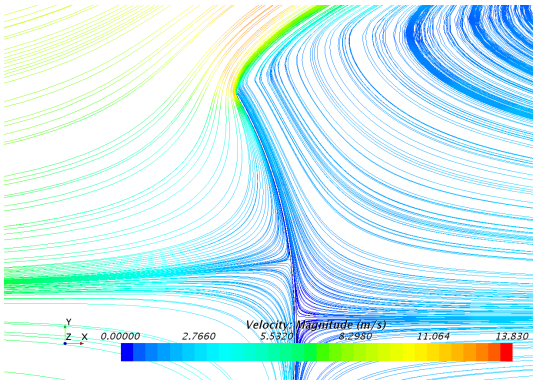

Figure 5.23: Top view, of constrained streamlines around the cambered sail model, at the height of CoE, in the normal computational domain, showing the angle by which the airflow separates from the sail.

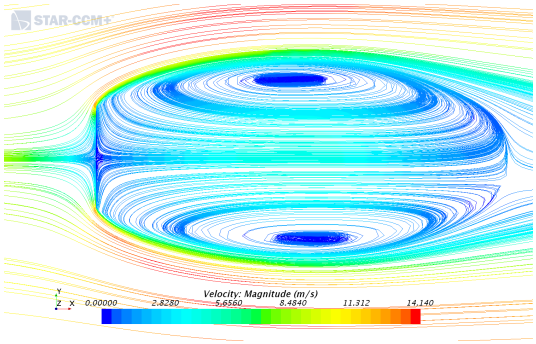

Figure 5.24: Top view, of constrained streamlin--es around the flat sail model, at the height of CoE, in the normal computational domain, showing two huge separation bubbles, as well as the length and width of the wake.

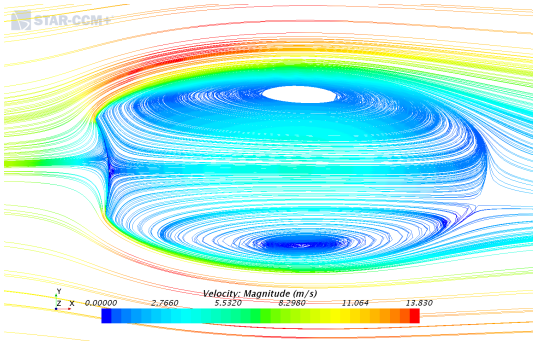

Figure 5.25: Top view, of constrained streamlines around the cambered sail model, at the height of CoE, in the normal computational domain, showing two huge separation bubbles, as well as the length and width of the wake.

In Fig. 5.22 - 5.23 it can be seen that the separation angle of the airflow, differs slightly between the sail models. The reason for carrying out the sail camber analysis, was because it was believed that the cambered sail model creates a wider wake and therefore also higher blockage. However, when studying the plots of the calculated drive force coefficients, for both domains, in Fig. 5.10, it becomes clear that the calculated drive force coefficients for the cambered sail model only are higher than the flat sail model for the sheet angles between 60° - 80° and higher for the flat sail model from 90° - 120°, for the normal domain. In Fig. 5.24 & 5.25, which shows 2D top views of the wake and the separation bubbles for the flat sail model and the cambered sail model, respectively, with a sheet angle of 90°, it can be seen that both the width and the length of the wake, behind the flat sail model, are slightly wider and longer than the wake behind the cambered sail model. The most probable reason for that the flat sail model generates higher drive force coefficients for sheet angles above 90° is that it has a larger projected sail area.

Residuals

Images of the residuals for the particular case presented in this Chapter, for both computational domains, can be seen in Fig. 5.26 & Fig. 5.27; images of the residuals for all other cases can be seen in Fig. A.278 - A.305, in Appendix.

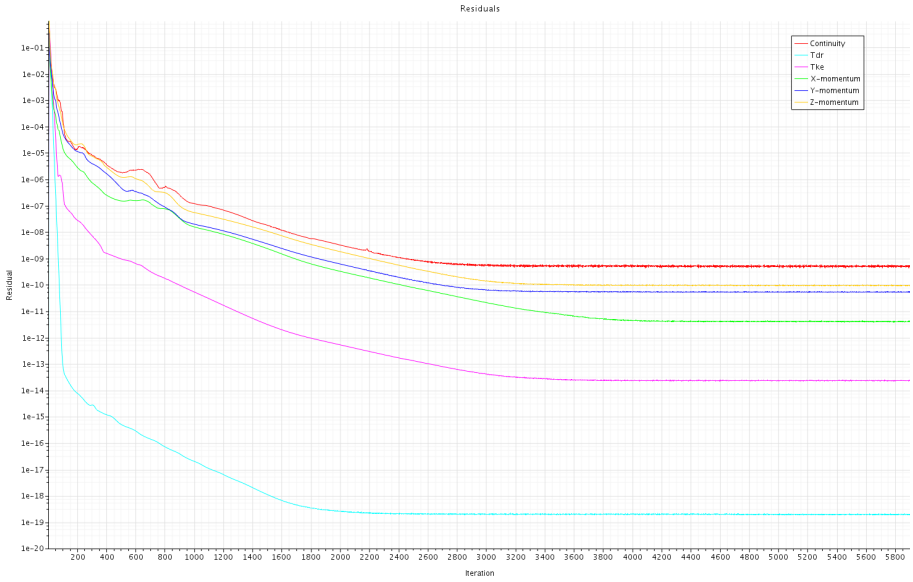

Figure 5.26: Residual vs iteration, from RANS simulations with the cambered sail model, with a sheet angle of 90°, in the normal computational domain & grid 3, showing the graphs of the Continuity (red), X-momentum (green), Y-momentum (blue), Z-momentum (yellow), Turbulent dissipation rate (cyan) and the Turbulent kinetic energy (purple).

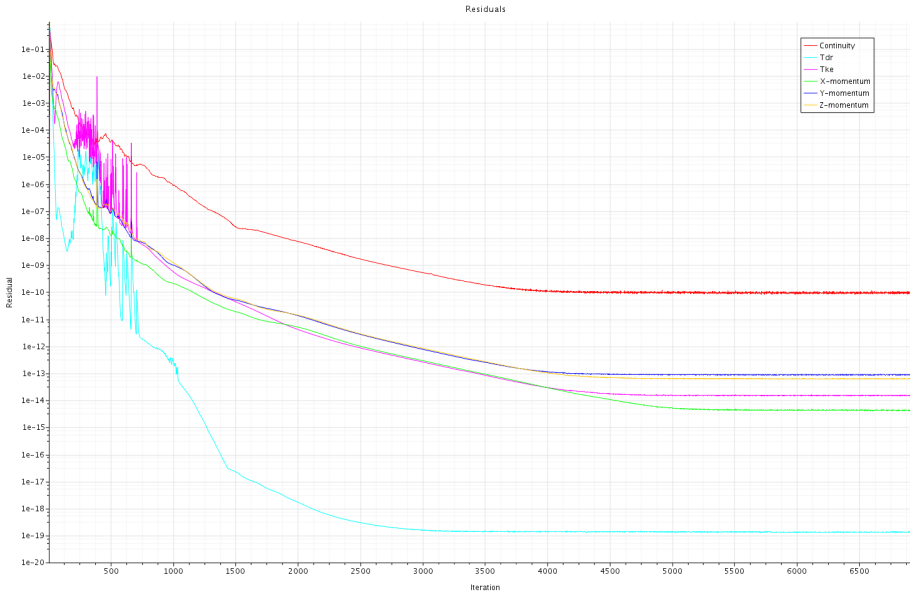

Figure 5.27: Residual vs iteration, from RANS simulations with the cambered sail model, with a sheet angle of 90°, in the large computational domain & grid 3, showing the graphs of the Continuity (red), X-momentum (green), Y-momentum (blue), Z-momentum (yellow), Turbulent dissipation rate (cyan) and the Turbulent kinetic energy (purple).

In Fig. 5.26, which shows the residuals for the normal computational domain, it can be

seen that the residual of the Continuity (red) converge after approximately 3000 iterations, the X-momentum (green) converge after 4000 iterations, the Y-momentum (blue) converge after 3000 iterations, the Z-momentum (yellow) converge after 3400 iterations, the turbulent dissipation rate (cyan) converge after approximately 2200 iterations and finally, the turbulent kinetic energy (purple) require approximately 3600 iterations before it converge.
In Fig. 5.27, which shows the residuals for the large computational domain, it can be seen that the residual of the Continuity (red) converge after approximately 4000 iterations, the X-momentum (green) converge after 5000 iterations, the Y-momentum (blue) converge after 4000 iterations, the Z-momentum (yellow) converge after 4500 iterations, the turbulent dissipation rate (cyan) converge after approximately 3500 iterations and finally, the turbulent kinetic energy (purple) after approximately 4500 iterations.

5.1.5 Detached-Eddy Simulation (DES)

To investigate whether or not an unsteady approach with DES would give results that were in better agreement with the experimental measurements, than the calculated results from the RANS simulations, a *sheet angle analysis* with DES, with Spalart-Allmaras (S-A) turbulence model was carried out. The same set of parameters that were used in the sail camber and sheet angle analysis for the RANS simulations were also used for DES, with the exception that, with DES, only the cambered sail model was used. The set of parameters for the DES can be seen in Table 4.21.

Drive Force Coefficients

In Fig 5.28 below, the average drive force coefficients from the last 100 000 iterations (2.5 physical seconds) from DES, with $S-A$ turbulence model, are plotted against the sheet angle δ [°], for both domains.

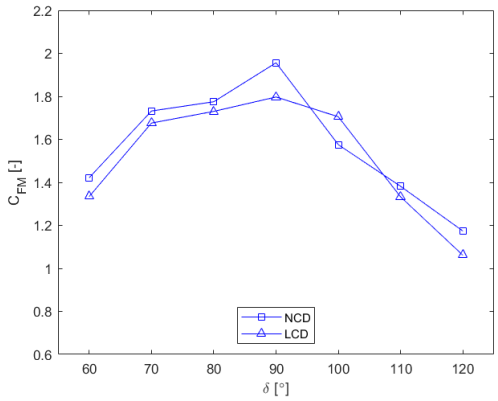

Figure 5.28: Average drive force coefficients C_{F_M} [-] from the last 100 000 iterations (2.5 physical seconds) from DES with S-A turbulence model vs the sheet angle δ [°], for both domains.

The corresponding data from Fig 5.28 is presented in Table A.11, in Appendix.

In Fig 5.28 the curves for the two domains in the low sheet angle range, i.e. 60° - 80°, are very parallel in appearance. The drive force coefficients for the normal domain are higher than those for the large domain, which they should be, but for the 90° - 120°, the parallelism cannot be seen and the drive force coefficient for the sheet angle 100° with the

large computational domain is larger than the corresponding drive force coefficient for the normal computational domain, which is nonphysical. It was therefore decided that the results from the RANS simulations, with the K-Epsilon turbulence model should be used for the calculation of the correction factors for blockage. Because of that, only the drive force coefficients C_{F_M} [-], from the DES results are presented in this project.

Flow Field Visualization

Fig. 5.29 & Fig. 5.30 below, shows 2D top view images of the velocity distribution and constrained streamlines, respectively, at a horizontal xy -plane, at the height of the center of effort (CoE) for the cambered sail model with a sheet angle of 90° in the normal domain. The corresponding side view images that shows the scalar quantities at a vertical xz -plane in the center of the domain can be seen in Fig. 5.31 & Fig. 5.32. For comparison reasons, the corresponding 2D top view image of the large domain of the velocity distribution, can be seen in Fig. 5.33. Only the case with the 90° sheet angle will be presented in this Chapter. The top- and side view images of the velocity distribution and constrained streamlines for the remaining sheet angles, for both domains, can be seen in Fig. A.306 - A.361, in Appendix.

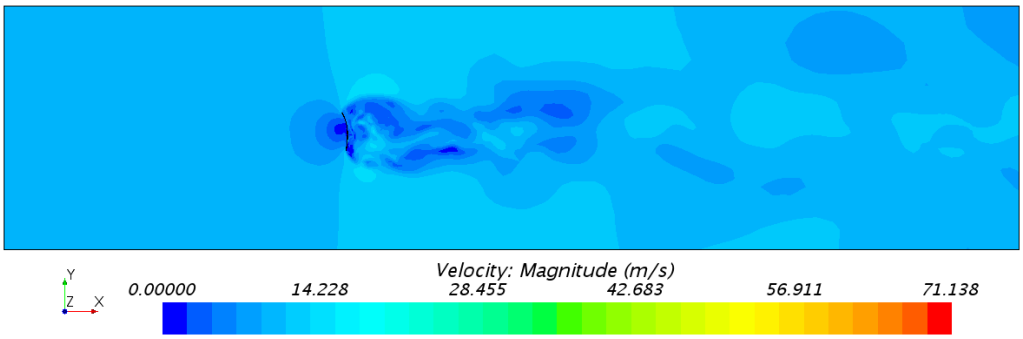

Figure 5.29: 2D Top view of the normal computational domain, showing the velocity distribution, at the height of the center of effort (CoE); the cambered sail model, with a sheet angle of 90°.

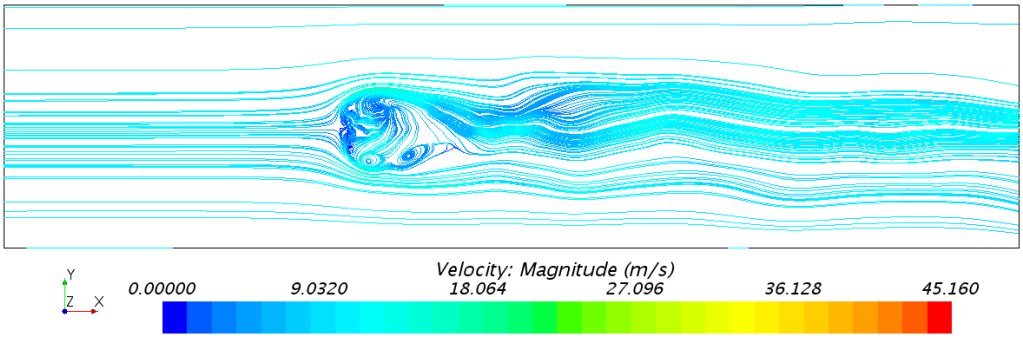

Figure 5.30: Top view, of the normal computational domain, showing constrained streamlines and the cambered sail model, with a sheet angle of 90°, at the height of the center of effort (CoE).

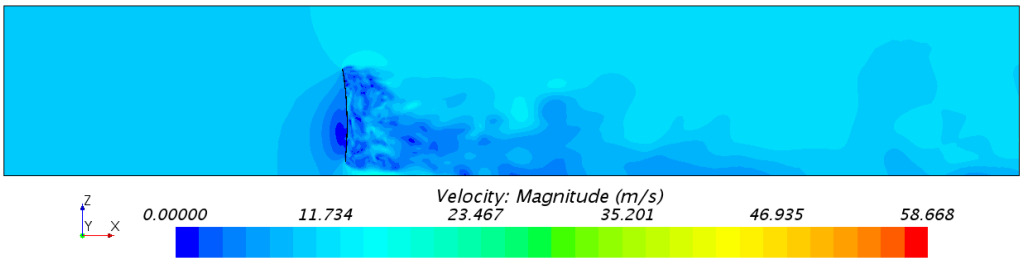

Figure 5.31: Side view, of the normal computational domain, showing the velocity distribution, at a centered xz-plane; the cambered sail model, with a sheet angle of 90°.

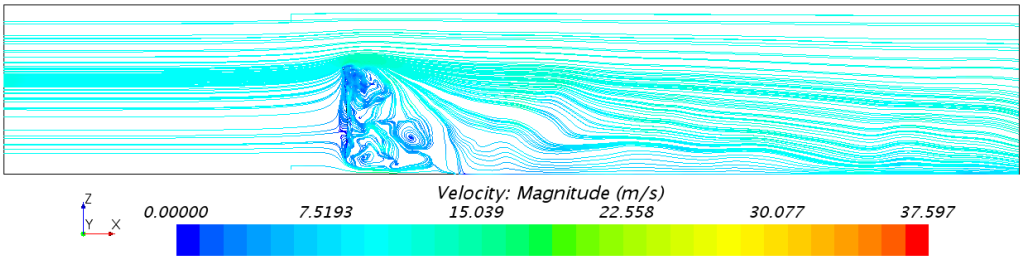

Figure 5.32: Side view, of the normal computational domain, showing constrained streamlines, at a centered xz-plane; the cambered sail model, with a sheet angle of 90°.

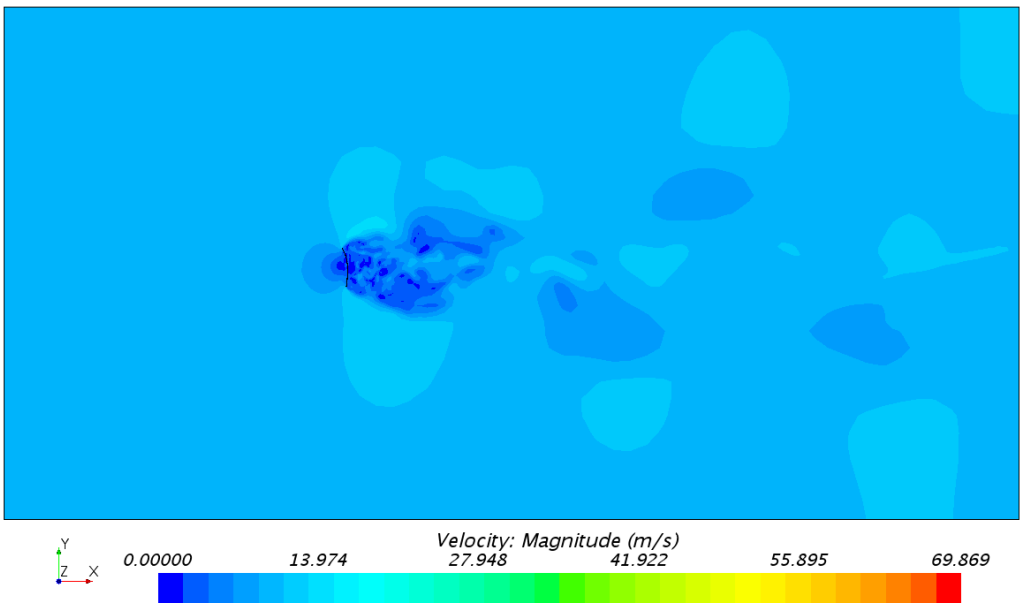

Figure 5.33: Top view of the large computational domain, showing the velocity distribution, at the height of the center of effort (CoE); the cambered sail model, with a sheet angle of 90°.

In Fig 5.29 and Fig 5.33, which show the velocity field, from a top view in the normal and large computational domain, respectively, it can be seen that DES managed better than RANS to resolve the small turbulent structures in the wake behind the sail model and also capture a somewhat oscillating behavior of the wake flow.

Residuals

An image of the residuals for the case with the 90° sheet angle can be seen in Fig. 5.34 below; images of the residuals for the remaining cases, from the sheet angle analysis, for both computational domains, can be seen in Fig. A.362 - A.375, in Appendix.

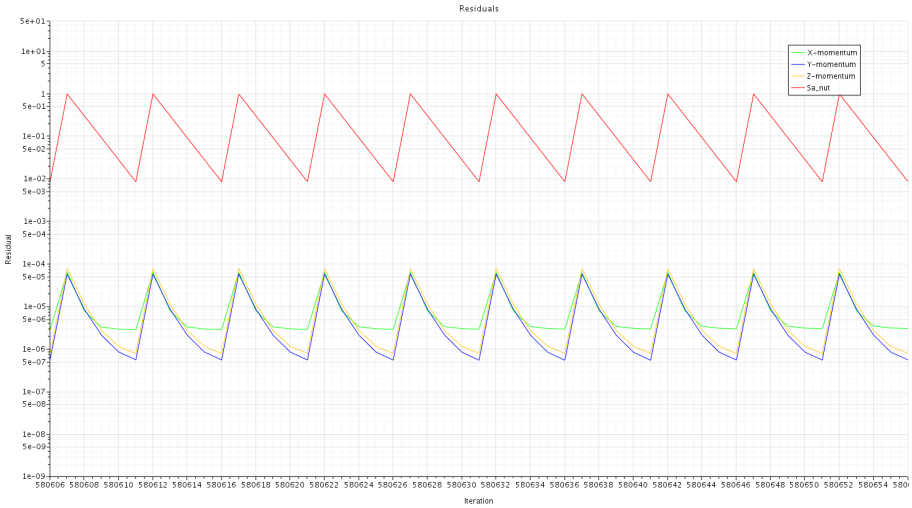

Figure 5.34: Residual vs iteration, from DES with the cambered sail model, with a sheet angle of 90°, in the normal computational domain & grid 3, showing the graphs of the X-momentum (green), Y-momentum (blue), Z-momentum (yellow) and Spalart-Allmaras Turbulent kinetic energy (red) of the last 50 iterations, with maximum 5 inner iterations.

In Fig. 5.34 the residuals of the last 50 iterations, with five inner iterations, are presented and it can be seen that the X-momentum residual (green) converges already after two inner iterations and that the Y- (blue) and the Z- (yellow) momentum residuals converges within five iterations. The appearance of the residual for Spalart-Allmaras turbulent kinetic energy (red) indicate that it might not converge within one time step.

5.1.6 Blockage Effects

As previously mentioned, the calculated results from the RANS simulations from the sail camber and sheet angle analysis, presented in Table A.7 & Table A.9 were used for the calculation of the blockage and the corresponding correction factors for all components, except for the lift force coefficient. The lift force coefficient was neglected because it's values are so low. Since the pitch moment coefficients are the product of the drive force coefficients and the vertical lever arm; the yaw moment coefficients are the product of the drive force coefficients and the horizontal lever arm, the measured pitch moment coefficients and measured yaw moment coefficients, from the wind tunnel tests, were corrected with the correction factors received with Eq. (4.77). Further, since the roll moment coefficients are the product of the side force coefficients and the vertical lever arm, the correction factors received with Eq. (4.78) were used for the correction of the measured roll moment coefficients.

Correction Factors from the Drive Force Coefficients

Fig. 5.35 below, shows a plot with correction factors, both calculated with the drive force coefficients C_{F_M} [-] that are received from the RANS simulations for the sail camber and

sheet angle analysis and extrapolated correction factors for the sheet angles: 50°, 130°, 140° & 150°. The extrapolated corrections factors were necessary when correcting the sheet angles for the headings 150° & 190°.

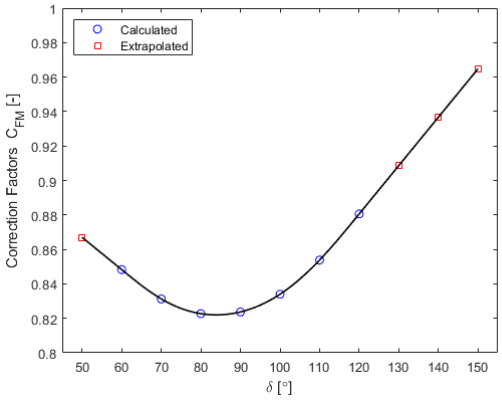

Figure 5.35: Extrapolation of the correction factors [-], from the drive force coefficients C_{F_M} [-], with the method "Least-Square Approximation by Natural Cubic Splines", with Matlab's *Curve Fitting Toolbox*.

The corresponding data from Fig. 5.35 are presented in Table 5.2 & Table 5.3.

Table 5.2: Blockage effects in %, calculated with the drive force coefficients C_{F_M} [-], retrieved from the RANS simulations, performed for the sail camber and sheet angle analysis, with the cambered sail model, as well as the calculated corresponding correction factors.

Sheet angle [°]	**60**	**70**	**80**	**90**	**100**	**110**	**120**
Blockage effects [%]	15.17	16.88	17.73	17.63	16.60	14.62	11.94
Correction factors [-]	0.8483	0.8312	0.8227	0.8237	0.8340	0.8538	0.8806

Table 5.3: Extrapolated blockage effects in [%], for the sheet angles: 50°, 130°, 140° & 150°, of the drive force coefficients C_{F_M} [-], using "Least-Square Approximation by Natural Cubic Splines", with Matlab's *Curve Fitting Toolbox* and the corresponding calculated correction factors [-].

Sheet angle [°]	**50**	**130**	**140**	**150**
Blockage effects [%]	13.30	9.13	6.33	3.52
Correction factors [-]	0.867	0.9087	0.9367	0.9648

The measured drive force coefficients, pitch moment coefficients and yaw moment coefficients from the wind tunnel tests were corrected by multiplying the correction factors in Table 5.2 & Table 5.3.

Correction Factors from the Side Force Coefficients

Fig. 5.36 below, shows a plot with correction factors, both calculated with the side force coefficients C_{F_S} [-], that are received from the RANS simulations for the sail camber and sheet angle analysis and extrapolated correction factors for the sheet angles: 50°, 130°, 140° & 150°. The extrapolated correction factors were necessary when correcting the sheet angles for the headings 150° & 190°.

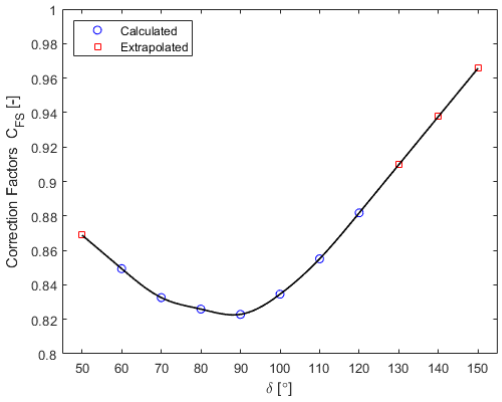

Figure 5.36: Extrapolation of the correction factors [-], from the side force coefficients C_{F_S} [-], with the method "Least-Square Approximation by Natural Cubic Splines", with Matlab's *Curve Fitting Toolbox*.

The corresponding data from Fig. 5.36 are presented in Table 5.4 & Table 5.5.

Table 5.4: Blockage effects in %, calculated with the side force coefficients C_{F_S} [-], retrieved from the RANS simulations, performed for the sail camber and sheet angle analysis, with the cambered sail model, as well as the calculated corresponding correction factors.

Sheet angle [°]	**60**	**70**	**80**	**90**	**100**	**110**	**120**
Blockage effects [%]	15.06	16.74	17.41	17.71	16.54	14.49	11.82
Correction factors [-]	0.8494	0.8326	0.8259	0.8229	0.8346	0.8551	0.8818

Table 5.5: Extrapolated blockage effects in [%], for the sheet angles: 50°, 130°, 140° & 150°, of the side force coefficients C_{F_S} [-], using "Least-Square Approximation by Natural Cubic Splines", with Matlab's *Curve Fitting Toolbox* and the corresponding calculated correction factors [-].

Sheet angle [°]	**50**	**130**	**140**	**150**
Blockage effects [%]	13.11	9.03	6.23	3.43
Correction factors [-]	0.8689	0.9097	0.9377	0.9657

The measured side force coefficients and roll moment coefficients from the wind tunnel tests were corrected by multiplying the correction factors in Table 5.4 & Table 5.5.

5.2 Experimental Tests

5.2.1 Mast Data (Full-Scale)

The outer radius a_i and the inner radius b_i, where the subscript $i = 1, 2$ represent respectively the mast bottom section and the mast top section of the full-scale aluminum mast, are presented in Table 5.6. The Young's modulus E_p and the calculated flexural rigidity EI_{p_i} for each section, where the subscript p stand for prototype, are presented there as well.

Table 5.6: The outer radius a_i and inner radius b_i, for the full-scale mast in aluminum, Young's modulus E and the calculated flexural rigidity EI_{p_i}.

Cross section: Tube			**Material: Aluminum**	
Section	a_i **E-3 [m]**	b_i **E-3 [m]**	E **[GPa]**	EI_{p_i} **[Nm^2]**
Bottom	31.75	28.75	60	15692
Top	25.60	23.60	60	5622

Flexural Tests

The variation of the mass, of the bottom sections and the top sections from the control weighing of the four different ILCA 7 masts in the initial phase of the flexural tests, are presented in Table 5.7.

Table 5.7: Results from the control weighing of the four different bottom sections and top sections.

Mast Nr.	**1**	**2**	**3**	**4**
Section		**mass [kg]**		
Bottom	2.894	2.882	2.888	2.737
Top	4.685	4.678	4.674	4.692

Fig. 5.37 below, shows the cuts and the theoretical displacement curve of the full-scale ILCA 7 mast as well as the loading points and the experimental displacement curve from the flexural tests. Note that the calculated average displacements are used when plotting the experimental displacement curve.

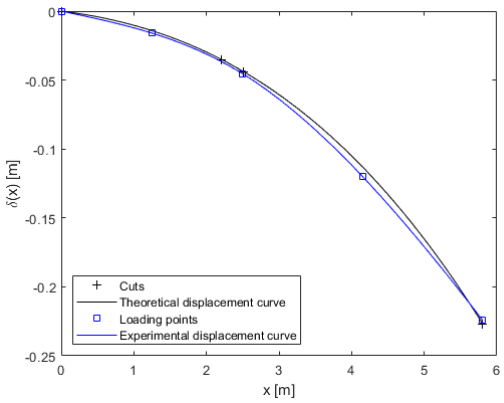

Figure 5.37: The cuts and the theoretical displacement curve as well as the loading points and the experimental displacement curve of the combined full-scale ILCA 7 mast.

The data from Fig. 5.37 are presented in Table 5.8 below.

Table 5.8: The results from the 5 experimental flexural tests shows the displacements of the mast under load, at the four loading points as well as the calculated average of the test series, that are used in the plot.

x-position [m]	**0.0000**	**1.2500**	**2.5000**	**4.1530**	**5.8050**
Test series			$\delta(x)$ [m]		
1	0.0000	0.0160	0.0460	0.1190	0.2170
2	0.0000	0.0155	0.0455	0.1200	0.2250
3	0.0000	0.0160	0.0450	0.1210	0.2280
4	0.0000	0.0165	0.0460	0.1205	0.2250
5	0.0000	0.0160	0.0450	0.1200	0.2265
Calculated average value					
Average	0.0000	0.0160	0.0455	0.1201	0.2243

The position at $x = 0.0000$ is as mentioned at the deck-level; the position at $x = 1.2500$ is the average value between the deck-level and the right edge of the overlap; the position at $x = 2.5000$ is the right edge of the overlap; the position at $x = 4.1530$ is the average value between the right edge of the overlap and the mast top; finally, the position at $x = 5.8050$ is the mast top.

Table 5.9 shows the corresponding theoretical data from the calculations of the displacements of the full-scale ILCA 7 mast.

Table 5.9: The corresponding data of $\delta(x)$, for the theoretical displacement curve in Fig. 5.37.

x [m]	0.0000	2.2050	2.5000	5.8050
$\delta(x)$ [m]	0.0000	0.0350	0.0440	0.2270

The first x-value corresponds to *cut 1* at the deck-level, the second x-value to *cut 2* at the left edge of the overlap, the third x-value to *cut 3* at the right edge of the overlap and the fourth x-value to the mast top.

5.2.2 Mast Data (Model-Scale)

For the mast model, it was desired to scale the flexural rigidity (EI) of the mast prototype and with Eq. (4.58), the flexural rigidity for each mast model section $(EI_i)_m$ were calculated. Then, the radii of the solid mast model sections a_{m_i} were calculated with Eq. (4.62), where the subscript $i = 1, 2, 3$ represent the mast bottom section, the mast top section and the mast foot, respectively. All these data as well as the lengths of each mast model section L_{m_i} and the Young's Modulus for the mast model E_m are presented in Table 5.10.

Table 5.10: Data, of the solid mast model sections.

Cross section: Solid		**Material: Stainless Steel**		
Section	a_{m_i} **E-3 [m]**	L_{m_i} **E-3 [m]**	E_m **[GPa]**	$(EI_m)_i$ **[Nm^2]**
Bottom	4.15	0.359	196	45.8
Top	3.20	0.4710	196	16.4
Mast foot	4.15	0.050	196	45.8

5.2.3 Scale Effects

By choosing the linear length scale factor $\alpha_L = 1/7$ and the velocity scale factor $\alpha_V = \sqrt{7}$ it was possible to receive equal strains in the sail and the same mast bend in both scales. How the mast model sections were scaled are explained in Chapter 4. Further, in Eq. (4.65) it could be seen that it was unfortunately not possible to scale the Reynolds number exactly. The consequences of the discrepancy were discussed in Section 4.1.8.

Geometrical Differences

Even though it was possible to scale the sail and use the cloth from a new full-scale MKII sail for the model sail, some geometrical differences could not be avoided. The sailmakers strived to scale all the small details that are mounted in the full-scale MKII sail, e.g. the new MKII sail, which is of bi-radial design, has a large number of overlapping panels and to get the model as accurate as possible the width of the overlapping panels were also scaled. This, however, required straight stitches instead of the usual zigzag stitches. Further, instead of a traditional eyelet, the sail model was equipped with thin U-shaped sailcloth *hooks*, where the trim controls the *cunningham* and *outhaul* were mounted. The window in the full-scale sail was deselected, because it should not influence the performance.

5.3 Wind Tunnel Tests

The results from the wind tunnel tests are presented in the order in which they are specified in the list below.

- Balance Tests
- Light Wind Tests
- Repeatability Tests
- Strong Wind Tests

5.3.1 Balance Tests

The balance tests, carried out after the wind tunnel tests, made it possible to quantify the balance measurement error and create correction factors for the measured forces and moments. The results from the balance tests are presented in Table 5.11, below. However, since the lift force component F_L that measured the force in the vertical z-direction, generally measured so low values during the tests, it was ignored for the balance tests. The tests showed that the wind tunnel balance measured too low values, so the two other force components and all three moments were corrected by dividing all measured wind tunnel data with the corresponding correction factor.

Table 5.11: Balance measurement errors, for each component, received from the balance tests, as well as the corresponding correction factors that are used for the correction of the measured experimental data.

Load component	F_M [N]	F_S [N]	M_P [Nm]	M_R [Nm]	M_Y [Nm]
Balance Error [%]	0.76	0.28	0.76	0.80	1.23
Correction factor [-]	0.9924	0.9972	0.9924	0.9920	0.9877

5.3.2 Light Wind Tests

The test matrix for the light wind tests, with the apparent wind speed $V_{AW} = 10.6$ m/s, consisted of five headings, three heel angles, and seven sheet angles; and for each configuration of these, three different settings with the kicker were tested. In this subsection, the corrected measured sail coefficients, received in the light wind tests, are presented. The lift force coefficients have, however, neither been corrected for the balance measurement error nor for the blockage effects; the reason for this, which has been mentioned earlier, was that the values for the lift force, which measured the vertical force component, were very low and therefore not of interest.

Drive Force Coefficients

In Fig. 5.38 - 5.52 below, the corrected measured drive force coefficients C_{F_M} [-] are plotted against the sheet angle δ [°], where LKT, MKT and HKT stands for Light Kicker Trim, Medium Kicker Trim and Hard Kicker Trim, respectively. The corresponding data from Fig. 5.38 - 5.52 are presented in Table A.12 - A.16, in Appendix.

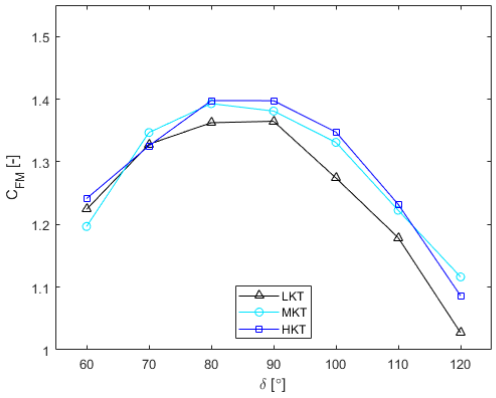

Figure 5.38: Corrected drive force coefficients C_{F_M} [-] vs sheet angle δ [°], for the three settings with the kicker: LKT, MKT and HKT, for the heading: 150° and the heel angle: 0°.

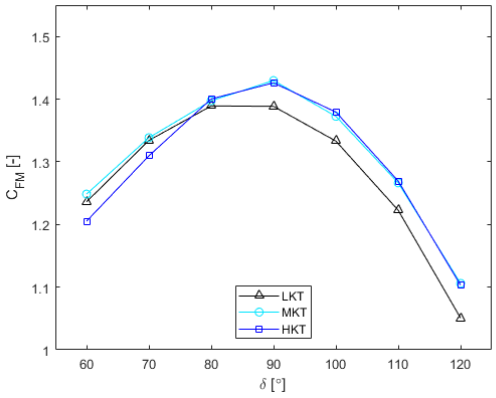

Figure 5.39: Corrected drive force coefficients C_{F_M} [-] vs sheet angle δ [°], for the three settings with the kicker: LKT, MKT and HKT, for the heading: 150° and the heel angle: 10°.

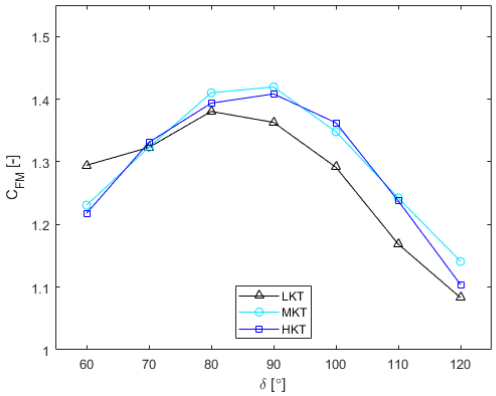

Figure 5.40: Corrected drive force coefficients C_{F_M} [-] vs sheet angle δ [°], for the three settings with the kicker: LKT, MKT and HKT, for the heading: 150° and the heel angle: 20°.

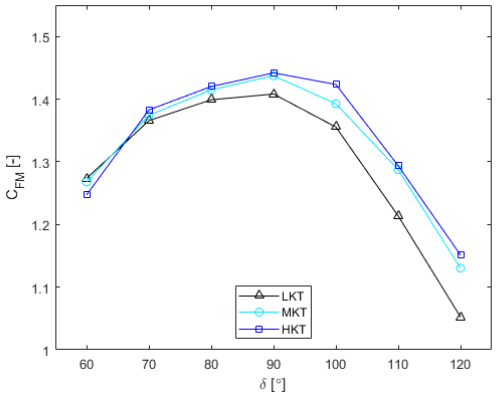

Figure 5.41: Corrected drive force coefficients C_{F_M} [-] vs sheet angle δ [°], for the three settings with the kicker: LKT, MKT and HKT, for the heading: 160° and the heel angle: 0°.

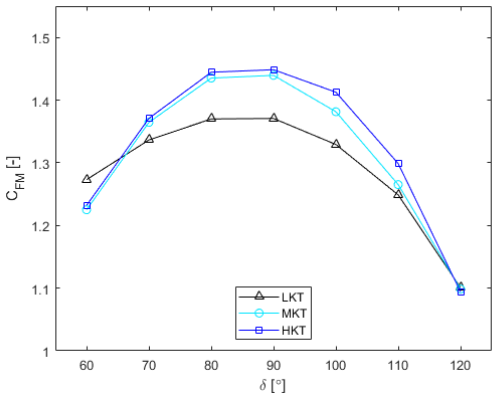

Figure 5.42: Corrected drive force coefficients C_{F_M} [-] vs sheet angle δ [°], for the three settings with the kicker: LKT, MKT and HKT, for the heading: 160° and the heel angle: 10°.

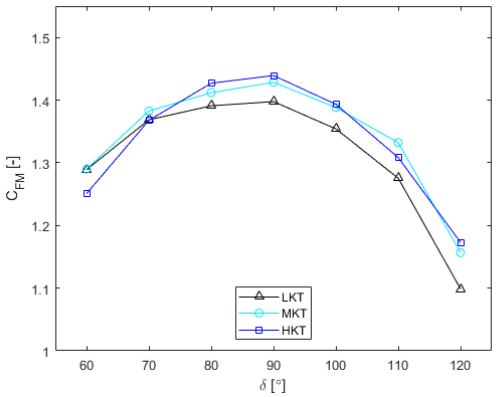

Figure 5.43: Corrected drive force coefficients C_{F_M} [-] vs sheet angle δ [°], for the three settings with the kicker: LKT, MKT and HKT, for the heading: 160° and the heel angle: 20°.

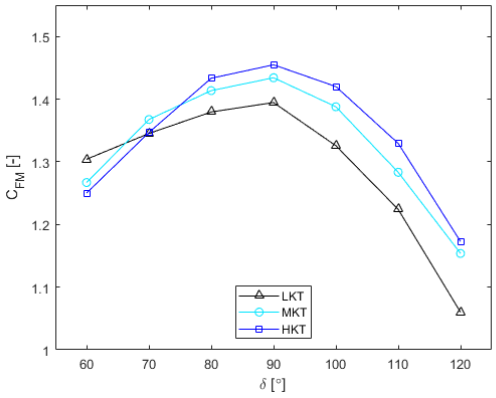

Figure 5.44: Corrected drive force coefficients C_{F_M} [-] vs sheet angle δ [°], for the three settings with the kicker: LKT, MKT and HKT, for the heading: 170° and the heel angle: 0°.

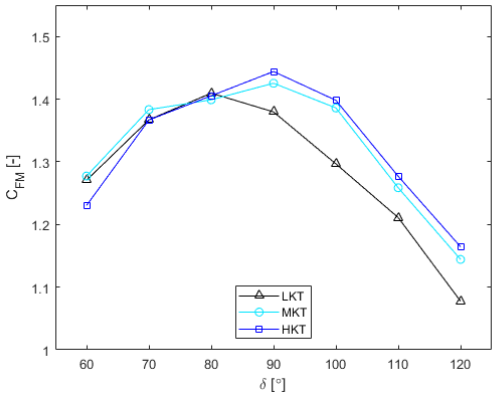

Figure 5.45: Corrected drive force coefficients C_{F_M} [-] vs sheet angle δ [°], for the three settings with the kicker: LKT, MKT and HKT, for the heading: 170° and the heel angle: 10°.

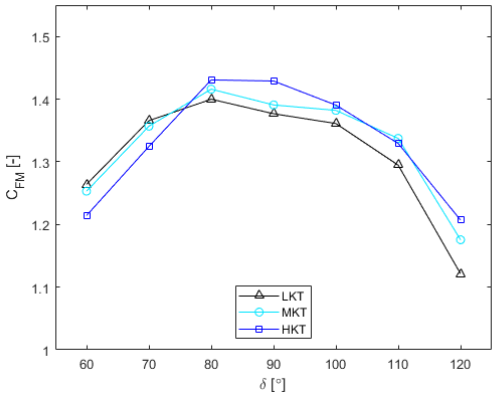

Figure 5.46: Corrected drive force coefficients C_{F_M} [-] vs sheet angle δ [°], for the three settings with the kicker: LKT, MKT and HKT, for the heading: 170° and the heel angle: 20°.

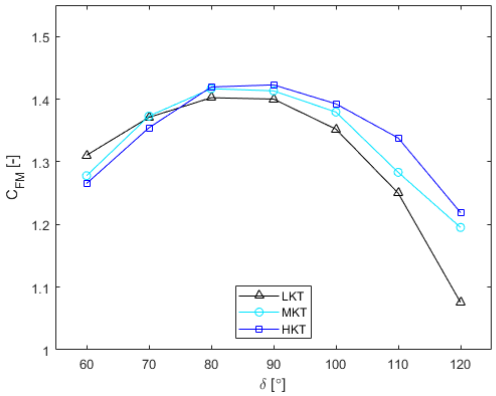

Figure 5.47: Corrected drive force coefficients C_{F_M} [-] vs sheet angle δ [°], for the three settings with the kicker: LKT, MKT and HKT, for the heading: 180° and the heel angle: 0°.

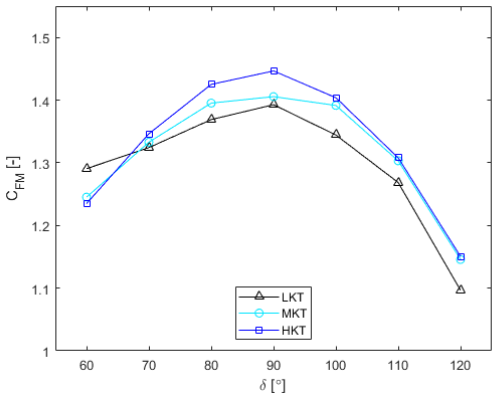

Figure 5.48: Corrected drive force coefficients C_{F_M} [-] vs sheet angle δ [°], for the three settings with the kicker: LKT, MKT and HKT, for the heading: 180° and the heel angle: 10°.

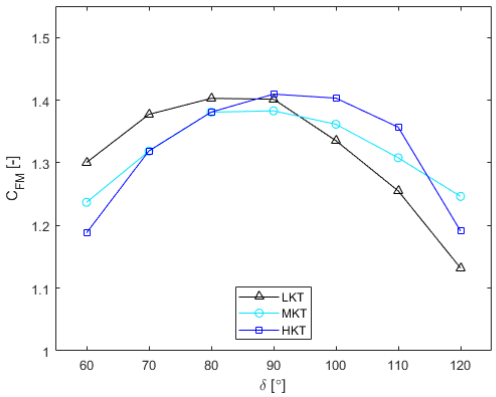

Figure 5.49: Corrected drive force coefficients C_{F_M} [-] vs sheet angle δ [°], for the three settings with the kicker: LKT, MKT and HKT, for the heading: 180° and the heel angle: 20°.

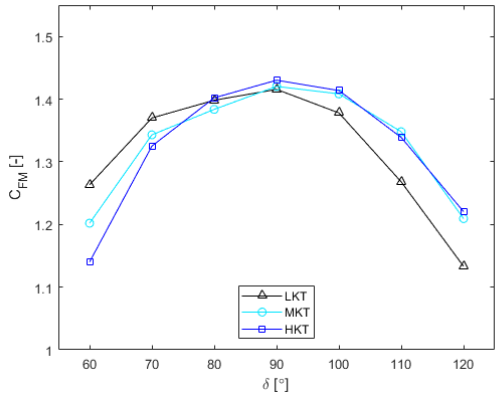

Figure 5.50: Corrected drive force coefficients C_{F_M} [-] vs sheet angle δ [°], for the three settings with the kicker: LKT, MKT and HKT, for the heading: 190° and the heel angle: 0°.

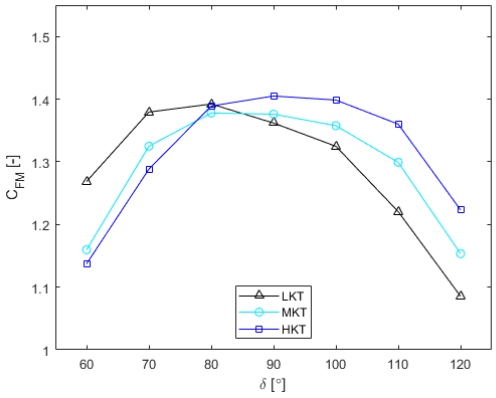

Figure 5.51: Corrected drive force coefficients C_{F_M} [-] vs sheet angle δ [°], for the three settings with the kicker: LKT, MKT and HKT, for the heading: 190° and the heel angle: 10°.

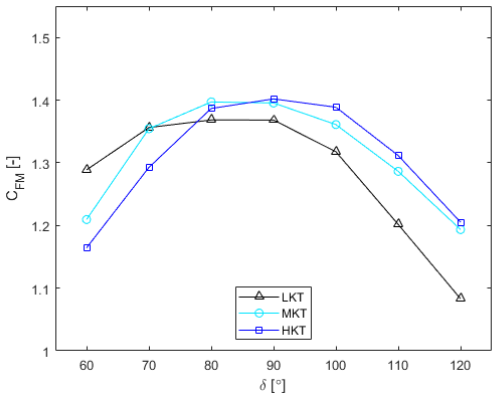

Figure 5.52: Corrected drive force coefficients C_{F_M} [-] vs sheet angle δ [°], for the three settings with the kicker: LKT, MKT and HKT, for the heading: 190° and the heel angle: 20°.

In Fig. 5.38 - 5.52 it can be seen that highest drive force coefficients are, for all three settings with the kicker, received with sheet angles in the range 80° - 100°, which is reasonable, because the force is proportional to the sail area and the largest projected sail area should be received with a sheet angle around 90°. Further, it can also be seen that the drive force coefficients received for the hard setting with the kicker in the sheet angle range 80° - 120° are overall higher than those received for the medium and light setting with the kicker, even though both the medium and light setting with the kicker gives the highest drive force coefficients for some single sheet angles. The light setting with the kicker gives overall the lowest drive force coefficients, except for the sheet angles 60° and 70°, for the headings 150° - 170°; in the heading range 180° - 190°, the drive force coefficients for the light setting with the kicker are for some heel angles, with the sheet angles 60° - 80°, higher than the drive force coefficients for the medium and hard setting with the kicker. It can also be seen that the drive force coefficients for the lower sheet angle range 60° - 80° are higher than those received in the higher sheet angle range, 100° - 120°.

Side Force Coefficients

In Fig. 5.53 - 5.67 below, the corrected measured side force coefficients C_{F_S} [-] are plotted against the sheet angle δ [°], where LKT, MKT and HKT stands for Light Kicker Trim, Medium Kicker Trim and Hard Kicker Trim, respectively. The corresponding data from Fig. 5.53 - 5.67 are presented in Table A.17 - A.21, in Appendix.

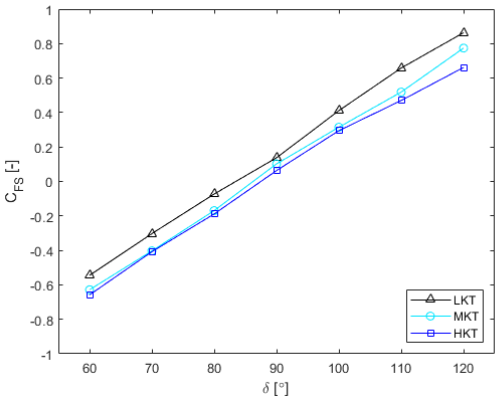

Figure 5.53: Corrected side force coefficients C_{F_S} [-] vs sheet angle δ [°], for the three settings with the kicker: LKT, MKT and HKT, for the heading: 150° and the heel angle: 0°.

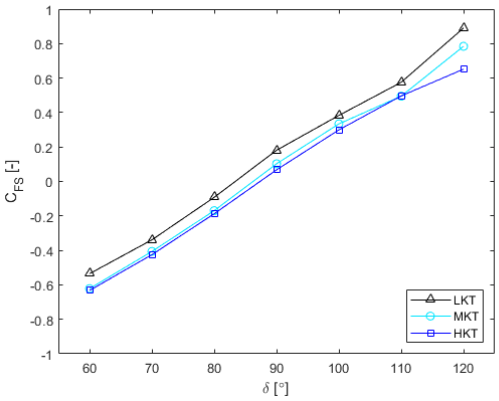

Figure 5.54: Corrected side force coefficients C_{F_S} [-] vs sheet angle δ [°], for the three settings with the kicker: LKT, MKT and HKT, for the heading: 150° and the heel angle: 10°.

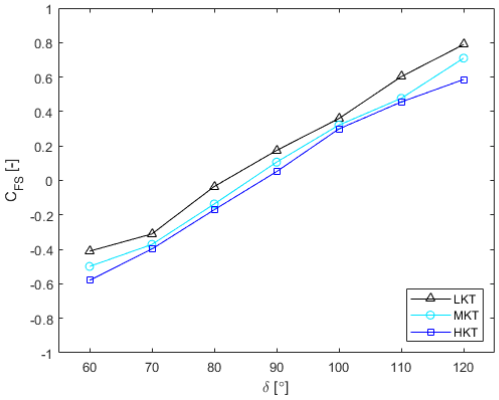

Figure 5.55: Corrected side force coefficients C_{F_S} [-] vs sheet angle δ [°], for the three settings with the kicker: LKT, MKT and HKT, for the heading: 150° and the heel angle: 20°.

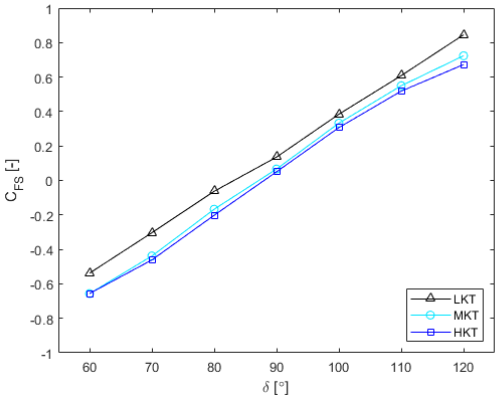

Figure 5.56: Corrected side force coefficients C_{F_S} [-] vs sheet angle δ [°], for the three settings with the kicker: LKT, MKT and HKT, for the heading: 160° and the heel angle: 0°.

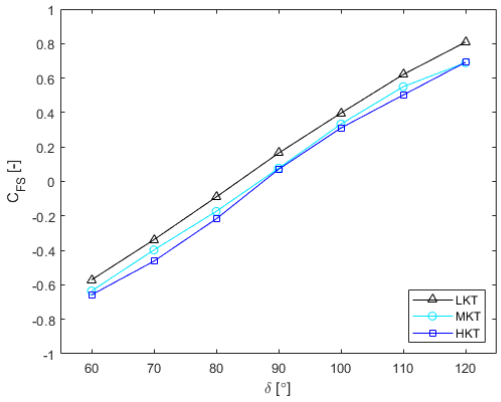

Figure 5.57: Corrected side force coefficients C_{F_S} [-] vs sheet angle δ [°], for the three settings with the kicker: LKT, MKT and HKT, for the heading: 160° and the heel angle: 10°.

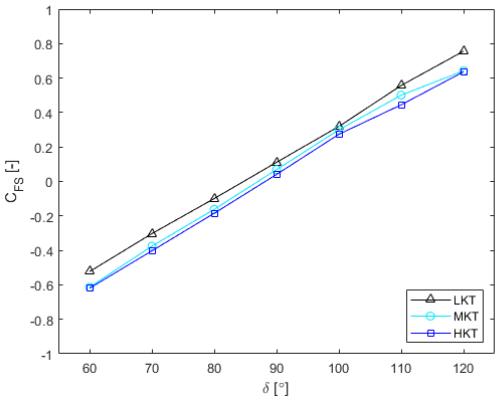

Figure 5.58: Corrected side force coefficients C_{F_S} [-] vs sheet angle δ [°], for the three settings with the kicker: LKT, MKT and HKT, for the heading: 160° and the heel angle: 20°.

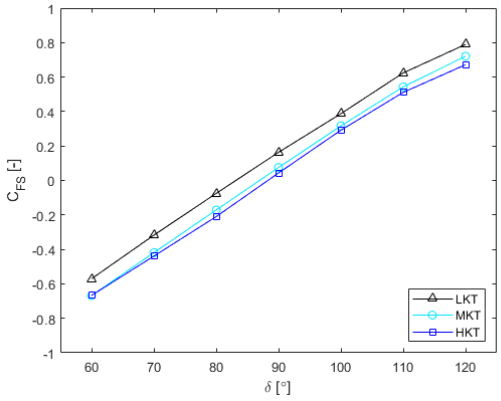

Figure 5.59: Corrected side force coefficients C_{F_S} [-] vs sheet angle δ [°], for the three settings with the kicker: LKT, MKT and HKT, for the heading: 170° and the heel angle: 0°.

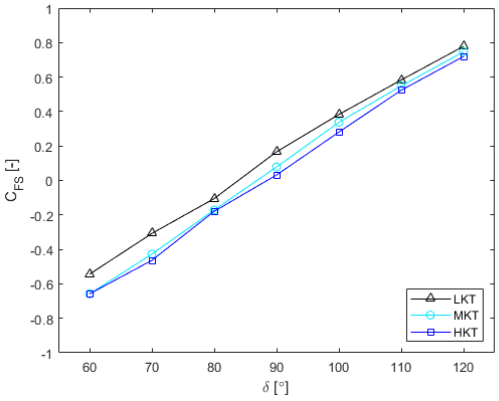

Figure 5.60: Corrected side force coefficients C_{F_S} [-] vs sheet angle δ [°], for the three settings with the kicker: LKT, MKT and HKT, for the heading: 170° and the heel angle: 10°.

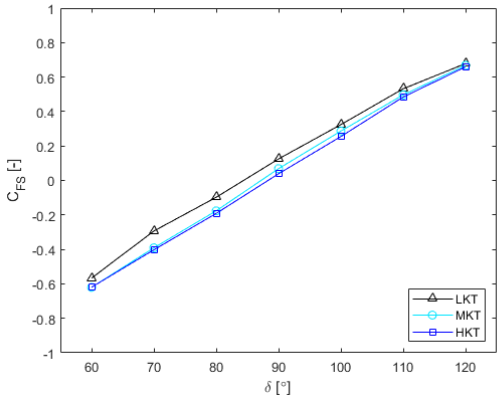

Figure 5.61: Corrected side force coefficients C_{F_S} [-] vs sheet angle δ [°], for the three settings with the kicker: LKT, MKT and HKT, for the heading: 170° and the heel angle: 20°.

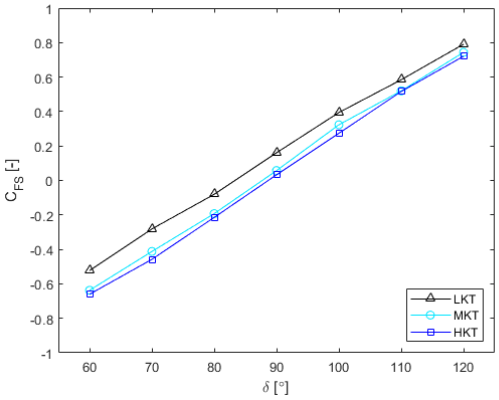

Figure 5.62: Corrected side force coefficients C_{F_S} [-] vs sheet angle δ [°], for the three settings with the kicker: LKT, MKT and HKT, for the heading: 180° and the heel angle: 0°.

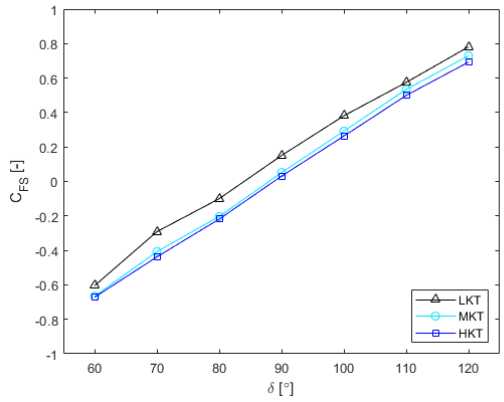

Figure 5.63: Corrected side force coefficients C_{F_S} [-] vs sheet angle δ [°], for the three settings with the kicker: LKT, MKT and HKT, for the heading: 180° and the heel angle: 10°.

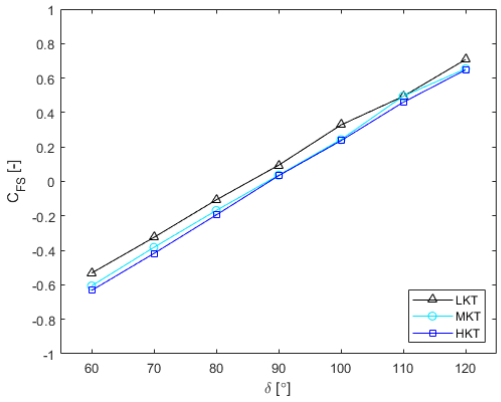

Figure 5.64: Corrected side force coefficients C_{F_S} [-] vs sheet angle δ [°], for the three settings with the kicker: LKT, MKT and HKT, for the heading: 180° and the heel angle: 20°.

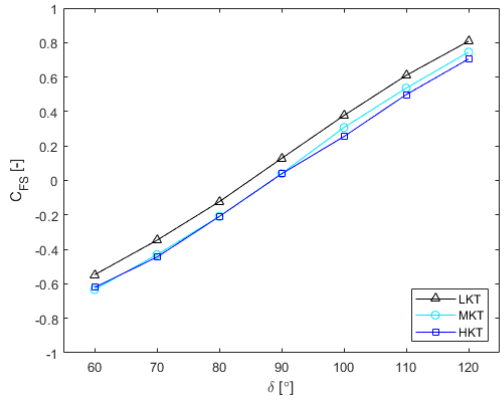

Figure 5.65: Corrected side force coefficients C_{F_S} [-] vs sheet angle δ [°], for the three settings with the kicker: LKT, MKT and HKT, for the heading: 190° and the heel angle: 0°.

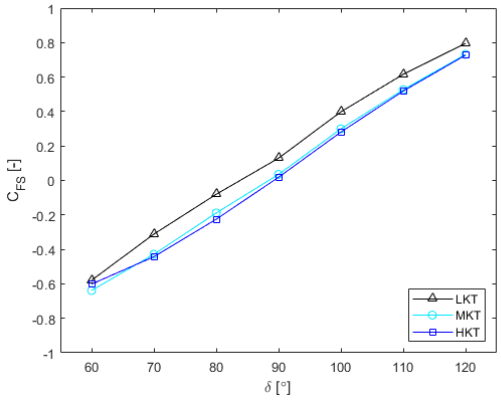

Figure 5.66: Corrected side force coefficients C_{F_S} [-] vs sheet angle δ [°], for the three settings with the kicker: LKT, MKT and HKT, for the heading: 190° and the heel angle: 10°.

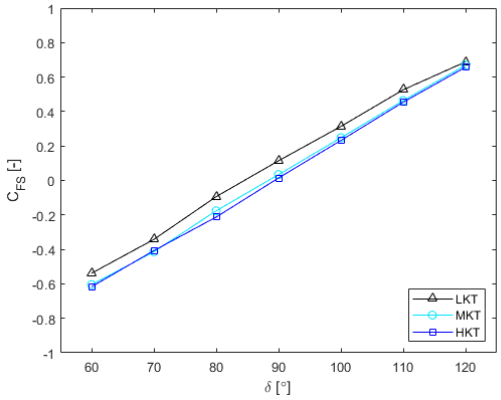

Figure 5.67: Corrected side force coefficients C_{F_S} [-] vs sheet angle δ [°], for the three settings with the kicker: LKT, MKT and HKT, for the heading: 190° and the heel angle: 20°.

In Fig. 5.53 - 5.67, it can be seen that the curves of the side force coefficients are overall very linear and more or less identical for the five different headings and the three different heel angles. The side force coefficients, received for the hard setting with the kicker are largest (negatively) in the lower sheet angle range 60° - 80° and lowest for the 90° sheet angle as well as in the high sheet angle range: 100° - 120°. The side force coefficients received for the medium setting with the kicker are thus more or less somewhere in between the corresponding side force coefficients, received for the hard and light setting with the kicker. It must be stressed that the sign of the coefficients only indicate the direction of the force.

Lift Force Coefficients

In Fig. 5.68 - 5.82 below, the partly corrected lift force coefficients C_{F_L} [-] are plotted against the sheet angle δ [°], where LKT, MKT and HKT stands for Light Kicker Trim, Medium Kicker Trim and Hard Kicker Trim, respectively. As previously mentioned, the lift forces are neither corrected for the balance measurement error nor for blockage effects, because of the very small values received for this force component. The corresponding data from Fig. 5.68 - 5.82 are presented in Table A.22 - A.26, in Appendix.

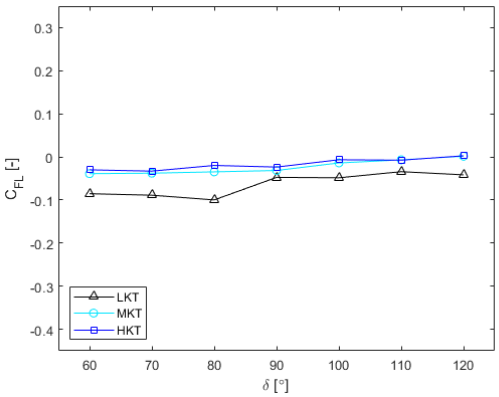

Figure 5.68: Partly corrected lift force coefficients C_{F_L} [-] vs sheet angle δ [°], for the three settings with the kicker: LKT, MKT and HKT, for the heading: 150° and the heel angle: 0°.

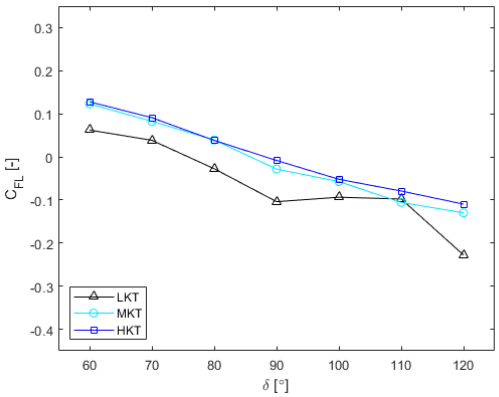

Figure 5.69: Partly corrected lift force coefficients C_{F_L} [-] vs sheet angle δ [°], for the three settings with the kicker: LKT, MKT and HKT, for the heading: 150° and the heel angle: 10°.

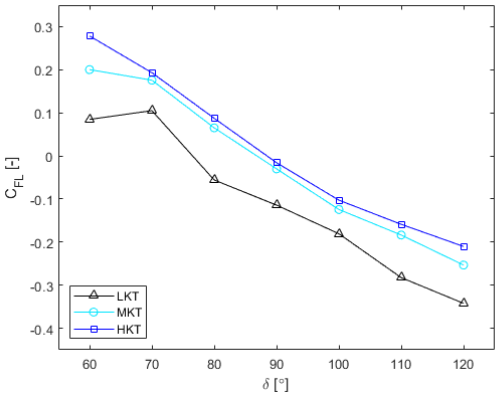

Figure 5.70: Partly corrected lift force coefficients C_{F_L} [-] vs sheet angle δ [°], for the three settings with the kicker: LKT, MKT and HKT, for the heading: 150° and the heel angle: 20°.

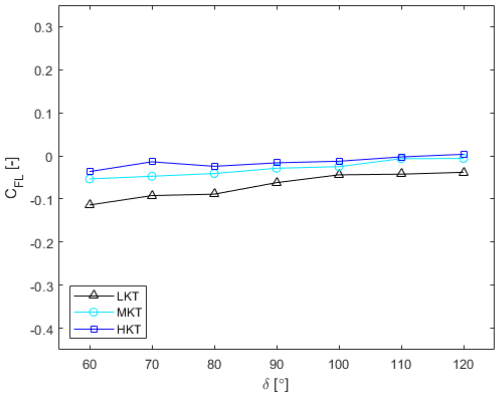

Figure 5.71: Partly corrected lift force coefficients C_{F_L} [-] vs sheet angle δ [°], for the three settings with the kicker: LKT, MKT and HKT, for the heading: 160° and the heel angle: 0°.

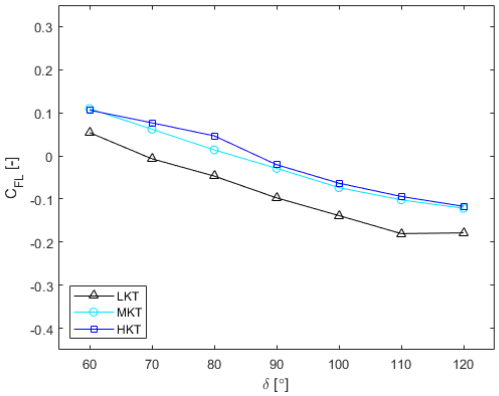

Figure 5.72: Partly corrected lift force coefficients C_{F_L} [-] vs sheet angle δ [°], for the three settings with the kicker: LKT, MKT and HKT, for the heading: 160° and the heel angle: 10°.

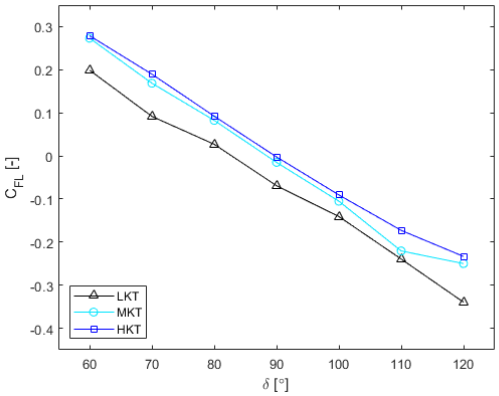

Figure 5.73: Partly corrected lift force coefficients C_{F_L} [-] vs sheet angle δ [°], for the three settings with the kicker: LKT, MKT and HKT, for the heading: 160° and the heel angle: 20°.

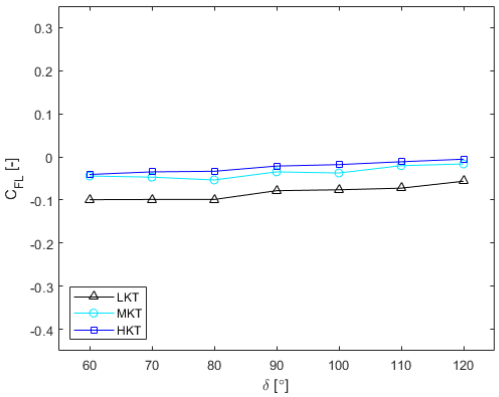

Figure 5.74: Partly corrected lift force coefficients C_{F_L} [-] vs sheet angle δ [°], for the three settings with the kicker: LKT, MKT and HKT, for the heading: 170° and the heel angle: 0°.

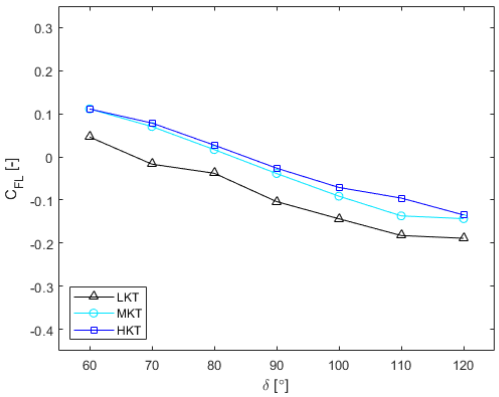

Figure 5.75: Partly corrected lift force coefficients C_{F_L} [-] vs sheet angle δ [°], for the three settings with the kicker: LKT, MKT and HKT, for the heading: 170° and the heel angle: 10°.

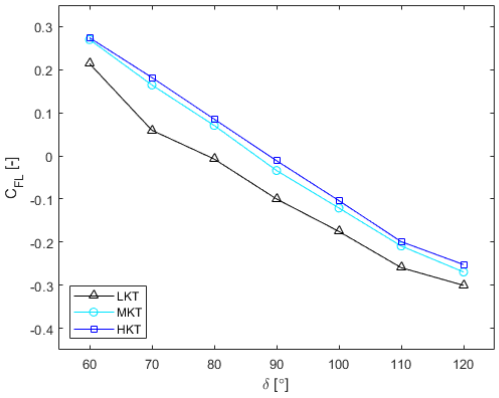

Figure 5.76: Partly corrected lift force coefficients C_{F_L} [-] vs sheet angle δ [°], for the three settings with the kicker: LKT, MKT and HKT, for the heading: 170° and the heel angle: 20°.

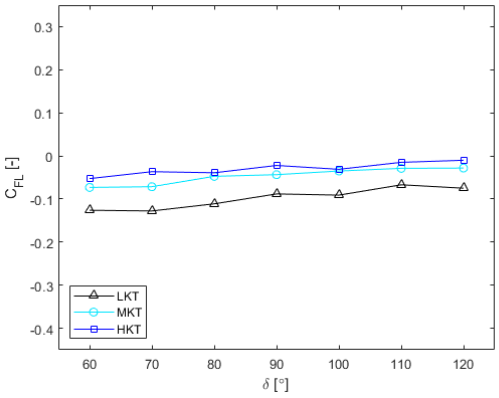

Figure 5.77: Partly corrected lift force coefficients C_{F_L} [-] vs sheet angle δ [°], for the three settings with the kicker: LKT, MKT and HKT, for the heading: 180° and the heel angle: 0°.

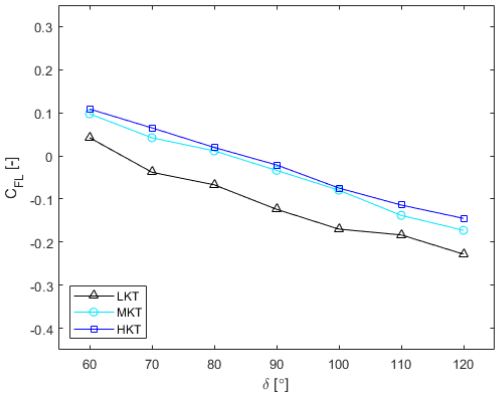

Figure 5.78: Partly corrected lift force coefficients C_{F_L} [-] vs sheet angle δ [°], for the three settings with the kicker: LKT, MKT and HKT, for the heading: 180° and the heel angle: 10°.

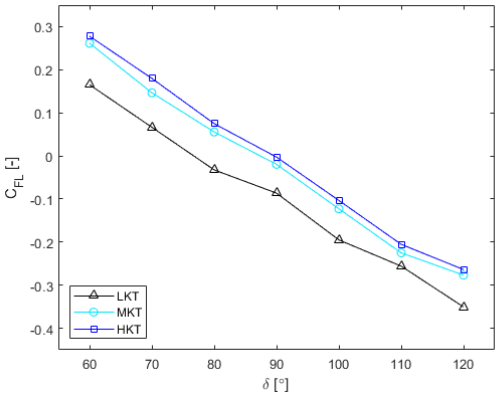

Figure 5.79: Partly corrected lift force coefficients C_{F_L} [-] vs sheet angle δ [°], for the three settings with the kicker: LKT, MKT and HKT, for the heading: 180° and the heel angle: 20°.

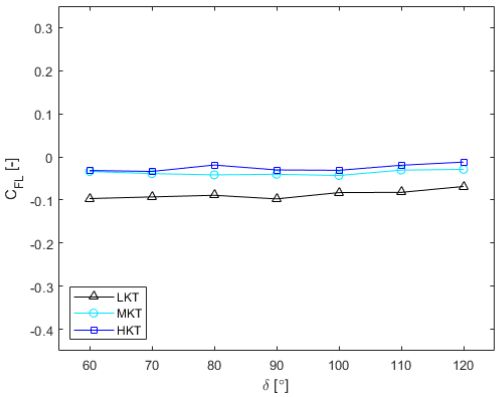

Figure 5.80: Partly corrected lift force coefficients C_{F_L} [-] vs sheet angle δ [°], for the three settings with the kicker: LKT, MKT and HKT, for the heading: 190° and the heel angle: 0°.

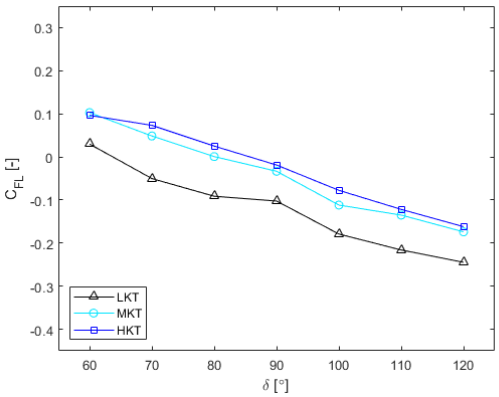

Figure 5.81: Partly corrected lift force coefficients C_{F_L} [-] vs sheet angle δ [°], for the three settings with the kicker: LKT, MKT and HKT, for the heading: 190° and the heel angle: 10°.

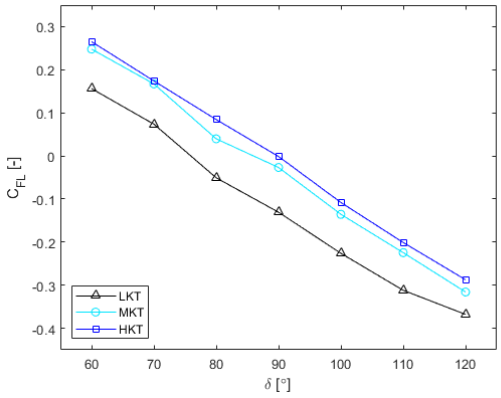

Figure 5.82: Partly corrected lift force coefficients C_{F_L} [-] vs sheet angle δ [°], for the three settings with the kicker: LKT, MKT and HKT, for the heading: 190° and the heel angle: 20°.

Studying the curves of the lift force coefficients, for the three settings with the kicker, in Fig. 5.68 - 5.82, it can be seen that the curves for the heel angle 0° are more or less linear and horizontal, for all five headings; the curves for the 10° heel angle have kept the linear appearance, but are rotated approximately around the 90° sheet angle. Same trend can be seen for the curves, for the 20° heel angle, i.e. the linearity is kept, but the curves are rotated more. Further, the lift force coefficients for the medium setting with the kicker are again somewhere in between those lift force coefficients, received for the hard and light setting with the kicker.

Pitch Moment Coefficients

In Fig. 5.83 - 5.97 below, the corrected measured pitch moment coefficients C_{M_P} [-] are plotted against the sheet angle δ [°], where LKT, MKT and HKT stands for Light Kicker Trim, Medium Kicker Trim and Hard Kicker Trim, respectively. The corresponding data from Fig. 5.83 - 5.97 are presented in Table A.27 - A.31, in Appendix.

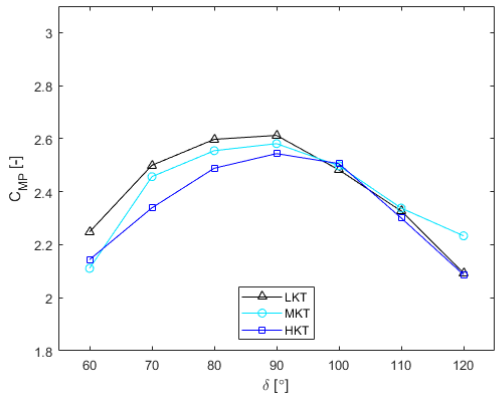

Figure 5.83: Corrected pitch moment coefficients C_{M_P} [-] vs sheet angle δ [°], for the three settings with the kicker: LKT, MKT and HKT, for the heading: 150° and the heel angle: 0°.

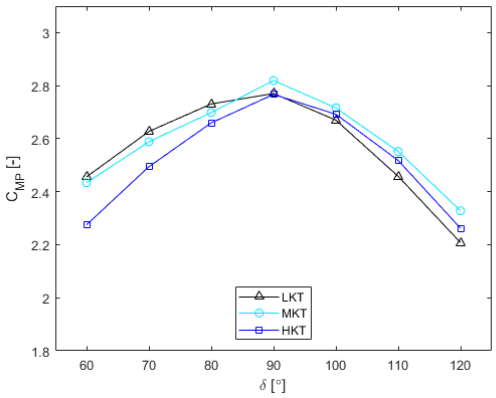

Figure 5.84: Corrected pitch moment coefficients C_{M_P} [-] vs sheet angle δ [°], for the three settings with the kicker: LKT, MKT and HKT, for the heading: 150° and the heel angle: 10°.

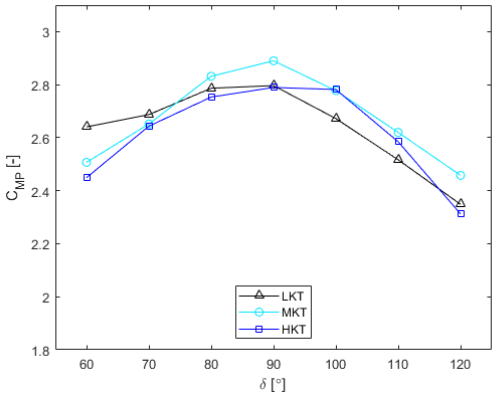

Figure 5.85: Corrected pitch moment coefficients C_{M_P} [-] vs sheet angle δ [°], for the three settings with the kicker: LKT, MKT and HKT, for the heading: 150° and the heel angle: 20°.

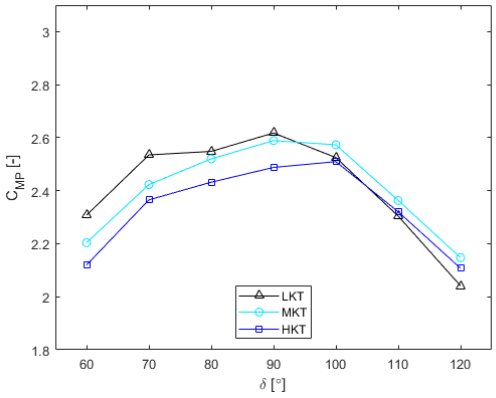

Figure 5.86: Corrected pitch moment coefficients C_{M_P} [-] vs sheet angle δ [°], for the three settings with the kicker: LKT, MKT and HKT, for the heading: 160° and the heel angle: 0°.

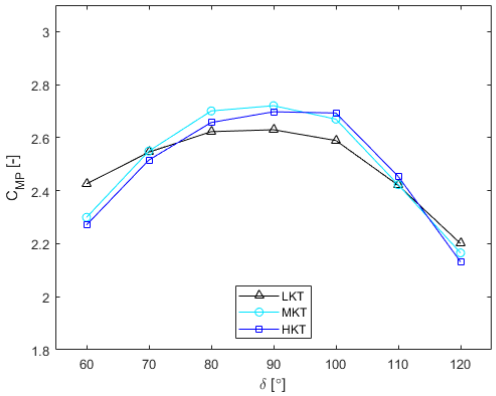

Figure 5.87: Corrected pitch moment coefficients C_{M_P} [-] vs sheet angle δ [°], for the three settings with the kicker: LKT, MKT and HKT, for the heading: 160° and the heel angle: 10°.

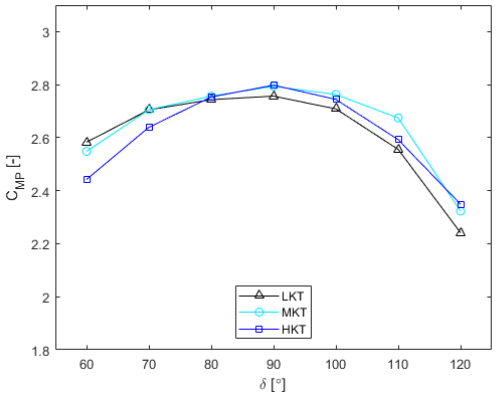

Figure 5.88: Corrected pitch moment coefficients C_{M_P} [-] vs sheet angle δ [°], for the three settings with the kicker: LKT, MKT and HKT, for the heading: 160° and the heel angle: 20°.

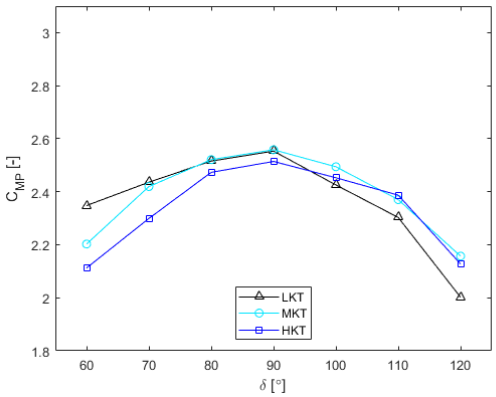

Figure 5.89: Corrected pitch moment coefficients C_{M_P} [-] vs sheet angle δ [°], for the three settings with the kicker: LKT, MKT and HKT, for the heading: 170° and the heel angle: 0°.

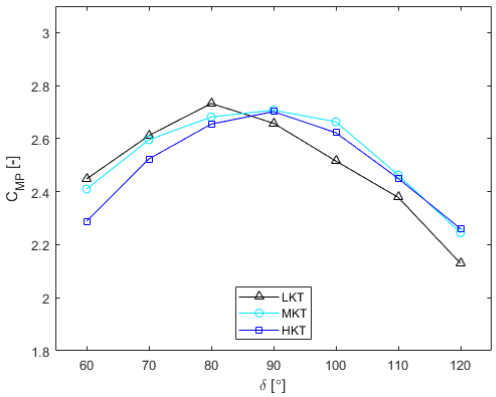

Figure 5.90: Corrected pitch moment coefficients C_{M_P} [-] vs sheet angle δ [°], for the three settings with the kicker: LKT, MKT and HKT, for the heading: 170° and the heel angle: 10°.

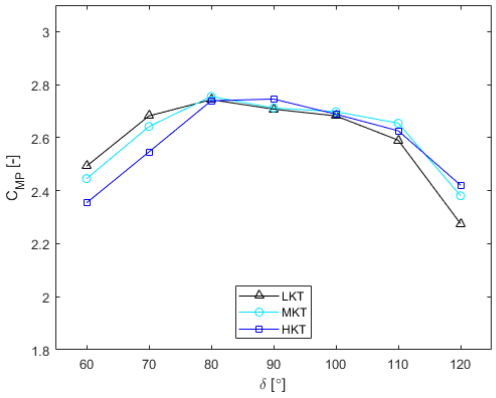

Figure 5.91: Corrected pitch moment coefficients C_{M_P} [-] vs sheet angle δ [°], for the three settings with the kicker: LKT, MKT and HKT, for the heading: 170° and the heel angle: 20°.

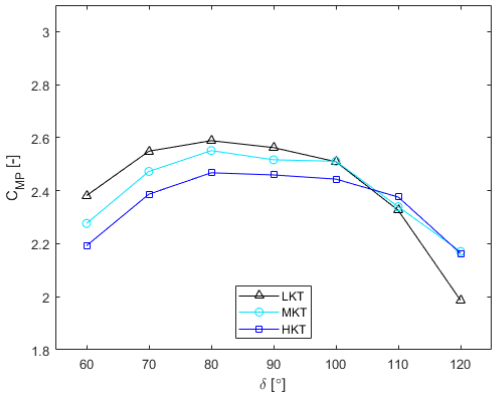

Figure 5.92: Corrected pitch moment coefficients C_{M_P} [-] vs sheet angle δ [°], for the three settings with the kicker: LKT, MKT and HKT, for the heading: 180° and the heel angle: 0°.

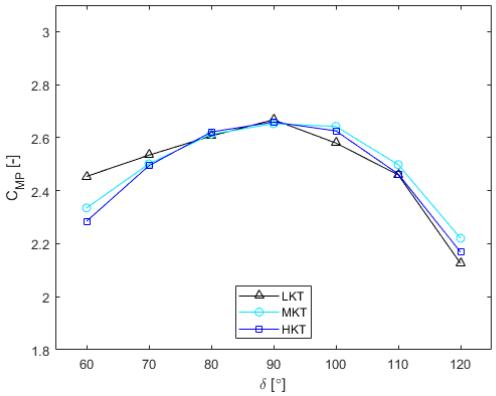

Figure 5.93: Corrected pitch moment coefficients C_{M_P} [-] vs sheet angle δ [°], for the three settings with the kicker: LKT, MKT and HKT, for the heading: 180° and the heel angle: 10°.

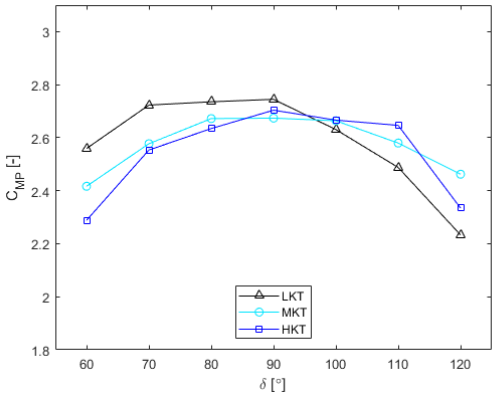

Figure 5.94: Corrected pitch moment coefficients C_{M_P} [-] vs sheet angle δ [°], for the three settings with the kicker: LKT, MKT and HKT, for the heading: 180° and the heel angle: 20°.

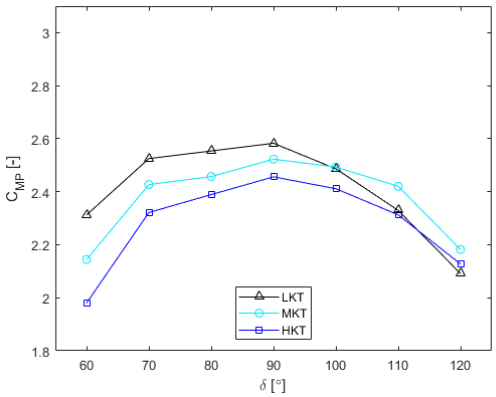

Figure 5.95: Corrected pitch moment coefficients C_{M_P} [-] vs sheet angle δ [°], for the three settings with the kicker: LKT, MKT and HKT, for the heading: 190° and the heel angle: 0°.

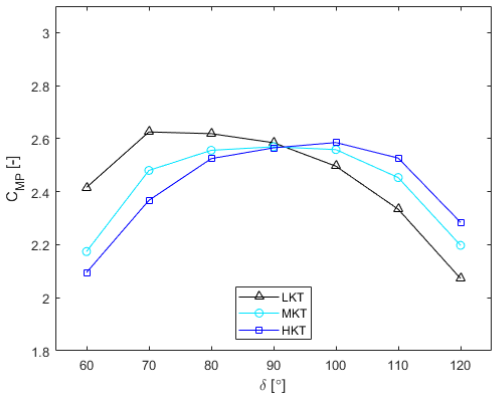

Figure 5.96: Corrected pitch moment coefficients C_{M_P} [-] vs sheet angle δ [°], for the three settings with the kicker: LKT, MKT and HKT, for the heading: 190° and the heel angle: 10°.

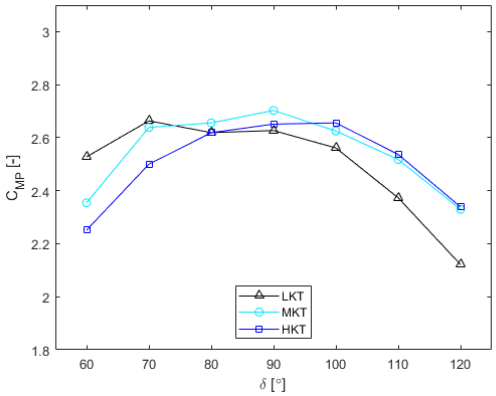

Figure 5.97: Corrected pitch moment coefficients C_{M_P} [-] vs sheet angle δ [°], for the three settings with the kicker: LKT, MKT and HKT, for the heading: 190° and the heel angle: 20°.

In Fig. 5.83 - 5.97 it can be seen that for the lower sheet angle range, 60° - 80°, the pitch moment coefficients are overall highest for the light setting with the kicker, followed by the medium and hard setting with the kicker. For the higher sheet angle range, 60° - 80°, the trend is different. For these sheet angles, the highest pitch moment coefficients are overall received for the medium setting with the kicker, followed by the hard and light setting with the kicker. For the 90° sheet angle, the highest pitch moment coefficients are overall received for either the medium or light setting with the kicker and occasionally for the hard setting with the kicker.

Roll Moment Coefficients

In Fig. 5.98 - 5.112 below, the corrected measured roll moment coefficients C_{M_R} [-] are plotted against the sheet angle δ [°], where LKT, MKT and HKT stands for Light Kicker Trim, Medium Kicker Trim and Hard Kicker Trim, respectively. The corresponding data from Fig. 5.98 - 5.112 are presented in Table A.32 - A.36, in Appendix.

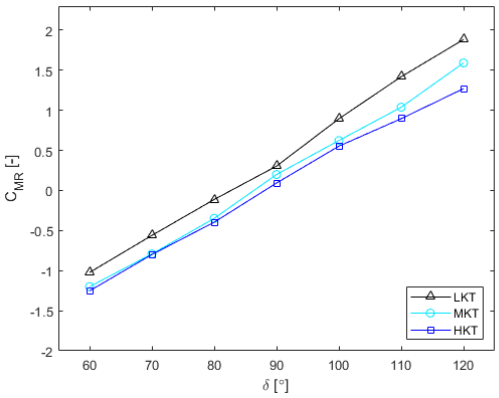

Figure 5.98: Corrected roll moment coefficients C_{M_R} [-] vs sheet angle δ [°], for the three settings with the kicker: LKT, MKT and HKT, for the heading: 150° and the heel angle: 0°.

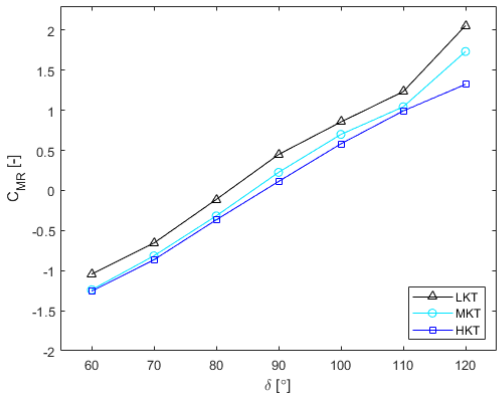

Figure 5.99: Corrected roll moment coefficients C_{M_R} [-] vs sheet angle δ [°], for the three settings with the kicker: LKT, MKT and HKT, for the heading: 150° and the heel angle: 10°.

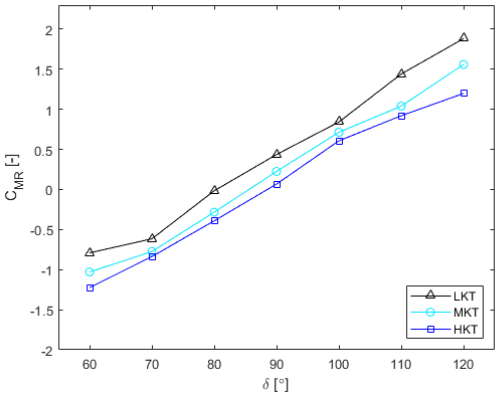

Figure 5.100: Corrected roll moment coefficients C_{M_R} [-] vs sheet angle δ [°], for the three settings with the kicker: LKT, MKT and HKT, for the heading: 150° and the heel angle: 20°.

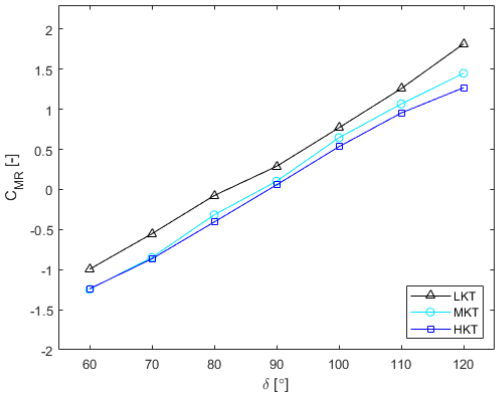

Figure 5.101: Corrected roll moment coefficients C_{M_R} [-] vs sheet angle δ [°], for the three settings with the kicker: LKT, MKT and HKT, for the heading: 160° and the heel angle: 0°.

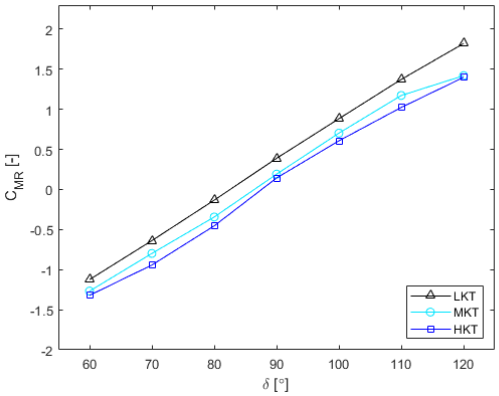

Figure 5.102: Corrected roll moment coefficients C_{M_R} [-] vs sheet angle δ [°], for the three settings with the kicker: LKT, MKT and HKT, for the heading: 160° and the heel angle: 10°.

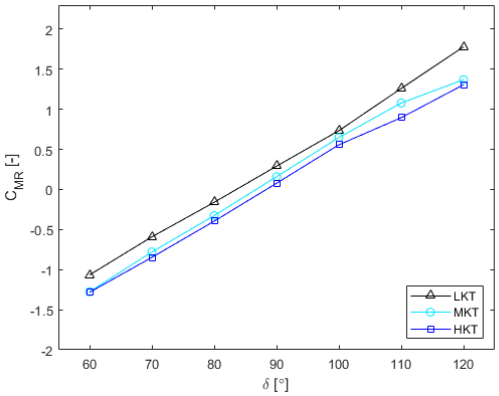

Figure 5.103: Corrected roll moment coefficients C_{M_R} [-] vs sheet angle δ [°], for the three settings with the kicker: LKT, MKT and HKT, for the heading: 160° and the heel angle: 20°.

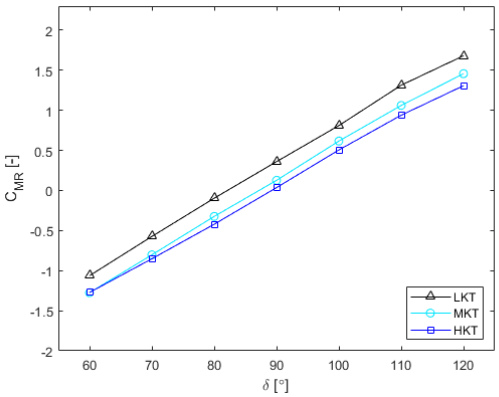

Figure 5.104: Corrected roll moment coefficients C_{M_R} [-] vs sheet angle δ [°], for the three settings with the kicker: LKT, MKT and HKT, for the heading: 170° and the heel angle: 0°.

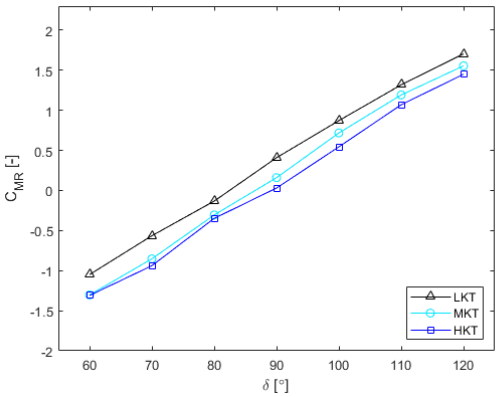

Figure 5.105: Corrected roll moment coefficients C_{M_R} [-] vs sheet angle δ [°], for the three settings with the kicker: LKT, MKT and HKT, for the heading: 170° and the heel angle: 10°.

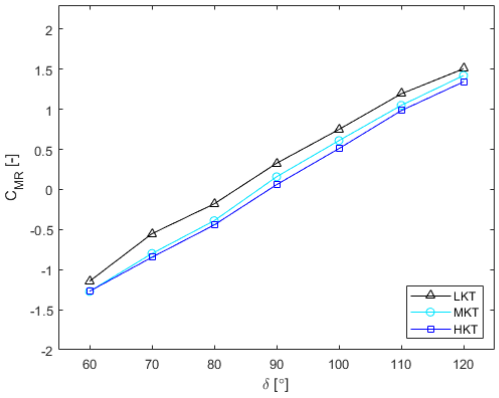

Figure 5.106: Corrected roll moment coefficients C_{M_R} [-] vs sheet angle δ [°], for the three settings with the kicker: LKT, MKT and HKT, for the heading: 170° and the heel angle: 20°.

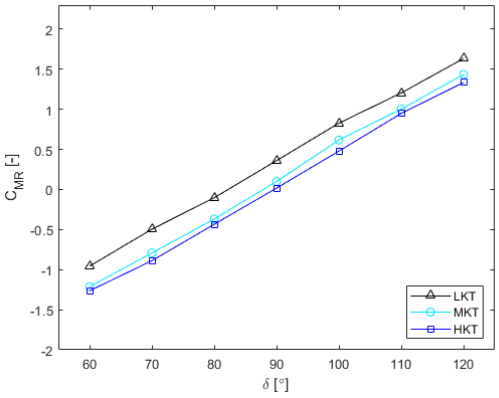

Figure 5.107: Corrected roll moment coefficients C_{M_R} [-] vs sheet angle δ [°], for the three settings with the kicker: LKT, MKT and HKT, for the heading: 180° and the heel angle: 0°.

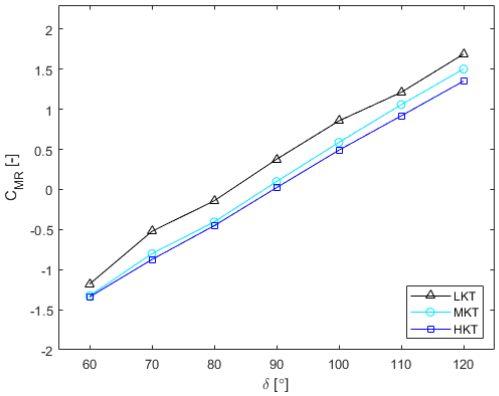

Figure 5.108: Corrected roll moment coefficients C_{M_R} [-] vs sheet angle δ [°], for the three settings with the kicker: LKT, MKT and HKT, for the heading: 180° and the heel angle: 10°.

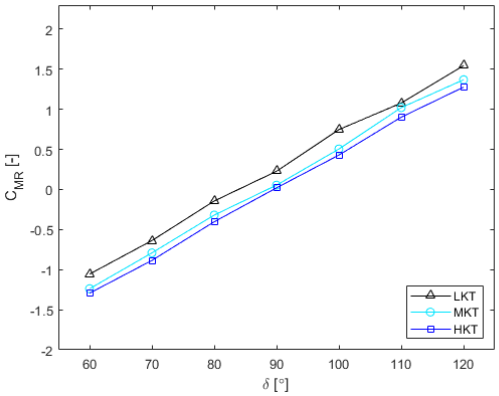

Figure 5.109: Corrected roll moment coefficients C_{M_R} [-] vs sheet angle δ [°], for the three settings with the kicker: LKT, MKT and HKT, for the heading: 180° and the heel angle: 20°.

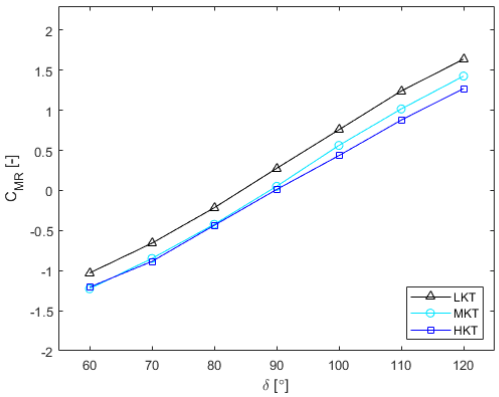

Figure 5.110: Corrected roll moment coefficients C_{M_R} [-] vs sheet angle δ [°], for the three settings with the kicker: LKT, MKT and HKT, for the heading: 190° and the heel angle: 0°.

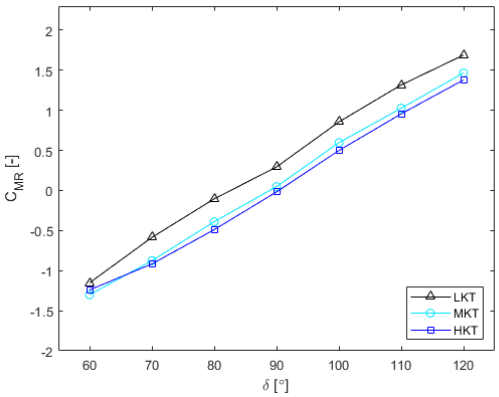

Figure 5.111: Corrected roll moment coefficients C_{M_R} [-] vs sheet angle δ [°], for the three settings with the kicker: LKT, MKT and HKT, for the heading: 190° and the heel angle: 10°.

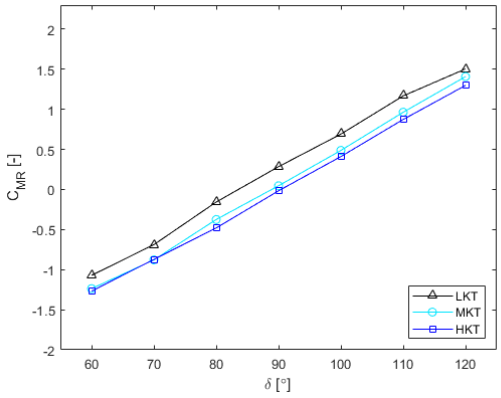

Figure 5.112: Corrected roll moment coefficients C_{M_R} [-] vs sheet angle δ [°], for the three settings with the kicker: LKT, MKT and HKT, for the heading: 190° and the heel angle: 20°.

The same linear appearance of the curves, as well as the overall trend of the different settings with the kicker that was seen for the side force coefficients, can also be seen for the roll moment coefficients in Fig. 5.98 - 5.112, i.e. the hard setting with the kicker is negatively larger than both the medium and light setting with the kicker for the sheet angle range, 60° - 80° and the opposite for the high sheet angle range.

Yaw Moment Coefficients

In Fig. 5.113 - 5.127 below, the corrected measured yaw moment coefficients C_{M_Y} [-] are plotted against the sheet angle δ [°], where LKT, MKT and HKT stands for Light Kicker Trim, Medium Kicker Trim and Hard Kicker Trim, respectively. The corresponding data from Fig. 5.113 - 5.127 are presented in Table A.37 - A.41, in Appendix.

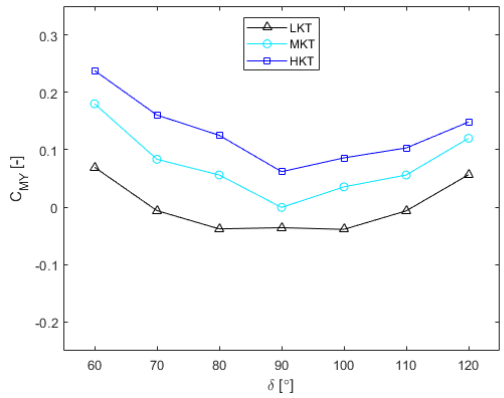

Figure 5.113: Corrected yaw moment coefficients C_{M_Y} [-] vs sheet angle δ [°], for the three settings with the kicker: LKT, MKT and HKT, for the heading: 150° and the heel angle: 0°.

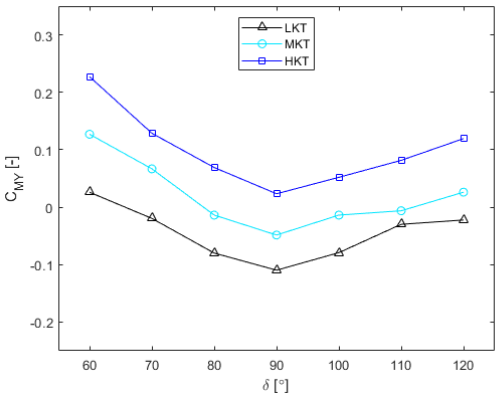

Figure 5.114: Corrected yaw moment coefficients C_{M_Y} [-] vs sheet angle δ [°], for the three settings with the kicker: LKT, MKT and HKT, for the heading: 150° and the heel angle: 10°.

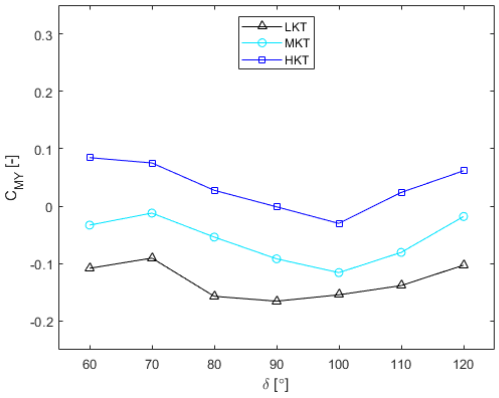

Figure 5.115: Corrected yaw moment coefficients C_{M_Y} [-] vs sheet angle δ [°], for the three settings with the kicker: LKT, MKT and HKT, for the heading: 150° and the heel angle: 20°.

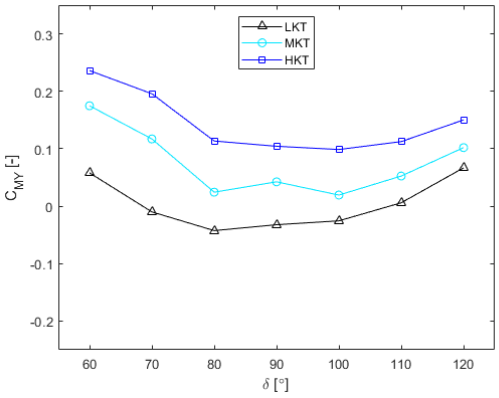

Figure 5.116: Corrected yaw moment coefficients C_{M_Y} [-] vs sheet angle δ [°], for the three settings with the kicker: LKT, MKT and HKT, for the heading: 160° and the heel angle: 0°.

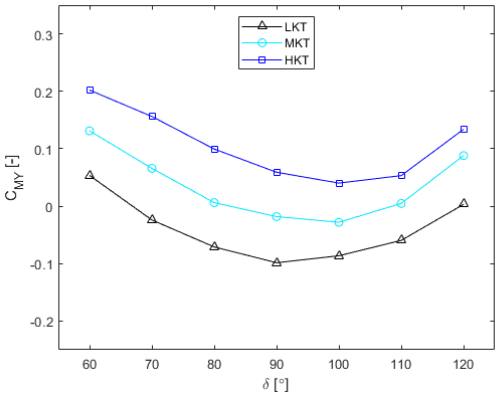

Figure 5.117: Corrected yaw moment coefficients C_{M_Y} [-] vs sheet angle δ [°], for the three settings with the kicker: LKT, MKT and HKT, for the heading: 160° and the heel angle: 10°.

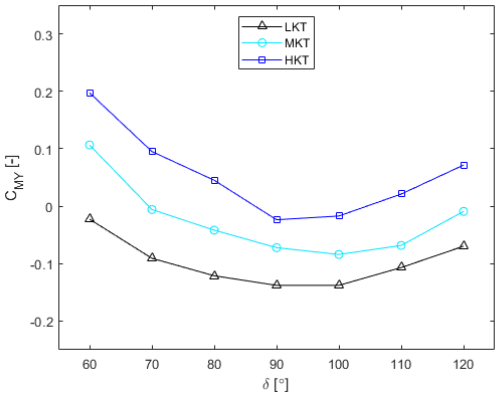

Figure 5.118: Corrected yaw moment coefficients C_{M_Y} [-] vs sheet angle δ [°], for the three settings with the kicker: LKT, MKT and HKT, for the heading: 160° and the heel angle: 20°.

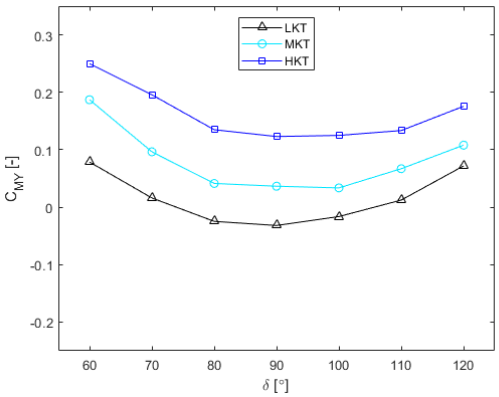

Figure 5.119: Corrected yaw moment coefficients C_{M_Y} [-] vs sheet angle δ [°], for the three settings with the kicker: LKT, MKT and HKT, for the heading: 170° and the heel angle: 0°.

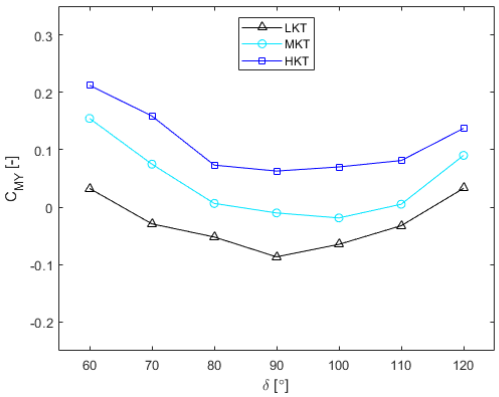

Figure 5.120: Corrected yaw moment coefficients C_{M_Y} [-] vs sheet angle δ [°], for the three settings with the kicker: LKT, MKT and HKT, for the heading: 170° and the heel angle: 10°.

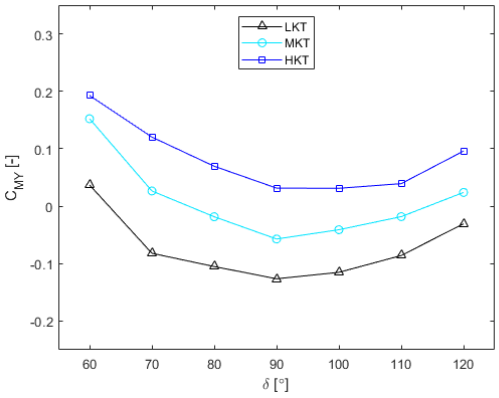

Figure 5.121: Corrected yaw moment coefficients C_{M_Y} [-] vs sheet angle δ [°], for the three settings with the kicker: LKT, MKT and HKT, for the heading: 170° and the heel angle: 20°.

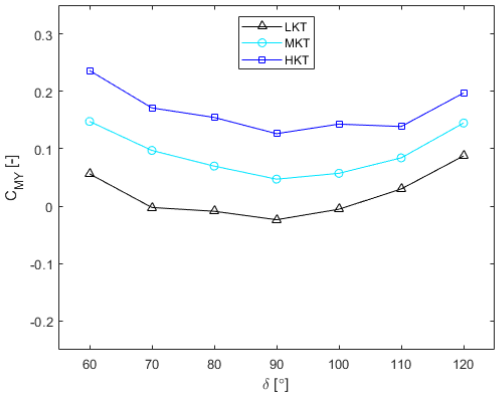

Figure 5.122: Corrected yaw moment coefficients C_{M_Y} [-] vs sheet angle δ [°], for the three settings with the kicker: LKT, MKT and HKT, for the heading: 180° and the heel angle: 0°.

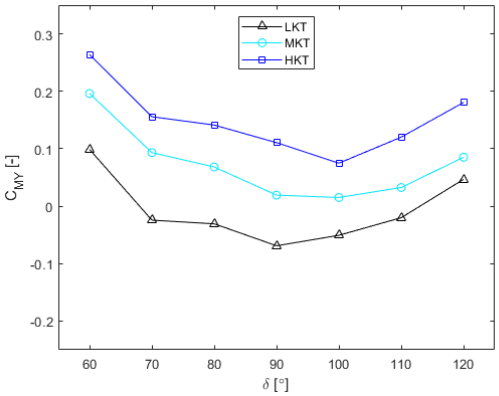

Figure 5.123: Corrected yaw moment coefficients C_{M_Y} [-] vs sheet angle δ [°], for the three settings with the kicker: LKT, MKT and HKT, for the heading: 180° and the heel angle: 10°.

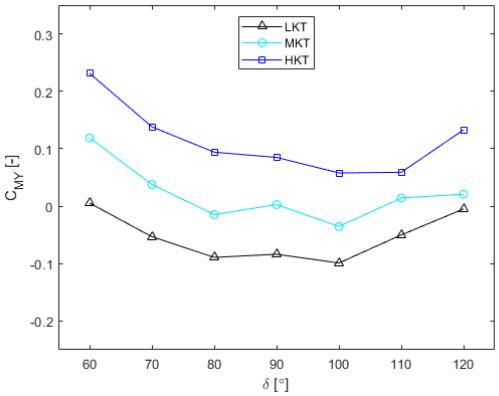

Figure 5.124: Corrected yaw moment coefficients C_{M_Y} [-] vs sheet angle δ [°], for the three settings with the kicker: LKT, MKT and HKT, for the heading: 180° and the heel angle: 20°.

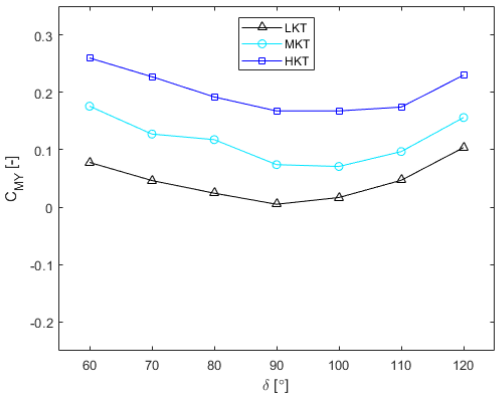

Figure 5.125: Corrected yaw moment coefficients C_{M_Y} [-] vs sheet angle δ [°], for the three settings with the kicker: LKT, MKT and HKT, for the heading: 190° and the heel angle: 0°.

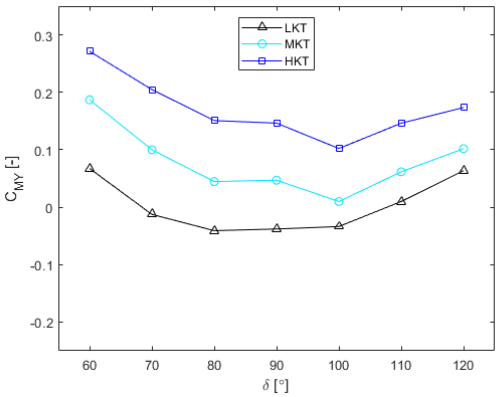

Figure 5.126: Corrected yaw moment coefficients C_{M_Y} [-] vs sheet angle δ [°], for the three settings with the kicker: LKT, MKT and HKT, for the heading: 190° and the heel angle: 10°.

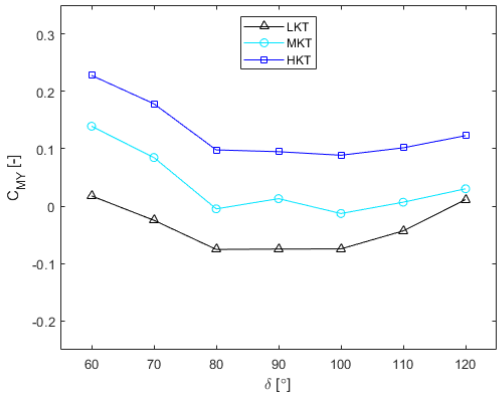

Figure 5.127: Corrected yaw moment coefficients C_{M_Y} [-] vs sheet angle δ [°], for the three settings with the kicker: LKT, MKT and HKT, for the heading: 190° and the heel angle: 20°.

When analyzing the yaw moments in Fig. 5.113 - 5.127 one has to keep in mind that the sign, i.e. plus or minus only has to do with where the force resultant is positioned, relative to the balance resolving center (BRC); since the wind tunnel balance measured positive moment as negative, all measurements of the yaw moments are multiplied with -1. A positive moment thus mean anti-clockwise rotation around the BRC and vice versa. In Fig. 5.113 - 5.127, it can be seen that the appearances of the curves, for all three settings with the kicker, are very alike. There are clear trends between the settings with the kicker and a global minimum is generally received for a sheet angle around 90°.

Repeatability Tests

Five separate repeatability tests with the apparent wind speed $V_{AW} = 10.6$ m/s were performed for the heel angles 0°, 10° & 20°, with a fix heading of 190° and with a fix sheet angle of 90°. For this configuration, the three settings with the kicker, i.e. LKT, MKT, and HKT, representing Light Kicker Trim, Medium Kicker Trim, and Hard Kicker Trim, respectively, were tested. Fig. 5.128 - 5.130 below, shows bar plots of the corrected measured drive force coefficients C_{F_M} for the five separate repeatability tests and in Fig. 5.131 the standard deviation σ [-] of the repeatability tests is plotted against the three heel angles: 0°, 10° & 20°, for each setting with the kicker. The corresponding data from Fig. 5.128 - 5.131 are presented in Table A.42, in Appendix.

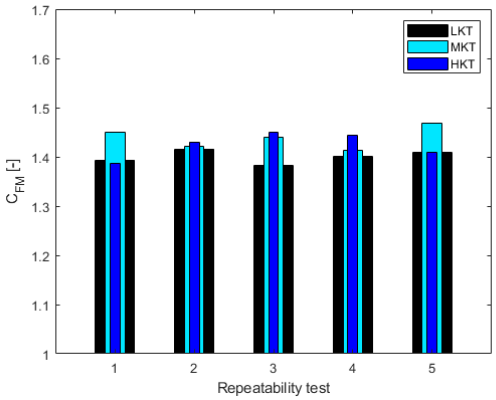

Figure 5.128: Corrected drive force coefficients C_{F_M} [-] vs repeatability test, for the three settings with the kicker: LKT, MKT and HKT, with a fix sheet angle of 90°, for the heading: 190° and the heel angle: 0°.

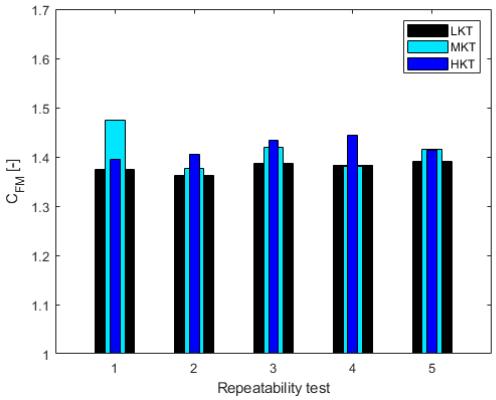

Figure 5.129: Corrected drive force coefficients C_{F_M} [-] vs repeatability test, for the three settings with the kicker: LKT, MKT and HKT, with a fix sheet angle of 90°, for the heading: 190° and the heel angle: 10°.

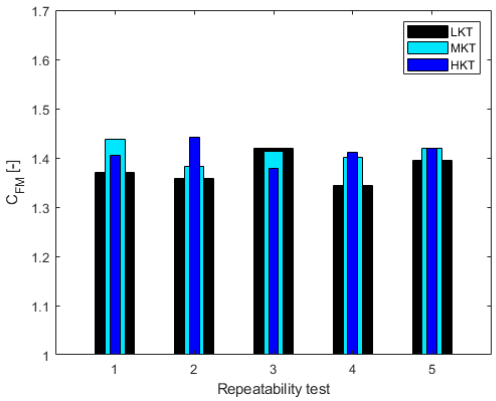

Figure 5.130: Corrected drive force coefficients C_{F_M} [-] vs repeatability test, for the three settings with the kicker: LKT, MKT and HKT, with a fix sheet angle of 90°, for the heading: 190° and the heel angle: 20°.

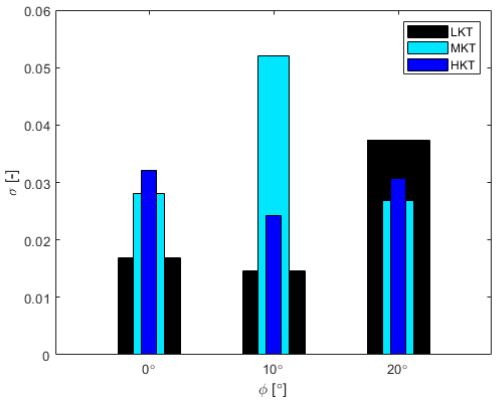

Figure 5.131: Standard deviation σ [-] of the repeatability tests vs heel angle ϕ [°], for the three settings with the kicker: LKT, MKT and HKT, for the heading: 190°.

Ideally, the drive force coefficients, for all 5 repeatability tests, for all heel angles, should be the same, but as can be seen in Fig. 5.128 - 5.130 the height of the bars vary. The standard deviation of the results, which can be seen in Fig. 5.131, shows that the dimensionless repeatability for the three settings with the kicker and the three heel angels are approximately somewhere between $1.5\% - 4\%$.

5.3.3 Strong Wind Tests

The test matrix for the experimental tests for the strong wind condition, with the apparent wind speed 18.5 m/s, is relatively small compared to the test matrix for the light wind condition. The strong wind condition only had two variables, which are the sheet angle and the kicker. The heading was kept at 180° and the heel angle kept at 0°. The corresponding data from Fig. 5.132 - 5.137 are presented in Table A.43 - A.48 in Appendix.

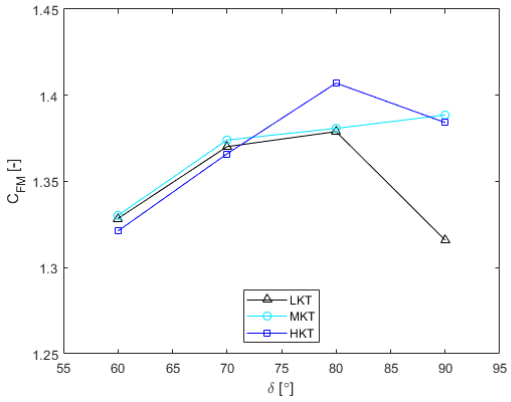

Figure 5.132: Corrected drive force coefficients C_{F_M} [-] vs sheet angle δ [°], for the three settings with the kicker: LKT, MKT and HKT, for the heading: 180° and the heel angle: 0°.

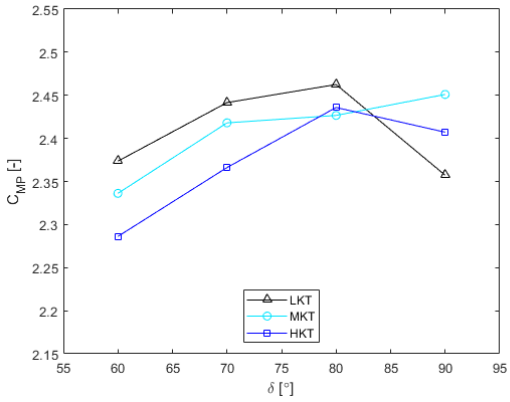

Figure 5.133: Corrected pitch moment coefficients C_{M_P} [-] vs sheet angle δ [°], for the three settings with the kicker: LKT, MKT and HKT, for the heading: 180° and the heel angle: 0°.

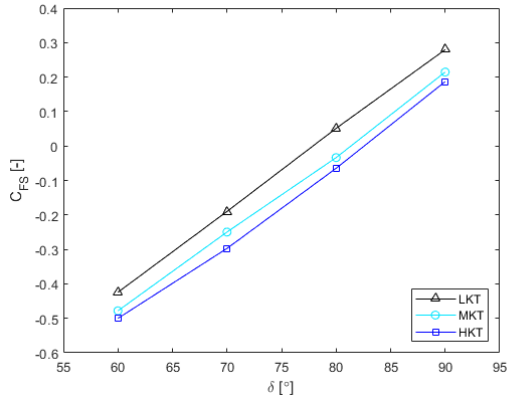

Figure 5.134: Corrected side force coefficients C_{F_S} [-] vs sheet angle δ [°], for the three settings with the kicker: LKT, MKT and HKT, for the heading: 180° and the heel angle: 0°.

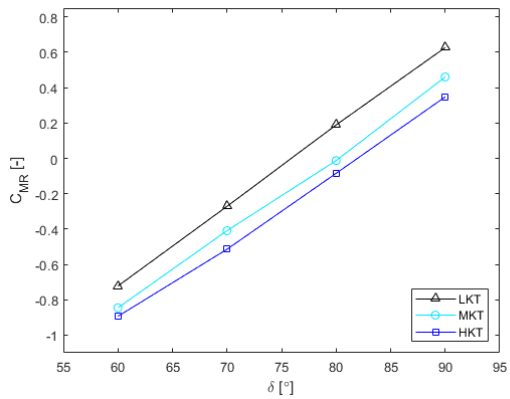

Figure 5.135: Corrected roll moment coefficients C_{M_R} [-] vs sheet angle δ [°], for the three settings with the kicker: LKT, MKT and HKT, for the heading: 180° and the heel angle: 0°.

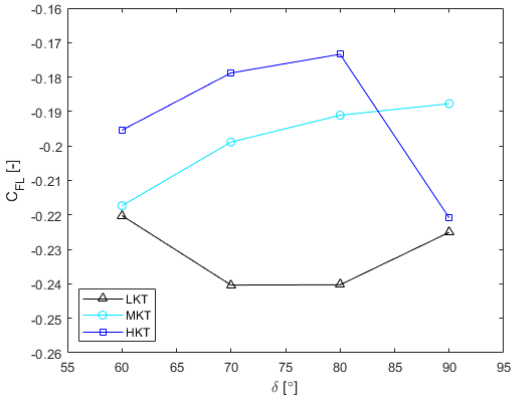

Figure 5.136: Corrected lift force coefficients C_{F_L} [-] vs sheet angle δ [°], for the three settings with the kicker: LKT, MKT and HKT, for the heading: 180° and the heel angle: 0°.

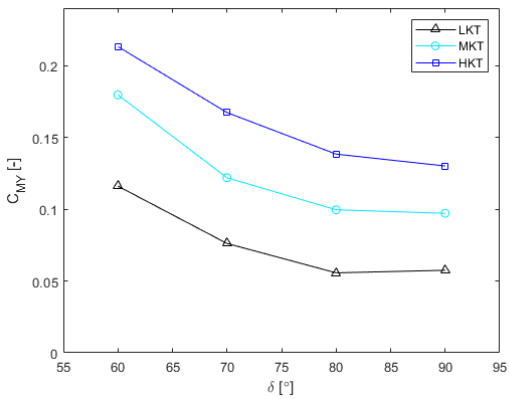

Figure 5.137: Corrected yaw moment coefficients C_{M_Y} [-] vs sheet angle δ [°], for the three settings with the kicker: LKT, MKT and HKT, for the heading: 180° and the heel angle: 0°.

In Fig. 5.132 it can be seen that the medium setting with the kicker receives the highest drive force coefficients for the 60°, 70° and 90° sheet angles. The curve for the hard setting with the kicker is more or less linear for the 60°, 70° and 80° sheet angles, where it peaks and then drops for the 90° sheet angle. The drive force coefficients received for the light setting with the kicker is only slightly lower than the ones received for the medium setting with the kicker, for the 60°, 70° and 80° sheet angles, but then suddenly drops for the 90° sheet angle. In Fig. 5.134 the highest pitch moment coefficients are received for the light setting with the kicker for the 60°, 70° and 80° sheet angles and then it drops for the 90° sheet angle, as it did for the drive force coefficients. The linear appearance of the curve for the hard setting with the kicker for the pitch moment coefficients is more or less identical to the appearance of the curve for the drive force coefficients. It thus peaks for the 80° sheet angle and drops for the 90° sheet angle. The only sheet angle where the medium setting with the kicker has the highest pitch moment coefficient is for the 90° sheet angle. In Fig. 5.134, where the side force coefficients are plotted, the appearance of the curves for all three settings with the kicker are very linear and parallel. It can be seen that for the 60° and 70° sheet angles, the hard setting with the kicker has the highest side force coefficients, the light setting with the kicker the lowest and the medium setting with the kicker somewhere in between the hard and the light setting with the kicker. For the 80° sheet angle the light setting with the kicker has a positive value, whereas the side force coefficients for the the medium and hard setting with the kicker have negative signs. Still the hard setting with the kicker has the highest side force coefficient, though. For the 90° sheet angle the light setting with the kicker now has the highest side force coefficient, followed by the medium and hard setting with the kicker. The situation is identical for the roll moment coefficients, which can be seen in Fig. 5.135. In Fig. 5.136 it can be seen that the light setting with the kicker has the highest lift force coefficients for all sheet angles and the hard setting with the kicker has the lowest for all sheet angles, except for 90° where the medium setting with the kicker has the lowest value. The lift force coefficient for the hard setting with the kicker drops again remarkably for the 90° sheet angle. In Fig. 5.137 it can be seen that the appearance of the curves for all three settings with the kicker are very parallel. The hard setting with the kicker gives the highest yaw moment coefficients for all sheet angles and the light setting with the kicker gives the lowest yaw moment coefficients for all sheet angles.

5.4 Validation

As previously mentioned, the validation is not a formal validation, as recommended by for example ITTC, but a comparison of modeled results with measured test results that has been corrected for all sources of error, except for blockage. Further, only the upright sailing condition with a heading of 180° and hard setting with the kicker is validated.

5.4.1 Plotted and Tabulated Data of Sail Coefficients

Fig. 5.138 - 5.149 below, show plots where the numerical results from the RANS simulations, with K-Epsilon turbulence model and the cambered sail model in the normal domain are compared with the measured results from the wind tunnel tests, that has been corrected for all sources of error, except for blockage. The corresponding data from Fig. 5.138 - 5.149, are presented in Table 5.12 further down.

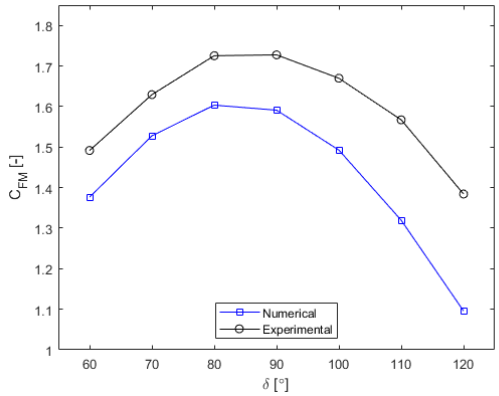

Figure 5.138: Numerical and experimental drive force coefficients C_{F_M} [-], vs sheet angle δ [°].

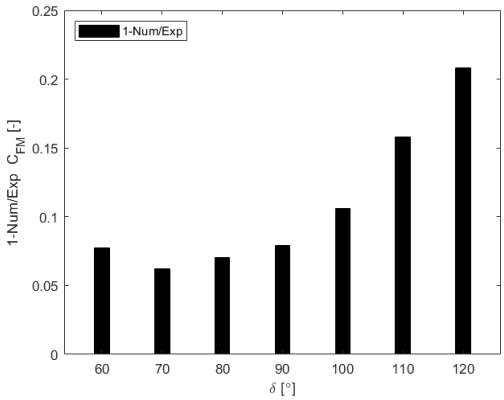

Figure 5.139: 1-Num/Exp ratio of the drive force coefficients C_{F_M} [-], vs sheet angle δ [°].

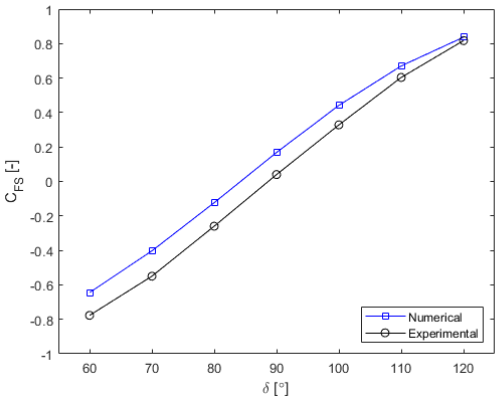

Figure 5.140: Numerical and experimental side force coefficients C_{F_S} [-], vs sheet angle δ [°].

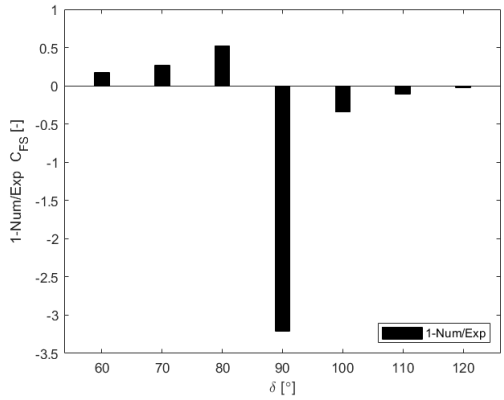

Figure 5.141: 1-Num/Exp ratio of the side force coefficients C_{F_S} [-], vs sheet angle δ [°].

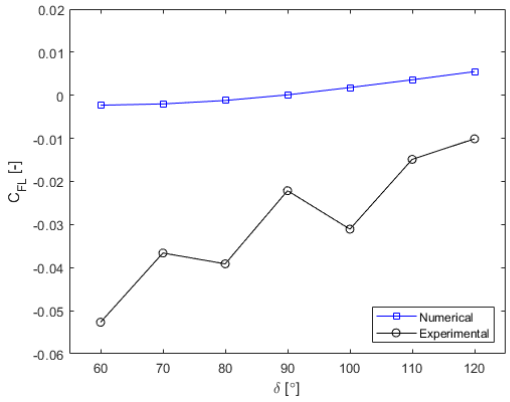

Figure 5.142: Numerical and experimental lift force coefficients C_{F_L} [-], vs sheet angle δ [°].

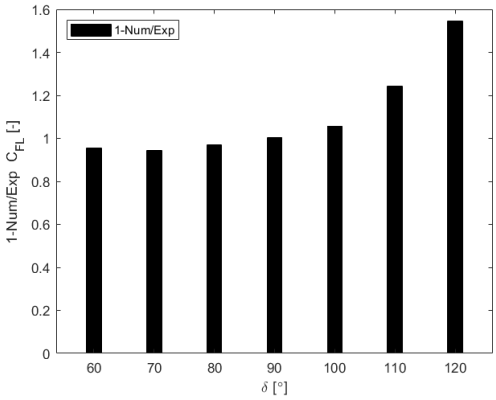

Figure 5.143: 1-Num/Exp ratio of the lift force coefficients C_{F_L} [-], vs sheet angle δ [°].

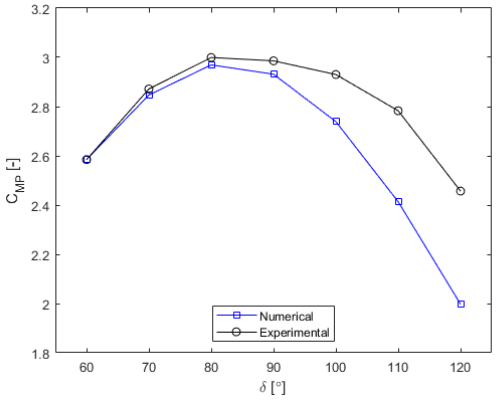

Figure 5.144: Numerical and experimental pitch moment coefficients C_{M_P} [-], vs sheet angle δ [°].

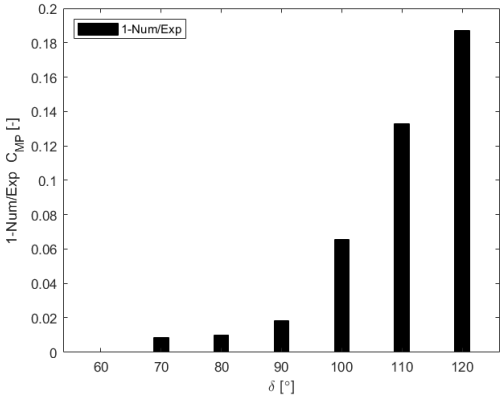

Figure 5.145: 1-Num/Exp ratio of the pitch moment coefficients C_{M_P} [-], vs sheet angle δ [°].

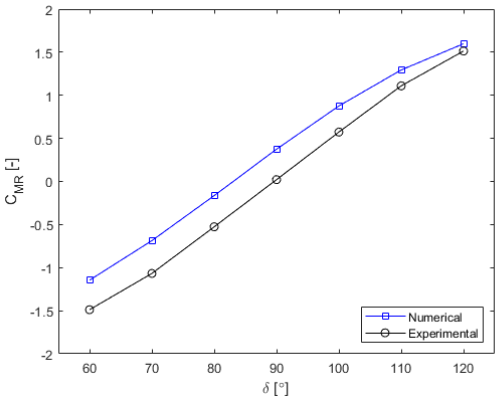

Figure 5.146: Numerical and experimental roll moment coefficients C_{M_R} [-], vs sheet angle δ [°].

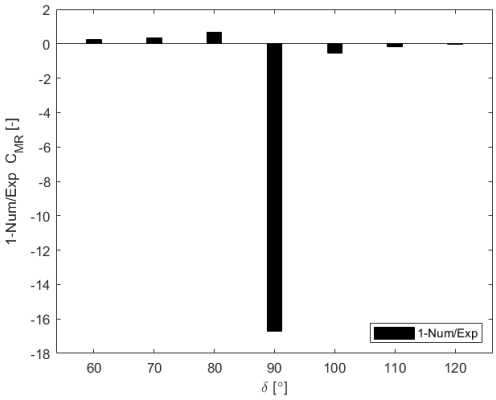

Figure 5.147: 1-Num/Exp ratio of the roll moment coefficients C_{M_R} [-], vs sheet angle δ [°].

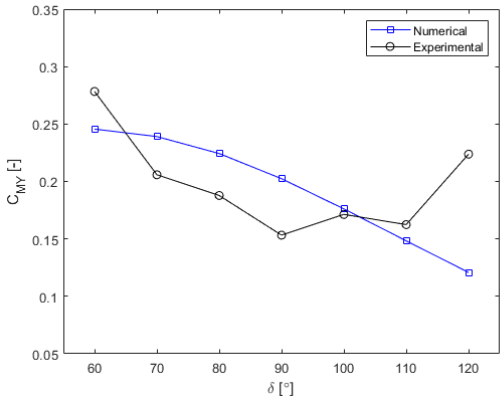

Figure 5.148: Numerical and experimental yaw moment coefficients C_{M_Y} [-], vs sheet angle δ [°].

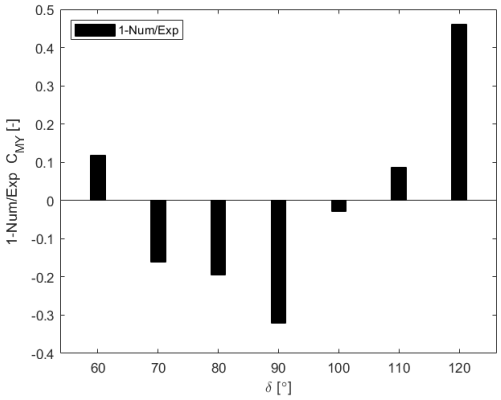

Figure 5.149: 1-Num/Exp ratio of the yaw moment coefficients C_{M_Y} [-], vs sheet angle δ [°].

Table 5.12: Tabulated data of the 1-num/exp ratio of the sail coefficients.

Sheet angle [°]	**60**	**70**	**80**	**90**	**100**	**110**	**120**
				1-Num/Exp			
C_{F_M} [-]	0.0772	0.0623	0.0706	0.0789	0.1061	0.1580	0.2084
C_{F_S} [-]	0.1703	0.2672	0.5255	-3.2070	-0.3453	-0.1108	-0.0245
C_{F_L} [-]	0.9563	0.9454	0.9693	1.0045	1.0579	1.2422	1.5445
C_{M_P} [-]	-0.0001	0.0085	0.0100	0.0182	0.0653	0.1328	0.1871
C_{M_R} [-]	0.2305	0.3567	0.6884	-16.6972	-0.5276	-0.1667	-0.0558
C_{M_Y} [-]	0.1176	-0.1616	-0.1944	-0.3206	-0.0280	0.0871	0.4602

In Fig. 5.138 it can be seen that the drive force coefficients from CFD are lower than the measured drive force coefficients, for all sheet angles. The appearances of the curves, however, are relatively similar, where the experimental measurements are very symmetric around a sheet angle of approximately 85°, which is reasonable. The 1-num/exp ratios for the drive force coefficients are presented in Fig. 5.139, and best agreement between the modeled and measured drive force coefficients is slightly above 6% for the 70° sheet angle. In Fig. 5.140, where the numerical and experimental side force coefficients are plotted, the appearances of the curves are relatively linear and parallel. The numerical side force coefficients are lower than the experimental side force coefficients in the low sheet angle range, i.e. between $60° - 80°$ and higher than the experimental side force coefficients between $90° - 120°$. The huge 1-num/exp ratio for the 90° sheet angle in Fig. 5.141 gives a misleading image that the agreement is very bad, which it not is. The reason for the high ratio is that one of the values, in this case the measured value, is very close to zero. In Table 5.12, where the ratios are presented, it can be seen that best agreement is around 2% for the 120° sheet angle.
The numerical and experimental lift force coefficients and the ratios in Fig. 5.142 & Fig. 5.143, respectively, shows relatively bad agreement for all sheet angles and that the numerical results are highly overpredicted. The lift force coefficients are however so small that they have not been used for any correction; the relevance of the lift force coefficients are therefore very low. In Fig. 5.144 it can be seen that the appearance of the curves for the pitch

moment coefficients are very alike the curves for the drive force coefficients, which is correct. The agreement between the modeled and measured pitch moment coefficients are comparatively very good between $60° - 90°$ and successively decreasing in the high sheet angle range. In Fig. 5.146 it can be seen that the appearance of the curves for the numerical and experimental roll moment coefficients are more or less identical to the corresponding curves for the side force coefficients, which is correct. As explained above, when any value is close to zero, as the measured roll moment in this case, the ratio becomes very large, which is misleading. This cannot be stressed enough, because it can be misinterpreted that the agreement therefore not is good, which is wrong. In Fig. 5.148 & Fig. 5.149 it can be seen that the agreement between the numerical and experimental yaw moment coefficients are generally low, except for the $100°$ sheet angle, where the agreement is within 3%.

6

Conclusions

Knowing how to sail the Olympic sailing class dinghy ILCA 7 for optimal VMG (velocity made good) on both the upwind leg and the downwind leg is of utmost importance for the ILCA 7 sailor. This knowledge can be learned by studying a so-called polar plot, which is the usual output from a VPP (velocity prediction program) where the aerodynamic coefficients are balanced against the hydrodynamic coefficients. To carry out a proper performance analysis of both legs of the ILCA 7 dinghy in a VPP, the aerodynamic coefficients for the MKII sail, in downwind conditions, first had to be retrieved.

In this report, it has been described how a sail model of the bi-radial MKII sail for the ILCA 7 dinghy was tested in Chalmers low-turbulence subsonic wind tunnel in a flat water sea state, for two different wind conditions, which corresponded to a light wind case and a strong wind case. The test matrix for the light wind case included five different headings, three different heel angles (upright sailing conditions included) seven different sheet angles and for each configuration of these variables, the sail model was tested for three different settings with the kicker. The test matrix for the strong wind condition, which simulated the case when the ILCA 7 dinghy is sailed dead downwind in a planing mode, was relatively small in comparison and covered only the heading of 180°, the upright sailing condition, four sheet angles and for each configuration of these variables, three settings with the kicker were tested.

Because of the manual testing procedure, when carrying out the wind tunnel tests, it was necessary to quantify the repeatability by calculating the standard deviation for a couple of general test cases. For the light wind condition, five separate repeatability tests were therefore carried out for each of the three heel angles. All repeatability tests were performed with a fix heading of 190°, a fixed sheet angle of 90° and with all three settings with the kicker. The mean value of the dimensionless standard deviation for the three different kicker settings, of the repeatability tests are approximately 2.5% for the 0° heel angle and 3% for the 10° and 20° heel angles.

Due to spatial restrictions of the test section, in Chalmers low-turbulence subsonic wind tunnel, which was the facility used for retrieving the aerodynamic coefficients, the sail and the mast had to be scaled; by choosing the proper linear length and velocity scale factors, the strain in the sail and the mast bend could be scaled properly. However, since it was not possible to scale the dimensionless Reynolds number exactly, neither kinematic nor dynamic similarity could be obtained. As explained in the report, the effects of not being able to scale the Reynolds number exactly is however relatively low, because the case analyzed has very low dependence on viscosity due to large fix separation at the edges of the sail.

Since Chalmers low-turbulence subsonic wind tunnel is of the semi-closed design, the measurements from the wind tunnel tests had to be corrected for blockage effects, caused by the presence of the lateral boundaries in the test section. This was achieved by performing steady RANS simulations and detached-eddy simulations (DES) for two computational domains of different sizes. One of the computational domains had the same cross-sectional area as the inlet of the test section of the wind tunnel and the other computational domain was an enlarged version, simulating an open test section. The blockage effects could then be isolated and calculated; the experimental coefficients corrected. The coefficients were also corrected for balance measurement errors, non-zero sampling errors and drag tare. For maximum accuracy, different turbulence models were tested in the initial phase of the numerical investigation.

In the grid dependence study, the observed order of convergence p and the estimation of uncertainty U_ϕ was 0.5 and 3.6 %, respectively, for grid 3 and the normal computational domain; 0.9 and 4.1 %, respectively, for grid 3 and the large computational domain. Since the received observed order of convergence were larger than zero, i.e. $p > 0$, monotonic convergence was received for both computational domains. Further, by receiving a safety factor of 1.25 for both computational domains, the generated grids were geometrically similar enough and the error estimations regarded as reliable. The corresponding uncertainty estimation for the finest grid, i.e. grid 1, presented in Fig. 5.4 & 5.5, showed that the estimation of uncertainty U_ϕ for the normal and the large computational domains were 1.8 % and 1.5 %, respectively. The verification analysis thus shows that the uncertainty is low with the used grid.

An informal validation was carried out where the numerical results were compared with experimental results. The validation showed that the numerical agreement with the experimental overall was relatively low. The reason for this must be the physical modeling, i.e the turbulence model and that wrong governing equations are solved. A non-stationary case has thus been solved with the equations for a stationary case. Even though a high accuracy of the agreement not was required because the results were used for small corrections, to model the flow characteristics more realistically, and perhaps get numerical results that are in better agreement with experimental results, unsteady RANS simulations and/or more attempts with DES should be performed.

Carrying out this project means that a complete set of aerodynamic coefficients for downwind sailing of the ILCA 7 dinghy is available. The set of coefficients can be downloaded from the homepage of Chalmers Sports and Technology [5] and used in a VPP for optimizing VMG in different wind conditions.

It is the authors hope that the results from this project will be useful for the Swedish elite ILCA 7 dinghy sailor who will have the honor of representing Sweden at the Summer Olympics 2024.

Bibliography

[1] Abbot, Ira H. and Von Doenhoff, Albert E. (1959). *Theory Of Wing Sections*. New York: Dover Publications Inc.

[2] Andersson, A., Barreng, A., Bohnsack, E., Lundin, L., Sahlberg, R., Werner, E. (2016). *Den flygande optimisten.* [Bachelor´s Thesis in Mechanical Engineering, Department of Shipping and Marine Technology, SJOX02-16-03] Gothenburg.

[3] Autodesk (2022). *Autodesk Inventor.* [Homepage].
Available at: https://www.autodesk.se/products/inventor/overview?plc=INVPROSA&term=1-YEAR&support=ADVANCED&quantity=1
[Accessed 28 Oct. 2022]

[4] Barlow, Jewel B., Rae, William H. and Pope, A. (1999). *Low-Speed Wind Tunnel Testing*, 3^{rd} edition. Toronto: John Wiley & Sons, inc.

[5] Chalmers Sports and Technology (2022). [Homepage].
Available at: https://www.chalmers.se/en/centres/sportstechnology/research/sports/sailing
[Accessed 28 Oct. 2022]

[6] Chernoray, V. and Davidson, L. (2018). *Low Turbulence Subsonic wind Tunnel.* [Homepage].
Available at: https://www.chalmers.se/en/departments/m2/simulator-labs/labs/chalmerswindtunnels/facility/Pages/Large-Scale-Low-Turbulence-Subsonic-wind-Tunnel.aspx
[Accessed 23 Jan. 2022]

[7] Crepier, P. (2017). *Ship Resistance Prediction: Verification And Validation Exercise On Unstructured Grids.* [Paper for the VII International Conference on Computational Methods in Marine Engineering, MARINE, 2017] the Netherlands.

[8] Davidson, L. (2020). *Fluid mechanics, turbulent flow and turbulence modeling.* [Homepage].
Available at: http://www.tfd.chalmers.se/ lada/MoF/ebook.html
[Accessed 23 Jan. 2022]

[9] Eca, L., and Hoekstra, M. (2014). *A procedure for the estimation of the numerical uncertainty of CFD calculations based on grid refinement studies.* [Journal of Computational Physics, (2014)].

[10] Fossati, F. (2007). *Aero-hydrodynamics and the performance of sailing yachts.* Milan: International Marine/McGraw-Hill

[11] Furness Controls (2022). *Electronic manometers for research applications.* [Online].
Available at: https://www.furness.com/us/product/fco560/?back=products&category=differential-pressure-manometers
[Accessed 23 Jan. 2022]

[12] Ideal Simulations (2022). *Courant Number.* [Online].
Available at: https://www.idealsimulations.com/resources/courant-number-cfd/
[Accessed 23 Jan. 2022]

[13] ILCA International Laser Class Association (2022). *ILCA Class Rules - One Design.* [pdf].
Available at: http://www.laserinternational.org/rules-and-regulations/laser-class-rules/
[Accessed 23 Jan. 2022]

[14] Institutionen för hållfasthetslära, KTH. (2010). *Handbok och formelsamling i Hållfasthetslära.* 7 *e* upplagan. Stockholm: Instant Book AB.

[15] ISEA 11th Conference of the International Sports Engineering Association (ISEA), Delft, Netherlands (2016). *The Engineering of SPORT 11*, [pdf].
Available at: http://toc.proceedings.com/31268webtoc.pdf
[Accessed 23 Jan. 2022]

[16] Johansson, B. (1997). *Measurements of Mean Velocities and Turbulence Intensities in the Working section of Wind Tunnel L2.* [pdf] Gothenburg.

[17] Jonsson, I and Busch, S (2015). *Wind Tunnel Test of a Double Blade Swept Propeller and Analysis of Real Geometry Effects.* [Master's Thesis, Department of Applied Mechanics, 2015-13] Gothenburg.

[18] Larsson, L., Eliasson, Rolf E. and Orych, M. (2016). *Principles of Yacht Design*, 4^{th} edition. London: Adlard Coles Nautical.

[19] Larsson, L. and Raven, Hoyte C. (2010). *The Principles of Naval Architecture Series, Ship Resistance and Flow.* New Jersey: The Society of Naval Architects and Marine Engineers (SNAME).

[20] Laser Performance (2022). *Laser Standard Mark II sail.* [Online].
Available at: http://shopeu.laserperformance.com/laser-standard-mark-ii-folded-sail/
[Accessed 23 Jan. 2022]

[21] Lindstrand, Levin, R and Peter, Jeremy. (2014). *CFD prediction of the effect of heel and trim on the resistance of an Olympic dinghy.* [Master's Thesis in Naval Architecture, Department of Shipping and Marine Technology, Division of Marine Design, 2014-14/304] Gothenburg.

[22] Lundh, Hans. (2008). *Grundläggande hållfasthetslära.* Stockholm: Instant Book AB.

[23] Marchaj, C A. (1979). *Aero-Hydrodynamics of Sailing*, London: Adlard Coles Limited.

[24] MARIN (2022). *MARIN*. [Homepage].
Available at: https://www.marin.nl/
[Accessed 23 Feb. 2022]

[25] McNeel (2022). *Rhino 3D*. [Homepage].
Available at: https://www.rhino3d.com/
[Accessed 23 Feb. 2022]

[26] Menter, F. R. (1992a). *Performance of Popular Turbulence Models for Attached and Separated Adverse Pressure Gradient Flow, AIAA J.*, Vol.30, pp. 2066-2072.

[27] NUMECA (2022). *FINE Marine*. [Homepage].
Available at: https://www.numeca.com/home
[Accessed 23 Feb. 2022]

[28] ORC (2022). *World Leader in Rating Technology*, [Homepage].
Available at: https://orc.org/index.asp?id=17
[Accessed 23 Feb. 2022]

[29] Pennanen, Mikka. (2016). *Optimal Sailor Position On An Olympic Dinghy*. [Master's Thesis in Naval Architecture, Department of Shipping and Marine Technology, 2016-16/367] Gothenburg.

[30] Powrie, T.S. (2007). *Aerodynamic analysis and performance prediction of a Laser Yacht*. [Project report 2007-ME44] Auckland, New Zealand.

[31] ReFRESCO, (2022). *Numerical Uncertainty Analysis-User Manual*. [pdf].
Version: 2018-rc 1
Available at: https://www.marin.nl/en/free-resources/verification-and-validation/verification-tools
[Accessed 23 Jan. 2022]

[32] Roache, P.J. (2009). *Fundamentals of Verification and Validation*, Albuquerque, New Mexico: Hermosa Publishers.

[33] SIEMENS (2022). *SIEMENS*. [Homepage].
Available at: https://www.sw.siemens.com/
[Accessed 23 Jan. 2022]

[34] SSF (2015). *SSF's Laser Guide*. [pdf]
Available at: http://www.svensksegling.se/globalassets/svenska-seglarforbundet-juniorsegling/2015-dokument/laserguide-online.pdf
[Accessed 23 Jan. 2022]

[35] Versteeg, H.K., Malalasekera, W. (2007). *An Introduction to Computational Fluid Dynamics, The Finite Volume Method*, 2^{nd} edition. Essex, England: Pearson Educational Limited.

[36] White, Frank M. (2011). *Fluid Mechanics*, 7^{th} edition. New York: The McGraw-Hill Companies Inc.

[37] Wikipedia (2022). *LabVIEW*, [Online].
Available at: https://en.wikipedia.org/wiki/LabVIEW
[Accessed 23 Jan. 2022]

[38] Wikipedia (2022). *Laser Dinghy*. [Online].
Available at: https://en.wikipedia.org/wiki/Laser%28dinghy%29
[Accessed 23 Jan. 2022]

[39] Wikipedia (2022). *Newton's laws of motion*, [Online].
Available at: https://en.wikipedia.org/wiki/Newton
[Accessed 23 Jan. 2022]

[40] Wikipedia (2022). *Pitot Tube*, [Online].
Available at: https://en.wikipedia.org/wiki/Pitot-tube
[Accessed 23 Jan. 2022]

A

Appendix

A.1 Turbulence

A.1.1 The Exact $\overline{v_i' v_j'}$ Equation

In [8] Davidson describes in a couple of steps how the most comprehensive turbulence model can be derived by deriving exact transport equations from the Navier-Stokes equation. The steps are as follow:

- Set up the momentum equation for the instantaneous velocity $v_i = \bar{v}_i + v_i' \longrightarrow$ Eq. (A)
- Time average $\longrightarrow$ equation for $\bar{v}_i$, Eq. (B)
- Subtract Eq. (B) from Eq. (A) $\longrightarrow$ equation for v_i', Eq. (C)
- Repeat the procedure for $v_j \longrightarrow$ equation for v_j', Eq. (D)
- Now multiply Eq. (C) with v_j' and Eq. (D) with v_i', time average and add them together $\longrightarrow$ equation for $\overline{v_i' v_j'}$

The final $\overline{v_i' v_j'}$-equation reads:

$$\begin{aligned}
\frac{\partial \overline{v_i' v_j'}}{\partial t} + \underbrace{\bar{v}_k \frac{\partial \overline{v_i' v_j'}}{\partial x_k}}_{C_{ij}} &= \underbrace{-\overline{v_i' v_k'} \frac{\partial \bar{v}_j}{\partial x_k} - \overline{v_j' v_k'} \frac{\partial \bar{v}_i}{\partial x_k}}_{P_{ij}} + \underbrace{\overline{\frac{p'}{\rho}\left(\frac{\partial v_i'}{\partial x_j} + \frac{\partial v_j'}{\partial x_i}\right)}}_{\Pi_{ij}} \\
&\underbrace{- \frac{\partial}{\partial x_k}\left[\overline{v_i' v_j' v_k'} + \frac{\overline{p' v_j'}}{\rho}\delta_{ik} + \frac{\overline{p' v_i'}}{\rho}\delta_{jk}\right]}_{D_{ij,t}} + \underbrace{\nu \frac{\partial^2 \overline{v_i' v_j'}}{\partial x_k \partial x_k}}_{D_{ij,\nu}} \\
&\underbrace{- g_i \beta \overline{v_j' \theta'} - g_j \beta \overline{v_i' \theta'}}_{G_{ij}} \underbrace{- 2\nu \overline{\frac{\partial v_i'}{\partial x_k}\frac{\partial v_j'}{\partial x_k}}}_{\varepsilon_{ij}}
\end{aligned} \tag{A.1}$$

where $D_{ij,t}$ and $D_{ij,\nu}$ respectively represents turbulent and viscous diffusion; the total diffusion thus reads: $D_{ij} = D_{ij,t} + D_{ij,\nu}$. Eq. (A.1) can also be written in a summarized way as:

$$C_{ij} = P_{ij} + \Pi_{ij} + D_{ij} + G_{ij} - \varepsilon_{ij}$$

where:

C_{ij} Convection

P_{ij} Production

Π_{ij} Pressure-strain

G_{ij} Buoyancy production

ε_{ij} Dissipation

Analyzing the terms in Eq. (A.1) in order to find which terms that are known and which terms that needs to be modeled. Reynolds stresses $\overline{v_i' v_j'}$ is obtained from the modeled $\overline{v_i' v_j'}$ equation and $\bar{v}_i$ is known from the momentum equation Eq. (2.23). The left hand side of Eq. (A.1) is thus known as well as the production term P_{ij} and the viscous part of the diffusion term, D_{ij}, i.e. D_{ij}^{ν} [8]. The buoyancy term, G_{ij} becomes known either by solving an exact transport equation for $\overline{v_i' \theta'}$, where $\theta = \bar{\theta} + \theta'$ is the instantaneous temperature, or by an approximate approach using *Boussinesq assumption*. The pressure-strain term, P_{ij} also has to be modeled as well as the turbulent diffusion term, D_{ij}^{t} and the dissipation, ε_{ij}.

A.1.2 The k Equation

The turbulent kinetic energy k is the sum of all normal Reynolds stresses [8], i.e.

$$k = \frac{1}{2} \sum_{i=1}^{3} \overline{v_i^2} = \frac{1}{2} \left(\overline{v_1^2} + v_2^2 + v_3^2 \right) \equiv \frac{1}{2} \overline{v_i' v_i'} \tag{A.2}$$

and by taking the *trace*, i.e. setting the indices $i = j$ of the equation for the Reynolds stresses $\overline{v_i' v_j'}$ and dividing with two, one receive the equation for the turbulent kinetic energy:

$$\begin{aligned} \frac{\partial k}{\partial t} + \underbrace{\bar{v}_i \frac{\partial k}{\partial x_j}}_{C^k} = & \underbrace{- \overline{v_i' v_j'} \frac{\partial \bar{v}_i}{\partial x_j}}_{P^k} \underbrace{- \nu \overline{\frac{\partial v_i'}{\partial x_j} \frac{\partial v_i'}{\partial x_j}}}_{\varepsilon} \\ & \underbrace{- \frac{\partial}{\partial x_j} \left\{ \overline{v_j' \left(\frac{p'}{\rho} + \frac{1}{2} v_i' v_i' \right)} \right\}}_{D_t^k} + \underbrace{\nu \frac{\partial^2 k}{\partial x_j \, \partial x_j}}_{D_\nu^k} \underbrace{- g_i \beta \overline{v_i' \theta'}}_{G^k} \end{aligned} \tag{A.3}$$

The total diffusion $D^k = D_t^k + D_\nu^k$ is decomposed into the turbulent and viscous diffusion D_t^k and D_ν^k, respectively and Eq. (A.3) can also be symbolically written as the $\overline{v_i' v_j'}$ equation were:

$$C^k = P^k + + D^k + G^k - \varepsilon$$

Analyzing the terms in Eq. (A.3), in order to establish which terms that are known and which has to be modeled, we obtain $\bar{v}_i$ from the momentum equation, Eq. (2.21) and the turbulent kinetic energy k is obtained from the modeled k equation. As in the $\overline{v_i' v_j'}$ equation, the viscous diffusion term $D^k_{i,\nu}$ is known as with the buoyancy term, G^k if either an exact transport equation is solved for $\overline{v_i' \theta'}$ or if the Boussinesq assumption is used. Thus, the pressure-strain term, P^k also has to be modeled as well as the turbulent diffusion term, D^k_t and the dissipation, ε.

A.1.3 The ε Equation

To express the turbulent viscosity, ν_t in eddy-viscosity models, two quantities are usually used and in the $k - \varepsilon$ model, k and ε are used [8]. The turbulent viscosity is estimated using dimensional analysis, where the turbulent velocity $\mathcal{U}$ is multiplied with the turbulent length scale $\mathcal{L}$:

$$\nu_t \propto \mathcal{U}\mathcal{L} \tag{A.4}$$

where the velocity scale is taken as $k^{1/2}$ and the length scale as $k^{3/2}/\varepsilon$, with the result that the turbulent viscosity is defined as:

$$\nu_t = C_\mu \frac{k^2}{\varepsilon} \tag{A.5}$$

where $C_\mu = 0.09$.

The ε transport equation can be derived exact, but it is very complicated according to Davidson who in [8] instead describe how the ε transport equation can be created with the usage of the k transport equation. The modeled equation of the ε transport equation reads:

$$\frac{\partial \varepsilon}{\partial t} + \bar{v}_j \frac{\partial \varepsilon}{\partial x_j} = \frac{\varepsilon}{k}\left(c_{\varepsilon 1} P^k + c_{\varepsilon 1} G^k - c_{\varepsilon 2}\varepsilon\right) + \frac{\partial}{\partial x_j}\left[\left(\nu + \frac{\nu_t}{\sigma_\varepsilon}\right)\frac{\partial \varepsilon}{\partial x_j}\right] \tag{A.6}$$

A.1.4 The Boussinesq Assumption

The *Boussinesq assumption* is named after the French mathematician and physicist *Joseph Valentin Boussinesq* who 1877 presented a method to model the Reynolds stresses in Eq. (2.23), by introducing a turbulent viscosity, ν_t, which is a flow property and not a fluid property. The Boussinesq assumption can be used when natural convection, i.e. buoyancy driven flows occurs. In [8], Davidson describes the procedure, by first considering the diffusion terms in Eq. (2.8), i.e. the momentum equation for incompressible flow, with constant viscosity, μ, which reads:

$$\frac{\partial}{\partial x_j}\left\{\mu\left(\frac{\partial \bar{v}_i}{\partial x_j} + \frac{\partial \bar{v}_j}{\partial x_i}\right)\right\} \tag{A.7}$$

With a change of the notation for the viscosity, μ for ν and introducing the turbulent viscosity, ν_t in Eq. (A.7), we receive:

Step 1:

$$\frac{\partial}{\partial x_j}\left\{\nu\left(\frac{\partial \bar{v}_i}{\partial x_j}+\frac{\partial \bar{v}_j}{\partial x_i}\right)-\overline{v_i' v_j'}\right\} \tag{A.8}$$

and in step 2, rewriting the diffusion terms, we get:

Step 2:

$$\frac{\partial}{\partial x_j}\left\{(\nu+\nu_t)\left(\frac{\partial \bar{v}_i}{\partial x_j}+\frac{\partial \bar{v}_j}{\partial x_i}\right)\right\} \tag{A.9}$$

Where it is emphasized that the turbulent viscosity, ν_t, is not constant. "Identification of" Eq. (A.8) & Eq. (A.9), results in an expression for the negative Reynolds stresses:

Step 3:

$$-\overline{v_i' v_j'}=\nu_t\left(\frac{\partial \bar{v}_i}{\partial x_j}+\frac{\partial \bar{v}_j}{\partial x_i}\right) \tag{A.10}$$

Since Eq. (A.10) not is valid for contraction, i.e. when i is set to j, the *trace* of the left hand side is added to to the right hand side in Eq. (A.10), which then reads:

Step 4:

$$\overline{v_i' v_j'}=-\nu_t\left(\frac{\partial \bar{v}_i}{\partial x_j}+\frac{\partial \bar{v}_j}{\partial x_i}\right)+\frac{1}{3}\delta_{ij}\,\overline{v_k' v_k'}=-2\,\nu\,\bar{s}_{ij}+\frac{2}{3}\delta_{ij}\,k \tag{A.11}$$

Inserting Eq. (A.11) in Eq. (2.23) the six unknown *Reynolds stresses* are replaced with a single unknown, i.e. the turbulent viscosity, ν_t and the momentum equation reads:

$$\begin{aligned}&\frac{\partial \rho_0\,\bar{v}_i}{\partial t}+\frac{\partial}{\partial x_j}\left(\rho_0\,\bar{v}_i\,\bar{v}_j\right)\\ =&-\frac{\partial \bar{p}\,B}{\partial x_i}+\frac{\partial}{\partial x_j}\left[(\mu+\mu_t)\left(\frac{\partial \bar{v}_i}{\partial x_j}+\frac{\partial \bar{v}_j}{\partial x_i}\right)\right]-\beta\,\rho_0\,(\bar{\theta}-\theta_0)\,g_i\end{aligned} \tag{A.12}$$

where the turbulent kinetic energy in the last term of Eq. (A.11) is included in the pressure term, i.e. $\bar{p}B=\bar{p}+2k/3$.

A.1.5 The $k-\varepsilon$ Model

The $k-\varepsilon$ model is an eddy-viscosity two-equation model that solves the transport equations for the turbulent kinetic viscosity, k and the turbulent dissipation, ε. The exact transport model for the turbulent kinetic energy, k was presented in Eq. (A.3) and the modeled

equation for k, Eq. (A.13), is received by inserting modeled assumptions for the production, P^k, production due to buoyancy, G^k and the diffusion, D^k, Eq. (A.14) - Eq. (A.16), respectively. The Reynolds stresses in the production term and the heat flux vector in the buoyancy term are received with the usage of Boussinesq assumption [8].

$$\begin{aligned} \frac{\partial k}{\partial t} + \bar{v}_j \frac{\partial k}{\partial x_j} = & \underbrace{\nu_t \left(\frac{\partial \bar{v}_i}{\partial x_j} + \frac{\partial \bar{v}_j}{\partial x_i} \right) \frac{\partial \bar{v}_i}{\partial x_j}}_{P^k} + \underbrace{g_i \, \beta \, \frac{\nu_t}{\sigma_\theta} \frac{\partial \bar{\theta}}{\partial x_i}}_{G^k} \\ & - \varepsilon + \underbrace{\frac{\partial}{\partial x_j} \left[\left(\nu + \frac{\nu_t}{\sigma_k} \right) \frac{\partial k}{\partial x_j} \right]}_{D^k} \end{aligned} \tag{A.13}$$

Production term:

$$\begin{aligned} P^k &= \left\{ \nu_t \left(\frac{\partial \bar{v}_i}{\partial x_j} + \frac{\partial \bar{v}_j}{\partial x_i} \right) - \frac{2}{3} \delta_{ij} \, k \right\} \frac{\partial \bar{v}_i}{\partial x_j} \\ &= \nu_t \left(\frac{\partial \bar{v}_i}{\partial x_j} + \frac{\partial \bar{v}_j}{\partial x_i} \right) \frac{\partial \bar{v}_i}{\partial x_j} = \nu_t \, 2 \, \bar{s}_{ij} \, (\, \bar{s}_{ij} + \Omega_{ij} \,) = 2 \, \nu_t \, \bar{s}_{ij} \, \bar{s}_{ij} \end{aligned} \tag{A.14}$$

$$\bar{s}_{ij} = \frac{1}{2} \left(\frac{\partial \bar{v}_i}{\partial x_j} + \frac{\partial \bar{v}_j}{\partial x_i} \right), \quad \Omega_{ij} = \frac{1}{2} \left(\frac{\partial \bar{v}_i}{\partial x_j} - \frac{\partial \bar{v}_j}{\partial x_i} \right), \quad \frac{\partial \bar{v}_i}{\partial x_j} = \bar{s}_{ij} + \Omega_{ij}$$

Buoyancy term:

$$G^k = - g_i \, \beta \, \overline{v_i' \, \theta'}, \quad \overline{v_i' \, \theta'} = - \alpha_t \frac{\partial \bar{\theta}}{\partial x_i}, \quad \alpha_t = \frac{\nu_t}{\sigma_\theta} \tag{A.15}$$

where $\overline{v_i' \, \theta'}$ is the heat flux vector, α_t is the turbulent thermal diffusivity and σ_θ is the turbulent Prandtl number.

Diffusion term:

$$D^k = \frac{\partial}{\partial x_j} \left[\left(\nu + \frac{\nu_t}{\sigma_k} \right) \frac{\partial k}{x_j} \right] \tag{A.16}$$

The modeled ε equation is received with the same method from Eq. (A.6), and reads:

$$\frac{\partial \varepsilon}{\partial t} + \bar{v}_j \frac{\partial \varepsilon}{\partial x_j} = \underbrace{\underbrace{\frac{\varepsilon}{k} c_{\varepsilon 1} \underbrace{\nu_t \left(\frac{\partial \bar{v}_i}{\partial x_j} + \frac{\partial \bar{v}_j}{\partial x_i} \right) \frac{\partial \bar{v}_i}{\partial x_j}}_{P^k}}_{P^\varepsilon} + \underbrace{\underbrace{\frac{\varepsilon}{k} c_{\varepsilon 1} \underbrace{g_i \beta \frac{\nu_t}{\sigma_\theta} \frac{\partial \bar{\theta}}{\partial x_i}}_{G^k}}_{G^\varepsilon} - \underbrace{c_{\varepsilon 2} \frac{\varepsilon^2}{k}}_{\Psi^\varepsilon} + \underbrace{\frac{\partial}{\partial x_j} \left[\left(\nu + \frac{\nu_t}{\sigma_\varepsilon} \right) \frac{\partial \varepsilon}{\partial x_j} \right]}_{D^\varepsilon}}_{} \tag{A.17}$$

Diffusion term:

$$D^\varepsilon = \frac{\partial}{\partial x_j} \left[\left(\nu + \frac{\nu_t}{\sigma_\varepsilon} \right) \frac{\partial \varepsilon}{x_j} \right] \tag{A.18}$$

Destruction term:

$$\Psi^\varepsilon = \frac{\varepsilon}{k} c_{\varepsilon 2} \varepsilon \tag{A.19}$$

A.2 Turbulence Intensity

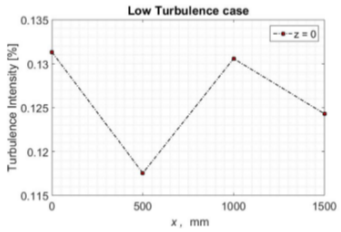

Figure A.1: The image shows the results from an investigation, carried out by the lab personnel of the wind tunnel facility, of the turbulence intensity [%] in the test section of Chalmers low-turbulence subsonic wind tunnel.

A.3 Acquisition Settings

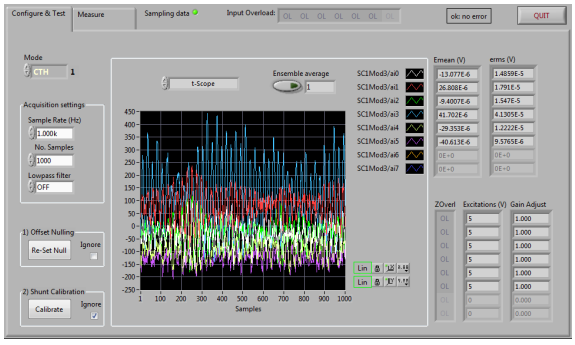

Figure A.2: The image shows the LabVIEW sampling window, with the Acquisition settings and the filtered data.

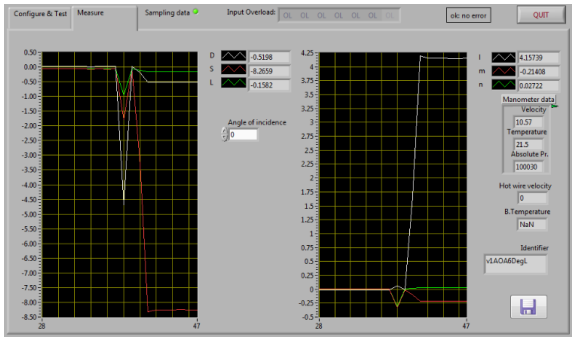

Figure A.3: The image shows the LabVIEW Measure tab with the three forces: D=drag, S=side and L=lift, the three moments: l=pitch, m=roll and n=yaw, the Manometer data: Velocity (U), Temperature (T), the Absolute Pressure (P) and the Identifier.

A.4 Numerical Investigation

A.4.1 Grid Dependence Study

Front Views of Grid 5-1, the Normal Domain & Flat Sail Model

In Fig. A.4 - A.8 below, the 5 grids of unstructured mesh of hexahedral cells with different resolution, of the normal domain with the flat sail model are presented and in Fig. A.9, which zoom in on the clew of the sail, some of the 50 prism-cell layers of grid 1 can be seen.

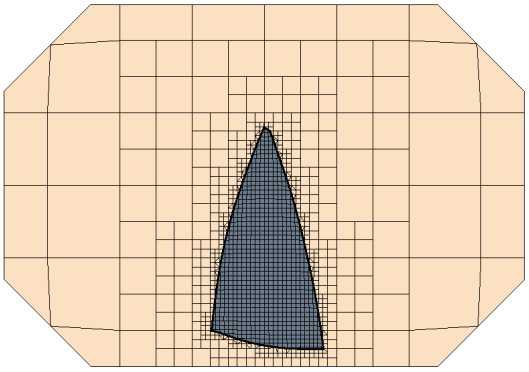

Figure A.4: Front view of the normal domain, grid 5 and the flat sail model.

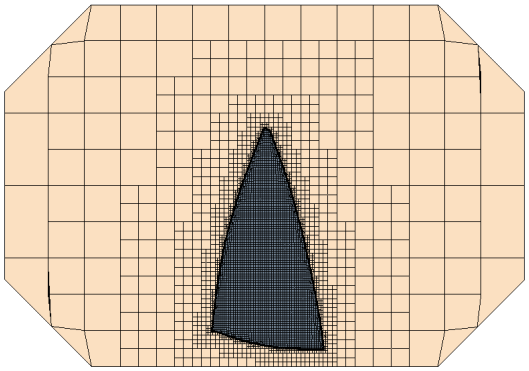

Figure A.5: Front view of the normal domain, grid 4 and the flat sail model.

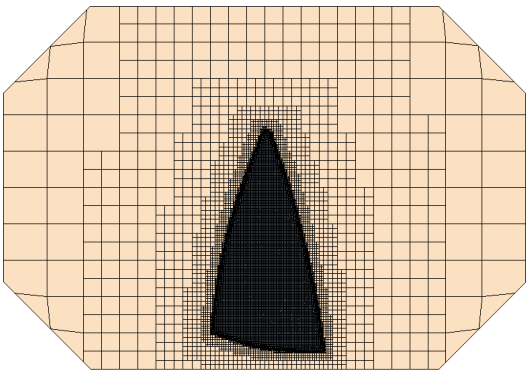

Figure A.6: Front view of the normal domain, grid 3 and the flat sail model.

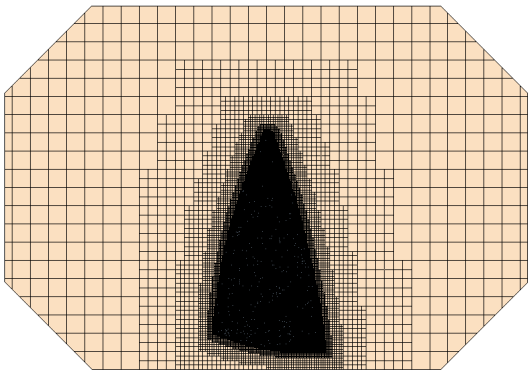

Figure A.7: Front view of the normal domain, grid 2 and the flat sail model.

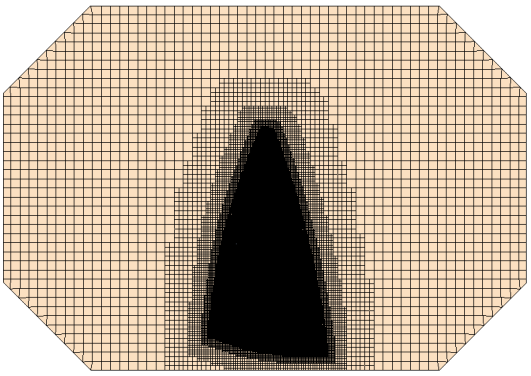

Figure A.8: Front view of the normal domain, grid 1 and the flat sail model.

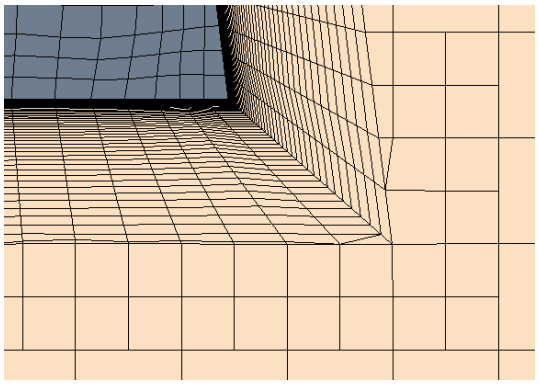

Figure A.9: Zoom of the clew, showing some of the prism-cell layers of grid 1, in the normal domain.

Top Views of Grid 5-1, the Normal Domain & Flat Sail Model

The top view images of grid 5-1 in Fig. A.10 - A.14 below, shows the full length and width of the normal domain.

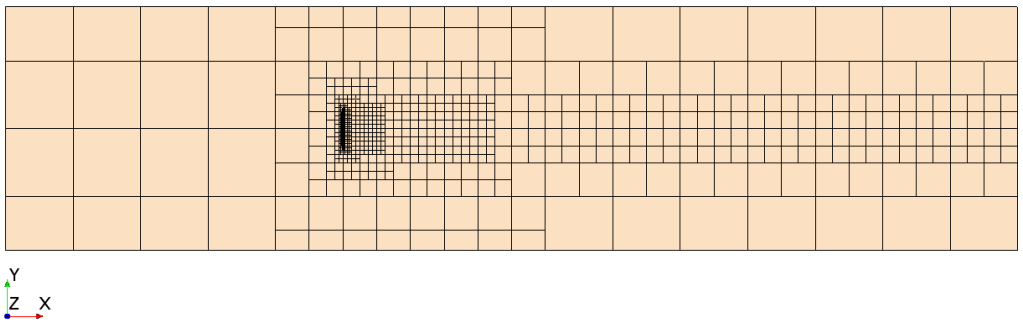

Figure A.10: Top view of the normal domain, grid 5 and the flat sail model.

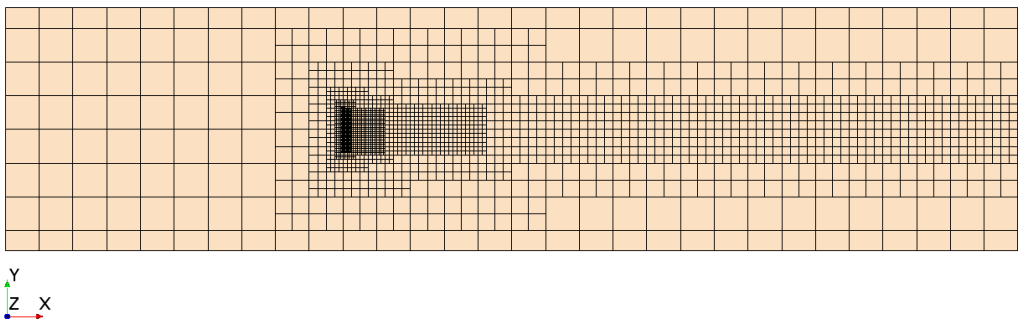

Figure A.11: Top view of the normal domain, grid 4 and the flat sail model.

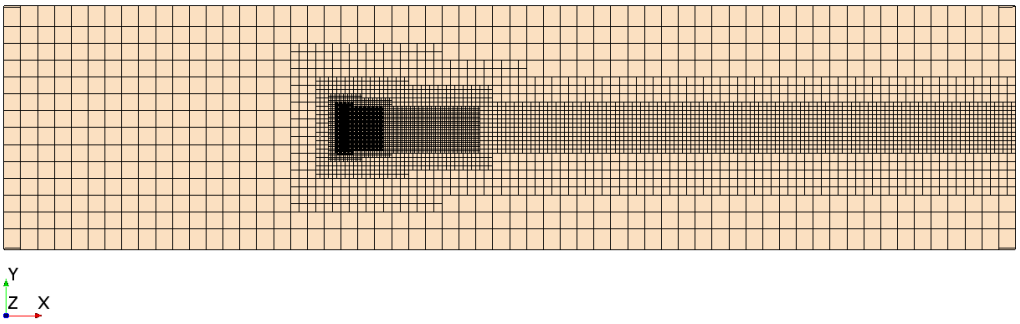

Figure A.12: Top view of the normal domain, grid 3 and the flat sail model.

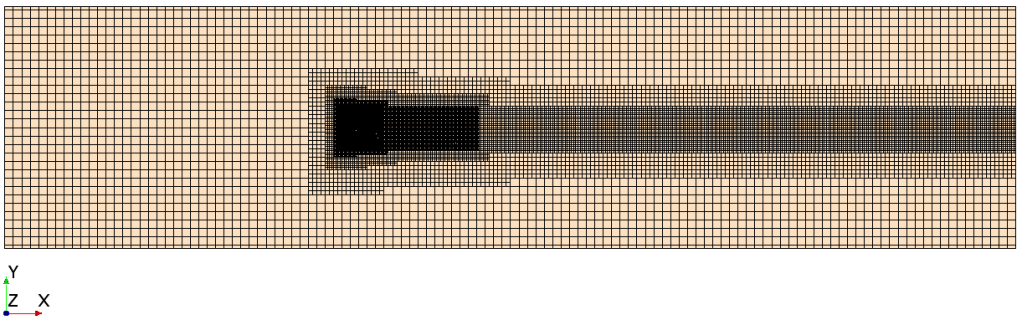

Figure A.13: Top view of the normal domain, grid 2 and the flat sail model.

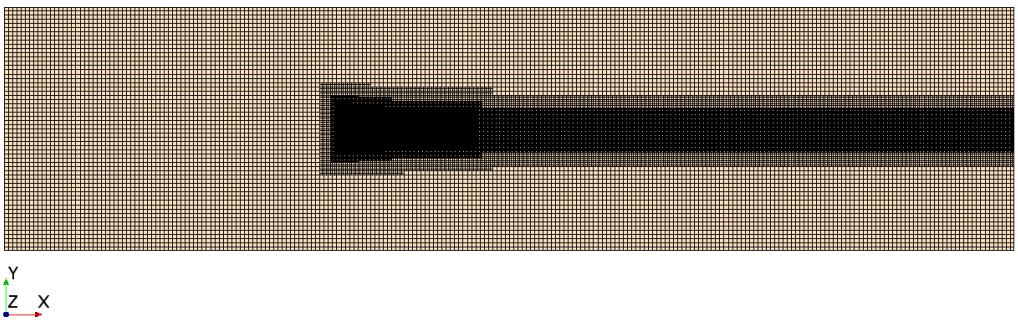

Figure A.14: Top view of the normal domain, grid 1 and the flat sail model.

Side Views of Grid 5-1, the Normal Domain & Flat Sail Model

The side view images of grid 5-1 in Fig. A.15 - A.19 below, shows the full length and height of the normal domain.

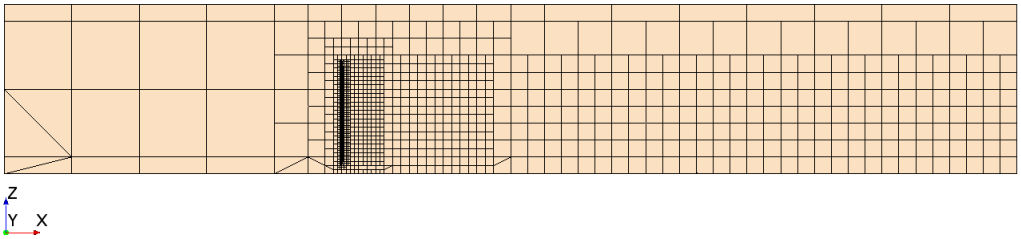

Figure A.15: Side view of the normal domain, grid 5 and the flat sail model.

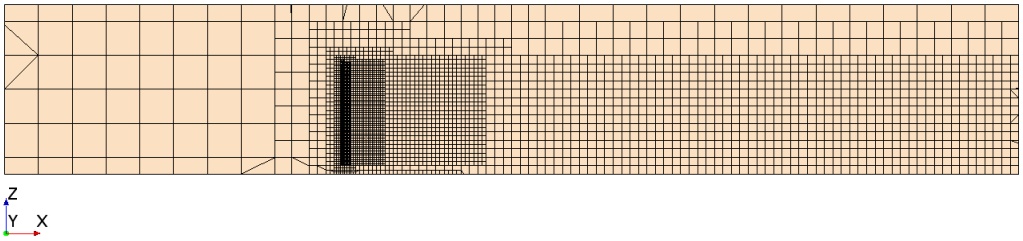

Figure A.16: Side view of the normal domain, grid 4 and the flat sail model.

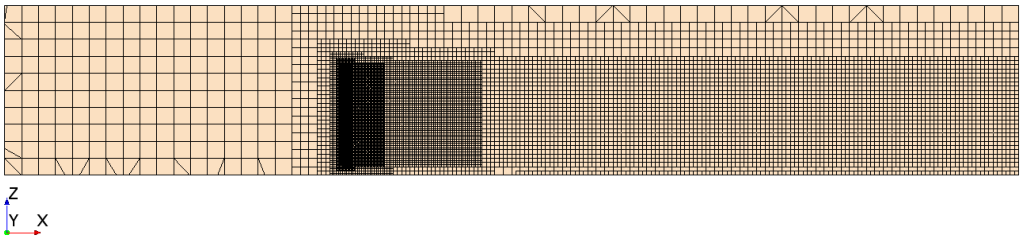

Figure A.17: Side view of the normal domain, grid 3 and the flat sail model.

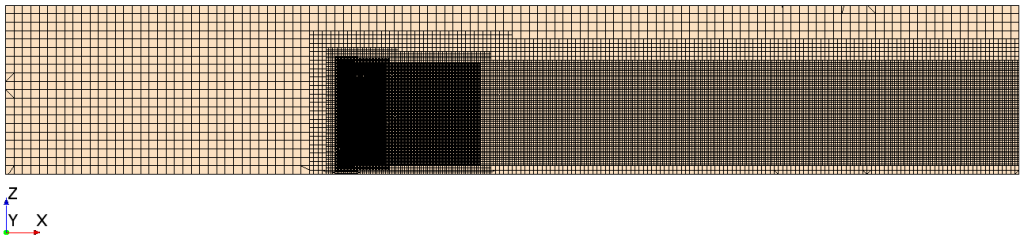

Figure A.18: Side view of the normal domain, grid 2 and the flat sail model.

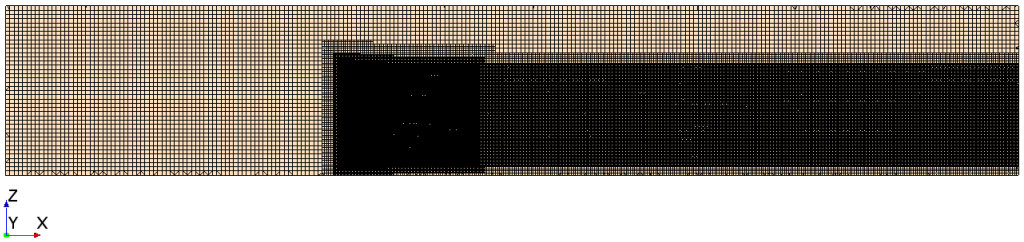

Figure A.19: Side view of the normal domain, grid 1 and the flat sail model.

Front Views of Grid 5-1, the Large Domain & Flat Sail Model

In Fig A.20 - A.24 below, the 5 grids, of unstructured mesh of hexahedral cells with different resolution, of the large domain with the flat sail model are presented and in Fig. A.25, which zoom in on the clew of the sail, some of the 50 prism-cell layers of grid 1 can be seen.

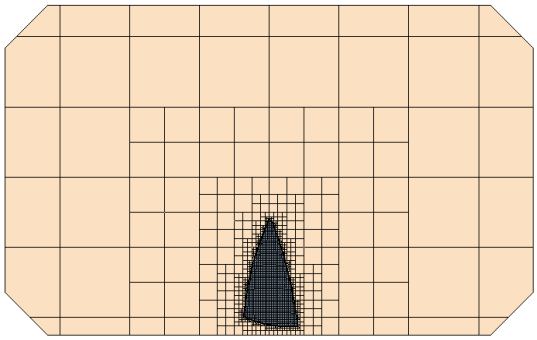

Figure A.20: Front view of the large domain, grid 5 and the flat sail model.

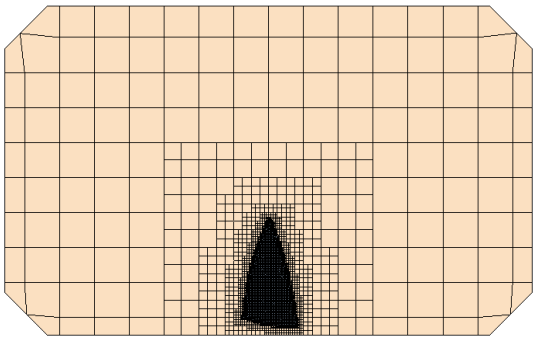

Figure A.21: Front view of the large domain, grid 4 and the flat sail model.

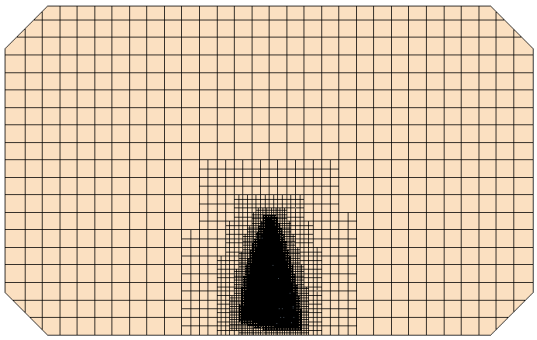

Figure A.22: Front view of the large domain, grid 3 and the flat sail model.

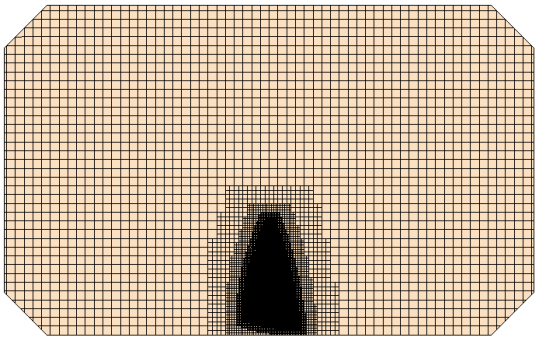

Figure A.23: Front view of the large domain, grid 2 and the flat sail model.

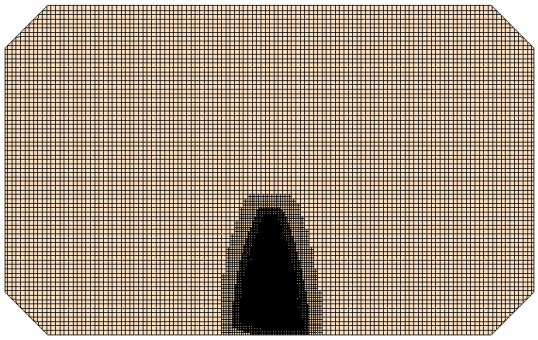

Figure A.24: Front view of the large domain, grid 1 and the flat sail model.

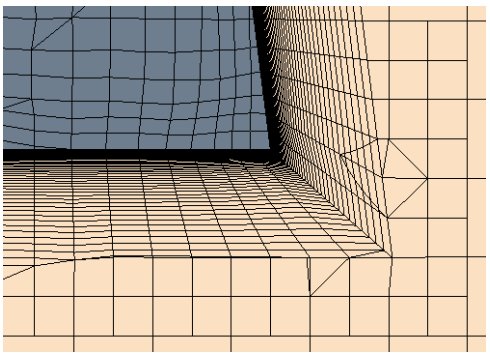

Figure A.25: Zoom of the clew, showing some of the prism-cell layers of grid 1, in the large domain.

Top Views of Grid 5-1, the Large Domain & Flat Sail Model

The top view images of grid 5-1 in Fig. A.26 - A.30 below, shows the full length and width of the large domain.

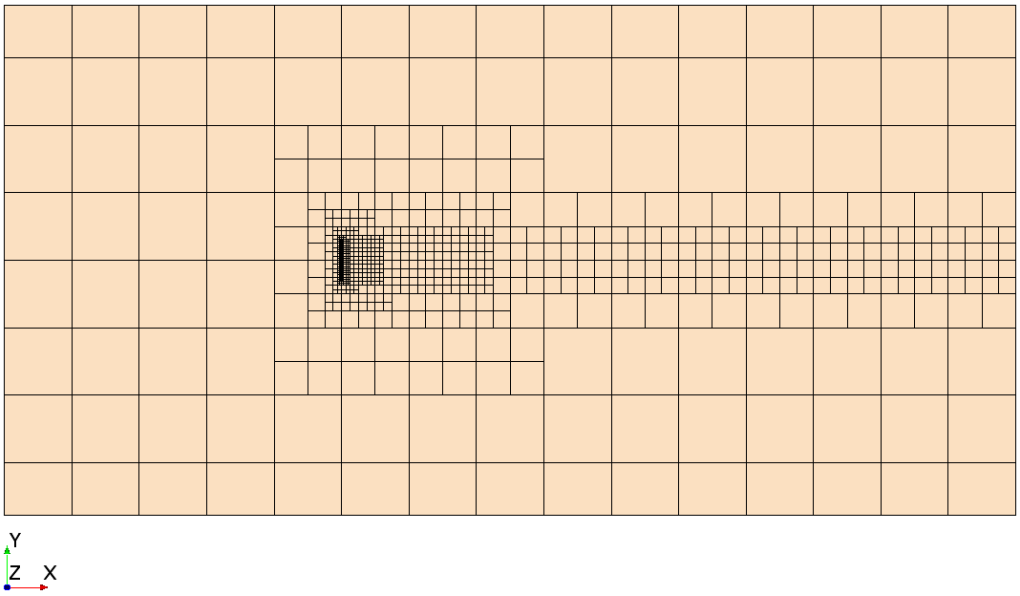

Figure A.26: Top view of the large domain, grid 5 and the flat sail model.

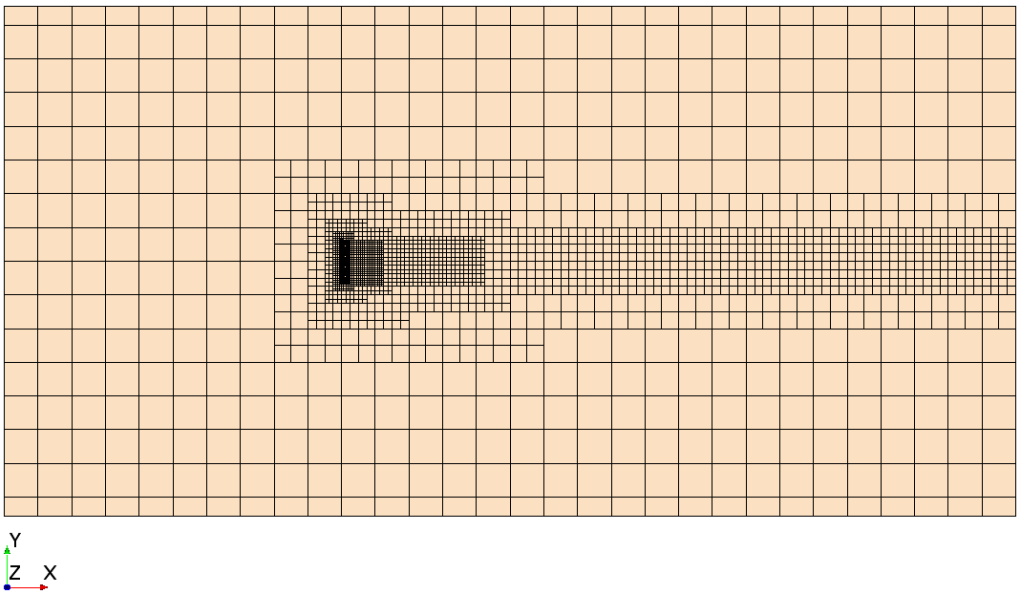

Figure A.27: Top view of the large domain, grid 4 and the flat sail model.

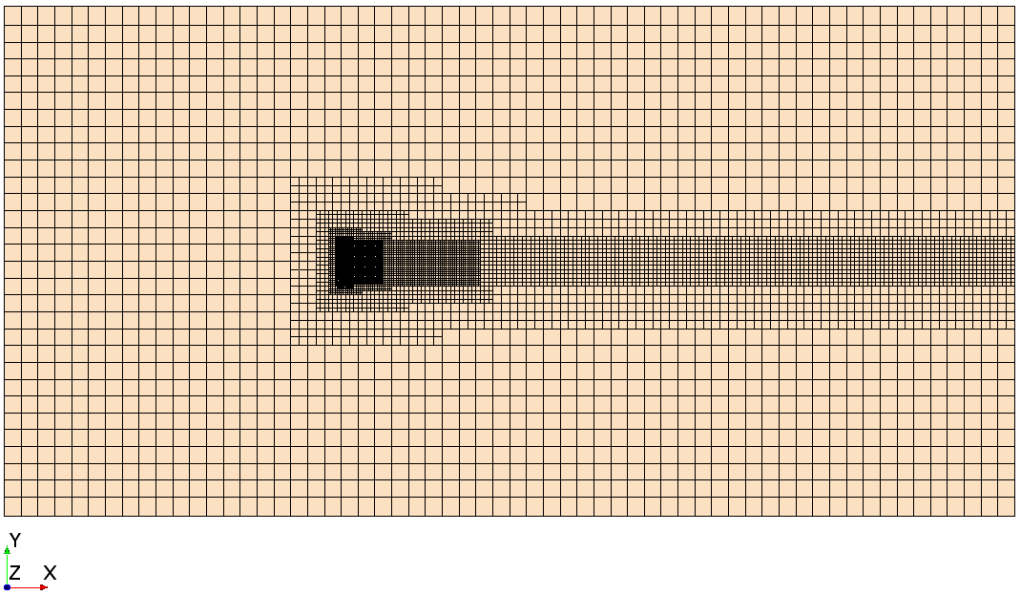

Figure A.28: Top view of the large domain, grid 3 and the flat sail model.

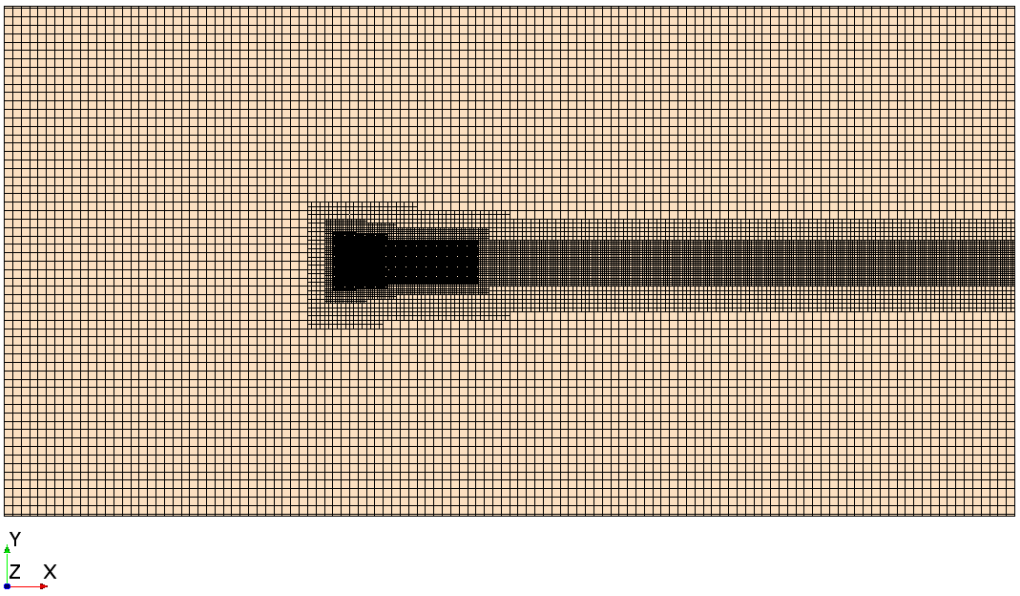

Figure A.29: Top view of the large domain, grid 2 and the flat sail model.

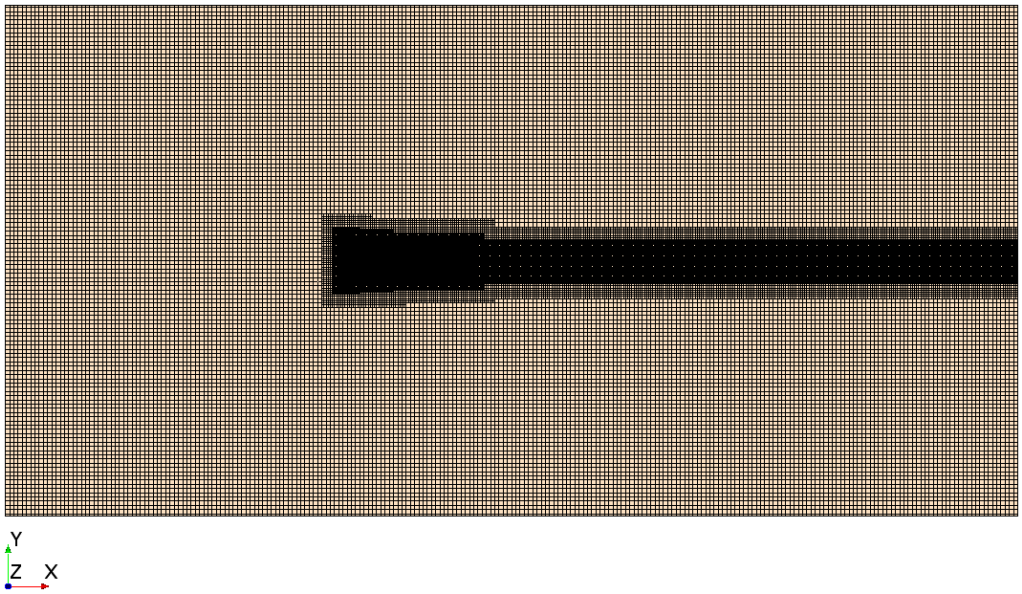

Figure A.30: Top view of the large domain, grid 1 and the flat sail model.

Side Views of Grid 5-1, the Large Domain & Flat Sail Model

The side view images of grid 5-1 in Fig. A.31 - A.35 below, shows the full length and height of the large domain.

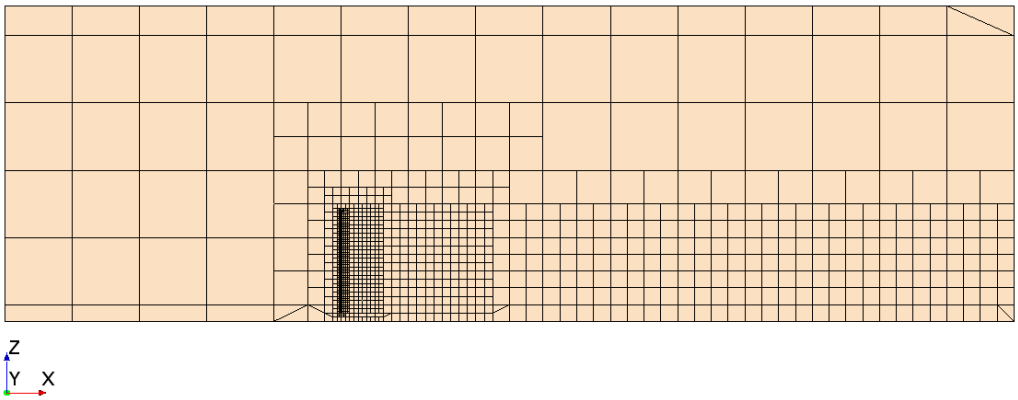

Figure A.31: Side view of the large domain, grid 5 and the flat sail model.

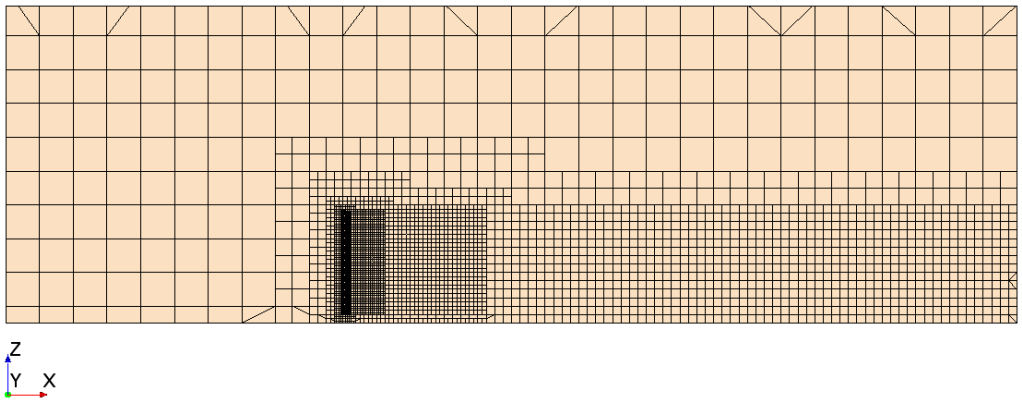

Figure A.32: Side view of the large domain, grid 4 and the flat sail model.

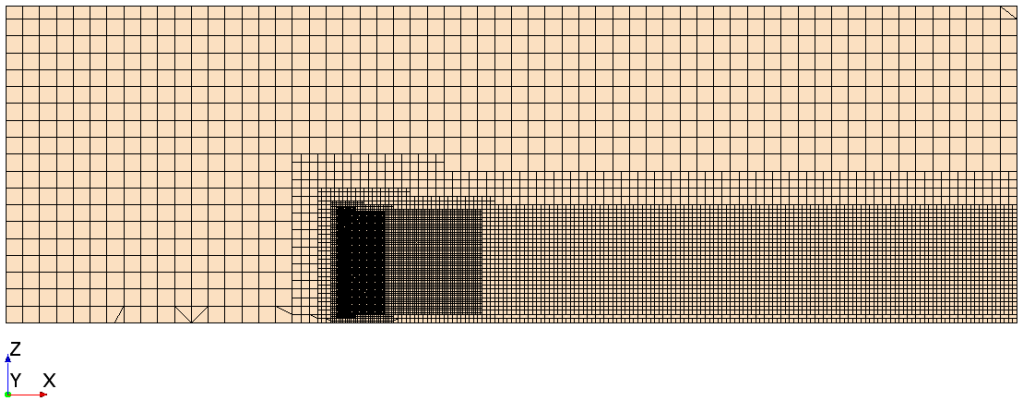

Figure A.33: Side view of the large domain, grid 3 and the flat sail model.

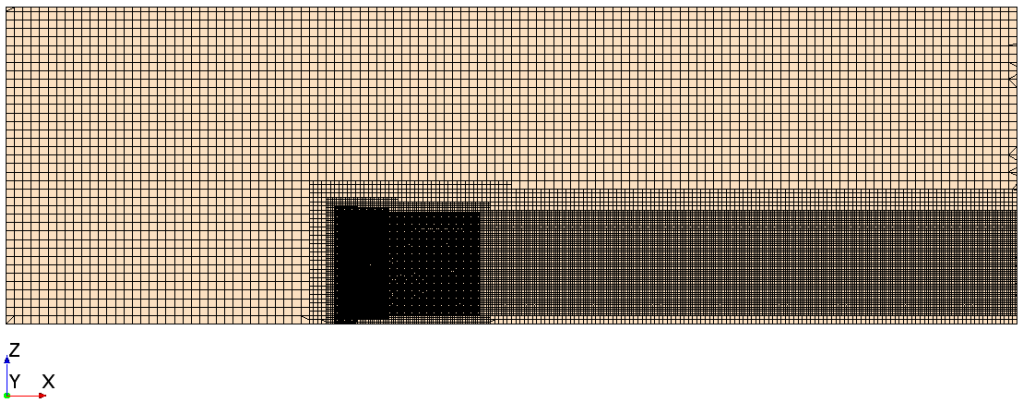

Figure A.34: Side view of the large domain, grid 2 and the flat sail model.

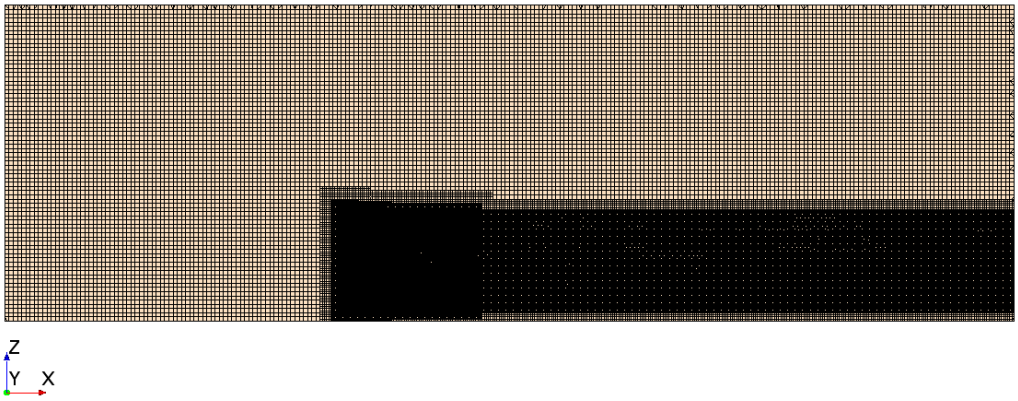

Figure A.35: Side view of the large domain, grid 1 and the flat sail model.

RANS Simulations

Tabulated Data

The corresponding data from Fig. 5.1 - 5.3 are presented in Table A.1 below.

Table A.1: Drive force coefficients C_{F_M} [-] and step size $1/\sqrt[3]{No.\ Cells}$, for each grid and both domains, presented in Fig. 5.1 - 5.3.

Grid	**1**	**2**	**3**	**4**	**5**
Normal Domain					
C_{F_M} [-]	1.5835	1.5921	1.6007	1.6351	1.6437
Step size [-]	0.00284	0.00514	0.00920	0.01680	0.03172
Large Domain					
C_{F_M} [-]	1.2478	1.2564	1.2737	1.3769	1.3511
Step size [-]	0.00280	0.00510	0.00913	0.01671	0.03153

Table A.2 below, show the difference in % of the drive force coefficients C_{F_M} and the step size, from Table A.1 above, with grid 1 as reference.

Table A.2: The difference in % between the drive force coefficients C_{F_M} [-] and the step size, from Table A.1, with grid 1 as reference.

Grid	**1**	**2**	**3**	**4**	**5**
Normal domain			$Diff.$ [%]		
C_{F_M} [-]	ref.	+0.5416	+1.0803	+3.2064	+3.7308
Step size [-]	ref.	+57.6441	+105.648	+142.159	+167.130
Large domain			$Diff.$ [%]		
C_{F_M} [-]	ref.	+0.6869	+ 2.0543	+9.8373	+7.9495
Step size [-]	ref.	+58.2278	+106.119	+142.594	+167.375

Flow Field Visualization

Top View Images

The top view images of the pressure distribution, velocity distribution, and constrained streamlines from the RANS simulations in the grid dependence study presented below, shows the scalar quantities at a horizontal xy-plane, at the height of the center of effort (CoE).

Pressure Distribution at CoE in the Normal Domain for Grid 5-1

Fig. A.36 - A.40 shows top view images of the pressure distribution, at CoE and the flat sail model with a sheet angle of 90° for grid 5-1 in the normal computational domain.

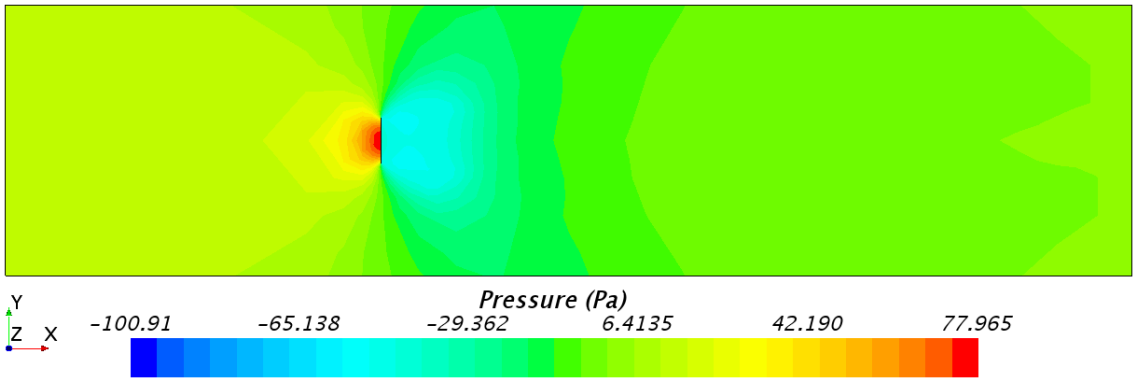

Figure A.36: Top view of the normal computational domain, with grid 5, showing the pressure distribution, at the height of the center of effort (CoE); the flat sail model with a sheet angle of 90°.

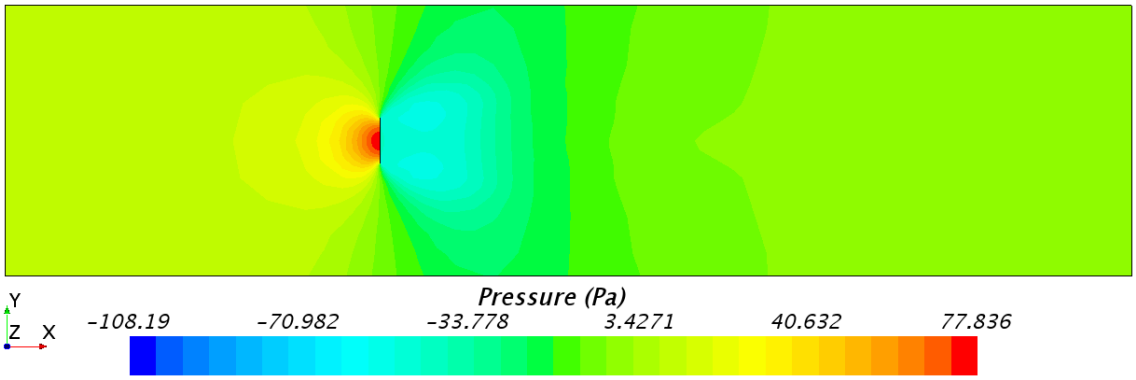

Figure A.37: Top view of the normal computational domain, with grid 4, showing the pressure distribution, at the height of the center of effort (CoE); the flat sail model with a sheet angle of 90°.

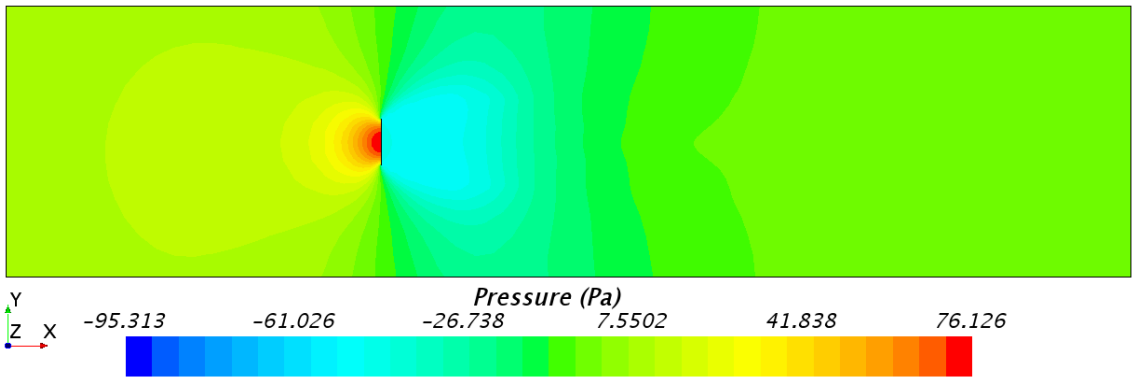

Figure A.38: Top view of the normal computational domain, with grid 3, showing the pressure distribution, at the height of the center of effort (CoE); the flat sail model with a sheet angle of 90°.

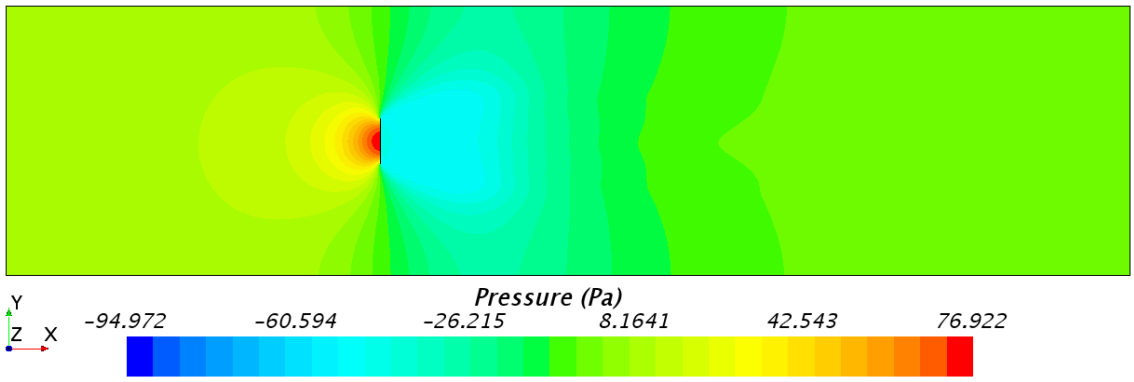

Figure A.39: Top view of the normal computational domain, with grid 2, showing the pressure distribution, at the height of the center of effort (CoE); the flat sail model with a sheet angle of 90°.

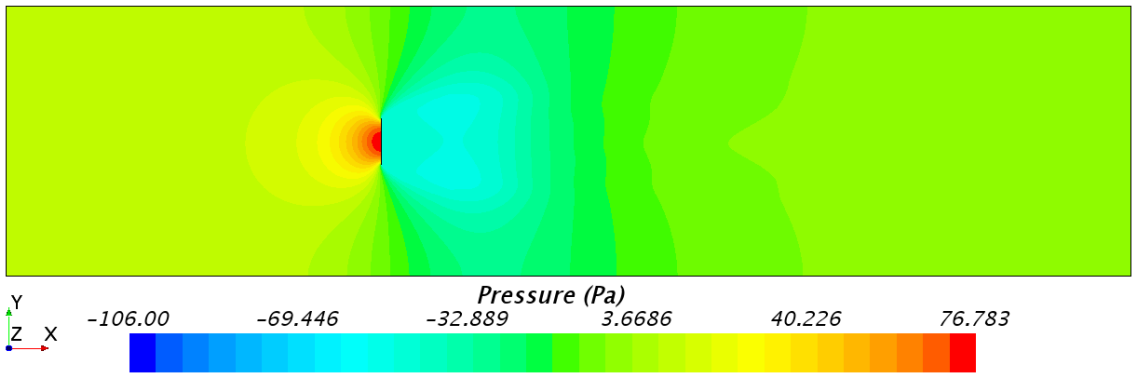

Figure A.40: Top view of the normal computational domain, with grid 1, showing the pressure distribution, at the height of the center of effort (CoE); the flat sail model with a sheet angle of 90°.

Velocity Distribution at CoE in the Normal Domain with Grid 5-1

Fig. A.41 - A.45 shows top view images of the velocity distribution, at CoE and the flat sail model with a sheet angle of 90° for grid 5-1 in the normal computational domain.

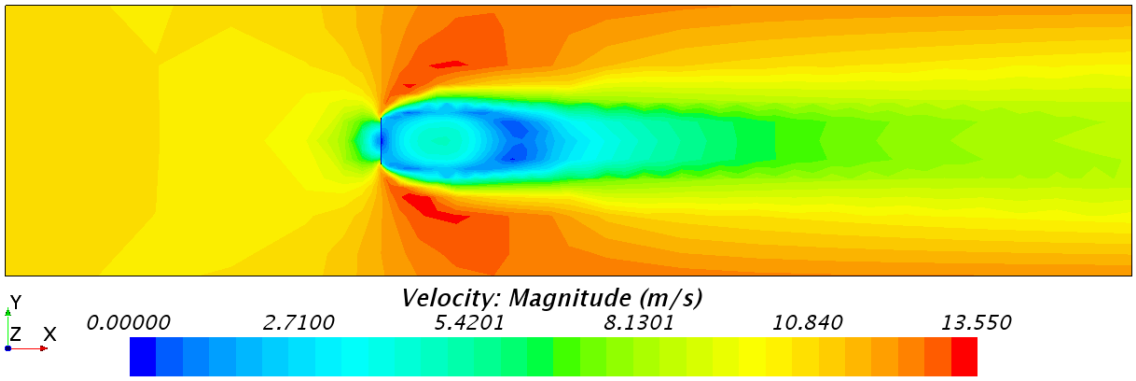

Figure A.41: Top view of the normal computational domain, with grid 5, showing the velocity distribution, at the height of the center of effort (CoE); the flat sail model, with a sheet angle of 90°.

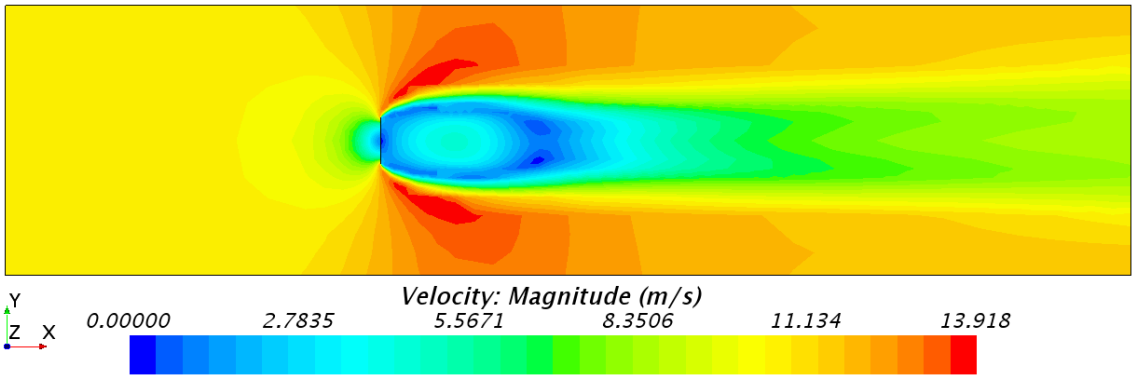

Figure A.42: Top view of the normal computational domain, with grid 4, showing the velocity distribution, at the height of the center of effort (CoE); the flat sail model, with a sheet angle of 90°.

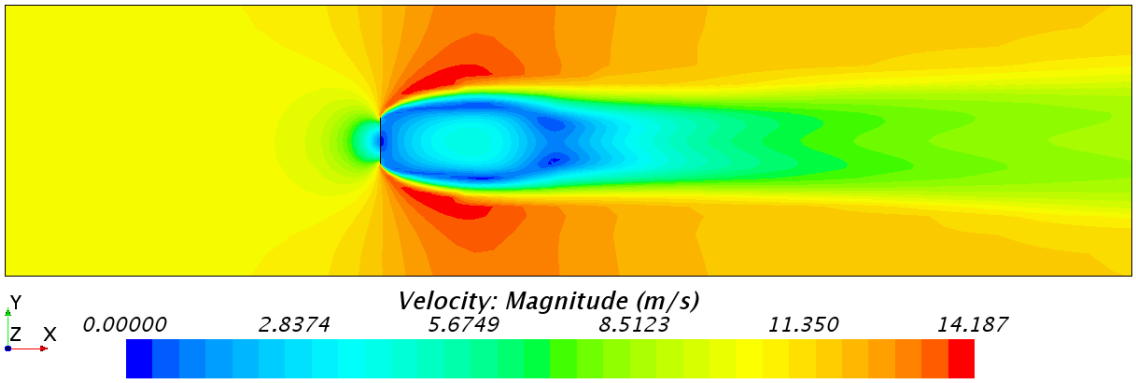

Figure A.43: Top view of the normal computational domain, with grid 3, showing the velocity distribution, at the height of the center of effort (CoE); the flat sail model, with a sheet angle of 90°.

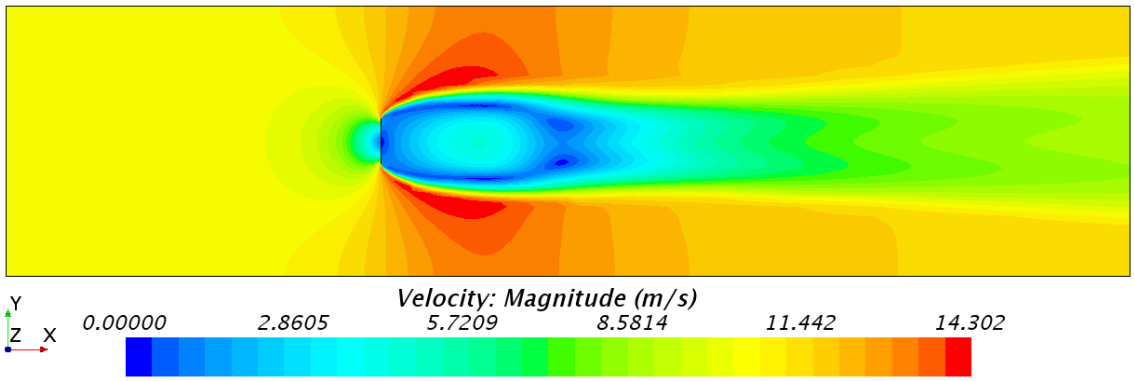

Figure A.44: Top view of the normal computational domain, with grid 2, showing the velocity distribution, at the height of the center of effort (CoE); the flat sail model, with a sheet angle of 90°.

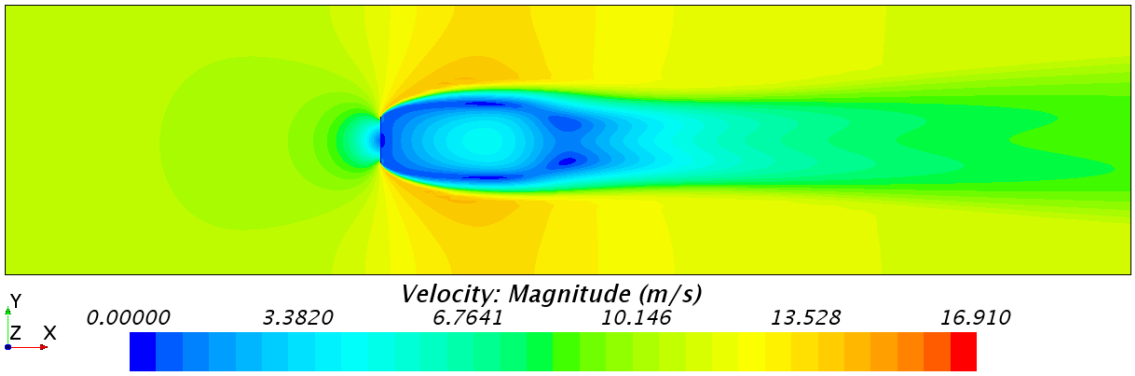

Figure A.45: Top view of the normal computational domain, with grid 1, showing the velocity distribution, at the height of the center of effort (CoE); the flat sail model, with a sheet angle of 90°.

Constrained Streamlines at CoE in the Normal Domain with Grid 5-1

Fig. A.46 - A.50 shows top view images of constrained streamlines, at CoE and the flat sail model with a sheet angle of 90° for grid 5-1 in the normal computational domain.

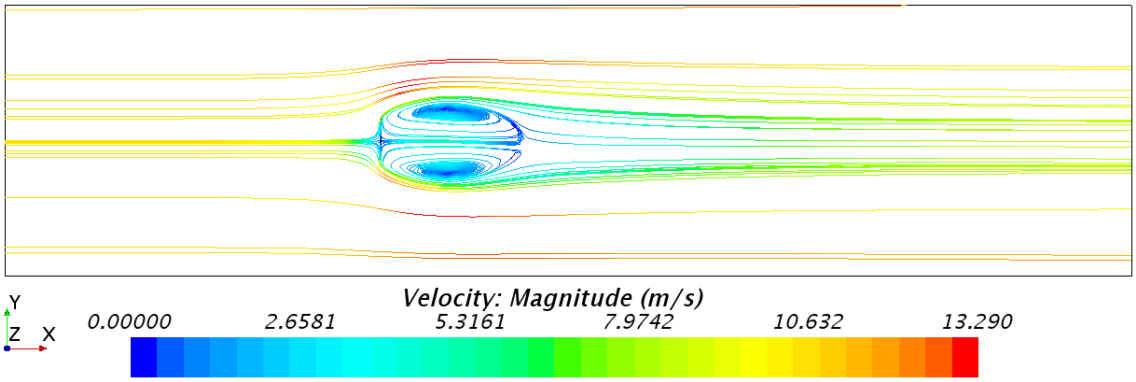

Figure A.46: Top view of the normal computational domain, with grid 5, showing constrained streamlines, at the height of the center of effort (CoE); the flat sail model, with a sheet angle of 90°.

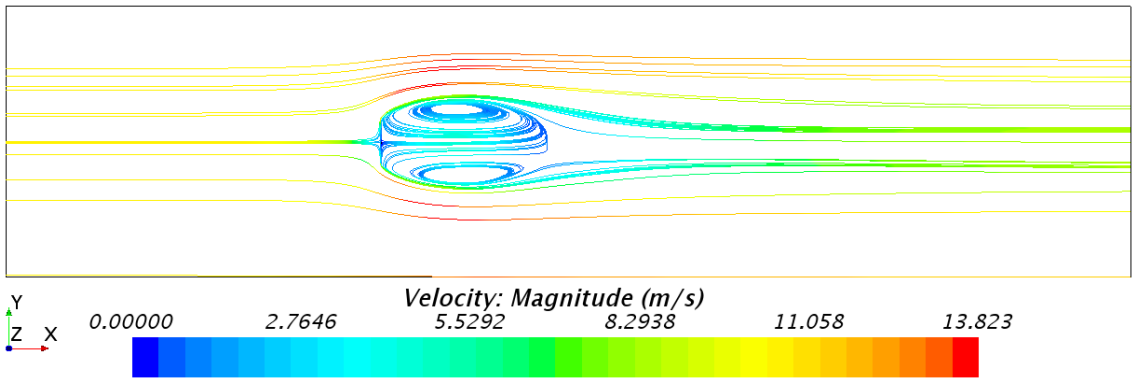

Figure A.47: Top view of the normal computational domain, with grid 4, showing constrained streamlines, at the height of the center of effort (CoE); the flat sail model, with a sheet angle of 90°.

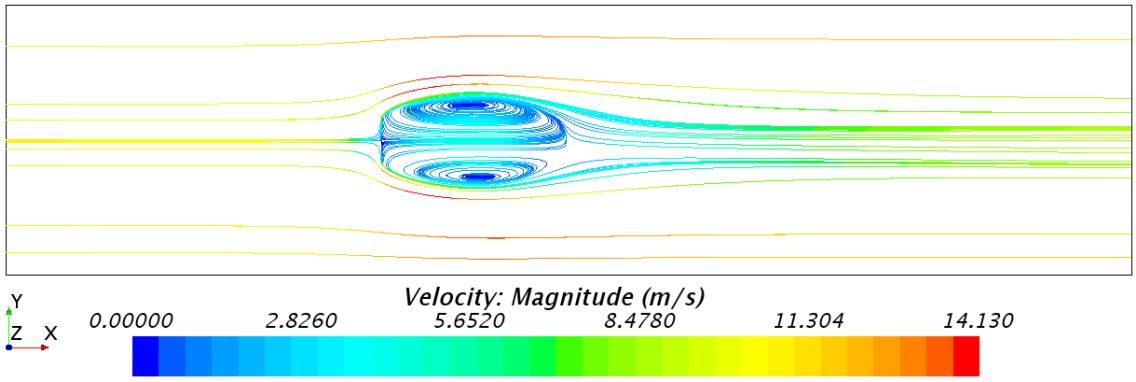

Figure A.48: Top view of the normal computational domain, with grid 3, showing constrained streamlines, at the height of the center of effort (CoE); the flat sail model, with a sheet angle of 90°.

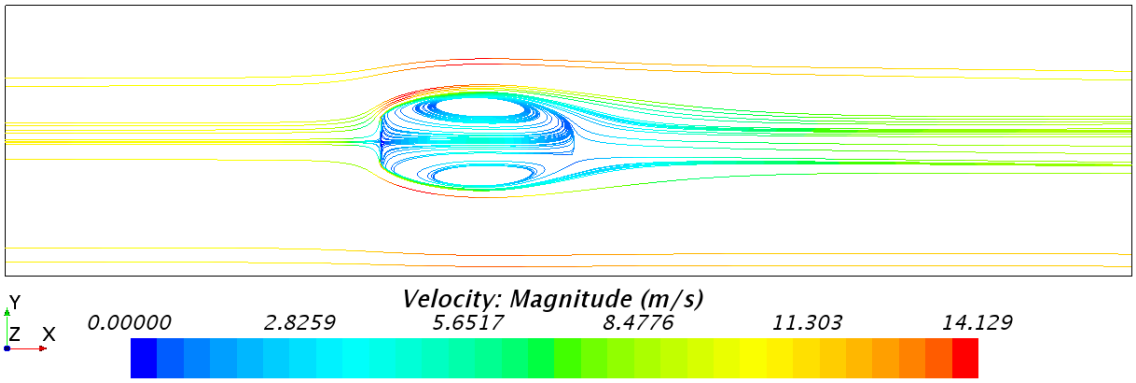

Figure A.49: Top view of the normal computational domain, with grid 2, showing constrained streamlines, at the height of the center of effort (CoE); the flat sail model, with a sheet angle of 90°.

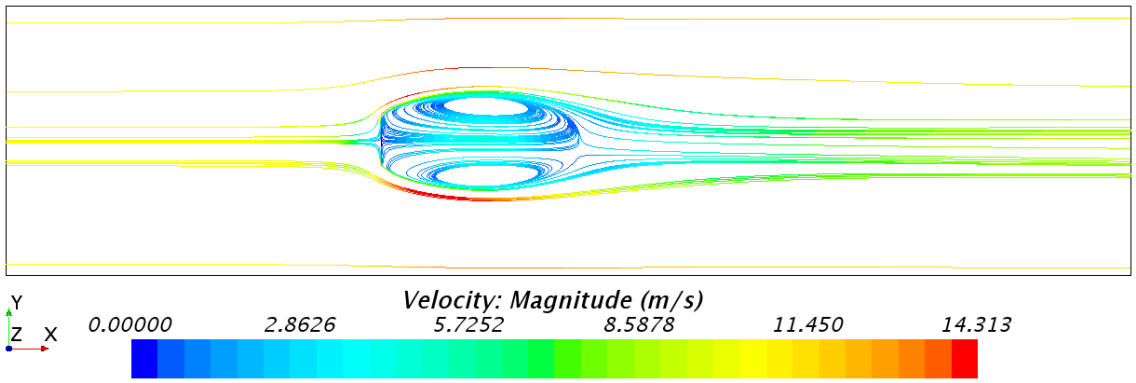

Figure A.50: Top view of the normal computational domain, with grid 1, showing constrained streamlines, at the height of the center of effort (CoE); the flat sail model, with a sheet angle of 90°.

Pressure Distribution at CoE in the Large Domain with Grid 5-1

Fig. A.51 - A.55 shows top view images of the pressure distribution, at CoE and the flat sail model with a sheet angle of 90° for grid 5-1 in the large computational domain.

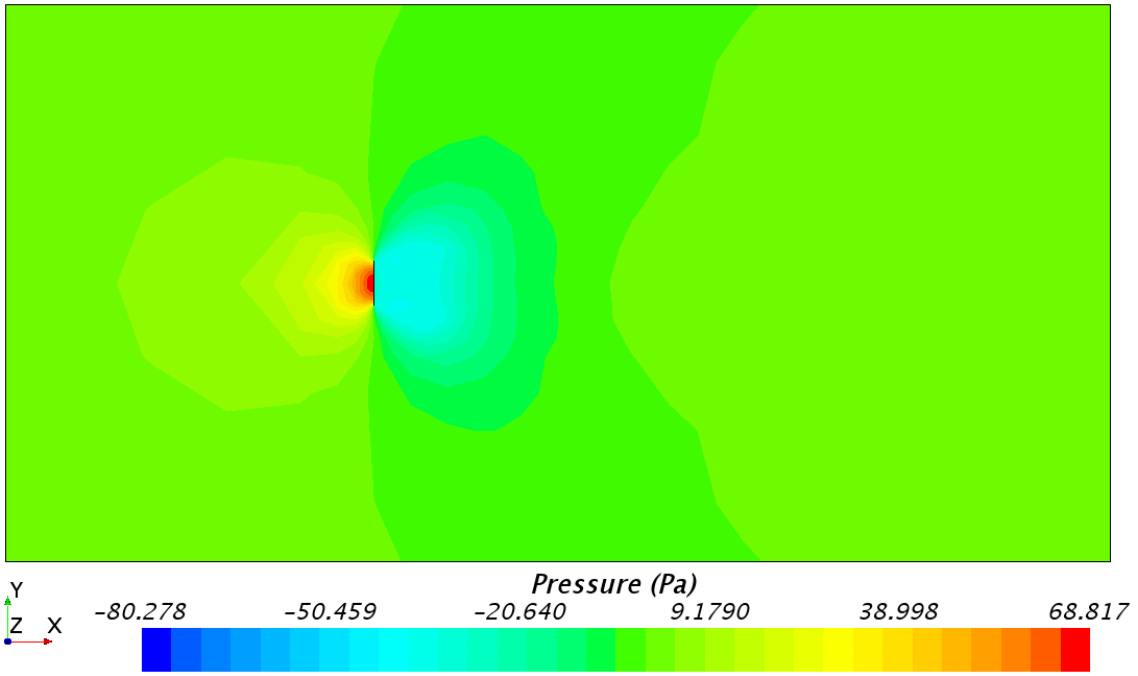

Figure A.51: Top view of the large computational domain, with grid 5, showing the pressure distribution, at the height of the center of effort (CoE); the flat sail model, with a sheet angle of 90°.

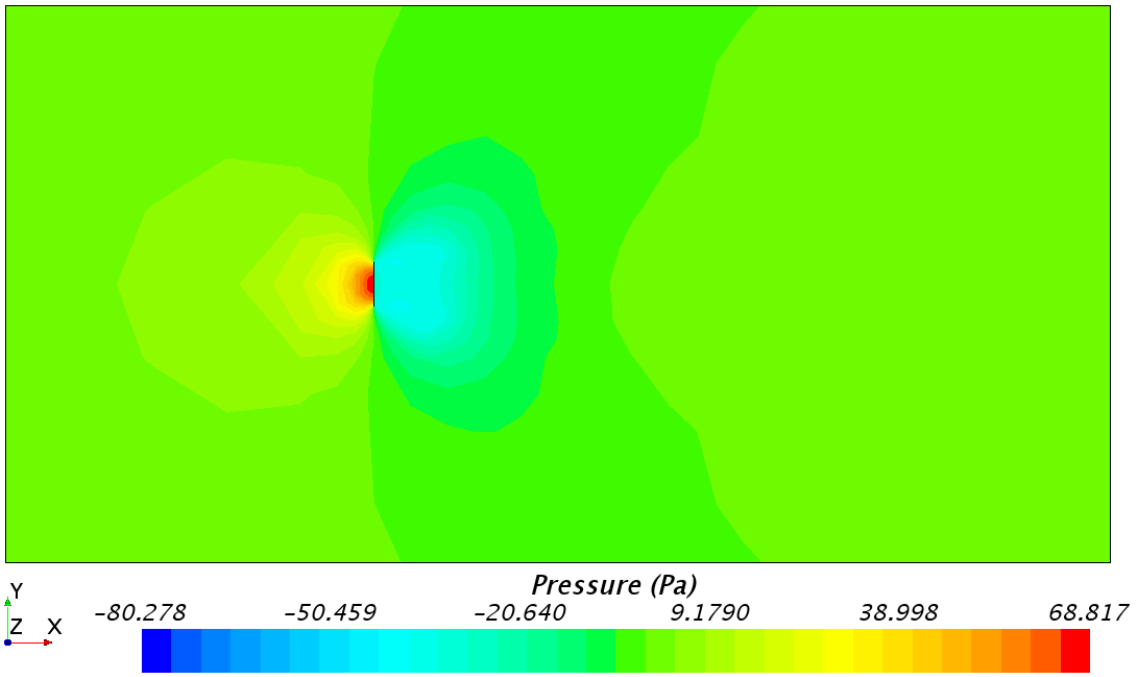

Figure A.52: Top view of the large computational domain, with grid 4, showing the pressure distribution, at the height of the center of effort (CoE); the flat sail model, with a sheet angle of 90°.

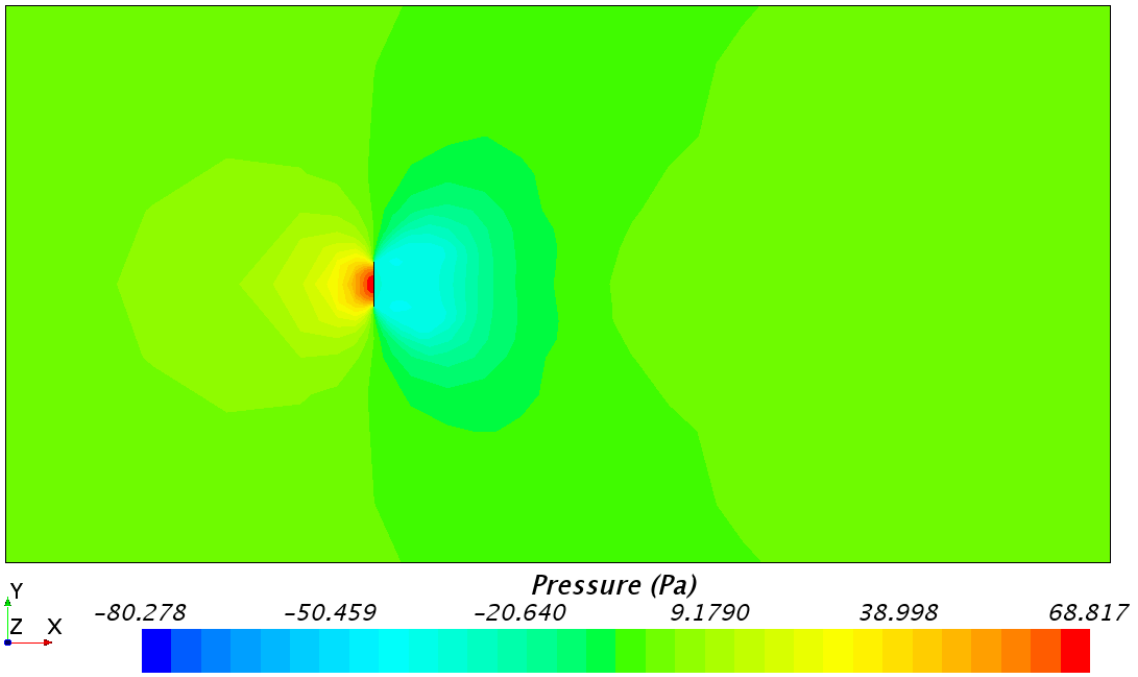

Figure A.53: Top view of the large computational domain, with grid 3, showing the pressure distribution, at the height of the center of effort (CoE); the flat sail model, with a sheet angle of 90°.

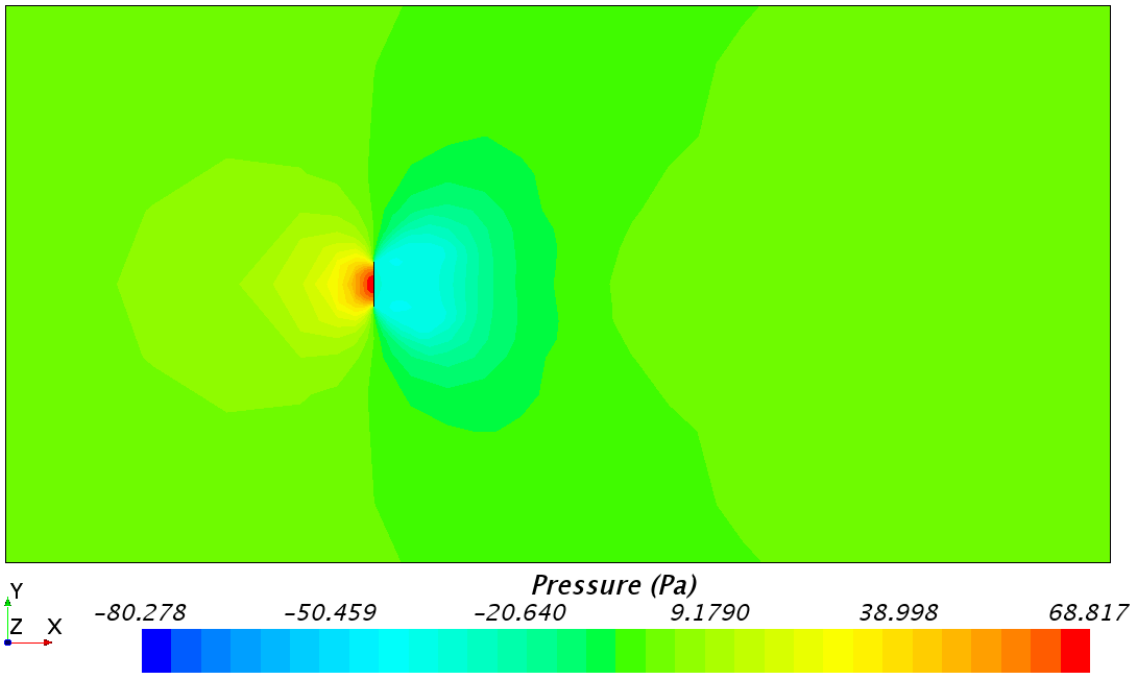

Figure A.54: Top view of the large computational domain, with grid 2, showing the pressure distribution, at the height of the center of effort (CoE); the flat sail model, with a sheet angle of 90°.

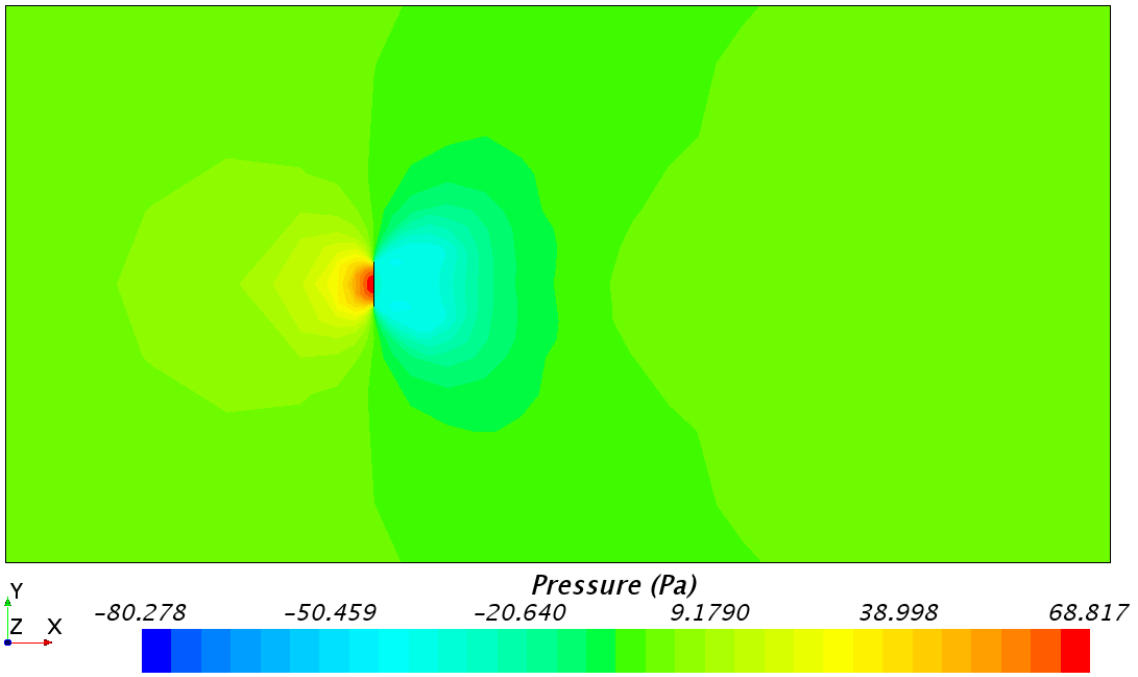

Figure A.55: Top view of the large computational domain, with grid 1, showing the pressure distribution, at the height of the center of effort (CoE); the flat sail model, with a sheet angle of 90°.

Velocity Distribution at CoE in the Large Domain with Grid 5-1

Fig. A.56 - A.60 shows top view images of the velocity distribution, at CoE and the flat sail model with a sheet angle of 90° for grid 5-1 in the large computational domain.

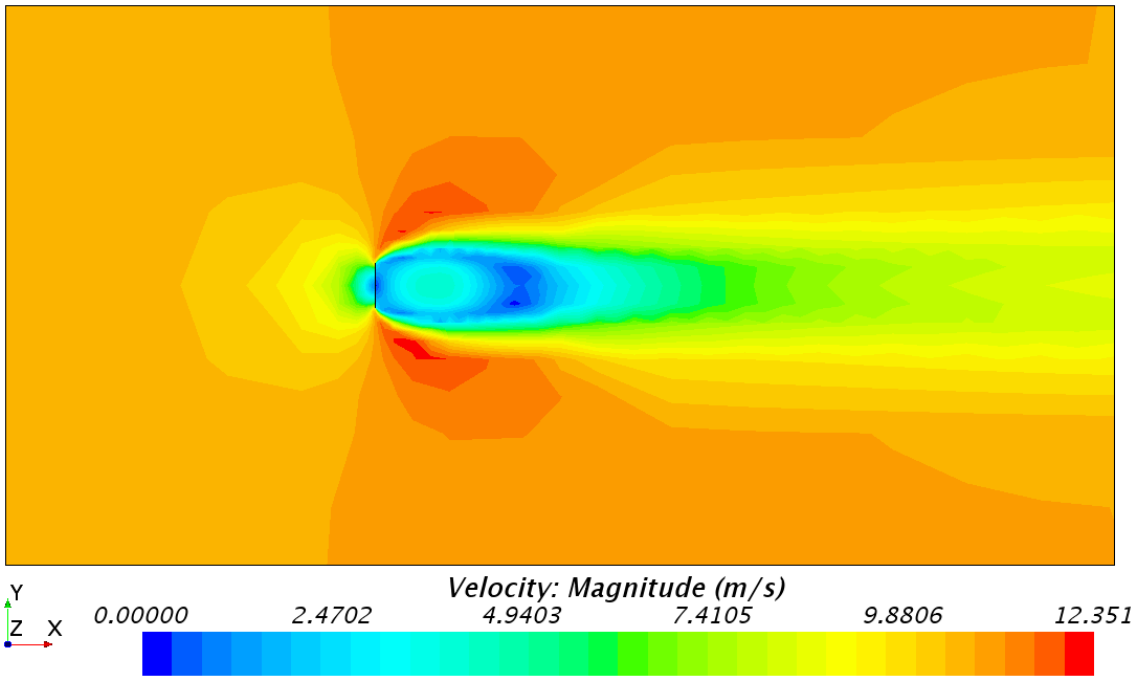

Figure A.56: Top view of the large computational domain, with grid 5, showing the velocity distribution, at the height of the center of effort (CoE); the flat sail model, with a sheet angle of 90°.

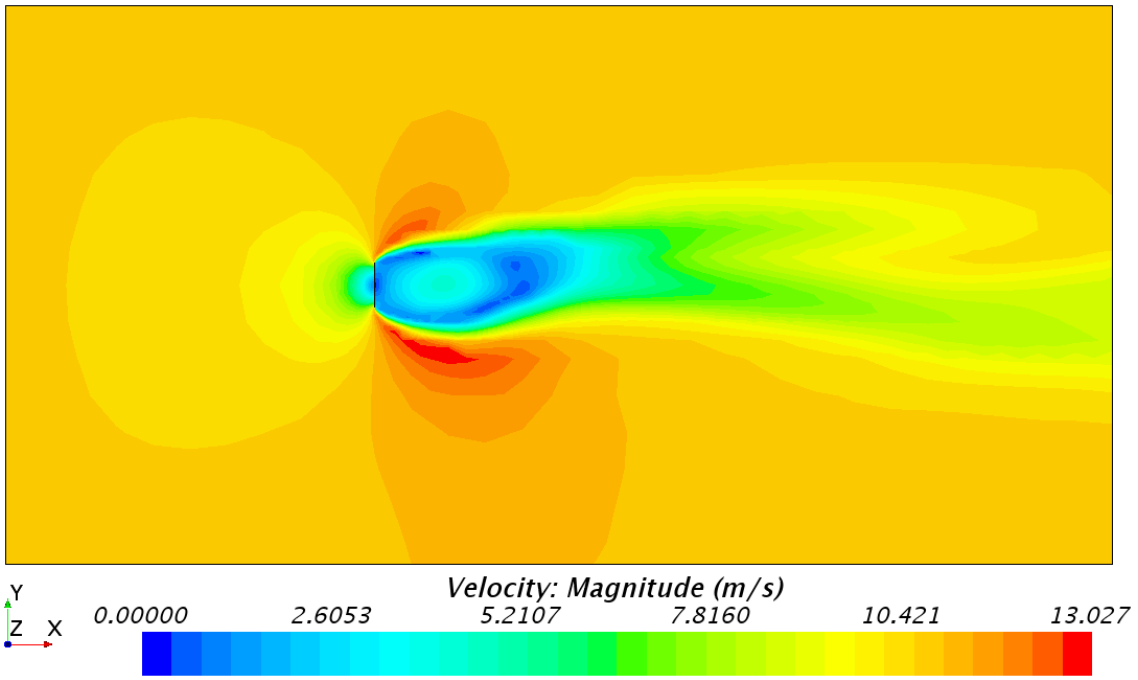

Figure A.57: Top view of the large computational domain, with grid 4, showing the velocity distribution, at the height of the center of effort (CoE); the flat sail model, with a sheet angle of 90°.

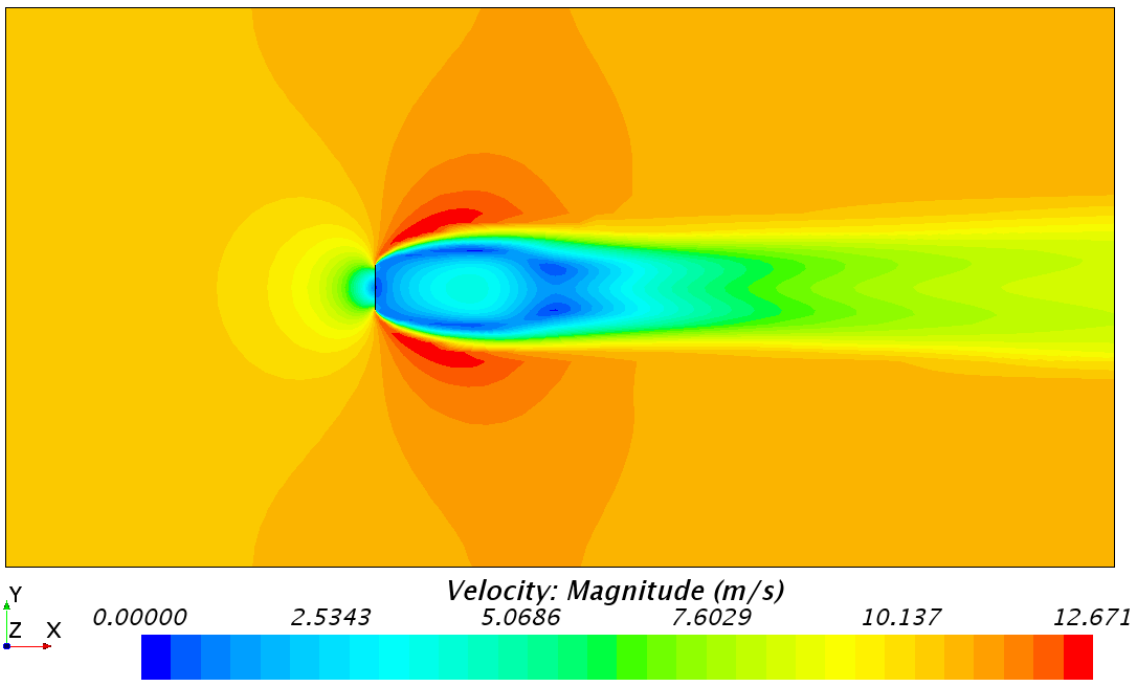

Figure A.58: Top view of the large computational domain, with grid 3, showing the velocity distribution, at the height of the center of effort (CoE); the flat sail model, with a sheet angle of 90°.

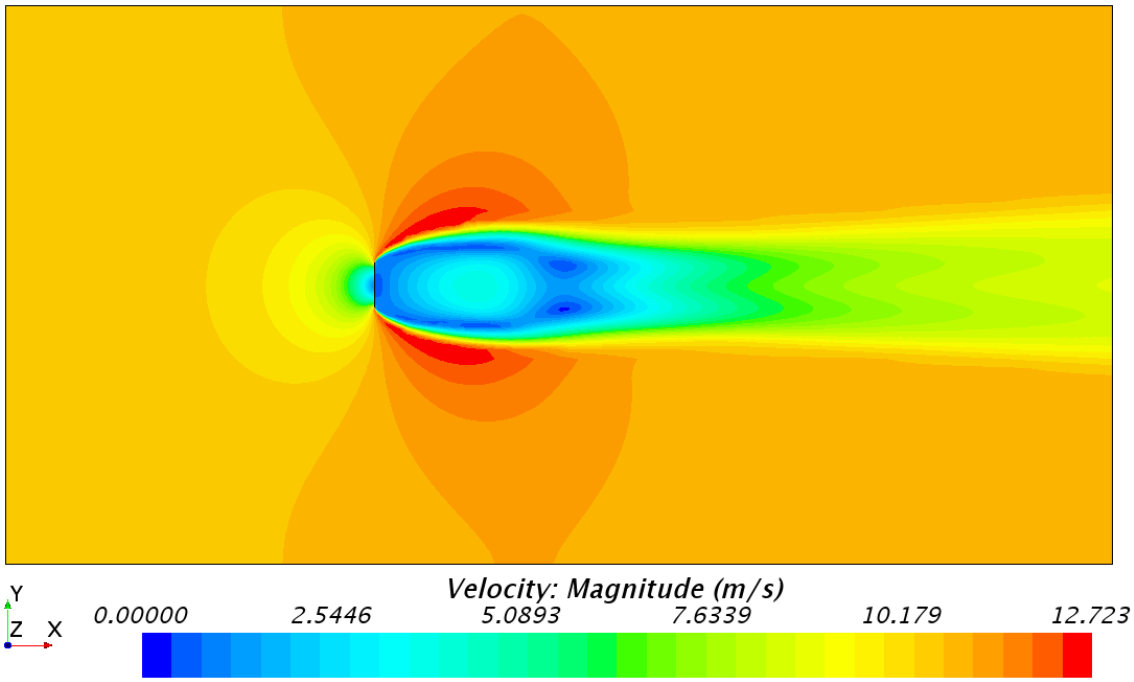

Figure A.59: Top view of the large computational domain, with grid 2, showing the velocity distribution, at the height of the center of effort (CoE); the flat sail model, with a sheet angle of 90°.

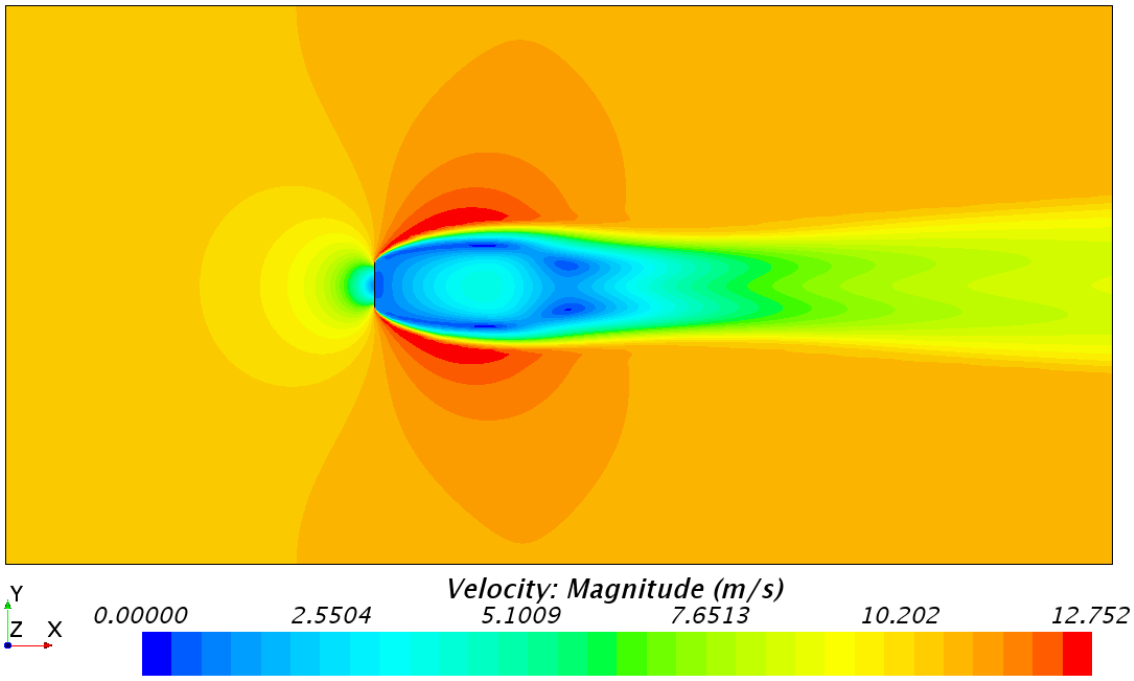

Figure A.60: Top view of the large computational domain, with grid 1, showing the velocity distribution, at the height of the center of effort (CoE); the flat sail model, with a sheet angle of 90°.

Constrained Streamlines at CoE in the Large Domain with Grid 5-1

Fig. A.61 - A.65 shows top view images of constrained streamlines, at CoE and the flat sail model with a sheet angle of 90° for grid 5-1 in the large computational domain.

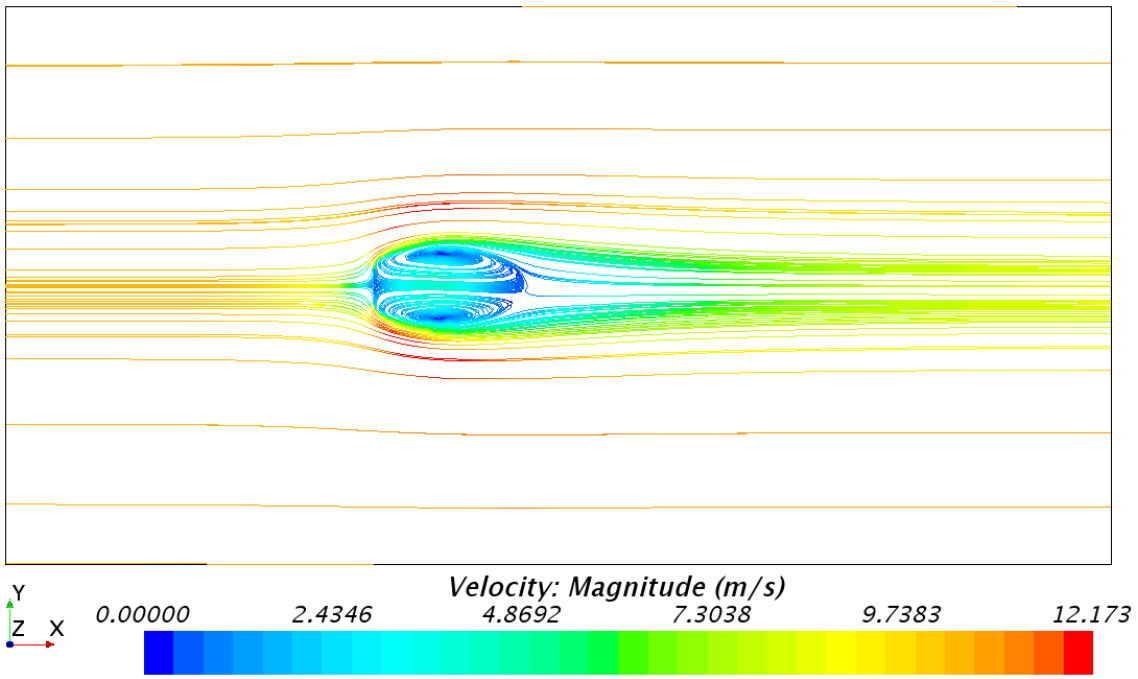

Figure A.61: Top view of the large computational domain, with grid 5, showing constrained streamlines, at the height of the center of effort (CoE); the flat sail model, with a sheet angle of 90°.

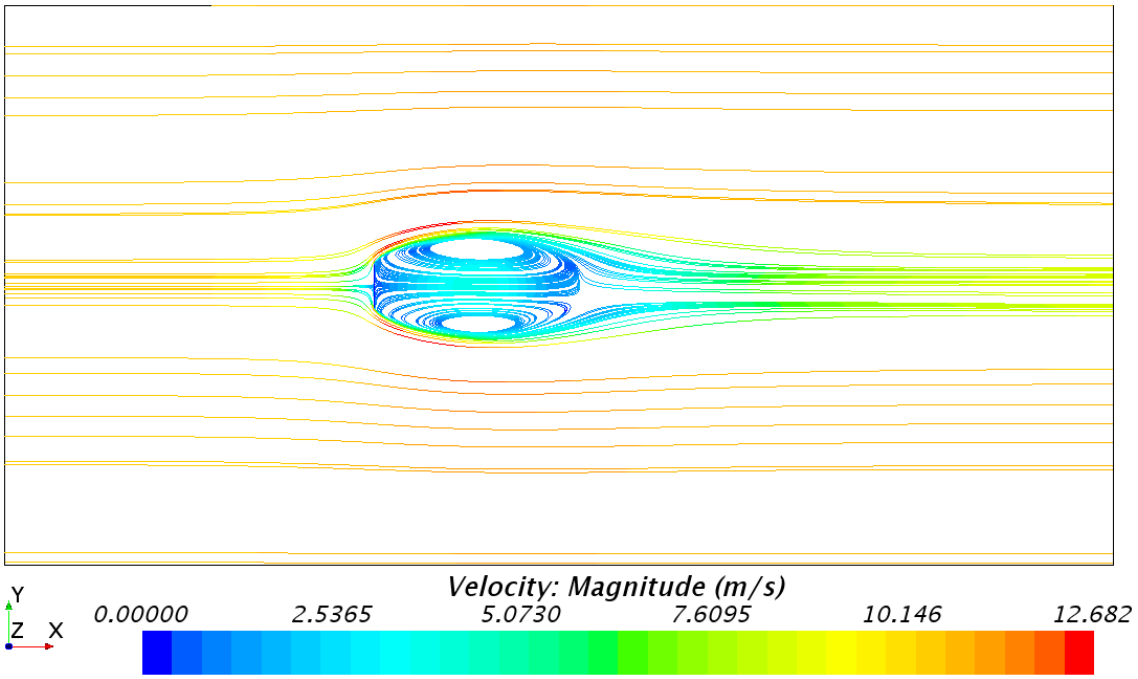

Figure A.62: Top view of the large computational domain, with grid 4, showing constrained streamlines, at the height of the center of effort (CoE); the flat sail model, with a sheet angle of 90°.

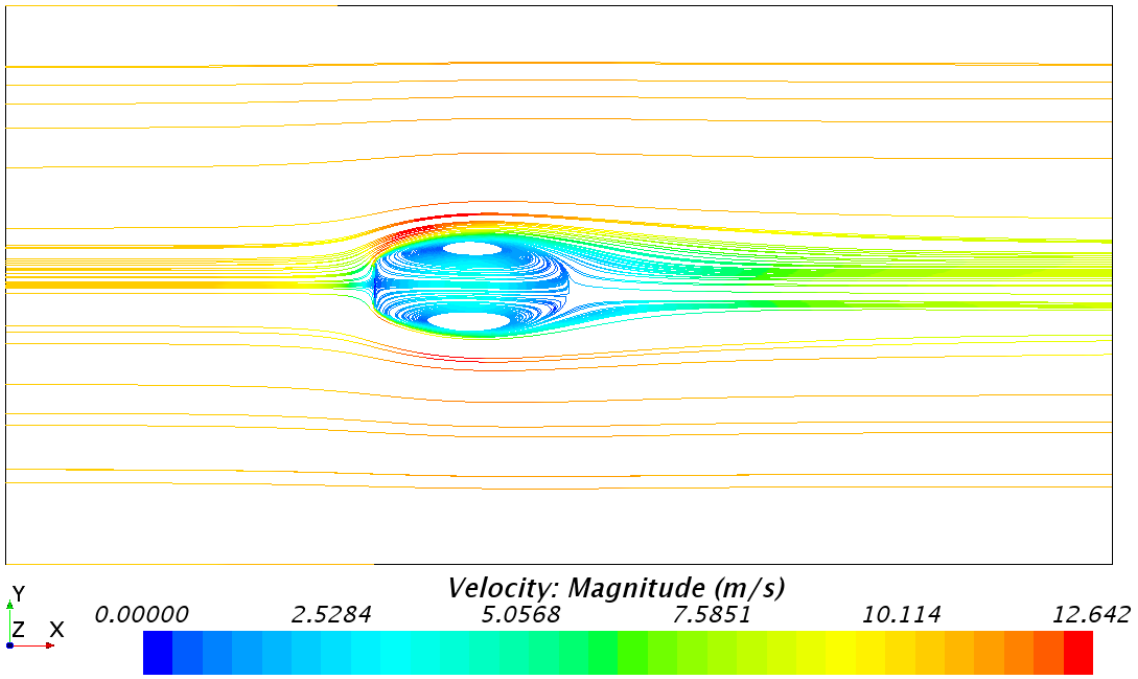

Figure A.63: Top view of the large computational domain, with grid 3, showing constrained streamlines, at the height of the center of effort (CoE); the flat sail model, with a sheet angle of 90°.

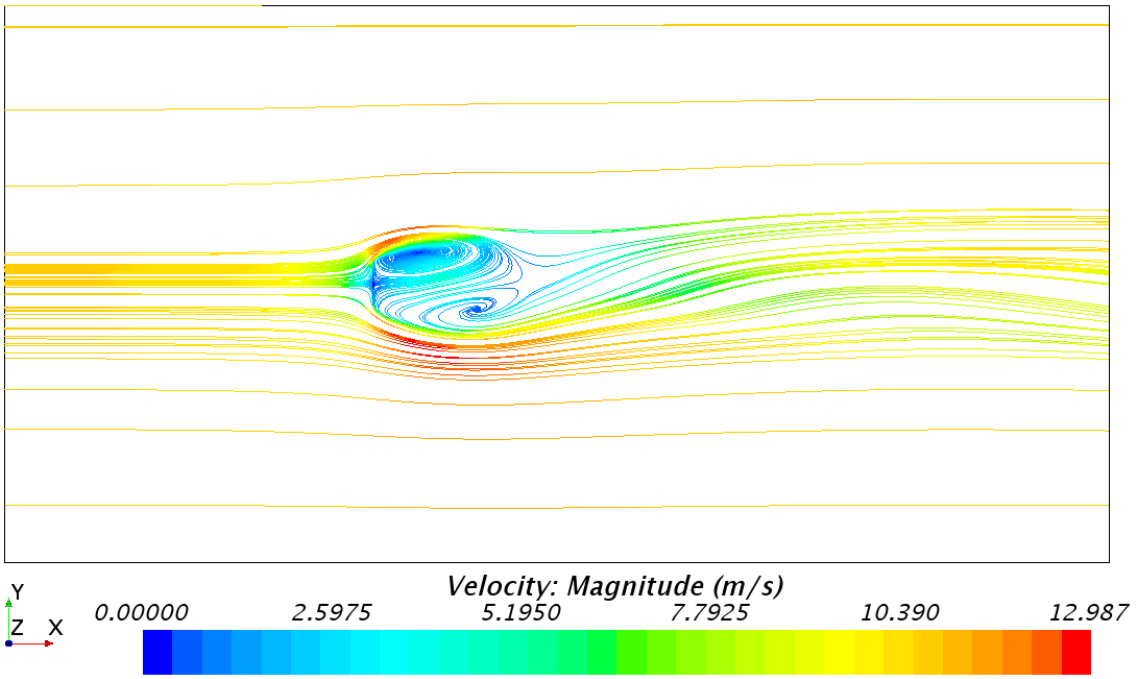

Figure A.64: Top view of the large computational domain, with grid 2, showing constrained streamlines, at the height of the center of effort (CoE); the flat sail model, with a sheet angle of 90°.

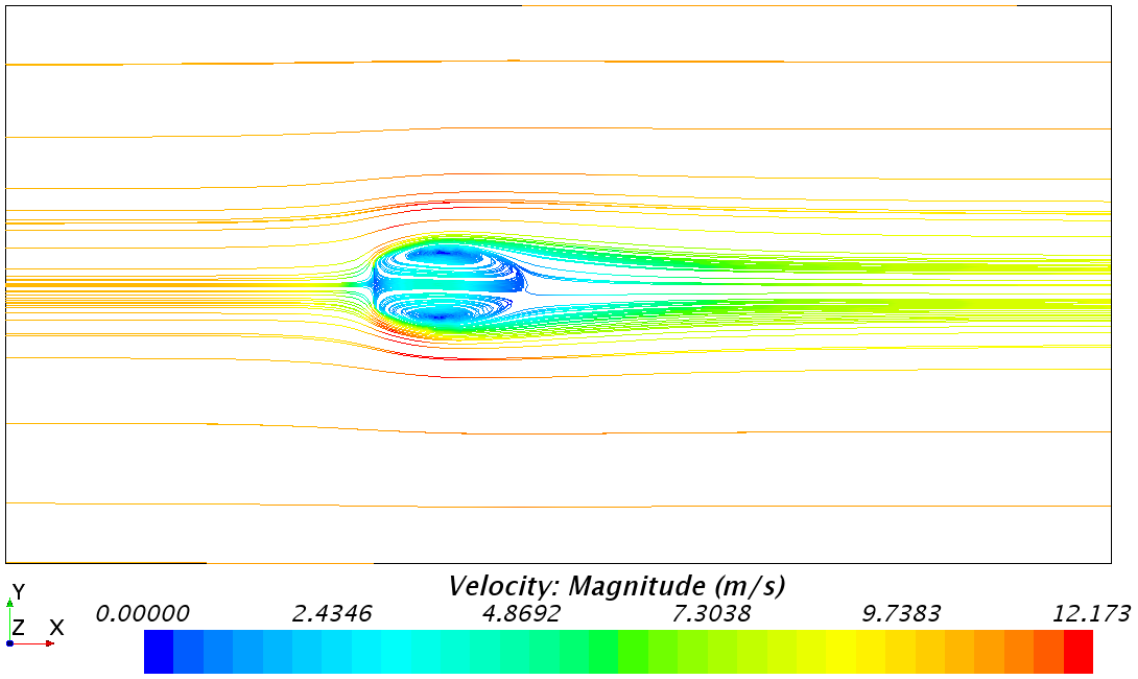

Figure A.65: Top view of the large computational domain, with grid 1, showing constrained streamlines, at the height of the center of effort (CoE); the flat sail model, with a sheet angle of 90°.

Side View Images

The corresponding side view images of the pressure distribution, velocity distribution, and constrained streamlines from the RANS simulations in the grid dependence study, shows the scalar quantities at a centered xz-plane.

Pressure Distribution at a Centered XZ-Plane in the Normal Domain for Grid 5-1

Fig. A.66 - A.70 shows the corresponding side view images of the pressure distribution, at a Centered xz-Plane for grid 5-1 in the normal computational domain and the flat sail model with a sheet angle of 90°.

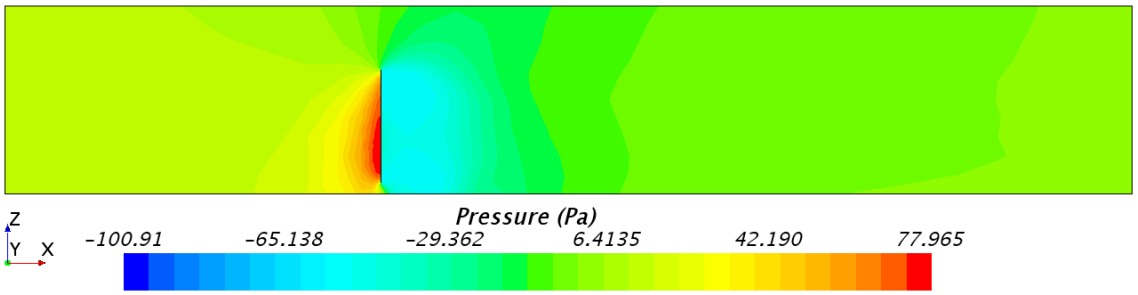

Figure A.66: Side view of the normal computational domain, with grid 5, showing the pressure distribution, at a centered xz-plane; the flat sail model, with a sheet angle of 90°.

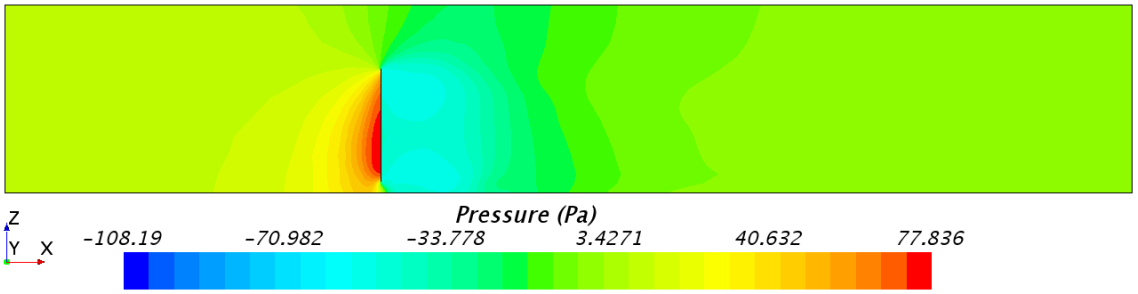

Figure A.67: Side view of the normal computational domain, with grid 4, showing the pressure distribution, at a centered xz-plane; the flat sail model, with a sheet angle of 90°.

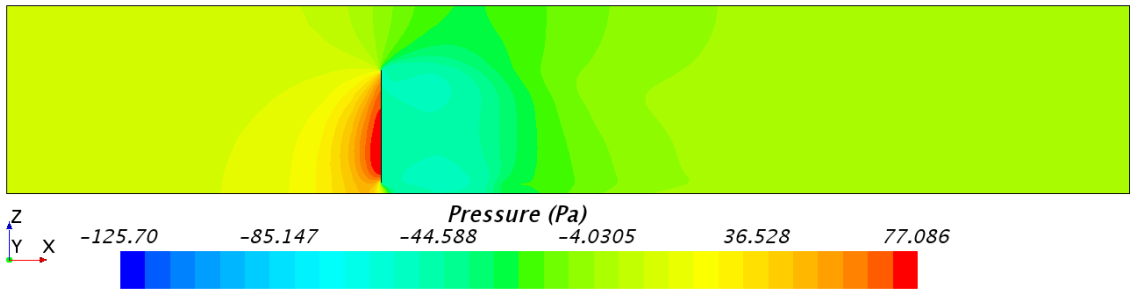

Figure A.68: Side view of the normal computational domain, with grid 3, showing the pressure distribution, at a centered xz-plane; the flat sail model, with a sheet angle of 90°.

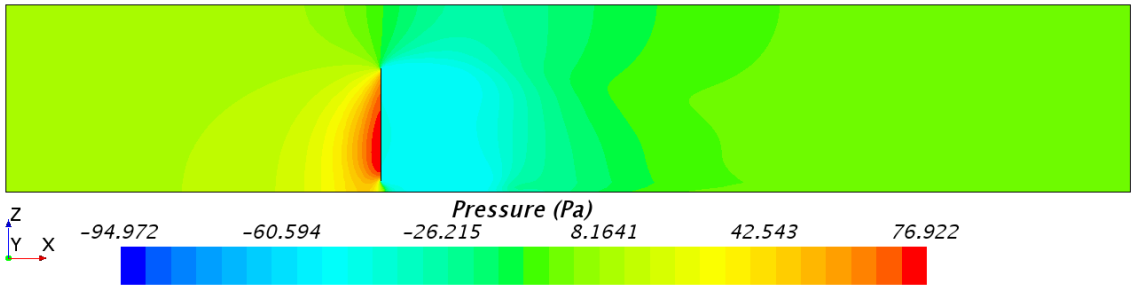

Figure A.69: Side view of the normal computational domain, with grid 2, showing the pressure distribution, at a centered xz-plane; the flat sail model, with a sheet angle of 90°.

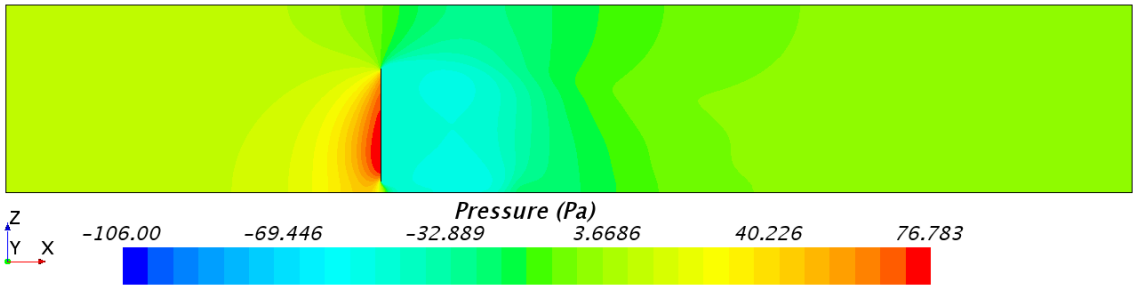

Figure A.70: Side view of the normal computational domain, with grid 1, showing the pressure distribution, at a centered xz-plane; the flat sail model, with a sheet angle of 90°.

Velocity Distribution at a Centered XZ-Plane in the Normal Domain for Grid 5-1

Fig. A.71 - A.75 shows the corresponding side view images of the velocity distribution, at a Centered xz-Plane for grid 5-1 in the normal computational domain and the flat sail model with a sheet angle of 90°.

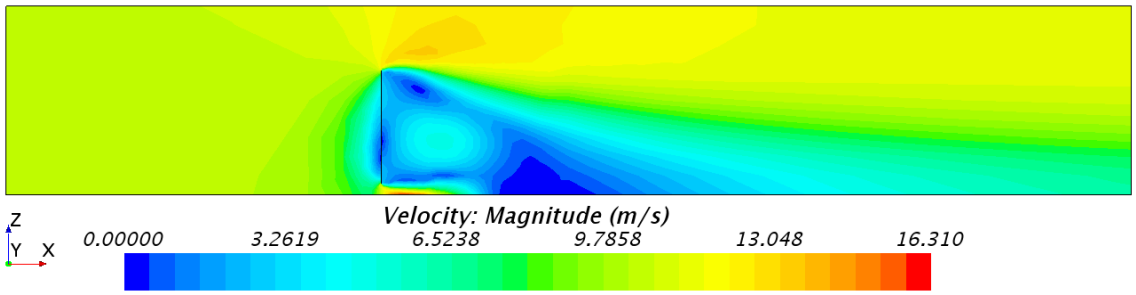

Figure A.71: Side view of the normal computational domain, with grid 5, showing the velocity distribution, at a centered xz-plane; the flat sail model, with a sheet angle of 90°.

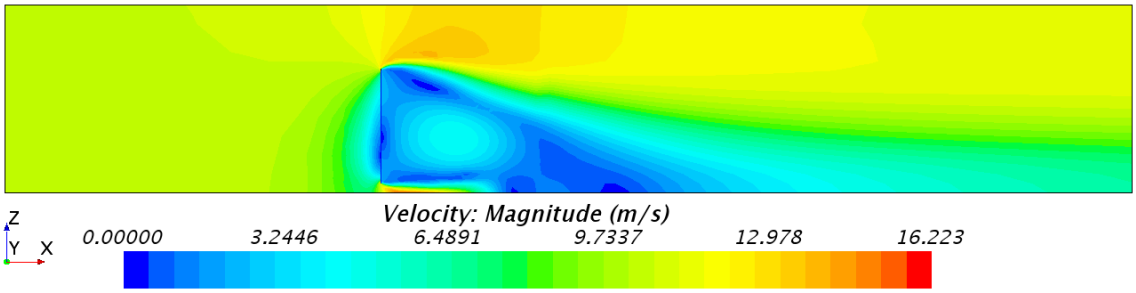

Figure A.72: Side view of the normal computational domain, with grid 4, showing the velocity distribution, at a centered xz-plane; the flat sail model, with a sheet angle of 90°.

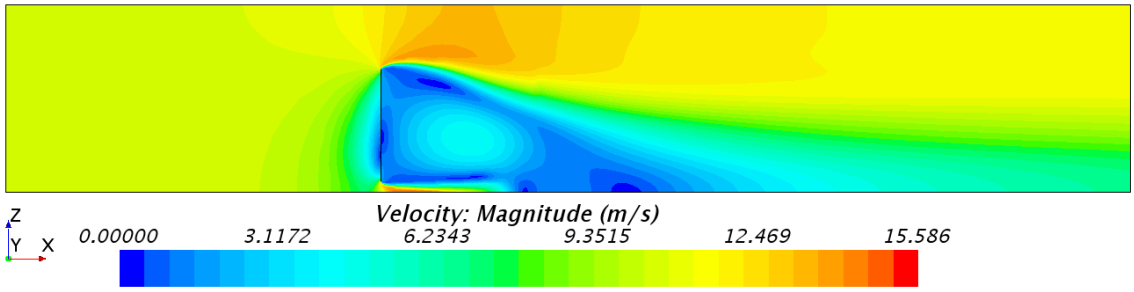

Figure A.73: Side view of the normal computational domain, with grid 3, showing the velocity distribution, at a centered xz-plane; the flat sail model, with a sheet angle of 90°.

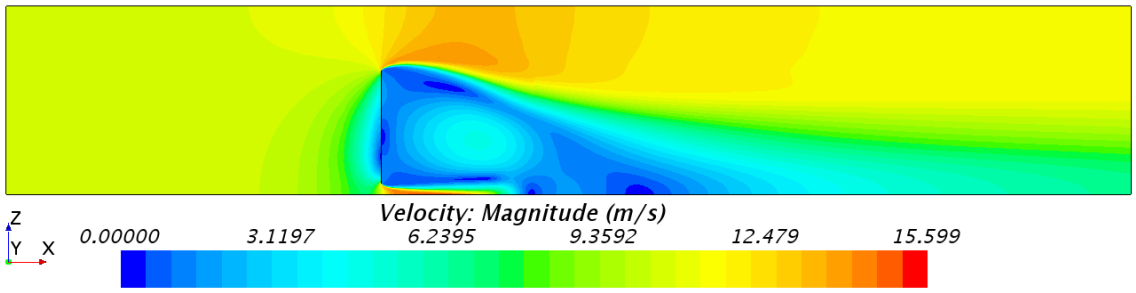

Figure A.74: Side view of the normal computational domain, with grid 2, showing the velocity distribution, at a centered xz-plane; the flat sail model, with a sheet angle of 90°.

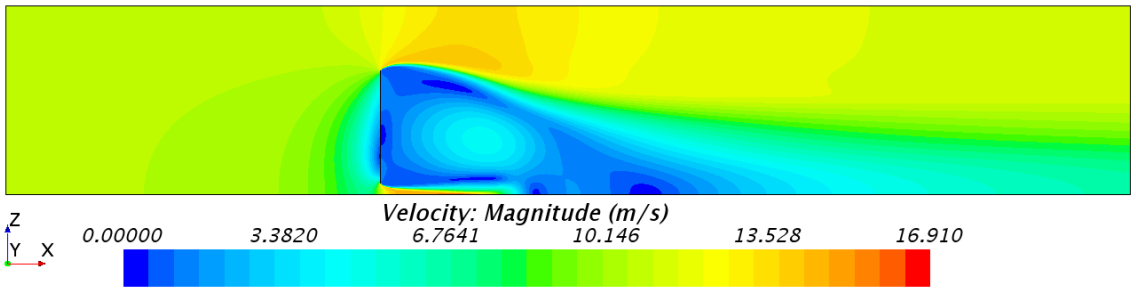

Figure A.75: Side view of the normal computational domain, with grid 1, showing the velocity distribution, at a centered xz-plane; the flat sail model, with a sheet angle of 90°.

Constrained Streamlines at a Centered XZ-Plane in the Normal Domain for Grid 5-1

Fig. A.76 - A.80 shows the corresponding side view images of constrained streamlines, at a Centered xz-Plane for grid 5-1 in the normal computational domain and the flat sail model with a sheet angle of 90°.

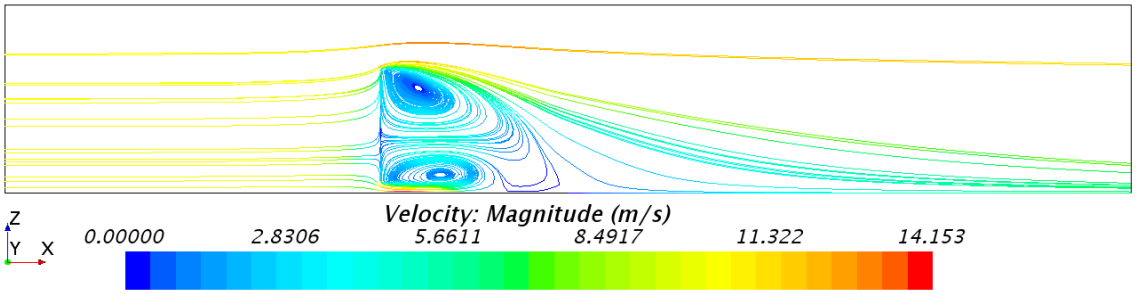

Figure A.76: Side view of the normal computational domain, with grid 5, showing constrained streamlines, at a centered xz-plane; the flat sail model, with a sheet angle of 90°.

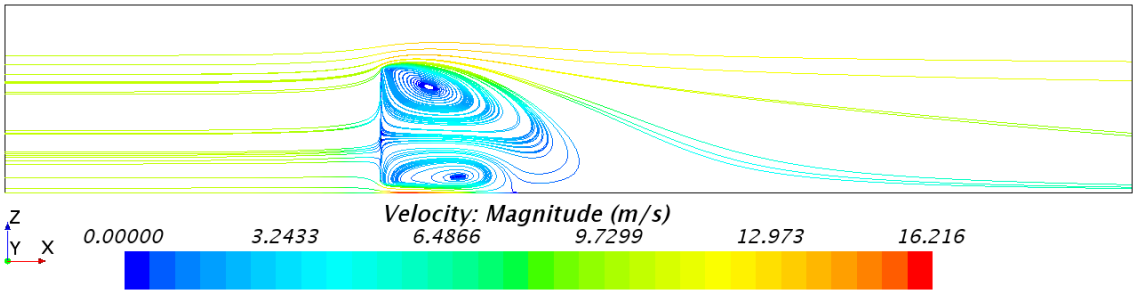

Figure A.77: Side view of the normal computational domain, with grid 4, showing constrained streamlines, at a centered xz-plane; the flat sail model, with a sheet angle of 90°.

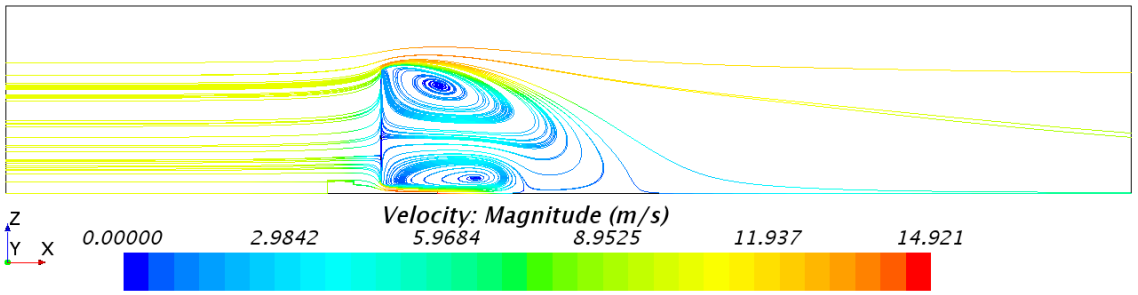

Figure A.78: Side view of the normal computational domain, with grid 3, showing constrained streamlines, at a centered xz-plane; the flat sail model, with a sheet angle of 90°.

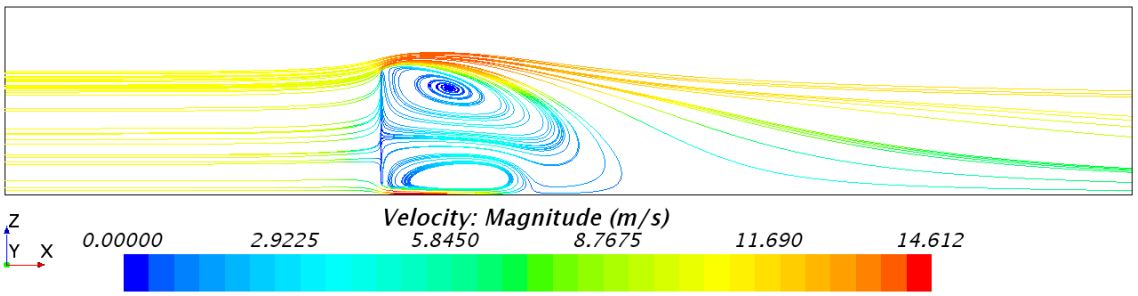

Figure A.79: Side view of the normal computational domain, with grid 2, showing constrained streamlines, at a centered xz-plane; the flat sail model, with a sheet angle of 90°.

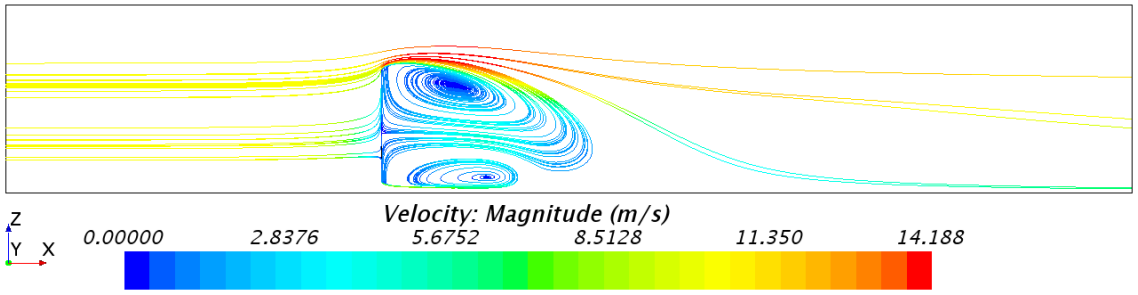

Figure A.80: Side view of the normal computational domain, with grid 1, showing constrained streamlines, at a centered xz-plane; the flat sail model, with a sheet angle of 90°.

Pressure Distribution at a Centered XZ-Plane in the Large Domain for Grid 5-1

Fig. A.81 - A.85 shows the corresponding side view images of the pressure distribution, at a Centered xz-plane for grid 5-1 in the large computational domain and the flat sail model with a sheet angle of 90°.

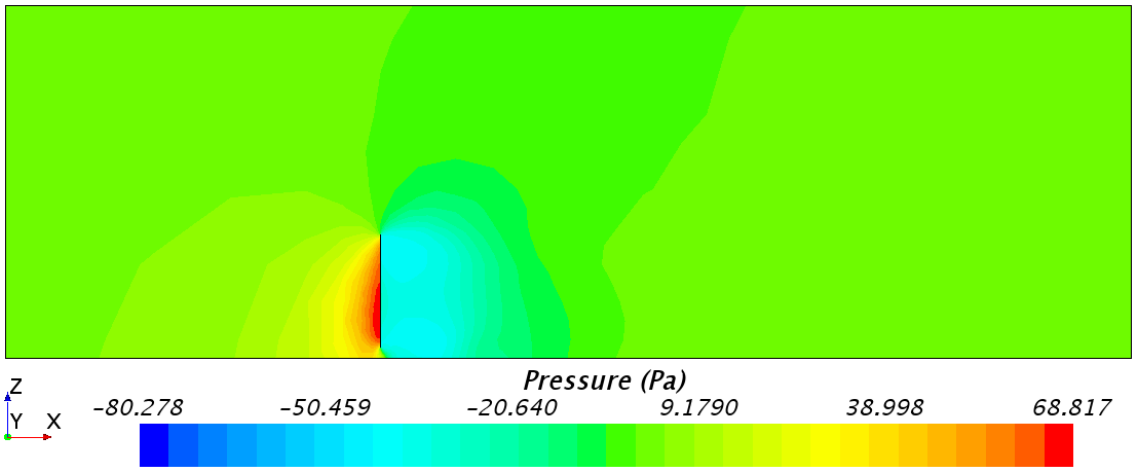

Figure A.81: Side view of the large computational domain, with grid 5, showing the pressure distribution, at a centered xz-plane; the flat sail model, with a sheet angle of 90°.

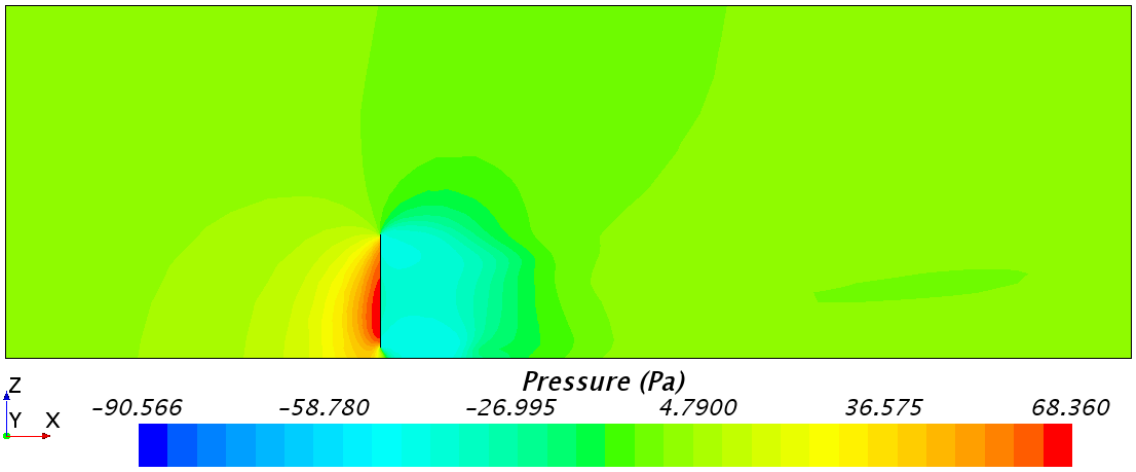

Figure A.82: Side view of the large computational domain, with grid 4, showing the pressure distribution, at a centered xz-plane; the flat sail model, with a sheet angle of 90°.

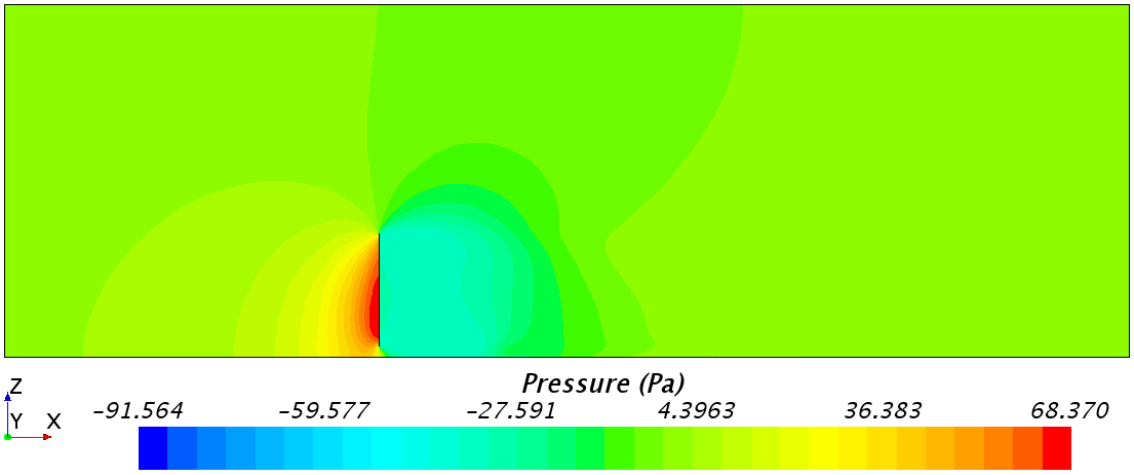

Figure A.83: Side view of the large computational domain, with grid 3, showing the pressure distribution, at a centered xz-plane; the flat sail model, with a sheet angle of 90°.

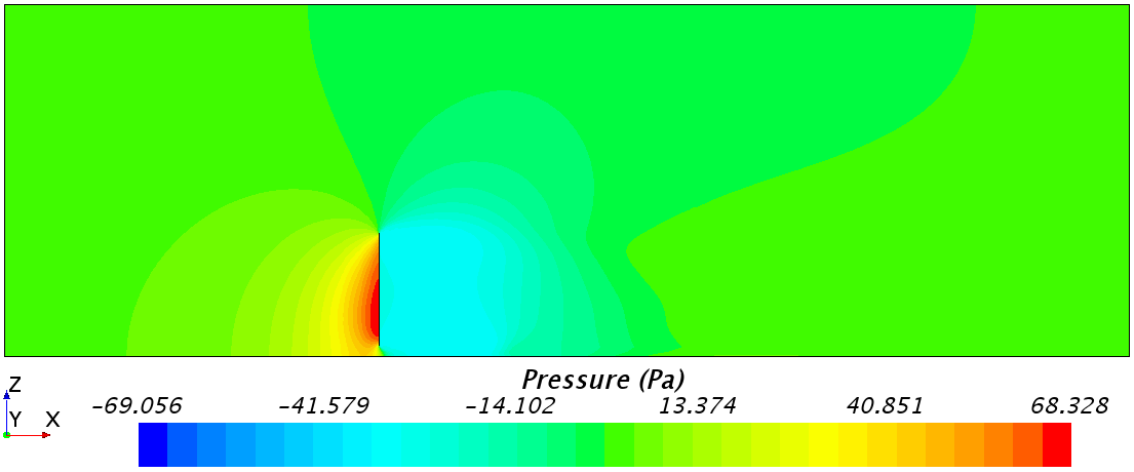

Figure A.84: Side view of the large computational domain, with grid 2, showing the pressure distribution, at a centered xz-plane; the flat sail model, with a sheet angle of 90°.

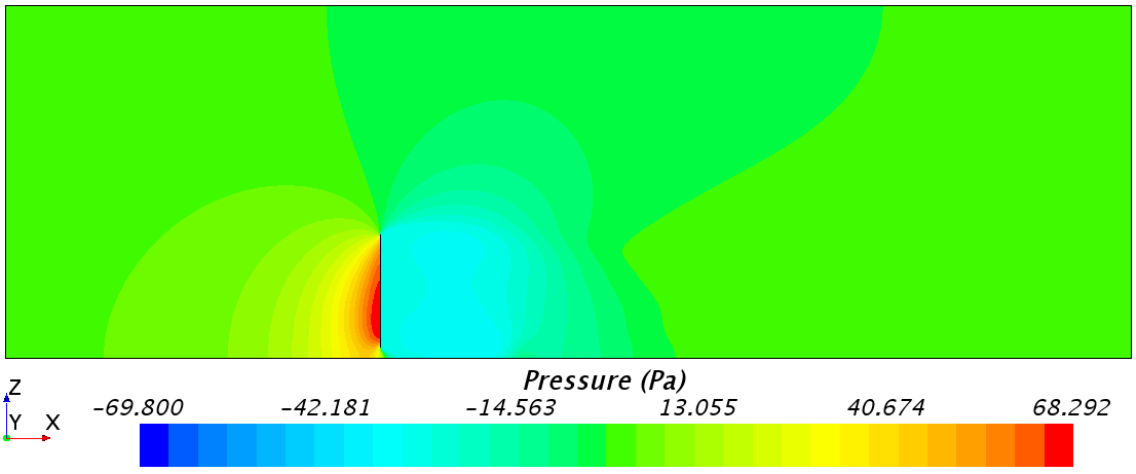

Figure A.85: Side view of the large computational domain, with grid 1, showing the pressure distribution, at a centered xz-plane; the flat sail model, with a sheet angle of 90°.

Velocity Distribution at a Centered XZ-Plane in the Large Domain for Grid 5-1

Fig. A.86 - A.90 shows the corresponding side view images of the velocity distribution, at a Centered xz-plane for grid 5-1 in the large computational domain and the flat sail model with a sheet angle of 90°.

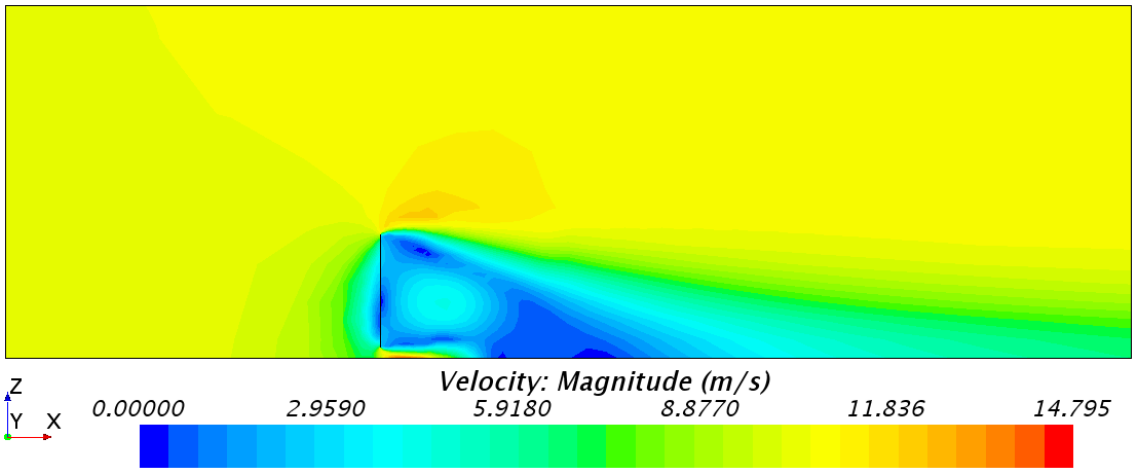

Figure A.86: Side view of the large computational domain, with grid 5, showing the velocity distribution, at a centered xz-plane; the flat sail model, with a sheet angle of 90°.

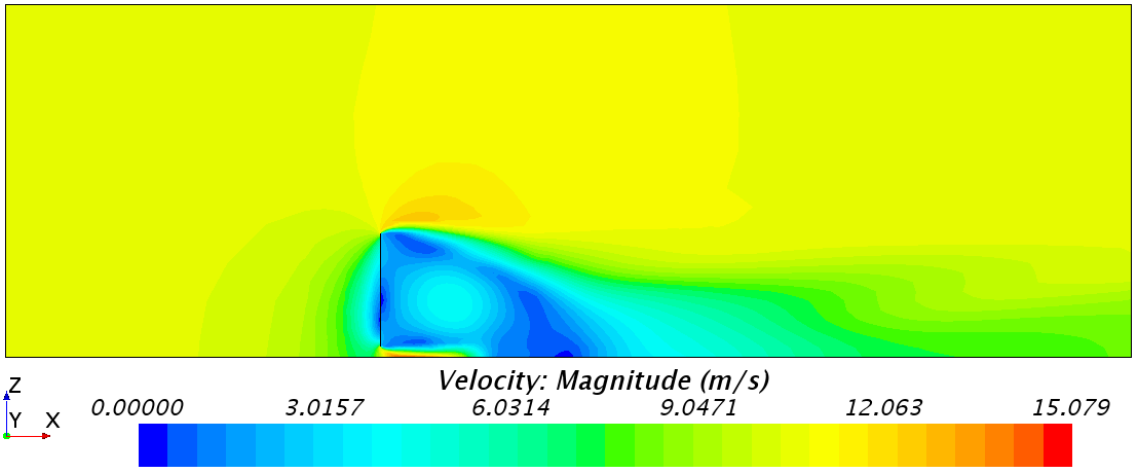

Figure A.87: Side view of the large computational domain, with grid 4, showing the velocity distribution, at a centered xz-plane; the flat sail model, with a sheet angle of 90°.

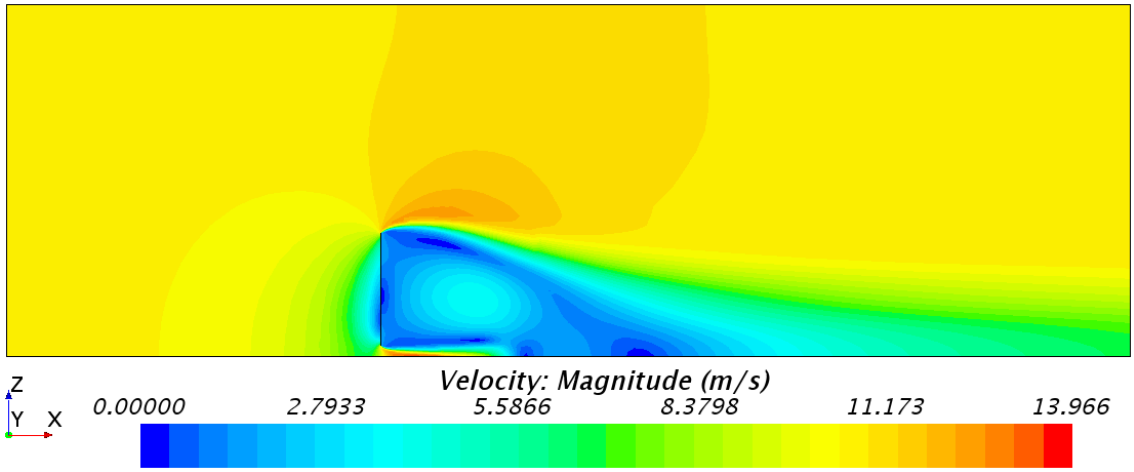

Figure A.88: Side view of the large computational domain, with grid 3, showing the velocity distribution, at a centered xz-plane; the flat sail model, with a sheet angle of 90°.

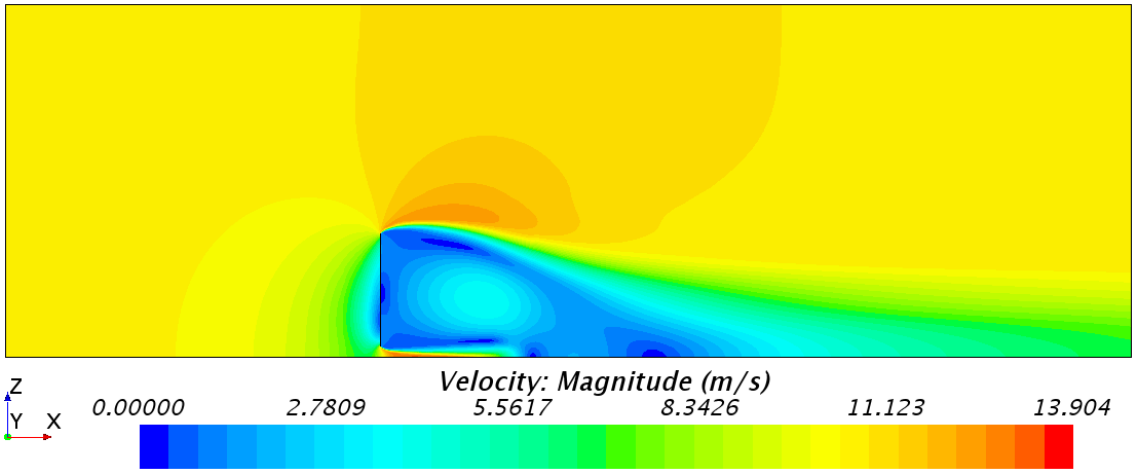

Figure A.89: Side view of the large computational domain, with grid 2, showing the velocity distribution, at a centered xz-plane; the flat sail model, with a sheet angle of 90°.

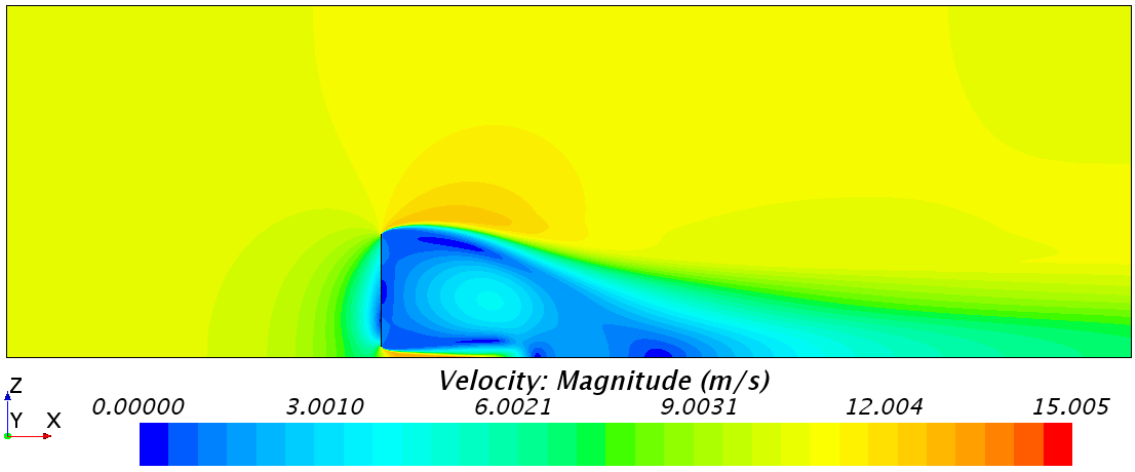

Figure A.90: Side view of the large computational domain, with grid 1, showing the velocity distribution, at a centered xz-plane; the flat sail model, with a sheet angle of 90°.

Constrained Streamlines at a Centered XZ-Plane in the Large Domain for Grid 5-1

Fig. A.91 - A.95 shows the corresponding side view images of constrained streamlines, at a Centered xz-plane for grid 5-1 in the large computational domain and the flat sail model with a sheet angle of 90°.

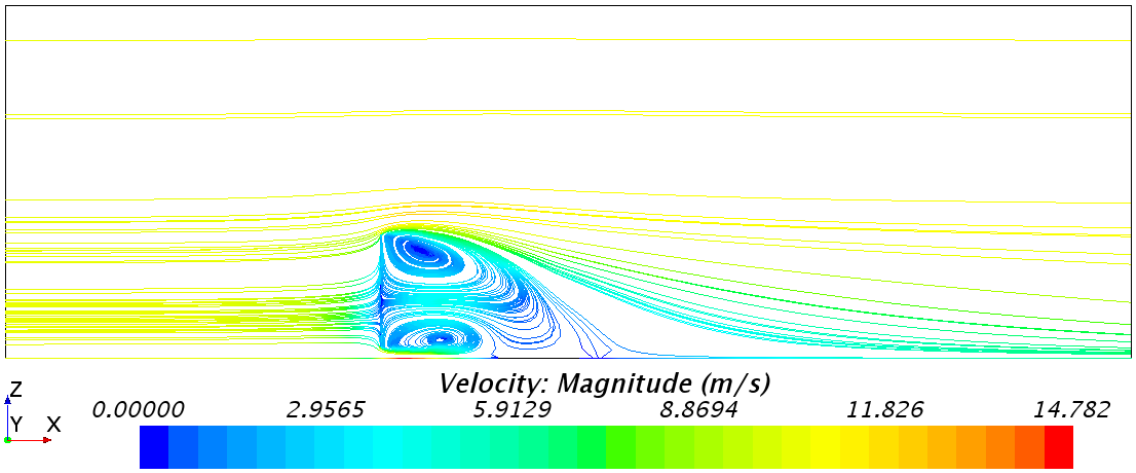

Figure A.91: Side view of the large computational domain, with grid 5, showing constrained streamlines, at a centered xz-plane; the flat sail model, with a sheet angle of 90°.

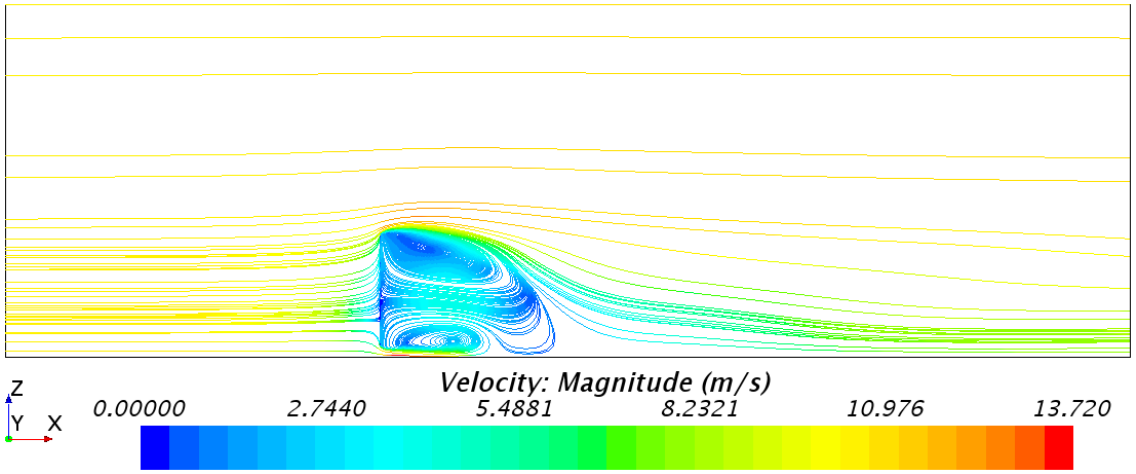

Figure A.92: Side view of the large computational domain, with grid 4, showing constrained streamlines, at a centered xz-plane; the flat sail model, with a sheet angle of 90°.

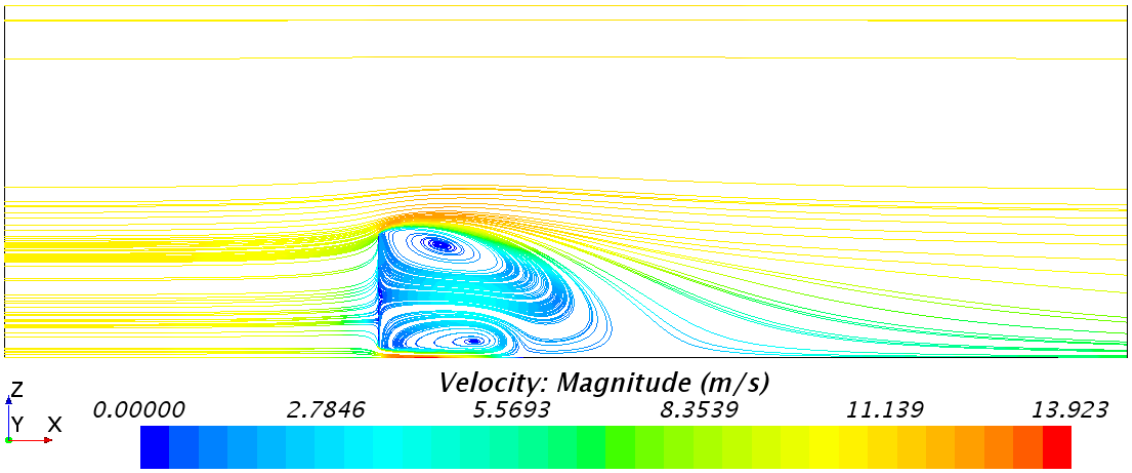

Figure A.93: Side view of the large computational domain, with grid 3, showing constrained streamlines, at a centered xz-plane; the flat sail model, with a sheet angle of 90°.

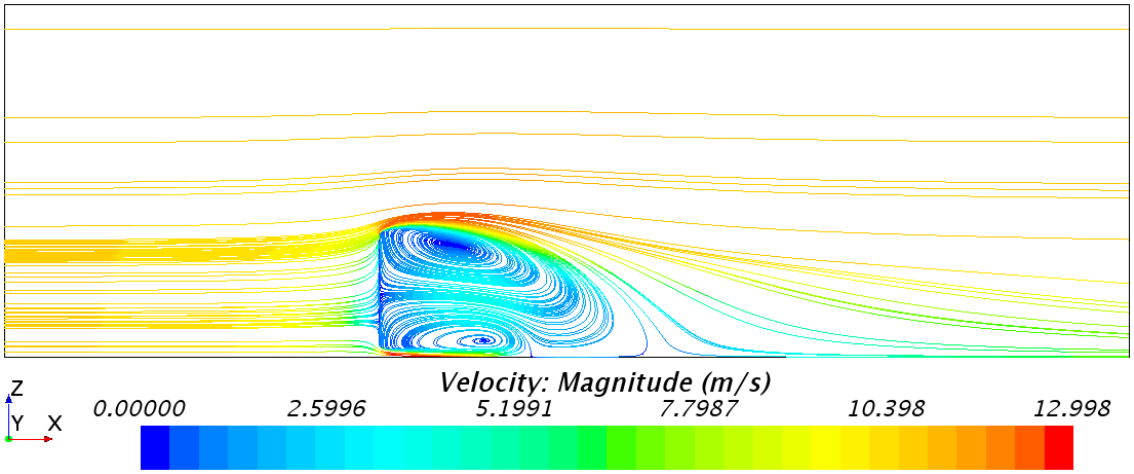

Figure A.94: Side view of the large computational domain, with grid 2, showing constrained streamlines, at a centered xz-plane; the flat sail model, with a sheet angle of 90°.

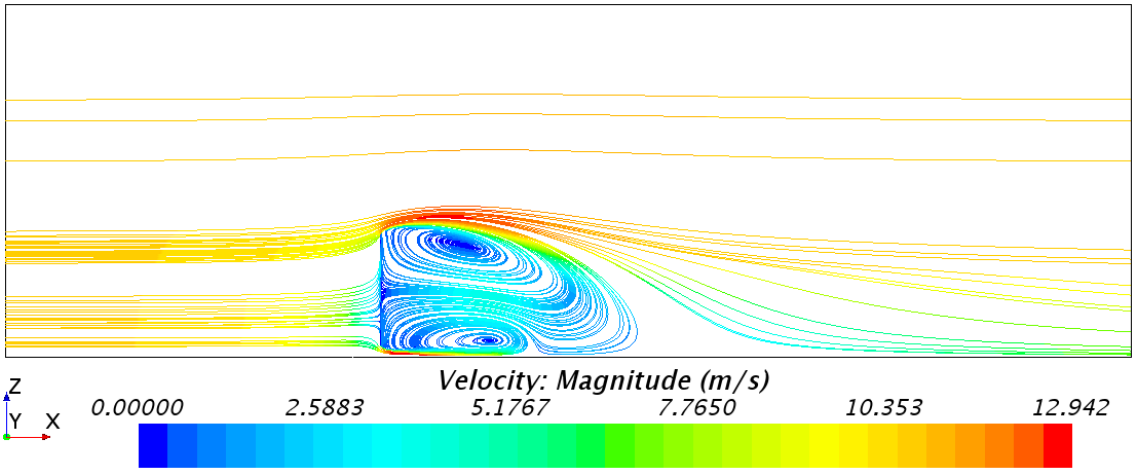

Figure A.95: Side view of the large computational domain, with grid 1, showing constrained streamlines, at a centered xz-plane; the flat sail model, with a sheet angle of 90°.

Residuals

Fig. A.96 - A.105 shows the residuals, from the RANS simulations that were performed in the grid dependence study.

Normal Domain with Grid 5

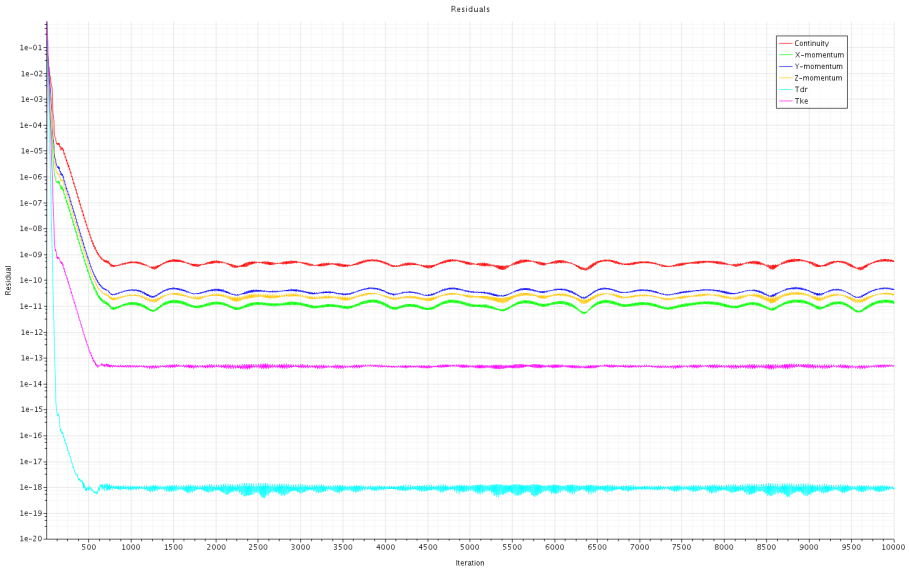

Figure A.96: Residual vs iteration, from the RANS simulations performed with the flat sail model, with a sheet angle of 90°, in the normal computational domain & grid 5, showing the graphs of the Continuity (red), X-momentum (green), Y-momentum (blue), Z-momentum (yellow), Turbulent dissipation rate (cyan) and the Turbulent kinetic energy (purple).

Normal Domain with Grid 4

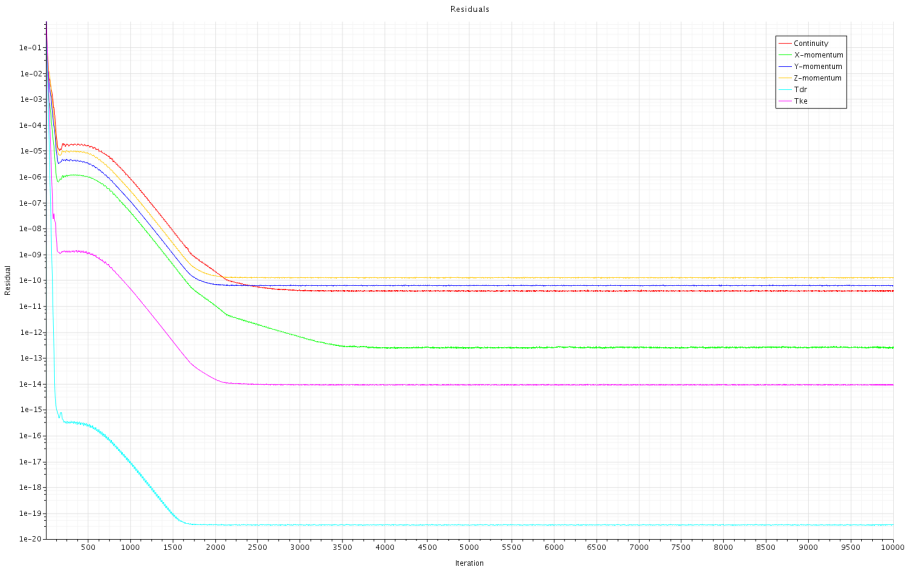

Figure A.97: Residual vs iteration, from the RANS simulations performed with the flat sail model, with a sheet angle of 90°, in the normal computational domain & grid 4, showing the graphs of the Continuity (red), X-momentum (green), Y-momentum (blue), Z-momentum (yellow), Turbulent dissipation rate (cyan) and the Turbulent kinetic energy (purple).

Normal Domain with Grid 3

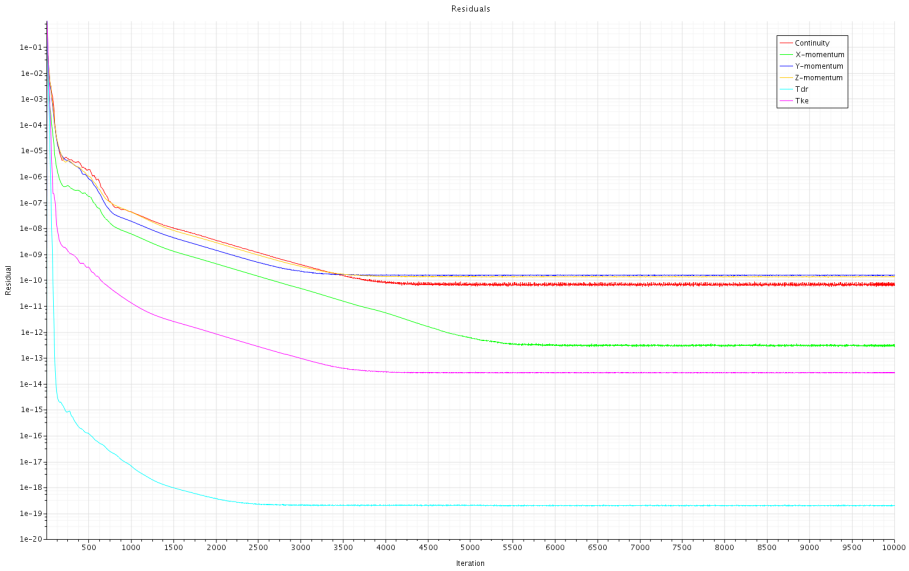

Figure A.98: Residual vs iteration, from the RANS simulations performed with the flat sail model, with a sheet angle of 90°, in the normal computational domain & grid 3, showing the graphs of the Continuity (red), X-momentum (green), Y-momentum (blue), Z-momentum (yellow), Turbulent dissipation rate (cyan) and the Turbulent kinetic energy (purple).

Normal Domain with Grid 2

Figure A.99: Residual vs iteration, from the RANS simulations performed with the flat sail model, with a sheet angle of 90°, in the normal computational domain & grid 2, showing the graphs of the Continuity (red), X-momentum (green), Y-momentum (blue), Z-momentum (yellow), Turbulent dissipation rate (cyan) and the Turbulent kinetic energy (purple).

Normal Domain with Grid 1

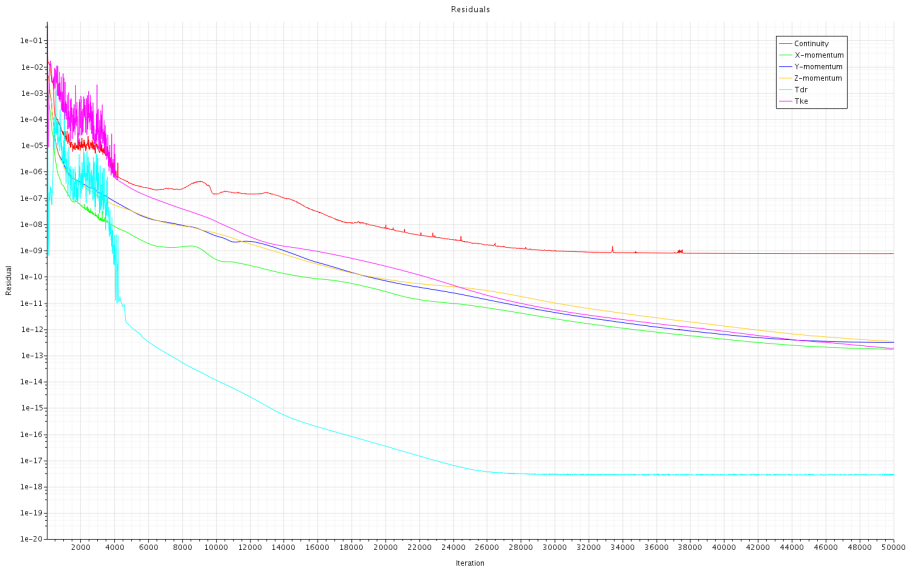

Figure A.100: Residual vs iteration, from the RANS simulations performed with the flat sail model, with a sheet angle of 90°, in the normal computational domain & grid 1, showing the graphs of the Continuity (red), X-momentum (green), Y-momentum (blue), Z-momentum (yellow), Turbulent dissipation rate (cyan) and the Turbulent kinetic energy (purple).

Large Domain with Grid 5

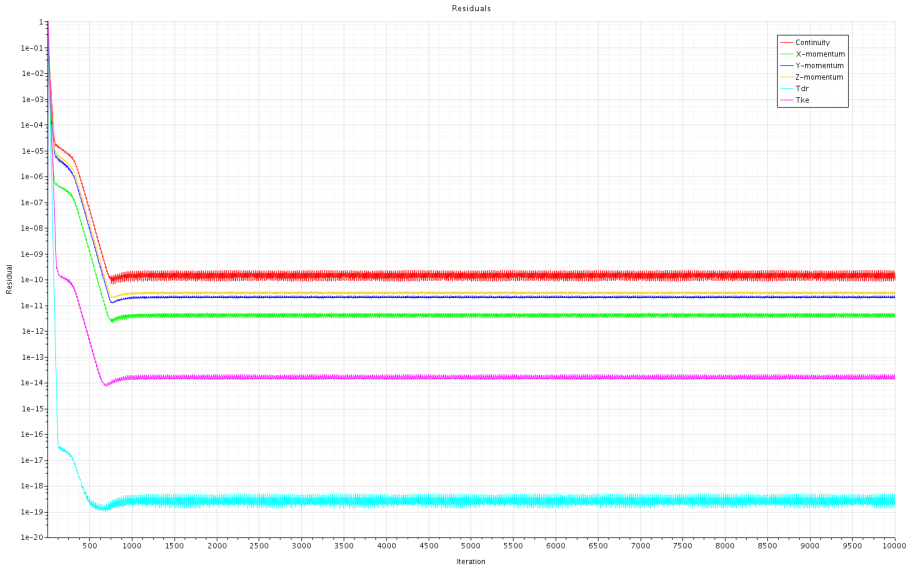

Figure A.101: Residual vs iteration, from the RANS simulations performed with the flat sail model, with a sheet angle of 90°, in the large computational domain & grid 5, showing the graphs of the Continuity (red), X-momentum (green), Y-momentum (blue), Z-momentum (yellow), Turbulent dissipation rate (cyan) and the Turbulent kinetic energy (purple).

Large Domain with Grid 4

Figure A.102: Residual vs iteration, from the RANS simulations performed with the flat sail model, with a sheet angle of 90°, in the large computational domain & grid 4, showing the graphs of the Continuity (red), X-momentum (green), Y-momentum (blue), Z-momentum (yellow), Turbulent dissipation rate (cyan) and the Turbulent kinetic energy (purple).

Large Domain with Grid 3

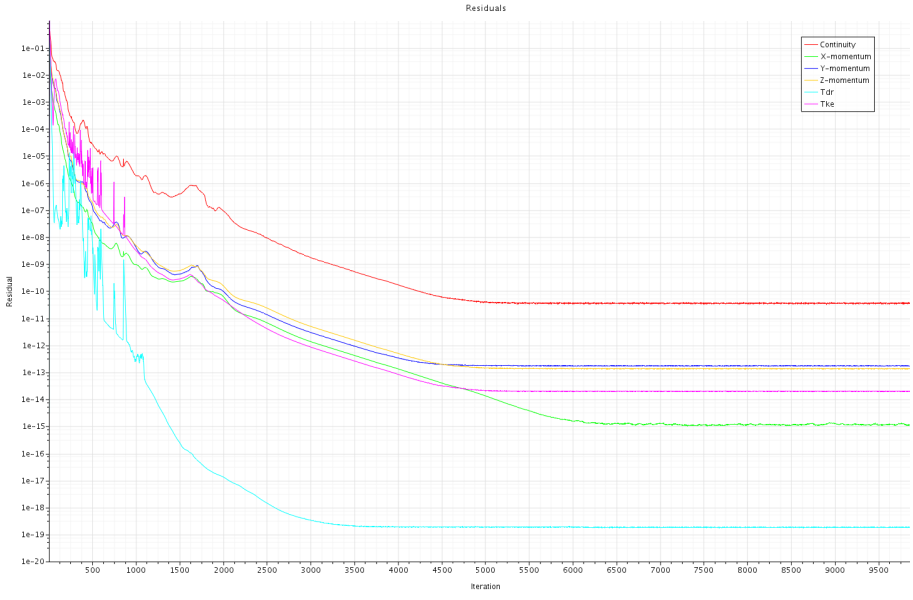

Figure A.103: Residual vs iteration, from the RANS simulations performed with the flat sail model, with a sheet angle of 90°, in the large computational domain & grid 3, showing the graphs of the Continuity (red), X-momentum (green), Y-momentum (blue), Z-momentum (yellow), Turbulent dissipation rate (cyan) and the Turbulent kinetic energy (purple).

Large Domain with Grid 2

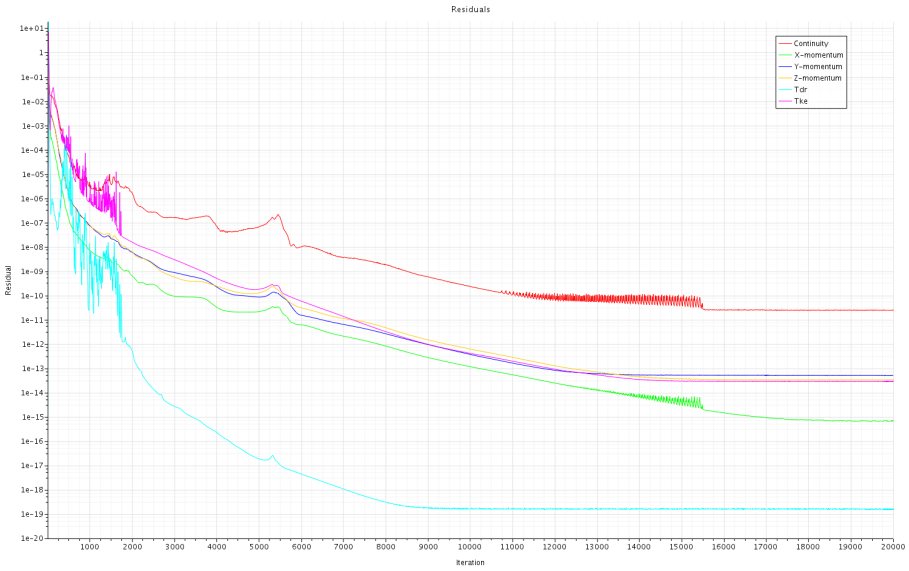

Figure A.104: Residual vs iteration, from the RANS simulations performed with the flat sail model, with a sheet angle of 90°, in the large computational domain & grid 2, showing the graphs of the Continuity (red), X-momentum (green), Y-momentum (blue), Z-momentum (yellow), Turbulent dissipation rate (cyan) and the Turbulent kinetic energy (purple).

Large Domain with Grid 1

Figure A.105: Residual vs iteration, from the RANS simulations performed with the flat sail model, with a sheet angle of 90°, in the large computational domain & grid 1, showing the graphs of the Continuity (red), X-momentum (green), Y-momentum (blue), Z-momentum (yellow), Turbulent dissipation rate (cyan) and the Turbulent kinetic energy (purple).

A.4.2 Verification Analysis of Discretization Uncertainty

ini-file & dat-file

The *ini*-file and the *dat*-file defined for the analysis of the normal domain can respectively be seen in Fig. A.106 & A.107 below.

```
[numerical_uncertainty]
CaseName=flatSailNormDom
DataFileName=verification_flatSailNormDom.dat
OutputFormat=PNG
IsUnsteady=No
GridStepSizeMethod=3
TimeStepsizeMethod=-1
UncertaintySolution=1
Showp=Yes
ShowAllUncertainties=Yes

; Grid Stepsize calculation method:
;       -1 ng=relative grid step size
;        1 ng=number of cells along one direction
;        2 ng=number of cells in the 2D grid
;        3 ng=number of cells in the 3D grid

; Time Stepsize calculation method:
;       -1 nt=relative time step size
;        1 nt=number of time steps
```

Figure A.106: The image shows the *ini*-file, read by the numerical uncertainty tool.

```
# This .dat-file contains input data
# for the simulated case with the flat
# sail model in the normal domain.
n_i     C_{FM}
0       5
0       0
43711276        1.5835
7371115 1.5921
1285998 1.6007
210969  1.6351
31340   1.6437
```

Figure A.107: The image shows the *dat*-file, read by the *ini*-file.

The command for the execution on GNU/Linux systems is presented below:

<path to the software> [[-i/- -input] <path to the ini-file>] [[-o/- -output]] <output-format>]

Tabulated data

The corresponding data from Fig. 5.4 - 5.5 are presented in Table A.3 below, where $h_i \,/\, h_1$ is the relative step size, ϕ_0 is the guess of the exact solution, ϕ_i is the result from the simulation, U is the estimated/discretization uncertainty, U_ϕ is the estimate of the uncertainty in the interval where the exact solution can be found with 95% certainty, p is the observed order of convergence, ϵ_Φ is the discretization error and F_s is the factor of safety.

Table A.3: Tabulated data from Fig. 5.4 & Fig. 5.5, from the RANS simulations, performed for the grid dependence study, with grid $1-5$ and the flat sail model, with a sheet angle of 90°, for both computational domains.

Grid	$h_i \,/\, h_1$	ϕ_0	ϕ_i	U	U_ϕ	p	ϵ_ϕ	F_s
Normal Domain								
1	1.00	1.56	1.58	0.03	1.8%	0.53	$2.34E-02$	1.25
2	1.81	1.56	1.59	0.04	2.5%	0.53	$3.20E-02$	1.25
3	3.24	1.56	1.60	0.06	3.6%	0.53	$4.35E-02$	1.25
4	5.92	1.56	1.64	0.09	5.7%	0.53	$5.98E-02$	1.25
5	11.17	1.56	1.64	0.10	6.6%	0.53	$8.36E-02$	1.25
Large Domain								
1	1.00	1.23	1.25	0.02	1.5%	0.86	$1.47E-02$	1.25
2	1.82	1.23	1.26	0.03	2.6%	0.86	$2.45E-02$	125
3	3.26	1.23	1.27	0.05	4.1%	0.86	$4.06E-02$	1.25
4	5.96	1.23	1.38	0.16	12.9%	0.86	$6.83E-02$	1.25
5	11.24	1.23	1.35	0.15	11.8%	0.86	$1.18E-01$	1.25

A.5 Sail Camber & Sheet Angle Analysis

A.5.1 Grid 3 of the Normal Domain & Cambered Sail Model

Fig. A.108 & Fig. A.109 below, shows the cambered sail model with a sheet angle of 90°, with grid 3, in the normal domain.

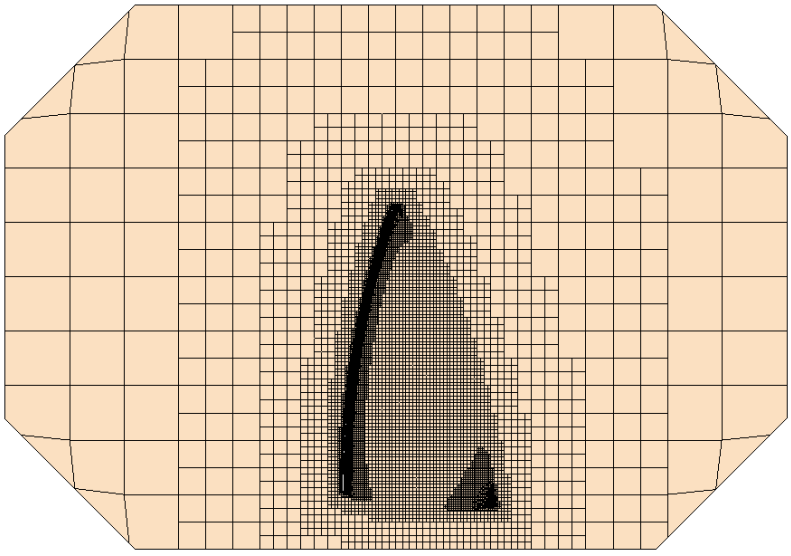

Figure A.108: Front view of the normal domain, grid 3 and the cambered sail model, with a sheet angle of 90°.

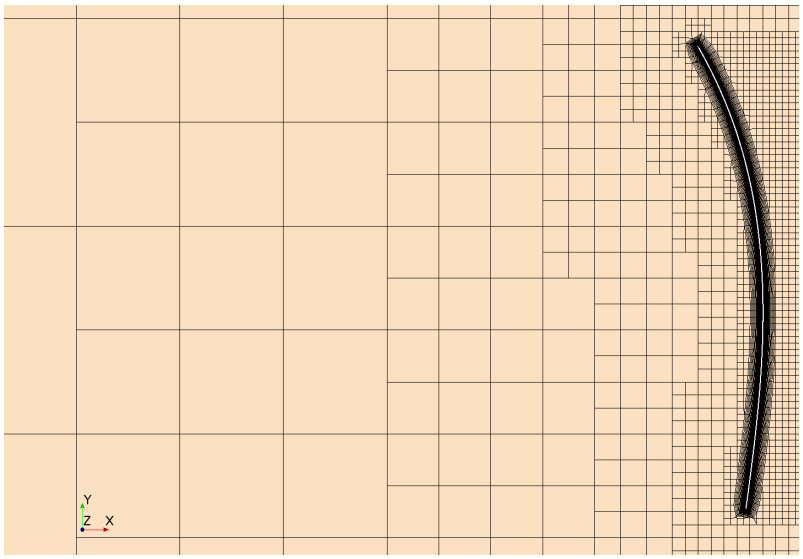

Figure A.109: Top view, zoom of the cambered sail model, with a sheet angle of 90°, showing the curvature of the sail, at the height of the center of effort (CoE) as well as the surface refinement degree and the diffusion depth (d), of the normal domain.

A.5.2 RANS Simulations

Turbulence Model Investigation

The drive force coefficients as well as the difference in % between the models, with K-Epsilon as reference, from the RANS simulations are presented in Table A.4 & Table A.5, respectively.

Table A.4: Drive force coefficients C_{F_M} [-] from the turbulence model investigation.

Turbulence model	$k-\varepsilon$	$SST\ k-\omega$	RST	$S-A$
Normal domain		C_{F_M} [-]		
Flat sail model	1.6017	1.6181	1.5879	1.7007
Cambered sail model	1.5910	1.5827	1.5766	1.6461
Large domain		C_{F_M} [-]		
Flat sail model	1.2766	1.2754	div.	1.4117
Cambered sail model	1.3105	1.3004	div.	1.4368

Table A.5: The difference in % between the turbulence models K-Epsilon, SST K-Omega, RST and S-A, with K-Epsilon as reference.

Turbulence model	$k-\varepsilon$	$SST\ k-\omega$	RST	$S-A$
Normal domain		$Diff.$ [%]		
Flat sail model	ref.	+1.0187	-0.8653	+5.9956
Cambered sail model	ref.	-0.5231	-0.9092	+3.4043
Large domain		$Diff.$ [%]		
Flat sail model	ref.	-0.0940	div.	+10.051
Cambered sail model	ref.	-0.7737	div.	+9.1945

From the turbulence model investigation, the K-Epsilon two-equation turbulence model was selected for the sail camber and sheet angle analysis. The only variable, for each sail model, in the analysis, was the sheet angle, which ranged from 60° - 120°, with increments of 10°. In this subsection the tabulated data is presented first and then flow field visualization images from the RANS simulations are presented.

Tabulated Data

The corresponding data from Fig. 5.10 - 5.15 in Chapter 5 are presented in Table A.6 - A.9 below.

Table A.6: Sail coefficients for the flat sail model in the normal domain.

Normal Domain & Flat Sail Model							
Sheet angle [°]	**60**	**70**	**80**	**90**	**100**	**110**	**120**
C_{F_M} [-]	1.1946	1.4080	1.5510	1.6017	1.5528	1.4103	1.1974
C_{F_S} [-]	-0.6865	-0.5104	-0.2724	0.0000	0.2727	0.5111	0.6880
C_{F_L} [-] (E-3)	0.6368	0.5852	0.5508	0.5852	0.5766	0.6282	0.7229
C_{M_P} [-]	2.1888	2.5726	2.8298	2.9212	2.8344	2.5801	2.1994
C_{M_R} [-]	-1.2574	-0.9321	-0.4969	-0.0000	0.4976	0.9349	1.2635
C_{M_Y} [-]	0.1329	0.1134	0.0857	0.0520	0.0168	-0.0160	-0.0435

Table A.7: Sail coefficients for the cambered sail model in the normal domain.

Normal Domain & Cambered Sail Model							
Sheet angle [°]	**60**	**70**	**80**	**90**	**100**	**110**	**120**
C_{F_M} [-]	1.3764	1.5278	1.6034	1.5910	1.4925	1.3195	1.0957
C_{F_S} [-]	-0.6448	-0.4030	-0.1232	0.1684	0.4417	0.6705	0.8374
C_{F_L} [-]	-0.0023	-0.0020	-0.0012	0.0001	0.0018	0.0036	0.0055
C_{M_P} [-]	2.5851	2.8473	2.9694	2.9316	2.7389	2.4135	1.9973
C_{M_R} [-]	-1.1454	-0.6868	-0.1640	0.3749	0.8764	1.2944	1.5983
C_{M_Y} [-]	0.2456	0.2391	0.2243	0.2024	0.1761	0.1483	0.1208

Table A.8: Sail coefficients for the flat sail model in the large domain.

Large Domain & Flat Sail Model							
Sheet angle [°]	**60**	**70**	**80**	**90**	**100**	**110**	**120**
C_{F_M} [-]	1.0046	1.1509	1.2445	1.2766	1.2445	1.1514	1.0068
C_{F_S} [-]	-0.5771	-0.4171	-0.2186	0.0000	0.2185	0.4172	0.5783
C_{F_L} [-] (E-3)	0.5680	0.4991	0.4561	0.4759	0.4710	0.5250	0.6110
C_{M_P} [-]	1.8379	2.0984	2.2647	2.3219	2.2659	2.1023	1.8464
C_{M_R} [-]	-1.0555	-0.7601	-0.3975	-0.0000	0.3977	0.7615	1.0603
C_{M_Y} [-]	0.1152	0.0957	0.0707	0.0420	0.0127	-0.0151	-0.0390

Table A.9: Sail coefficients for the cambered sail model in the large domain.

Large Domain & Cambered Sail Model							
Sheet angle [°]	**60**	**70**	**80**	**90**	**100**	**110**	**120**
C_{F_M} [-]	1.1675	1.2699	1.3191	1.3105	1.2447	1.1266	0.9648
C_{F_S} [-]	-0.5477	-0.3356	-0.1018	0.1386	0.3686	0.5733	0.7384
C_{F_L} [-]	-0.0022	-0.0021	-0.0015	-0.0003	0.0012	0.0031	0.0049
C_{M_P} [-]	2.1910	2.3636	2.4386	2.4104	2.2808	2.0588	1.7579
C_{M_R} [-]	-0.9723	-0.5712	-0.1355	0.3079	0.7303	1.1057	1.4086
C_{M_Y} [-]	0.2093	0.1993	0.1846	0.1662	0.1458	0.1250	0.1049

In Table A.10 below, the difference in % of the drive force coefficients C_{F_M} [-] from Table A.6 - A.9 above, are presented as an example of the effect of having a camber in the sail.

Table A.10: The difference in % of the drive force coefficients C_{F_M}, received from the sail camber analysis with RANS simulations, for both domains, with the flat sail model as reference.

Sheet angle [°]	**60**	**70**	**80**	**90**	**100**	**110**	**120**
Normal Domain				$Diff.$ [%]			
Flat sail model	ref.	ref.	ref.	ref.	ref.	ref.	ref.
Cambered sail model	+14.142	+8.1613	+3.3223	-0.6703	-3.9602	-6.6525	-8.8701
Large Domain				$Diff.$ [%]			
Flat sail model	ref.	ref.	ref.	ref.	ref.	ref.	ref.
Cambered sail model	+14.999	+9.8315	+5.8199	+2.6207	+0.0161	-2.1774	-4.2605

Flow Field Visualization

The top view images of the pressure distribution, velocity distribution, and constrained streamlines, shows the scalar quantities at a horizontal xy-plane, at the height of the center of effort (CoE); the corresponding side-view images shows the scalar quantities at a vertical xz-plane in the center of the domain.

Top View Images

Pressure Distribution at CoE with the Flat Sail Model in the Normal Domain

Fig. A.110 - A.116 shows top view images of the pressure distribution, for the seven different sheet angles with the flat sail model in the normal computational domain.

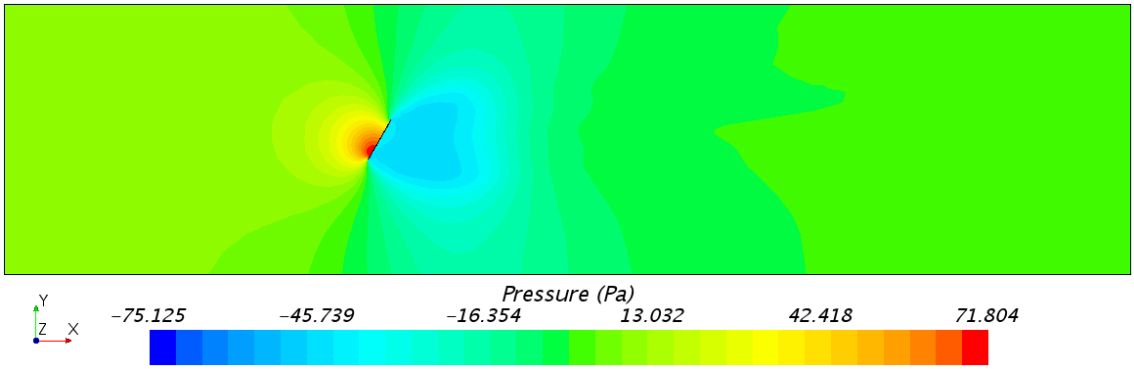

Figure A.110: Top view of the normal computational domain, showing the pressure distribution, at the height of the center of effort (CoE); the flat sail model, with a sheet angle of 60°.

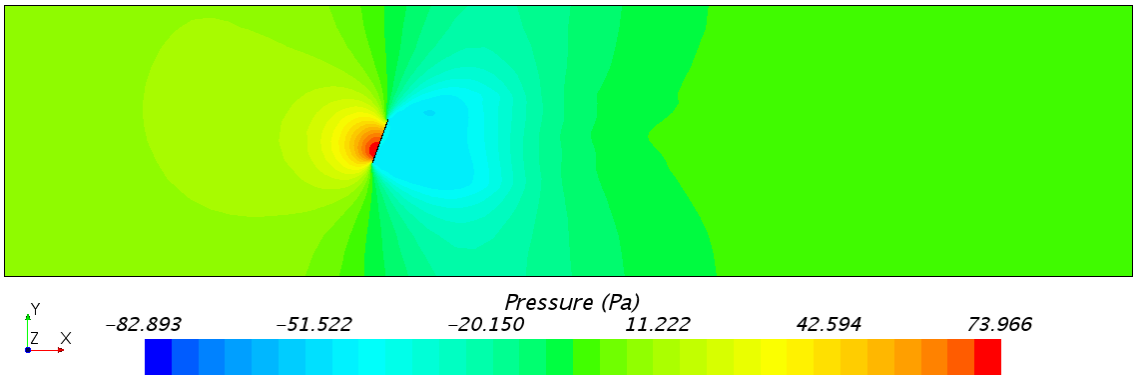

Figure A.111: Top view of the normal computational domain, showing the pressure distribution, at the height of the center of effort (CoE); the flat sail model, with a sheet angle of 70°.

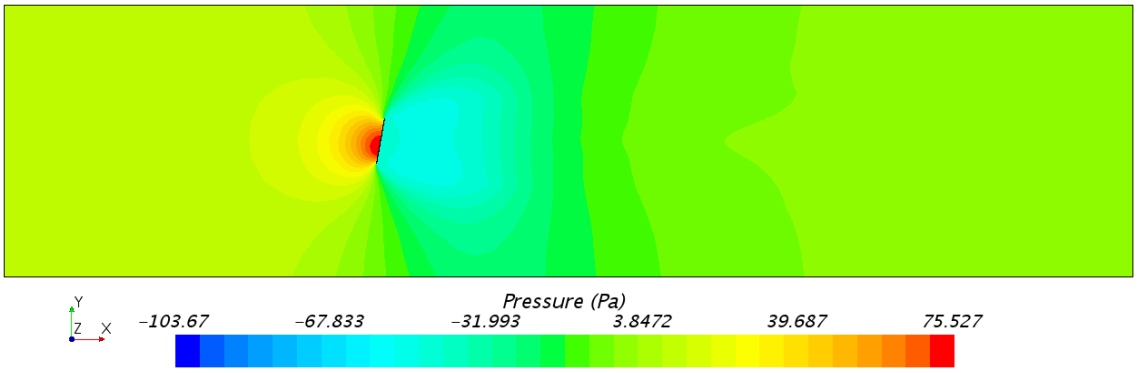

Figure A.112: Top view of the normal computational domain, showing the pressure distribution, at the height of the center of effort (CoE); the flat sail model, with a sheet angle of 80°.

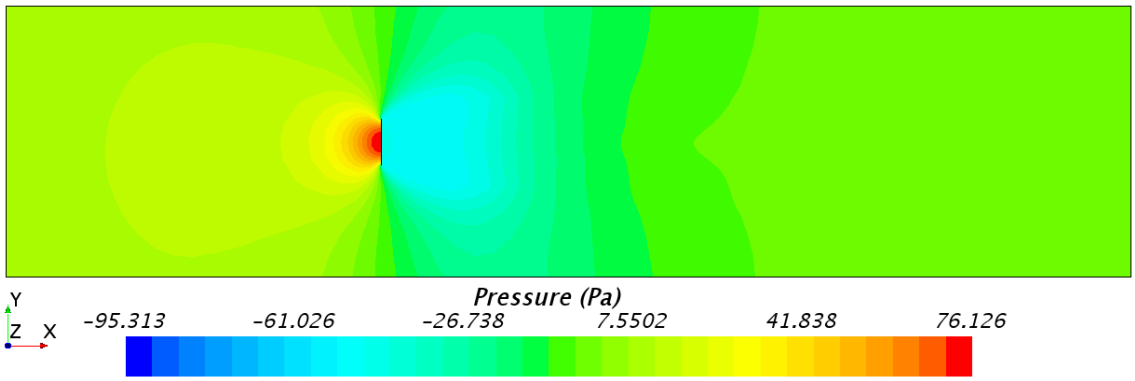

Figure A.113: Top view of the normal computational domain, showing the pressure distribution, at the height of the center of effort (CoE); the flat sail model, with a sheet angle of 90°.

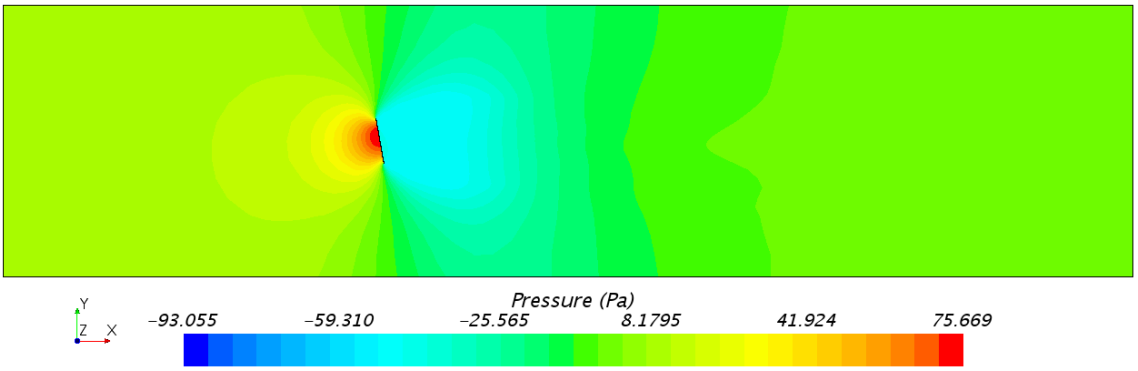

Figure A.114: Top view of the normal computational domain, showing the pressure distribution, at the height of the center of effort (CoE); the flat sail model, with a sheet angle of 100°.

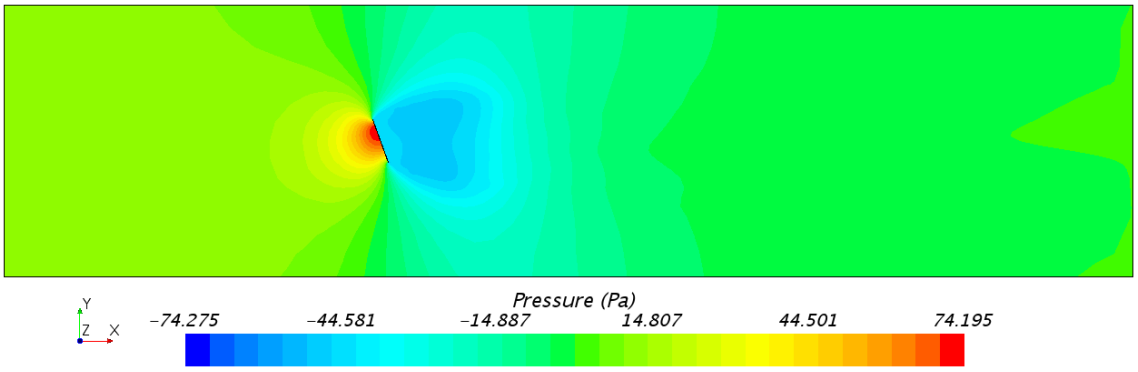

Figure A.115: Top view of the normal computational domain, showing the pressure distribution, at the height of the center of effort (CoE); the flat sail model, with a sheet angle of 110°.

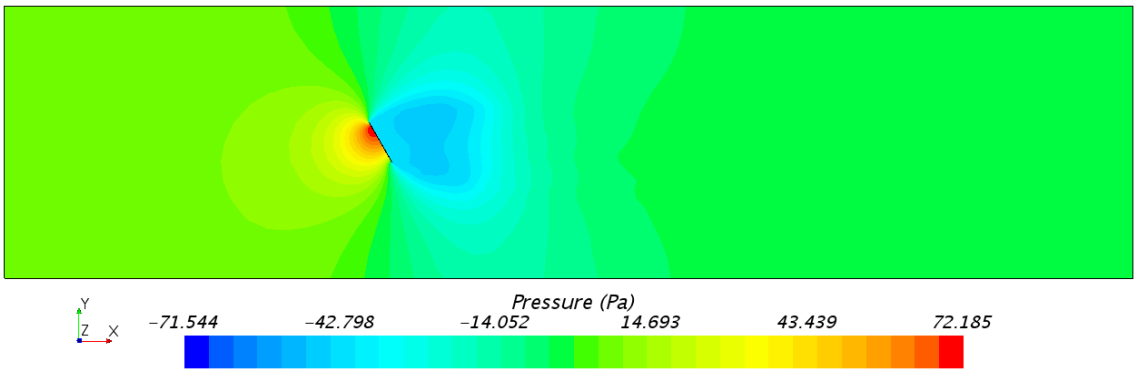

Figure A.116: Top view of the normal computational domain, showing the pressure distribution, at the height of the center of effort (CoE); the flat sail model, with a sheet angle of 120°.

Pressure Distribution at CoE with the Cambered Sail Model in the Normal Domain

Fig. A.117 - A.123 shows top view images of the pressure distribution, for the seven different sheet angles with the cambered sail model in the normal computational domain.

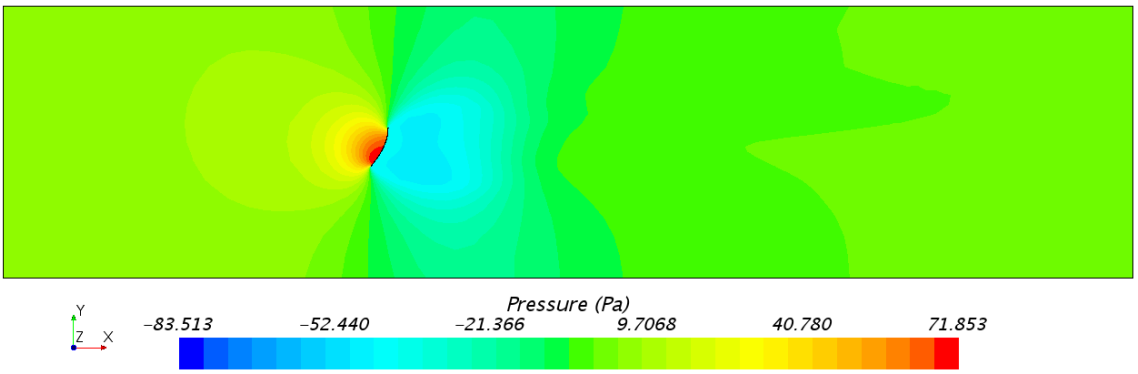

Figure A.117: Top view of the normal computational domain, showing the pressure distribution, at the height of the center of effort (CoE); the cambered sail model, with a sheet angle of 60°.

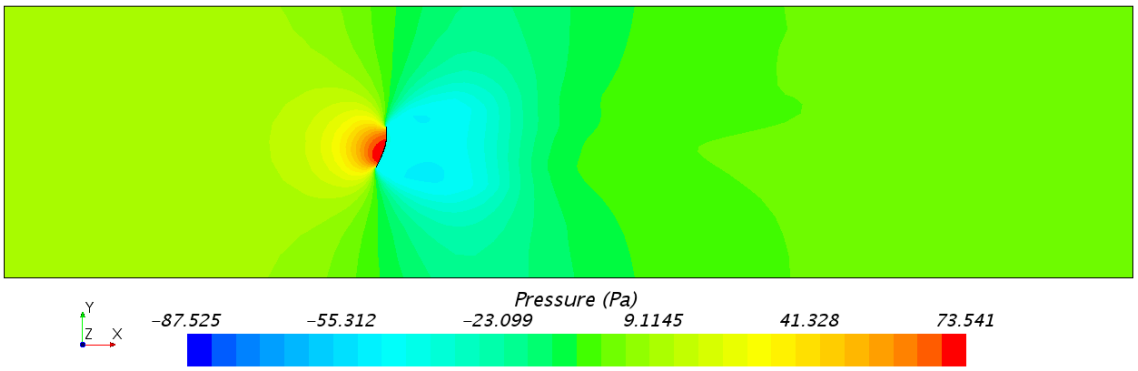

Figure A.118: Top view of the normal computational domain, showing the pressure distribution, at the height of the center of effort (CoE); the cambered sail model, with a sheet angle of 70°.

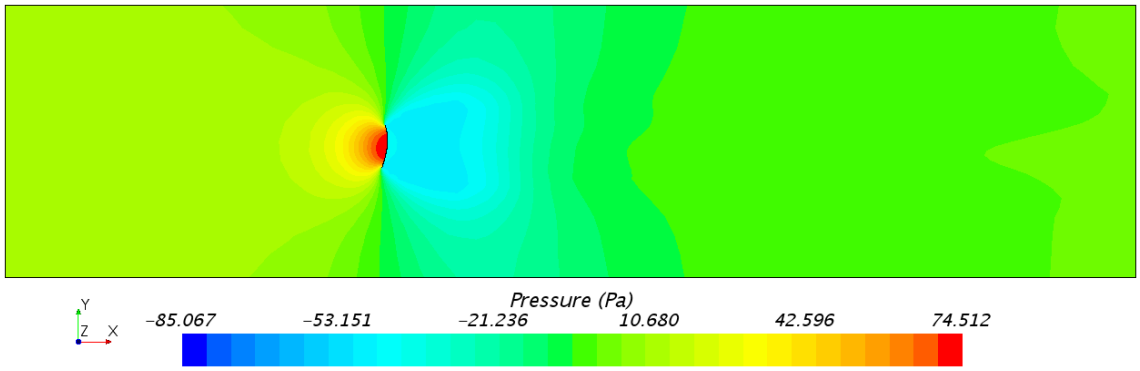

Figure A.119: Top view of the normal computational domain, showing the pressure distribution, at the height of the center of effort (CoE); the cambered sail model, with a sheet angle of 80°.

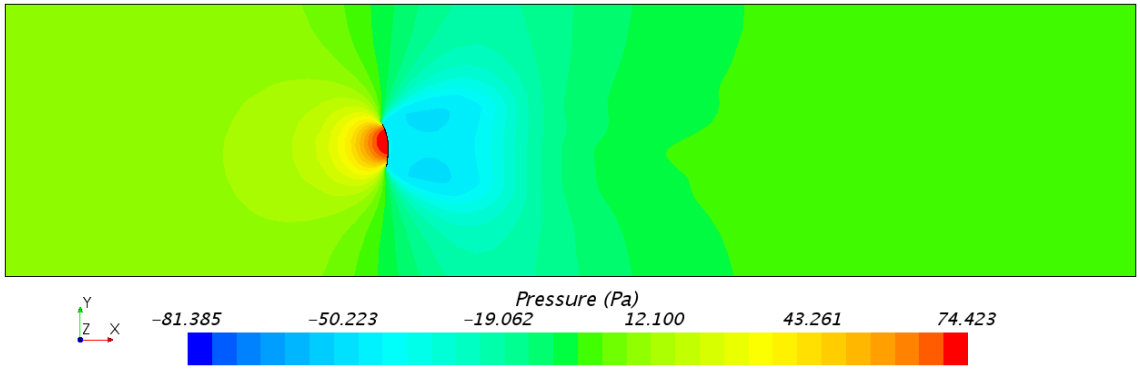

Figure A.120: Top view of the normal computational domain, showing the pressure distribution, at the height of the center of effort (CoE); the cambered sail model, with a sheet angle of 90°.

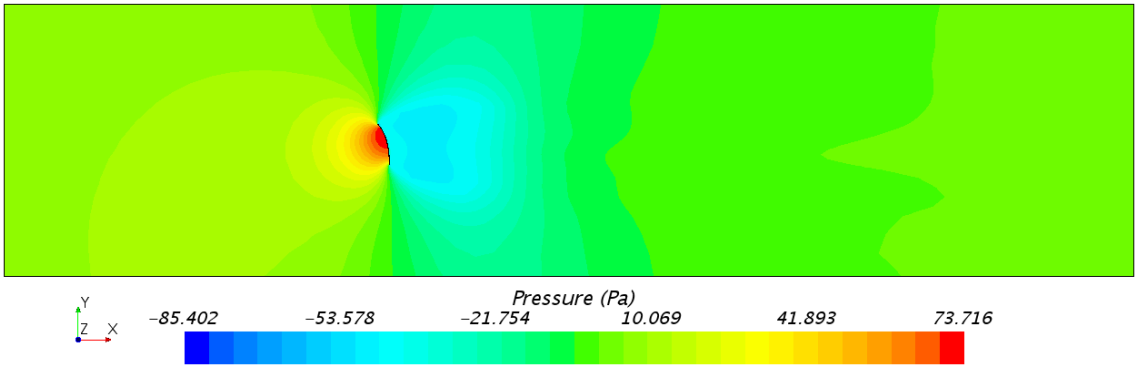

Figure A.121: Top view of the normal computational domain, showing the pressure distribution, at the height of the center of effort (CoE); the cambered sail model, with a sheet angle of 100°.

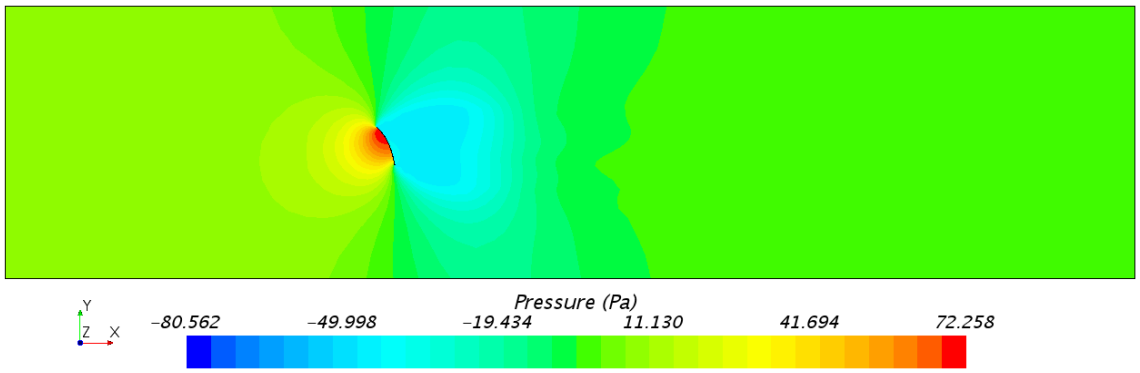

Figure A.122: Top view of the normal computational domain, showing the pressure distribution, at the height of the center of effort (CoE); the cambered sail model, with a sheet angle of 110°.

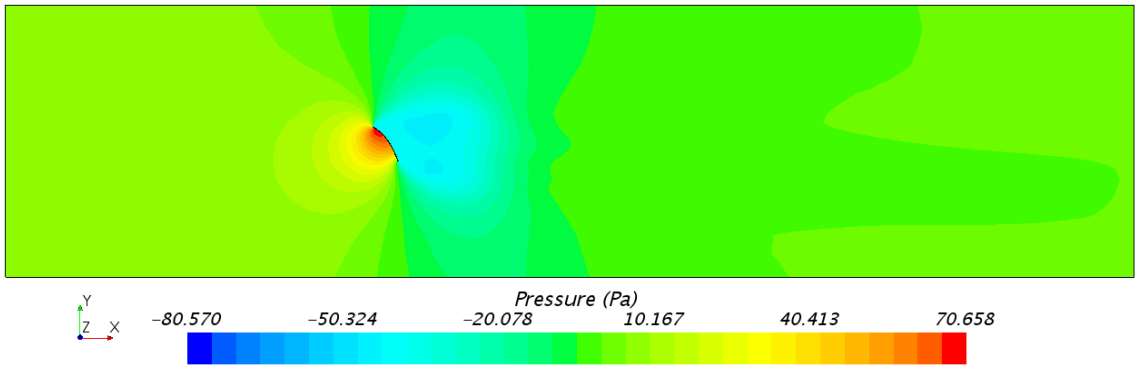

Figure A.123: Top view of the normal computational domain, showing the pressure distribution, at the height of the center of effort (CoE); the cambered sail model, with a sheet angle of 120°.

Velocity Distribution at CoE with the Flat Sail Model in the Normal Domain

Fig. A.124 - A.130 shows top view images of the velocity distribution, for the seven different sheet angles with the flat sail model in the normal computational domain.

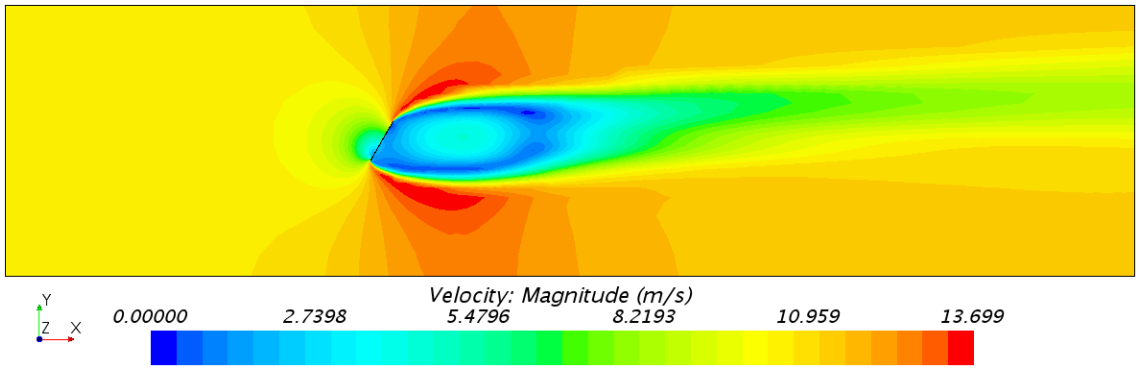

Figure A.124: Top view of the normal computational domain, showing the velocity distribution, at the height of the center of effort (CoE); the flat sail model, with a sheet angle of 60°.

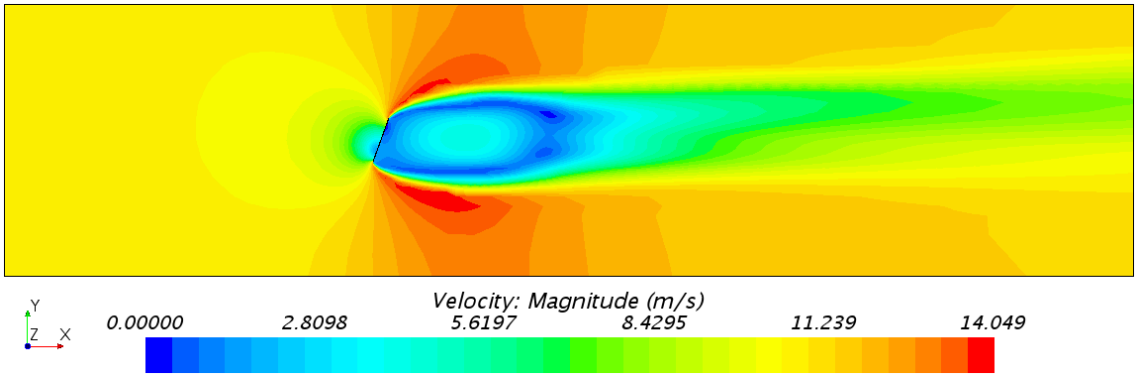

Figure A.125: Top view of the normal computational domain, showing the velocity distribution, at the height of the center of effort (CoE); the flat sail model, with a sheet angle of 70°.

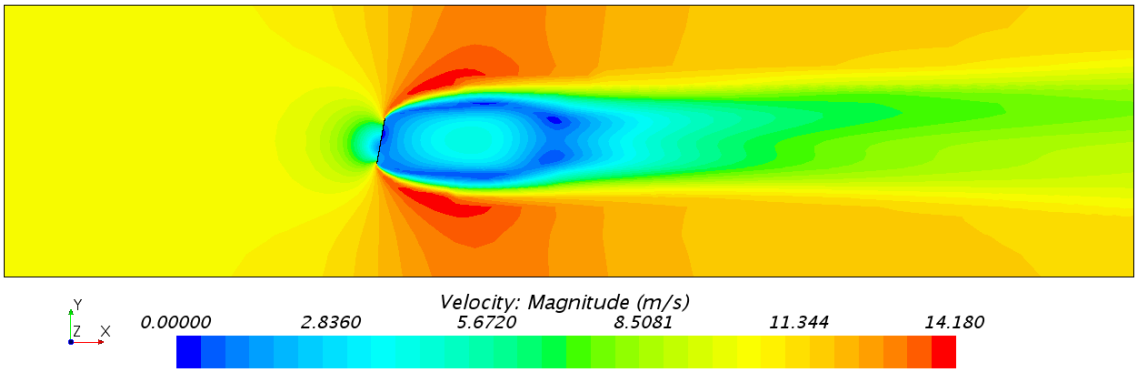

Figure A.126: Top view of the normal computational domain, showing the velocity distribution, at the height of the center of effort (CoE); the flat sail model, with a sheet angle of 80°.

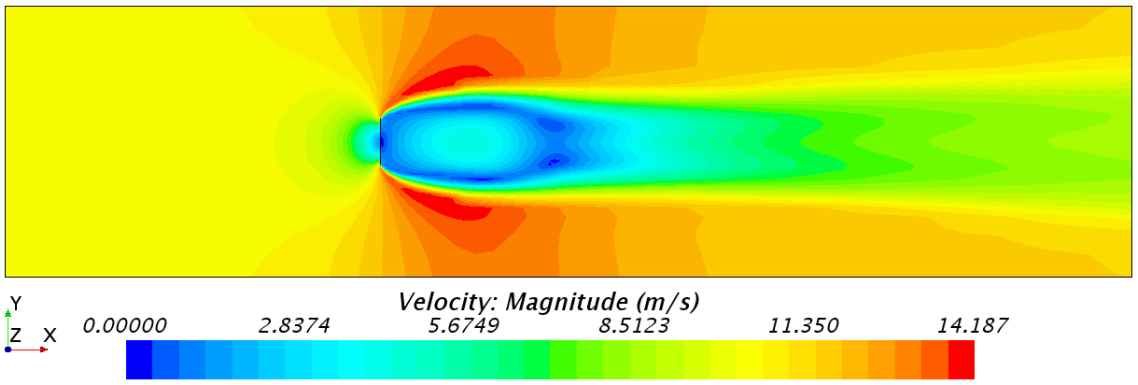

Figure A.127: Top view of the normal computational domain, showing the velocity distribution, at the height of the center of effort (CoE); the flat sail model, with a sheet angle of 90°.

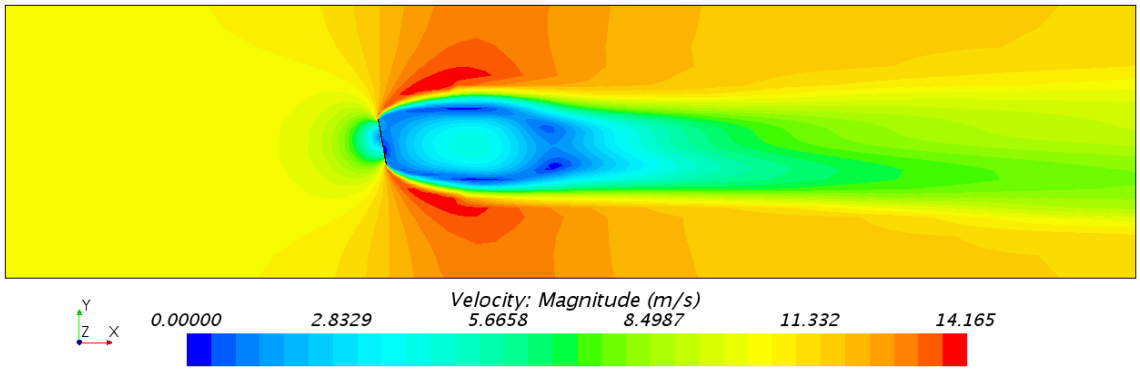

Figure A.128: Top view of the normal computational domain, showing the velocity distribution, at the height of the center of effort (CoE); the flat sail model, with a sheet angle of 100°.

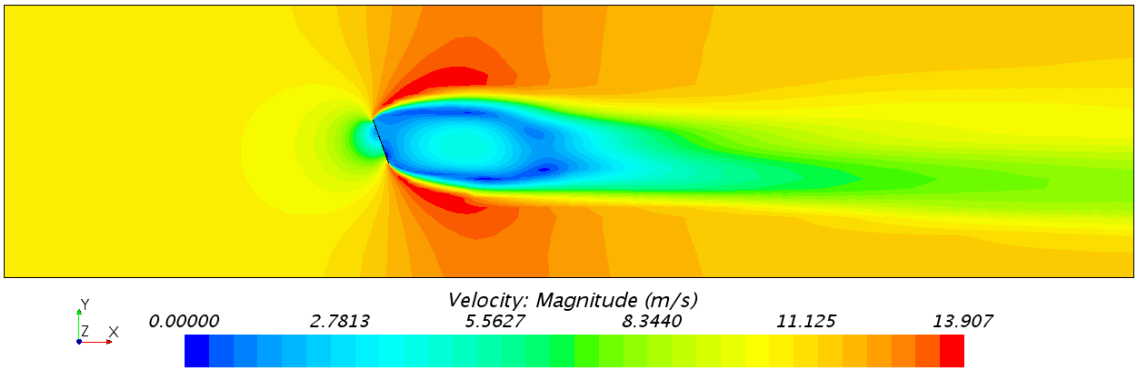

Figure A.129: Top view of the normal computational domain, showing the velocity distribution, at the height of the center of effort (CoE); the flat sail model, with a sheet angle of 110°.

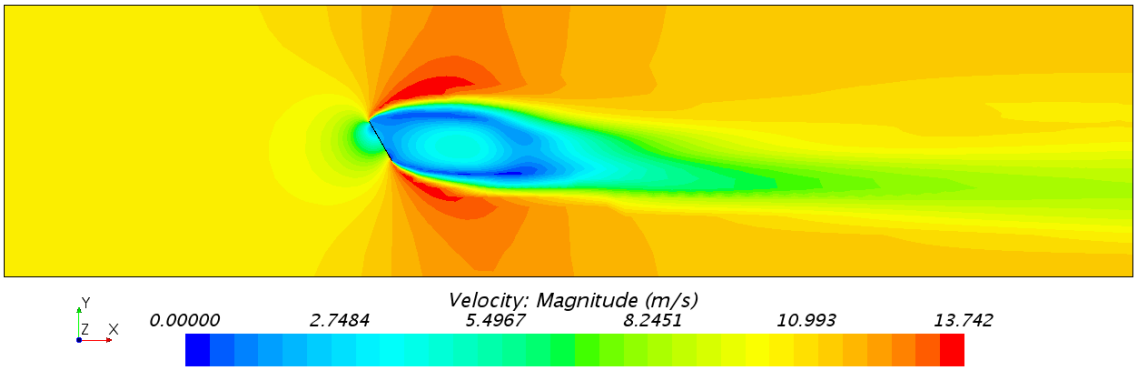

Figure A.130: Top view of the normal computational domain, showing the velocity distribution, at the height of the center of effort (CoE); the flat sail model, with a sheet angle of 120°.

Velocity Distribution at CoE with the Cambered Sail Model in the Normal Domain

Fig. A.131 - A.137 shows top view images of the velocity distribution, for the seven different sheet angles with the cambered sail model in the normal computational domain.

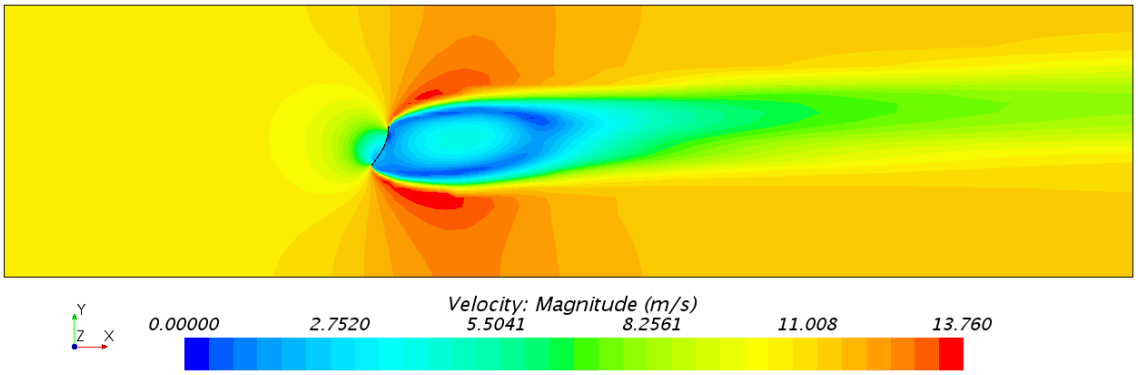

Figure A.131: Top view of the normal computational domain, showing the velocity distribution, at the height of the center of effort (CoE); the cambered sail model, with a sheet angle of 60°.

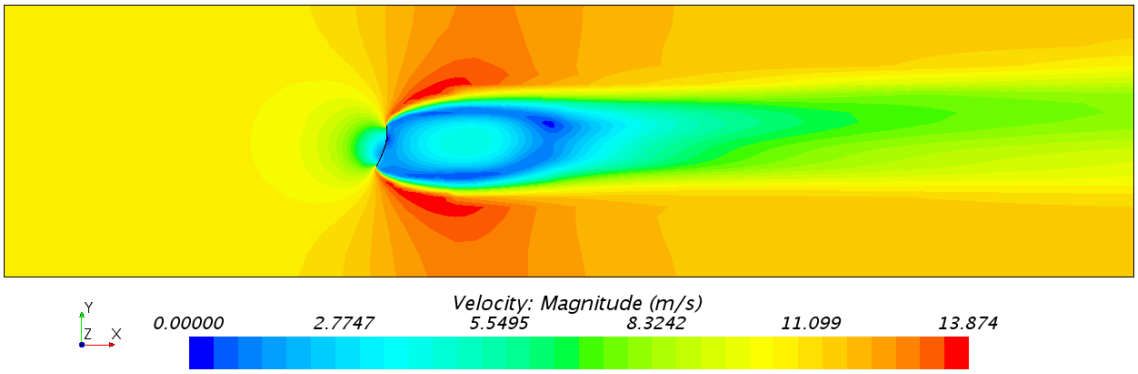

Figure A.132: Top view of the normal computational domain, showing the velocity distribution, at the height of the center of effort (CoE); the cambered sail model, with a sheet angle of 70°.

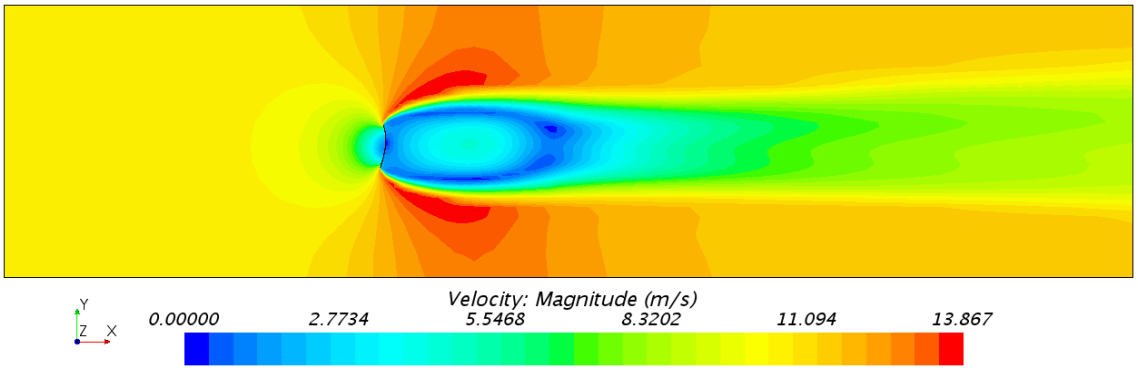

Figure A.133: Top view of the normal computational domain, showing the velocity distribution, at the height of the center of effort (CoE); the cambered sail model, with a sheet angle of 80°.

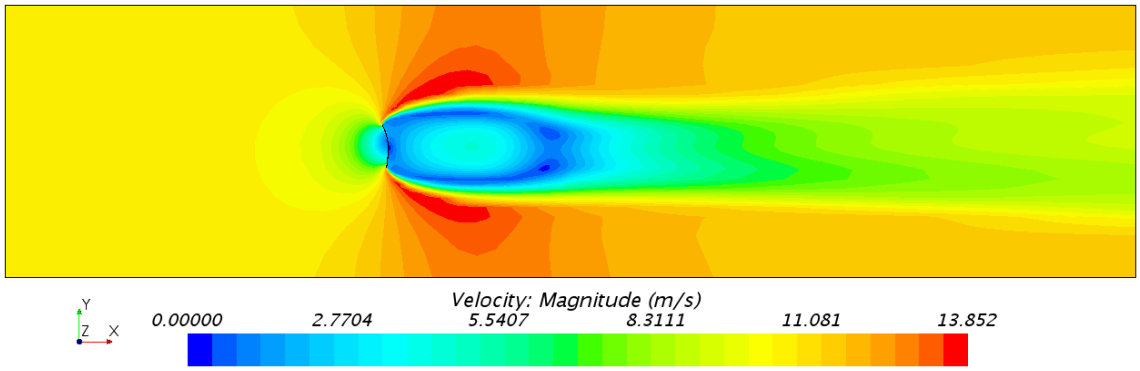

Figure A.134: Top view of the normal computational domain, showing the velocity distribution, at the height of the center of effort (CoE); the cambered sail model, with a sheet angle of 90°.

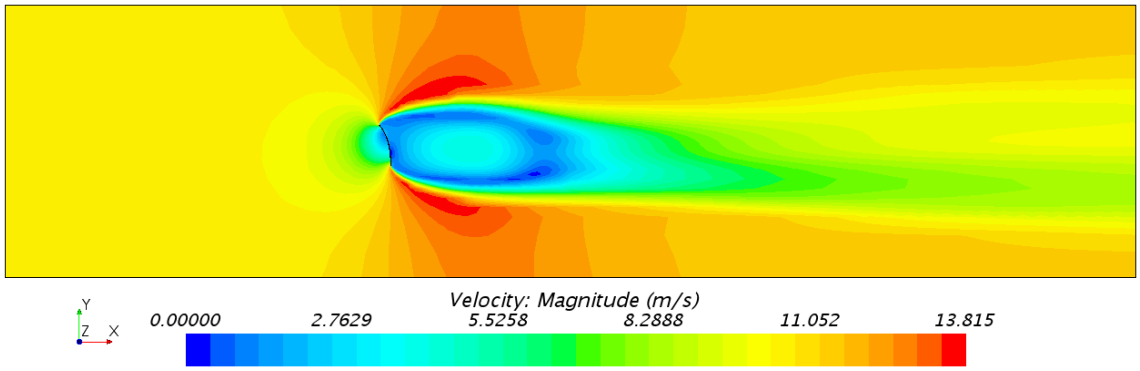

Figure A.135: Top view of the normal computational domain, showing the velocity distribution, at the height of the center of effort (CoE); the cambered sail model, with a sheet angle of 100°.

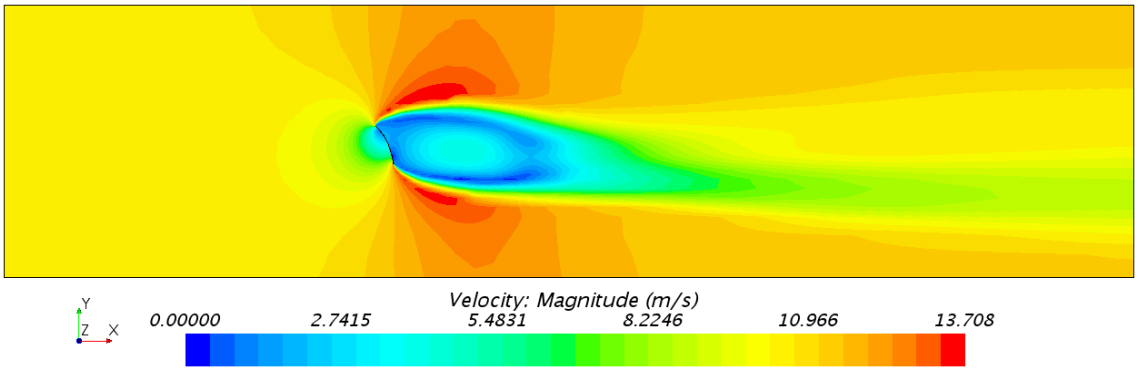

Figure A.136: Top view of the normal computational domain, showing the velocity distribution, at the height of the center of effort (CoE); the cambered sail model, with a sheet angle of 110°.

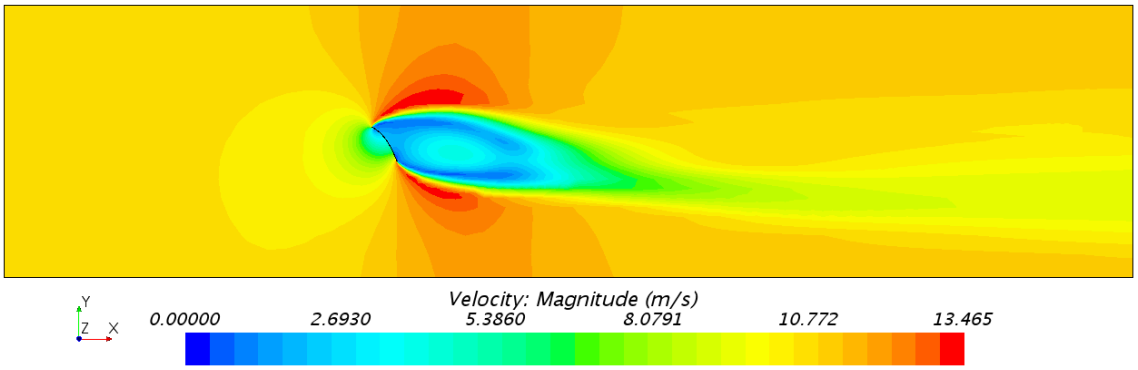

Figure A.137: Top view of the normal computational domain, showing the velocity distribution, at the height of the center of effort (CoE); the cambered sail model, with a sheet angle of 120°.

Constrained Streamlines at CoE with the Flat Sail Model in the Normal Domain

Fig. A.138 - A.144 shows top view images of constrained streamlines, for the seven different sheet angles with the flat sail model in the normal computational domain.

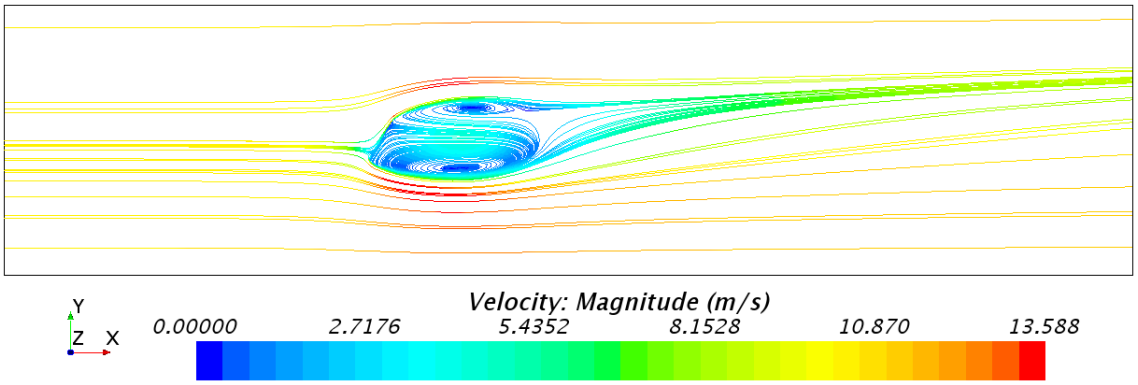

Figure A.138: Top view of the normal computational domain, showing constrained streamlines, at the height of the center of effort (CoE); the flat sail model, with a sheet angle of 60°.

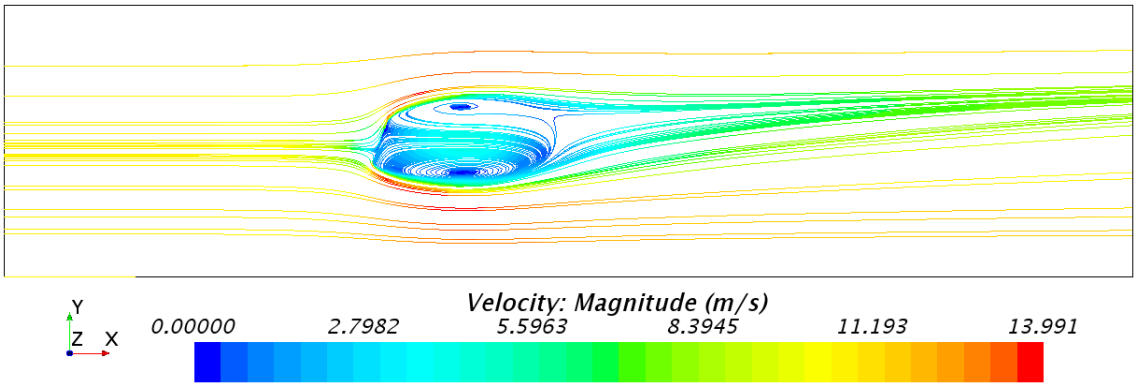

Figure A.139: Top view of the normal computational domain, showing constrained streamlines, at the height of the center of effort (CoE); the flat sail model, with a sheet angle of 70°.

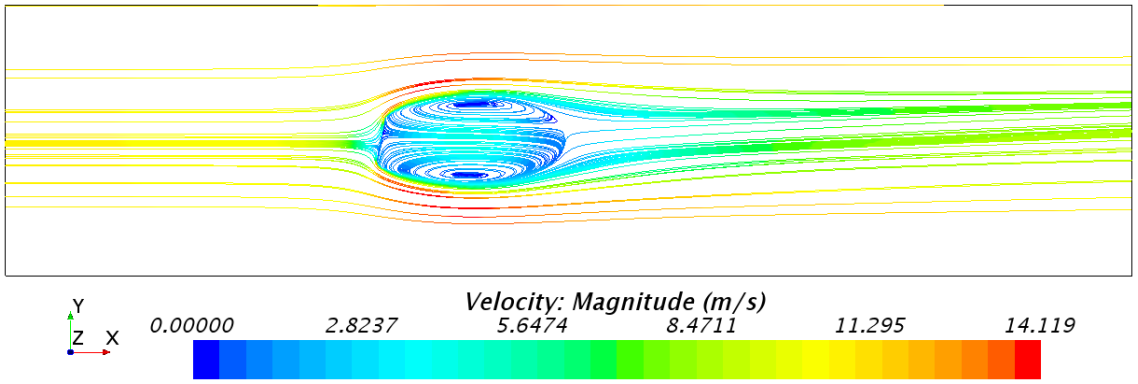

Figure A.140: Top view of the normal computational domain, showing constrained streamlines, at the height of the center of effort (CoE); the flat sail model, with a sheet angle of 80°.

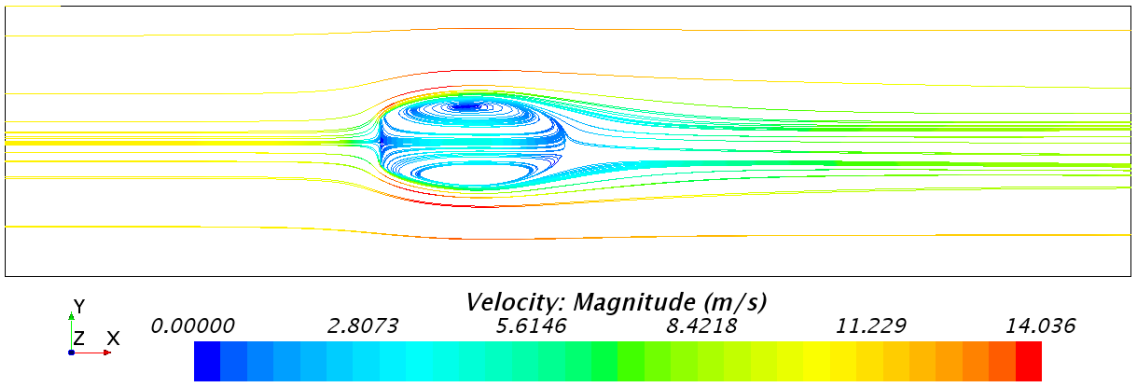

Figure A.141: Top view of the normal computational domain, showing constrained streamlines, at the height of the center of effort (CoE); the flat sail model, with a sheet angle of 90°.

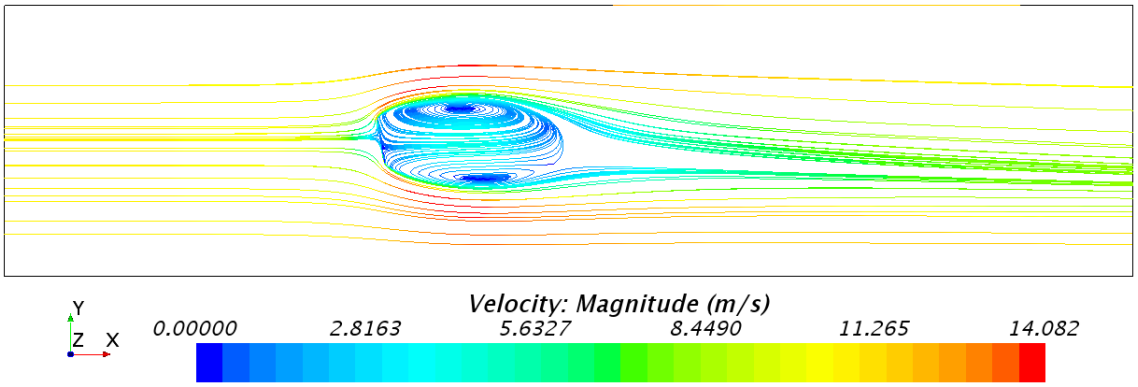

Figure A.142: Top view of the normal computational domain, showing constrained streamlines, at the height of the center of effort (CoE); the flat sail model, with a sheet angle of 100°.

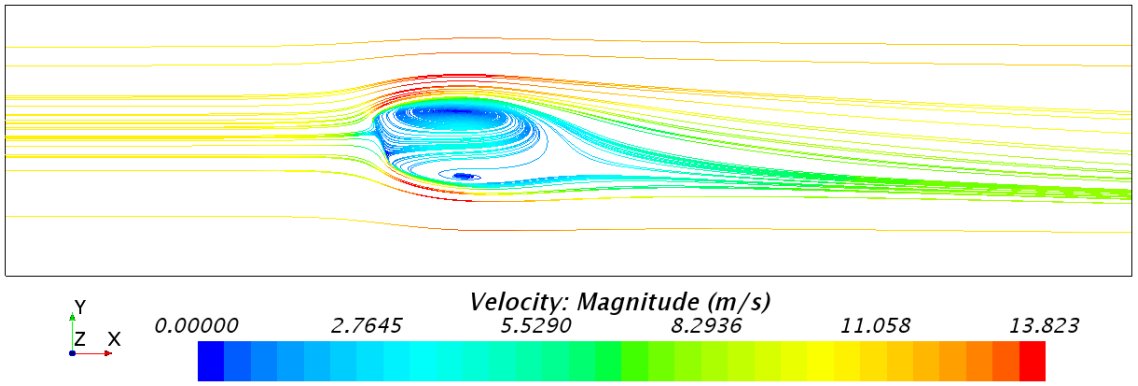

Figure A.143: Top view of the normal computational domain, showing constrained streamlines, at the height of the center of effort (CoE); the flat sail model, with a sheet angle of 110°.

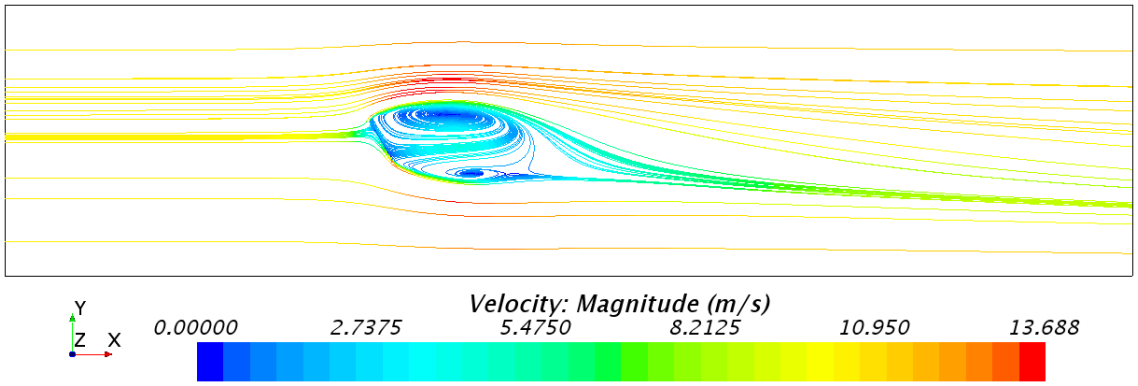

Figure A.144: Top view of the normal computational domain, showing constrained streamlines, at the height of the center of effort (CoE); the flat sail model, with a sheet angle of 120°.

Constrained Streamlines at CoE with the Cambered Sail Model in the Normal Domain

Fig. A.145 - A.151 shows top view images of constrained streamlines, for the seven different sheet angles with the cambered sail model in the normal computational domain.

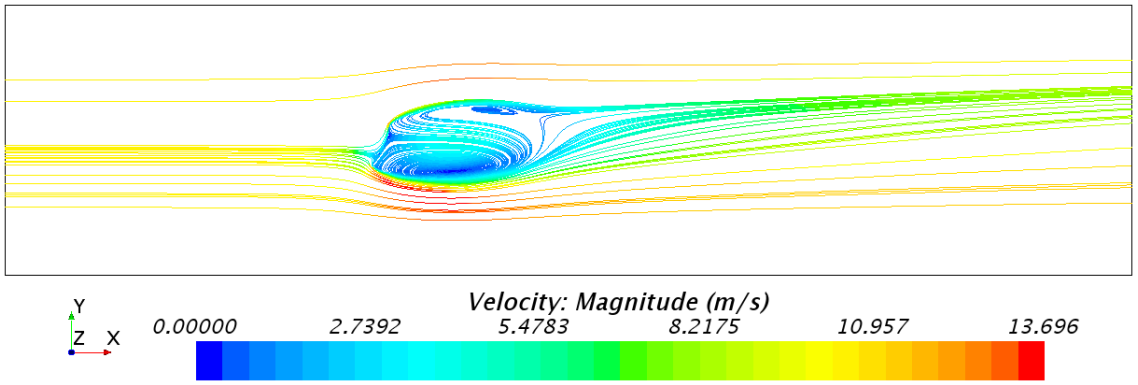

Figure A.145: Top view of the normal computational domain, showing constrained streamlines, at the height of the center of effort (CoE); the cambered sail model, with a sheet angle of 60°.

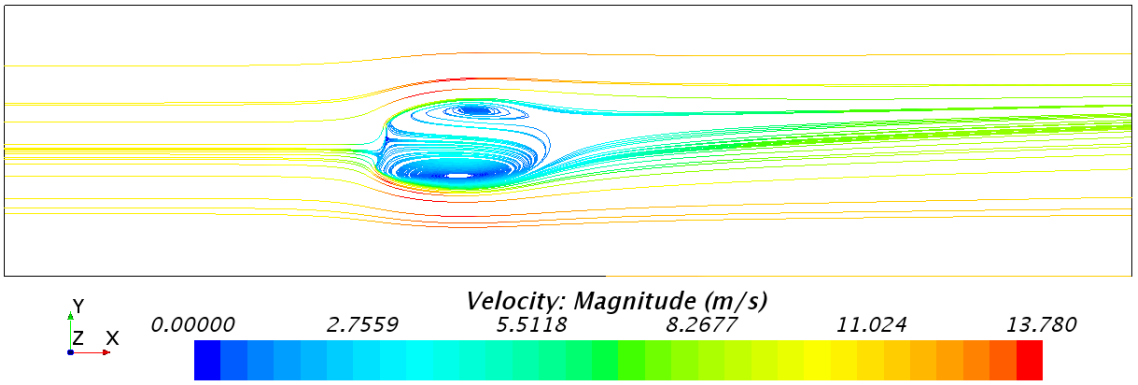

Figure A.146: Top view of the normal computational domain, showing constrained streamlines, at the height of the center of effort (CoE); the cambered sail model, with a sheet angle of 70°.

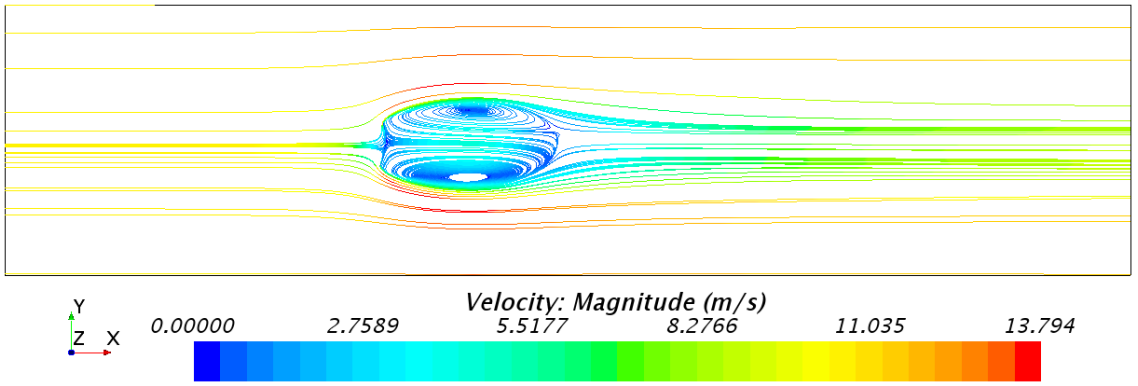

Figure A.147: Top view of the normal computational domain, showing constrained streamlines, at the height of the center of effort (CoE); the cambered sail model, with a sheet angle of 80°.

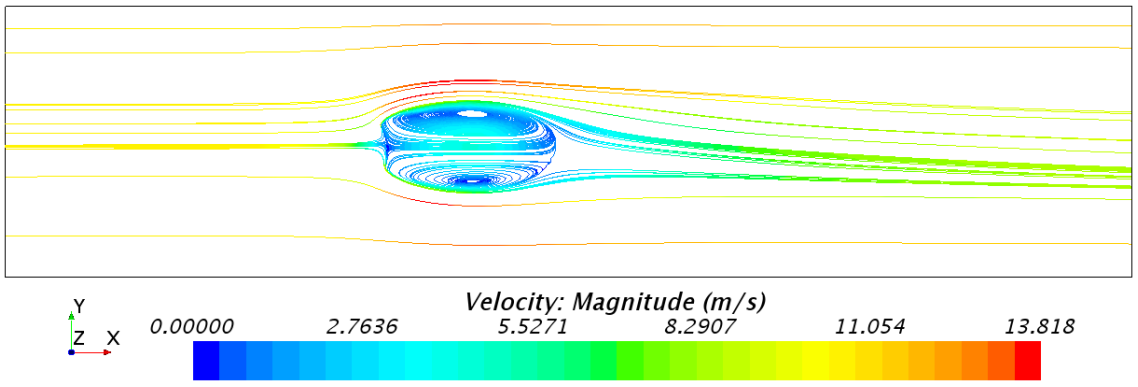

Figure A.148: Top view of the normal computational domain, showing constrained streamlines, at the height of the center of effort (CoE); the cambered sail model, with a sheet angle of 90°.

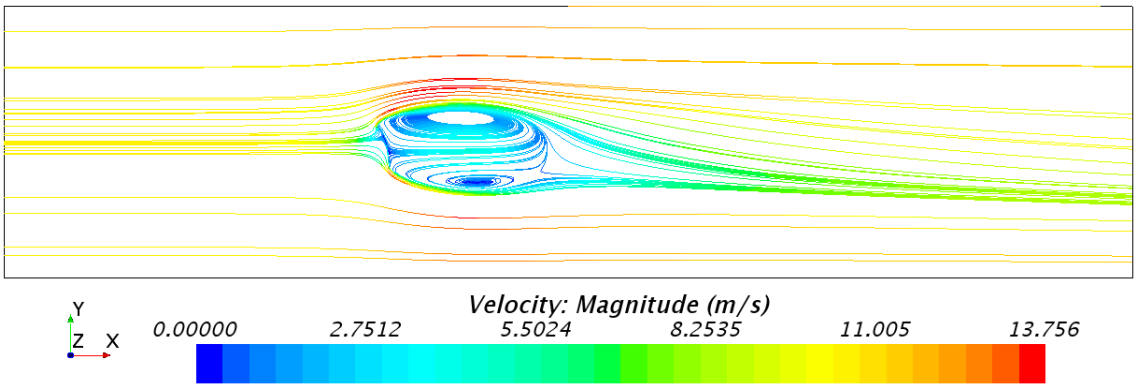

Figure A.149: Top view of the normal computational domain, showing constrained streamlines, at the height of the center of effort (CoE); the cambered sail model, with a sheet angle of 100°.

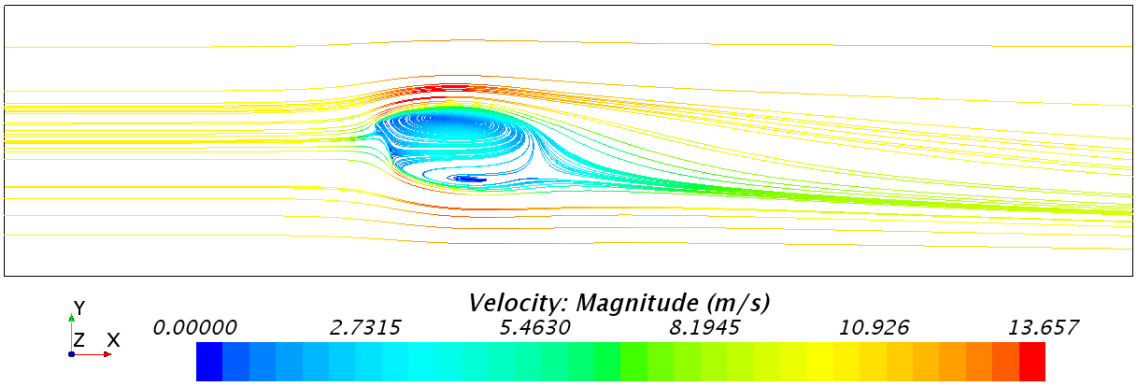

Figure A.150: Top view of the normal computational domain, showing constrained streamlines, at the height of the center of effort (CoE); the cambered sail model, with a sheet angle of 110°.

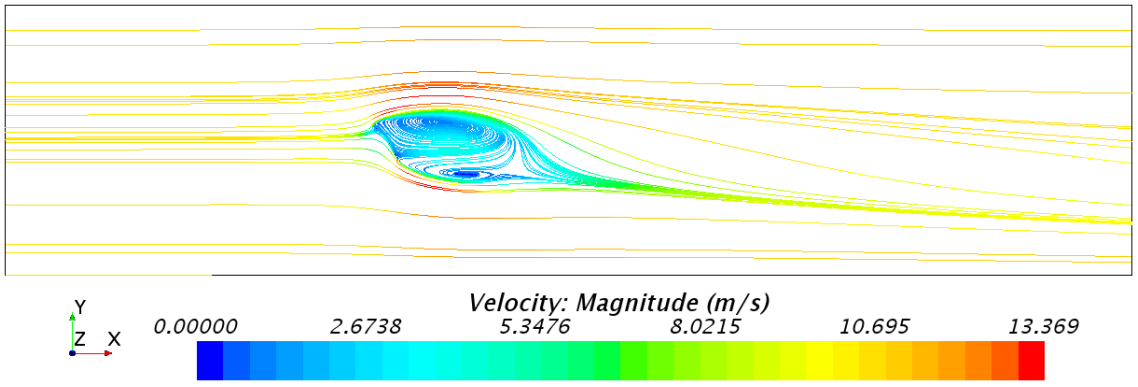

Figure A.151: Top view of the normal computational domain, showing constrained streamlines, at the height of the center of effort (CoE); the cambered sail model, with a sheet angle of 120°.

Pressure Distribution at CoE with the Flat Sail Model in the Large Domain

Fig. A.152 - A.158 shows top view images of the pressure distribution, for the seven different sheet angles with the flat sail model in the large computational domain.

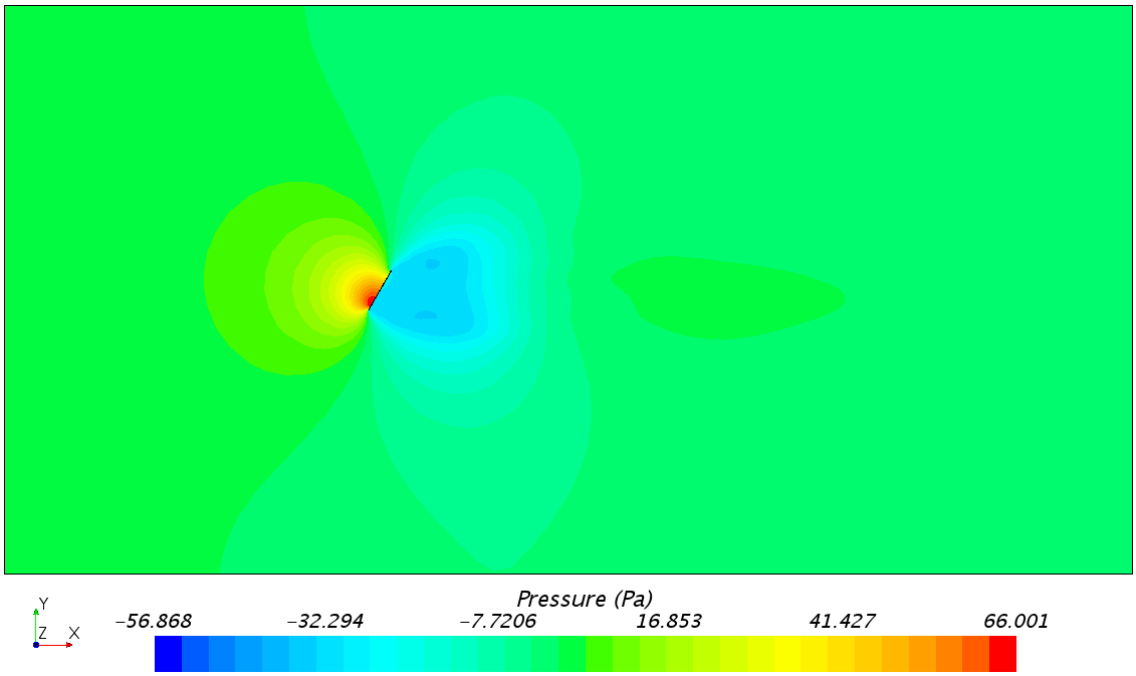

Figure A.152: Top view of the large computational domain, showing the pressure distribution, at the height of the center of effort (CoE); the flat sail model, with a sheet angle of 60°.

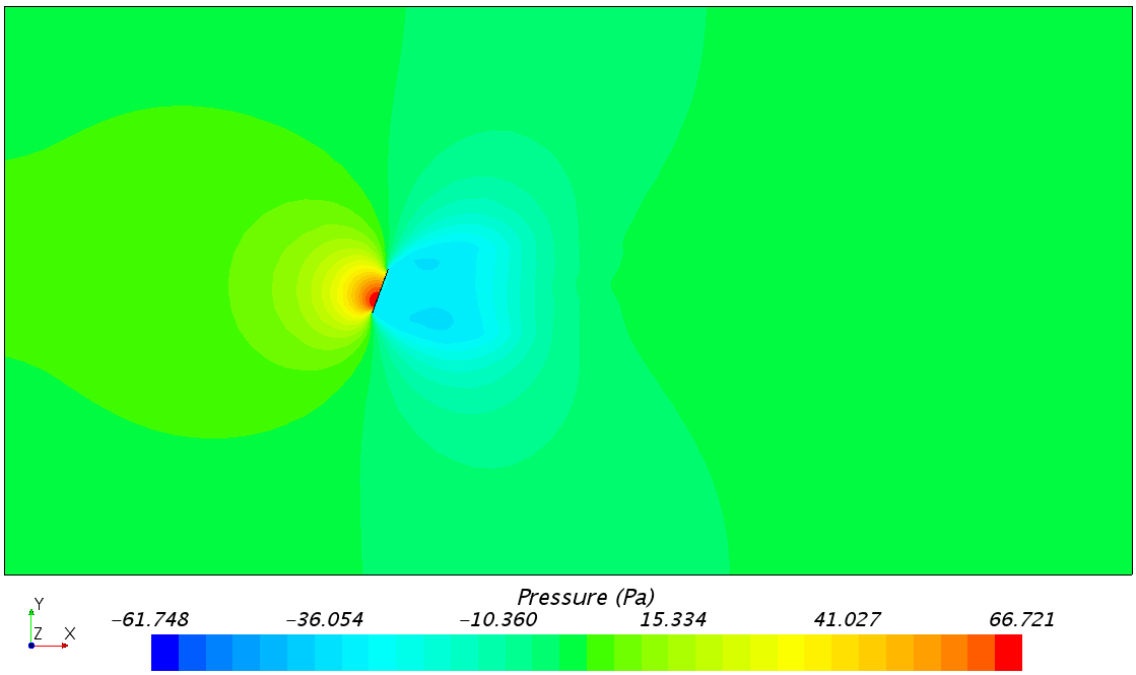

Figure A.153: Top view of the large computational domain, showing the pressure distribution, at the height of the center of effort (CoE); the flat sail model, with a sheet angle of 70°.

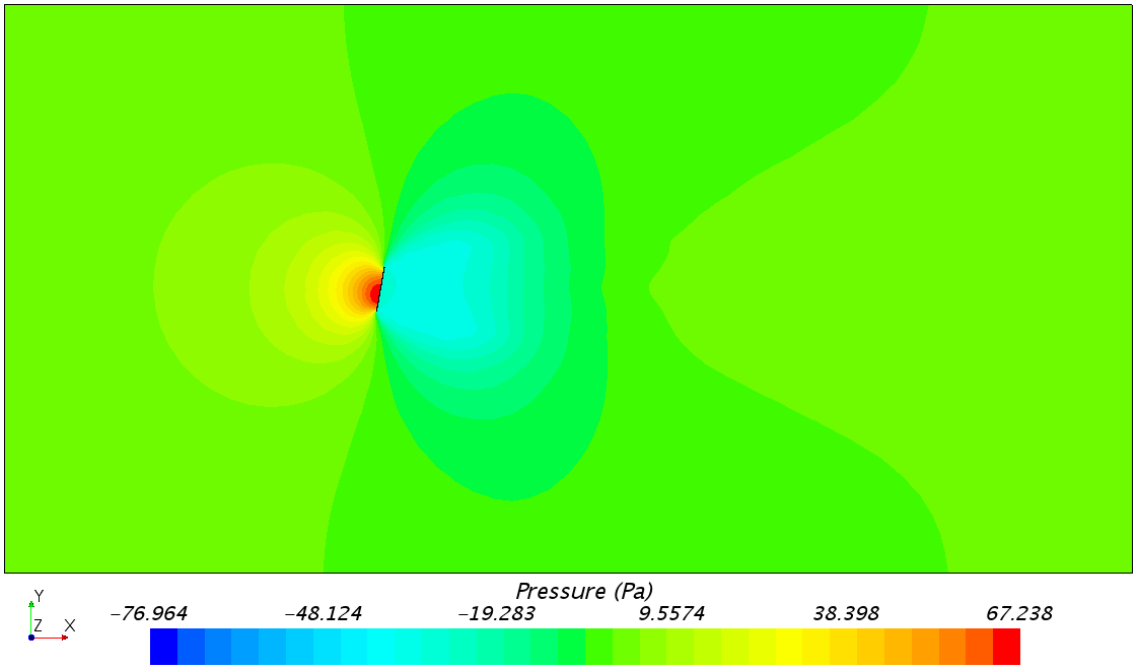

Figure A.154: Top view of the large computational domain, showing the pressure distribution, at the height of the center of effort (CoE); the flat sail model, with a sheet angle of 80°.

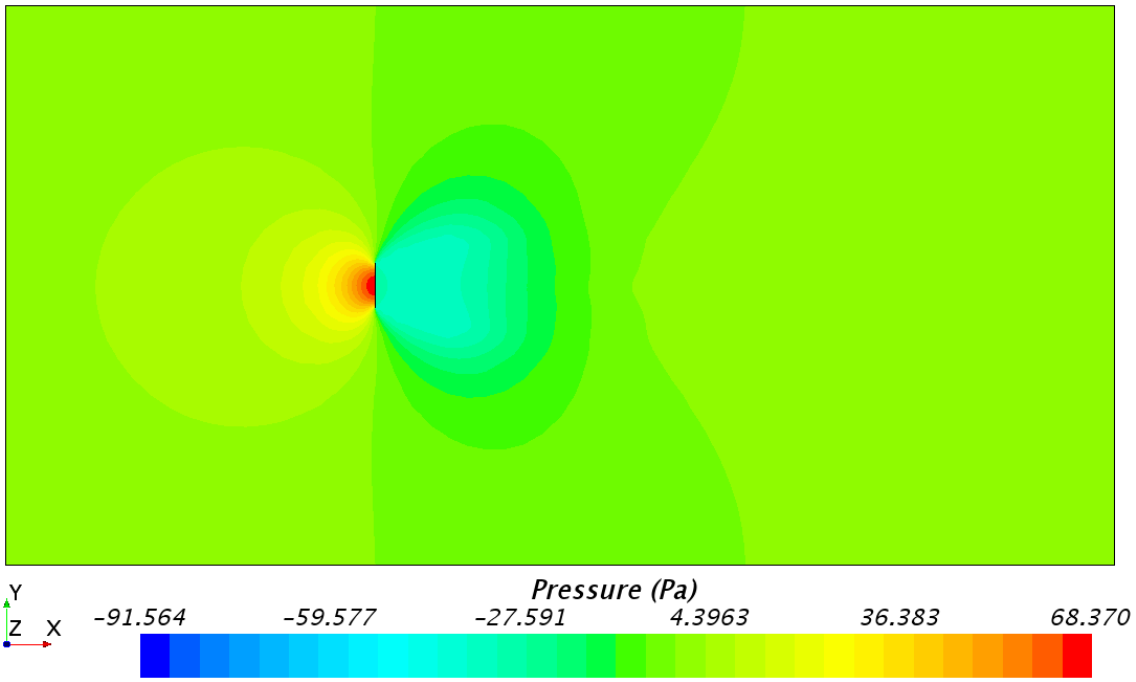

Figure A.155: Top view of the large computational domain, showing the pressure distribution, at the height of the center of effort (CoE); the flat sail model, with a sheet angle of 90°.

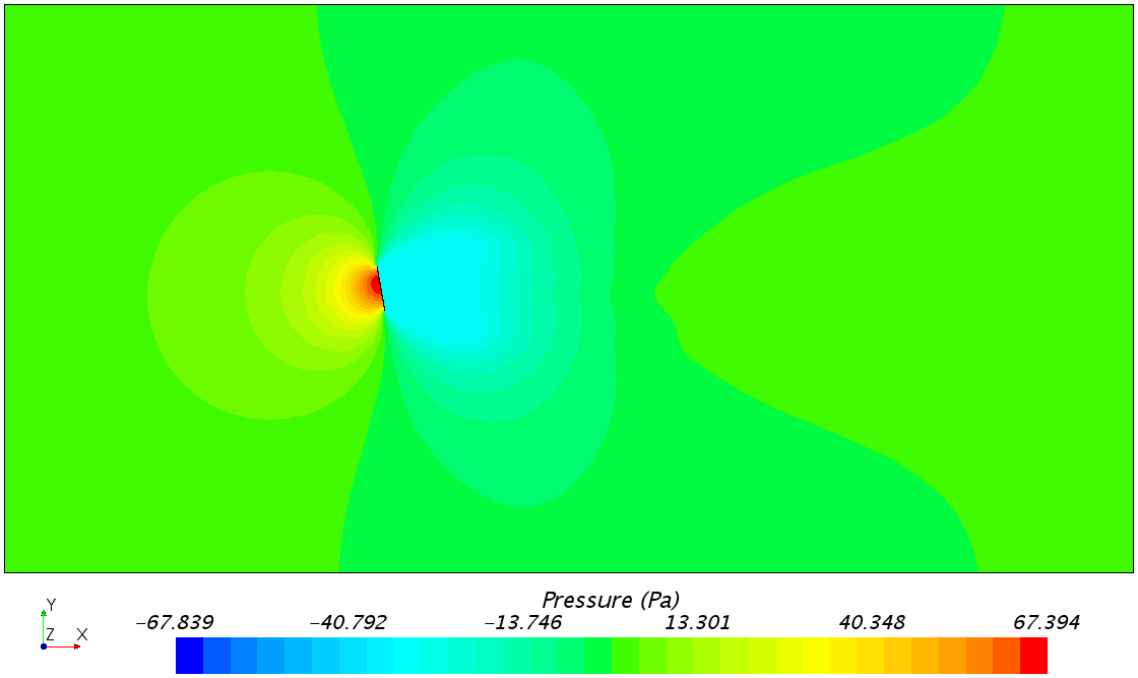

Figure A.156: Top view of the large computational domain, showing the pressure distribution, at the height of the center of effort (CoE); the flat sail model, with a sheet angle of 100°.

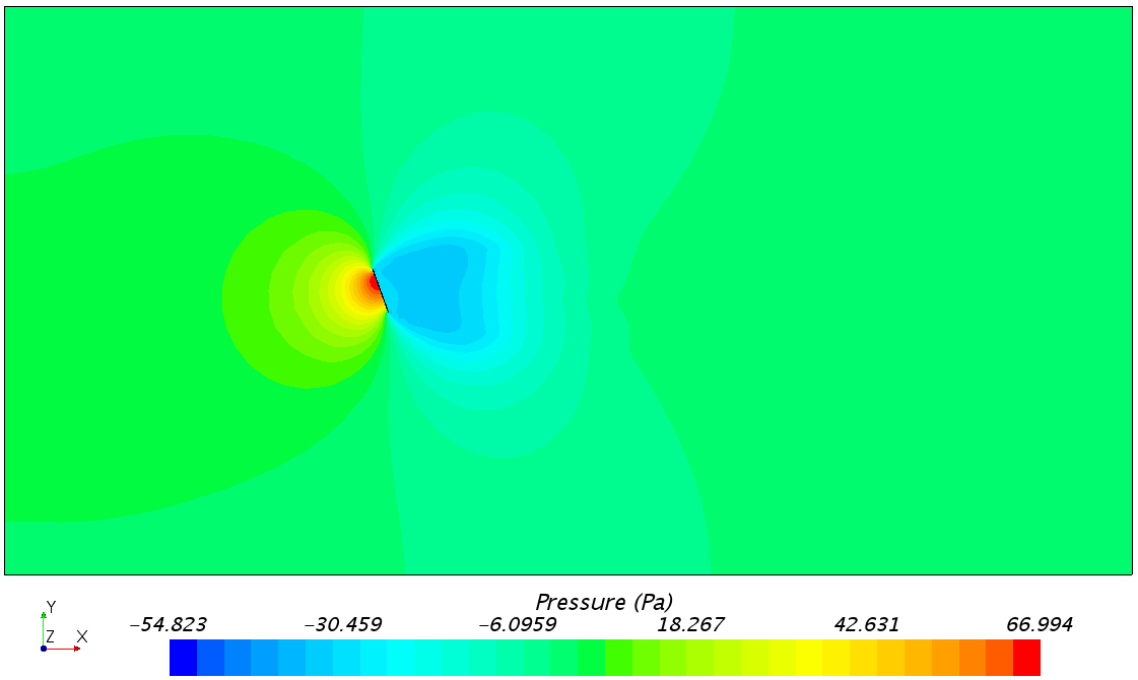

Figure A.157: Top view of the large computational domain, showing the pressure distribution, at the height of the center of effort (CoE); the flat sail model, with a sheet angle of 110°.

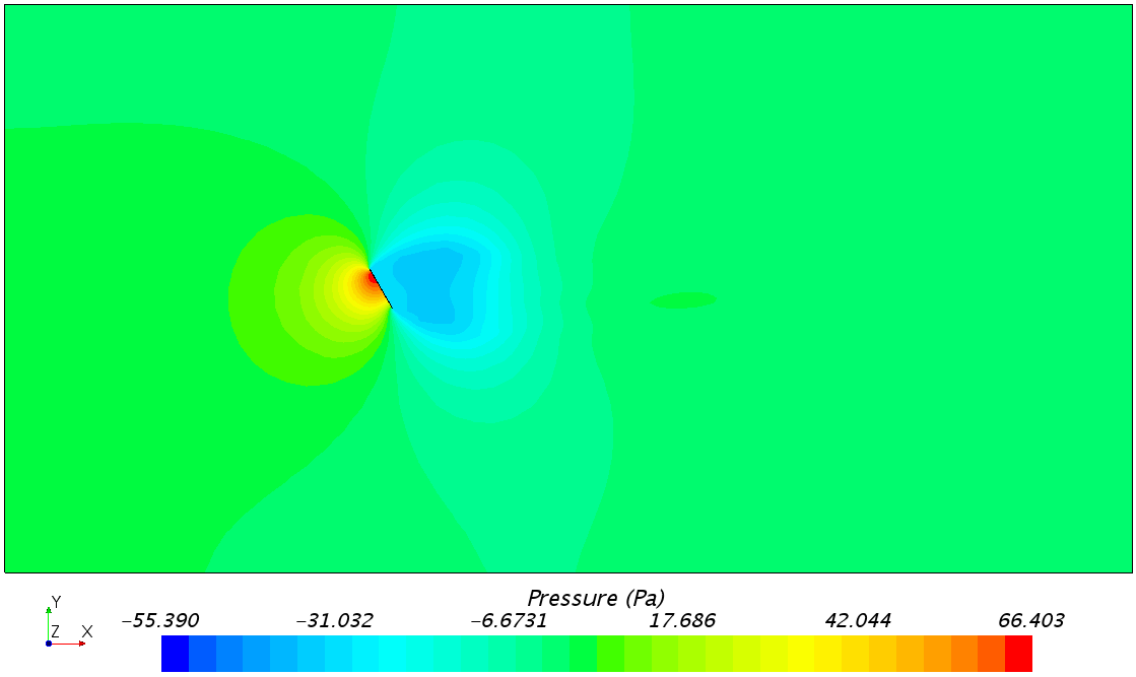

Figure A.158: Top view of the large computational domain, showing the pressure distribution, at the height of the center of effort (CoE); the Flat sail model, with a sheet angle of 120°.

Pressure Distribution at CoE with the Cambered Sail Model in the Large Domain

Fig. A.159 - A.165 shows top view images of the pressure distribution, for the seven different sheet angles with the cambered sail model in the large computational domain.

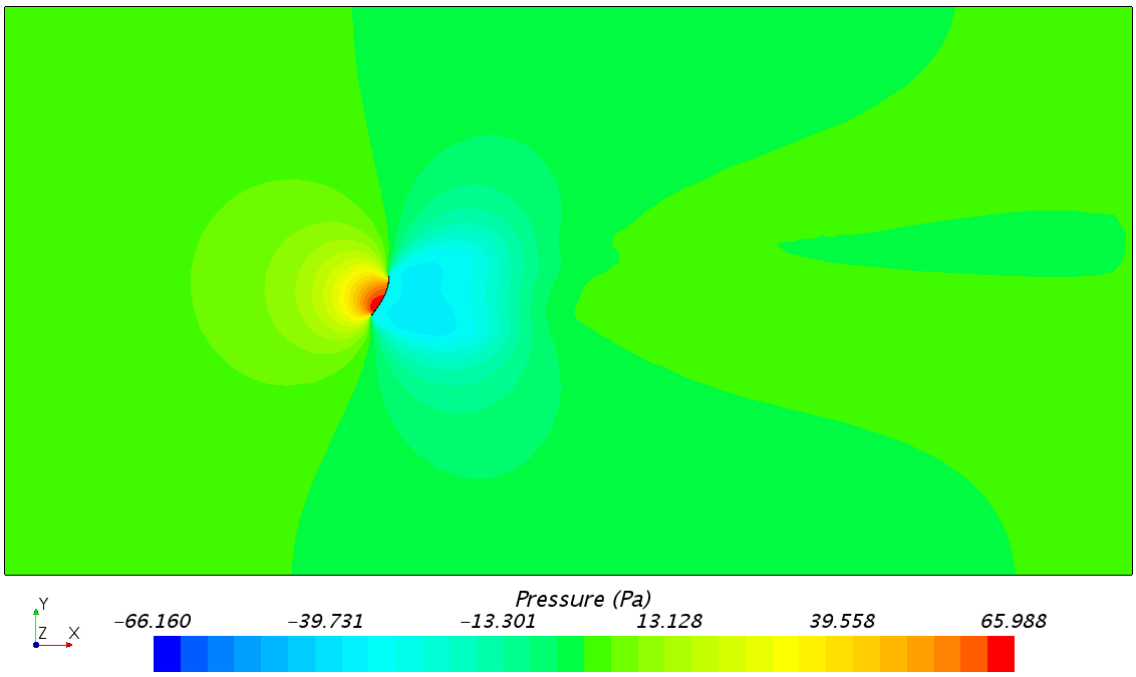

Figure A.159: Top view of the large computational domain, showing the pressure distribution, at the height of the center of effort (CoE); the cambered sail model, with a sheet angle of 60°.

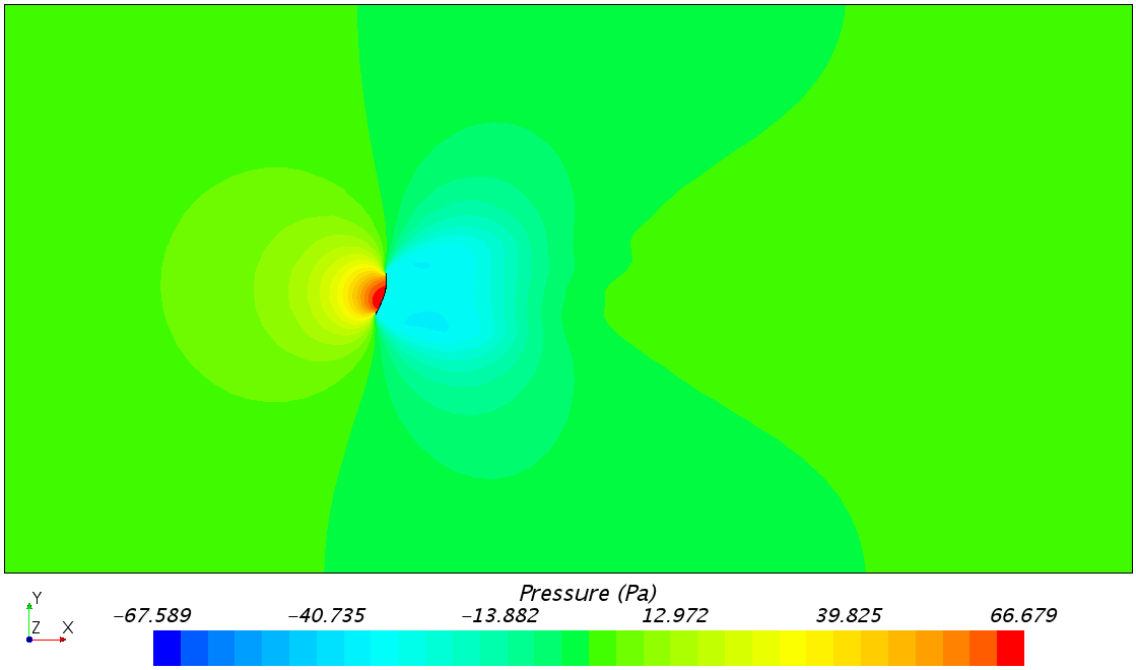

Figure A.160: Top view of the large computational domain, showing the pressure distribution, at the height of the center of effort (CoE); the cambered sail model, with a sheet angle of 70°.

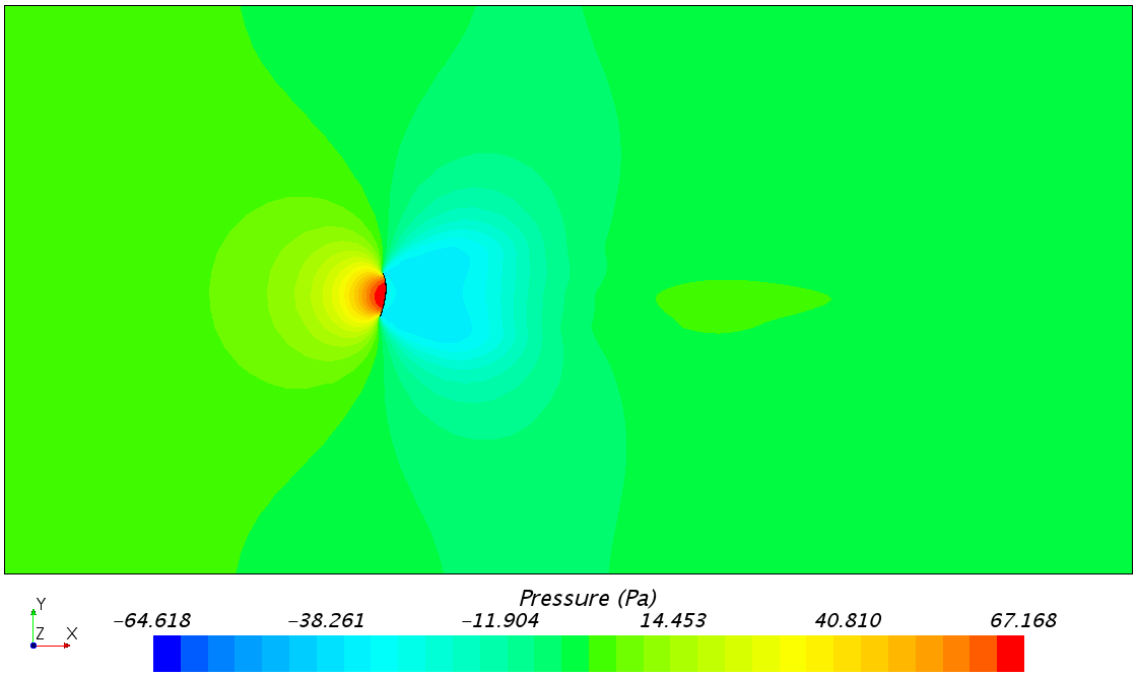

Figure A.161: Top view of the large computational domain, showing the pressure distribution, at the height of the center of effort (CoE); the cambered sail model, with a sheet angle of 80°.

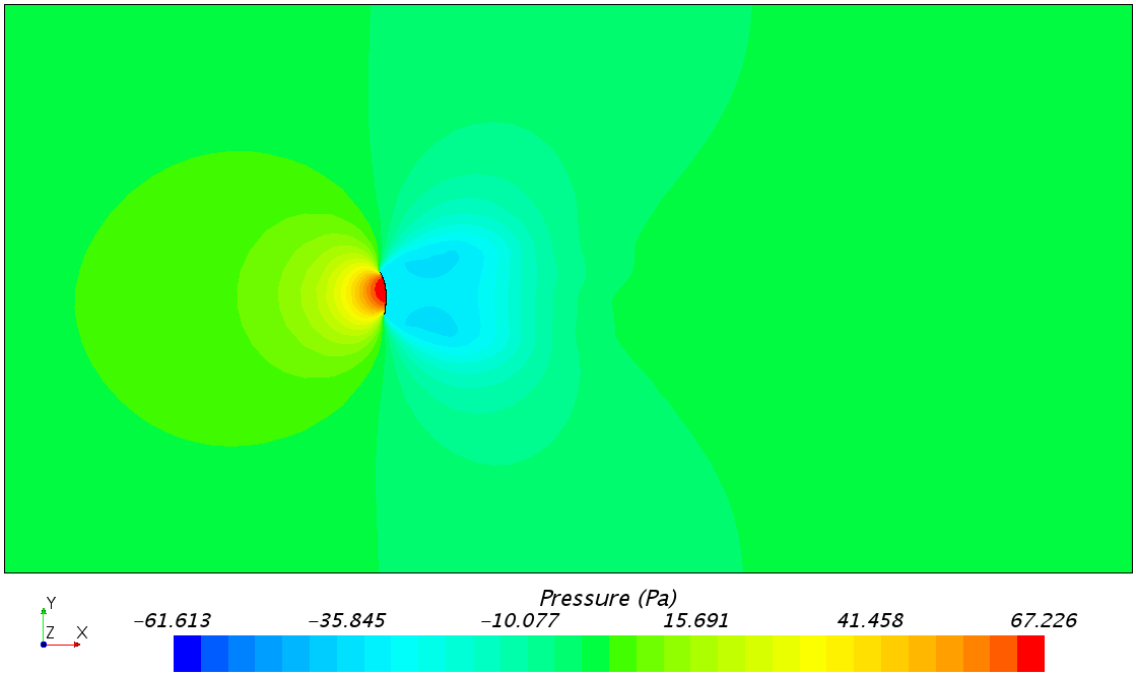

Figure A.162: Top view of the large computational domain, showing the pressure distribution, at the height of the center of effort (CoE); the cambered sail model, with a sheet angle of 90°.

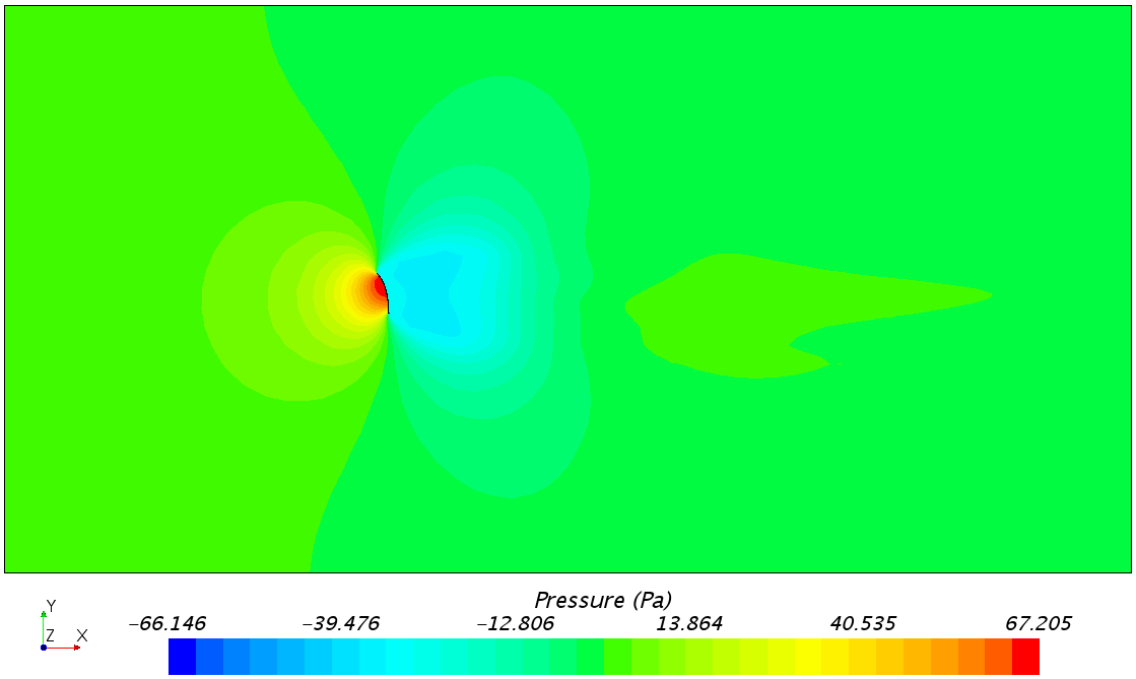

Figure A.163: Top view of the large computational domain, showing the pressure distribution, at the height of the center of effort (CoE); the cambered sail model, with a sheet angle of 100°.

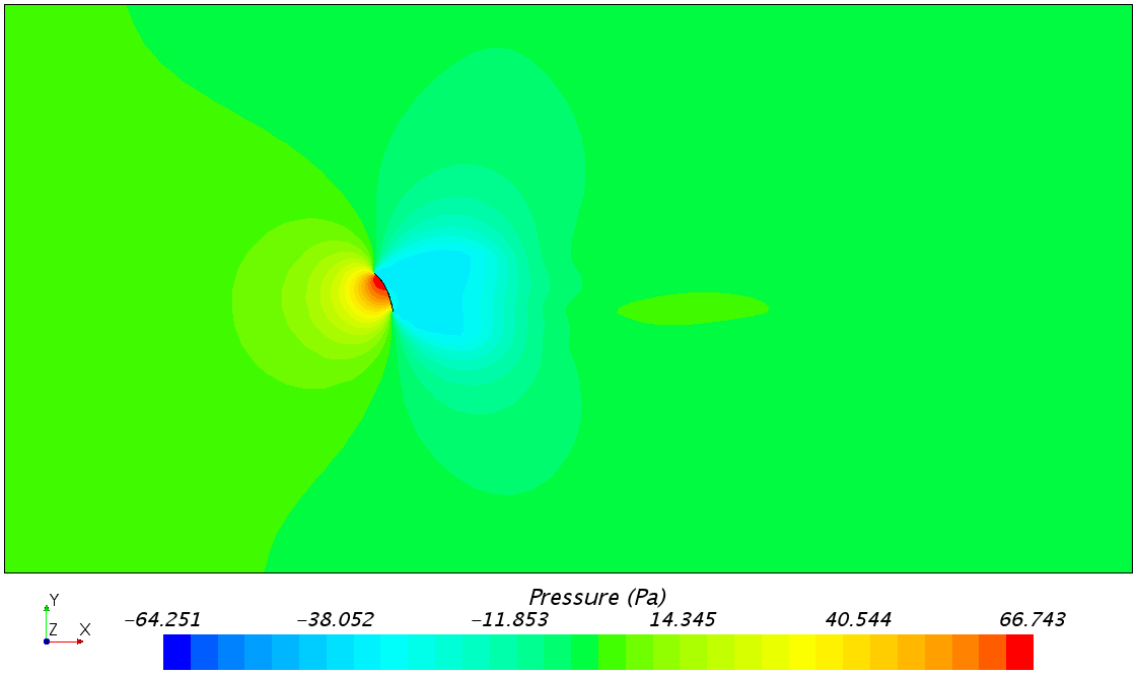

Figure A.164: Top view of the large computational domain, showing the pressure distribution, at the height of the center of effort (CoE); the cambered sail model, with a sheet angle of 110°.

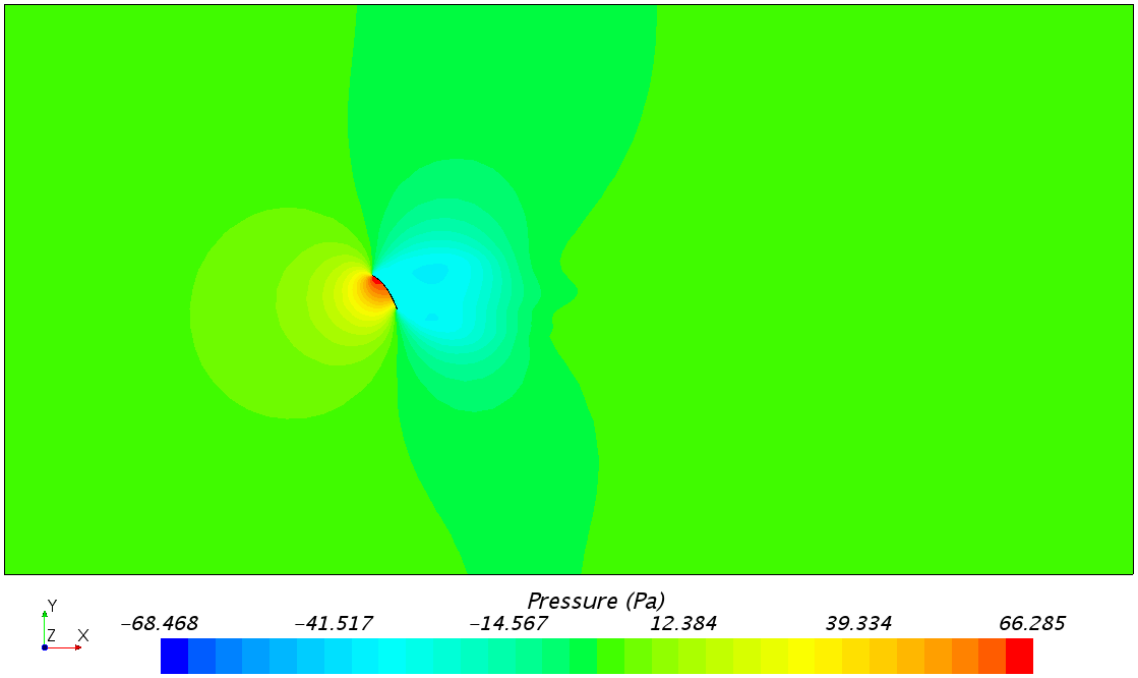

Figure A.165: Top view of the large computational domain, showing the pressure distribution, at the height of the center of effort (CoE); the cambered sail model, with a sheet angle of 120°.

Velocity Distribution at CoE with the Flat Sail Model in the Large Domain

Fig. A.166 - A.172 shows top view images of the velocity distribution, for the seven different sheet angles with the flat sail model in the large computational domain.

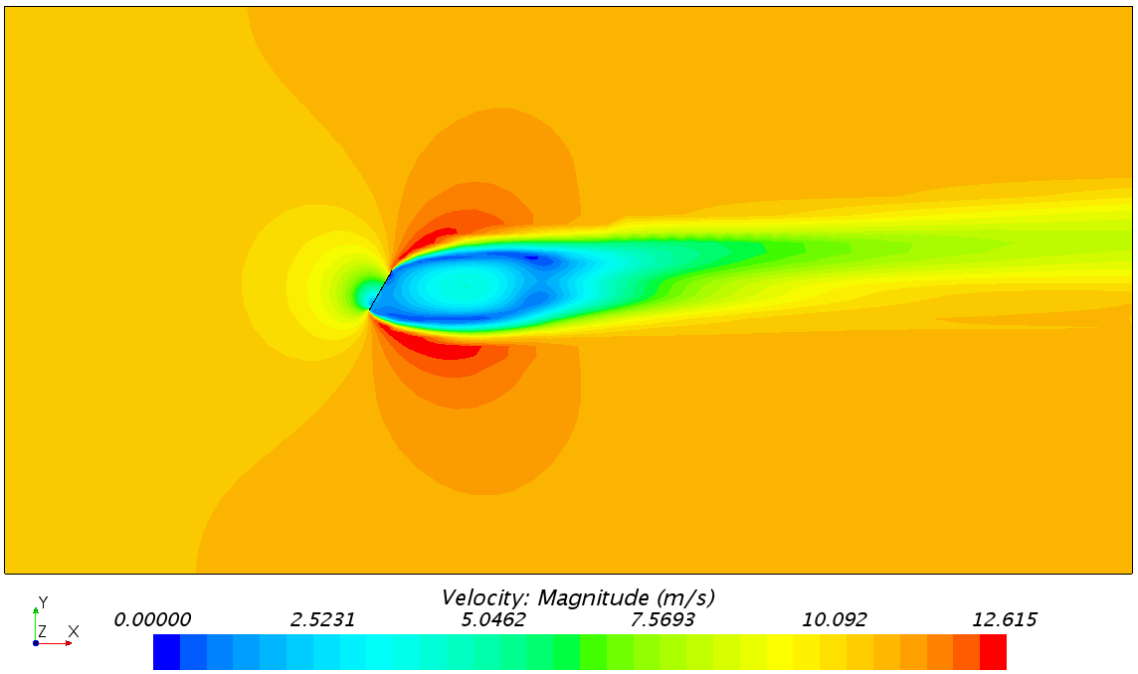

Figure A.166: Top view of the large computational domain, showing the velocity distribution, at the height of the center of effort (CoE); the flat sail model, with a sheet angle of 60°.

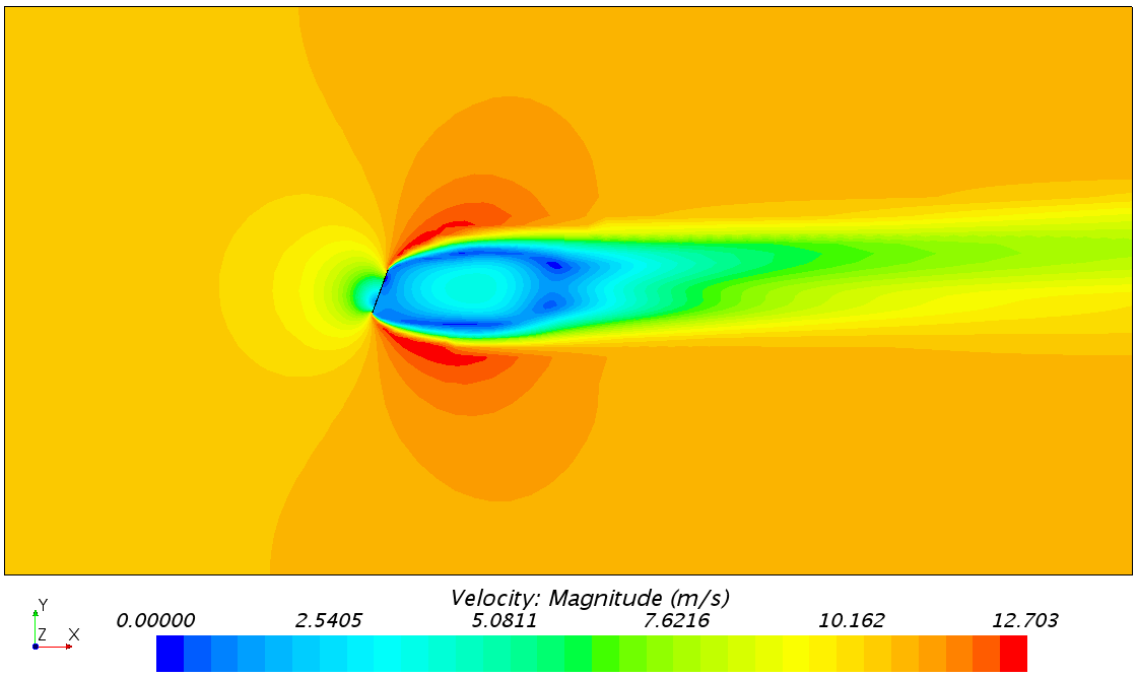

Figure A.167: Top view of the large computational domain, showing the velocity distribution, at the height of the center of effort (CoE); the flat sail model, with a sheet angle of 70°.

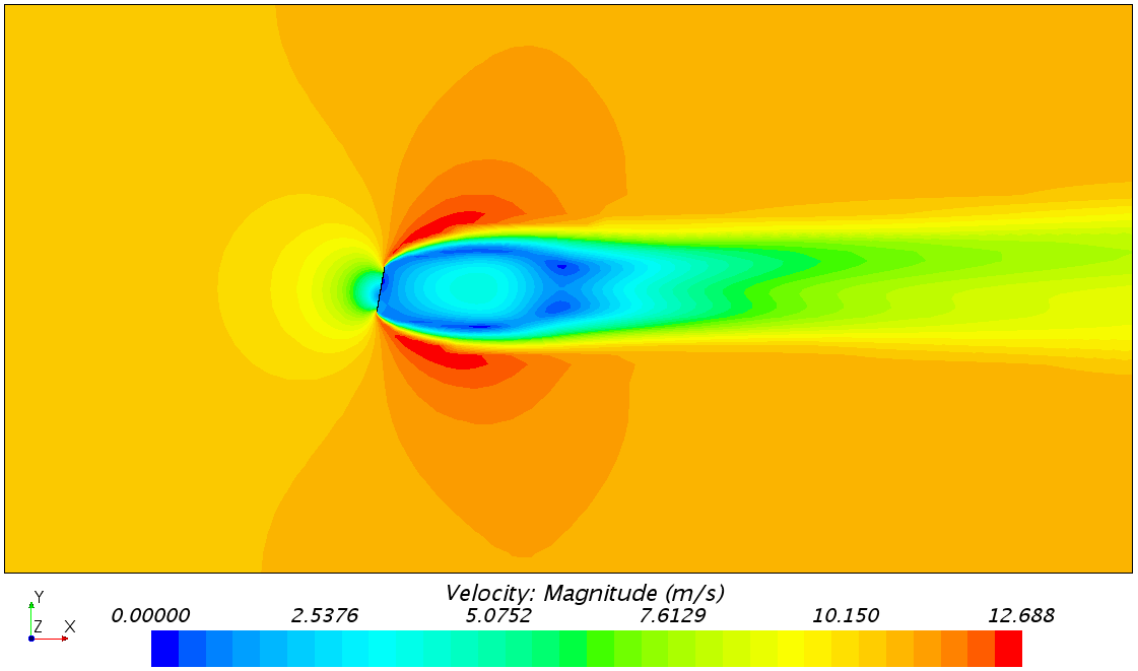

Figure A.168: Top view of the large computational domain, showing the velocity distribution, at the height of the center of effort (CoE); the flat sail model, with a sheet angle of 80°.

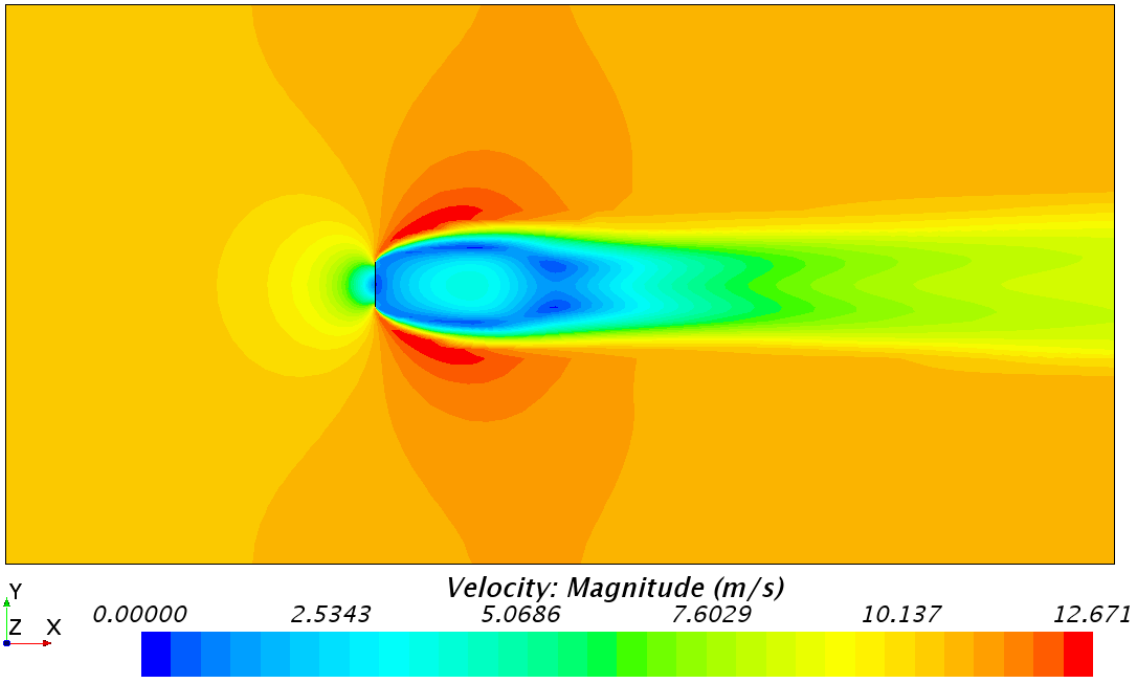

Figure A.169: Top view of the large computational domain, showing the velocity distribution, at the height of the center of effort (CoE); the flat sail model, with a sheet angle of 90°.

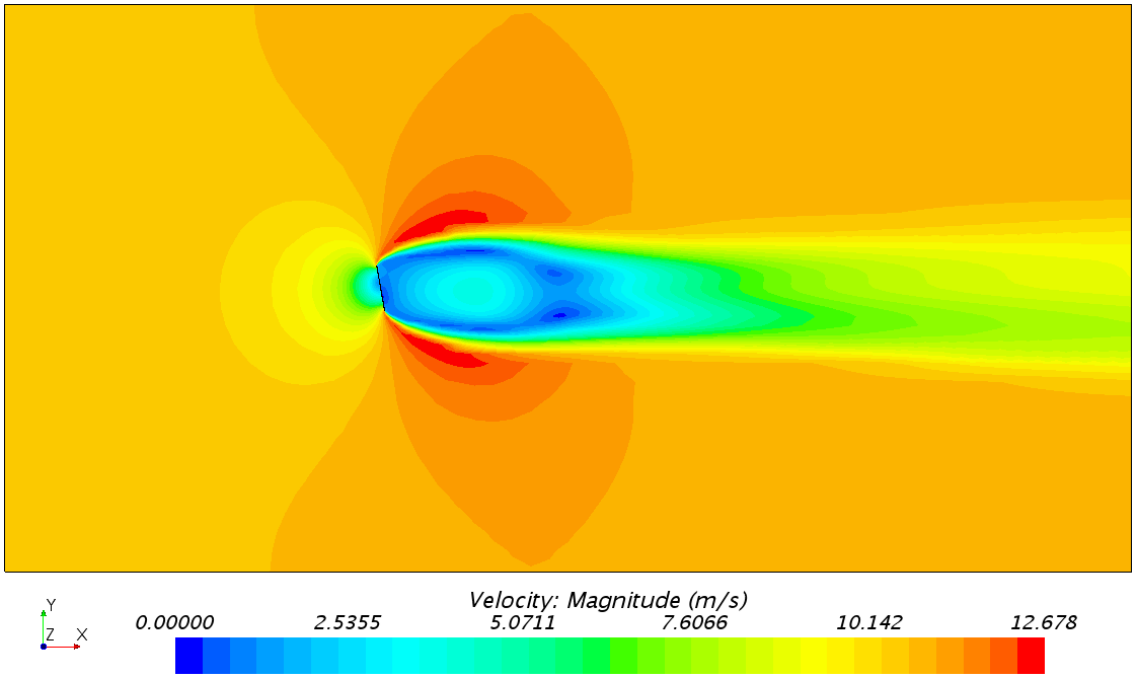

Figure A.170: Top view of the large computational domain, showing the velocity distribution, at the height of the center of effort (CoE); the flat sail model, with a sheet angle of 100°.

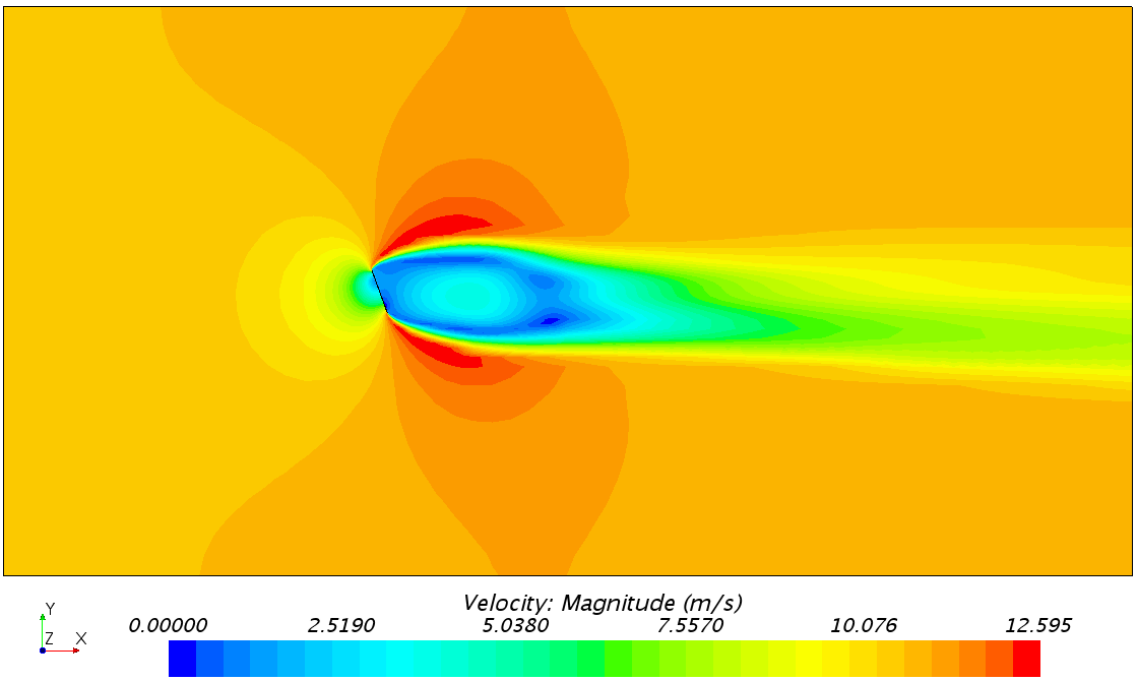

Figure A.171: Top view of the large computational domain, showing the velocity distribution, at the height of the center of effort (CoE); the flat sail model, with a sheet angle of 110°.

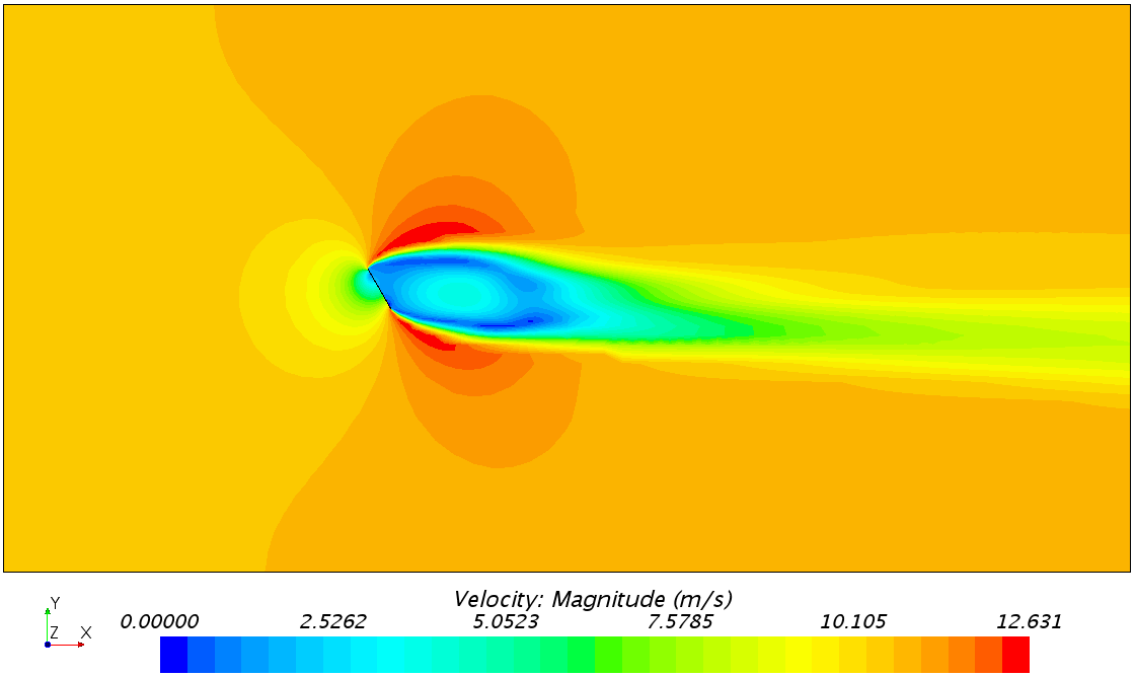

Figure A.172: Top view of the large computational domain, showing the velocity distribution, at the height of the center of effort (CoE); the flat sail model, with a sheet angle of 120°.

Velocity Distribution at CoE with the Cambered Sail Model in the Large Domain

Fig. A.173 - A.179 shows top view images of the velocity distribution, for the seven different sheet angles with the cambered sail model in the large computational domain.

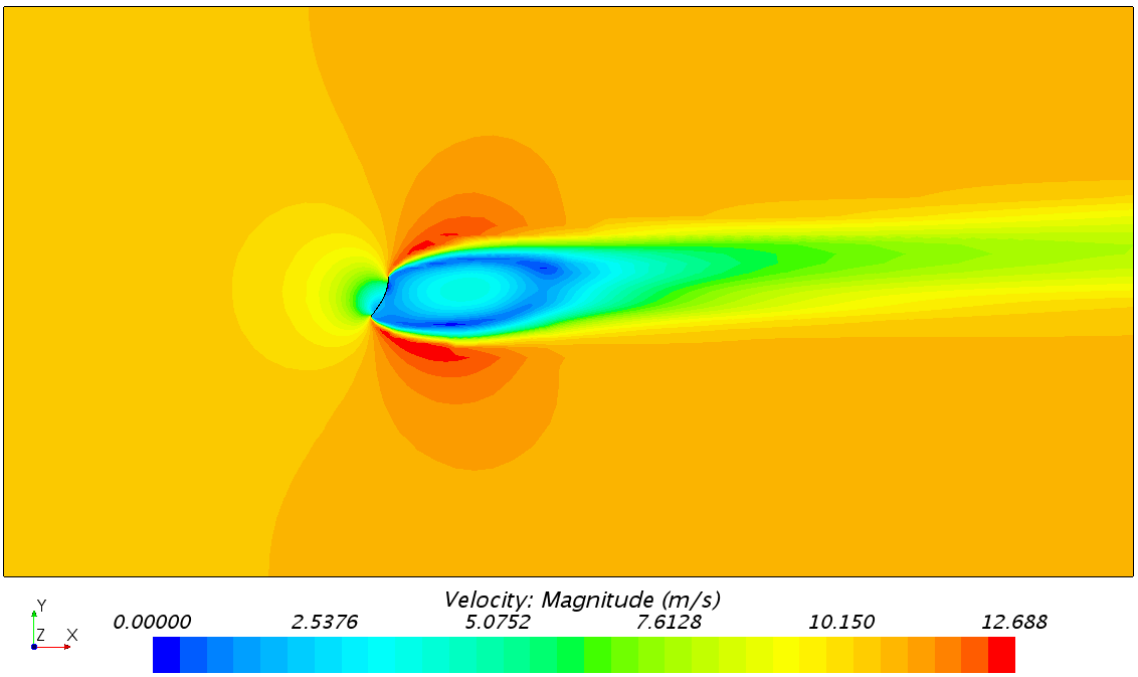

Figure A.173: Top view of the large computational domain, showing the velocity distribution, at the height of the center of effort (CoE); the cambered sail model, with a sheet angle of 60°.

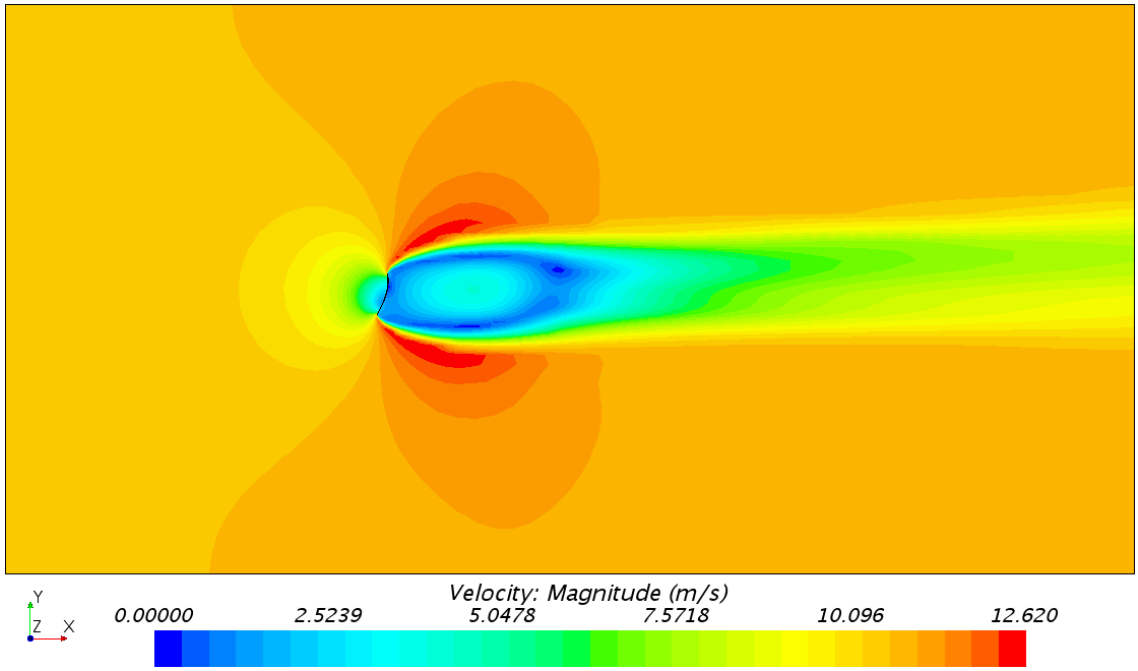

Figure A.174: Top view of the large computational domain, showing the velocity distribution, at the height of the center of effort (CoE); the cambered sail model, with a sheet angle of 70°.

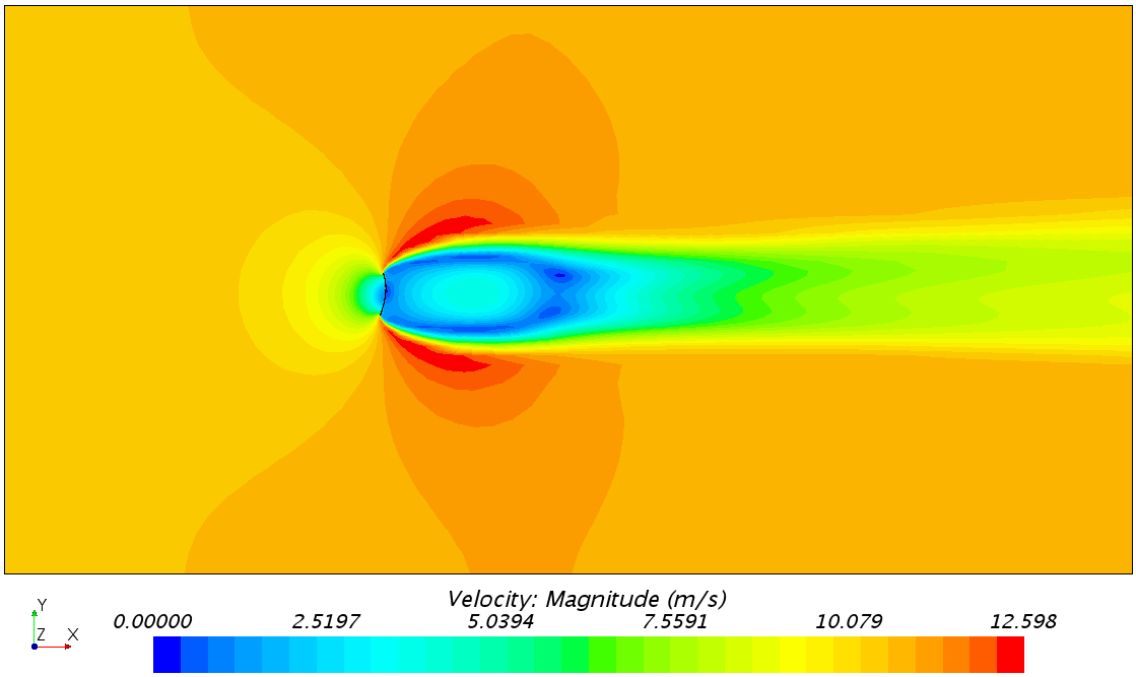

Figure A.175: Top view of the large computational domain, showing the velocity distribution, at the height of the center of effort (CoE); the cambered sail model, with a sheet angle of 80°.

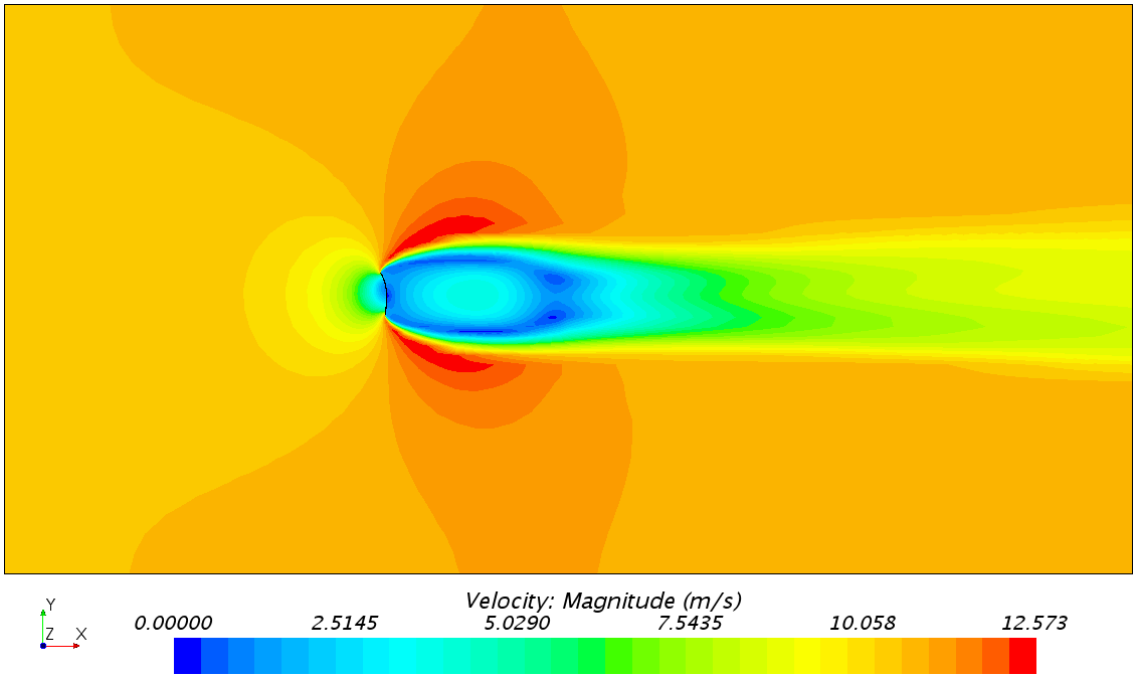

Figure A.176: Top view of the large computational domain, showing the velocity distribution, at the height of the center of effort (CoE); the cambered sail model, with a sheet angle of 90°.

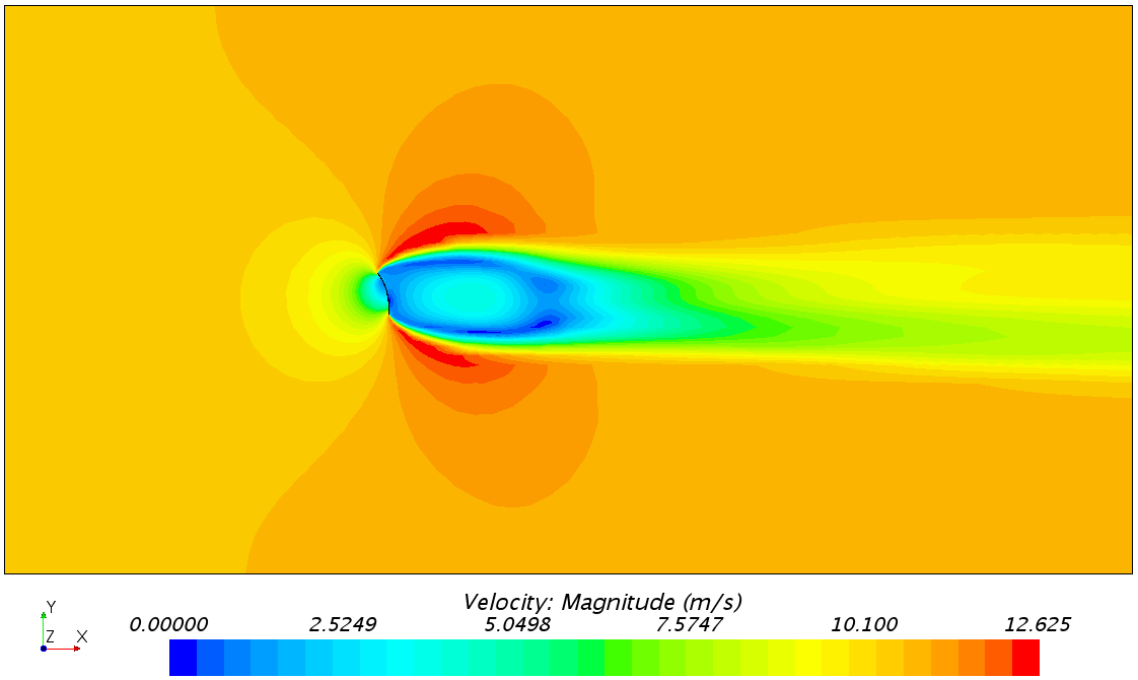

Figure A.177: Top view of the large computational domain, showing the velocity distribution, at the height of the center of effort (CoE); the cambered sail model, with a sheet angle of 100°.

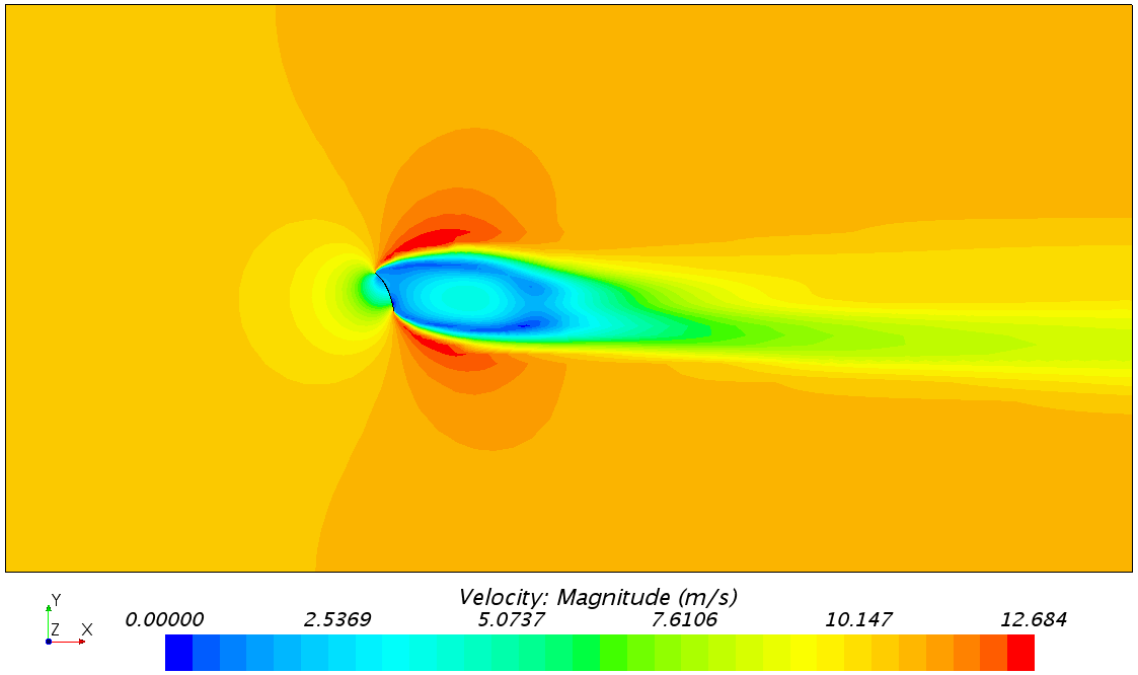

Figure A.178: Top view of the large computational domain, showing the velocity distribution, at the height of the center of effort (CoE); the cambered sail model, with a sheet angle of 110°.

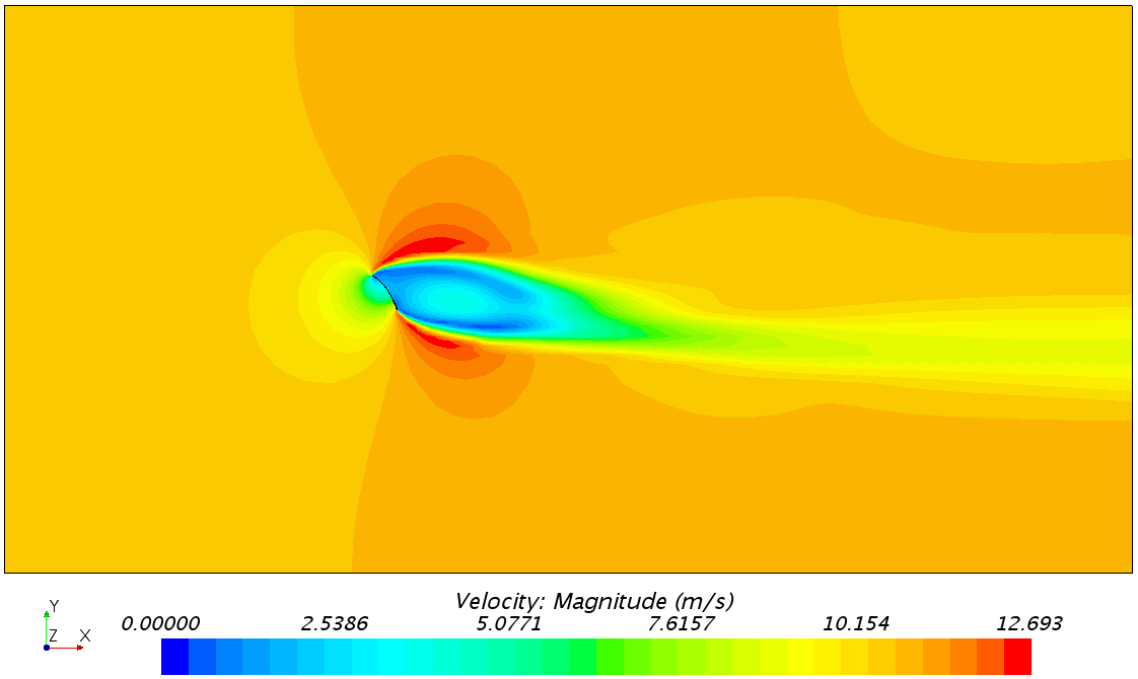

Figure A.179: Top view of the large computational domain, showing the velocity distribution, at the height of the center of effort (CoE); the cambered sail model, with a sheet angle of 120°.

Constrained Streamlines at CoE with the Flat Sail Model in the Large Domain

Fig. A.180 - A.186 shows top view images of constrained streamlines, for the seven different sheet angles with the flat sail model in the large computational domain.

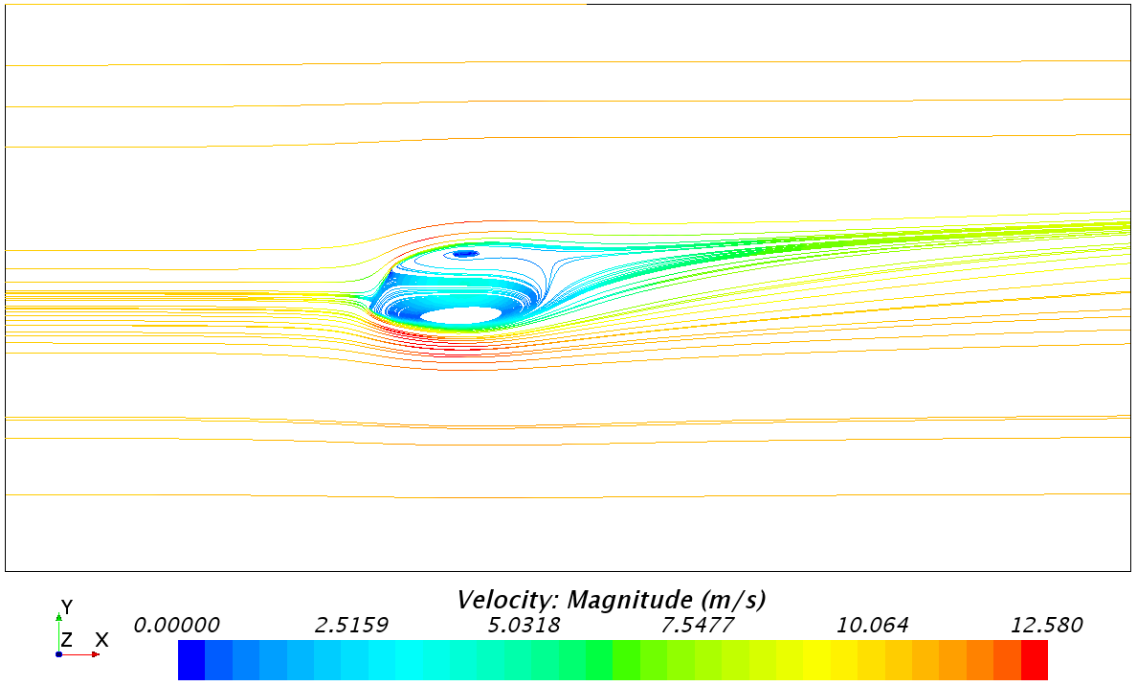

Figure A.180: Top view of the large computational domain, showing constrained streamlines, at the height of the center of effort (CoE); the flat sail model, with a sheet angle of 60°.

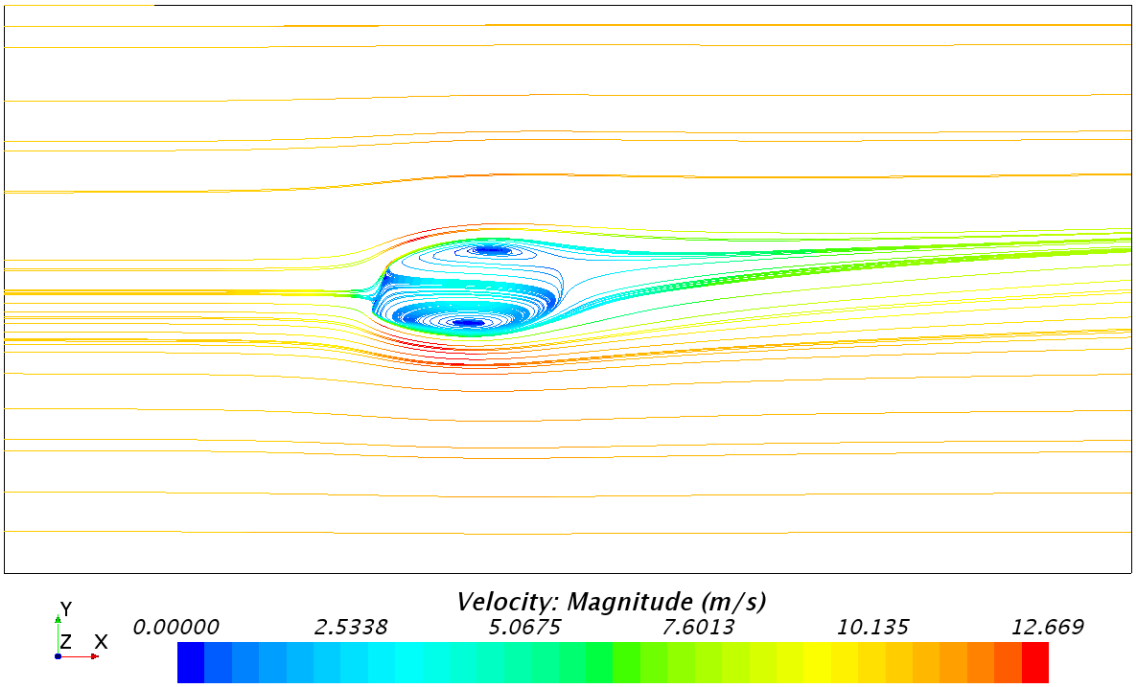

Figure A.181: Top view of the large computational domain, showing constrained streamlines, at the height of the center of effort (CoE); the flat sail model, with a sheet angle of 70°.

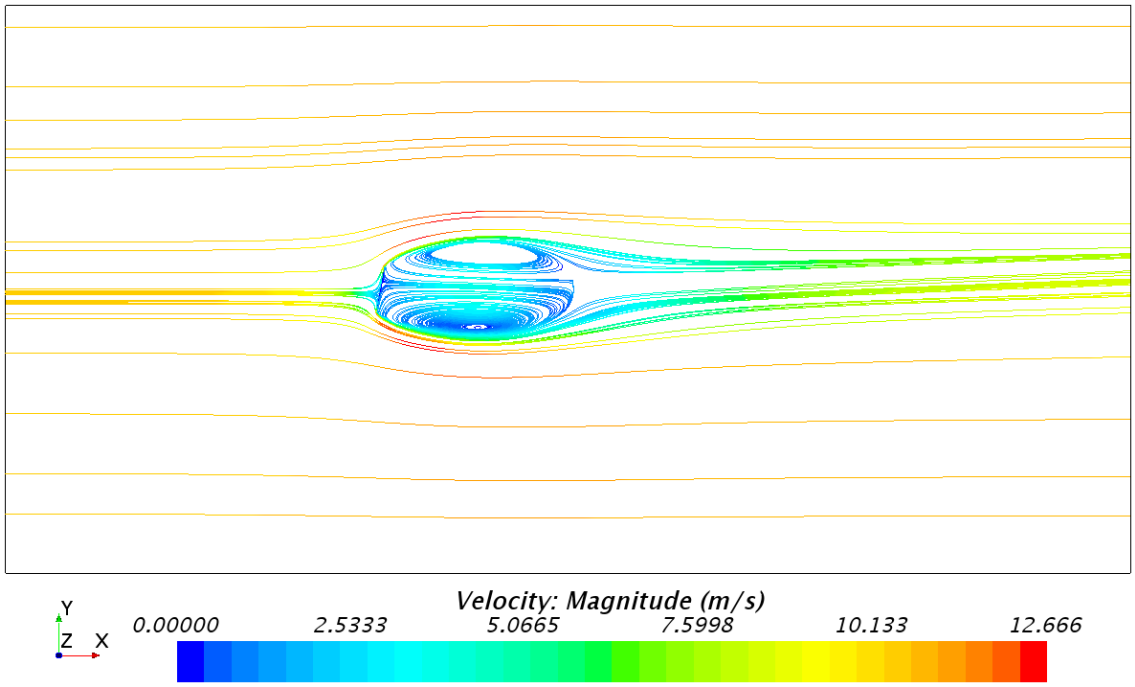

Figure A.182: Top view of the large computational domain, showing constrained streamlines, at the height of the center of effort (CoE); the flat sail model, with a sheet angle of 80°.

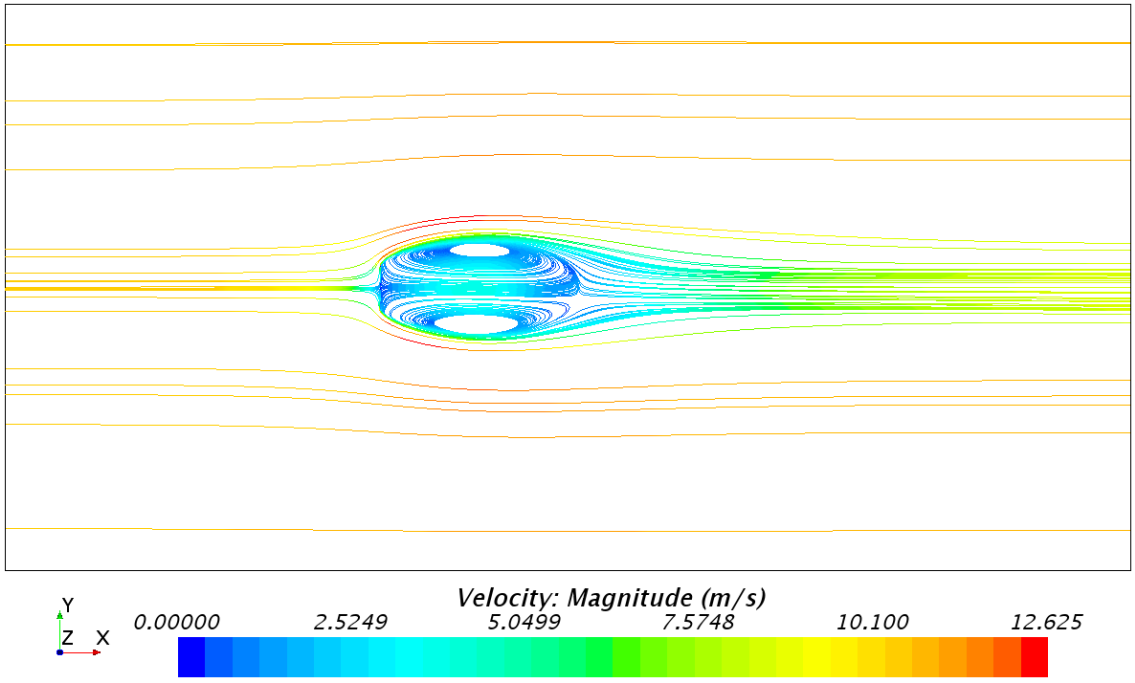

Figure A.183: Top view of the large computational domain, showing constrained streamlines, at the height of the center of effort (CoE); the flat sail model, with a sheet angle of 90°.

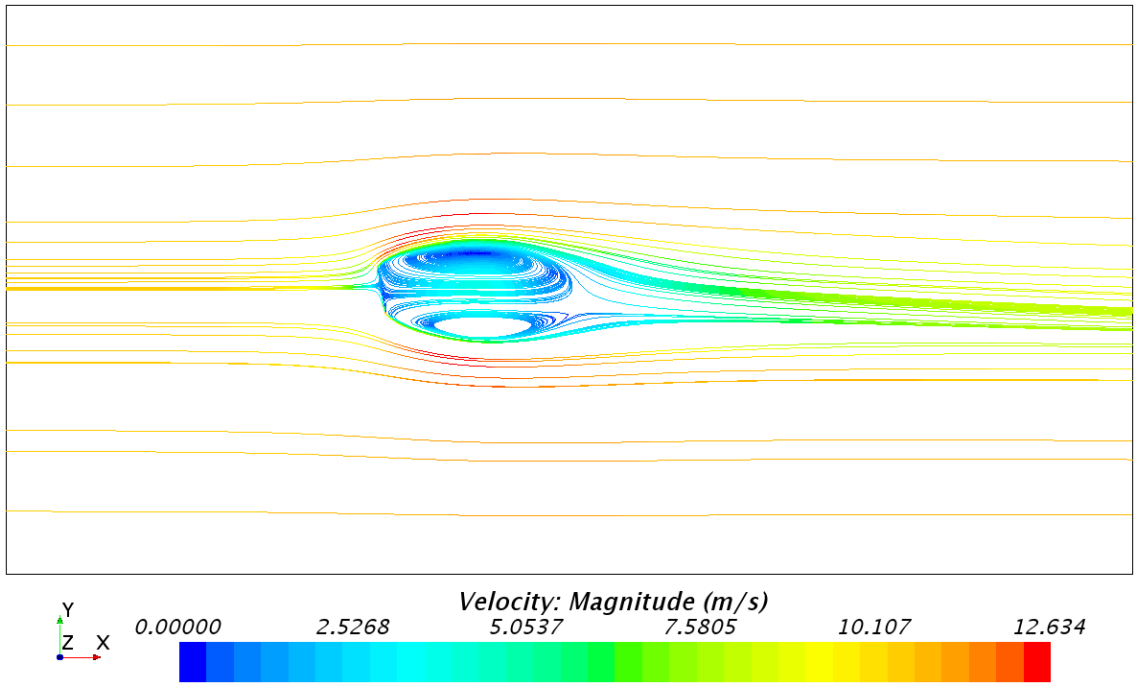

Figure A.184: Top view of the large computational domain, showing constrained streamlines, at the height of the center of effort (CoE); the flat sail model, with a sheet angle of 100°.

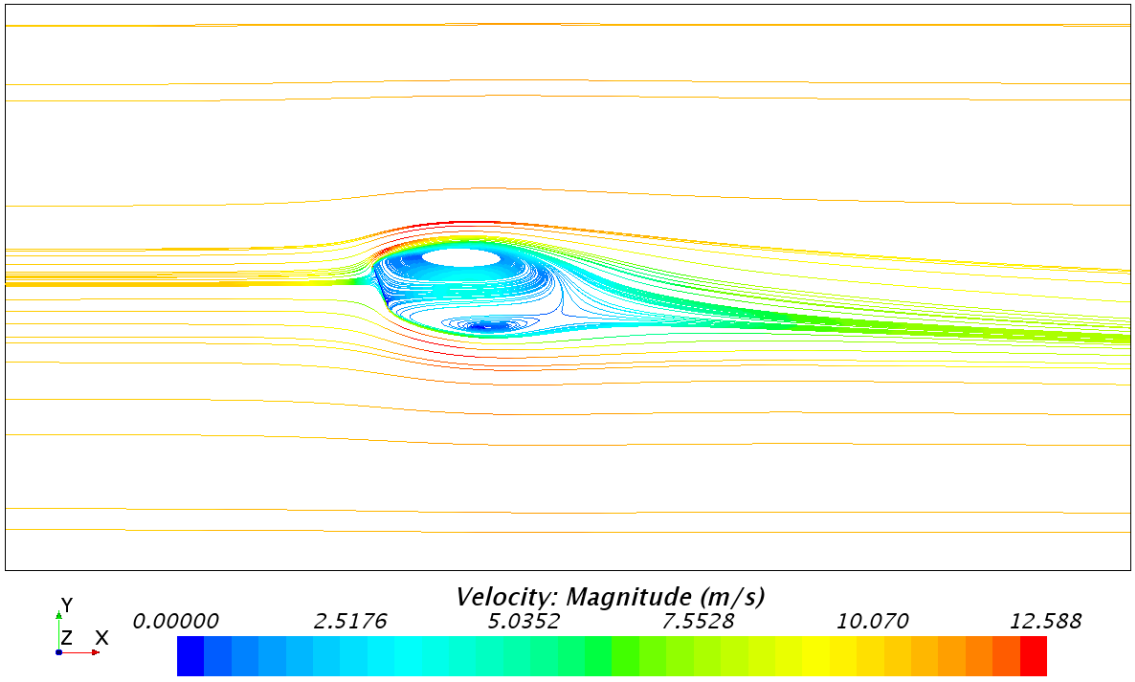

Figure A.185: Top view of the large computational domain, showing constrained streamlines, at the height of the center of effort (CoE); the flat sail model, with a sheet angle of 110°.

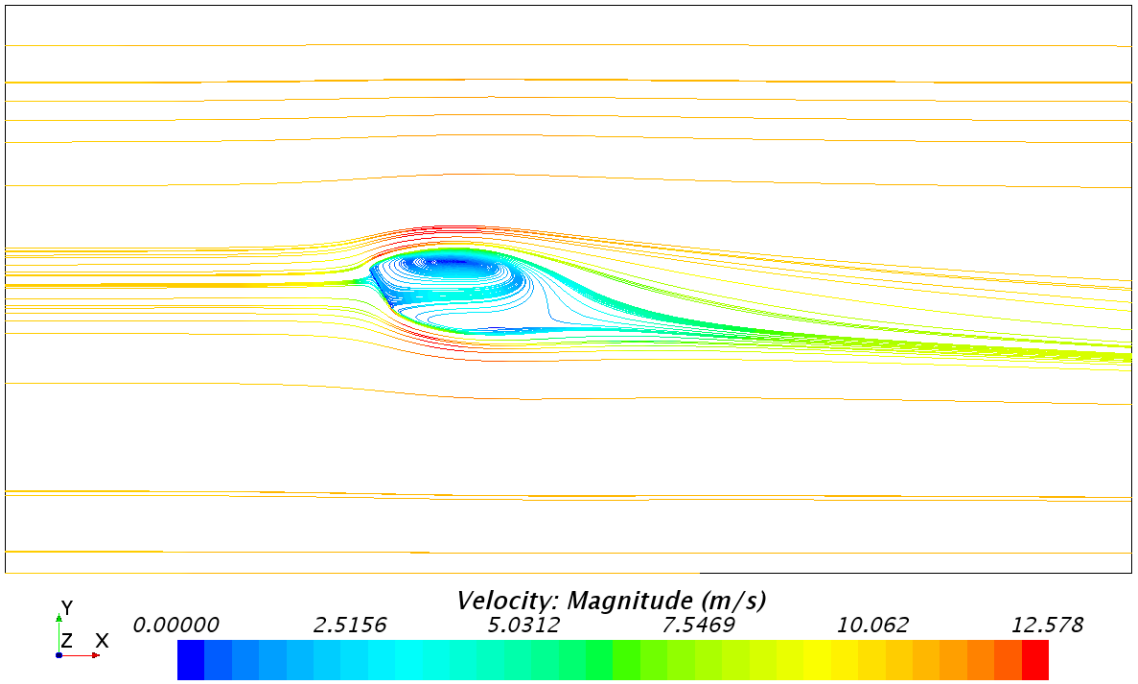

Figure A.186: Top view of the large computational domain, showing constrained streamlines, at the height of the center of effort (CoE); the flat sail model, with a sheet angle of 120°.

Constrained Streamlines at CoE with the Cambered Sail Model in the Large Domain

Fig. A.187 - A.193 shows top view images of constrained streamlines, for the seven different sheet angles with the cambered sail model in the large computational domain.

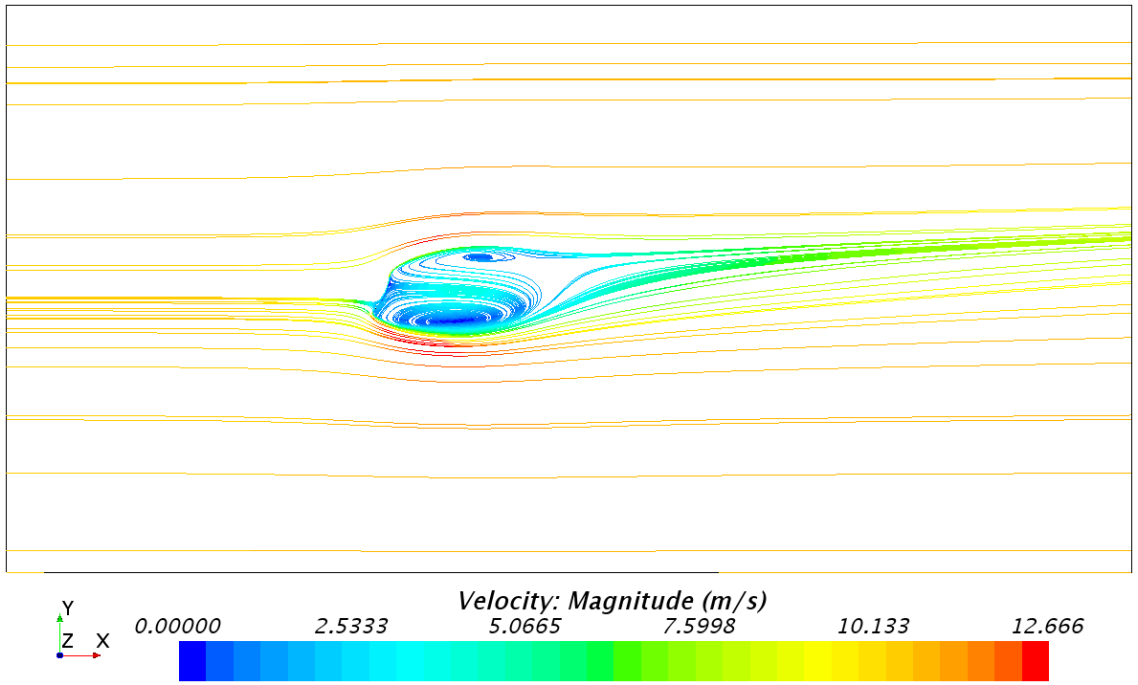

Figure A.187: Top view of the large computational domain, showing constrained streamlines, at the height of the center of effort (CoE); the cambered sail model, with a sheet angle of 60°.

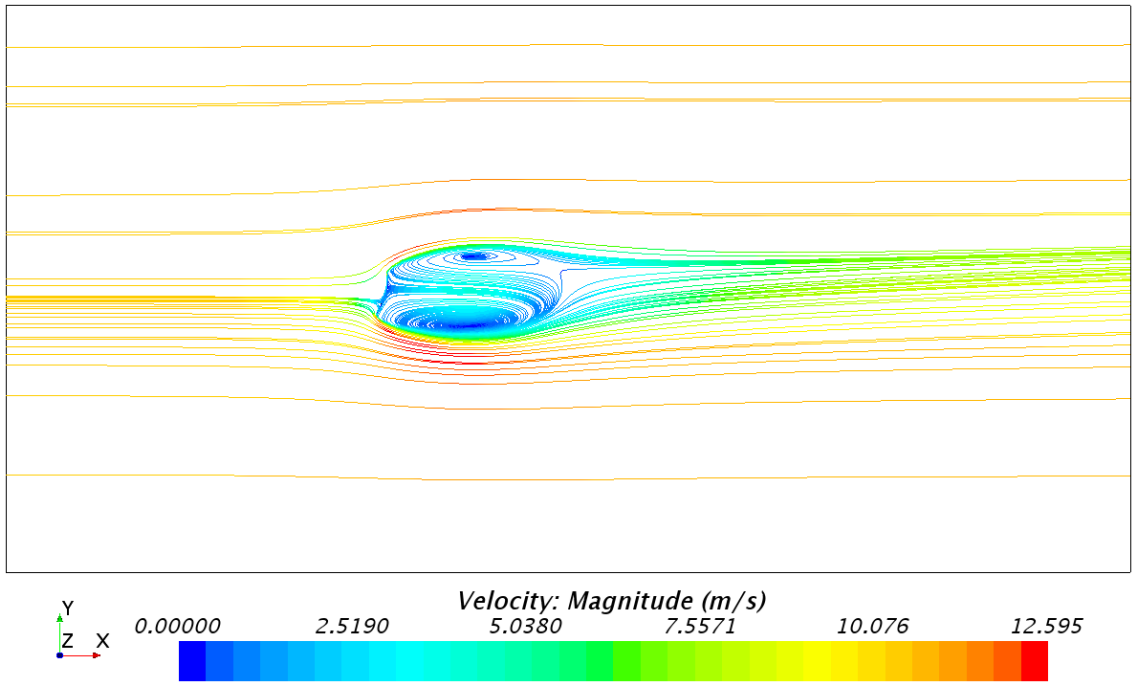

Figure A.188: Top view of the large computational domain, showing constrained streamlines, at the height of the center of effort (CoE); the cambered sail model, with a sheet angle of 70°.

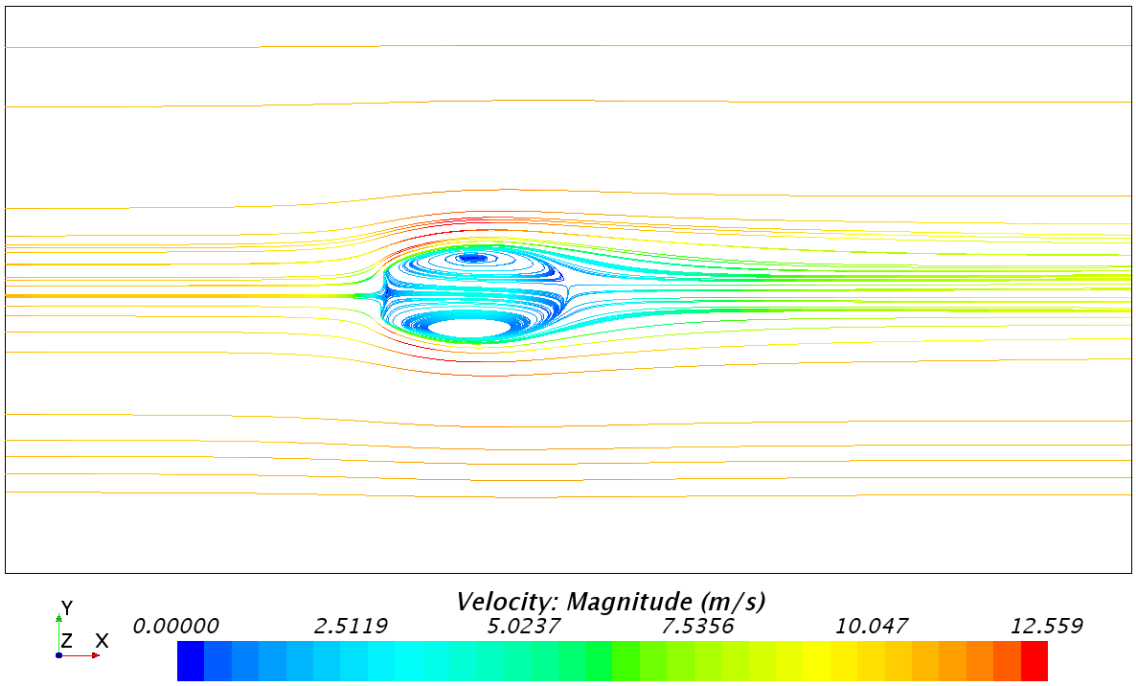

Figure A.189: Top view of the large computational domain, showing constrained streamlines, at the height of the center of effort (CoE); the cambered sail model, with a sheet angle of 80°.

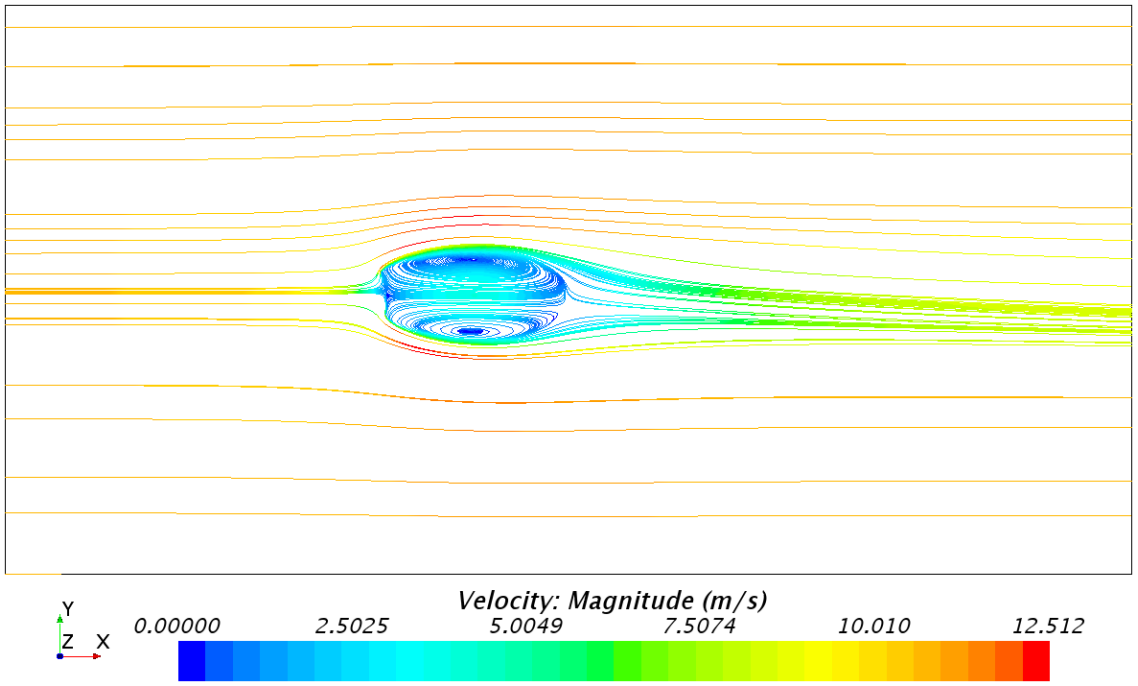

Figure A.190: Top view of the large computational domain, showing constrained streamlines, at the height of the center of effort (CoE); the cambered sail model, with a sheet angle of 90°.

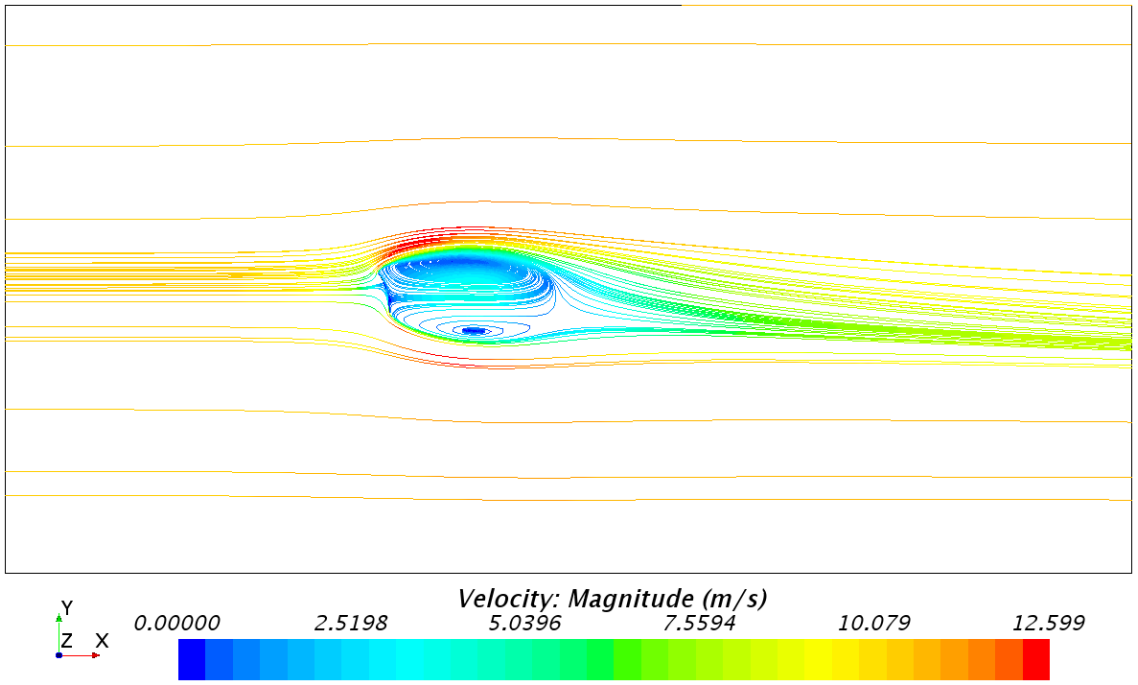

Figure A.191: Top view of the large computational domain, showing constrained streamlines, at the height of the center of effort (CoE); the cambered sail model, with a sheet angle of 100°.

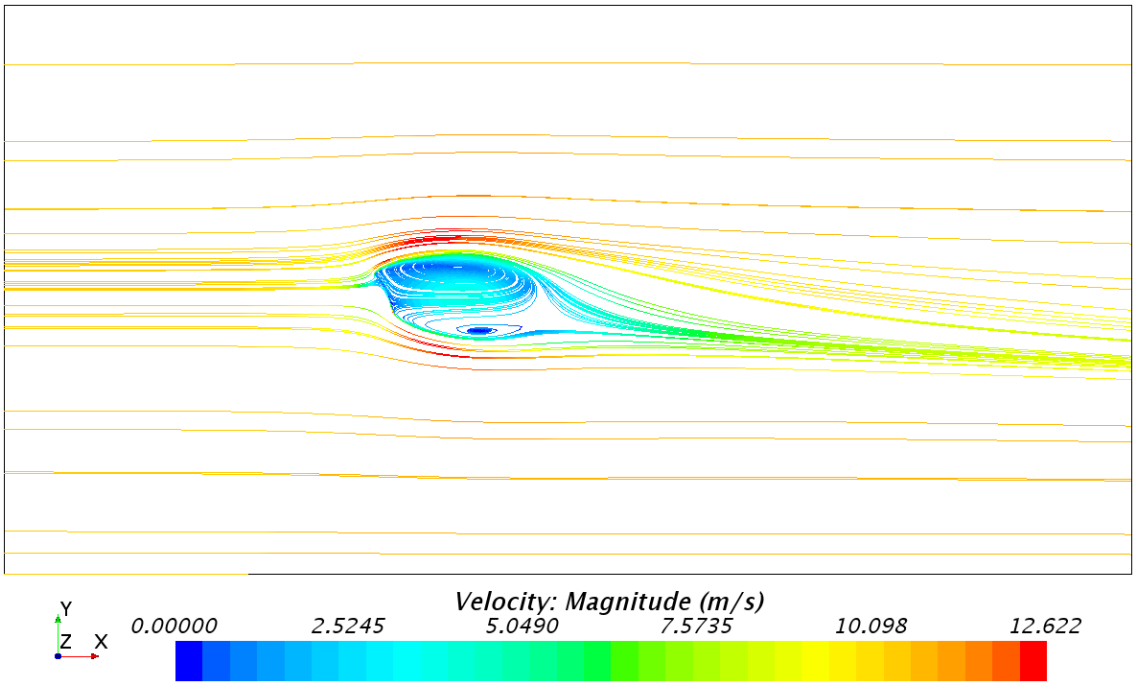

Figure A.192: Top view of the large computational domain, showing constrained streamlines, at the height of the center of effort (CoE); the cambered sail model, with a sheet angle of 110°.

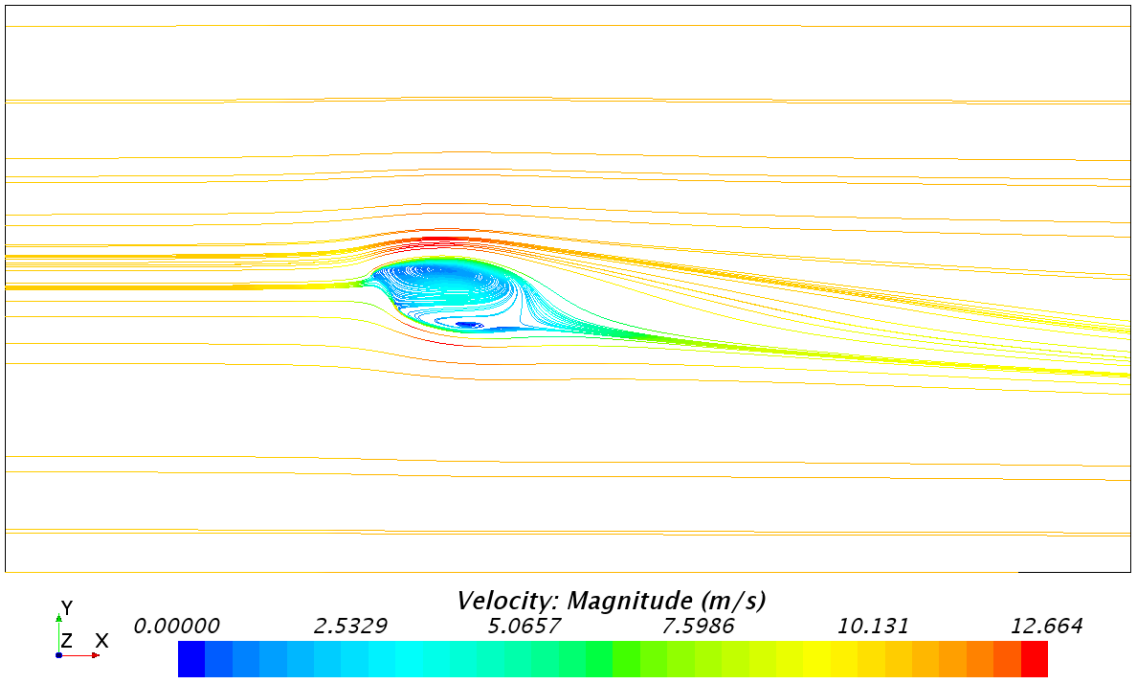

Figure A.193: Top view of the large computational domain, showing constrained streamlines, at the height of the center of effort (CoE); the cambered sail model, with a sheet angle of 120°.

Side View Images

Pressure Distribution at a centered XZ-plane with the Flat Sail Model in the Normal Domain

Fig. A.194 - A.200 shows the corresponding side view images of the pressure distribution, for the seven different sheet angles with the flat sail model and with grid 3 in the normal computational domain.

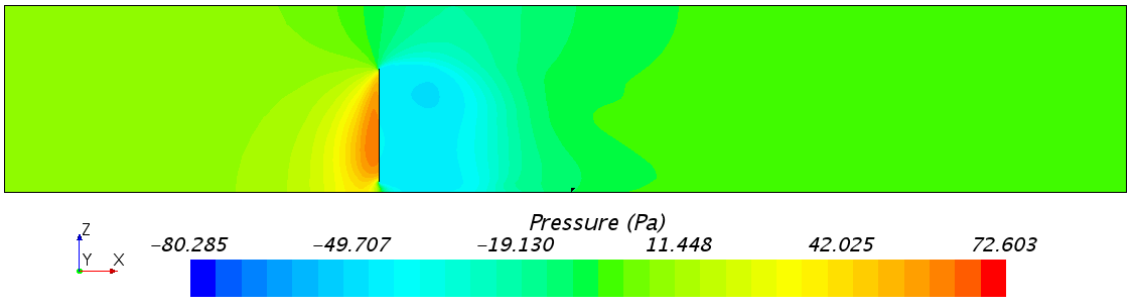

Figure A.194: Side view of the normal computational domain, showing the pressure distribution, at a centered xz-plane; the flat sail model, with a sheet angle of 60°.

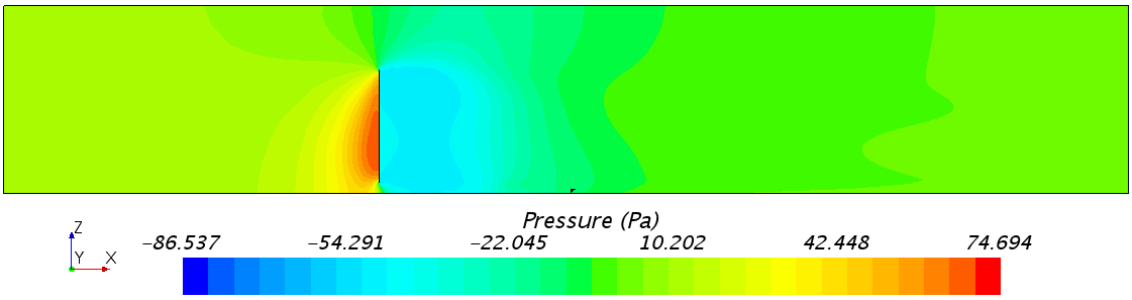

Figure A.195: Side view of the normal computational domain, showing the pressure distribution, at a centered xz-plane; the flat sail model, with a sheet angle of 70°.

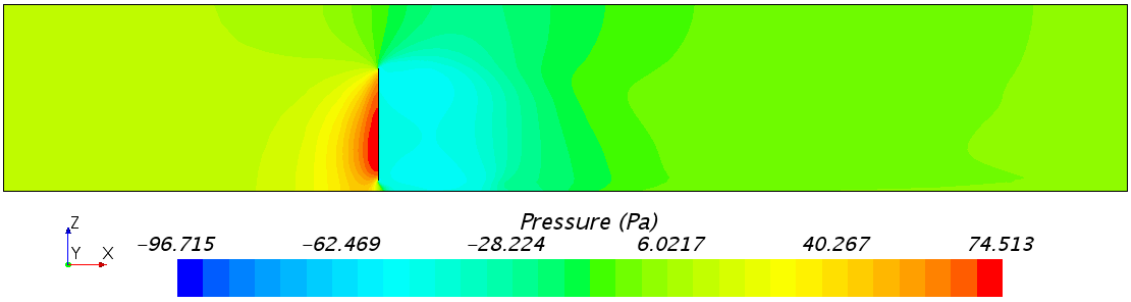

Figure A.196: Side view of the normal computational domain, showing the pressure distribution, at a centered xz-plane; the flat sail model, with a sheet angle of 80°.

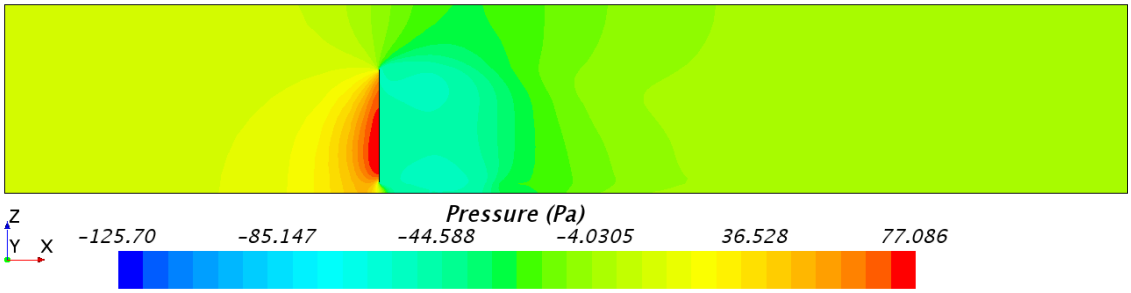

Figure A.197: Side view of the normal computational domain, showing the pressure distribution, at a centered xz-plane; the flat sail model, with a sheet angle of 90°.

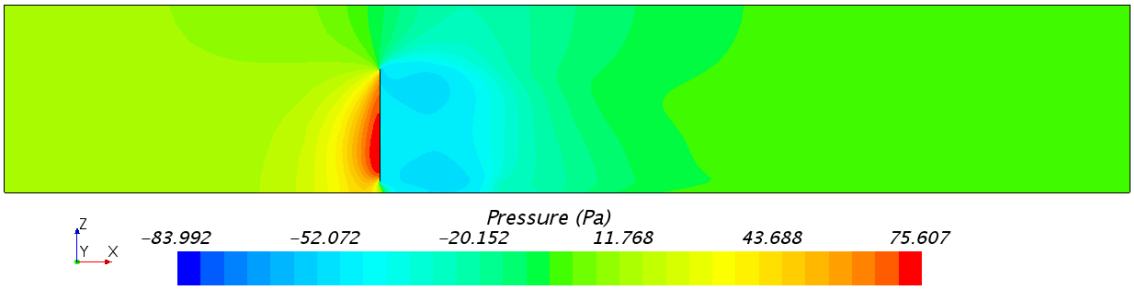

Figure A.198: Side view of the normal computational domain, showing the pressure distribution, at a centered xz-plane; the flat sail model, with a sheet angle of 100°.

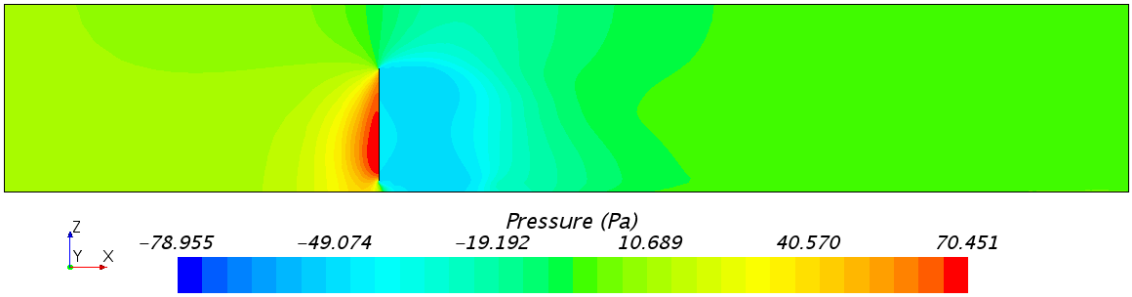

Figure A.199: Side view of the normal computational domain, showing the pressure distribution, at a centered xz-plane; the flat sail model, with a sheet angle of 110°.

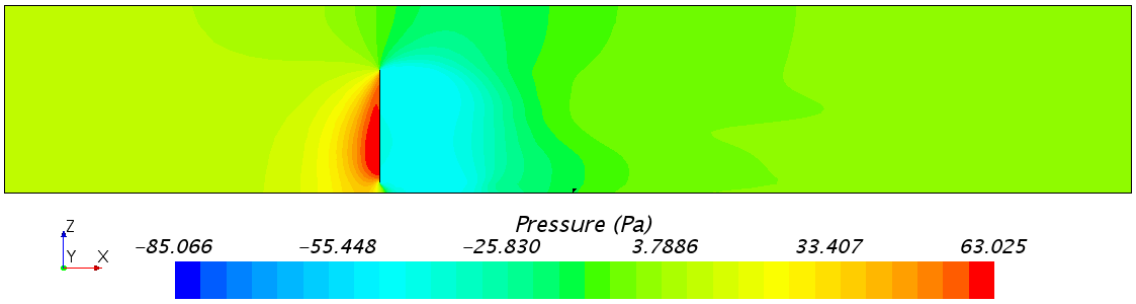

Figure A.200: Side view of the normal computational domain, showing the pressure distribution, at a centered xz-plane; the flat sail model, with a sheet angle of 120°.

Pressure Distribution at a centered XZ-plane with the Cambered Sail Model in the Normal Domain

Fig. A.201 - A.207 shows the corresponding side view images of the pressure distribution, for the seven different sheet angles with the cambered sail model and with grid 3 in the normal computational domain.

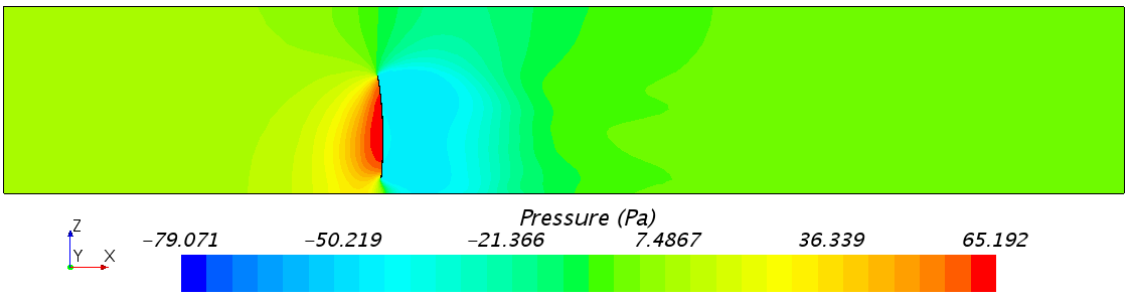

Figure A.201: Side view of the normal computational domain, showing the pressure distribution, at a centered xz-plane; the cambered sail model, with a sheet angle of 60°.

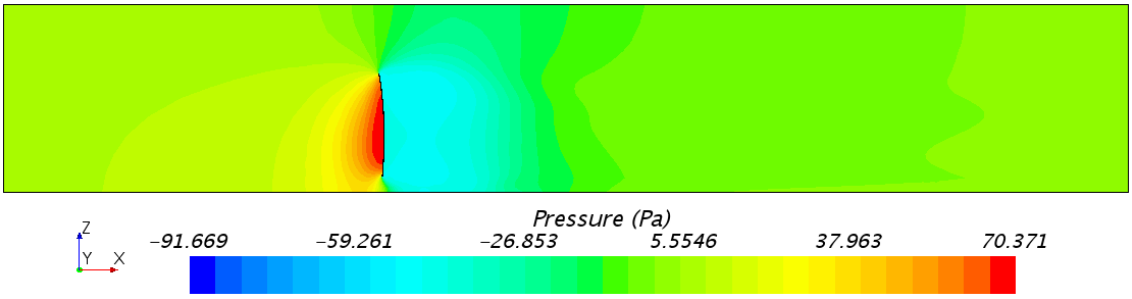

Figure A.202: Side view of the normal computational domain, showing the pressure distribution, at a centered xz-plane; the cambered sail model, with a sheet angle of 70°.

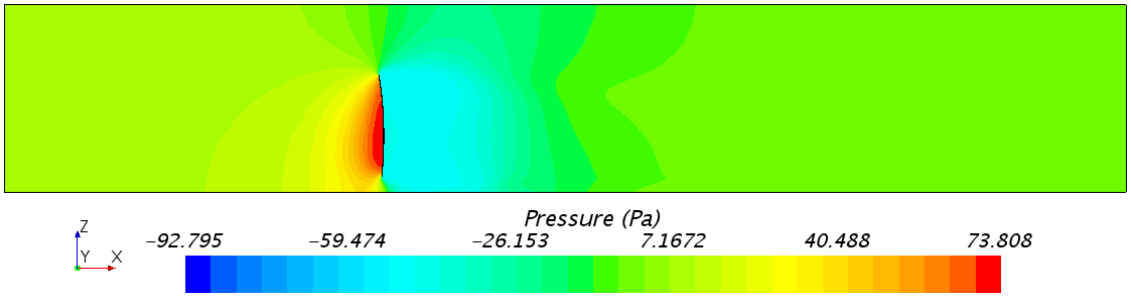

Figure A.203: Side view of the normal computational domain, showing the pressure distribution, at a centered xz-plane; the cambered sail model, with a sheet angle of 80°.

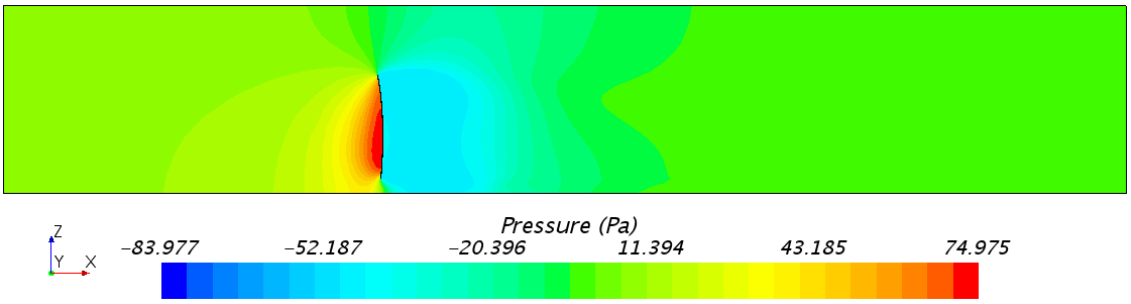

Figure A.204: Side view of the normal computational domain, showing the pressure distribution, at a centered xz-plane; the cambered sail model, with a sheet angle of 90°.

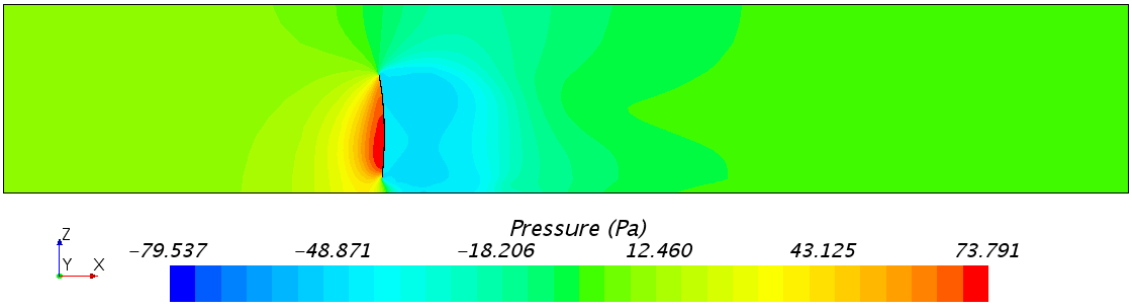

Figure A.205: Side view of the normal computational domain, showing the pressure distribution, at a centered xz-plane; the cambered sail model, with a sheet angle of 100°.

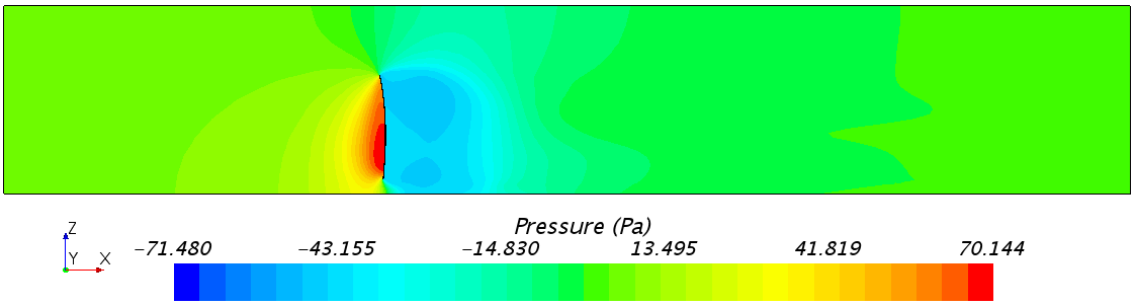

Figure A.206: Side view of the normal computational domain, showing the pressure distribution, at a centered xz-plane; the cambered sail model, with a sheet angle of 110°.

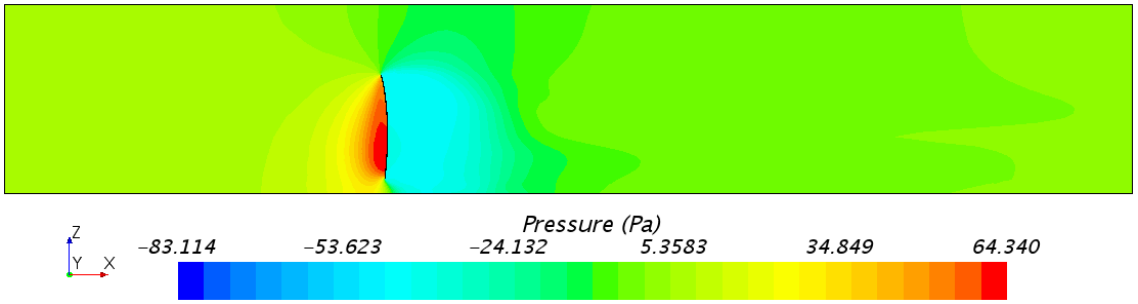

Figure A.207: Side view of the normal computational domain, showing the pressure distribution, at a centered xz-plane; the cambered sail model, with a sheet angle of 120°.

Velocity Distribution at a centered XZ-plane with the Flat Sail Model in the Normal Domain

Fig. A.208 - A.214 shows the corresponding side view images of the velocity distribution, for the seven different sheet angles with the flat sail model and with grid 3 in the normal computational domain.

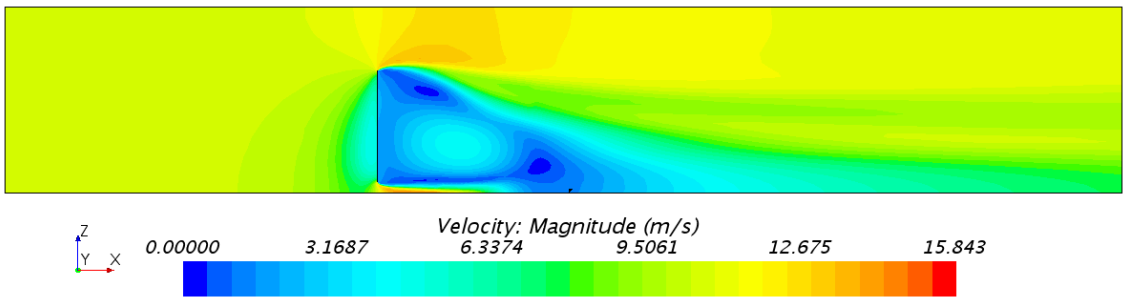

Figure A.208: Side view of the normal computational domain, showing the velocity distribution, at a centered xz-plane; the flat sail model, with a sheet angle of 60°.

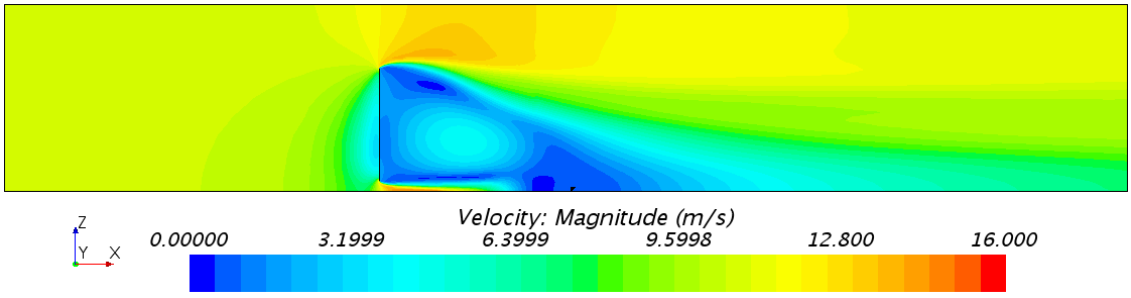

Figure A.209: Side view of the normal computational domain, showing the velocity distribution, at a centered xz-plane; the flat sail model, with a sheet angle of 70°.

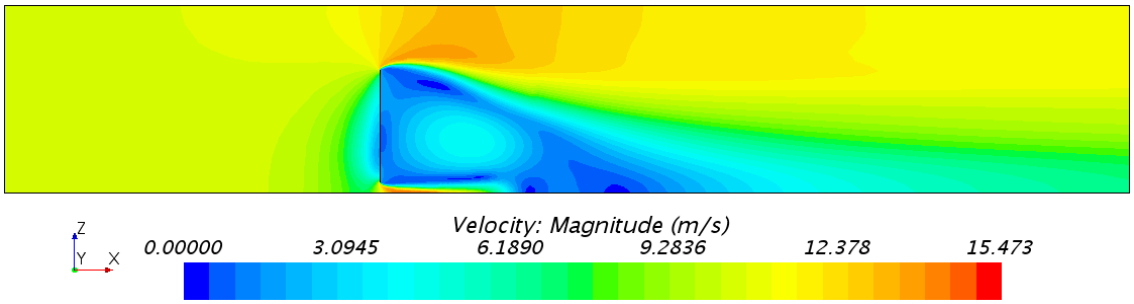

Figure A.210: Side view of the normal computational domain, showing the velocity distribution, at a centered xz-plane; the flat sail model, with a sheet angle of 80°.

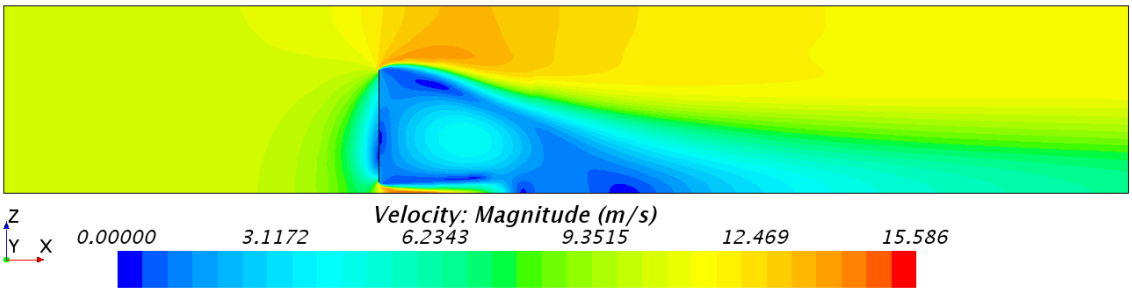

Figure A.211: Side view of the normal computational domain, showing the velocity distribution, at a centered xz-plane; the flat sail model, with a sheet angle of 90°.

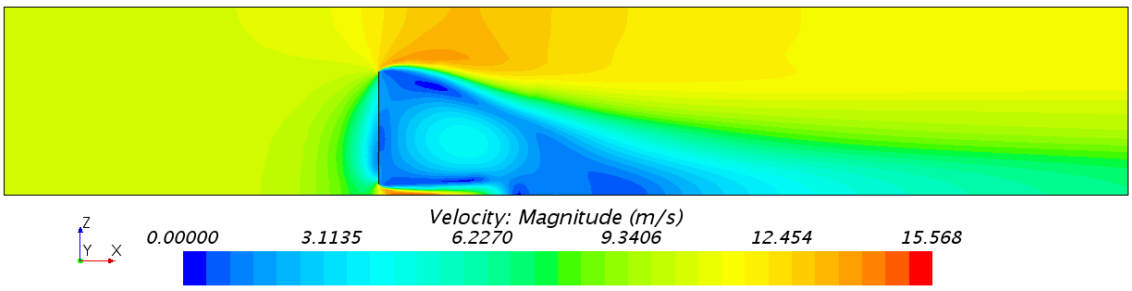

Figure A.212: Side view of the normal computational domain, showing the velocity distribution, at a centered xz-plane; the flat sail model, with a sheet angle of 100°.

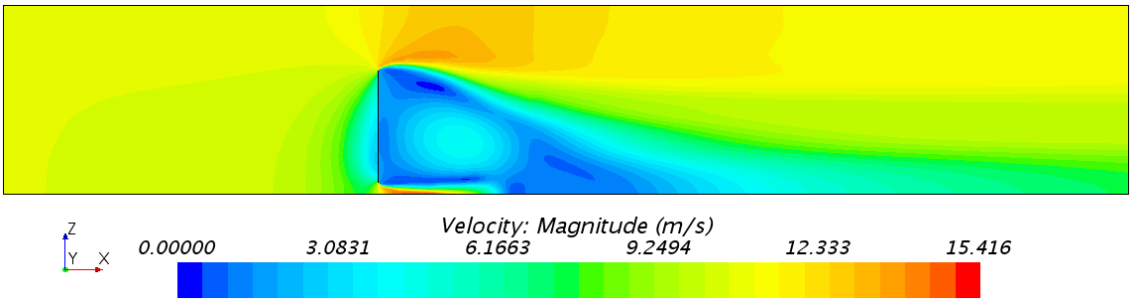

Figure A.213: Side view of the normal computational domain, showing the velocity distribution, at a centered xz-plane; the flat sail model, with a sheet angle of 110°.

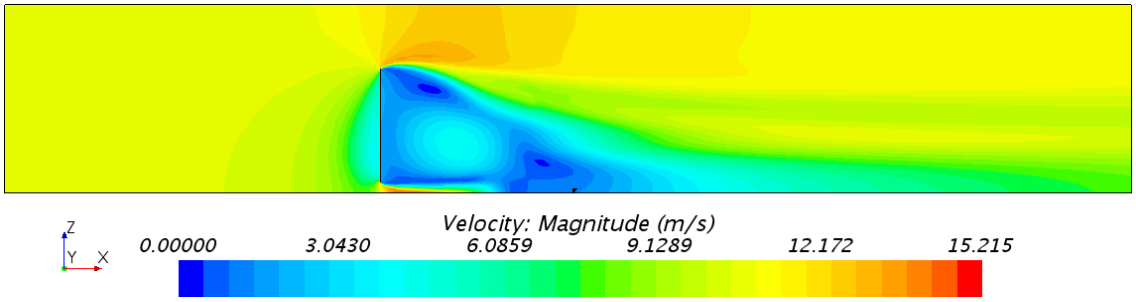

Figure A.214: Side view of the normal computational domain, showing the velocity distribution, at a centered xz-plane; the flat sail model, with a sheet angle of 120°.

Velocity Distribution at a centered XZ-plane with the Cambered Sail Model in the Normal Domain

Fig. A.215 - A.221 shows the corresponding side view images of the velocity distribution, for the seven different sheet angles with the cambered sail model and with grid 3 in the normal computational domain.

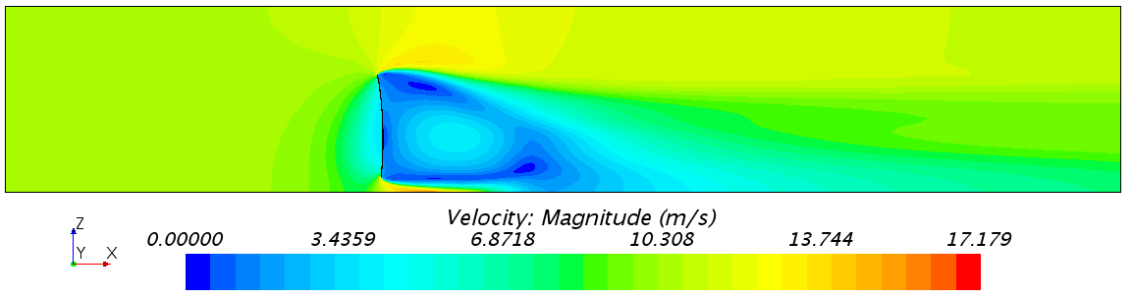

Figure A.215: Side view of the normal computational domain, showing the velocity distribution, at a centered xz-plane; the cambered sail model, with a sheet angle of 60°.

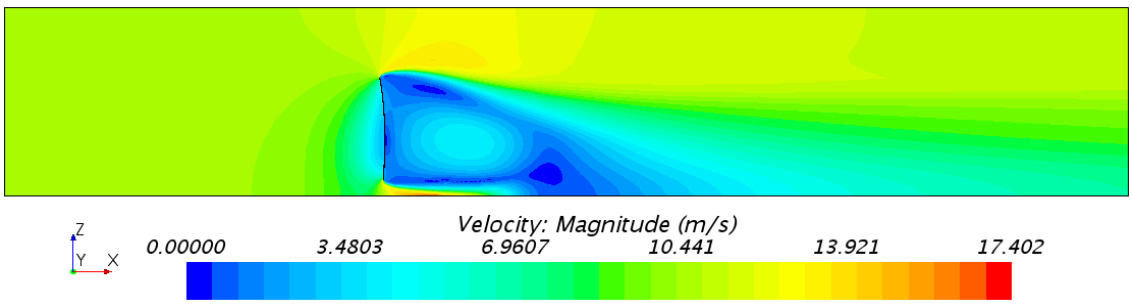

Figure A.216: Side view of the normal computational domain, showing the velocity distribution, at a centered xz-plane; the cambered sail model, with a sheet angle of 70°.

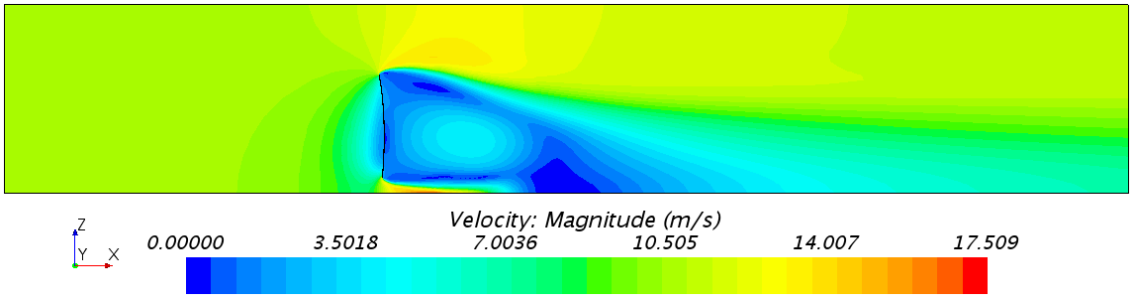

Figure A.217: Side view of the normal computational domain, showing the velocity distribution, at a centered xz-plane; the cambered sail model, with a sheet angle of 80°.

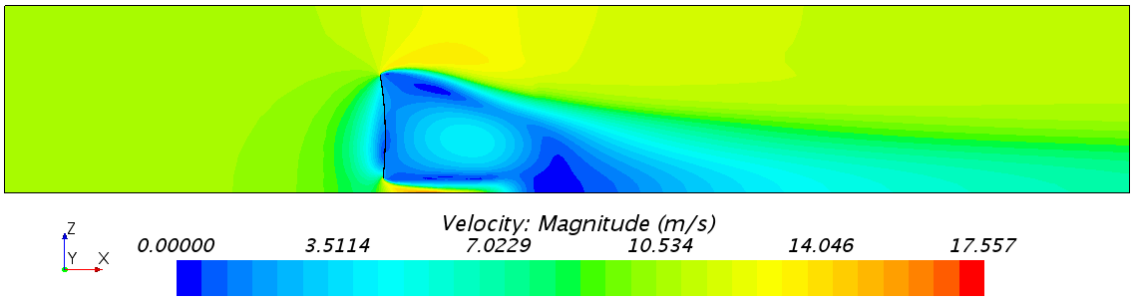

Figure A.218: Side view of the normal computational domain, showing the velocity distribution, at a centered xz-plane; the cambered sail model, with a sheet angle of 90°.

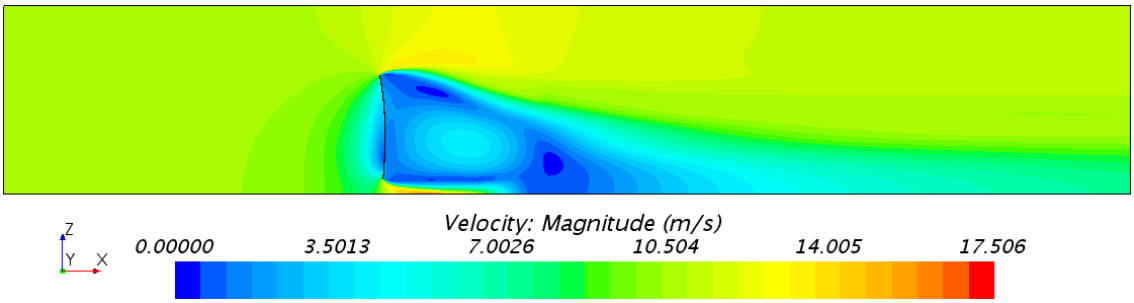

Figure A.219: Side view of the normal computational domain, showing the velocity distribution, at a centered xz-plane; the cambered sail model, with a sheet angle of 100°.

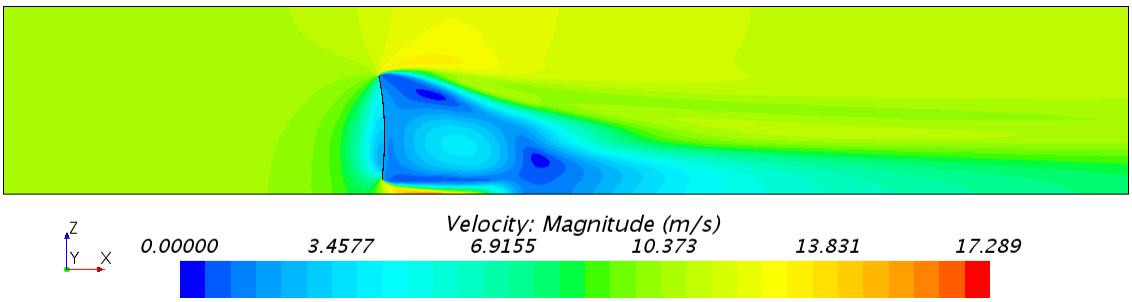

Figure A.220: Side view of the normal computational domain, showing the velocity distribution, at a centered xz-plane; the cambered sail model, with a sheet angle of 110°.

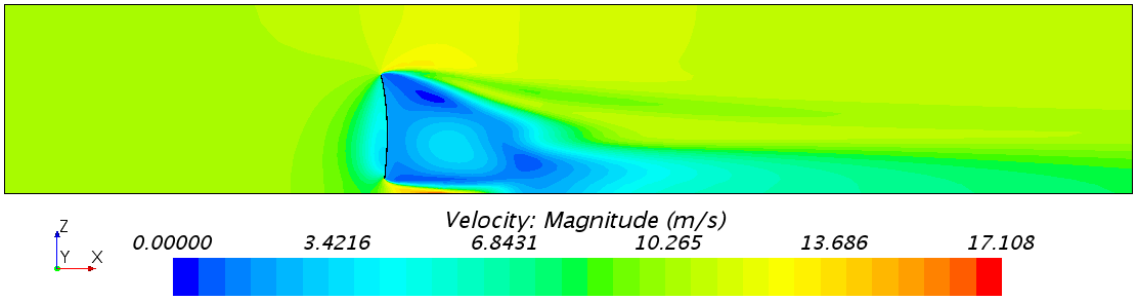

Figure A.221: Side view of the normal computational domain, showing the velocity distribution, at a centered xz-plane; the cambered sail model, with a sheet angle of 120°.

Constrained Streamlines at a centered XZ-plane with the Flat Sail Model in the Normal Domain

Fig. A.222 - A.228 shows the corresponding side view images of constrained streamlines, for the seven different sheet angles with the flat sail model and with grid 3 in the normal computational domain.

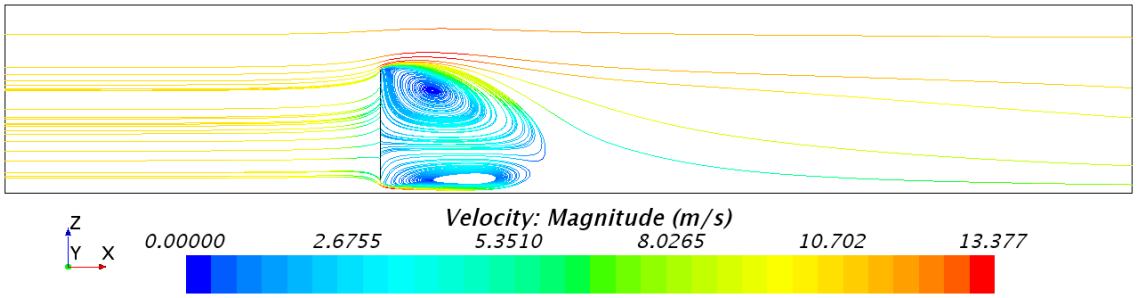

Figure A.222: Side view of the normal computational domain, showing constrained streamlines, at a centered xz-plane; the flat sail model, with a sheet angle of 60°.

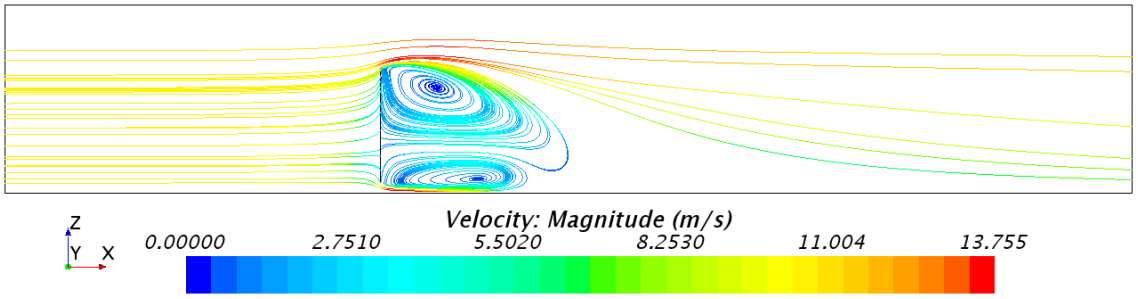

Figure A.223: Side view of the normal computational domain, showing constrained streamlines, at a centered xz-plane; the flat sail model, with a sheet angle of 70°.

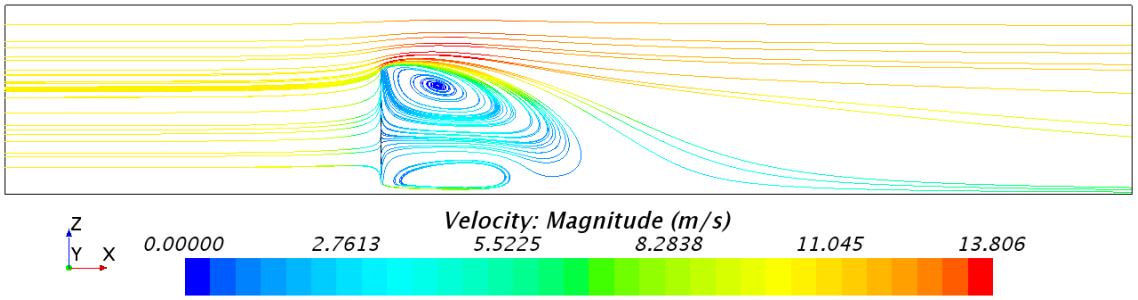

Figure A.224: Side view of the normal computational domain, showing constrained streamlines, at a centered xz-plane; the flat sail model, with a sheet angle of 80°.

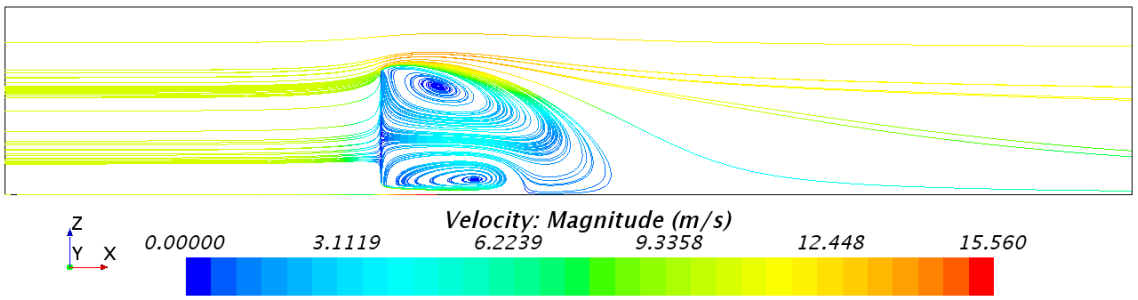

Figure A.225: Side view of the normal computational domain, showing constrained streamlines, at a centered xz-plane; the flat sail model, with a sheet angle of 90°.

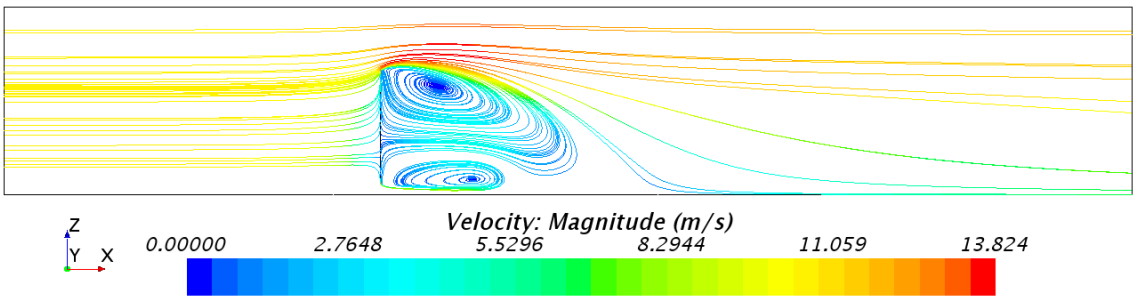

Figure A.226: Side view of the normal computational domain, showing constrained streamlines, at a centered xz-plane; the flat sail model, with a sheet angle of 100°.

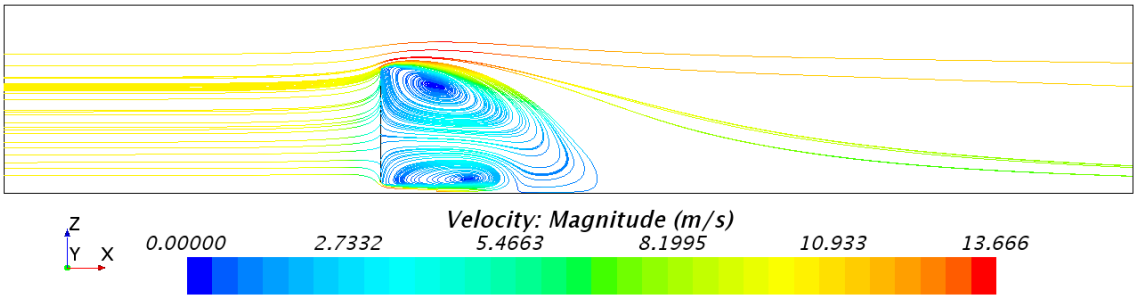

Figure A.227: Side view of the normal computational domain, showing constrained streamlines, at a centered xz-plane; the flat sail model, with a sheet angle of 110°.

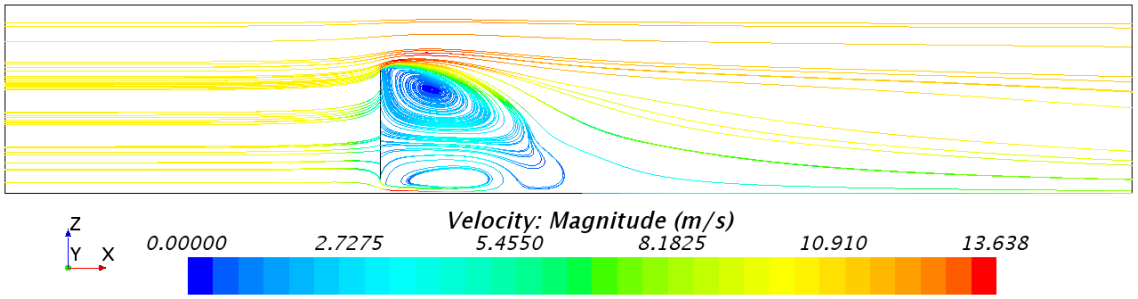

Figure A.228: Side view of the normal computational domain, showing constrained streamlines, at a centered xz-plane; the flat sail model, with a sheet angle of 120°.

Constrained Streamlines at a centered XZ-plane with the Cambered Sail Model in the Normal Domain

Fig. A.229 - A.235 shows the corresponding side view images of constrained streamlines, for the seven different sheet angles with the cambered sail model and with grid 3 in the normal computational domain.

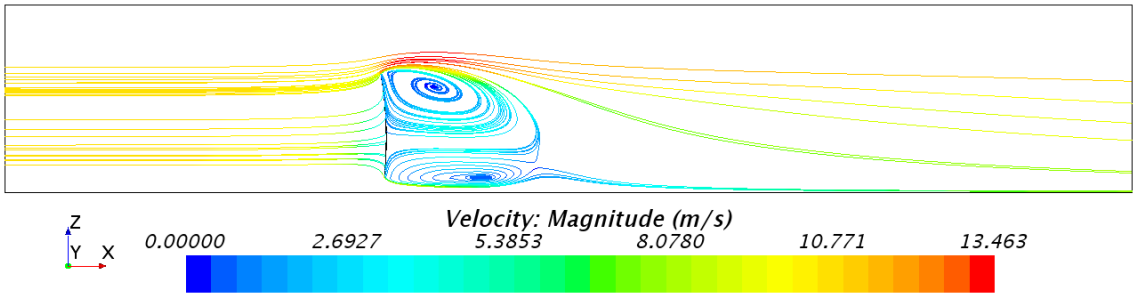

Figure A.229: Side view of the normal computational domain, showing constrained streamlines, at a centered xz-plane; the cambered sail model, with a sheet angle of 60°.

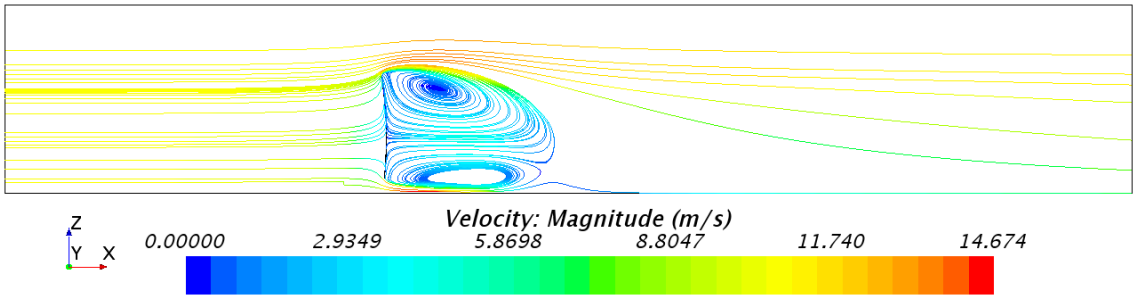

Figure A.230: Side view of the normal computational domain, showing constrained streamlines, at a centered xz-plane; the cambered sail model, with a sheet angle of 70°.

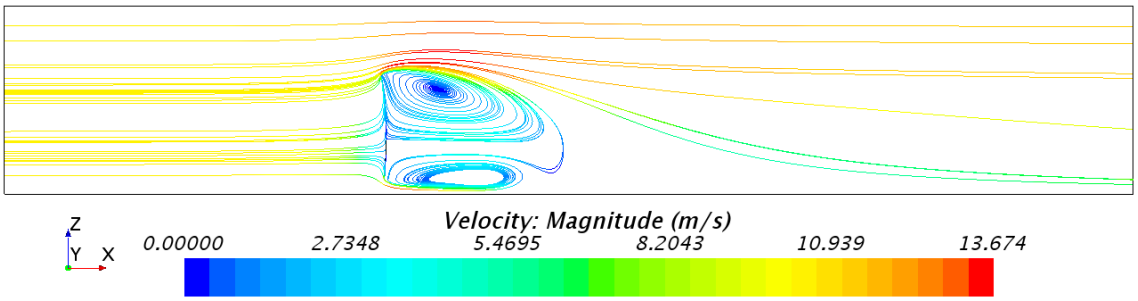

Figure A.231: Side view of the normal computational domain, showing constrained streamlines, at a centered xz-plane; the cambered sail model, with a sheet angle of 80°.

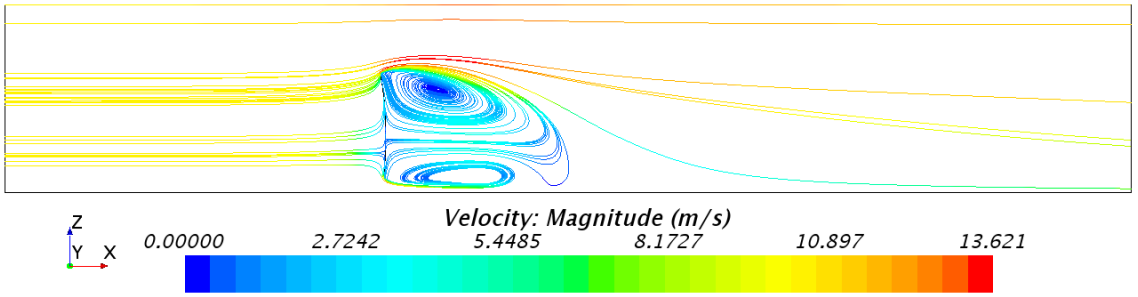

Figure A.232: Side view of the normal computational domain, showing constrained streamlines, at a centered xz-plane; the cambered sail model, with a sheet angle of 90°.

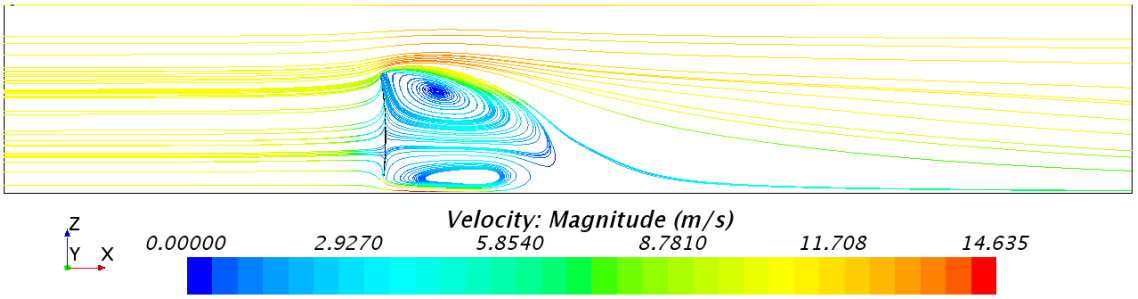

Figure A.233: Side view of the normal computational domain, showing constrained streamlines, at a centered xz-plane; the cambered sail model, with a sheet angle of 100°.

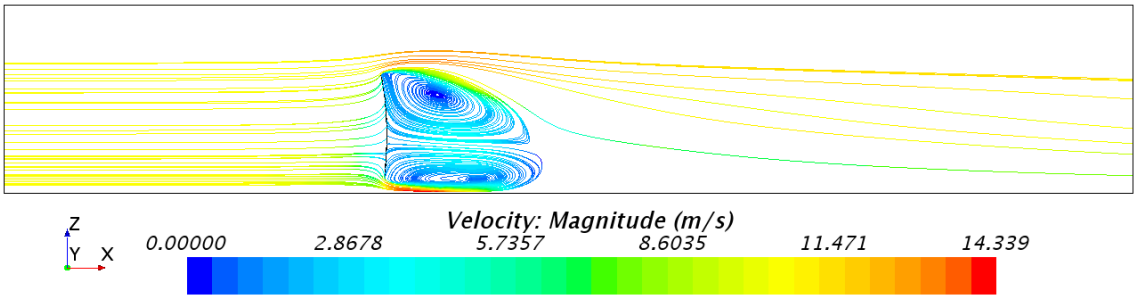

Figure A.234: Side view of the normal computational domain, showing constrained streamlines, at a centered xz-plane; the cambered sail model, with a sheet angle of 110°.

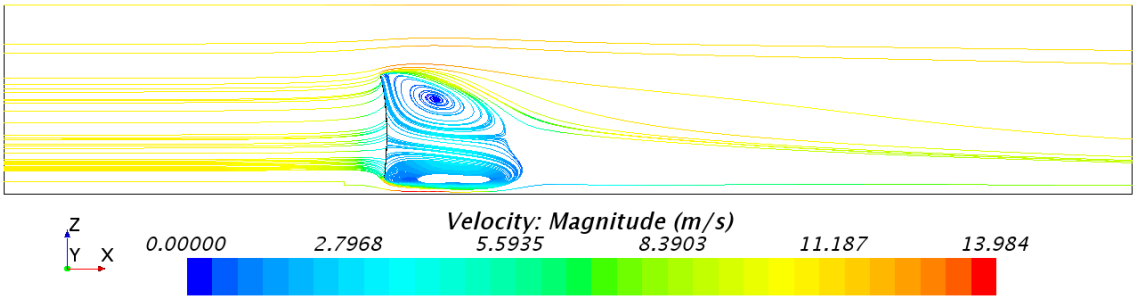

Figure A.235: Side view of the normal computational domain, showing constrained streamlines, at a centered xz-plane; the cambered sail model, with a sheet angle of 120°.

Pressure Distribution at a centered XZ-plane with the Flat Sail Model in the Large Domain

Fig. A.236 - A.242 shows the corresponding side view images of the pressure distribution, for the seven different sheet angles with the flat sail model and with grid 3 in the large computational domain.

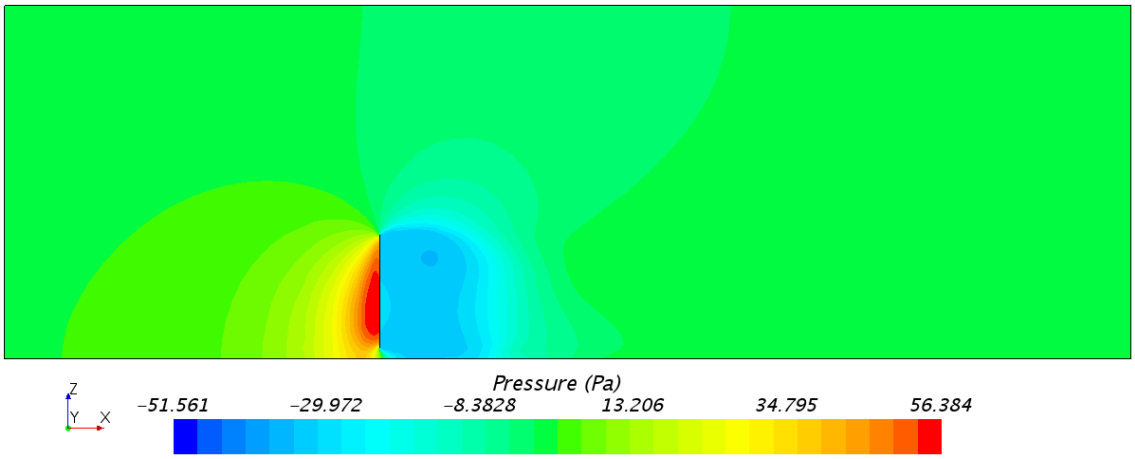

Figure A.236: Side view of the large computational domain, showing the pressure distribution, at a centered xz-plane; the flat sail model, with a sheet angle of 60°.

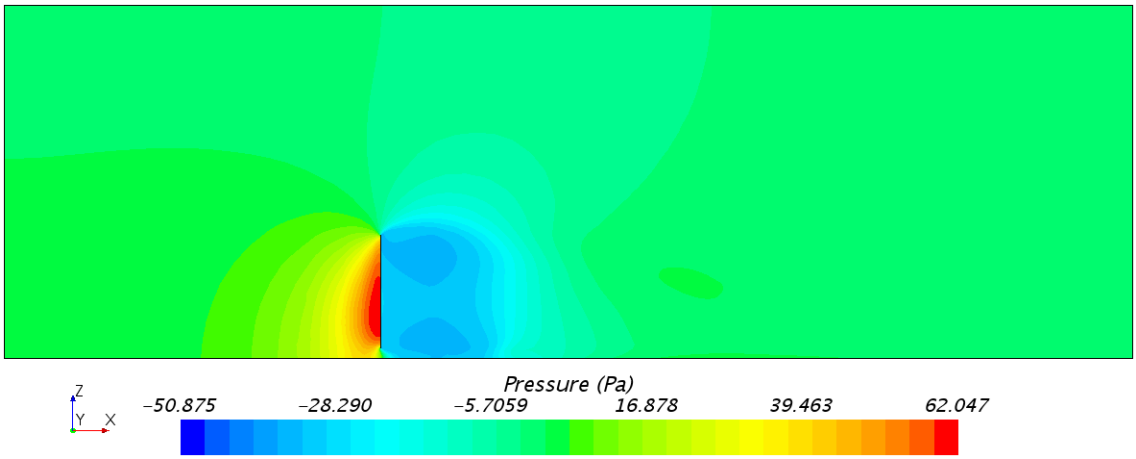

Figure A.237: Side view of the large computational domain, showing the pressure distribution, at a centered xz-plane; the flat sail model, with a sheet angle of 70°.

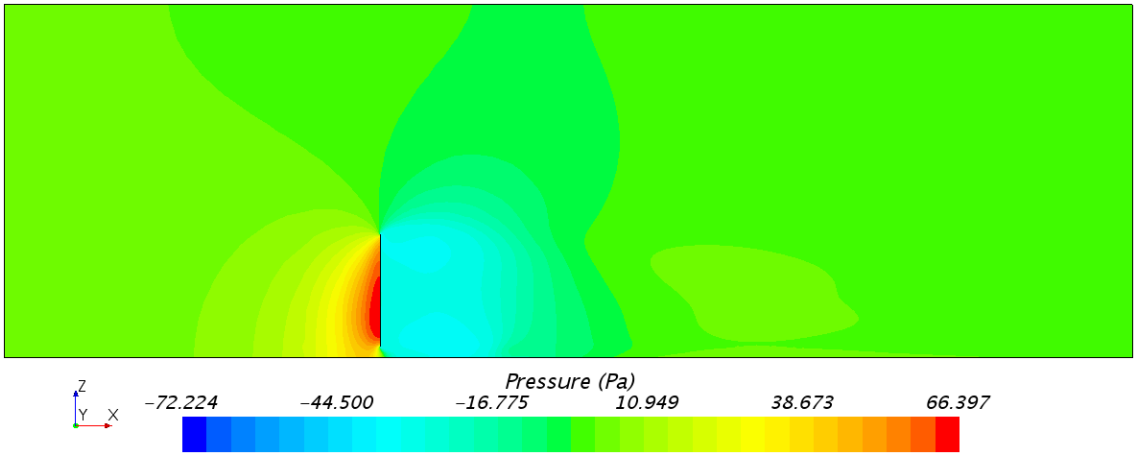

Figure A.238: Side view of the large computational domain, showing the pressure distribution, at a centered xz-plane; the flat sail model, with a sheet angle of 80°.

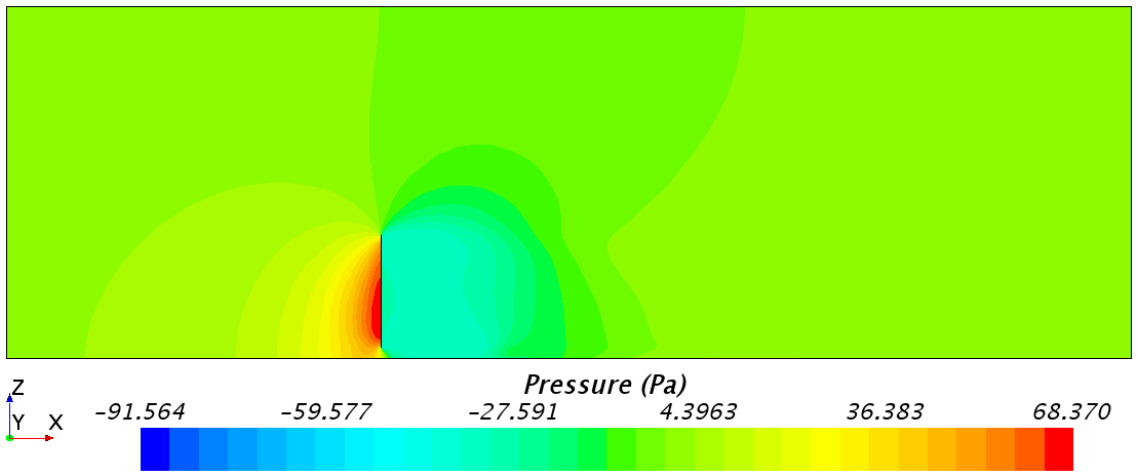

Figure A.239: Side view of the large computational domain, showing the pressure distribution, at a centered xz-plane; the flat sail model, with a sheet angle of 90°.

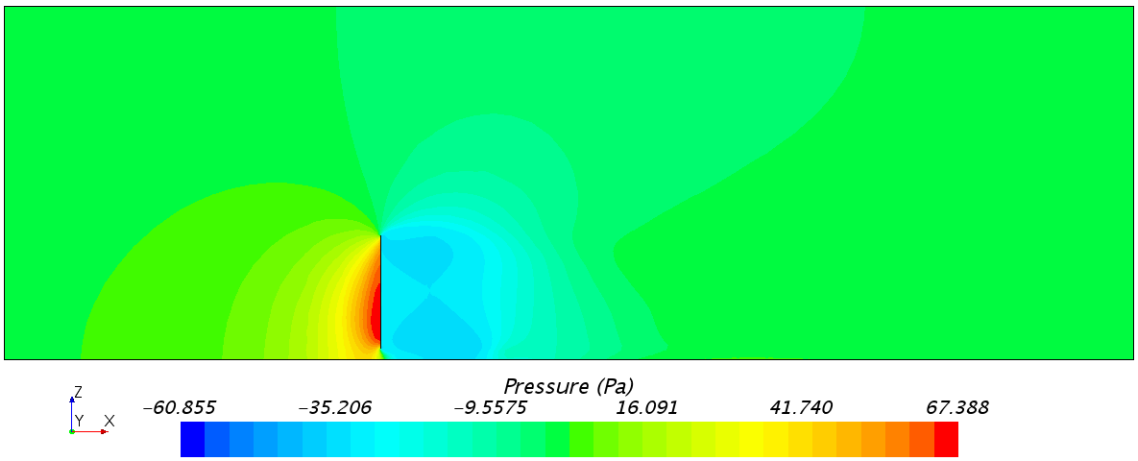

Figure A.240: Side view of the large computational domain, showing the pressure distribution, at a centered xz-plane; the flat sail model, with a sheet angle of 100°.

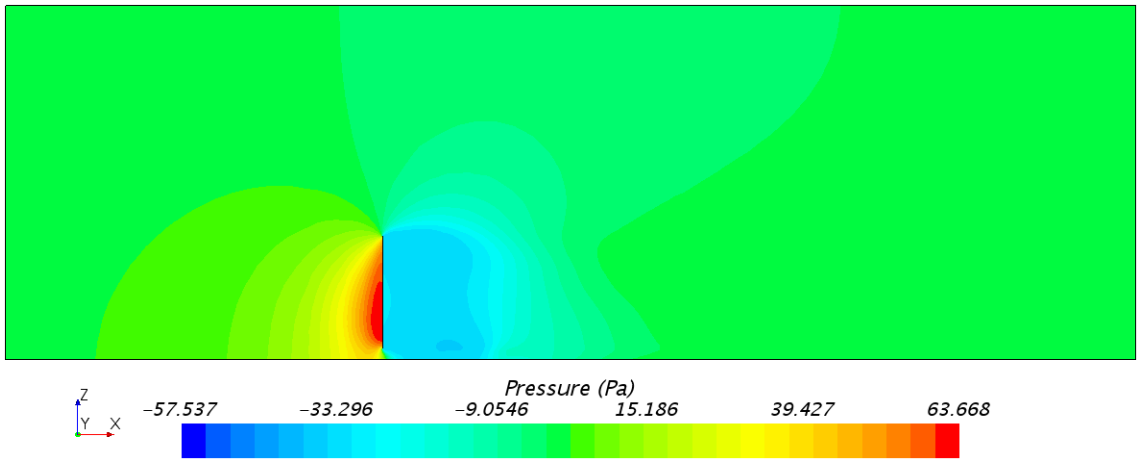

Figure A.241: Side view of the large computational domain, showing the pressure distribution, at a centered xz-plane; the flat sail model, with a sheet angle of 110°.

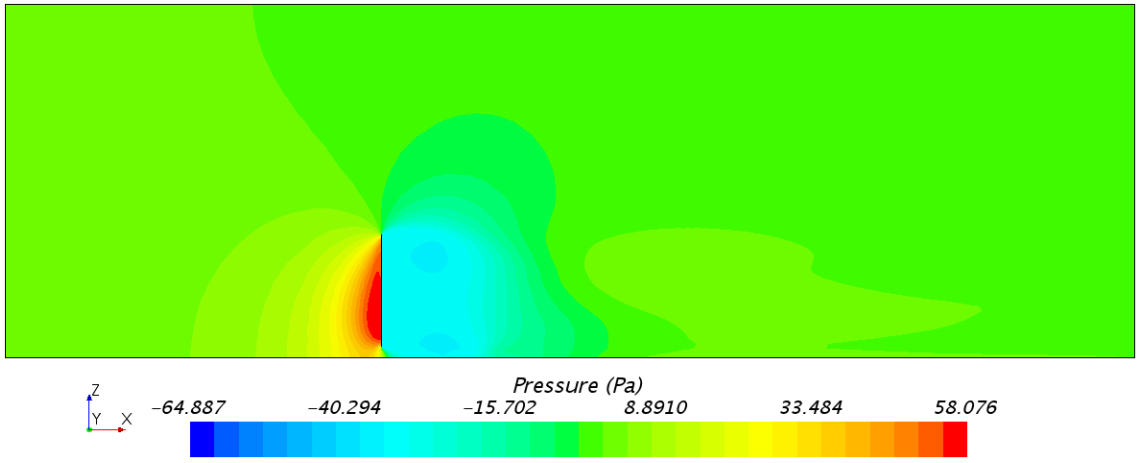

Figure A.242: Side view of the large computational domain, showing the pressure distribution, at a centered xz-plane; the flat sail model, with a sheet angle of 120°.

Pressure Distribution at a centered XZ-plane with the Cambered Sail Model in the Large Domain

Fig. A.243 - A.249 shows the corresponding side view images of the pressure distribution, for the seven different sheet angles with the cambered sail model and with grid 3 in the large computational domain.

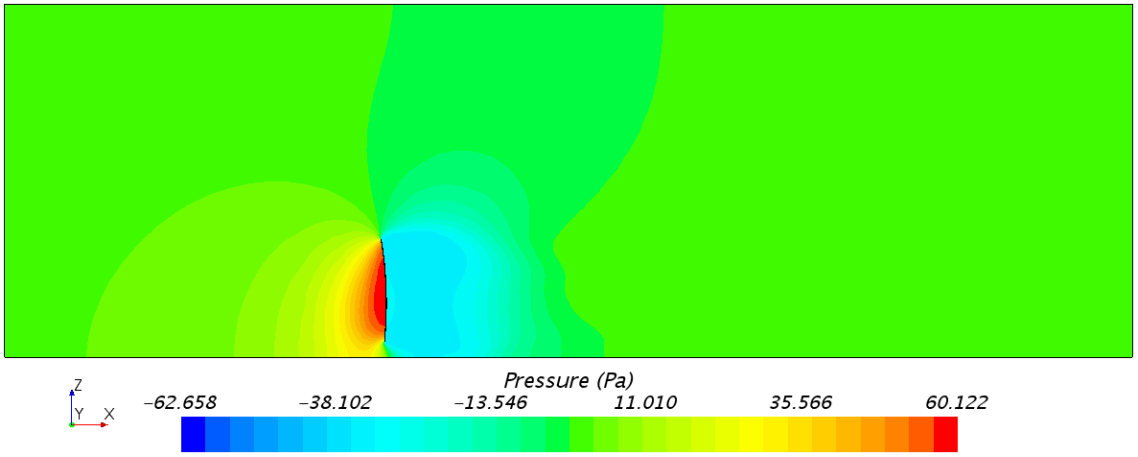

Figure A.243: Side view of the large computational domain, showing the pressure distribution, at a centered xz-plane; the cambered sail model, with a sheet angle of 60°.

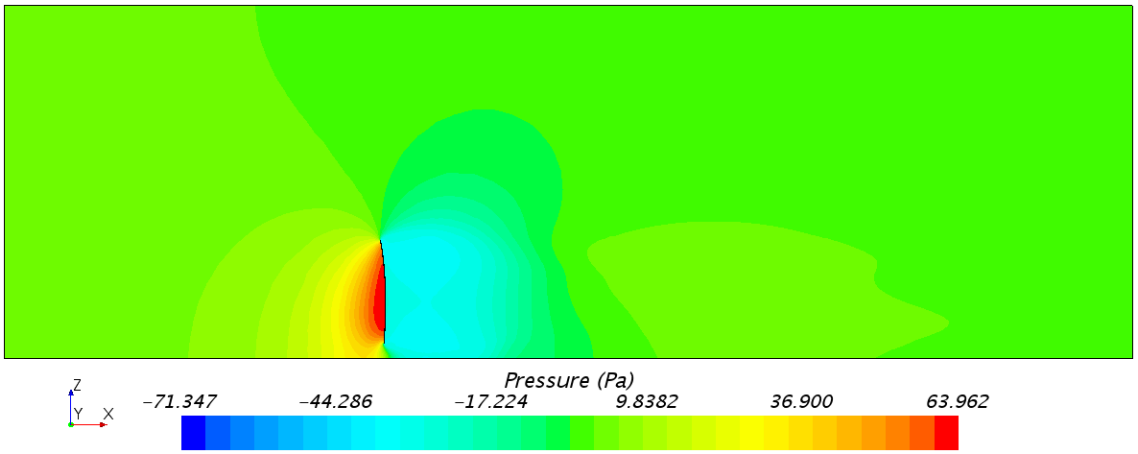

Figure A.244: Side view of the large computational domain, showing the pressure distribution, at a centered xz-plane; the cambered sail model, with a sheet angle of 70°.

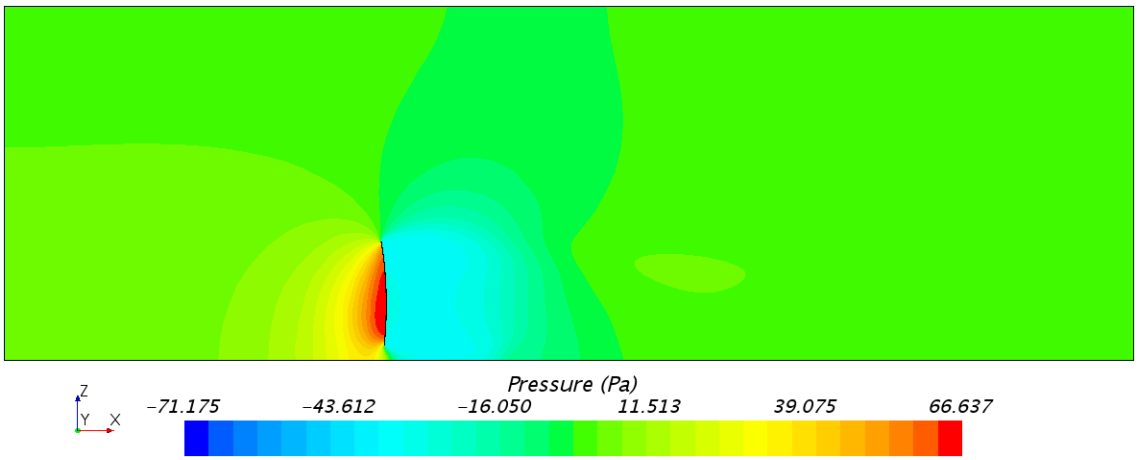

Figure A.245: Side view of the large computational domain, showing the pressure distribution, at a centered xz-plane; the cambered sail model, with a sheet angle of 80°.

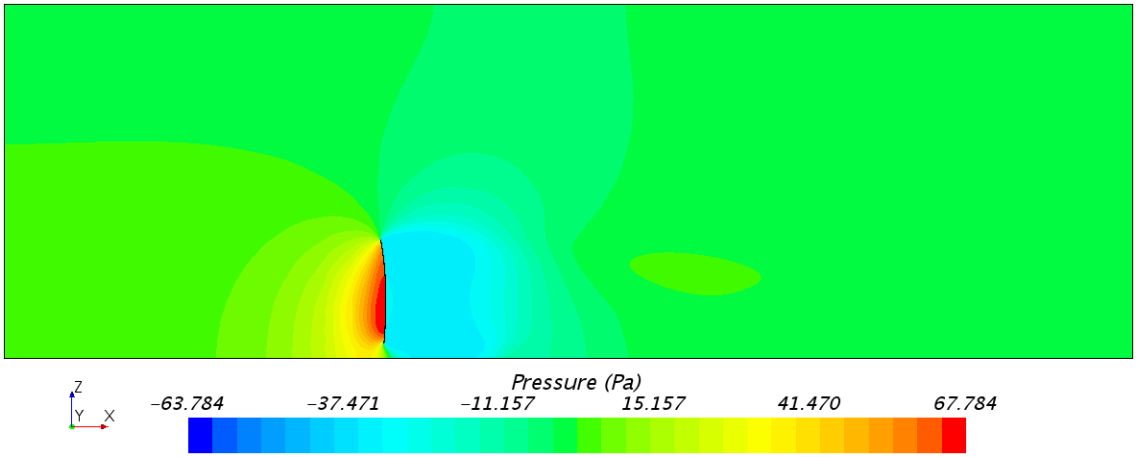

Figure A.246: Side view of the large computational domain, showing the pressure distribution, at a centered xz-plane; the cambered sail model, with a sheet angle of 90°.

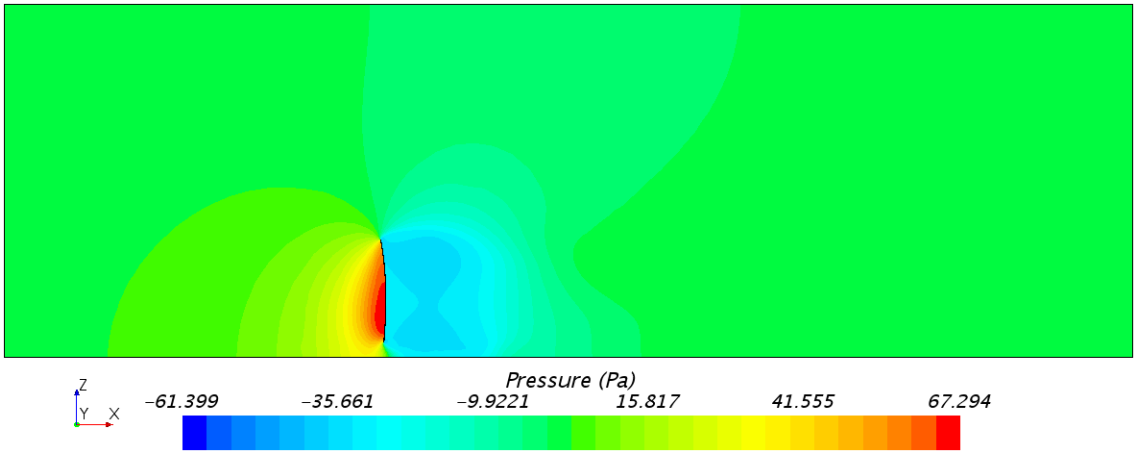

Figure A.247: Side view of the large computational domain, showing the pressure distribution, at a centered xz-plane; the cambered sail model, with a sheet angle of 100°.

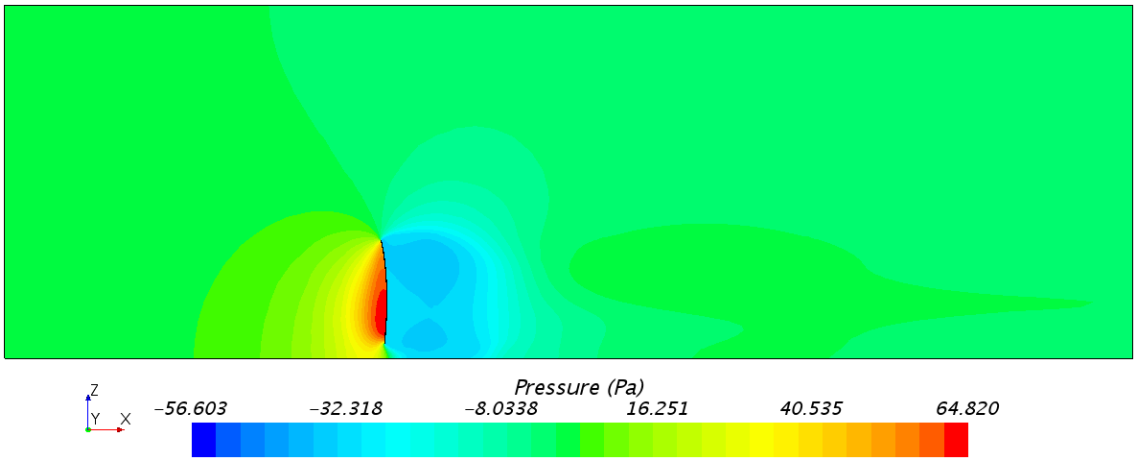

Figure A.248: Side view of the large computational domain, showing the pressure distribution, at a centered xz-plane; the cambered sail model, with a sheet angle of 110°.

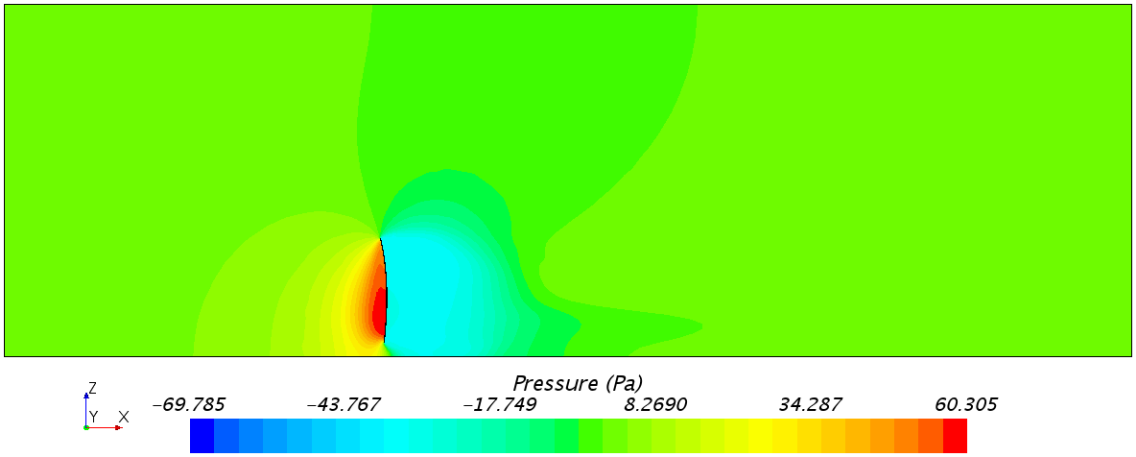

Figure A.249: Side view of the large computational domain, showing the pressure distribution, at a centered xz-plane; the cambered sail model, with a sheet angle of 120°.

Velocity Distribution at a centered XZ-plane with the Flat Sail Model in the Large Domain

Fig. A.250 - A.256 shows the corresponding side view images of the velocity distribution, for the seven different sheet angles with the flat sail model and with grid 3 in the large computational domain.

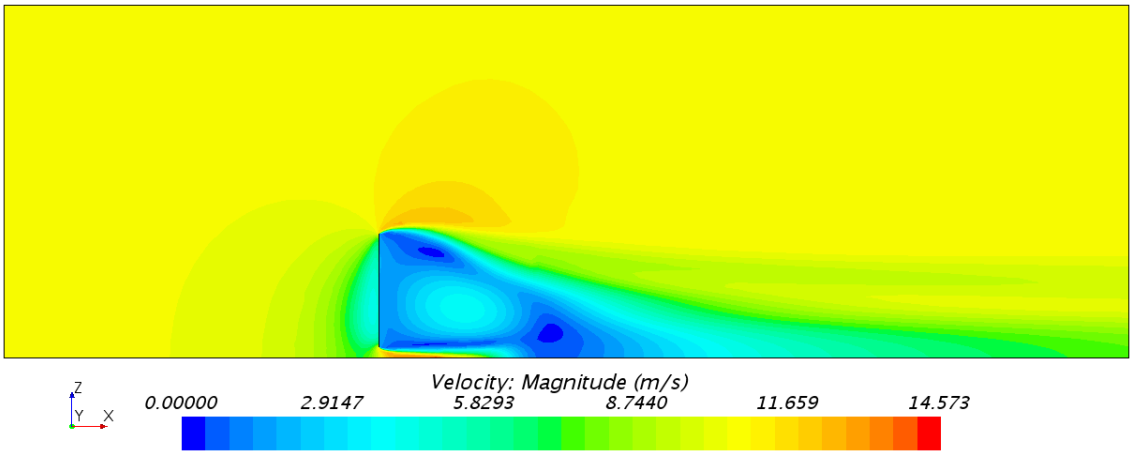

Figure A.250: Side view of the large computational domain, showing the velocity distribution, at a centered xz-plane; the flat sail model, with a sheet angle of 60°.

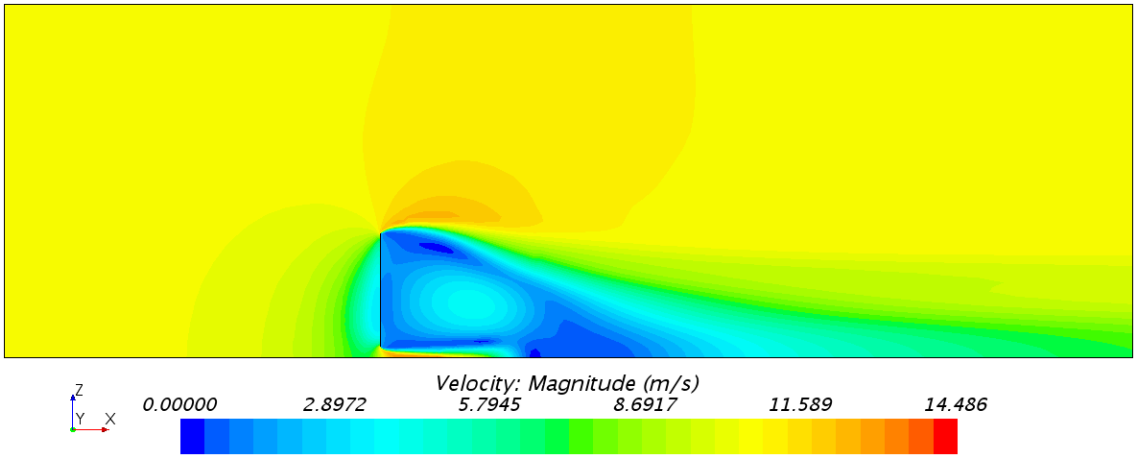

Figure A.251: Side view of the large computational domain, showing the velocity distribution, at a centered xz-plane; the flat sail model, with a sheet angle of 70°.

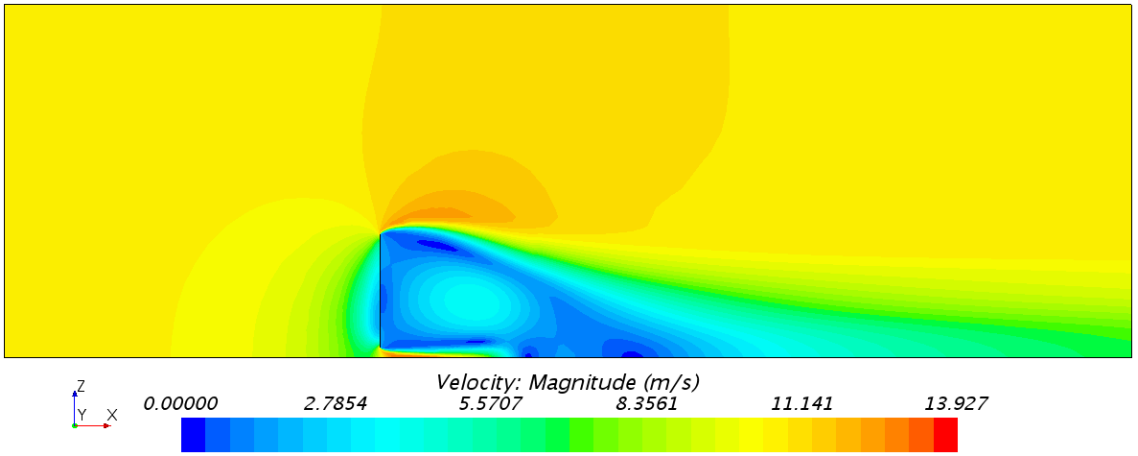

Figure A.252: Side view of the large computational domain, showing the velocity distribution, at a centered xz-plane; the flat sail model, with a sheet angle of 80°.

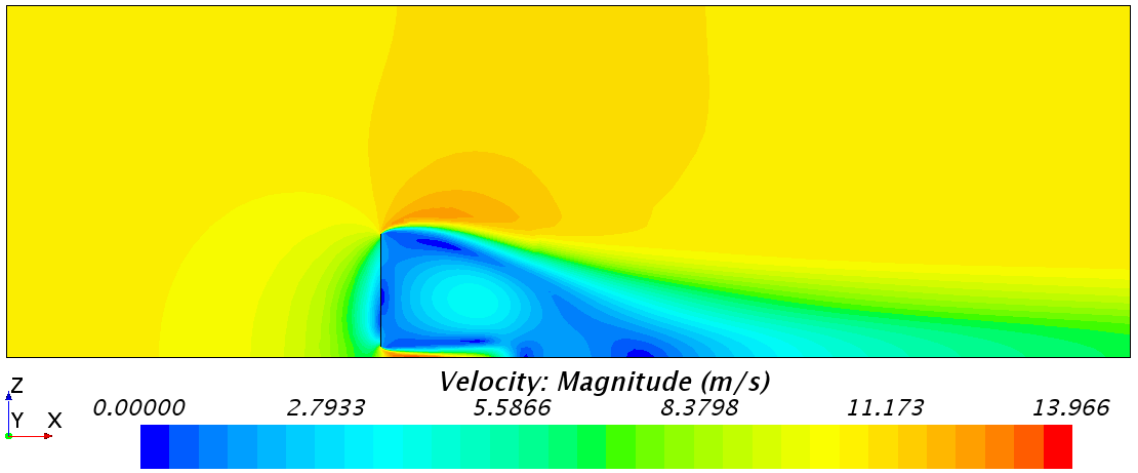

Figure A.253: Side view of the large computational domain, showing the velocity distribution, at a centered xz-plane; the flat sail model, with a sheet angle of 90°.

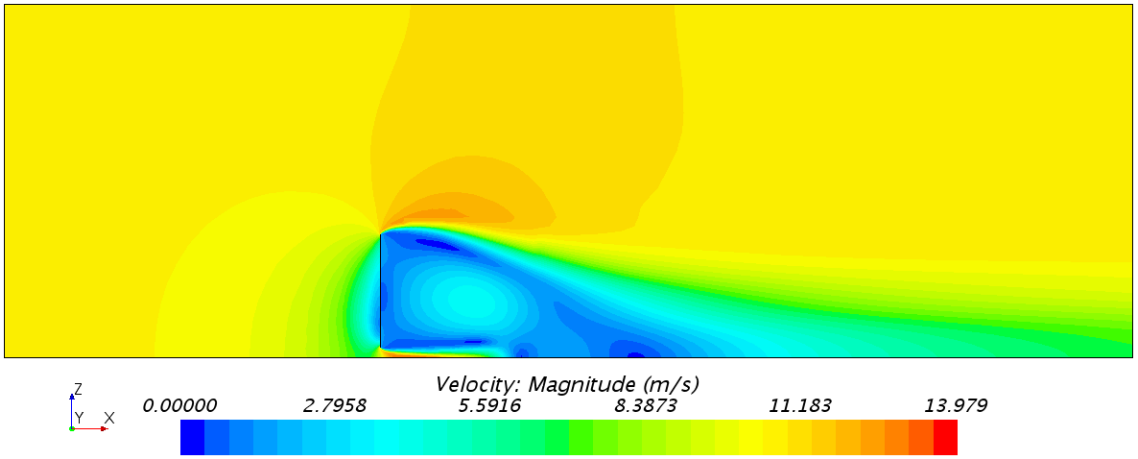

Figure A.254: Side view of the large computational domain, showing the velocity distribution, at a centered xz-plane; the flat sail model, with a sheet angle of 100°.

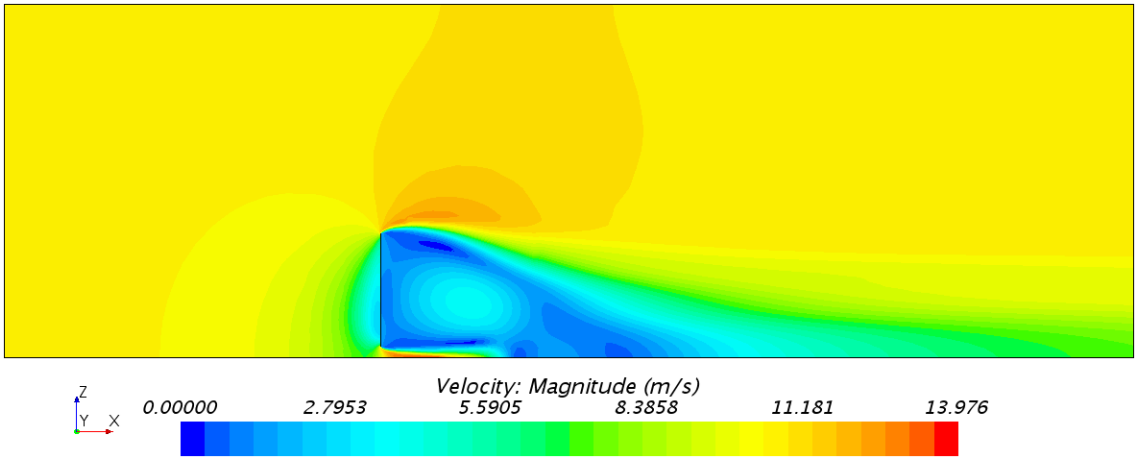

Figure A.255: Side view of the large computational domain, showing the velocity distribution, at a centered xz-plane; the flat sail model, with a sheet angle of 110°.

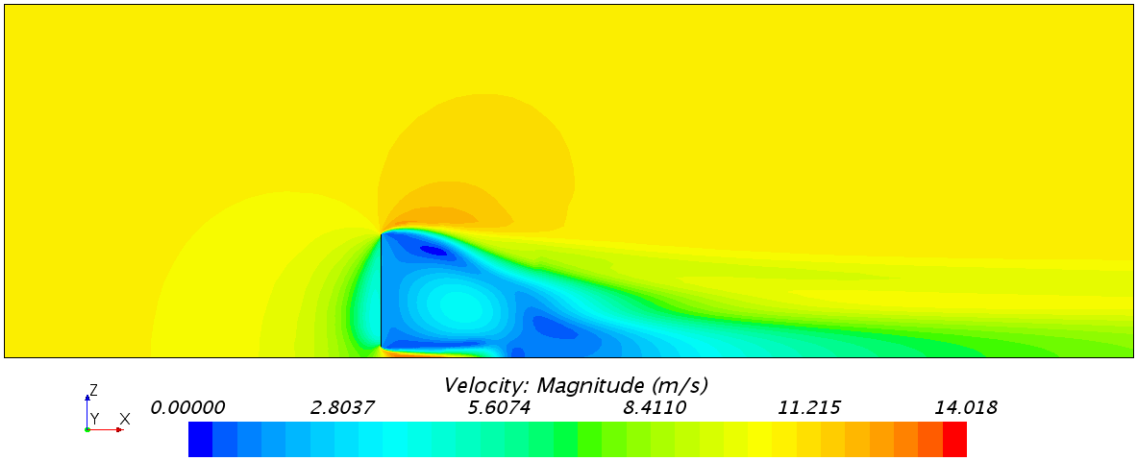

Figure A.256: Side view of the large computational domain, showing the velocity distribution, at a centered xz-plane; the flat sail model, with a sheet angle of 120°.

Velocity Distribution at a centered XZ-plane with the Cambered Sail Model in the Large Domain

Fig. A.257 - A.263 shows the corresponding side view images of the velocity distribution, for the seven different sheet angles with the cambered sail model and with grid 3 in the large computational domain.

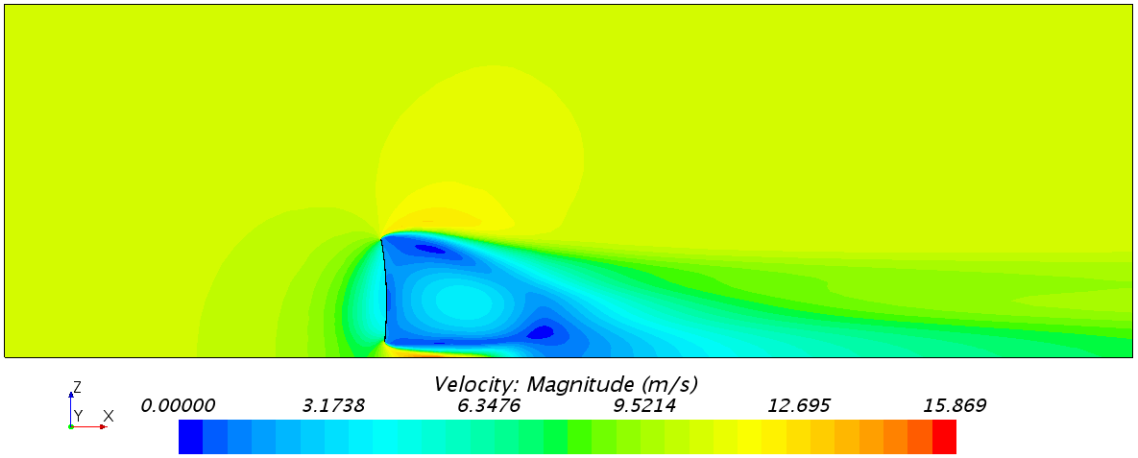

Figure A.257: Side view of the large computational domain, showing the velocity distribution, at a centered xz-plane; the cambered sail model, with a sheet angle of 60°.

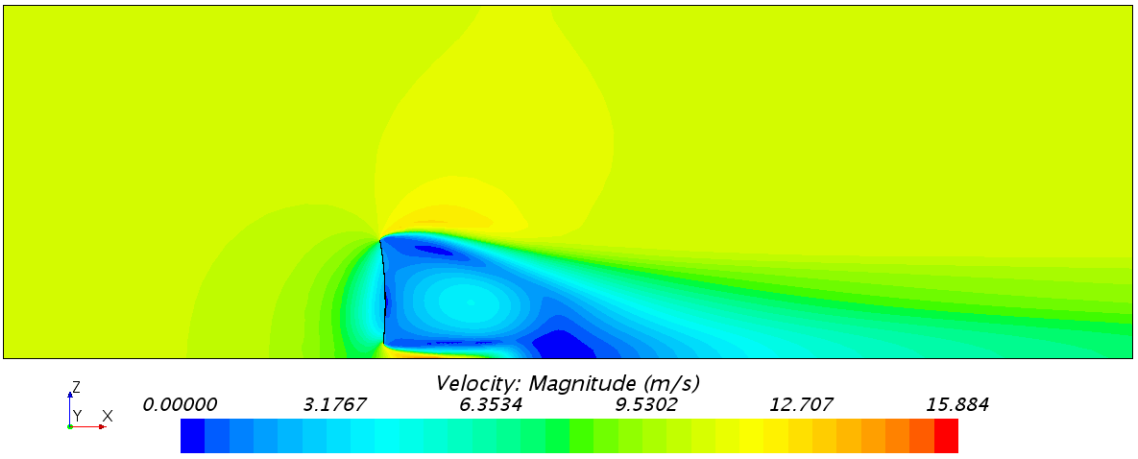

Figure A.258: Side view of the large computational domain, showing the velocity distribution, at a centered xz-plane; the cambered sail model, with a sheet angle of 70°.

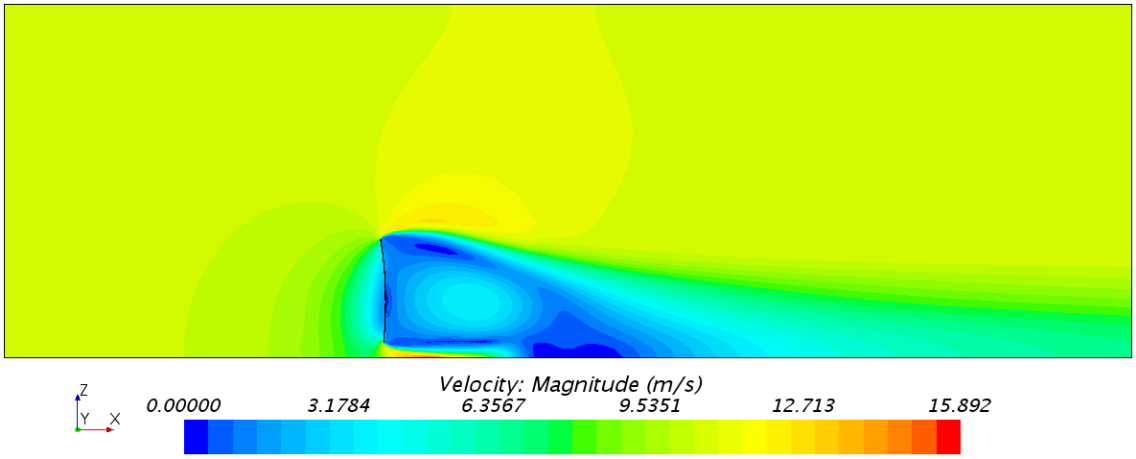

Figure A.259: Side view of the large computational domain, showing the velocity distribution, at a centered xz-plane; the cambered sail model, with a sheet angle of 80°.

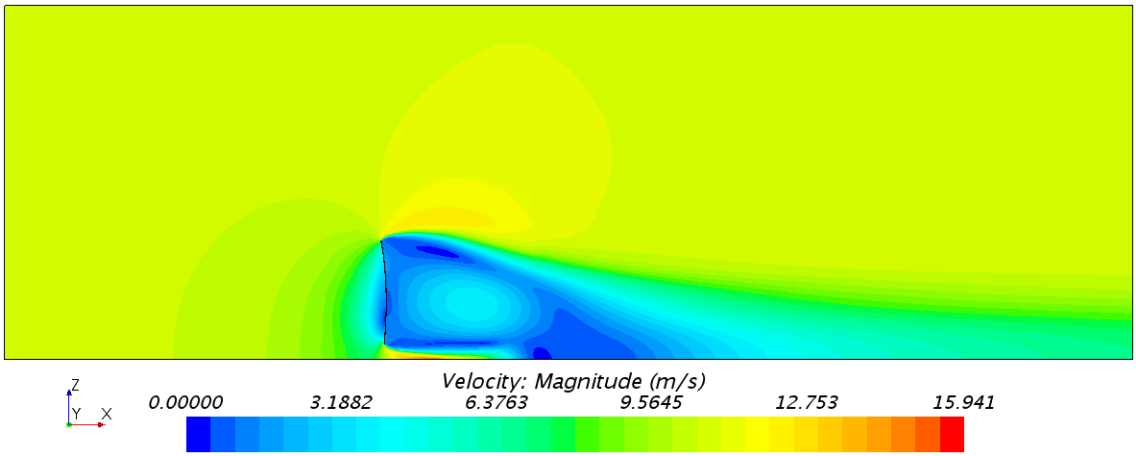

Figure A.260: Side view of the large computational domain, showing the velocity distribution, at a centered xz-plane; the cambered sail model, with a sheet angle of 90°.

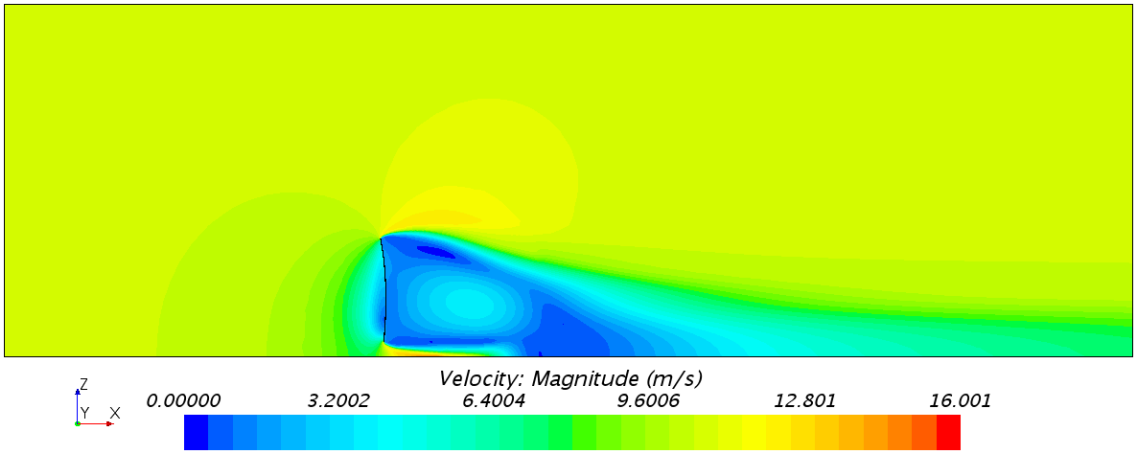

Figure A.261: Side view of the large computational domain, showing the velocity distribution, at a centered xz-plane; the cambered sail model, with a sheet angle of 100°.

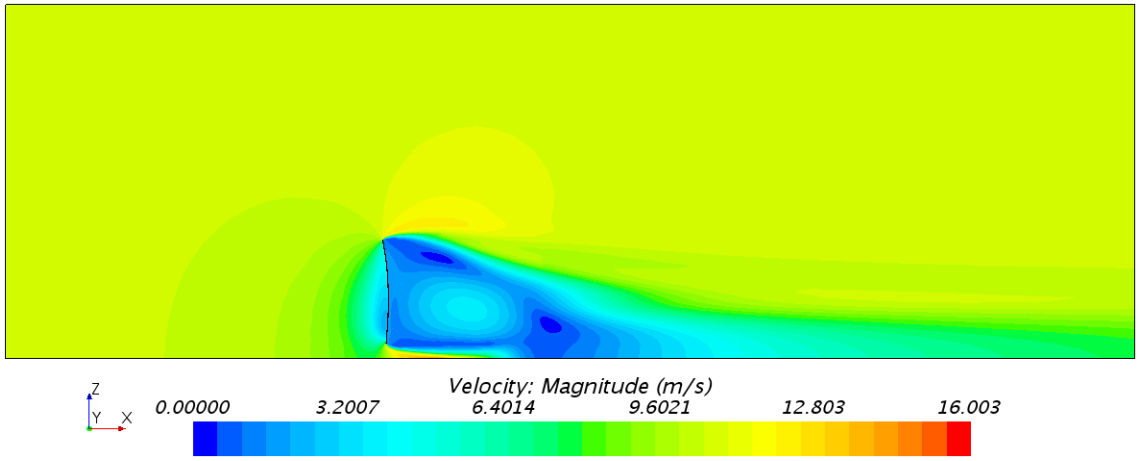

Figure A.262: Side view of the large computational domain, showing the velocity distribution, at a centered xz-plane; the cambered sail model, with a sheet angle of 110°.

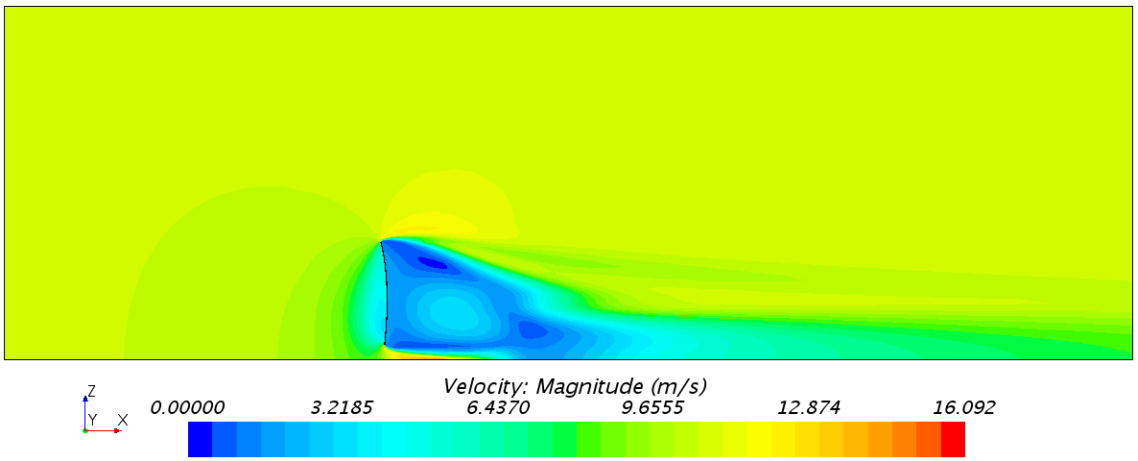

Figure A.263: Side view of the large computational domain, showing the velocity distribution, at a centered xz-plane; the cambered sail model, with a sheet angle of 120°.

Constrained Streamlines at a centered XZ-plane with the Flat Sail Model in the Large Domain

Fig. A.264 - A.270 shows the corresponding side view images of constrained streamlines, for the seven different sheet angles with the flat sail model and with grid 3 in the large computational domain.

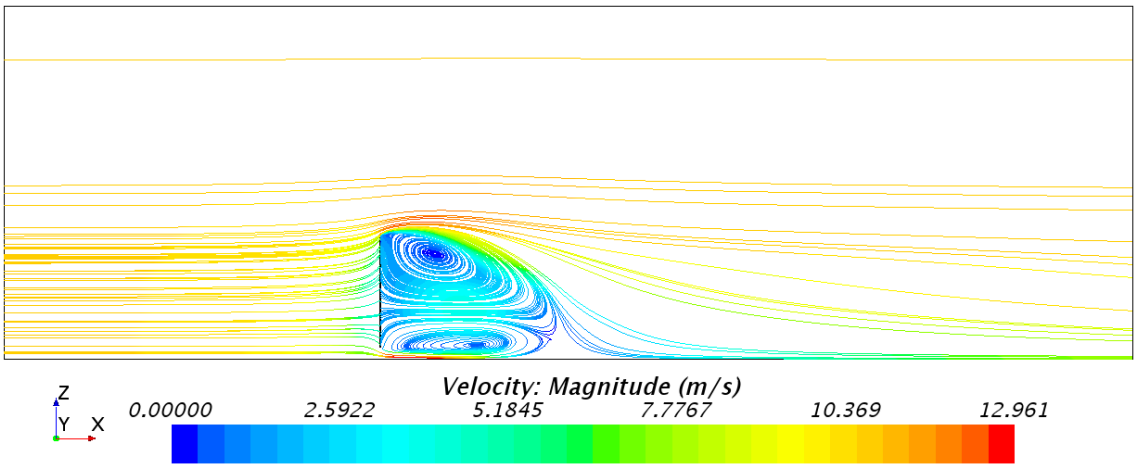

Figure A.264: Side view of the large computational domain, showing constrained streamlines, at a centered xz-plane; the flat sail model, with a sheet angle of 60°.

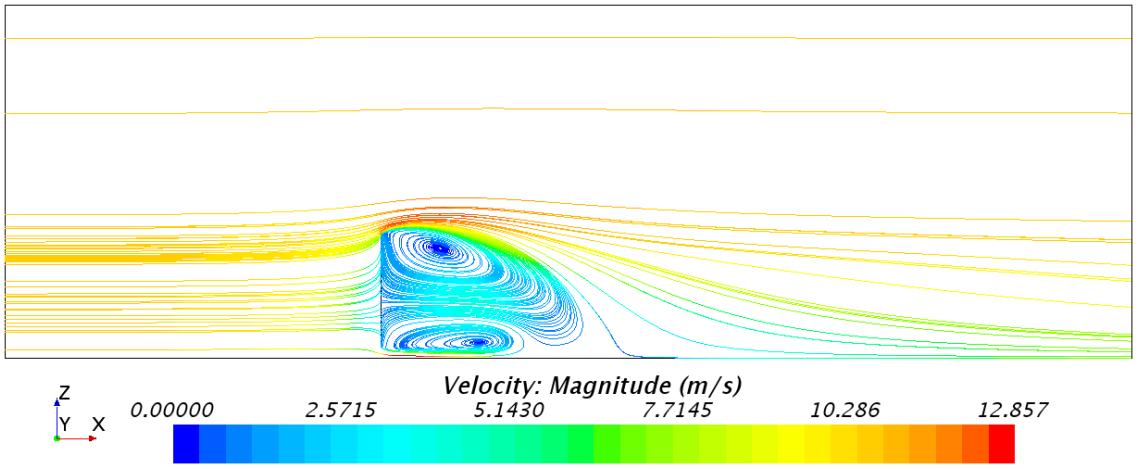

Figure A.265: Side view of the large computational domain, showing constrained streamlines, at a centered xz-plane; the flat sail model, with a sheet angle of 70°.

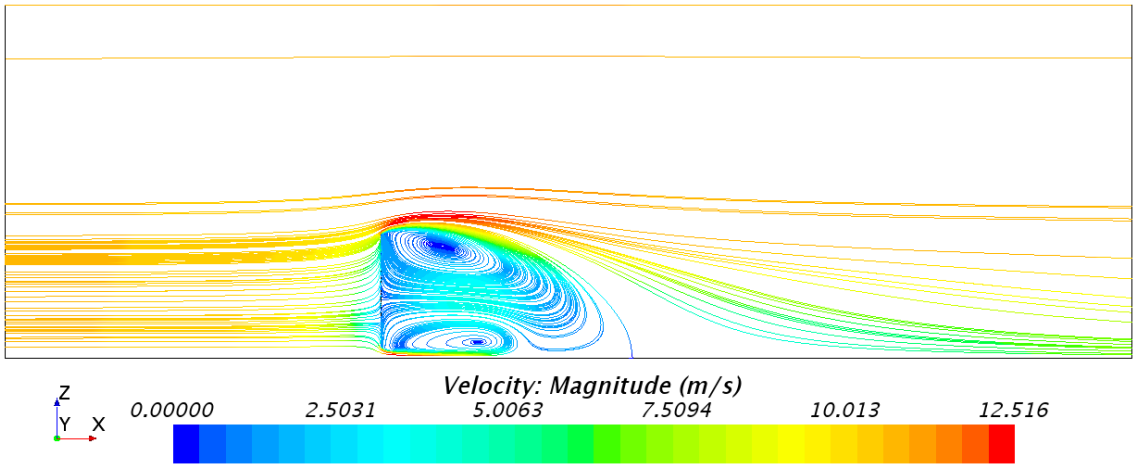

Figure A.266: Side view of the large computational domain, showing constrained streamlines, at a centered xz-plane; the flat sail model, with a sheet angle of 80°.

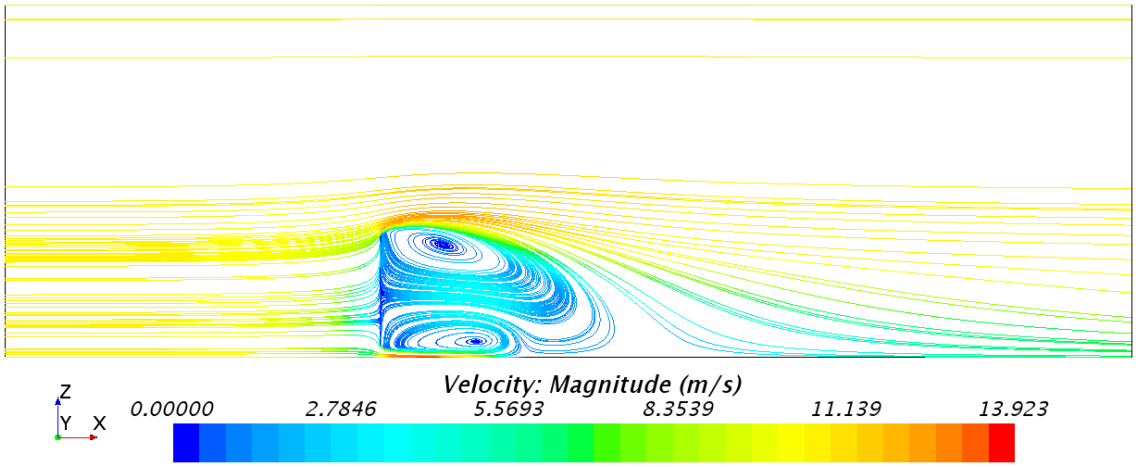

Figure A.267: Side view of the large computational domain, showing constrained streamlines, at a centered xz-plane; the flat sail model, with a sheet angle of 90°.

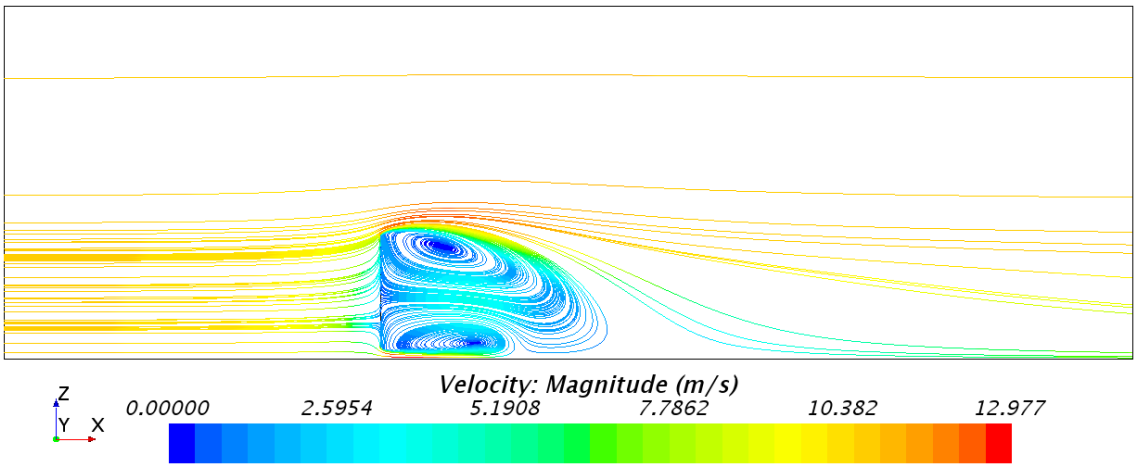

Figure A.268: Side view of the large computational domain, showing constrained streamlines, at a centered xz-plane; the flat sail model, with a sheet angle of 100°.

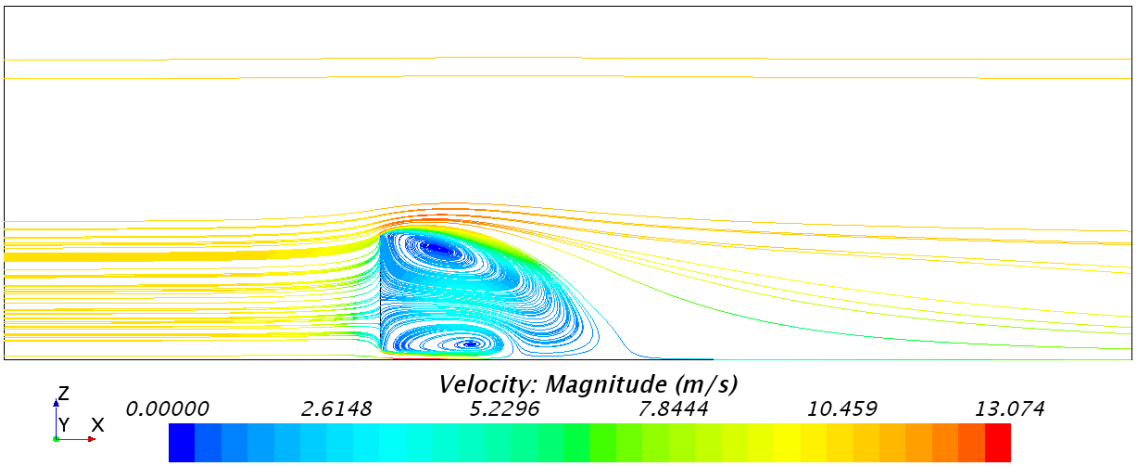

Figure A.269: Side view of the large computational domain, showing constrained streamlines, at a centered xz-plane; the flat sail model, with a sheet angle of 110°.

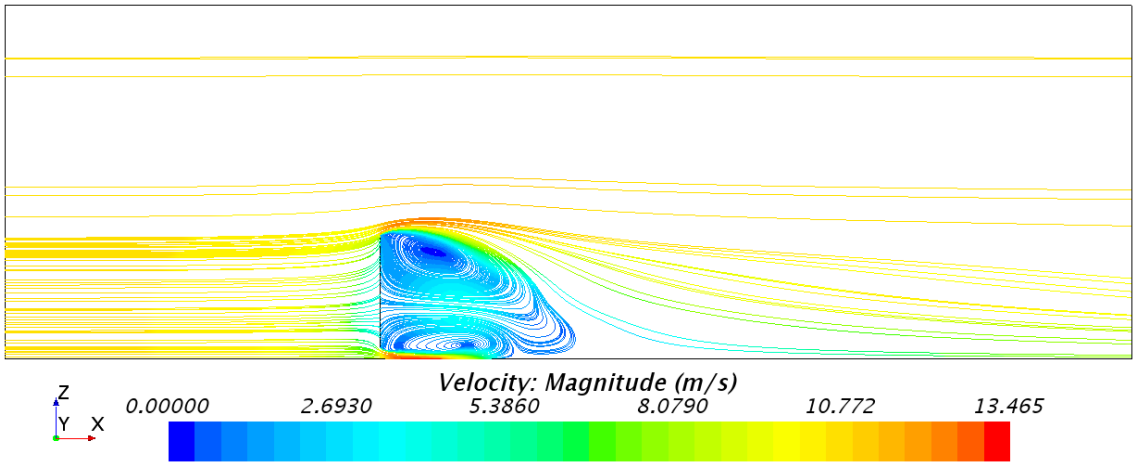

Figure A.270: Side view of the large computational domain, showing constrained streamlines, at a centered xz-plane; the flat sail model, with a sheet angle of 120°.

Constrained Streamlines at a centered XZ-plane with the Cambered Sail Model in the Large Domain

Fig. A.271 - A.277 shows the corresponding side view images of constrained streamlines, for the seven different sheet angles with the cambered sail model and with grid 3 in the large computational domain.

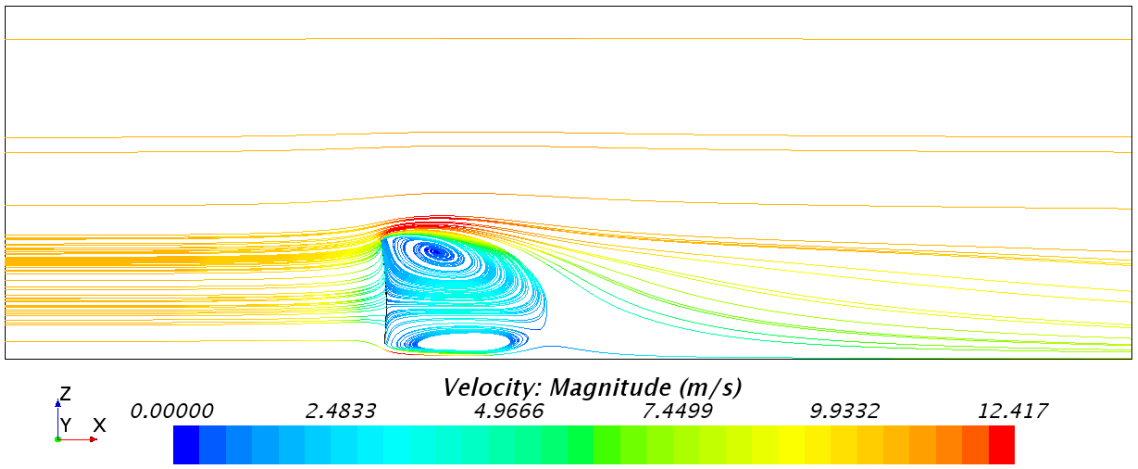

Figure A.271: Side view of the large computational domain, showing constrained streamlines, at a centered xz-plane; the cambered sail model, with a sheet angle of 60°.

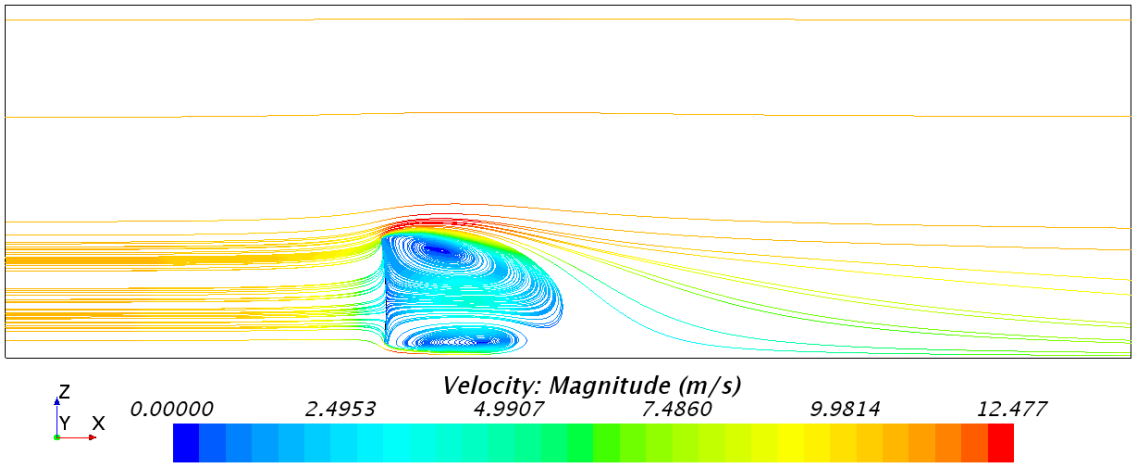

Figure A.272: Side view of the large computational domain, showing constrained streamlines, at a centered xz-plane; the cambered sail model, with a sheet angle of 70°.

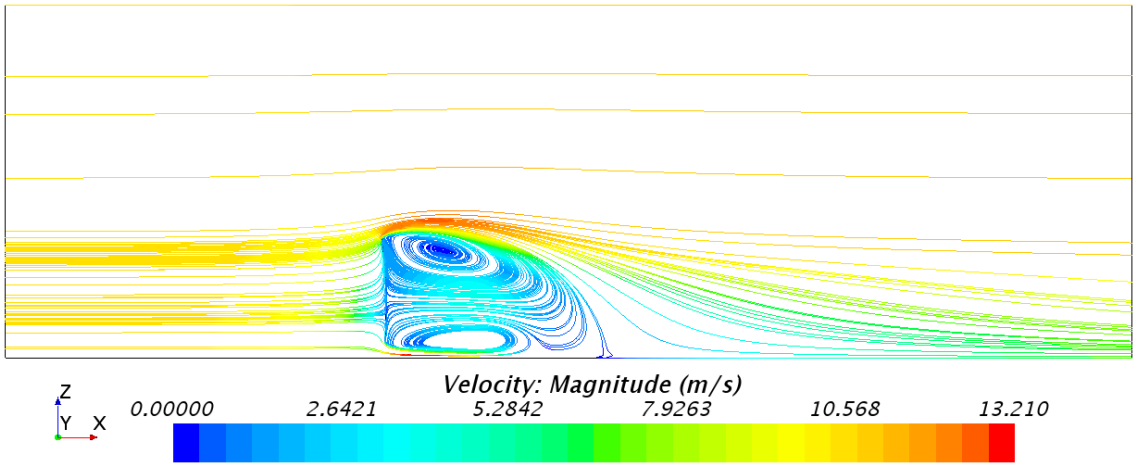

Figure A.273: Side view of the large computational domain, showing constrained streamlines, at a centered xz-plane; the cambered sail model, with a sheet angle of 80°.

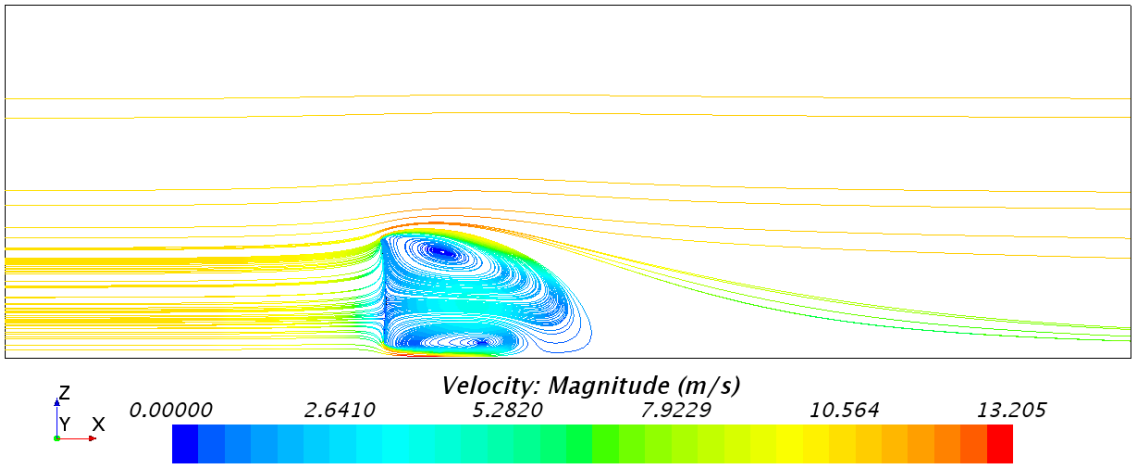

Figure A.274: Side view of the large computational domain, showing constrained streamlines, at a centered xz-plane; the cambered sail model, with a sheet angle of 90°.

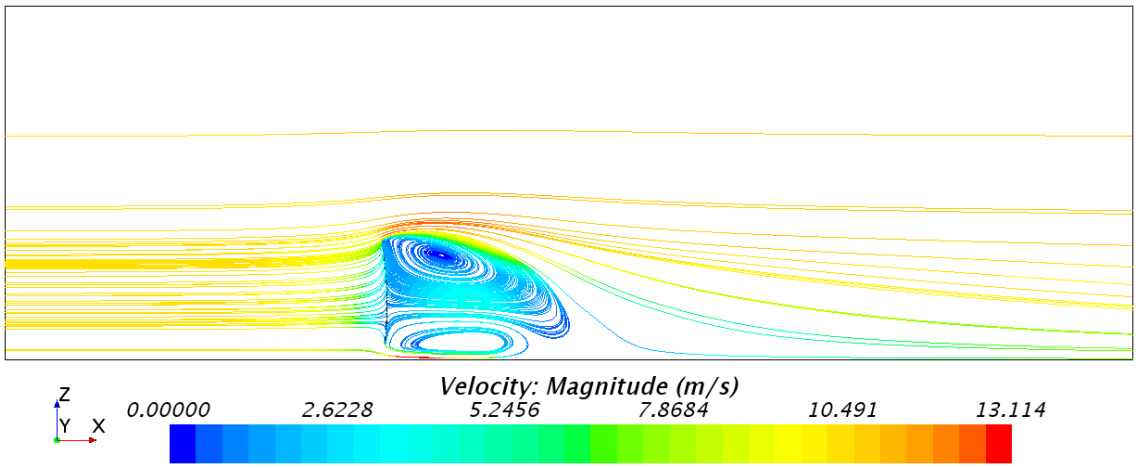

Figure A.275: Side view of the large computational domain, showing constrained streamlines, at a centered xz-plane; the cambered sail model, with a sheet angle of 100°.

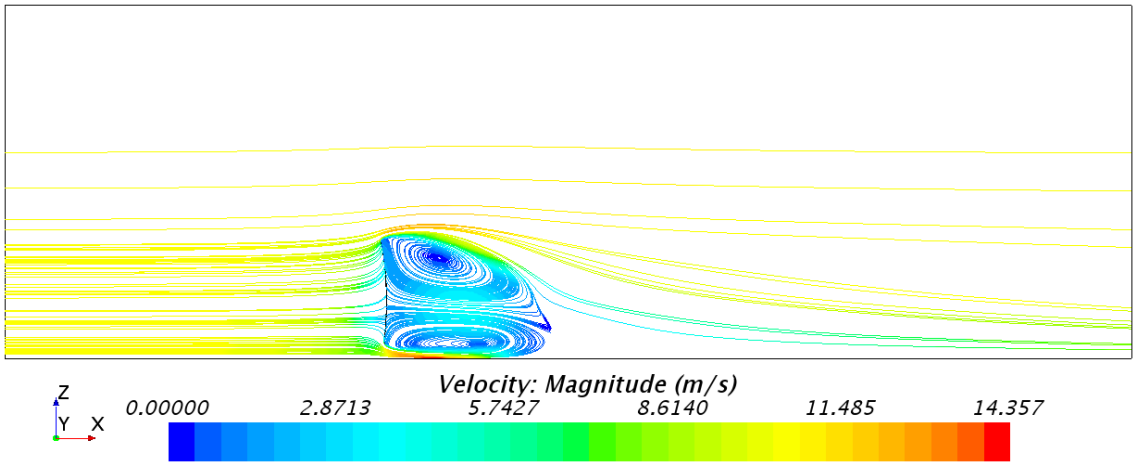

Figure A.276: Side view of the large computational domain, showing constrained streamlines, at a centered xz-plane; the cambered sail model, with a sheet angle of 110°.

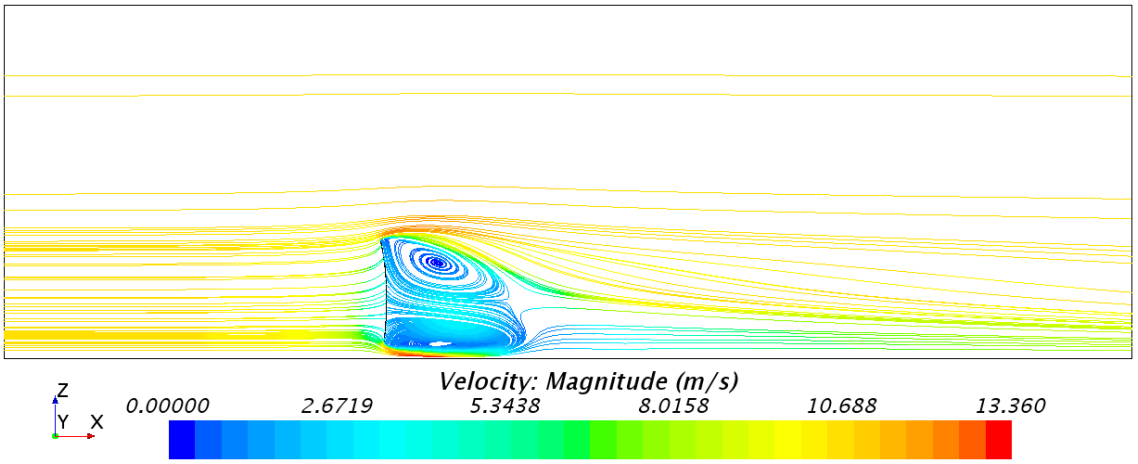

Figure A.277: Side view of the large computational domain, showing constrained streamlines, at a centered xz-plane; the cambered sail model, with a sheet angle of 120°.

Residuals

Fig. A.278 - A.305 shows the residuals, from all RANS simulations that were performed in the sail camber and sheet angle analysis, for both sail models and for both computational domains.

Flat Sail Model with Sheet Angle 60° and the Normal Domain

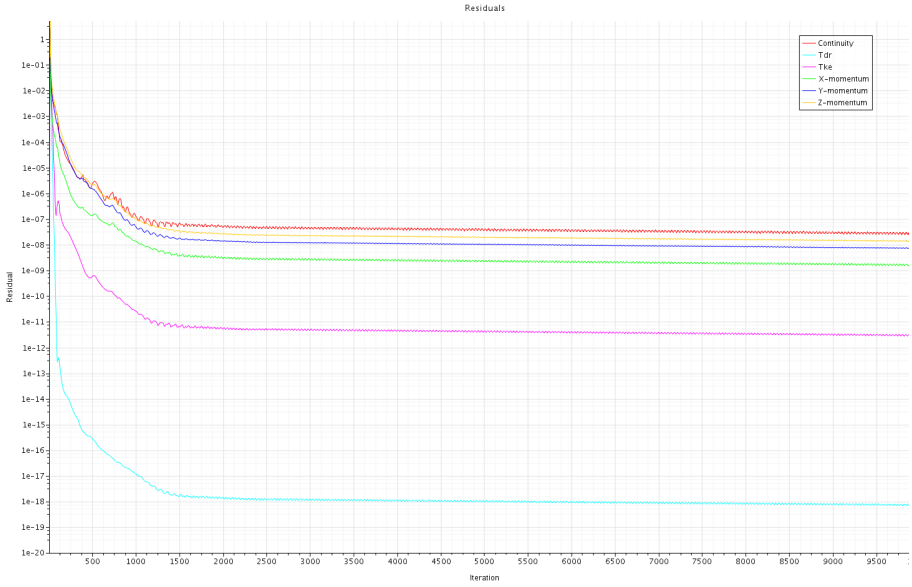

Figure A.278: Residual vs iteration, from RANS simulations with the flat sail model, with a sheet angle of 60°, in the normal computational domain & grid 3, showing the graphs of the Continuity (red), X-momentum (green), Y-momentum (blue), Z-momentum (yellow), Turbulent dissipation rate (cyan) and the Turbulent kinetic energy (purple).

Flat Sail Model with Sheet Angle 70° and the Normal Domain

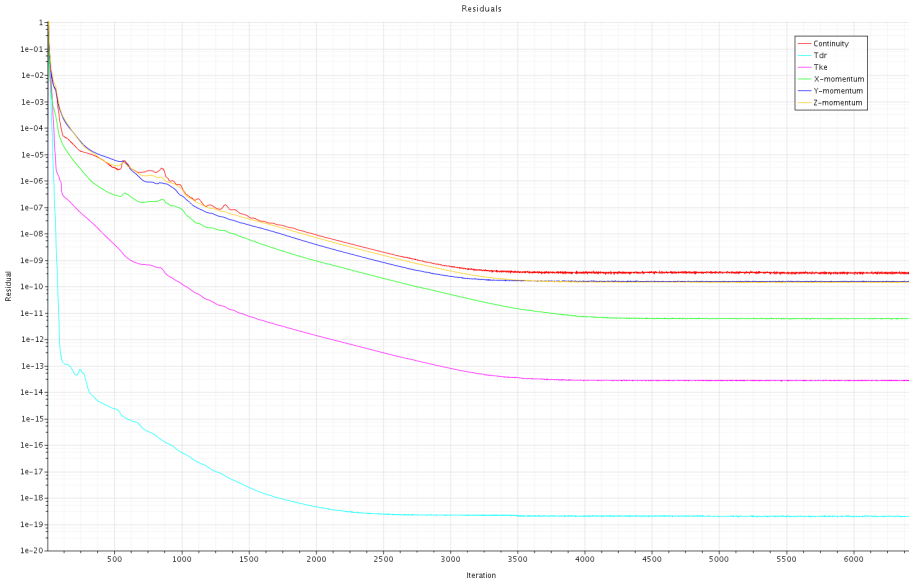

Figure A.279: Residual vs iteration, from RANS simulations with the flat sail model, with a sheet angle of 70°, in the normal computational domain & grid 3, showing the graphs of the Continuity (red), X-momentum (green), Y-momentum (blue), Z-momentum (yellow), Turbulent dissipation rate (cyan) and the Turbulent kinetic energy (purple).

Flat Sail Model with Sheet Angle 80° and the Normal Domain

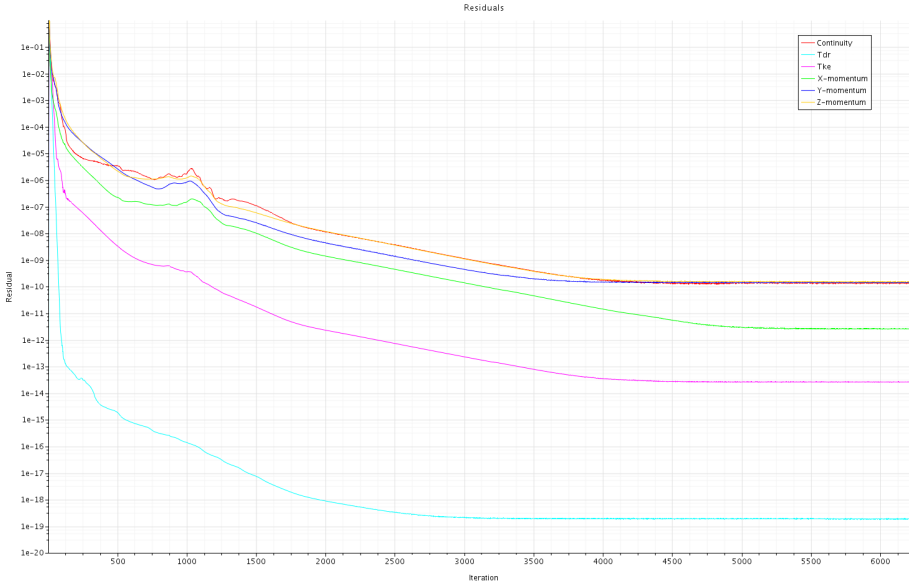

Figure A.280: Residual vs iteration, from RANS simulations with the flat sail model, with a sheet angle of 80°, in the normal computational domain & grid 3, showing the graphs of the Continuity (red), X-momentum (green), Y-momentum (blue), Z-momentum (yellow), Turbulent dissipation rate (cyan) and the Turbulent kinetic energy (purple).

Flat Sail Model with Sheet Angle 90° and the Normal Domain

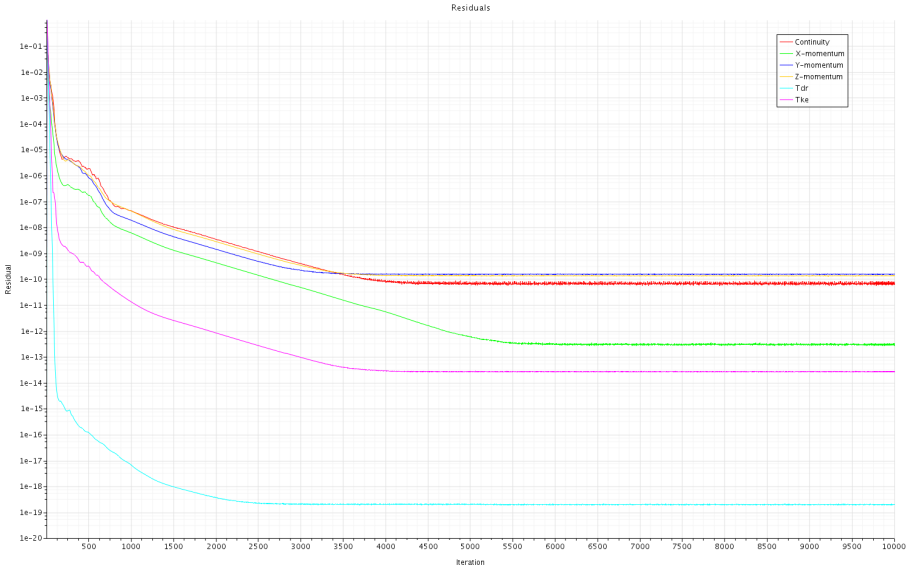

Figure A.281: Residual vs iteration, from RANS simulations with the flat sail model, with a sheet angle of 90°, in the normal computational domain & grid 3, showing the graphs of the Continuity (red), X-momentum (green), Y-momentum (blue), Z-momentum (yellow), Turbulent dissipation rate (cyan) and the Turbulent kinetic energy (purple).

Flat Sail Model with Sheet Angle 100° and the Normal Domain

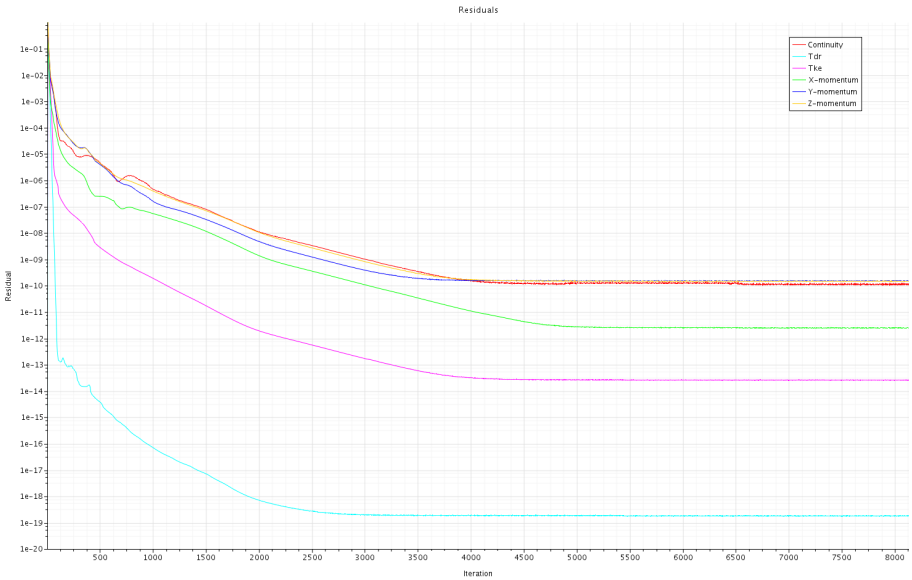

Figure A.282: Residual vs iteration, from RANS simulations with the flat sail model, with a sheet angle of 100°, in the normal computational domain & grid 3, showing the graphs of the Continuity (red), X-momentum (green), Y-momentum (blue), Z-momentum (yellow), Turbulent dissipation rate (cyan) and the Turbulent kinetic energy (purple).

Flat Sail Model with Sheet Angle 110° and the Normal Domain

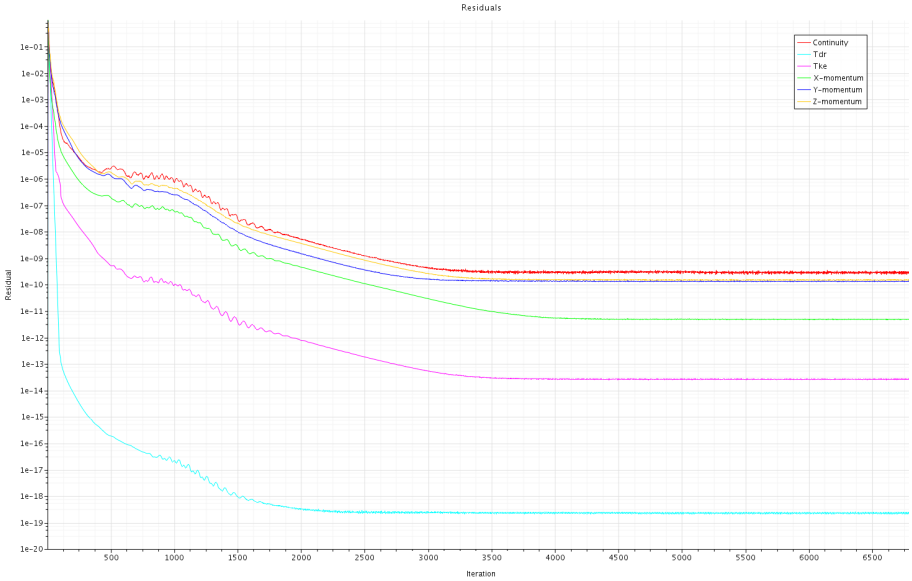

Figure A.283: Residual vs iteration, from RANS simulations with the flat sail model, with a sheet angle of 110°, in the normal computational domain & grid 3, showing the graphs of the Continuity (red), X-momentum (green), Y-momentum (blue), Z-momentum (yellow), Turbulent dissipation rate (cyan) and the Turbulent kinetic energy (purple).

Flat Sail Model with Sheet Angle 120° and the Normal Domain

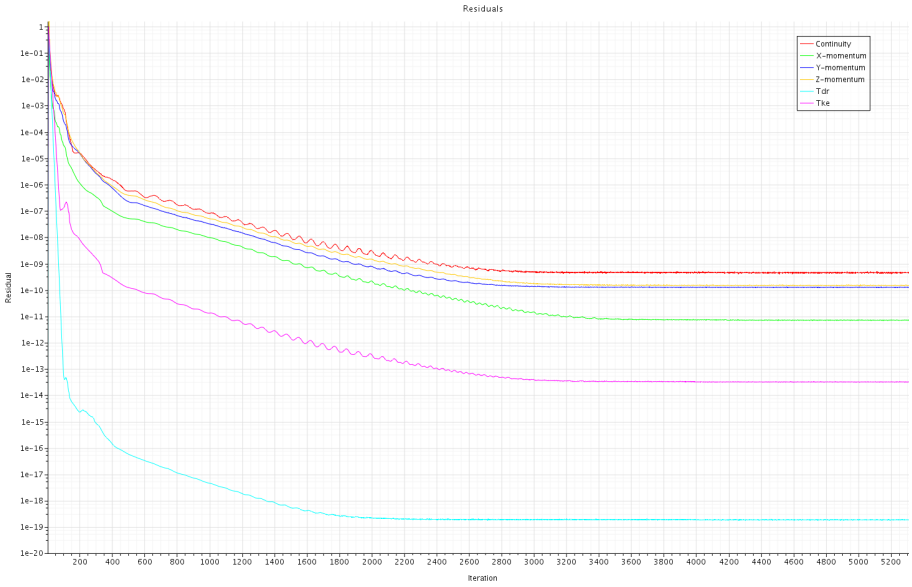

Figure A.284: Residual vs iteration, from RANS simulations with the flat sail model, with a sheet angle of 120°, in the normal computational domain & grid 3, showing the graphs of the Continuity (red), X-momentum (green), Y-momentum (blue), Z-momentum (yellow), Turbulent dissipation rate (cyan) and the Turbulent kinetic energy (purple).

Cambered Sail Model with Sheet Angle 60° and the Normal Domain

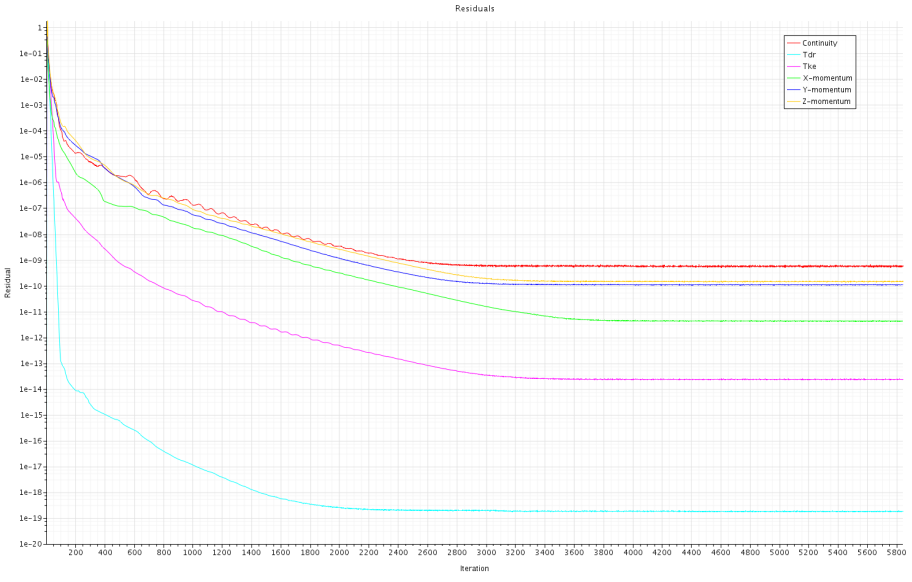

Figure A.285: Residual vs iteration, from RANS simulations with the cambered sail model, with a sheet angle of 60°, in the normal computational domain & grid 3, showing the graphs of the Continuity (red), X-momentum (green), Y-momentum (blue), Z-momentum (yellow), Turbulent dissipation rate (cyan) and the Turbulent kinetic energy (purple).

Cambered Sail Model with Sheet Angle 70° and the Normal Domain

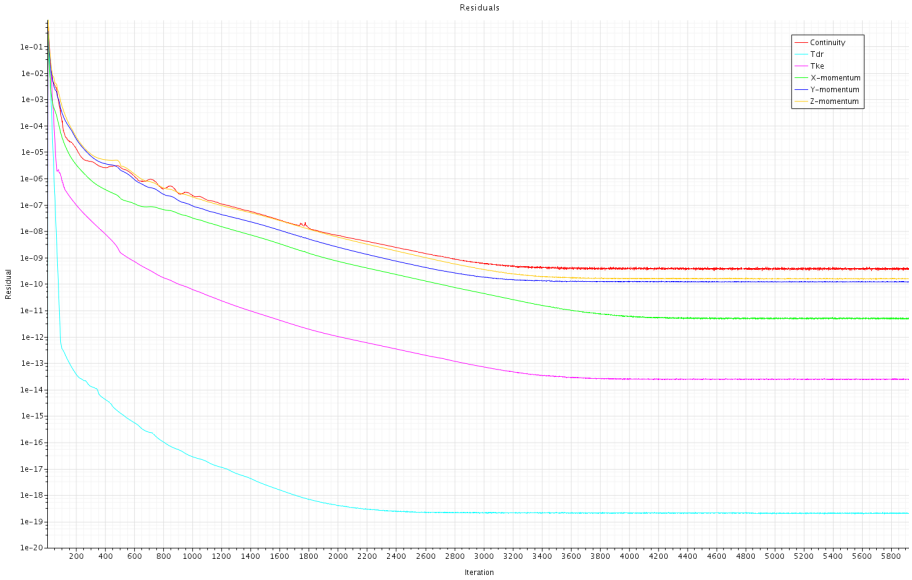

Figure A.286: Residual vs iteration, from RANS simulations with the cambered sail model, with a sheet angle of 70°, in the normal computational domain & grid 3, showing the graphs of the Continuity (red), X-momentum (green), Y-momentum (blue), Z-momentum (yellow), Turbulent dissipation rate (cyan) and the Turbulent kinetic energy (purple).

Cambered Sail Model with Sheet Angle 80° and the Normal Domain

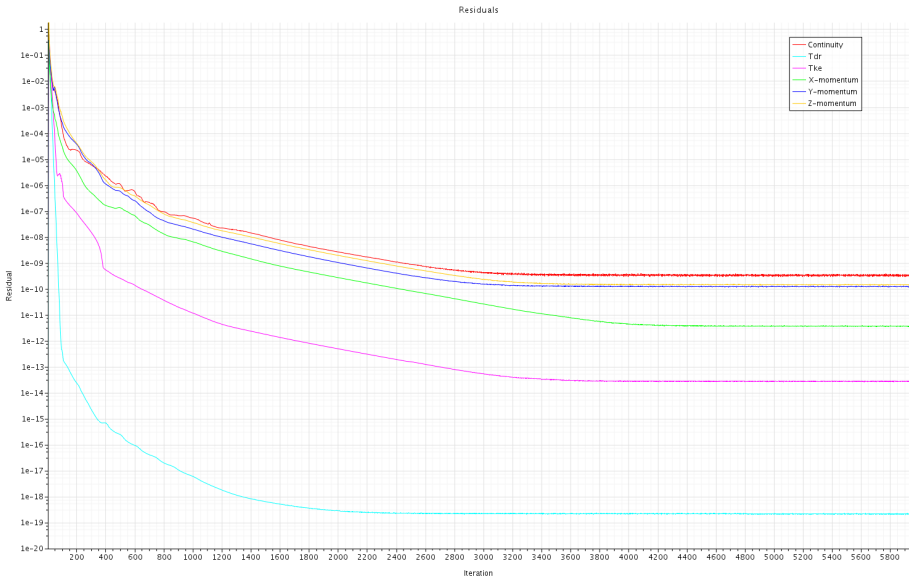

Figure A.287: Residual vs iteration, from RANS simulations with the cambered sail model, with a sheet angle of 80°, in the normal computational domain & grid 3, showing the graphs of the Continuity (red), X-momentum (green), Y-momentum (blue), Z-momentum (yellow), Turbulent dissipation rate (cyan) and the Turbulent kinetic energy (purple).

Cambered Sail Model with Sheet Angle 90° and the Normal Domain

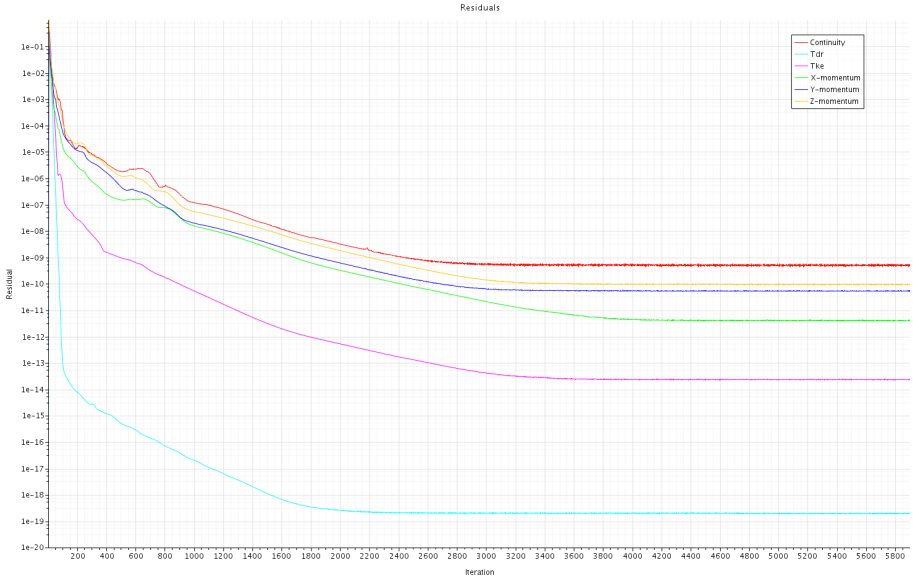

Figure A.288: Residual vs iteration, from RANS simulations with the cambered sail model, with a sheet angle of 90°, in the normal computational domain & grid 3, showing the graphs of the Continuity (red), X-momentum (green), Y-momentum (blue), Z-momentum (yellow), Turbulent dissipation rate (cyan) and the Turbulent kinetic energy (purple).

Cambered Sail Model with Sheet Angle 100° and the Normal Domain

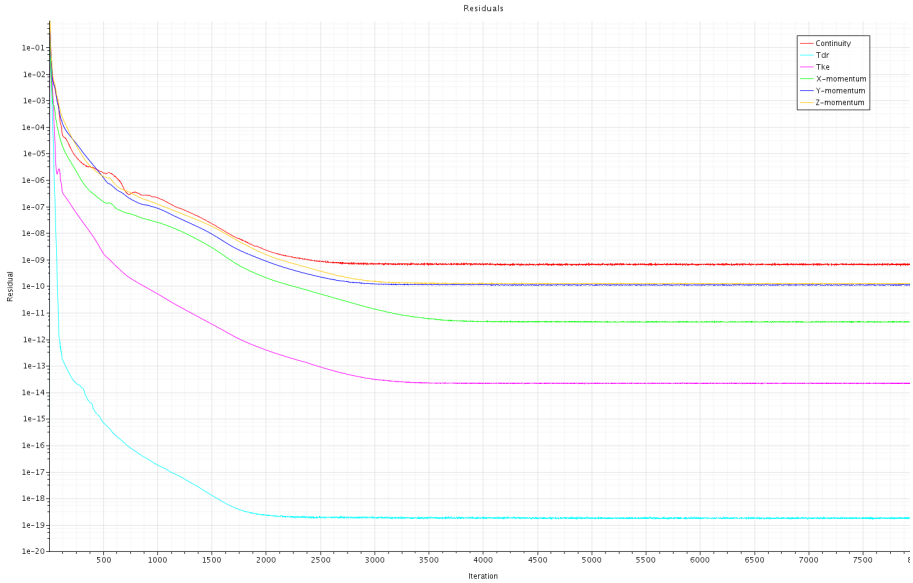

Figure A.289: Residual vs iteration, from RANS simulations with the cambered sail model, with a sheet angle of 100°, in the normal computational domain & grid 3, showing the graphs of the Continuity (red), X-momentum (green), Y-momentum (blue), Z-momentum (yellow), Turbulent dissipation rate (cyan) and the Turbulent kinetic energy (purple).

Cambered Sail Model with Sheet Angle 110° and the Normal Domain

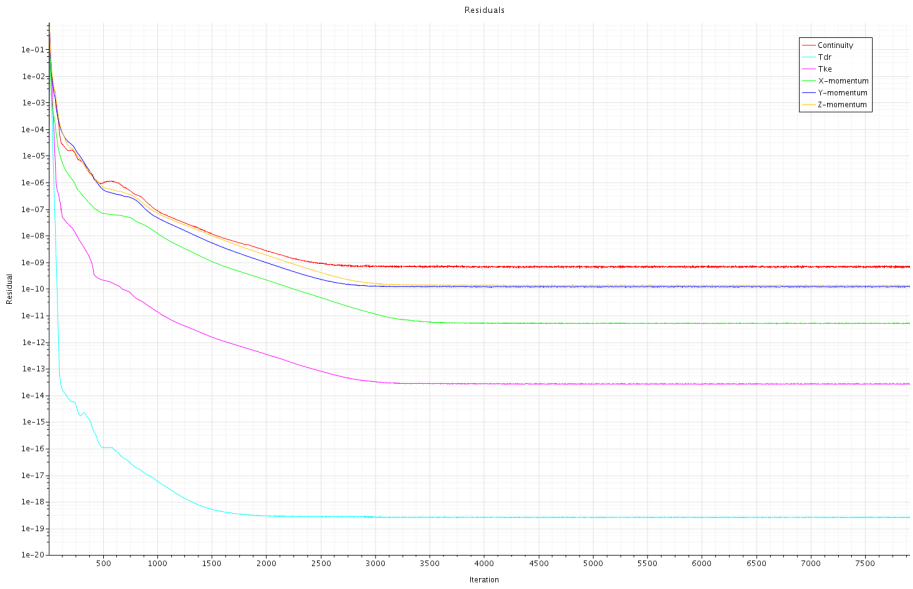

Figure A.290: Residual vs iteration, from RANS simulations with the cambered sail model, with a sheet angle of 110°, in the normal computational domain & grid 3, showing the graphs of the Continuity (red), X-momentum (green), Y-momentum (blue), Z-momentum (yellow), Turbulent dissipation rate (cyan) and the Turbulent kinetic energy (purple).

Cambered Sail Model with Sheet Angle 120° and the Normal Domain

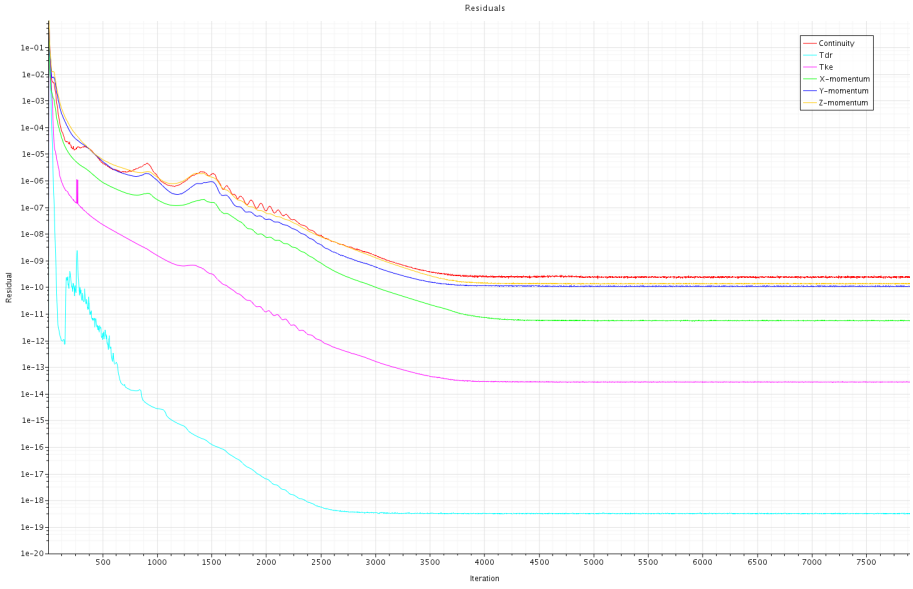

Figure A.291: Residual vs iteration, from RANS simulations with the cambered sail model, with a sheet angle of 120°, in the normal computational domain & grid 3, showing the graphs of the Continuity (red), X-momentum (green), Y-momentum (blue), Z-momentum (yellow), Turbulent dissipation rate (cyan) and the Turbulent kinetic energy (purple).

Flat Sail Model with Sheet Angle 60° and the Large Domain

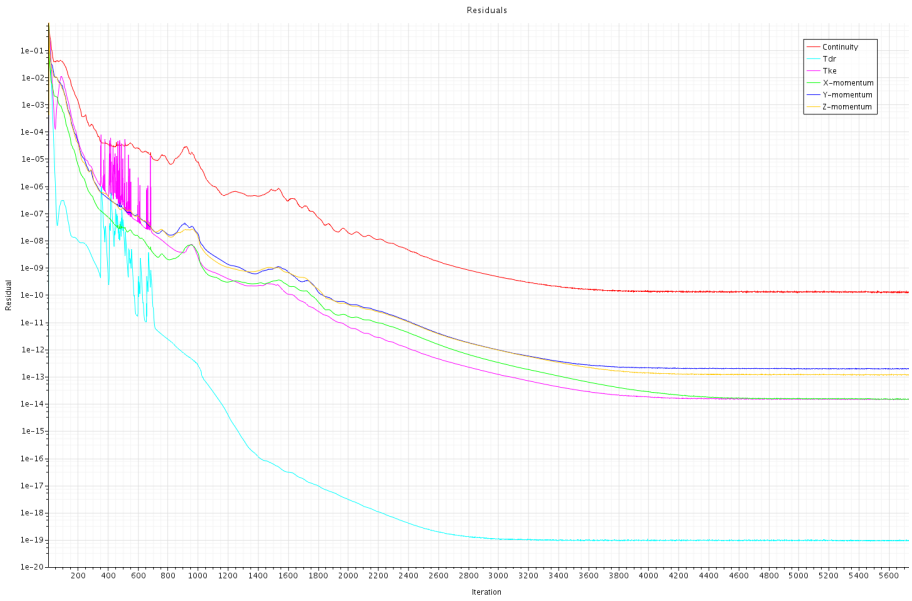

Figure A.292: Residual vs iteration, from RANS simulations with the flat sail model, with a sheet angle of 60°, in the large computational domain & grid 3, showing the graphs of the Continuity (red), X-momentum (green), Y-momentum (blue), Z-momentum (yellow), Turbulent dissipation rate (cyan) and the Turbulent kinetic energy (purple).

Flat Sail Model with Sheet Angle 70° and the Large Domain

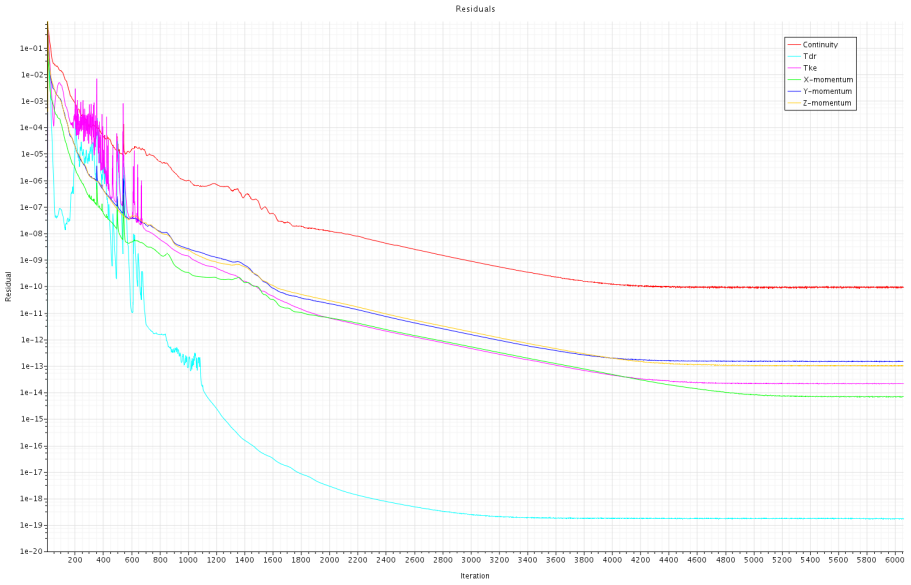

Figure A.293: Residual vs iteration, from RANS simulations with the flat sail model, with a sheet angle of 70°, in the large computational domain & grid 3, showing the graphs of the Continuity (red), X-momentum (green), Y-momentum (blue), Z-momentum (yellow), Turbulent dissipation rate (cyan) and the Turbulent kinetic energy (purple).

Flat Sail Model with Sheet Angle 80° and the Large Domain

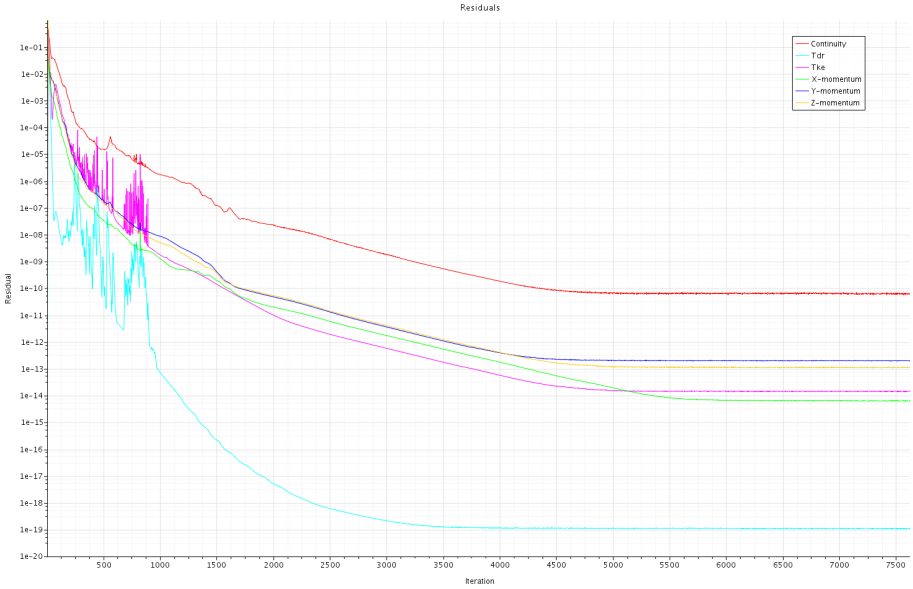

Figure A.294: Residual vs iteration, from RANS simulations with the flat sail model, with a sheet angle of 80°, in the large computational domain & grid 3, showing the graphs of the Continuity (red), X-momentum (green), Y-momentum (blue), Z-momentum (yellow), Turbulent dissipation rate (cyan) and the Turbulent kinetic energy (purple).

Flat Sail Model with Sheet Angle 90° and the Large Domain

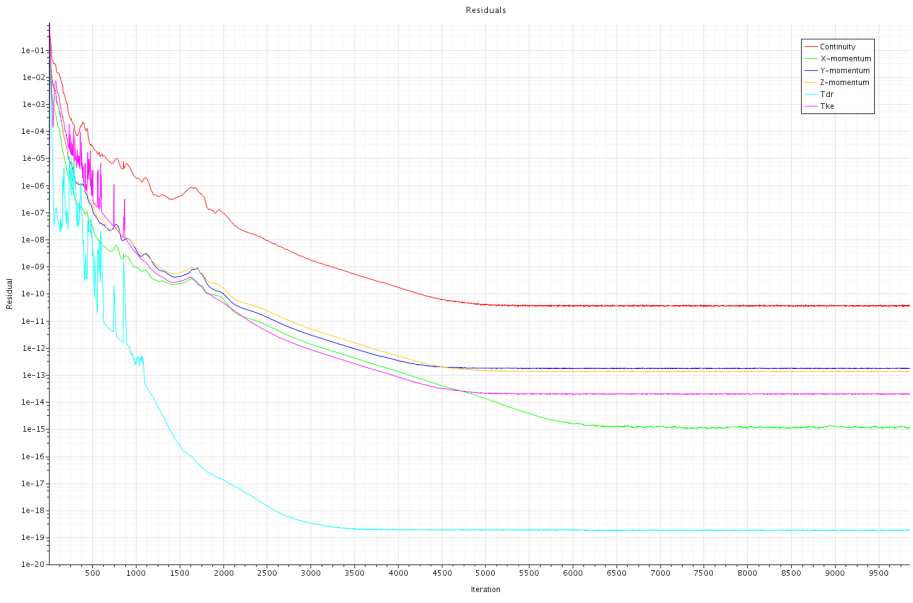

Figure A.295: Residual vs iteration, from RANS simulations with the flat sail model, with a sheet angle of 90°, in the large computational domain & grid 3, showing the graphs of the Continuity (red), X-momentum (green), Y-momentum (blue), Z-momentum (yellow), Turbulent dissipation rate (cyan) and the Turbulent kinetic energy (purple).

Flat Sail Model with Sheet Angle 100° and the Large Domain

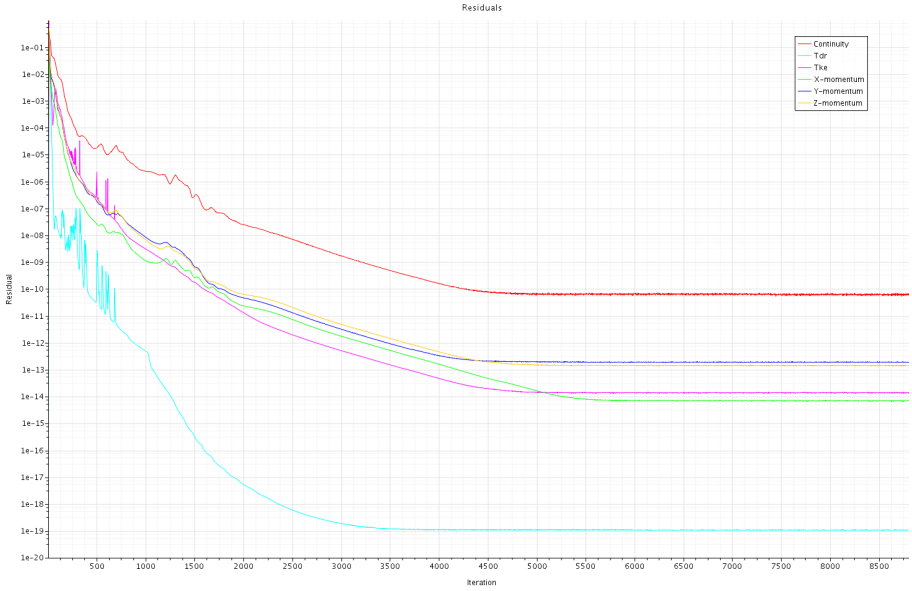

Figure A.296: Residual vs iteration, from RANS simulations with the flat sail model, with a sheet angle of 100°, in the large computational domain & grid 3, showing the graphs of the Continuity (red), X-momentum (green), Y-momentum (blue), Z-momentum (yellow), Turbulent dissipation rate (cyan) and the Turbulent kinetic energy (purple).

Flat Sail Model with Sheet Angle 110° and the Large Domain

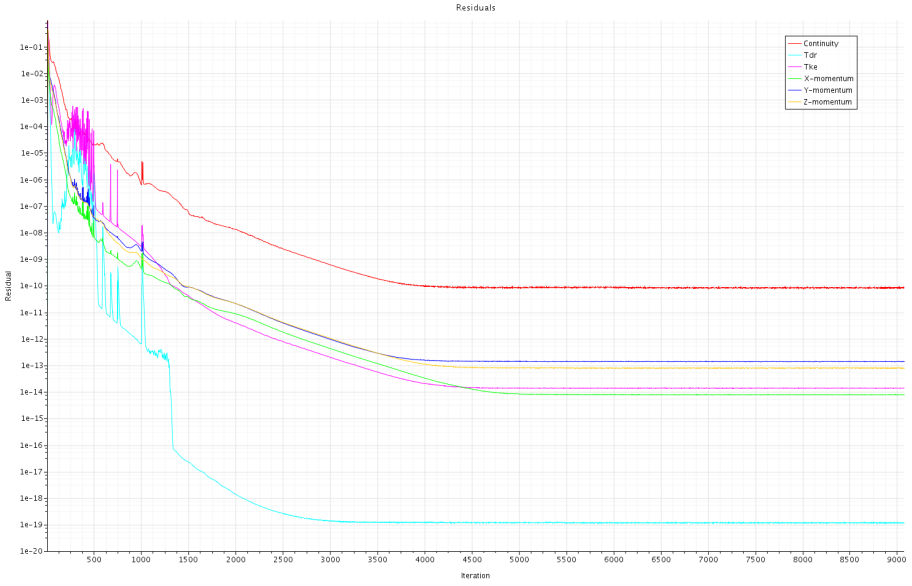

Figure A.297: Residual vs iteration, from RANS simulations with the flat sail model, with a sheet angle of 110°, in the large computational domain & grid 3, showing the graphs of the Continuity (red), X-momentum (green), Y-momentum (blue), Z-momentum (yellow), Turbulent dissipation rate (cyan) and the Turbulent kinetic energy (purple).

Flat Sail Model with Sheet Angle 120° and the Large Domain

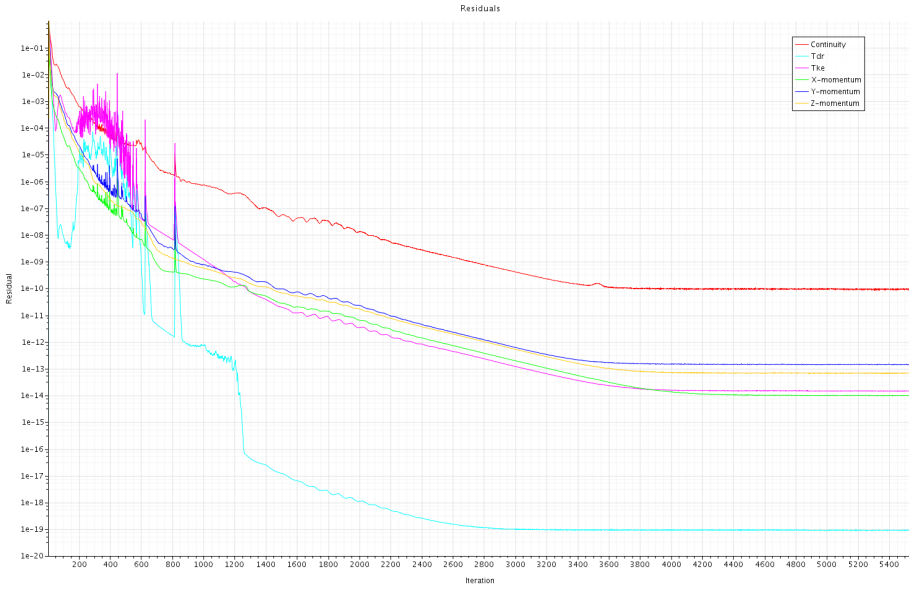

Figure A.298: Residual vs iteration, from RANS simulations with the flat sail model, with a sheet angle of 120°, in the large computational domain & grid 3, showing the graphs of the Continuity (red), X-momentum (green), Y-momentum (blue), Z-momentum (yellow), Turbulent dissipation rate (cyan) and the Turbulent kinetic energy (purple).

Cambered Sail Model with Sheet Angle 60° and the Large Domain

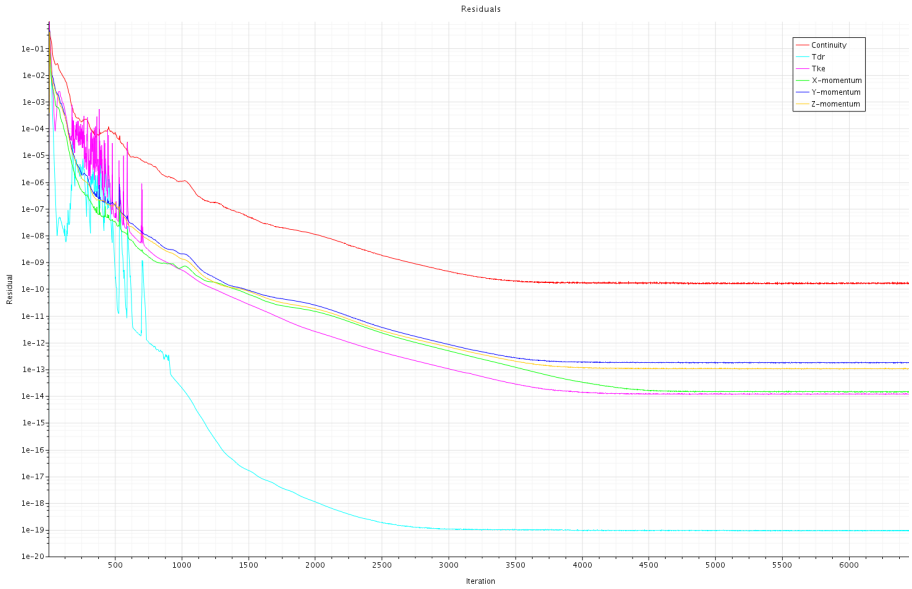

Figure A.299: Residual vs iteration, from RANS simulations with the cambered sail model, with a sheet angle of 60°, in the large computational domain & grid 3, showing the graphs of the Continuity (red), X-momentum (green), Y-momentum (blue), Z-momentum (yellow), Turbulent dissipation rate (cyan) and the Turbulent kinetic energy (purple).

Cambered Sail Model with Sheet Angle 70° and the Large Domain

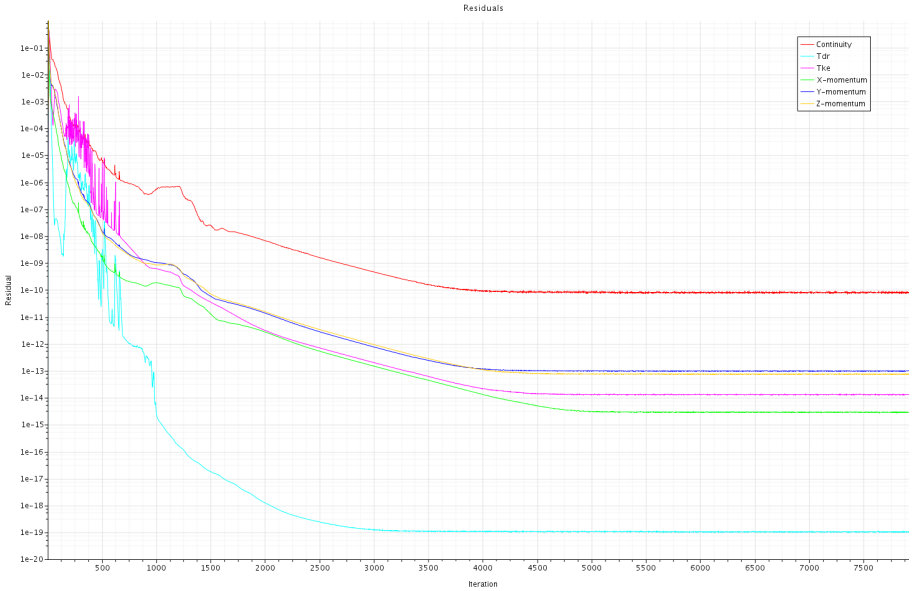

Figure A.300: Residual vs iteration, from RANS simulations with the cambered sail model, with a sheet angle of 70°, in the large computational domain & grid 3, showing the graphs of the Continuity (red), X-momentum (green), Y-momentum (blue), Z-momentum (yellow), Turbulent dissipation rate (cyan) and the Turbulent kinetic energy (purple).

Cambered Sail Model with Sheet Angle 80° and the Large Domain

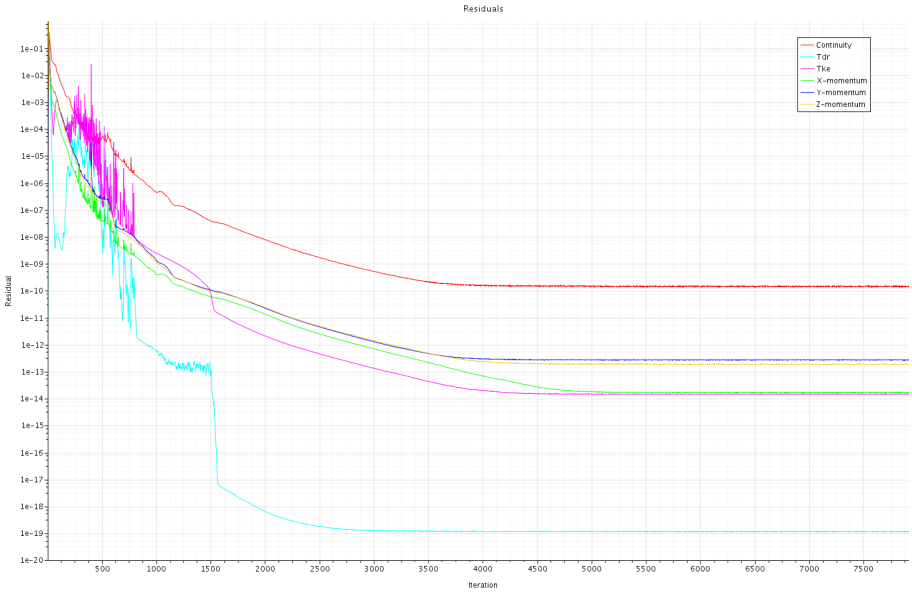

Figure A.301: Residual vs iteration, from RANS simulations with the cambered sail model, with a sheet angle of 80°, in the large computational domain & grid 3, showing the graphs of the Continuity (red), X-momentum (green), Y-momentum (blue), Z-momentum (yellow), Turbulent dissipation rate (cyan) and the Turbulent kinetic energy (purple).

Cambered Sail Model with Sheet Angle 90° and the Large Domain

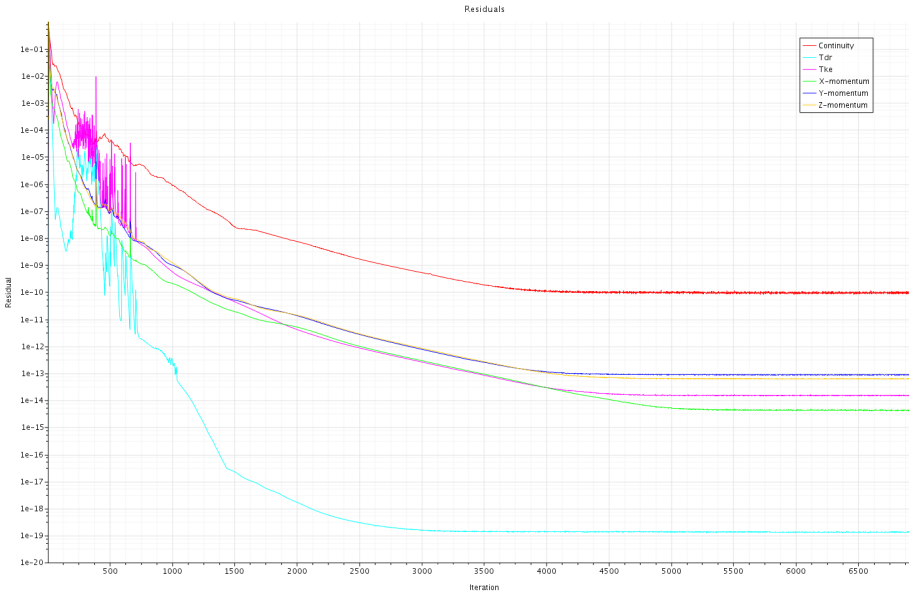

Figure A.302: Residual vs iteration, from RANS simulations with the cambered sail model, with a sheet angle of 90°, in the large computational domain & grid 3, showing the graphs of the Continuity (red), X-momentum (green), Y-momentum (blue), Z-momentum (yellow), Turbulent dissipation rate (cyan) and the Turbulent kinetic energy (purple).

Cambered Sail Model with Sheet Angle 100° and the Large Domain

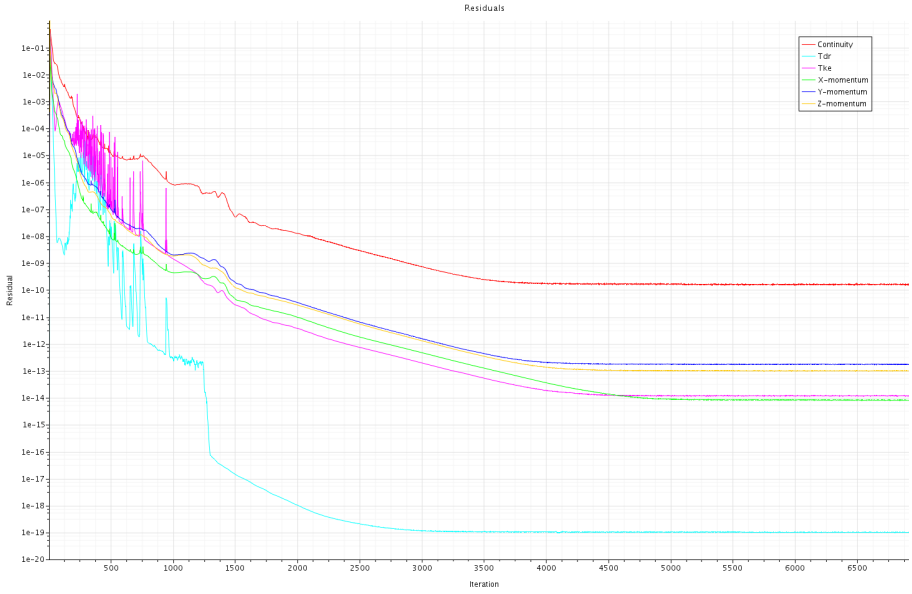

Figure A.303: Residual vs iteration, from RANS simulations with the cambered sail model, with a sheet angle of 100°, in the large computational domain & grid 3, showing the graphs of the Continuity (red), X-momentum (green), Y-momentum (blue), Z-momentum (yellow), Turbulent dissipation rate (cyan) and the Turbulent kinetic energy (purple).

Cambered Sail Model with Sheet Angle 110° and the Large Domain

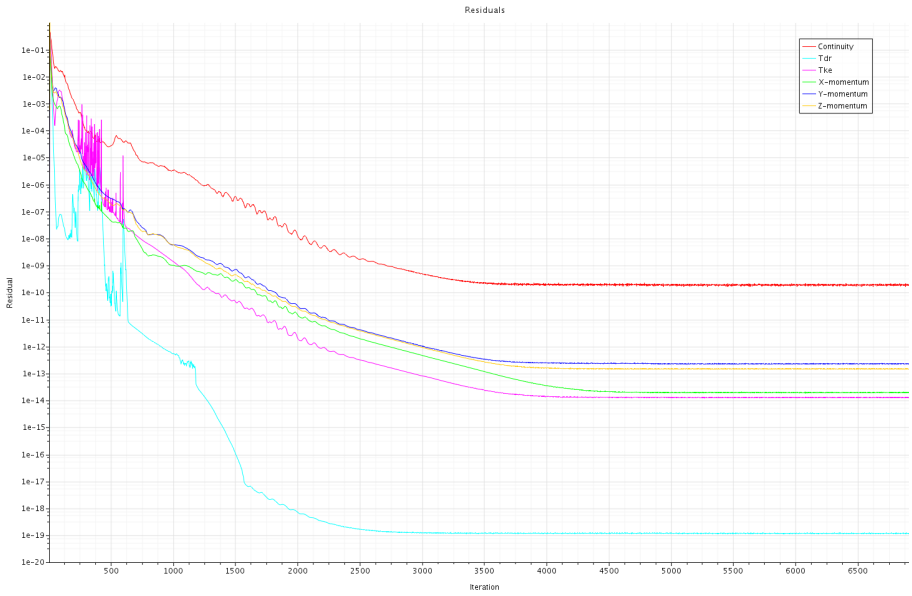

Figure A.304: Residual vs iteration, from RANS simulations with the cambered sail model, with a sheet angle of 110°, in the large computational domain & grid 3, showing the graphs of the Continuity (red), X-momentum (green), Y-momentum (blue), Z-momentum (yellow), Turbulent dissipation rate (cyan) and the Turbulent kinetic energy (purple).

Cambered Sail Model with Sheet Angle 120° and the Large Domain

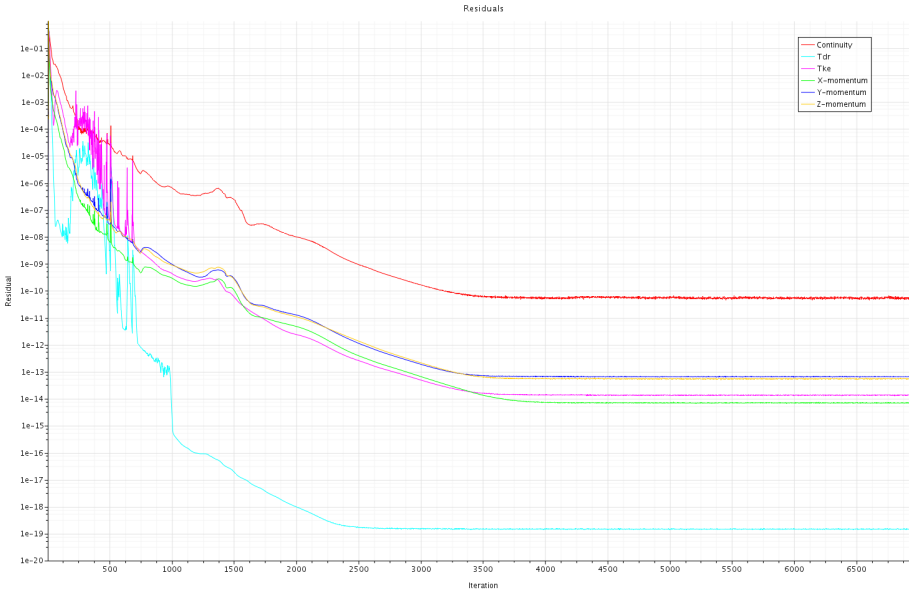

Figure A.305: Residual vs iteration, from RANS simulations with the cambered sail model, with a sheet angle of 120°, in the large computational domain & grid 3, showing the graphs of the Continuity (red), X-momentum (green), Y-momentum (blue), Z-momentum (yellow), Turbulent dissipation rate (cyan) and the Turbulent kinetic energy (purple).

A.5.3 Detached-Eddy Simulations (DES)

Tabulated Data

The average drive force coefficients from Fig 5.28 are presented in Table A.11 below.

Table A.11: Average drive force coefficients C_{F_M} [-], from the last 100 000 iterations (2.5 physical seconds) from DES, with Spalart-Allmaras (S-A) turbulence model.

Sheet angle [°]	**60**	**70**	**80**	**90**	**100**	**110**	**120**
Normal domain				C_{F_M} [-]			
DES	1.4216	1.7320	1.7750	1.9562	1.5752	1.3817	1.1738
Large domain				C_{F_M} [-]			
DES	1.3341	1.6759	1.7301	1.7971	1.7051	1.3325	1.0611

Flow Field Visualization

The top view images of the velocity distribution and constrained streamlines, shows the scalar quantities at a horizontal xy -plane, at the height of the center of effort (CoE) and the corresponding side-view images, shows the scalar quantities at a vertical XZ -plane in the center of the domain.

Top View Images

Velocity Distribution at CoE with the Cambered Sail Model in the Normal Domain

Fig. A.306 - A.312 shows top view images of the velocity distribution, for the seven different sheet angles with the cambered sail model in the normal computational domain.

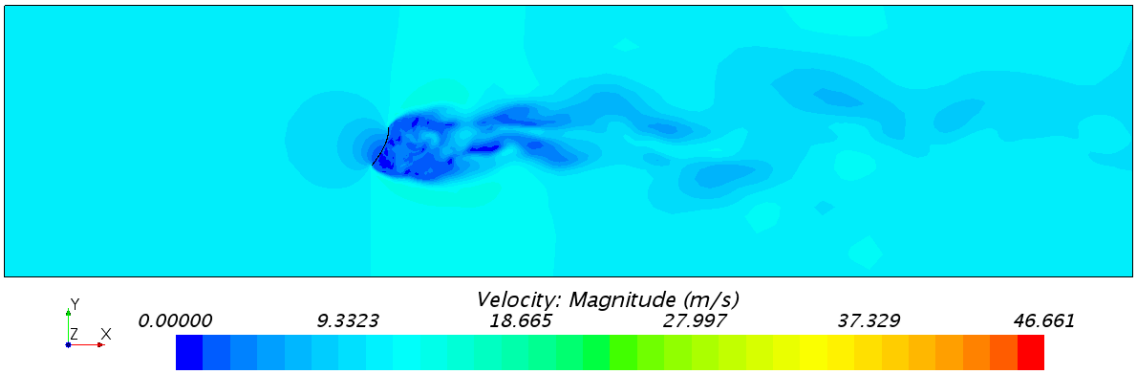

Figure A.306: Top view of the normal computational domain, showing the velocity distribution, at the height of the center of effort (CoE); the cambered sail model, with a sheet angle of 60°.

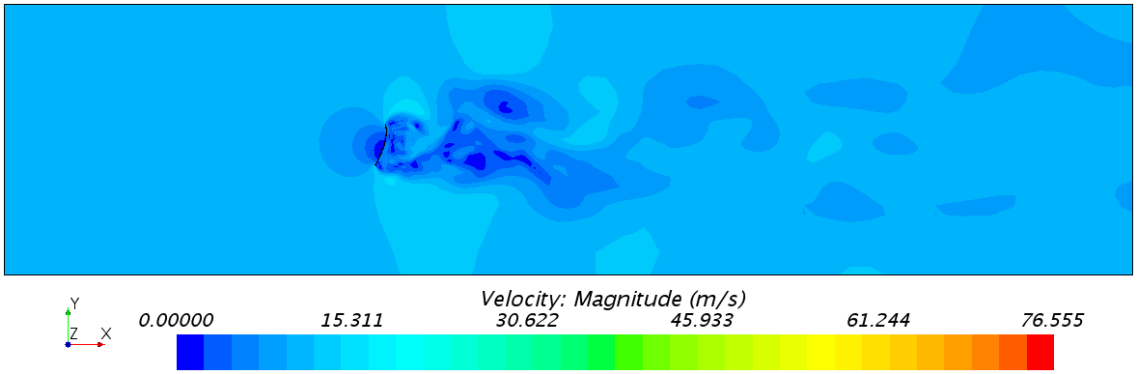

Figure A.307: Top view of the normal computational domain, showing the velocity distribution, at the height of the center of effort (CoE); the cambered sail model, with a sheet angle of 70°.

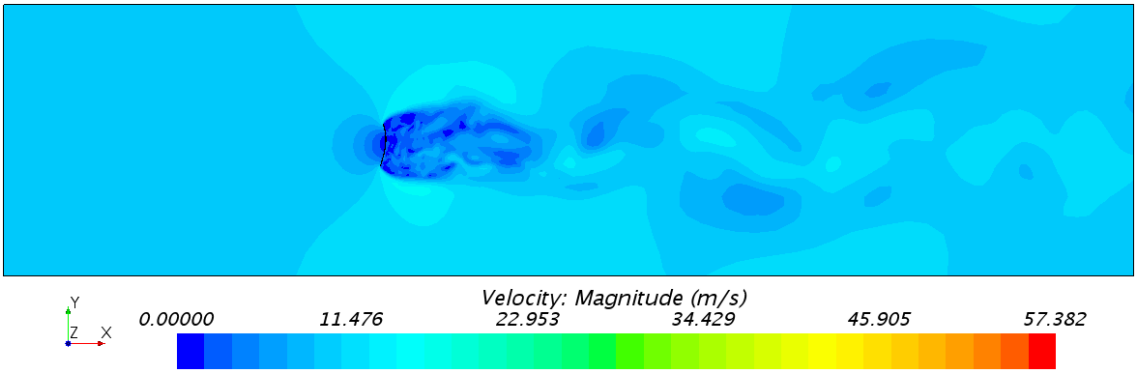

Figure A.308: Top view of the normal computational domain, showing the velocity distribution, at the height of the center of effort (CoE); the cambered sail model, with a sheet angle of 80°.

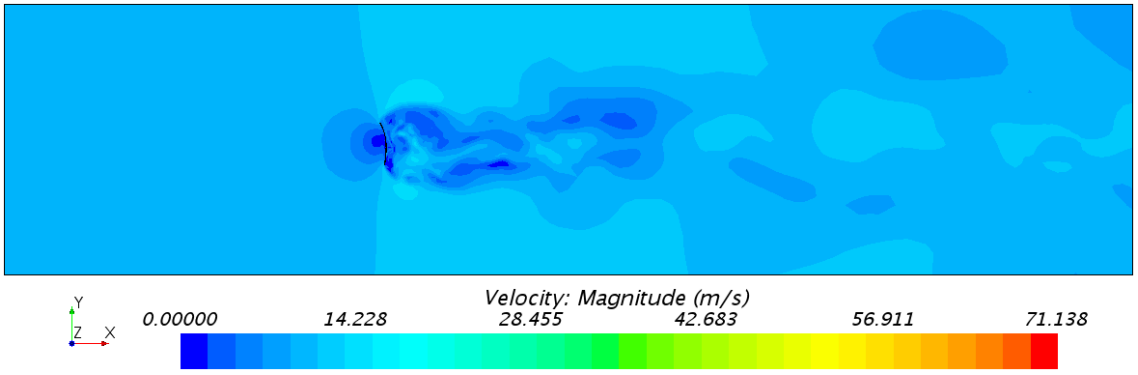

Figure A.309: Top view of the normal computational domain, showing the velocity distribution, at the height of the center of effort (CoE); the cambered sail model, with a sheet angle of 90°.

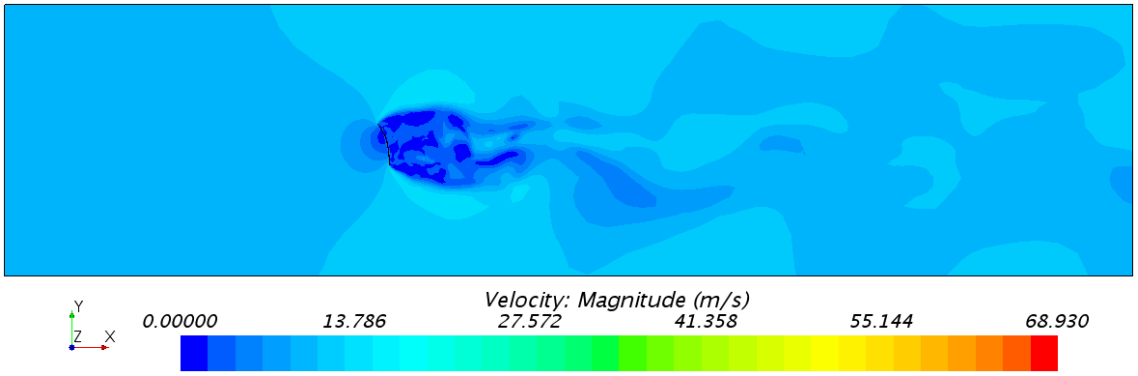

Figure A.310: Top view of the normal computational domain, showing the velocity distribution, at the height of the center of effort (CoE); the cambered sail model, with a sheet angle of 100°.

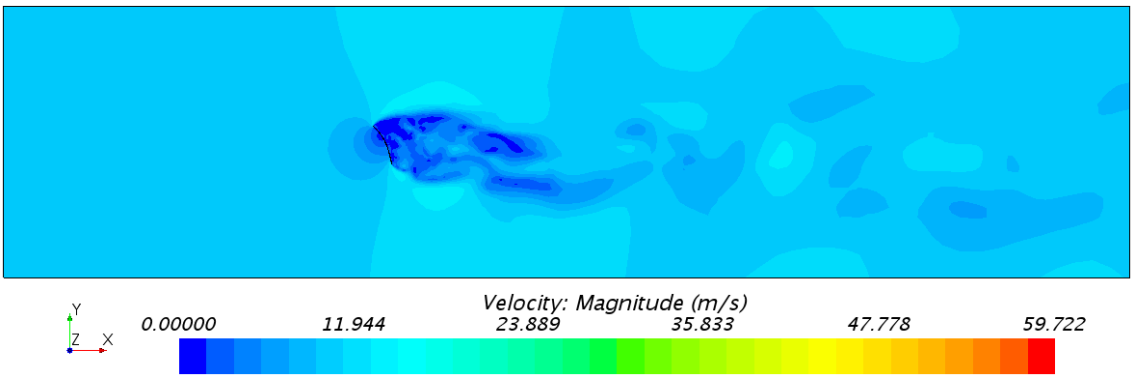

Figure A.311: Top view of the normal computational domain, showing the velocity distribution, at the height of the center of effort (CoE); the cambered sail model, with a sheet angle of 110°.

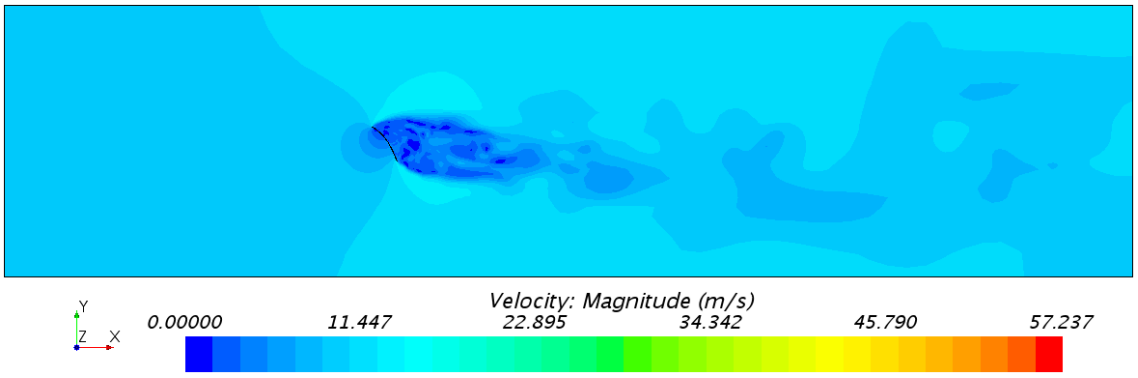

Figure A.312: Top view of the normal computational domain, showing the velocity distribution, at the height of the center of effort (CoE); the cambered sail model, with a sheet angle of 120°.

Constrained Streamlines at CoE with the Cambered Sail Model in the Normal Domain

Fig. A.313 - A.319 shows top view images of constrained streamlines, for the seven different sheet angles with the cambered sail model in the normal computational domain.

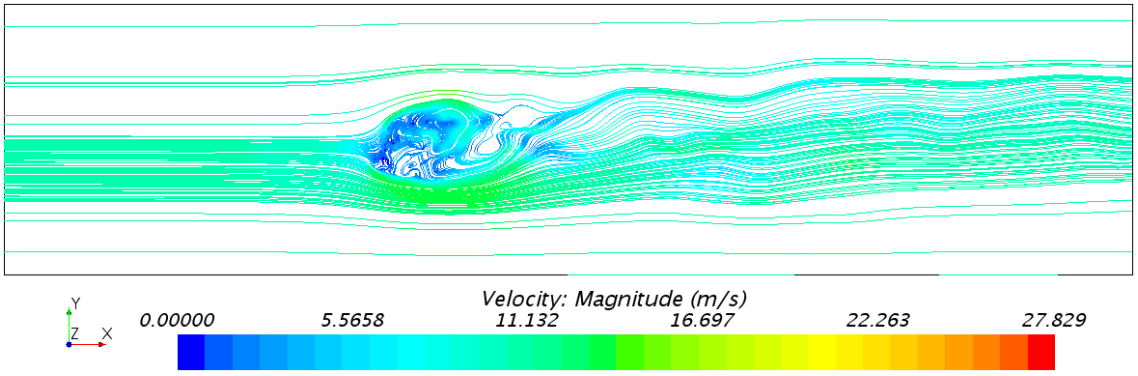

Figure A.313: Top view, of the normal computational domain, showing constrained streamlines and the cambered sail model, with a sheet angle of 60°, at the height of the center of effort (CoE).

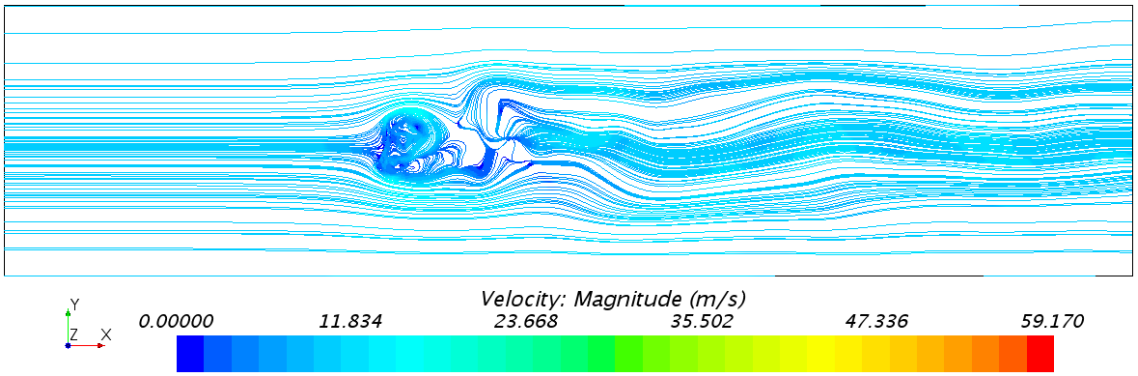

Figure A.314: Top view, of the normal computational domain, showing constrained streamlines and the cambered sail model, with a sheet angle of 70°, at the height of the center of effort (CoE).

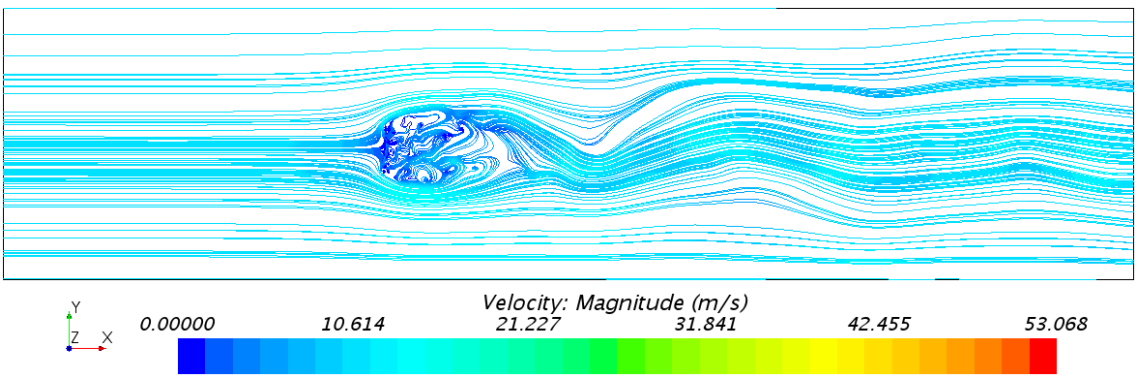

Figure A.315: Top view, of the normal computational domain, showing constrained streamlines and the cambered sail model, with a sheet angle of 80°, at the height of the center of effort (CoE).

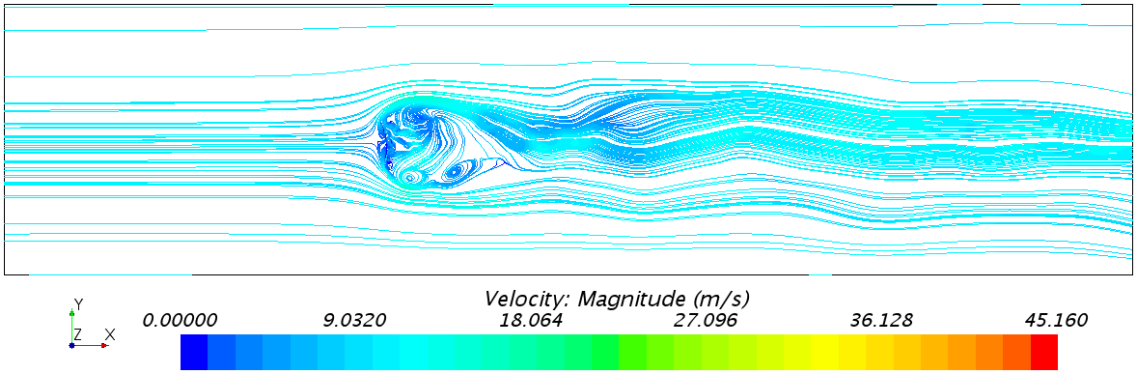

Figure A.316: Top view, of the normal computational domain, showing constrained streamlines and the cambered sail model, with a sheet angle of 90°, at the height of the center of effort (CoE).

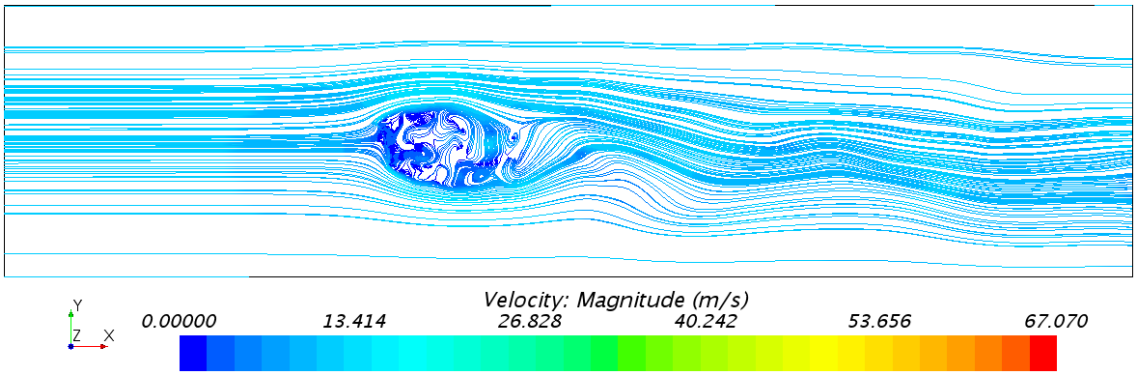

Figure A.317: Top view, of the normal computational domain, showing constrained streamlines and the cambered sail model, with a sheet angle of 100°, at the height of the center of effort (CoE).

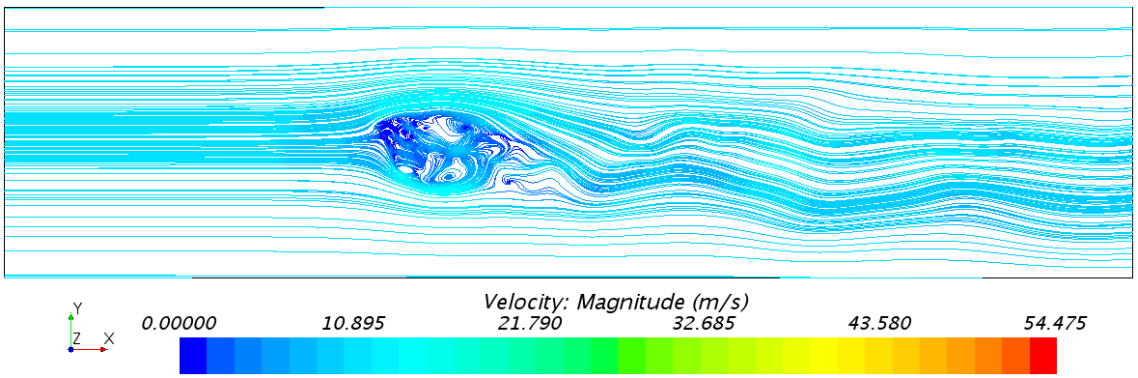

Figure A.318: Top view, of the normal computational domain, showing constrained streamlines and the cambered sail model, with a sheet angle of 110°, at the height of the center of effort (CoE).

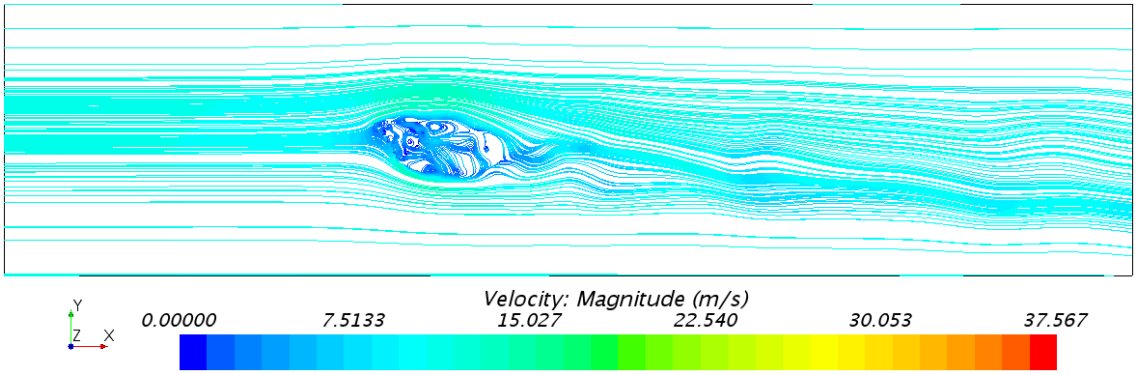

Figure A.319: Top view, of the normal computational domain, showing constrained streamlines and the cambered sail model, with a sheet angle of 120°, at the height of the center of effort (CoE).

Velocity Distribution at CoE with the Cambered Sail Model in the Large Domain

Fig. A.320 - A.326 shows top view images of the velocity distribution, for the seven different sheet angles with the cambered sail model in the large computational domain.

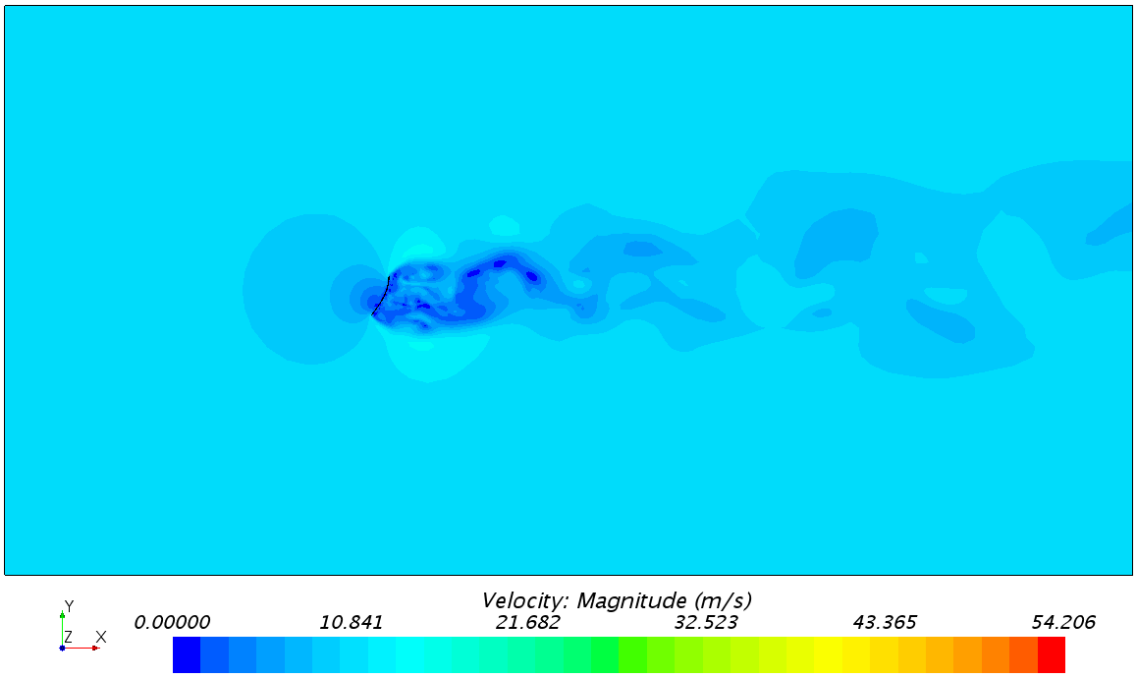

Figure A.320: Top view of the large computational domain, showing the velocity distribution, at the height of the center of effort (CoE); the cambered sail model, with a sheet angle of 60°.

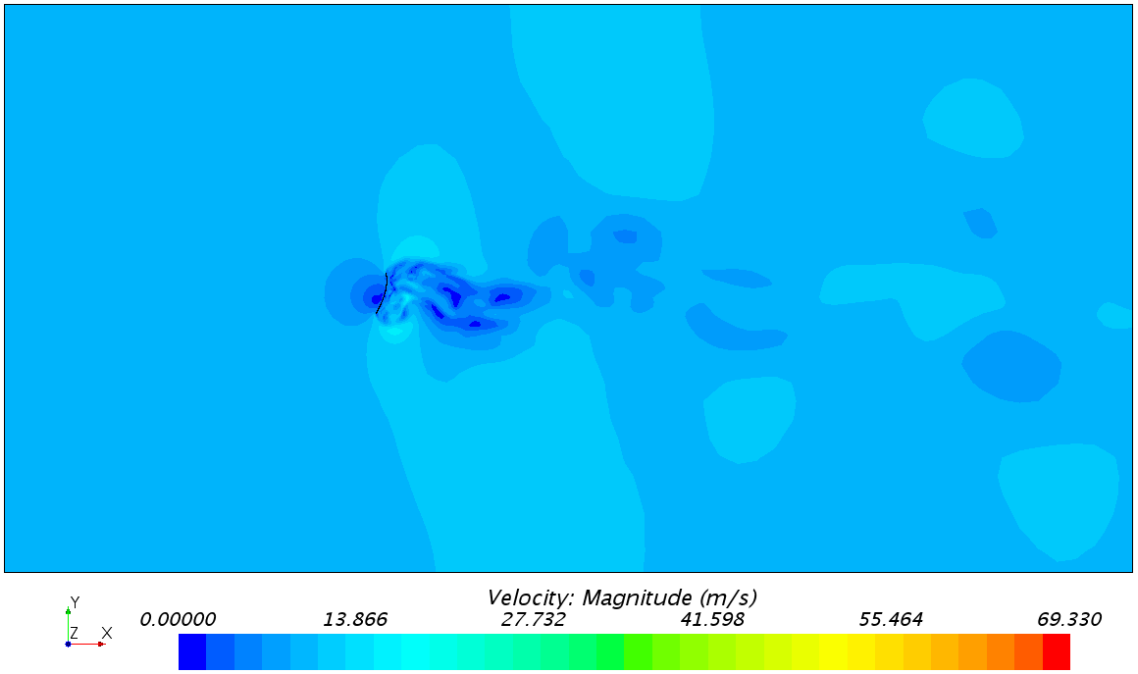

Figure A.321: Top view of the large computational domain, showing the velocity distribution, at the height of the center of effort (CoE); the cambered sail model, with a sheet angle of 70°.

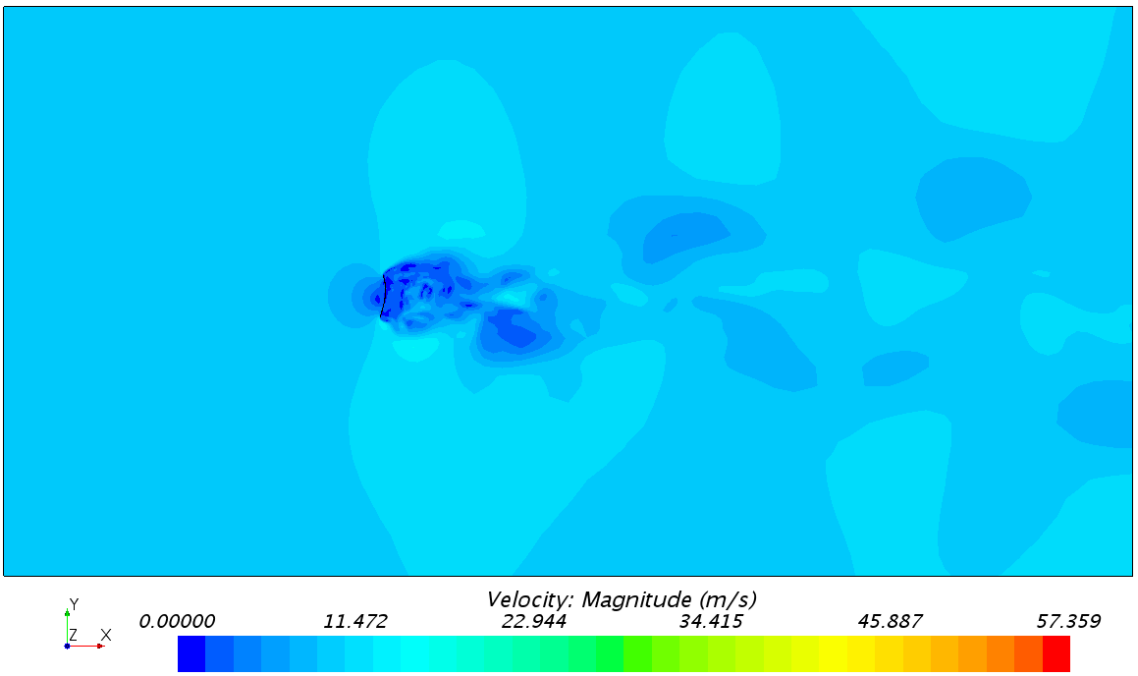

Figure A.322: Top view of the large computational domain, showing the velocity distribution, at the height of the center of effort (CoE); the cambered sail model, with a sheet angle of 80°.

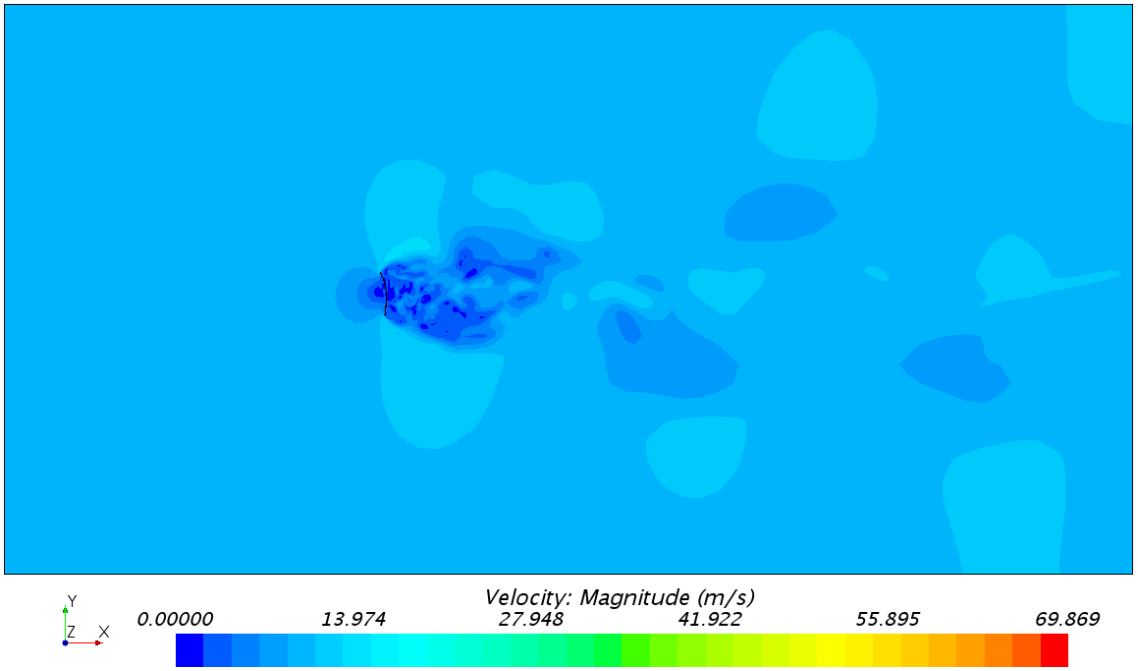

Figure A.323: Top view of the large computational domain, showing the velocity distribution, at the height of the center of effort (CoE); the cambered sail model, with a sheet angle of 90°.

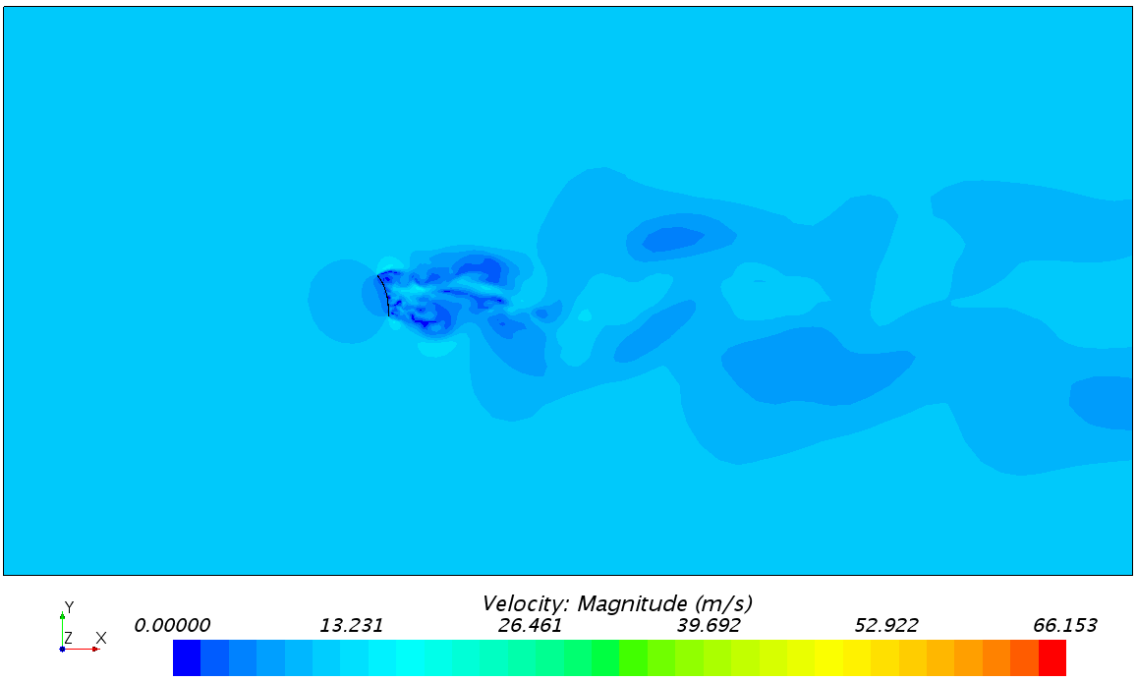

Figure A.324: Top view of the large computational domain, showing the velocity distribution, at the height of the center of effort (CoE); the cambered sail model, with a sheet angle of 100°.

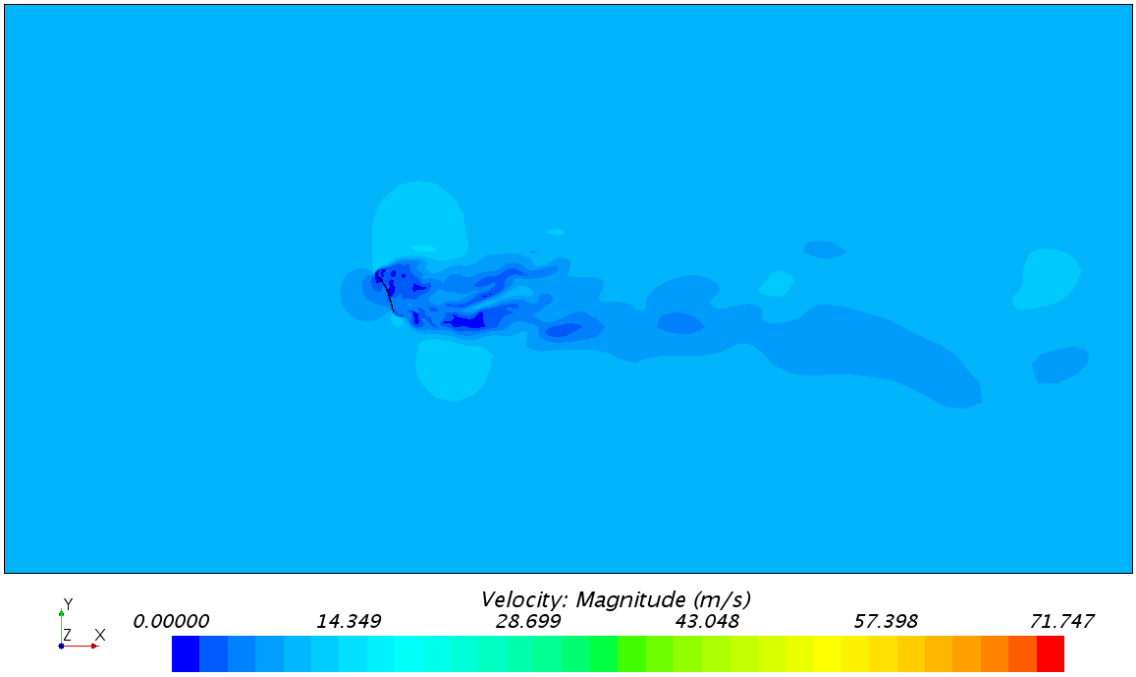

Figure A.325: Top view of the large computational domain, showing the velocity distribution, at the height of the center of effort (CoE); the cambered sail model, with a sheet angle of 110°.

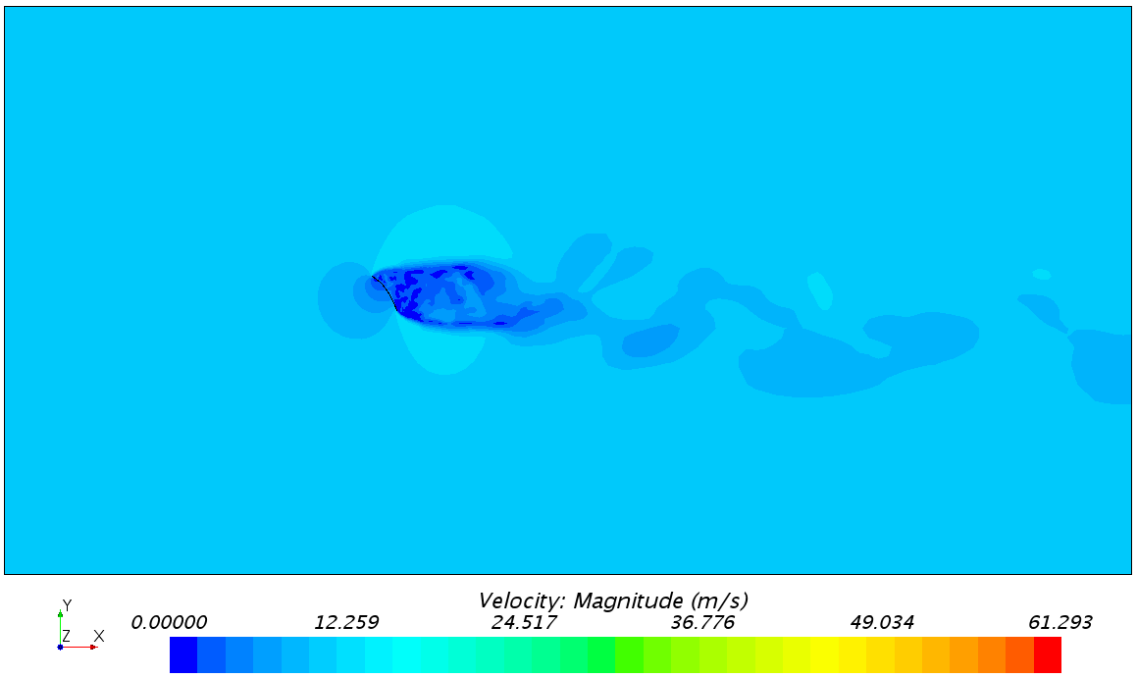

Figure A.326: Top view of the large computational domain, showing the velocity distribution, at the height of the center of effort (CoE); the cambered sail model, with a sheet angle of 120°.

Constrained Streamlines at CoE with the Cambered Sail Model in the Large Domain

Fig. A.327 - A.333 shows top view images of constrained streamlines, for the seven different sheet angles with the cambered sail model in the large computational domain.

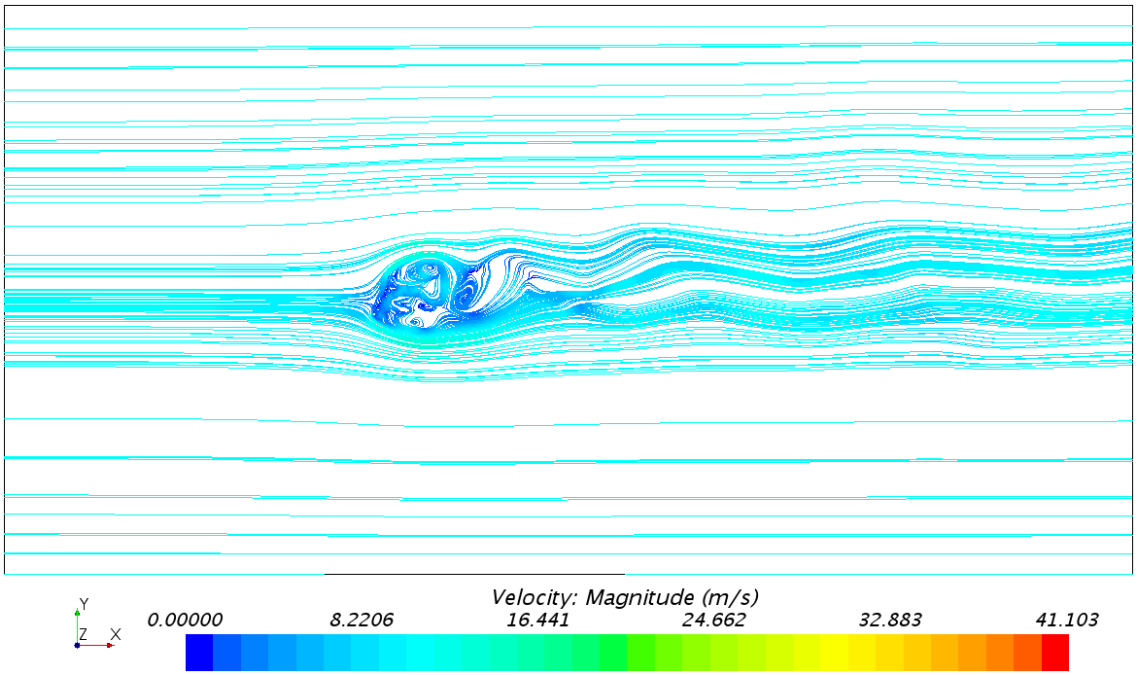

Figure A.327: Top view, of the large computational domain, showing constrained streamlines and the cambered sail model, with a sheet angle of 60°, at the height of the center of effort (CoE).

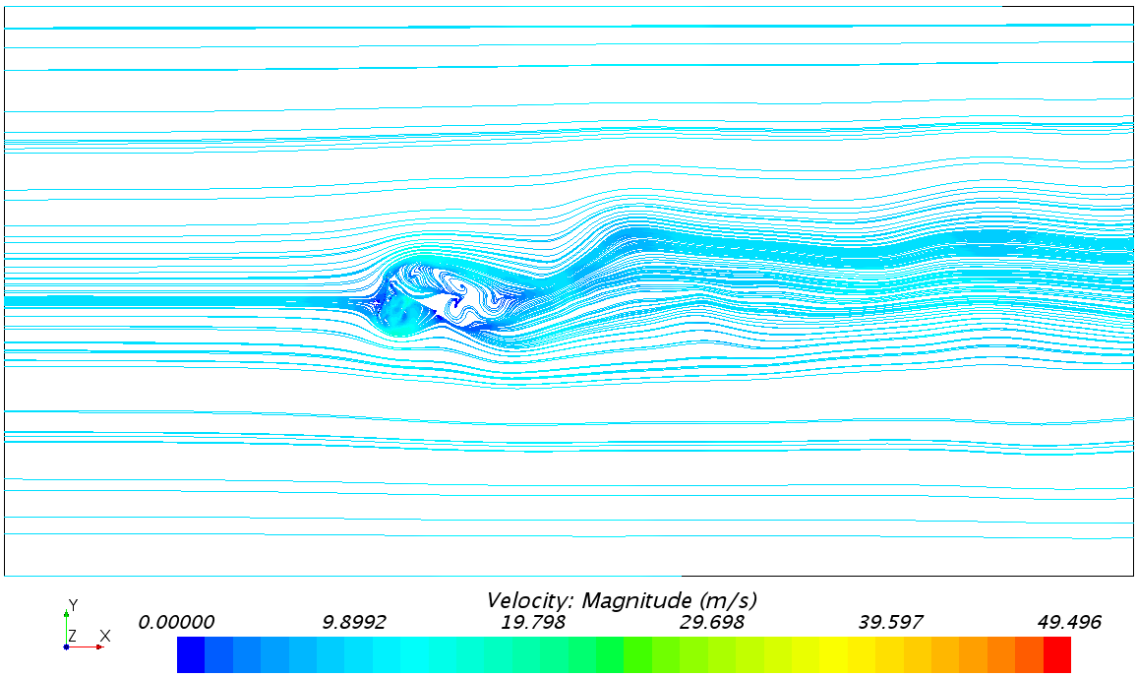

Figure A.328: Top view, of the large computational domain, showing constrained streamlines and the cambered sail model, with a sheet angle of 70°, at the height of the center of effort (CoE).

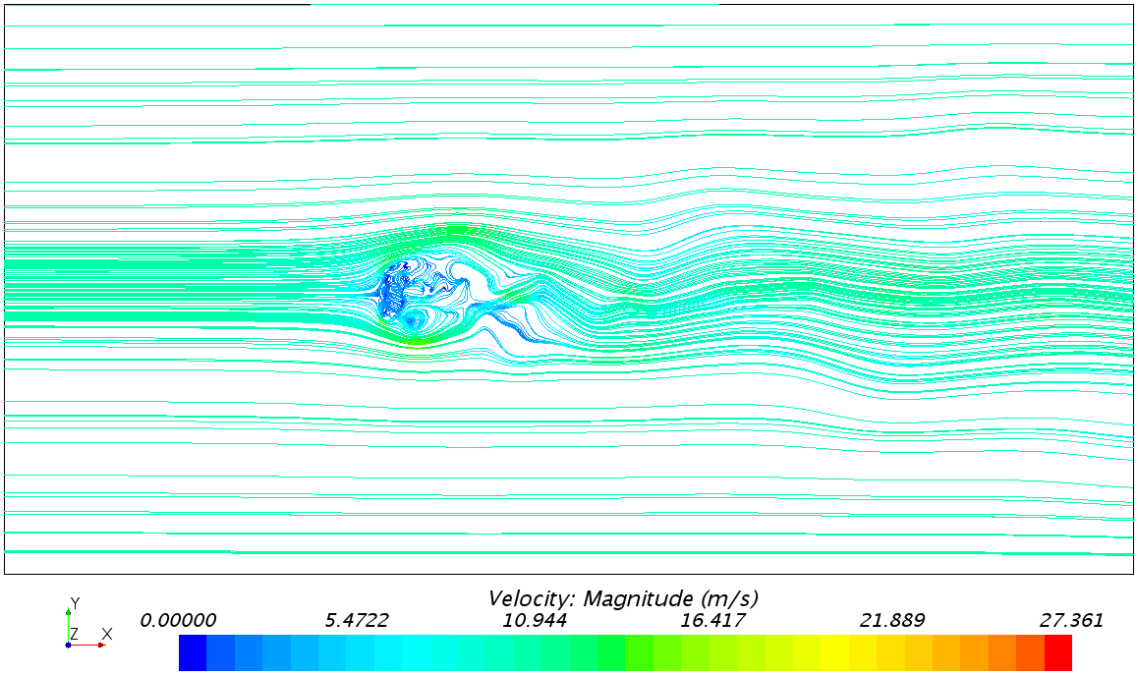

Figure A.329: Top view, of the large computational domain, showing constrained streamlines and the cambered sail model, with a sheet angle of 80°, at the height of the center of effort (CoE).

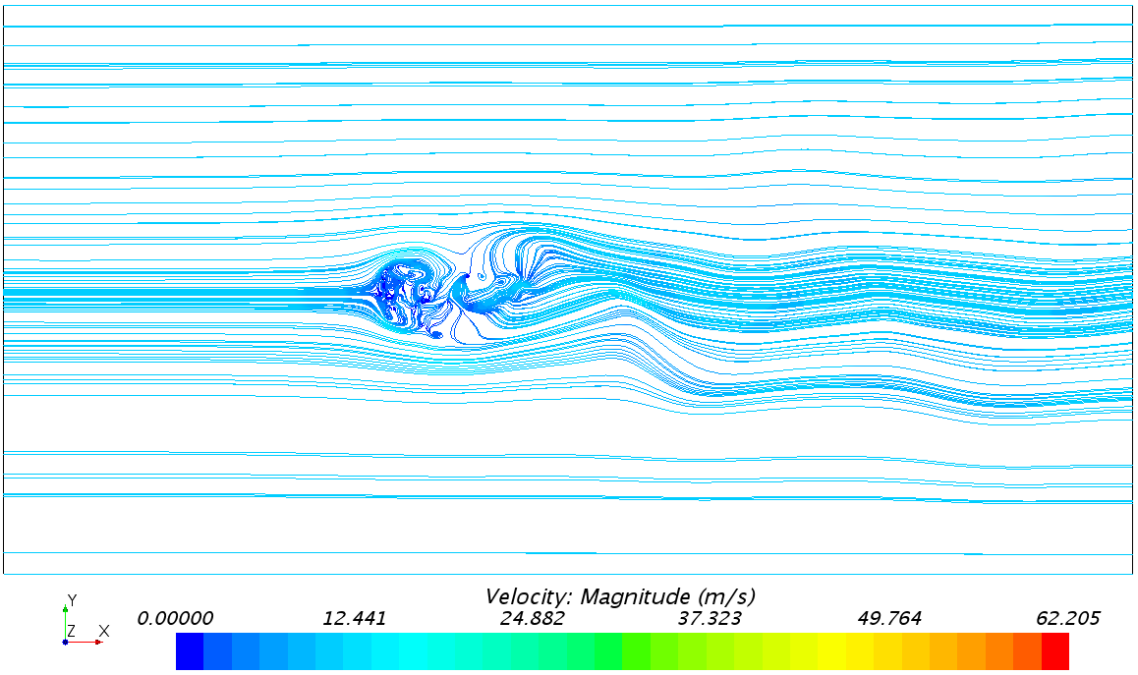

Figure A.330: Top view, of the large computational domain, showing constrained streamlines and the cambered sail model, with a sheet angle of 90°, at the height of the center of effort (CoE).

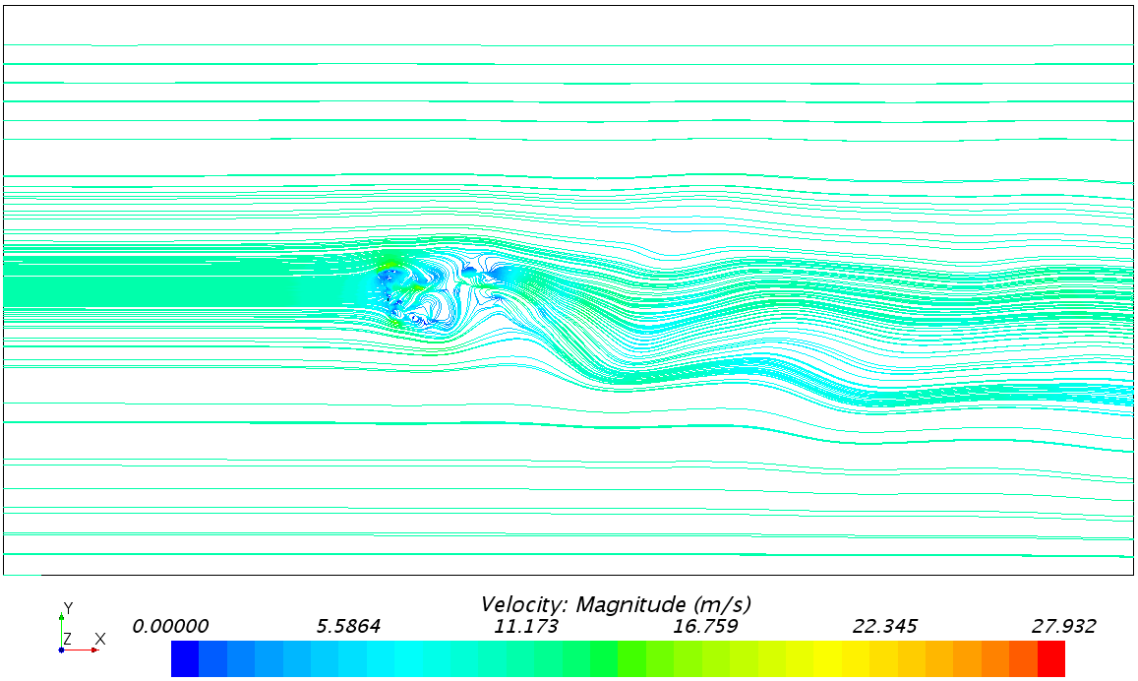

Figure A.331: Top view, of the large computational domain, showing constrained streamlines and the cambered sail model, with a sheet angle of 100°, at the height of the center of effort (CoE).

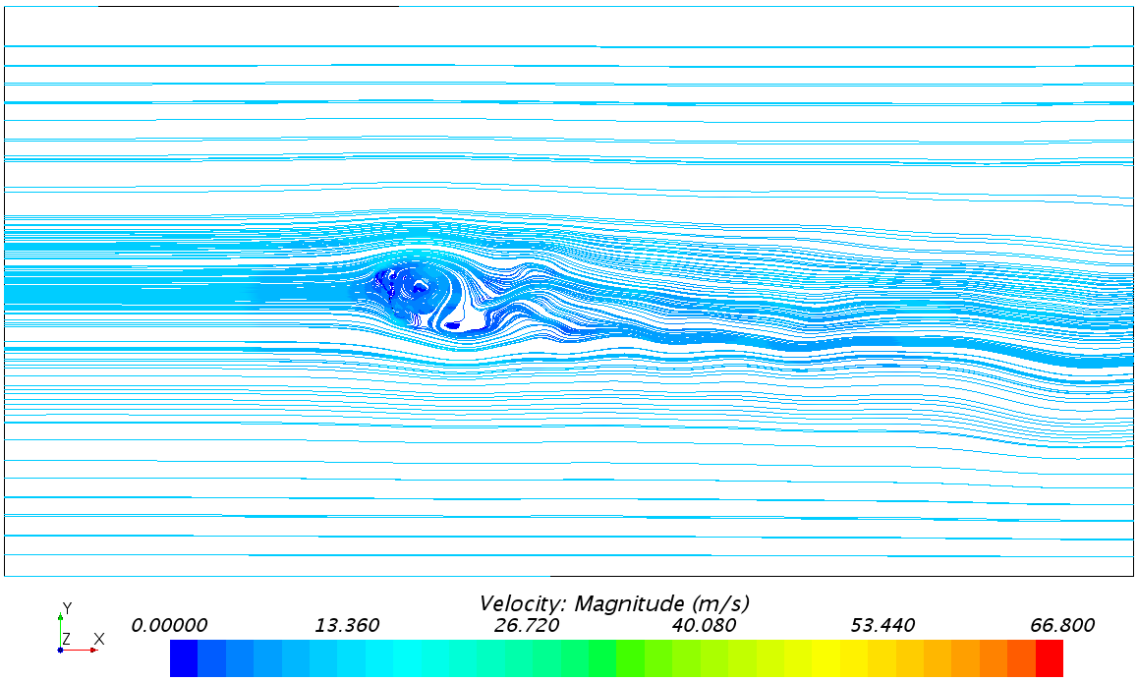

Figure A.332: Top view, of the large computational domain, showing constrained streamlines and the cambered sail model, with a sheet angle of 110°, at the height of the center of effort (CoE).

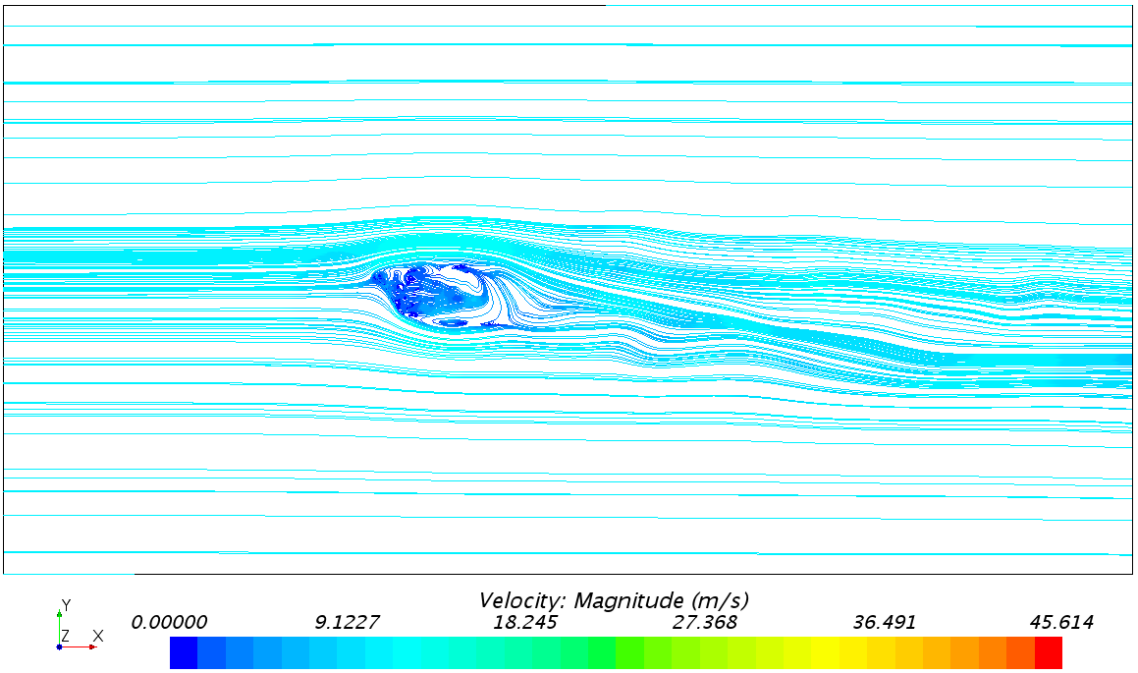

Figure A.333: Top view, of the large computational domain, showing constrained streamlines and the cambered sail model, with a sheet angle of 120°, at the height of the center of effort (CoE).

Side View Images

Velocity distribution at a centered XZ-plane with the cambered Sail Model in the Normal Domain

Fig. A.334 - A.340 shows the corresponding side view images of the velocity distribution, for the seven different sheet angles with the cambered sail model and with grid 3 in the normal computational domain.

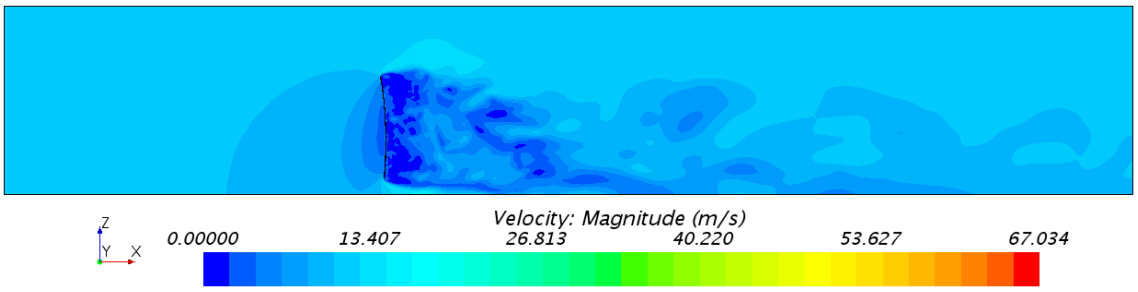

Figure A.334: Side view, of the normal computational domain, showing the velocity distribution, at a centered xz-plane; the cambered sail model, with a sheet angle of 60°.

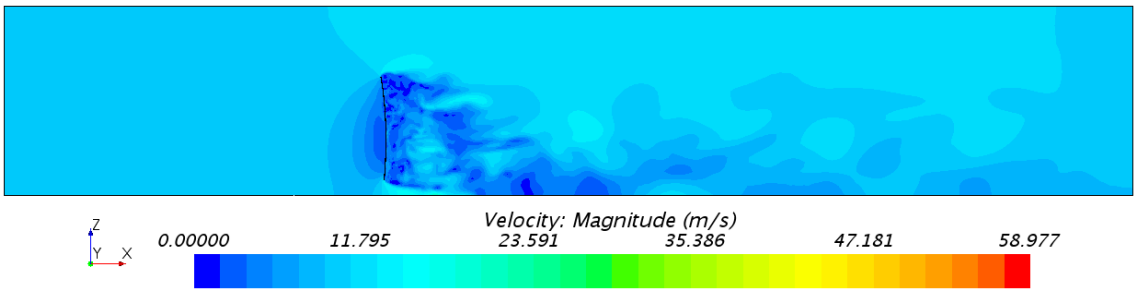

Figure A.335: Side view, of the normal computational domain, showing the velocity distribution, at a centered xz-plane; the cambered sail model, with a sheet angle of 70°.

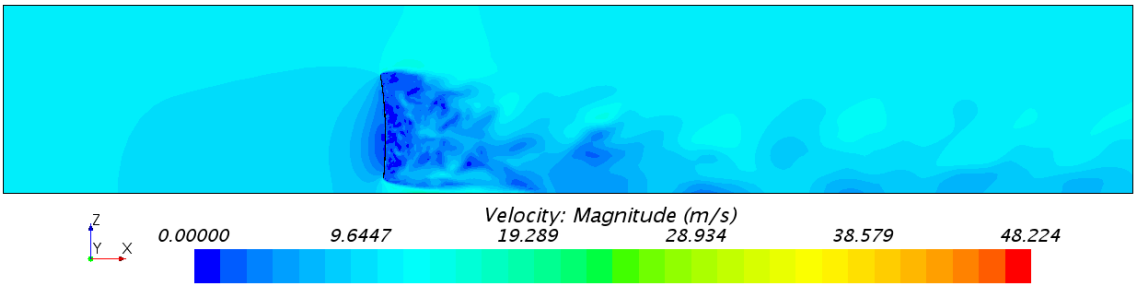

Figure A.336: Side view, of the normal computational domain, showing the velocity distribution, at a centered xz-plane; the cambered sail model, with a sheet angle of 80°.

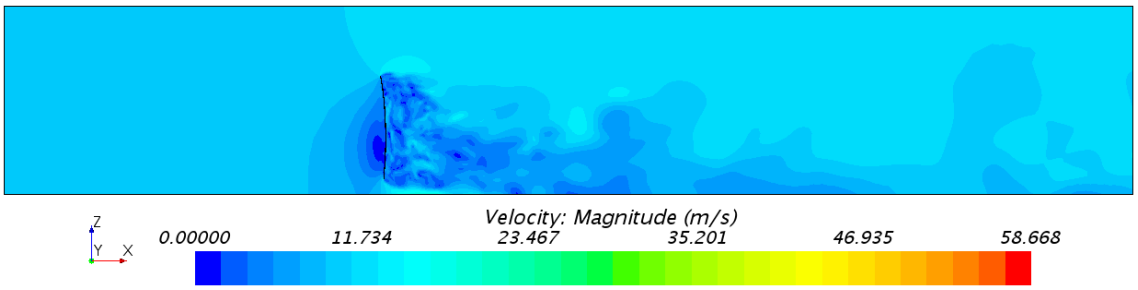

Figure A.337: Side view, of the normal computational domain, showing the velocity distribution, at a centered xz-plane; the cambered sail model, with a sheet angle of 90°.

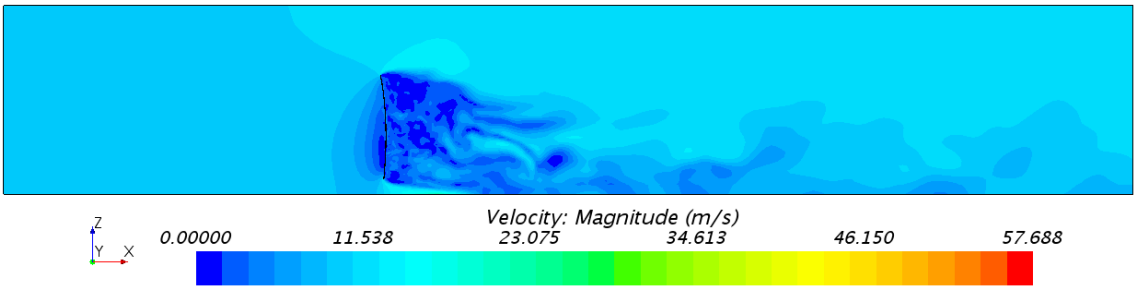

Figure A.338: Side view, of the normal computational domain, showing the velocity distribution, at a centered xz-plane; the cambered sail model, with a sheet angle of 100°.

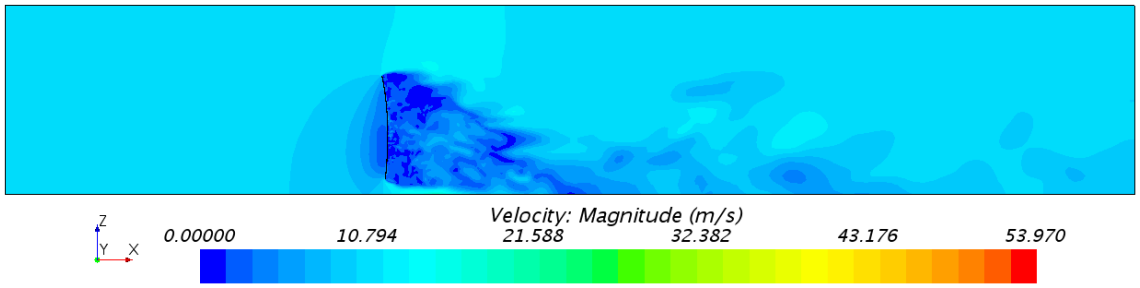

Figure A.339: Side view, of the normal computational domain, showing the velocity distribution, at a centered xz-plane; the cambered sail model, with a sheet angle of 110°.

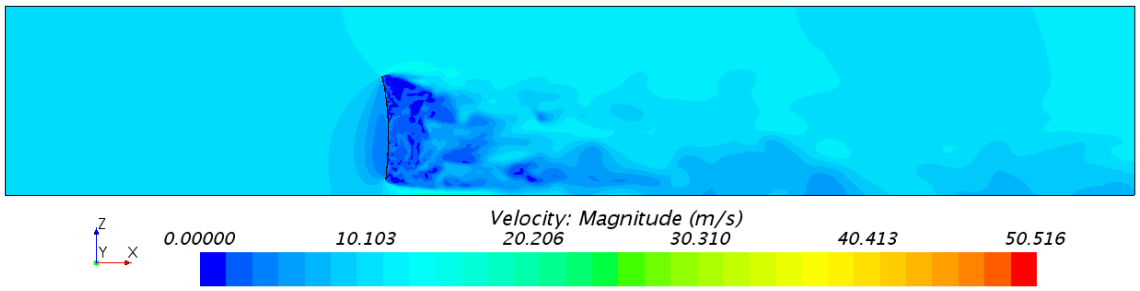

Figure A.340: Side view, of the normal computational domain, showing the velocity distribution, at a centered xz-plane; the cambered sail model, with a sheet angle of 120°.

Constrained Streamlines at a centered XZ-plane with the Cambered Sail Model in the Normal Domain

Fig. A.341 - A.347 shows the corresponding side view images of constrained streamlines, for the seven different sheet angles with the cambered sail model and with grid 3 in the normal computational domain.

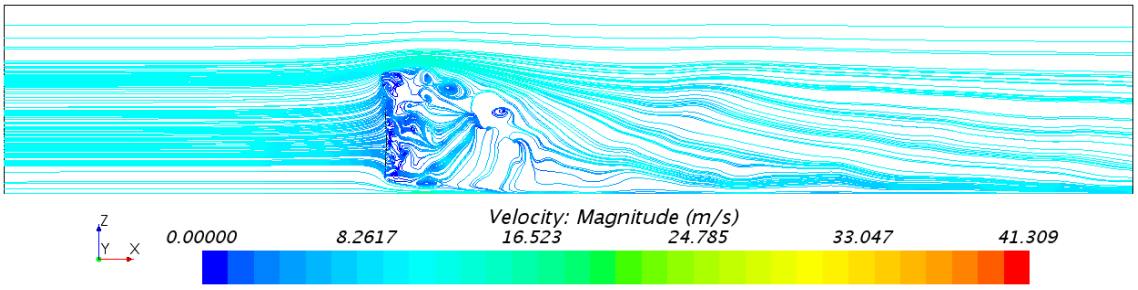

Figure A.341: Side view, of the normal computational domain, showing constrained streamlines, at a centered xz-plane; the cambered sail model, with a sheet angle of 60°.

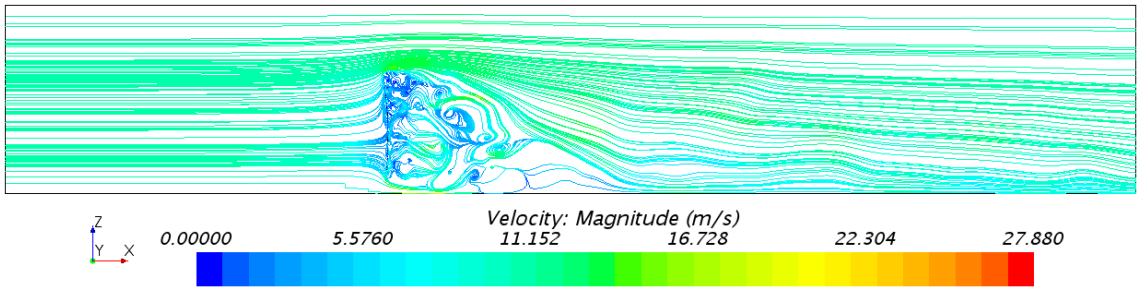

Figure A.342: Side view, of the normal computational domain, showing constrained streamlines, at a centered xz-plane; the cambered sail model, with a sheet angle of 70°.

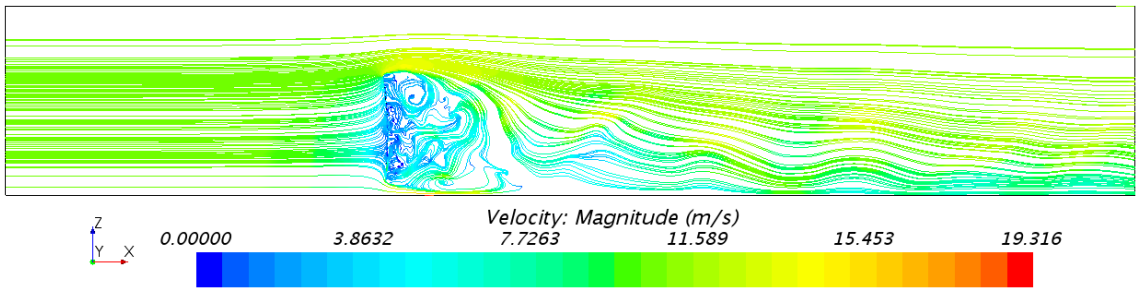

Figure A.343: Side view, of the normal computational domain, showing constrained streamlines, at a centered xz-plane; the cambered sail model, with a sheet angle of 80°.

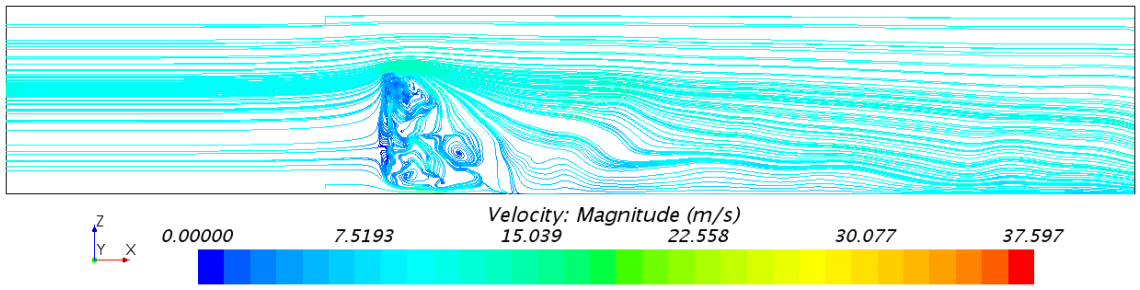

Figure A.344: Side view, of the normal computational domain, showing constrained streamlines, at a centered xz-plane; the cambered sail model, with a sheet angle of 90°.

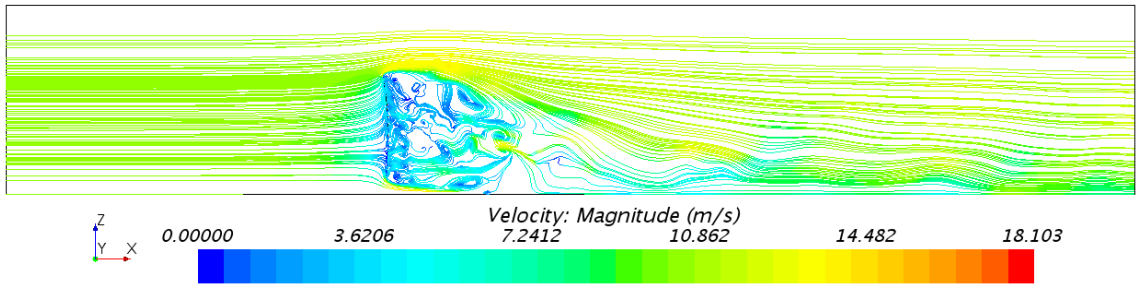

Figure A.345: Side view, of the normal computational domain, showing constrained streamlines, at a centered xz-plane; the cambered sail model, with a sheet angle of 100°.

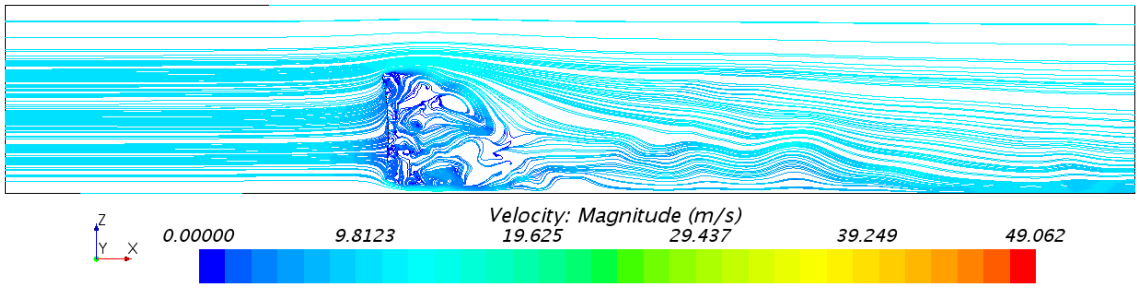

Figure A.346: Side view, of the normal computational domain, showing constrained streamlines, at a centered xz-plane; the cambered sail model, with a sheet angle of 110°.

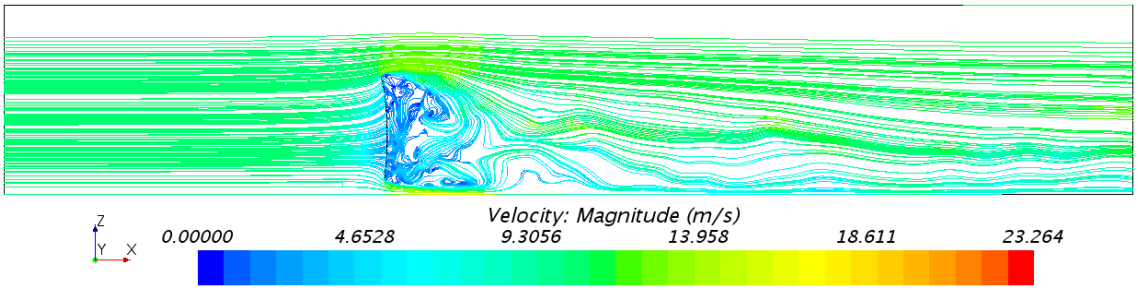

Figure A.347: Side view, of the normal computational domain, showing constrained streamlines, at a centered xz-plane; the cambered sail model, with a sheet angle of 120°.

Velocity distribution at a centered XZ-plane with the Cambered Sail Model in the Large Domain

Fig. A.348 - A.354 shows the corresponding side view images of constrained streamlines, for the seven different sheet angles with the cambered sail model and with grid 3 in the large computational domain.

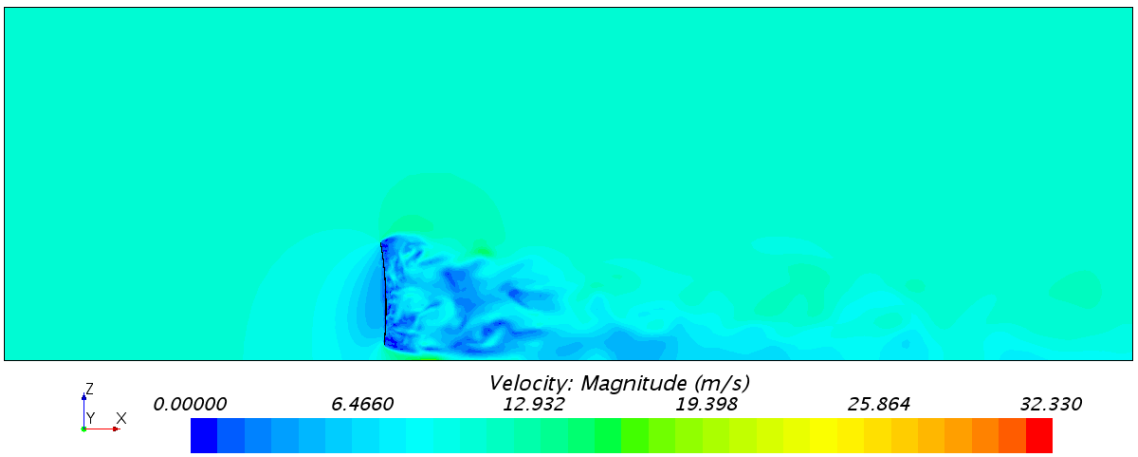

Figure A.348: Side view, of the large computational domain, showing the velocity distribution, at a centered xz-plane; the cambered sail model, with a sheet angle of 60°.

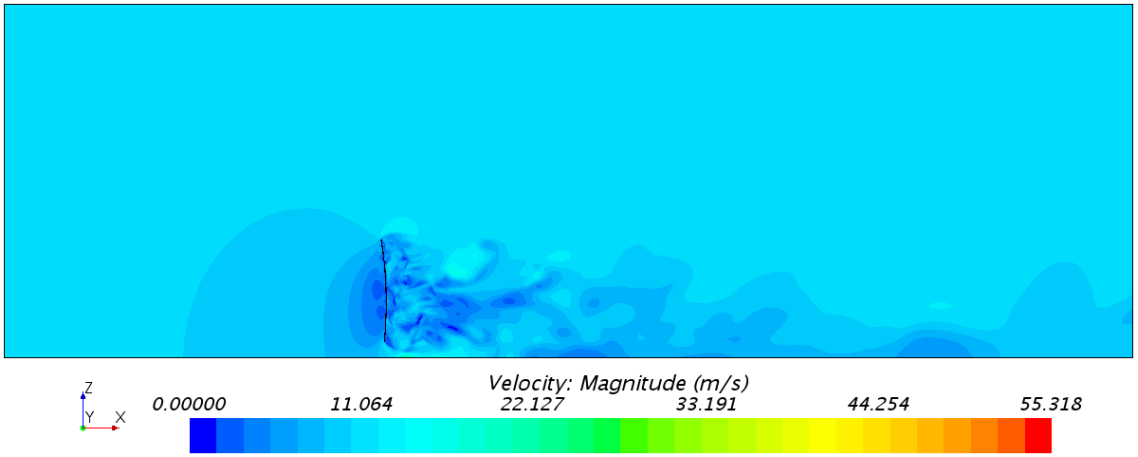

Figure A.349: Side view, of the large computational domain, showing the velocity distribution, at a centered xz-plane; the cambered sail model, with a sheet angle of 70°.

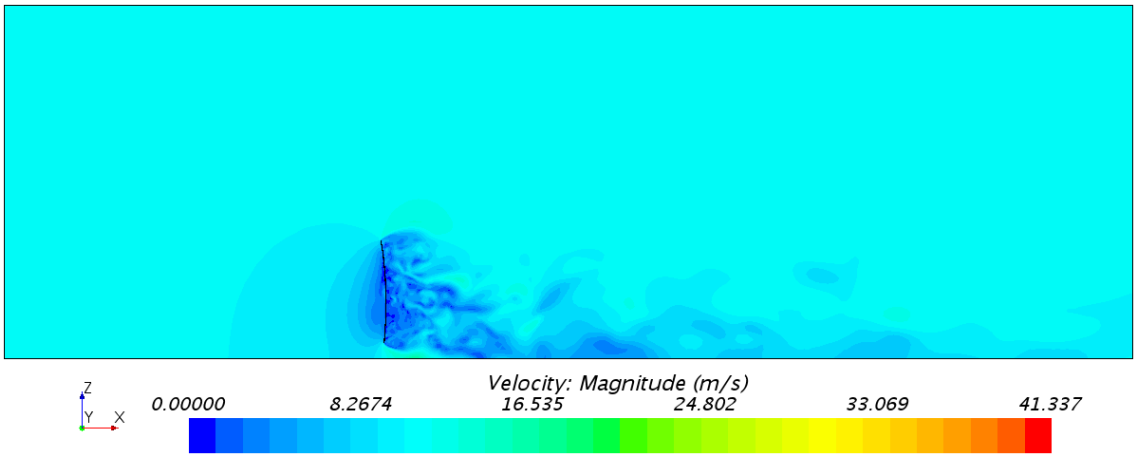

Figure A.350: Side view, of the large computational domain, showing the velocity distribution, at a centered xz-plane; the cambered sail model, with a sheet angle of 80°.

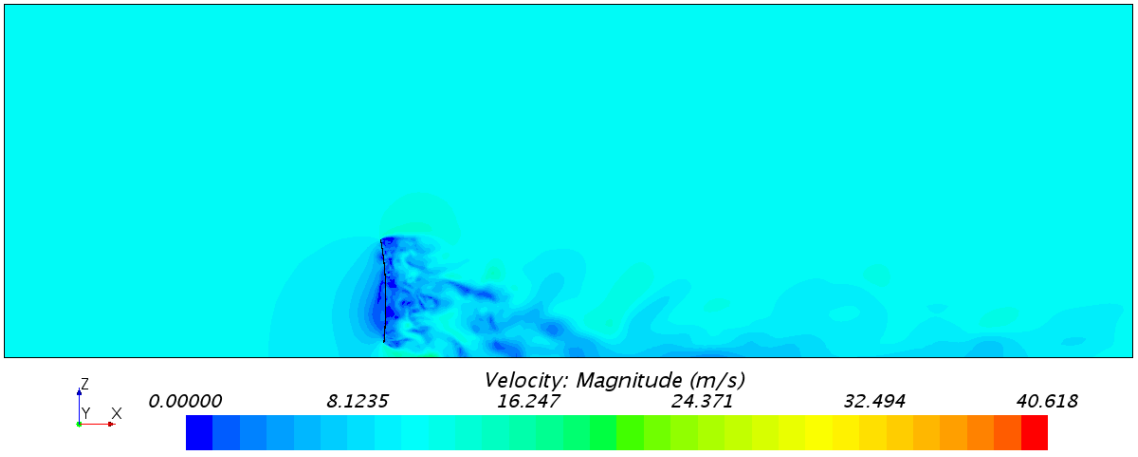

Figure A.351: Side view, of the large computational domain, showing the velocity distribution, at a centered xz-plane; the cambered sail model, with a sheet angle of 90°.

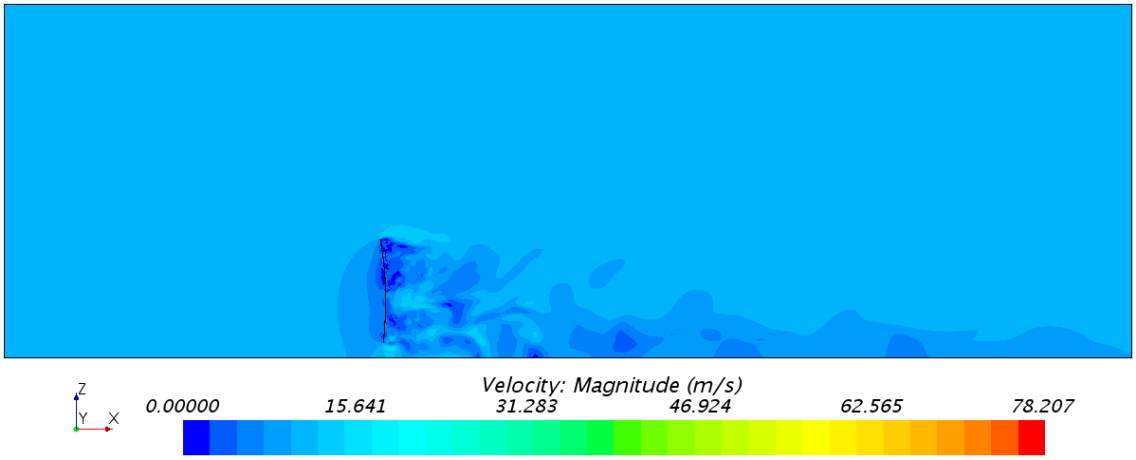

Figure A.352: Side view, of the large computational domain, showing the velocity distribution, at a centered xz-plane; the cambered sail model, with a sheet angle of 100°.

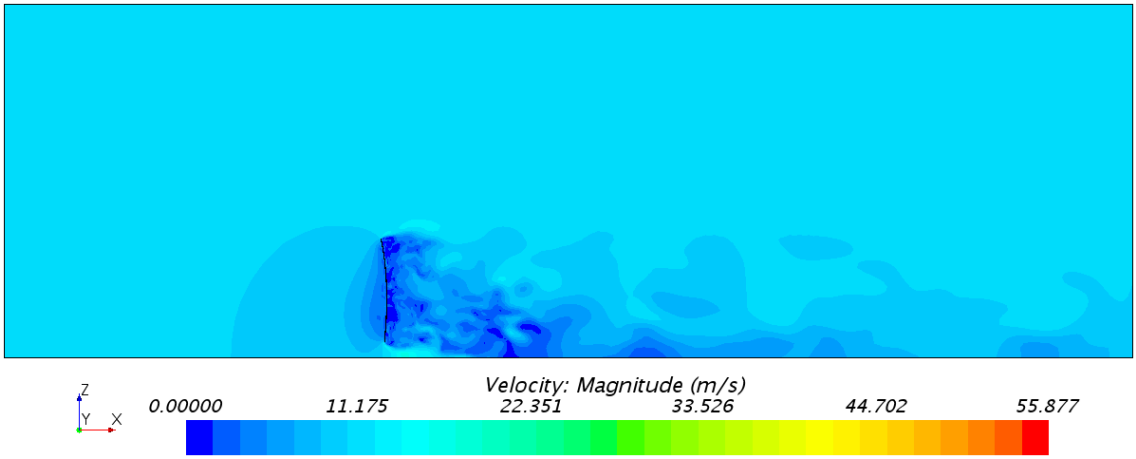

Figure A.353: Side view, of the large computational domain, showing the velocity distribution, at a centered xz-plane; the cambered sail model, with a sheet angle of 110°.

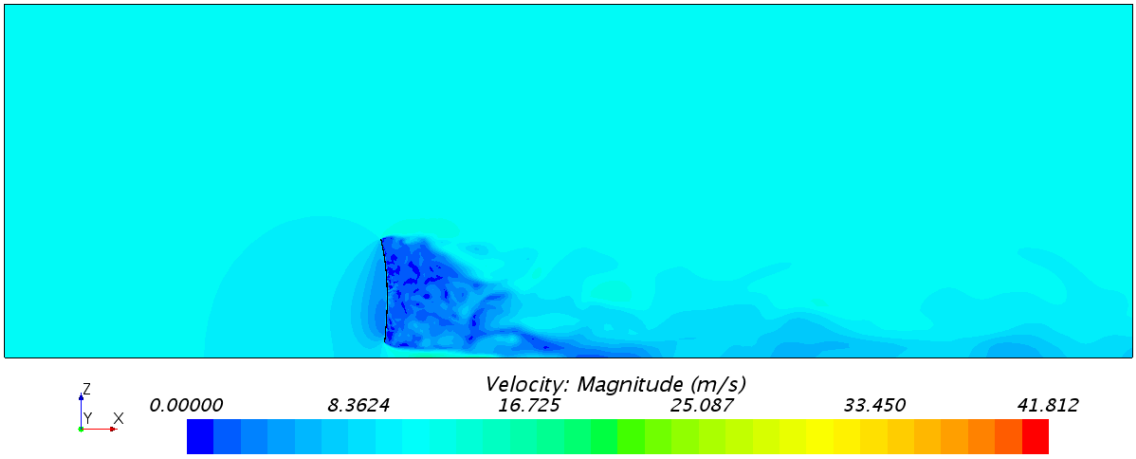

Figure A.354: Side view, of the large computational domain, showing the velocity distribution, at a centered xz-plane; the cambered sail model, with a sheet angle of 120°.

Constrained Streamlines at a centered XZ-plane with the Cambered Sail Model in the Large Domain

Fig. A.341 - A.347 shows the corresponding side view images of constrained streamlines, for the seven different sheet angles with the cambered sail model and with grid 3 in the normal computational domain.

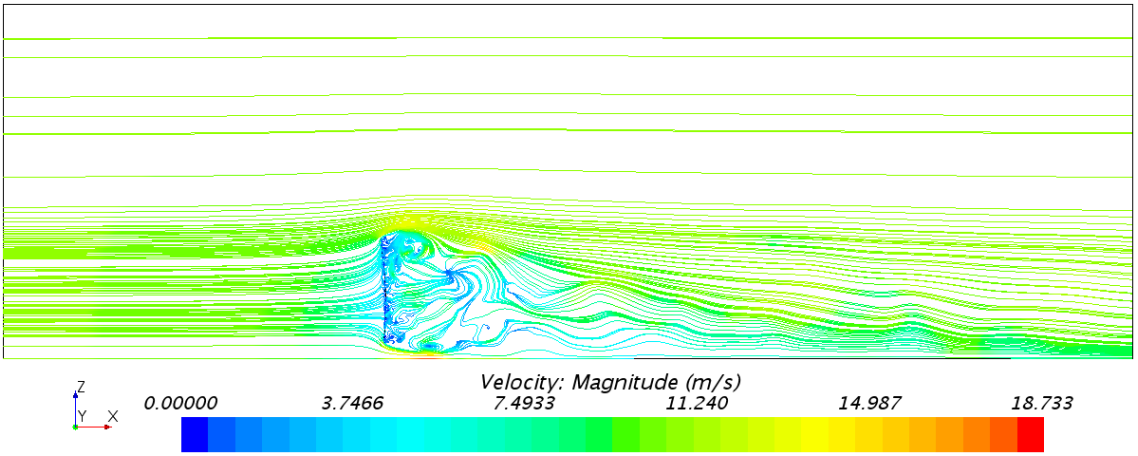

Figure A.355: Side view, of the large computational domain, showing constrained streamlines, at a centered xz-plane; the cambered sail model, with a sheet angle of 60°.

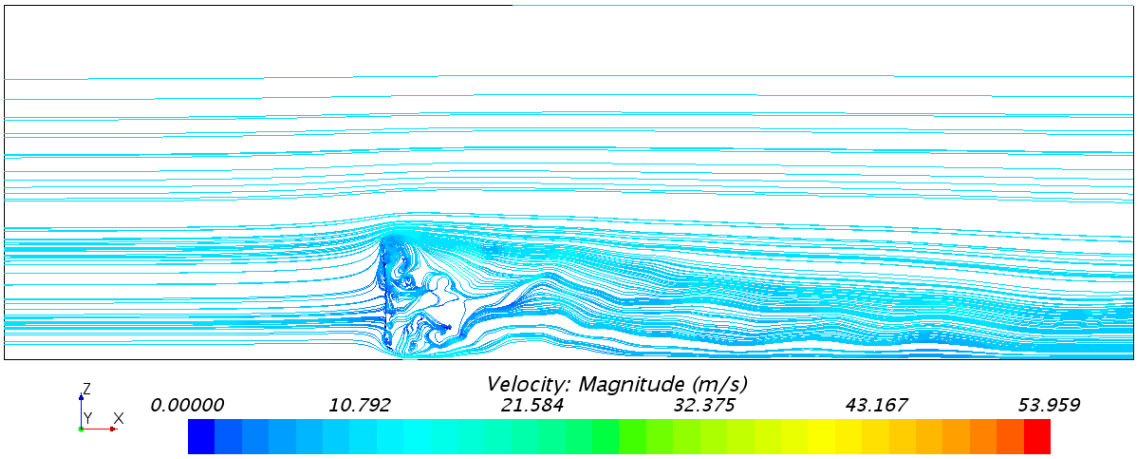

Figure A.356: Side view, of the large computational domain, showing constrained streamlines, at a centered xz-plane; the cambered sail model, with a sheet angle of 70°.

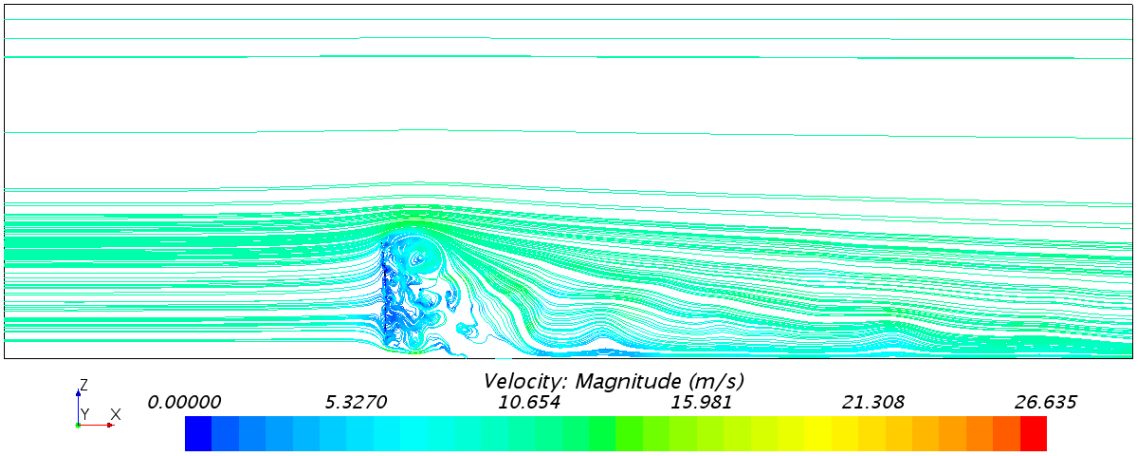

Figure A.357: Side view, of the large computational domain, showing constrained streamlines, at a centered xz-plane; the cambered sail model, with a sheet angle of 80°.

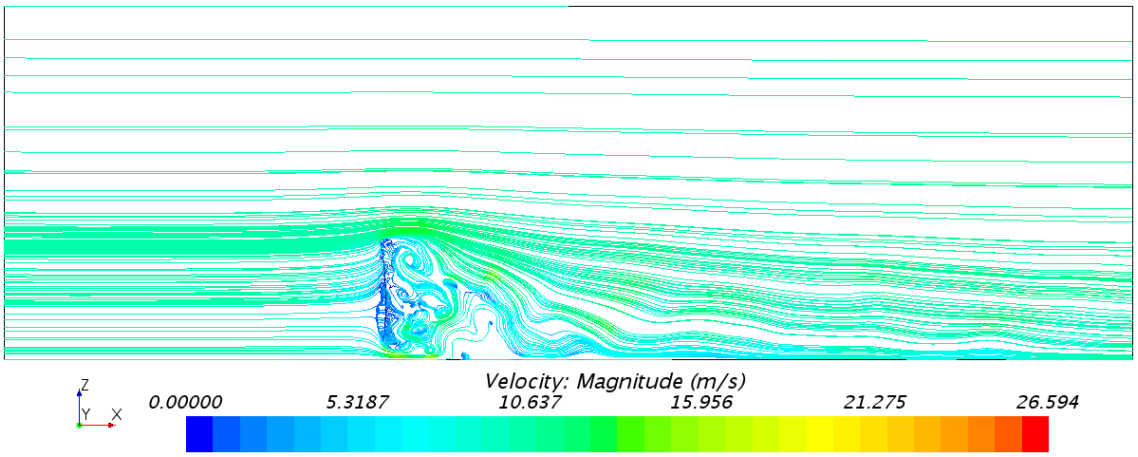

Figure A.358: Side view, of the large computational domain, showing constrained streamlines, at a centered xz-plane; the cambered sail model, with a sheet angle of 90°.

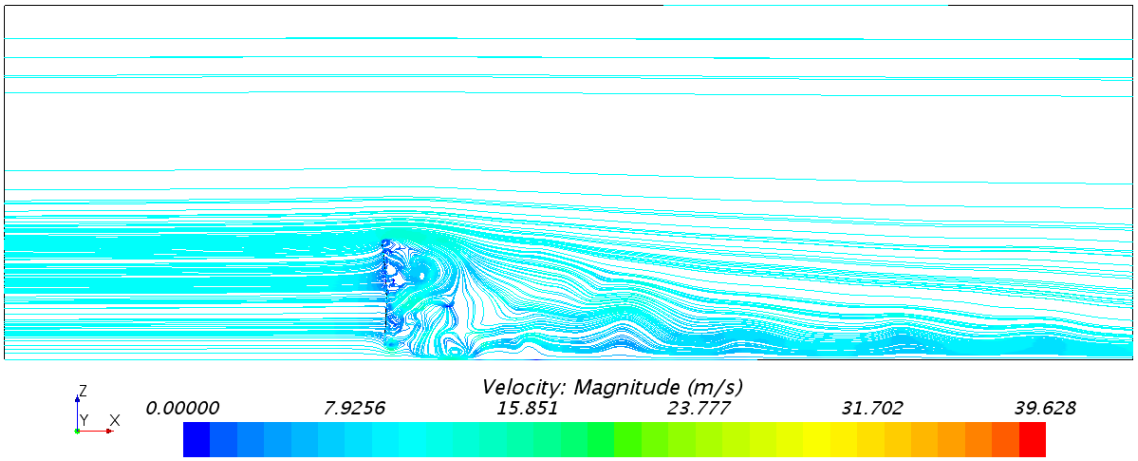

Figure A.359: Side view, of the large computational domain, showing constrained streamlines, at a centered xz-plane; the cambered sail model, with a sheet angle of 100°.

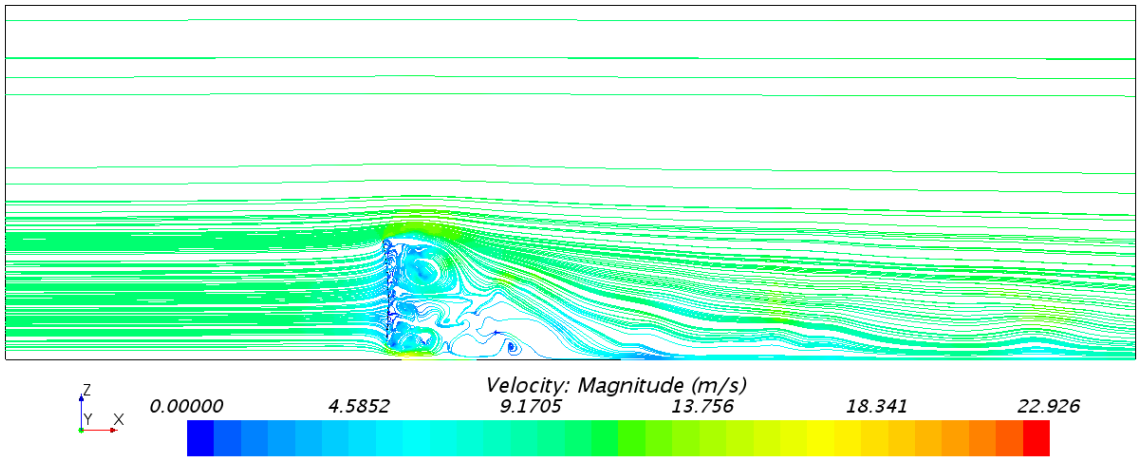

Figure A.360: Side view, of the large computational domain, showing constrained streamlines, at a centered xz-plane; the cambered sail model, with a sheet angle of 110°.

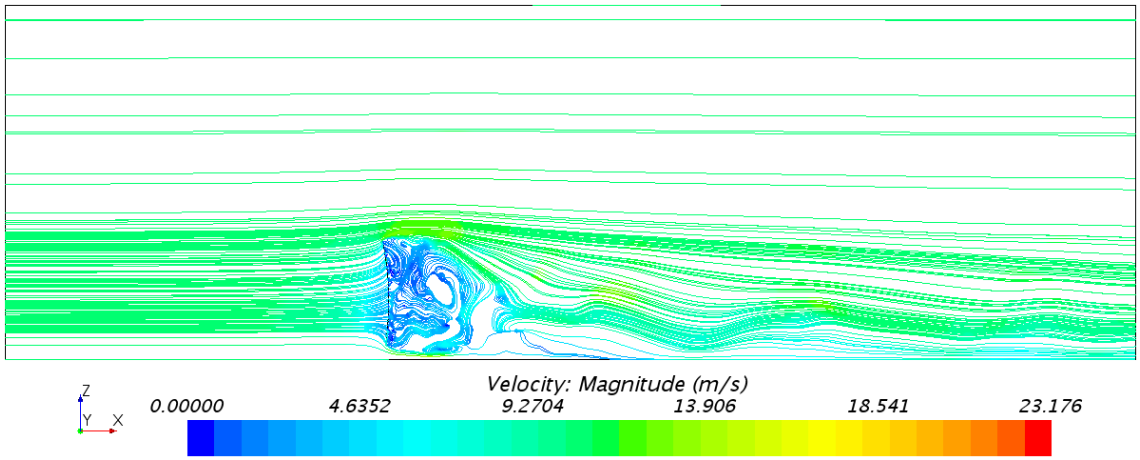

Figure A.361: Side view, of the large computational domain, showing constrained streamlines, at a centered xz-plane; the cambered sail model, with a sheet angle of 120°.

Residuals

Fig. A.362 - A.375 shows the residuals, from the sheet angle analysis performed with DES for both computational domains.

Cambered Sail Model with Sheet Angle 60° and the Normal Domain

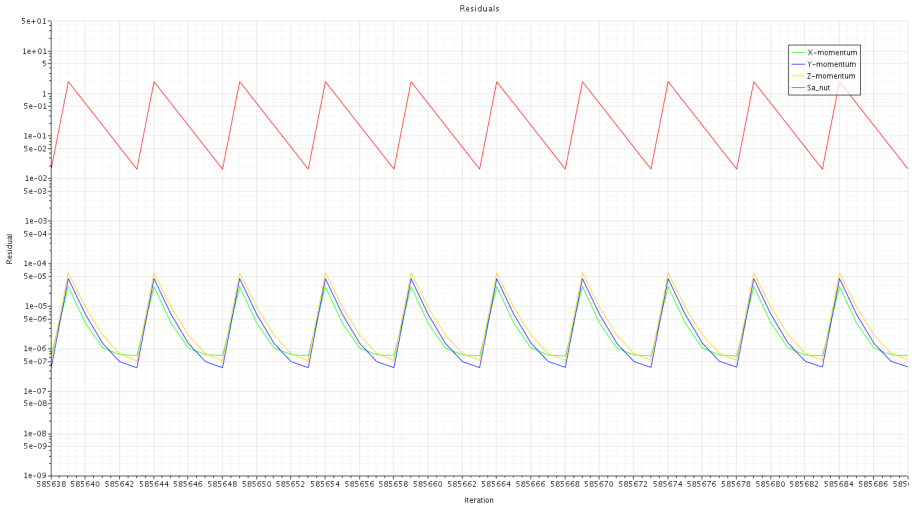

Figure A.362: Residual vs iteration, from DES with the cambered sail model, with a sheet angle of 60°, in the normal computational domain & grid 3, showing the graphs of the X-momentum (green), Y-momentum (blue), Z-momentum (yellow) and Spalart-Allmaras Turbulent kinetic energy (red) of the last 50 iterations, with maximum 5 inner iterations.

Cambered Sail Model with Sheet Angle 70° and the Normal Domain

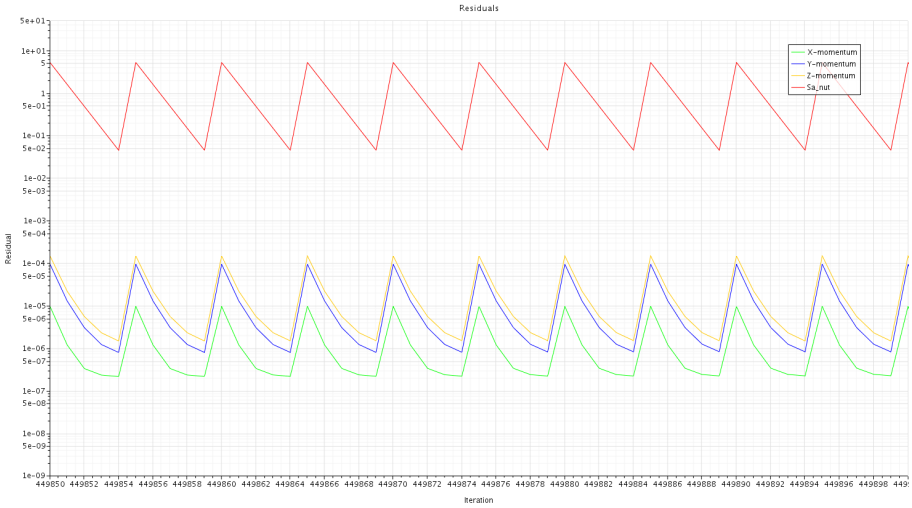

Figure A.363: Residual vs iteration, from DES with the cambered sail model, with a sheet angle of 70°, in the normal computational domain & grid 3, showing the graphs of the X-momentum (green), Y-momentum (blue), Z-momentum (yellow) and Spalart-Allmaras Turbulent kinetic energy (red) of the last 50 iterations, with maximum 5 inner iterations.

Cambered Sail Model with Sheet Angle 80° and the Normal Domain

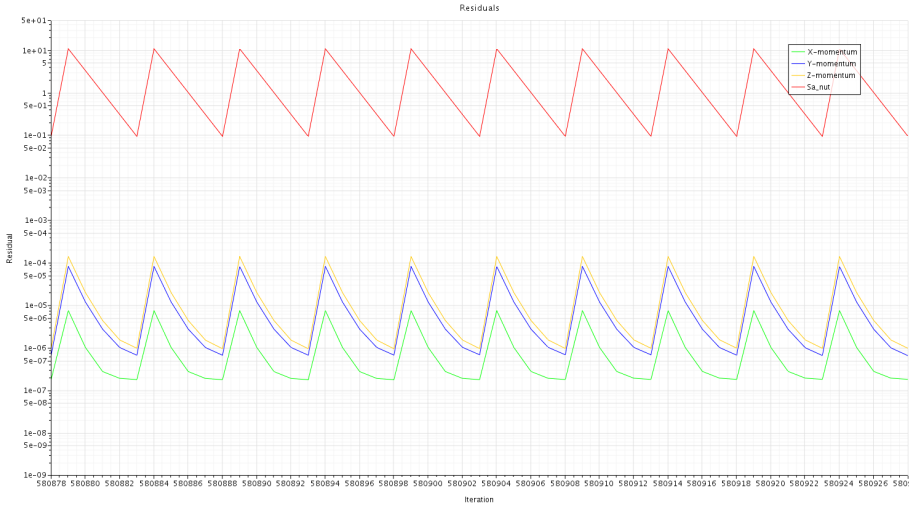

Figure A.364: Residual vs iteration, from DES with the cambered sail model, with a sheet angle of 80°, in the normal computational domain & grid 3, showing the graphs of the X-momentum (green), Y-momentum (blue), Z-momentum (yellow) and Spalart-Allmaras Turbulent kinetic energy (red) of the last 50 iterations, with maximum 5 inner iterations.

Cambered Sail Model with Sheet Angle 90° and the Normal Domain

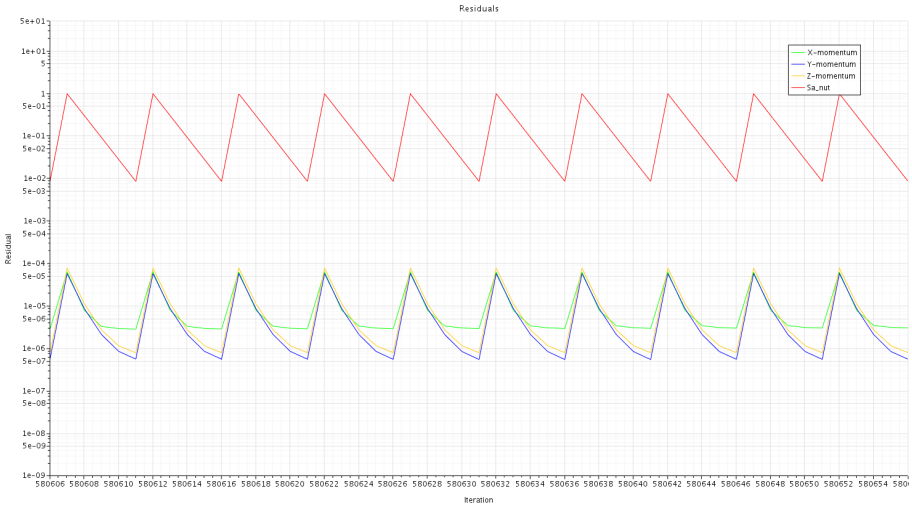

Figure A.365: Residual vs iteration, from DES with the cambered sail model, with a sheet angle of 90°, in the normal computational domain & grid 3, showing the graphs of the X-momentum (green), Y-momentum (blue), Z-momentum (yellow) and Spalart-Allmaras Turbulent kinetic energy (red) of the last 50 iterations, with maximum 5 inner iterations.

Cambered Sail Model with Sheet Angle 100° and the Normal Domain

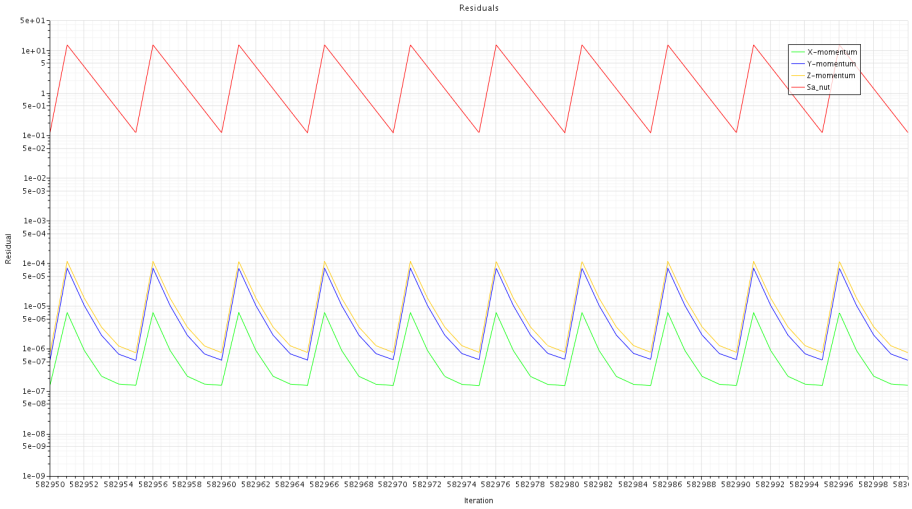

Figure A.366: Residual vs iteration, from DES with the cambered sail model, with a sheet angle of 100°, in the normal computational domain & grid 3, showing the graphs of the X-momentum (green), Y-momentum (blue), Z-momentum (yellow) and Spalart-Allmaras Turbulent kinetic energy (red) of the last 50 iterations, with maximum 5 inner iterations.

Cambered Sail Model with Sheet Angle 110° and the Normal Domain

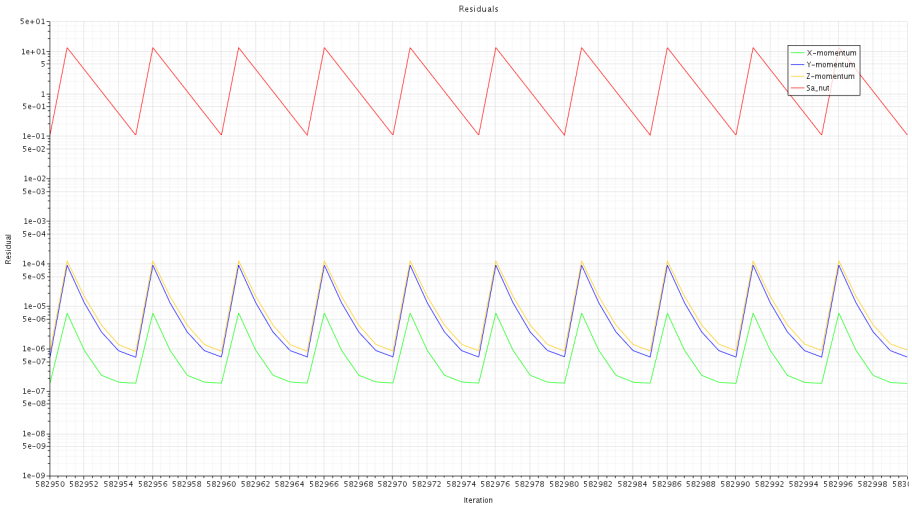

Figure A.367: Residual vs iteration, from DES with the cambered sail model, with a sheet angle of 110°, in the normal computational domain & grid 3, showing the graphs of the X-momentum (green), Y-momentum (blue), Z-momentum (yellow) and Spalart-Allmaras Turbulent kinetic energy (red) of the last 50 iterations, with maximum 5 inner iterations.

Cambered Sail Model with Sheet Angle 120° and the Normal Domain

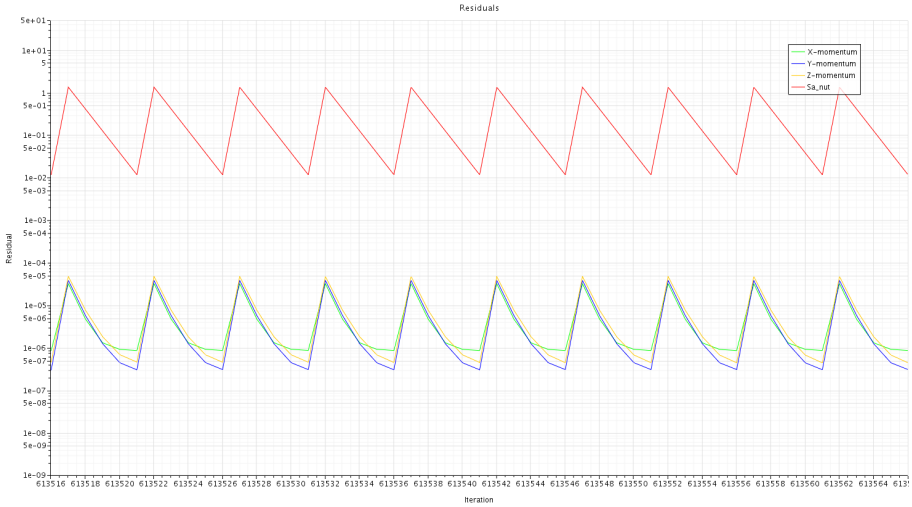

Figure A.368: Residual vs iteration, from DES with the cambered sail model, with a sheet angle of 120°, in the normal computational domain & grid 3, showing the graphs of the X-momentum (green), Y-momentum (blue), Z-momentum (yellow) and Spalart-Allmaras Turbulent kinetic energy (red) of the last 50 iterations, with maximum 5 inner iterations.

Cambered Sail Model with Sheet Angle 60° and the Large Domain

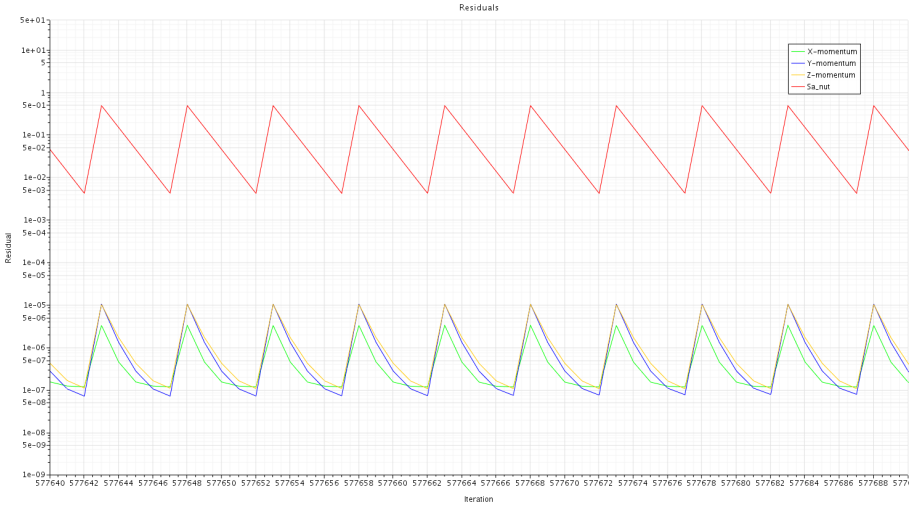

Figure A.369: Residual vs iteration, from DES with the cambered sail model, with a sheet angle of 60°, in the large computational domain & grid 3, showing the graphs of the X-momentum (green), Y-momentum (blue), Z-momentum (yellow) and Spalart-Allmaras Turbulent kinetic energy (red) of the last 50 iterations, with maximum 5 inner iterations.

Cambered Sail Model with Sheet Angle 70° and the Large Domain

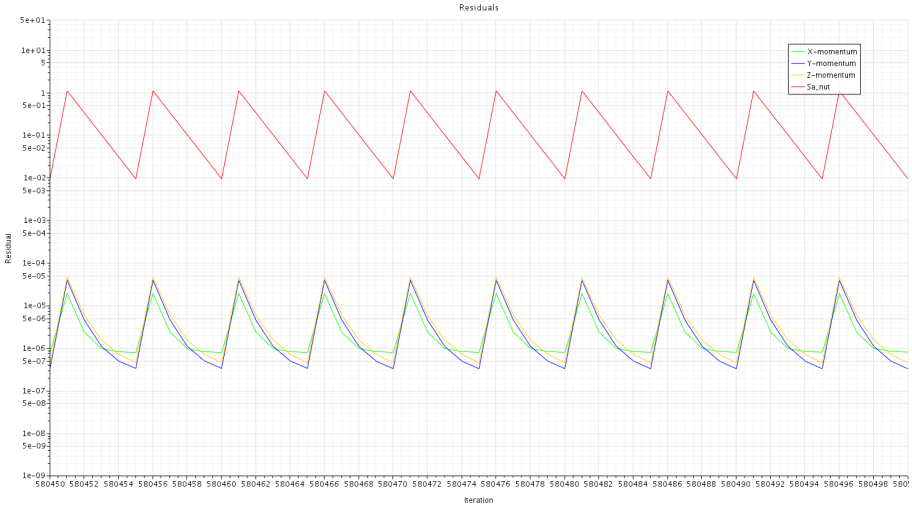

Figure A.370: Residual vs iteration, from DES with the cambered sail model, with a sheet angle of 70°, in the large computational domain & grid 3, showing the graphs of the X-momentum (green), Y-momentum (blue), Z-momentum (yellow) and Spalart-Allmaras Turbulent kinetic energy (red) of the last 50 iterations, with maximum 5 inner iterations.

Cambered Sail Model with Sheet Angle 80° and the Large Domain

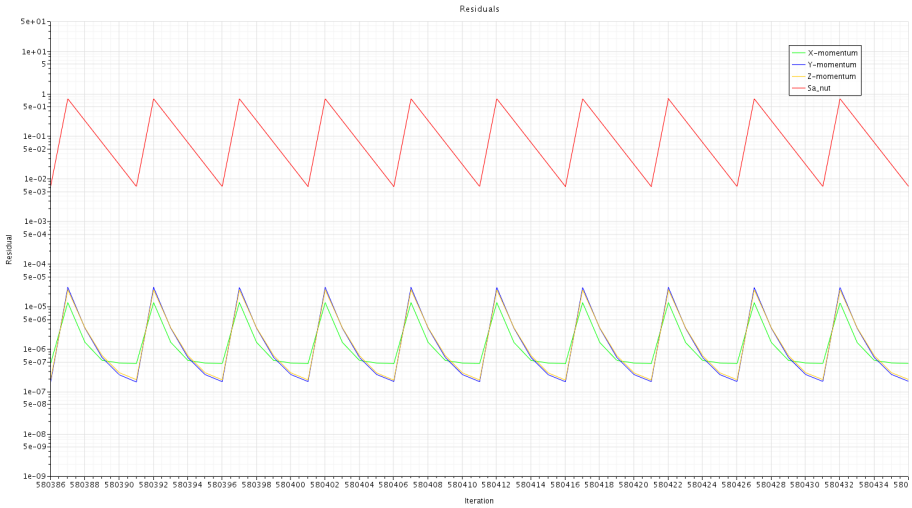

Figure A.371: Residual vs iteration, from DES with the cambered sail model, with a sheet angle of 80°, in the large computational domain & grid 3, showing the graphs of the X-momentum (green), Y-momentum (blue), Z-momentum (yellow) and Spalart-Allmaras Turbulent kinetic energy (red) of the last 50 iterations, with maximum 5 inner iterations.

Cambered Sail Model with Sheet Angle 90° and the Large Domain

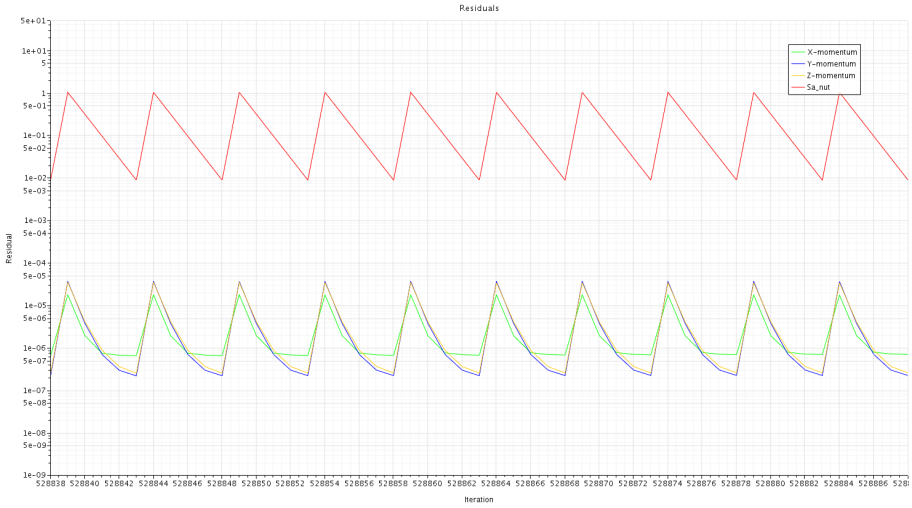

Figure A.372: Residual vs iteration, from DES with the cambered sail model, with a sheet angle of 90°, in the large computational domain & grid 3, showing the graphs of the X-momentum (green), Y-momentum (blue), Z-momentum (yellow) and Spalart-Allmaras Turbulent kinetic energy (red) of the last 50 iterations, with maximum 5 inner iterations.

Cambered Sail Model with Sheet Angle 100° and the Large Domain

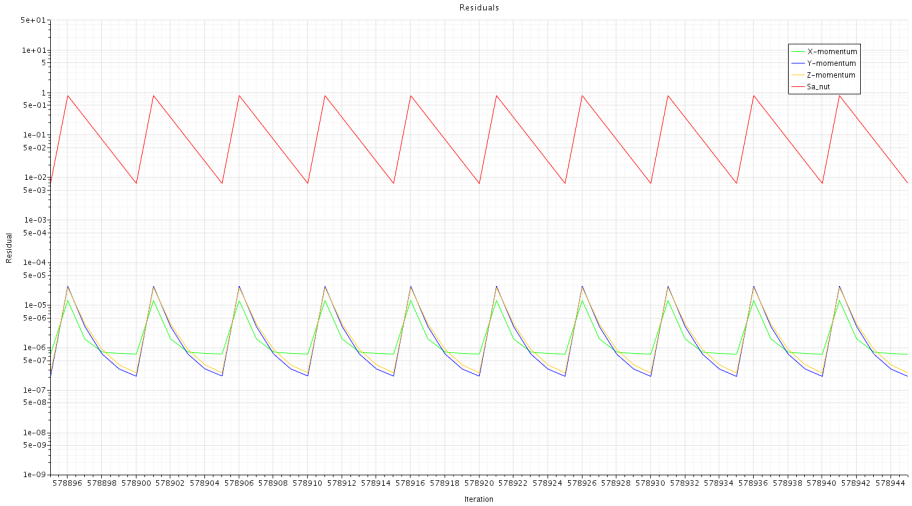

Figure A.373: Residual vs iteration, from DES with the cambered sail model, with a sheet angle of 100°, in the large computational domain & grid 3, showing the graphs of the X-momentum (green), Y-momentum (blue), Z-momentum (yellow) and Spalart-Allmaras Turbulent kinetic energy (red) of the last 50 iterations, with maximum 5 inner iterations.

Cambered Sail Model with Sheet Angle 110° and the Large Domain

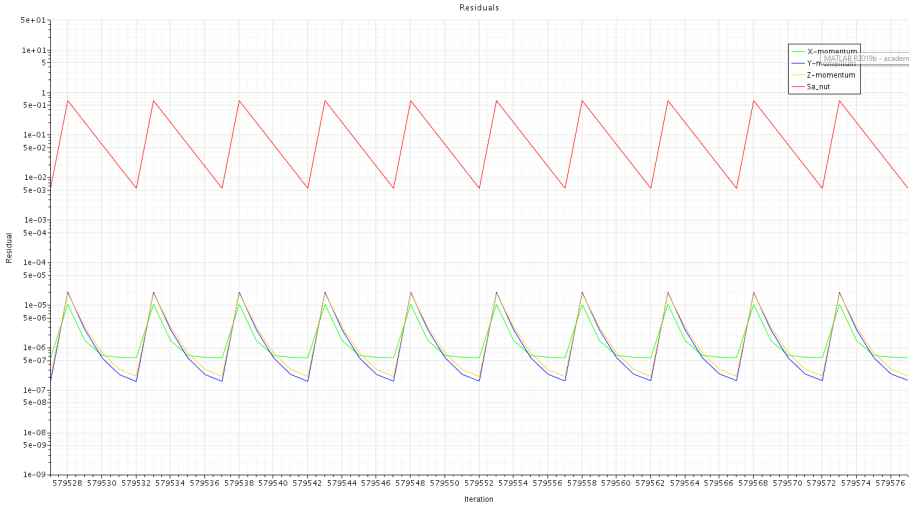

Figure A.374: Residual vs iteration, from DES with the cambered sail model, with a sheet angle of 110°, in the large computational domain & grid 3, showing the graphs of the X-momentum (green), Y-momentum (blue), Z-momentum (yellow) and Spalart-Allmaras Turbulent kinetic energy (red) of the last 50 iterations, with maximum 5 inner iterations.

Cambered Sail Model with Sheet Angle 120° and the Large Domain

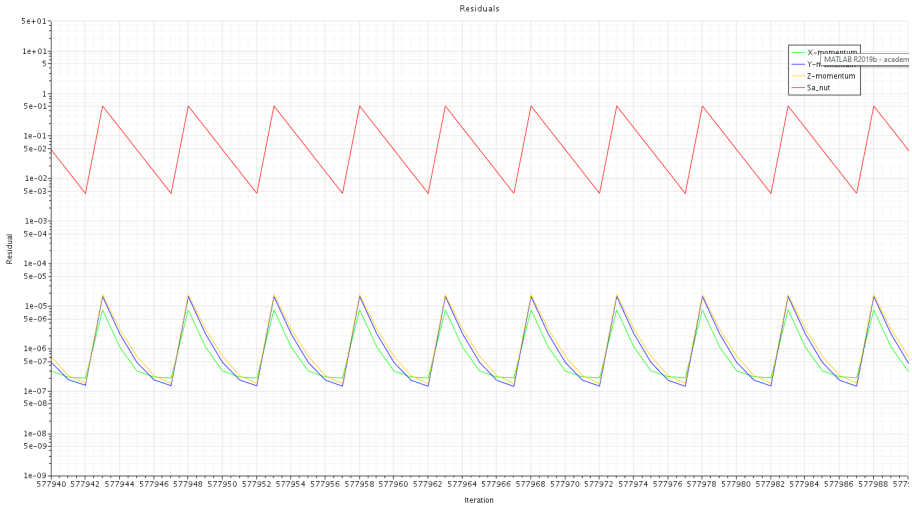

Figure A.375: Residual vs iteration, from DES with the cambered sail model, with a sheet angle of 120°, in the large computational domain & grid 3, showing the graphs of the X-momentum (green), Y-momentum (blue), Z-momentum (yellow) and Spalart-Allmaras Turbulent kinetic energy (red) of the last 50 iterations, with maximum 5 inner iterations.

A.6 Wind Tunnel Tests

A.6.1 Light Wind Tests

Drive Force Coefficients

The corresponding data from Fig. 5.38 - 5.52 are presented in Table A.12 - A.16 below.

Table A.12: Corrected drive force coefficients C_{F_M} [-] for the cases with a heading of 150°, where LKT, MKT and HKT, stands for Light Kicker Trim, Medium Kicker Trim and Hard Kicker Trim, respectively.

Heading: 150°							
Sheet angle [°]	**60**	**70**	**80**	**90**	**100**	**110**	**120**
Heel angle: 0°				C_{F_M} [-]			
LKT	1.2240	1.3280	1.3624	1.3647	1.2742	1.1789	1.0272
MKT	1.1968	1.3467	1.3928	1.3810	1.3310	1.2226	1.1163
HKT	1.2413	1.3254	1.3976	1.3976	1.3475	1.2321	1.0863
Heel angle: 10°				C_{F_M} [-]			
LKT	1.2362	1.3341	1.3892	1.3885	1.3330	1.2226	1.0507
MKT	1.2485	1.3385	1.3974	1.4297	1.3726	1.2664	1.1060
HKT	1.2052	1.3095	1.4004	1.4260	1.3794	1.2693	1.1032
Heel angle: 20°				C_{F_M} [-]			
LKT	1.2945	1.3229	1.3804	1.3629	1.2913	1.1687	1.0831
MKT	1.2308	1.3232	1.4101	1.4195	1.3480	1.2424	1.1409
HKT	1.2178	1.3311	1.3936	1.4083	1.3623	1.2377	1.1040

Table A.13: Corrected drive force coefficients C_{F_M} [-] for the cases with a heading of 160°, where LKT, MKT and HKT, stands for Light Kicker Trim, Medium Kicker Trim and Hard Kicker Trim, respectively.

Heading: 160°							
Sheet angle [°]	**60**	**70**	**80**	**90**	**100**	**110**	**120**
Heel angle: 0°				C_{F_M} [-]			
LKT	1.2736	1.3656	1.3989	1.4082	1.3555	1.2136	1.0523
MKT	1.2678	1.3743	1.4149	1.4374	1.3927	1.2875	1.1302
HKT	1.2471	1.3828	1.4201	1.4419	1.4235	1.2937	1.1511
Heel angle: 10°				C_{F_M} [-]			
LKT	1.2731	1.3364	1.3700	1.3708	1.3293	1.2487	1.1006
MKT	1.2250	1.3645	1.4352	1.4395	1.3815	1.2652	1.0985
HKT	1.2320	1.3709	1.4445	1.4486	1.4127	1.2987	1.0941
Heel angle: 20°				C_{F_M} [-]			
LKT	1.2891	1.3686	1.3910	1.3976	1.3541	1.2755	1.0987
MKT	1.2900	1.3827	1.4119	1.4285	1.3882	1.3323	1.1566
HKT	1.2507	1.3677	1.4270	1.4393	1.3934	1.3084	1.1730

Table A.14: Corrected drive force coefficients C_{F_M} [-] for the cases with a heading of 170°, where LKT, MKT and HKT, stands for Light Kicker Trim, Medium Kicker Trim and Hard Kicker Trim, respectively.

Heading: 170°							
Sheet angle [°]	**60**	**70**	**80**	**90**	**100**	**110**	**120**
Heel angle: 0°				C_{F_M} [-]			
LKT	1.3041	1.3452	1.3795	1.3946	1.3256	1.2240	1.0599
MKT	1.2669	1.3675	1.4136	1.4341	1.3878	1.2833	1.1537
HKT	1.2500	1.3467	1.4333	1.4548	1.4201	1.3294	1.1727
Heel angle: 10°				C_{F_M} [-]			
LKT	1.2705	1.3670	1.4096	1.3796	1.2967	1.2110	1.0776
MKT	1.2772	1.3833	1.3989	1.4254	1.3860	1.2585	1.1442
HKT	1.2304	1.3667	1.4054	1.4441	1.3981	1.2769	1.1644
Heel angle: 20°				C_{F_M} [-]			
LKT	1.2640	1.3656	1.3999	1.3767	1.3611	1.2946	1.1213
MKT	1.2531	1.3568	1.4159	1.3907	1.3821	1.3373	1.1755
HKT	1.2143	1.3244	1.4307	1.4289	1.3905	1.3293	1.2069

Table A.15: Corrected drive force coefficients C_{F_M} [-] for the cases with a heading of 180°, where LKT, MKT and HKT, stands for Light Kicker Trim, Medium Kicker Trim and Hard Kicker Trim, respectively.

Heading: 180°							
Sheet angle [°]	**60**	**70**	**80**	**90**	**100**	**110**	**120**
Heel angle: 0°				C_{F_M} [-]			
LKT	1.3104	1.3709	1.4023	1.4001	1.3521	1.2499	1.0755
MKT	1.2778	1.3730	1.4166	1.4132	1.3794	1.2832	1.1952
HKT	1.2653	1.3542	1.4194	1.4228	1.3925	1.3380	1.2189
Heel angle: 10°				C_{F_M} [-]			
LKT	1.2907	1.3243	1.3690	1.3927	1.3443	1.2685	1.0965
MKT	1.2452	1.3329	1.3953	1.4056	1.3915	1.3032	1.1457
HKT	1.2349	1.3463	1.4252	1.4466	1.4039	1.3080	1.1505
Heel angle: 20°				C_{F_M} [-]			
LKT	1.3005	1.3772	1.4029	1.4015	1.3353	1.2552	1.1320
MKT	1.2369	1.3186	1.3808	1.3829	1.3615	1.3080	1.2464
HKT	1.1882	1.3190	1.3810	1.4096	1.4032	1.3569	1.1911

Table A.16: Corrected drive force coefficients C_{F_M} [-] for the cases with a heading of 190°, where LKT, MKT and HKT, stands for Light Kicker Trim, Medium Kicker Trim and Hard Kicker Trim, respectively.

Heading: 190°							
Sheet angle [°]	**60**	**70**	**80**	**90**	**100**	**110**	**120**
Heel angle: 0°				C_{F_M} [-]			
LKT	1.2633	1.3699	1.3982	1.4156	1.3780	1.2680	1.1332
MKT	1.2020	1.3430	1.3837	1.4203	1.4084	1.3480	1.2093
HKT	1.1401	1.3251	1.4021	1.4302	1.4137	1.3390	1.2205
Heel angle: 10°				C_{F_M} [-]			
LKT	1.2686	1.3794	1.3922	1.3619	1.3247	1.2205	1.0854
MKT	1.1595	1.3250	1.3778	1.3760	1.3577	1.2992	1.1533
HKT	1.1372	1.2883	1.3891	1.4050	1.3986	1.3601	1.2232
Heel angle: 20°				C_{F_M} [-]			
LKT	1.2888	1.3563	1.3684	1.3683	1.3176	1.2016	1.0830
MKT	1.2095	1.3544	1.3971	1.3955	1.3611	1.2864	1.1934
HKT	1.1643	1.2926	1.3867	1.4020	1.3887	1.3116	1.2052

Side Force Coefficients

The corresponding data from Fig. 5.53 - 5.67 are presented in Table A.17 - A.21 below.

Table A.17: Corrected side force coefficients C_{F_S} [-] for the cases with a heading of 150°, where LKT, MKT and HKT, stands for Light Kicker Trim, Medium Kicker Trim and Hard Kicker Trim, respectively.

Heading: 150°							
Sheet angle [°]	**60**	**70**	**80**	**90**	**100**	**110**	**120**
Heel angle: 0°				C_{F_S} [-]			
LKT	-0.5449	-0.3028	-0.0728	0.1378	0.4112	0.6583	0.8633
MKT	-0.6285	-0.4030	-0.1691	0.1019	0.3150	0.5188	0.7739
HKT	-0.6580	-0.4078	-0.1885	0.0633	0.2950	0.4700	0.6616
Heel angle: 10°				C_{F_S} [-]			
LKT	-0.5353	-0.3388	-0.0920	0.1813	0.3834	0.5755	0.8906
MKT	-0.6217	-0.4063	-0.1695	0.1027	0.3342	0.4949	0.7844
HKT	-0.6324	-0.4250	-0.1874	0.0676	0.2995	0.4965	0.6518
Heel angle: 20°				C_{F_S} [-]			
LKT	-0.4103	-0.3104	-0.0352	0.1743	0.3595	0.6025	0.7886
MKT	-0.4988	-0.3715	-0.1368	0.1063	0.3214	0.4765	0.7097
HKT	-0.5799	-0.3979	-0.1702	0.0512	0.2992	0.4556	0.5859

Table A.18: Corrected side force coefficients C_{F_S} [-] for the cases with a heading of 160°, where LKT, MKT and HKT, stands for Light Kicker Trim, Medium Kicker Trim and Hard Kicker Trim, respectively.

Heading: 160°							
Sheet angle [°]	**60**	**70**	**80**	**90**	**100**	**110**	**120**
Heel angle: 0°				C_{F_S} [-]			
LKT	-0.5380	-0.3032	-0.0627	0.1358	0.3846	0.6084	0.8454
MKT	-0.6565	-0.4383	-0.1669	0.0665	0.3326	0.5495	0.7236
HKT	-0.6562	-0.4613	-0.2018	0.0505	0.3070	0.5184	0.6725
Heel angle: 10°				C_{F_S} [-]			
LKT	-0.5710	-0.3381	-0.0903	0.1644	0.3964	0.6207	0.8089
MKT	-0.6355	-0.3976	-0.1738	0.0765	0.3330	0.5498	0.6893
HKT	-0.6581	-0.4628	-0.2174	0.0704	0.3103	0.5017	0.6919
Heel angle: 20°				C_{F_S} [-]			
LKT	-0.5230	-0.3028	-0.0993	0.1114	0.3194	0.5572	0.7563
MKT	-0.6136	-0.3757	-0.1620	0.0691	0.2995	0.5010	0.6419
HKT	-0.6196	-0.4027	-0.1847	0.0410	0.2739	0.4450	0.6365

Table A.19: Corrected side force coefficients C_{F_S} [-] for the cases with a heading of 170°, where LKT, MKT and HKT, stands for Light Kicker Trim, Medium Kicker Trim and Hard Kicker Trim, respectively.

Heading: 170°							
Sheet angle [°]	**60**	**70**	**80**	**90**	**100**	**110**	**120**
Heel angle: 0°				C_{F_S} [-]			
LKT	-0.5705	-0.3173	-0.0752	0.1635	0.3877	0.6241	0.7896
MKT	-0.6682	-0.4188	-0.1716	0.0752	0.3166	0.5433	0.7208
HKT	-0.6671	-0.4391	-0.2099	0.0435	0.2917	0.5113	0.6716
Heel angle: 10°				C_{F_S} [-]			
LKT	-0.5439	-0.3074	-0.1053	0.1663	0.3831	0.5832	0.7784
MKT	-0.6577	-0.4274	-0.1713	0.0783	0.3374	0.5489	0.7469
HKT	-0.6582	-0.4636	-0.1790	0.0317	0.2808	0.5238	0.7196
Heel angle: 20°				C_{F_S} [-]			
LKT	-0.5667	-0.2934	-0.0975	0.1251	0.3244	0.5321	0.6785
MKT	-0.6202	-0.3909	-0.1763	0.0687	0.2868	0.4965	0.6677
HKT	-0.6195	-0.4025	-0.1914	0.0390	0.2551	0.4843	0.6591

Table A.20: Corrected side force coefficients C_{F_S} [-] for the cases with a heading of 180°, where LKT, MKT and HKT, stands for Light Kicker Trim, Medium Kicker Trim and Hard Kicker Trim, respectively.

Heading: 180°							
Sheet angle [°]	**60**	**70**	**80**	**90**	**100**	**110**	**120**
Heel angle: 0°				C_{F_S} [-]			
LKT	-0.5228	-0.2816	-0.0803	0.1610	0.3944	0.5845	0.7905
MKT	-0.6373	-0.4122	-0.1924	0.0573	0.3233	0.5199	0.7434
HKT	-0.6601	-0.4579	-0.2144	0.0329	0.2740	0.5162	0.7208
Heel angle: 10°				C_{F_S} [-]			
LKT	-0.6048	-0.2914	-0.0999	0.1506	0.3812	0.5749	0.7814
MKT	-0.6662	-0.4075	-0.2033	0.0516	0.2922	0.5343	0.7295
HKT	-0.6720	-0.4379	-0.2185	0.0309	0.2634	0.4993	0.6927
Heel angle: 20°				C_{F_S} [-]			
LKT	-0.5319	-0.3247	-0.1070	0.0941	0.3278	0.4939	0.7077
MKT	-0.6060	-0.3825	-0.1686	0.0364	0.2427	0.4948	0.6536
HKT	-0.6326	-0.4180	-0.1946	0.0331	0.2364	0.4595	0.6474

Table A.21: Corrected side force coefficients C_{F_S} [-] for the cases with a heading of 190°, where LKT, MKT and HKT, stands for Light Kicker Trim, Medium Kicker Trim and Hard Kicker Trim, respectively.

Heading: 190°							
Sheet angle [°]	**60**	**70**	**80**	**90**	**100**	**110**	**120**
Heel angle: 0°				C_{F_S} [-]			
LKT	-0.5473	-0.3472	-0.1236	0.1280	0.3768	0.6100	0.8081
MKT	-0.6332	-0.4309	-0.2090	0.0398	0.3069	0.5362	0.7447
HKT	-0.6205	-0.4450	-0.2098	0.0381	0.2548	0.4983	0.7048
Heel angle: 10°				C_{F_S} [-]			
LKT	-0.5790	-0.3113	-0.0802	0.1294	0.3985	0.6159	0.7959
MKT	-0.6384	-0.4286	-0.1888	0.0354	0.2996	0.5263	0.7317
HKT	-0.6013	-0.4427	-0.2252	0.0185	0.2808	0.5189	0.7272
Heel angle: 20°				C_{F_S} [-]			
LKT	-0.5385	-0.3420	-0.0939	0.1143	0.3137	0.5262	0.6885
MKT	-0.6049	-0.4138	-0.1761	0.0342	0.2481	0.4637	0.6694
HKT	-0.6169	-0.4070	-0.2125	0.0145	0.2324	0.4542	0.6575

Lift Force Coefficients

The corresponding data from Fig. 5.68 - 5.82 are presented in Table A.22 - A.26 below.

Table A.22: Partly corrected lift force coefficients C_{F_L} [-] for the cases with a heading of 150°, where LKT, MKT and HKT, stands for Light Kicker Trim, Medium Kicker Trim and Hard Kicker Trim, respectively.

Heading: 150°							
Sheet angle [°]	**60**	**70**	**80**	**90**	**100**	**110**	**120**
Heel angle: 0°				C_{F_L} [-]			
LKT	-0.0854	-0.0889	-0.0998	-0.0475	-0.0484	-0.0343	-0.0416
MKT	-0.0389	-0.0377	-0.0347	-0.0315	-0.0140	-0.0068	0.0016
HKT	-0.0300	-0.0330	-0.0198	-0.0236	-0.0066	-0.0075	0.0026
Heel angle: 10°				C_{F_L} [-]			
LKT	0.0624	0.0386	-0.0274	-0.1038	-0.0935	-0.0977	-0.2276
MKT	0.1231	0.0827	0.0393	-0.0282	-0.0572	-0.1055	-0.1298
HKT	0.1281	0.0910	0.0384	-0.0082	-0.0519	-0.0792	-0.1095
Heel angle: 20°				C_{F_L} [-]			
LKT	0.0848	0.1051	-0.0559	-0.1142	-0.1807	-0.2825	-0.3422
MKT	0.2003	0.1758	0.0652	-0.0300	-0.1244	-0.1837	-0.2534
HKT	0.2785	0.1931	0.0874	-0.0158	-0.1027	-0.1588	-0.2102

Table A.23: Partly corrected lift force coefficients C_{F_L} [-] for the cases with a heading of 160°, where LKT, MKT and HKT, stands for Light Kicker Trim, Medium Kicker Trim and Hard Kicker Trim, respectively.

Heading: 160°							
Sheet angle [°]	**60**	**70**	**80**	**90**	**100**	**110**	**120**
Heel angle: 0°				C_{F_L} [-]			
LKT	-0.1139	-0.0921	-0.0888	-0.0620	-0.0439	-0.0423	-0.0381
MKT	-0.0534	-0.0472	-0.0408	-0.0287	-0.0249	-0.0064	-0.0059
HKT	-0.0364	-0.0137	-0.0242	-0.0161	-0.0124	-0.0023	0.0037
Heel angle: 10°				C_{F_L} [-]			
LKT	0.0541	-0.0066	-0.0468	-0.0974	-0.1384	-0.1803	-0.1786
MKT	0.1097	0.0620	0.0141	-0.0287	-0.0735	-0.1020	-0.1216
HKT	0.1063	0.0769	0.0466	-0.0203	-0.0632	-0.0941	-0.1170
Heel angle: 20°				C_{F_L} [-]			
LKT	0.1991	0.0918	0.0271	-0.0691	-0.1408	-0.2394	-0.3396
MKT	0.2733	0.1688	0.0826	-0.0150	-0.1052	-0.2207	-0.2499
HKT	0.2790	0.1898	0.0923	-0.0023	-0.0906	-0.1729	-0.2334

Table A.24: Partly corrected lift force coefficients C_{F_L} [-] for the cases with a heading of 170°, where LKT, MKT and HKT, stands for Light Kicker Trim, Medium Kicker Trim and Hard Kicker Trim, respectively.

Heading: 170°							
Sheet angle [°]	**60**	**70**	**80**	**90**	**100**	**110**	**120**
Heel angle: 0°				C_{F_L} [-]			
LKT	-0.0992	-0.0988	-0.0988	-0.0784	-0.0763	-0.0725	-0.0565
MKT	-0.0443	-0.0470	-0.0535	-0.0347	-0.0373	-0.0203	-0.0163
HKT	-0.0407	-0.0347	-0.0333	-0.0213	-0.0178	-0.0112	-0.0053
Heel angle: 10°				C_{F_L} [-]			
LKT	0.0463	-0.0168	-0.0379	-0.1037	-0.1436	-0.1825	-0.1889
MKT	0.1114	0.0705	0.0170	-0.0385	-0.0911	-0.1368	-0.1433
HKT	0.1113	0.0787	0.0274	-0.0260	-0.0708	-0.0955	-0.1347
Heel angle: 20°				C_{F_L} [-]			
LKT	0.2142	0.0596	-0.0072	-0.1000	-0.1753	-0.2594	-0.3005
MKT	0.2701	0.1647	0.0707	-0.0339	-0.1209	-0.2091	-0.2695
HKT	0.2742	0.1820	0.0854	-0.0111	-0.1038	-0.1991	-0.2522

Table A.25: Partly corrected lift force coefficients C_{F_L} [-] for the cases with a heading of 180°, where LKT, MKT and HKT, stands for Light Kicker Trim, Medium Kicker Trim and Hard Kicker Trim, respectively.

Heading: 180°							
Sheet angle [°]	**60**	**70**	**80**	**90**	**100**	**110**	**120**
Heel angle: 0°				C_{F_L} [-]			
LKT	-0.1261	-0.1278	-0.1112	-0.0882	-0.0910	-0.0670	-0.0749
MKT	-0.0731	-0.0715	-0.0474	-0.0435	-0.0351	-0.0288	-0.0282
HKT	-0.0527	-0.0366	-0.0391	-0.0221	-0.0311	-0.0149	-0.0101
Heel angle: 10°				C_{F_L} [-]			
LKT	0.0424	-0.0379	-0.0670	-0.1239	-0.1699	-0.1834	-0.2280
MKT	0.0977	0.0422	0.0117	-0.0335	-0.0796	-0.1380	-0.1727
HKT	0.1089	0.0651	0.0196	-0.0209	-0.0746	-0.1140	-0.1449
Heel angle: 20°				C_{F_L} [-]			
LKT	0.1652	0.0665	-0.0325	-0.0864	-0.1950	-0.2559	-0.3506
MKT	0.2616	0.1466	0.0556	-0.0196	-0.1229	-0.2251	-0.2767
HKT	0.2778	0.1799	0.0749	-0.0028	-0.1034	-0.2053	-0.2638

Table A.26: Partly corrected lift force coefficients C_{F_L} [-] for the cases with a heading of 190°, where LKT, MKT and HKT, stands for Light Kicker Trim, Medium Kicker Trim and Hard Kicker Trim, respectively.

Heading: 190°							
Sheet angle [°]	**60**	**70**	**80**	**90**	**100**	**110**	**120**
Heel angle: 0°				C_{F_L} [-]			
LKT	-0.0967	-0.0928	-0.0891	-0.0974	-0.0828	-0.0823	-0.0686
MKT	-0.0338	-0.0387	-0.0416	-0.0403	-0.0430	-0.0306	-0.0289
HKT	-0.0315	-0.0338	-0.0188	-0.0302	-0.0311	-0.0193	-0.0120
Heel angle: 10°				C_{F_L} [-]			
LKT	0.0299	-0.0502	-0.0913	-0.1024	-0.1790	-0.2161	-0.2446
MKT	0.1029	0.0486	0.0008	-0.0333	-0.1117	-0.1351	-0.1740
HKT	0.0965	0.0734	0.0252	-0.0188	-0.0775	-0.1218	-0.1619
Heel angle: 20°				C_{F_L} [-]			
LKT	0.1562	0.0738	-0.0508	-0.1308	-0.2261	-0.3119	-0.3679
MKT	0.2479	0.1672	0.0397	-0.0268	-0.1356	-0.2246	-0.3159
HKT	0.2652	0.1741	0.0844	-0.0013	-0.1081	-0.2010	-0.2874

Pitch Moment Coefficients

The corresponding data from Fig. 5.83 - 5.97 are presented in Table A.27 - A.31 below.

Table A.27: Corrected pitch moment coefficients C_{M_P} [-] for the cases with a heading of 150°, where LKT, MKT and HKT, stands for Light Kicker Trim, Medium Kicker Trim and Hard Kicker Trim, respectively.

Heading: 150°							
Sheet angle [°]	**60**	**70**	**80**	**90**	**100**	**110**	**120**
Heel angle: 0°				C_{M_P} [-]			
LKT	2.2485	2.4996	2.5976	2.6125	2.4822	2.3270	2.0937
MKT	2.1110	2.4567	2.5548	2.5814	2.4980	2.3382	2.2335
HKT	2.1437	2.3390	2.4886	2.5437	2.5060	2.3008	2.0872
Heel angle: 10°				C_{M_P} [-]			
LKT	2.4560	2.6274	2.7310	2.7705	2.6700	2.4580	2.2079
MKT	2.4339	2.5886	2.6987	2.8192	2.7162	2.5517	2.3282
HKT	2.2752	2.4943	2.6597	2.7672	2.6922	2.5179	2.2622
Heel angle: 20°				C_{M_P} [-]			
LKT	2.6409	2.6871	2.7867	2.7965	2.6721	2.5166	2.3487
MKT	2.5071	2.6517	2.8317	2.8901	2.7775	2.6200	2.4579
HKT	2.4495	2.6436	2.7534	2.7895	2.7818	2.5846	2.3125

Table A.28: Corrected pitch moment coefficients C_{M_P} [-] for the cases with a heading of 160°, where LKT, MKT and HKT, stands for Light Kicker Trim, Medium Kicker Trim and Hard Kicker Trim, respectively.

Heading: 160°							
Sheet angle [°]	**60**	**70**	**80**	**90**	**100**	**110**	**120**
Heel angle: 0°				C_{M_P} [-]			
LKT	2.3079	2.5350	2.5484	2.6178	2.5250	2.3043	2.0411
MKT	2.2039	2.4232	2.5201	2.5891	2.5731	2.3631	2.1474
HKT	2.1198	2.3654	2.4321	2.4879	2.5096	2.3206	2.1075
Heel angle: 10°				C_{M_P} [-]			
LKT	2.4258	2.5456	2.6229	2.6300	2.5893	2.4205	2.2007
MKT	2.2995	2.5496	2.7009	2.7208	2.6700	2.4225	2.1653
HKT	2.2709	2.5158	2.6574	2.6978	2.6932	2.4540	2.1318
Heel angle: 20°				C_{M_P} [-]			
LKT	2.5830	2.7051	2.7437	2.7568	2.7086	2.5558	2.2413
MKT	2.5485	2.7055	2.7570	2.7937	2.7632	2.6744	2.3228
HKT	2.4426	2.6394	2.7536	2.7983	2.7443	2.5926	2.3489

Table A.29: Corrected pitch moment coefficients C_{M_P} [-] for the cases with a heading of 170°, where LKT, MKT and HKT, stands for Light Kicker Trim, Medium Kicker Trim and Hard Kicker Trim, respectively.

Heading: 170°							
Sheet angle [°]	**60**	**70**	**80**	**90**	**100**	**110**	**120**
Heel angle: 0°				C_{M_P} [-]			
LKT	2.3479	2.4359	2.5156	2.5532	2.4255	2.3030	2.0019
MKT	2.2026	2.4195	2.5210	2.5583	2.4942	2.3702	2.1570
HKT	2.1124	2.2991	2.4731	2.5142	2.4526	2.3871	2.1275
Heel angle: 10°				C_{M_P} [-]			
LKT	2.4481	2.6120	2.7329	2.6583	2.5157	2.3787	2.1297
MKT	2.4100	2.5958	2.6819	2.7077	2.6637	2.4631	2.2449
HKT	2.2885	2.5237	2.6553	2.7022	2.6226	2.4502	2.2603
Heel angle: 20°				C_{M_P} [-]			
LKT	2.4926	2.6821	2.7434	2.7077	2.6822	2.5907	2.2757
MKT	2.4456	2.6421	2.7552	2.7122	2.6981	2.6549	2.3810
HKT	2.3543	2.5462	2.7392	2.7459	2.6887	2.6261	2.4210

Table A.30: Corrected pitch moment coefficients C_{M_P} [-] for the cases with a heading of 180°, where LKT, MKT and HKT, stands for Light Kicker Trim, Medium Kicker Trim and Hard Kicker Trim, respectively.

Heading: 180°							
Sheet angle [°]	**60**	**70**	**80**	**90**	**100**	**110**	**120**
Heel angle: 0°				C_{M_P} [-]			
LKT	2.3817	2.5491	2.5888	2.5626	2.5094	2.3260	1.9865
MKT	2.2765	2.4729	2.5514	2.5167	2.5111	2.3397	2.1705
HKT	2.1926	2.3869	2.4677	2.4595	2.4439	2.3762	2.1635
Heel angle: 10°				C_{M_P} [-]			
LKT	2.4539	2.5342	2.6063	2.6678	2.5799	2.4596	2.1257
MKT	2.3350	2.5011	2.6130	2.6528	2.6426	2.4983	2.2207
HKT	2.2847	2.4942	2.6215	2.6591	2.6258	2.4632	2.1684
Heel angle: 20°				C_{M_P} [-]			
LKT	2.5594	2.7231	2.7354	2.7448	2.6306	2.4877	2.2332
MKT	2.4168	2.5774	2.6721	2.6738	2.6639	2.5798	2.4622
HKT	2.2884	2.5535	2.6345	2.7038	2.6663	2.6465	2.3345

Table A.31: Corrected pitch moment coefficients C_{M_P} [-] for the cases with a heading of 190°, where LKT, MKT and HKT, stands for Light Kicker Trim, Medium Kicker Trim and Hard Kicker Trim, respectively.

Heading: 190°							
Sheet angle [°]	**60**	**70**	**80**	**90**	**100**	**110**	**120**
Heel angle: 0°				C_{M_P} [-]			
LKT	2.3124	2.5250	2.5537	2.5828	2.4863	2.3294	2.0911
MKT	2.1443	2.4269	2.4571	2.5227	2.4931	2.4205	2.1818
HKT	1.9801	2.3216	2.3892	2.4561	2.4112	2.3127	2.1270
Heel angle: 10°				C_{M_P} [-]			
LKT	2.4164	2.6255	2.6190	2.5848	2.4963	2.3339	2.0727
MKT	2.1743	2.4803	2.5562	2.5695	2.5588	2.4533	2.1978
HKT	2.0954	2.3674	2.5248	2.5655	2.5855	2.5271	2.2843
Heel angle: 20°				C_{M_P} [-]			
LKT	2.5278	2.6636	2.6191	2.6270	2.5613	2.3732	2.1213
MKT	2.3543	2.6387	2.6559	2.7029	2.6253	2.5177	2.3296
HKT	2.2512	2.5000	2.6190	2.6512	2.6559	2.5369	2.3390

Roll Moment Coefficients

The corresponding data from Fig. 5.98 - 5.112 are presented in Table A.32 - A.36 below.

Table A.32: Corrected roll moment coefficients C_{M_R} [-] for the cases with a heading of 150°, where LKT, MKT and HKT, stands for Light Kicker Trim, Medium Kicker Trim and Hard Kicker Trim, respectively.

Heading: 150°							
Sheet angle [°]	**60**	**70**	**80**	**90**	**100**	**110**	**120**
Heel angle: 0°				C_{M_R} [-]			
LKT	-1.0227	-0.5604	-0.1123	0.3045	0.8948	1.4195	1.8837
MKT	-1.2000	-0.7915	-0.3481	0.1994	0.6234	1.0390	1.5914
HKT	-1.2523	-0.7992	-0.3959	0.0932	0.5532	0.8961	1.2709
Heel angle: 10°				C_{M_R} [-]			
LKT	-1.0449	-0.6562	-0.1123	0.4494	0.8550	1.2334	2.0576
MKT	-1.2398	-0.8156	-0.3174	0.2263	0.6998	1.0438	1.7340
HKT	-1.2569	-0.8650	-0.3668	0.1121	0.5824	0.9923	1.3246
Heel angle: 20°				C_{M_R} [-]			
LKT	-0.7909	-0.6155	-0.0164	0.4364	0.8427	1.4405	1.8828
MKT	-1.0298	-0.7745	-0.2832	0.2254	0.7139	1.0403	1.5595
HKT	-1.2240	-0.8375	-0.3912	0.0677	0.6074	0.9204	1.1988

Table A.33: Corrected roll moment coefficients C_{M_R} [-] for the cases with a heading of 160°, where LKT, MKT and HKT, stands for Light Kicker Trim, Medium Kicker Trim and Hard Kicker Trim, respectively.

Heading: 160°							
Sheet angle [°]	**60**	**70**	**80**	**90**	**100**	**110**	**120**
Heel angle: 0°				C_{M_R} [-]			
LKT	-0.9944	-0.5523	-0.0757	0.2890	0.7699	1.2587	1.8174
MKT	-1.2459	-0.8481	-0.3169	0.1029	0.6455	1.0673	1.4506
HKT	-1.2392	-0.8655	-0.4060	0.0576	0.5339	0.9545	1.2701
Heel angle: 10°				C_{M_R} [-]			
LKT	-1.1241	-0.6379	-0.1332	0.3892	0.8831	1.3730	1.8214
MKT	-1.2678	-0.7981	-0.3435	0.1912	0.7031	1.1730	1.4197
HKT	-1.3207	-0.9426	-0.4542	0.1434	0.6073	1.0236	1.3989
Heel angle: 20°				C_{M_R} [-]			
LKT	-1.0657	-0.5907	-0.1597	0.2910	0.7343	1.2605	1.7807
MKT	-1.2764	-0.7796	-0.3265	0.1596	0.6488	1.0794	1.3705
HKT	-1.2833	-0.8469	-0.3951	0.0779	0.5578	0.8962	1.3068

Table A.34: Corrected roll moment coefficients C_{M_R} [-] for the cases with a heading of 170°, where LKT, MKT and HKT, stands for Light Kicker Trim, Medium Kicker Trim and Hard Kicker Trim, respectively.

Heading: 170°							
Sheet angle [°]	**60**	**70**	**80**	**90**	**100**	**110**	**120**
Heel angle: 0°				C_{M_R} [-]			
LKT	-1.0630	-0.5736	-0.0963	0.3601	0.8103	1.3137	1.6813
MKT	-1.2753	-0.8027	-0.3238	0.1269	0.6168	1.0611	1.4574
HKT	-1.2720	-0.8522	-0.4211	0.0360	0.5059	0.9396	1.3078
Heel angle: 10°				C_{M_R} [-]			
LKT	-1.0492	-0.5646	-0.1322	0.4092	0.8720	1.3184	1.7048
MKT	-1.3031	-0.8531	-0.3054	0.1599	0.7182	1.1922	1.5552
HKT	-1.3098	-0.9384	-0.3484	0.0305	0.5447	1.0696	1.4508
Heel angle: 20°				C_{M_R} [-]			
LKT	-1.1450	-0.5521	-0.1790	0.3270	0.7490	1.1933	1.5061
MKT	-1.2716	-0.7994	-0.3895	0.1583	0.6098	1.0496	1.4219
HKT	-1.2701	-0.8463	-0.4426	0.0599	0.5102	0.9838	1.3435

Table A.35: Corrected roll moment coefficients C_{M_R} [-] for the cases with a heading of 180°, where LKT, MKT and HKT, stands for Light Kicker Trim, Medium Kicker Trim and Hard Kicker Trim, respectively.

Heading: 180°							
Sheet angle [°]	**60**	**70**	**80**	**90**	**100**	**110**	**120**
Heel angle: 0°				C_{M_R} [-]			
LKT	-0.9566	-0.4960	-0.1030	0.3602	0.8274	1.2047	1.6338
MKT	-1.2123	-0.7919	-0.3693	0.0989	0.6169	1.0026	1.4355
HKT	-1.2643	-0.8889	-0.4346	0.0174	0.4788	0.9487	1.3349
Heel angle: 10°				C_{M_R} [-]			
LKT	-1.1804	-0.5224	-0.1413	0.3771	0.8559	1.2124	1.6892
MKT	-1.3259	-0.8013	-0.4053	0.0984	0.5880	1.0582	1.5028
HKT	-1.3406	-0.8742	-0.4520	0.0227	0.4905	0.9188	1.3522
Heel angle: 20°				C_{M_R} [-]			
LKT	-1.0553	-0.6378	-0.1433	0.2276	0.7475	1.0789	1.5451
MKT	-1.2383	-0.7912	-0.3292	0.0545	0.5052	1.0213	1.3691
HKT	-1.2937	-0.8853	-0.4029	0.0205	0.4295	0.9026	1.2768

Table A.36: Corrected roll moment coefficients C_{M_R} [-] for the cases with a heading of 190°, where LKT, MKT and HKT, stands for Light Kicker Trim, Medium Kicker Trim and Hard Kicker Trim, respectively.

Heading: 190°							
Sheet angle [°]	**60**	**70**	**80**	**90**	**100**	**110**	**120**
Heel angle: 0°				C_{M_R} [-]			
LKT	-1.0298	-0.6579	-0.2158	0.2757	0.7576	1.2410	1.6384
MKT	-1.2262	-0.8487	-0.4222	0.0517	0.5621	1.0172	1.4272
HKT	-1.2059	-0.8855	-0.4356	0.0119	0.4351	0.8782	1.2719
Heel angle: 10°				C_{M_R} [-]			
LKT	-1.1520	-0.5857	-0.1046	0.2937	0.8555	1.3173	1.6899
MKT	-1.3018	-0.8766	-0.3902	0.0485	0.5969	1.0266	1.4671
HKT	-1.2405	-0.9166	-0.4889	0.0178	0.4988	0.9563	1.3797
Heel angle: 20°				C_{M_R} [-]			
LKT	-1.0711	-0.6883	-0.1564	0.2847	0.6914	1.1677	1.5046
MKT	-1.2372	-0.8784	-0.3748	0.0465	0.4878	0.9638	1.4088
HKT	-1.2679	-0.8722	-0.4802	0.0164	0.4113	0.8740	1.2988

Yaw Moment Coefficients

The corresponding data from Fig. 5.113 - 5.127 are presented in Table A.37 - A.41 below. Note that since the wind tunnel balance measured positive yaw moments as negative, all data were multiplied with -1.

Table A.37: Yaw moment coefficients C_{M_Y} [-] for the cases with a heading of 150°, where LKT, MKT and HKT, stands for Light Kicker Trim, Medium Kicker Trim and Hard Kicker Trim, respectively.

Heading: 150°							
Sheet angle [°]	**60**	**70**	**80**	**90**	**100**	**110**	**120**
Heel angle: 0°				C_{M_Y} [-]			
LKT	0.0695	-0.0060	-0.0378	-0.0357	-0.0387	-0.0064	0.0565
MKT	0.1801	0.0834	0.0561	-0.0004	0.0354	0.0560	0.1200
HKT	0.2378	0.1605	0.1252	0.0618	0.0858	0.1032	0.1483
Heel angle: 10°				C_{M_Y} [-]			
LKT	0.0260	-0.0196	-0.0799	-0.1097	-0.0792	-0.0298	-0.0223
MKT	0.1270	0.0668	-0.0138	-0.0485	-0.0138	-0.0062	0.0261
HKT	0.2272	0.1287	0.0691	0.0234	0.0520	0.0816	0.1194
Heel angle: 20°				C_{M_Y} [-]			
LKT	-0.1081	-0.0904	-0.1569	-0.1654	-0.1543	-0.1382	-0.1027
MKT	-0.0329	-0.0120	-0.0538	-0.0917	-0.1157	-0.0805	-0.0179
HKT	0.0845	0.0753	0.0276	-0.0011	-0.0300	0.0240	0.0616

Table A.38: Yaw moment coefficients C_{M_Y} [-] for the cases with a heading of 160°, where LKT, MKT and HKT, stands for Light Kicker Trim, Medium Kicker Trim and Hard Kicker Trim, respectively.

Heading: 160°							
Sheet angle [°]	**60**	**70**	**80**	**90**	**100**	**110**	**120**
Heel angle: 0°				C_{M_Y} [-]			
LKT	0.0579	-0.0100	-0.0425	-0.0323	-0.0255	0.0059	0.0667
MKT	0.1748	0.1170	0.0244	0.0424	0.0194	0.0525	0.1020
HKT	0.2360	0.1958	0.1135	0.1043	0.0987	0.1125	0.1502
Heel angle: 10°				C_{M_Y} [-]			
LKT	0.0535	-0.0240	-0.0710	-0.0984	-0.0863	-0.0596	0.0031
MKT	0.1312	0.0658	0.0062	-0.0182	-0.0280	0.0048	0.0880
HKT	0.2021	0.1562	0.0995	0.0591	0.0402	0.0532	0.1338
Heel angle: 20°				C_{M_Y} [-]			
LKT	-0.0226	-0.0908	-0.1212	-0.1379	-0.1379	-0.1068	-0.0697
MKT	0.1066	-0.0058	-0.0417	-0.0722	-0.0841	-0.0684	-0.0091
HKT	0.1974	0.0952	0.0451	-0.0236	-0.0171	0.0211	0.0716

Table A.39: Yaw moment coefficients C_{M_Y} [-] for the cases with a heading of 170°, where LKT, MKT and HKT, stands for Light Kicker Trim, Medium Kicker Trim and Hard Kicker Trim, respectively.

Heading: 170°							
Sheet angle [°]	**60**	**70**	**80**	**90**	**100**	**110**	**120**
Heel angle: 0°				C_{M_Y} [-]			
LKT	0.0786	0.0160	-0.0247	-0.0319	-0.0163	0.0124	0.0718
MKT	0.1870	0.0964	0.0413	0.0365	0.0336	0.0670	0.1080
HKT	0.2498	0.1957	0.1349	0.1230	0.1250	0.1335	0.1757
Heel angle: 10°				C_{M_Y} [-]			
LKT	0.0326	-0.0290	-0.0520	-0.0865	-0.0648	-0.0323	0.0328
MKT	0.1546	0.0749	0.0065	-0.0100	-0.0187	0.0051	0.0902
HKT	0.2122	0.1587	0.0732	0.0629	0.0700	0.0813	0.1372
Heel angle: 20°				C_{M_Y} [-]			
LKT	0.0369	-0.0820	-0.1051	-0.1264	-0.1152	-0.0859	-0.0306
MKT	0.1523	0.0265	-0.0184	-0.0572	-0.0410	-0.0182	0.0239
HKT	0.1926	0.1203	0.0695	0.0315	0.0311	0.0392	0.0960

Table A.40: Yaw moment coefficients C_{M_Y} [-] for the cases with a heading of 180°, where LKT, MKT and HKT, stands for Light Kicker Trim, Medium Kicker Trim and Hard Kicker Trim, respectively.

Heading: 180°							
Sheet angle [°]	**60**	**70**	**80**	**90**	**100**	**110**	**120**
Heel angle: 0°				C_{M_Y} [-]			
LKT	0.0562	-0.0023	-0.0089	-0.0236	-0.0053	0.0299	0.0875
MKT	0.1476	0.0971	0.0698	0.0470	0.0572	0.0841	0.1448
HKT	0.2361	0.1711	0.1545	0.1262	0.1429	0.1387	0.1971
Heel angle: 10°				C_{M_Y} [-]			
LKT	0.0988	-0.0243	-0.0307	-0.0690	-0.0507	-0.0201	0.0467
MKT	0.1962	0.0933	0.0683	0.0192	0.0151	0.0325	0.0852
HKT	0.2641	0.1558	0.1413	0.1106	0.0749	0.1202	0.1806
Heel angle: 20°				C_{M_Y} [-]			
LKT	0.0054	-0.0532	-0.0892	-0.0837	-0.0989	-0.0501	-0.0049
MKT	0.1190	0.0377	-0.0147	0.0027	-0.0353	0.0143	0.0208
HKT	0.2313	0.1382	0.0940	0.0849	0.0579	0.0590	0.1329

Table A.41: Yaw moment coefficients C_{M_Y} [-] for the cases with a heading of 190°, where LKT, MKT and HKT, stands for Light Kicker Trim, Medium Kicker Trim and Hard Kicker Trim, respectively.

Heading: 190°							
Sheet angle [°]	**60**	**70**	**80**	**90**	**100**	**110**	**120**
Heel angle: 0°				C_{M_Y} [-]			
LKT	0.0779	0.0464	0.0244	0.0051	0.0168	0.0468	0.1038
MKT	0.1758	0.1273	0.1176	0.0740	0.0709	0.0968	0.1561
HKT	0.2597	0.2271	0.1919	0.1675	0.1676	0.1743	0.2299
Heel angle: 10°				C_{M_Y} [-]			
LKT	0.0674	-0.0126	-0.0409	-0.0380	-0.0337	0.0099	0.0636
MKT	0.1869	0.1001	0.0446	0.0470	0.0098	0.0616	0.1019
HKT	0.2713	0.2048	0.1508	0.1463	0.1022	0.1462	0.1735
Heel angle: 20°				C_{M_Y} [-]			
LKT	0.0179	-0.0245	-0.0753	-0.0747	-0.0744	-0.0430	0.0116
MKT	0.1392	0.0847	-0.0047	0.0131	-0.0128	0.0069	0.0303
HKT	0.2277	0.1783	0.0980	0.0949	0.0887	0.1016	0.1228

Repeatability Tests

The corresponding data from Fig. 5.128 - 5.131 are presented in Table A.42 below.

Table A.42: Corrected drive force coefficients C_{F_M} [-] and standard deviation σ [-], for the 5 separate repeatability tests that were carried out with the heading 190° and the fix sheet angle 90°, for the three heel angles and the three trims with the kicker, where LKT, MKT and HKT, stands for Light Kicker Trim, Medium Kicker Trim and Hard Kicker Trim, respectively.

Heading: 190°						
Rep. test:	**1**	**2**	**3**	**4**	**5**	**1 - 5**
Heel angle: 0°			C_{F_M} [-]			σ [-]
LKT	1.3938	1.4158	1.3817	1.4012	1.4085	0.0168
MKT	1.4495	1.4205	1.4407	1.4133	1.4694	0.0281
HKT	1.3872	1.4304	1.4494	1.4434	1.4089	0.0322
Heel angle: 10°			C_{F_M} [-]			σ [-]
LKT	1.3737	1.3626	1.3863	1.3834	1.3912	0.0146
MKT	1.4748	1.3768	1.4189	1.3808	1.4161	0.0520
HKT	1.3944	1.4058	1.4330	1.4435	1.4142	0.0243
Heel angle: 20°			C_{F_M} [-]			σ [-]
LKT	1.3704	1.3572	1.4185	1.3434	1.3942	0.0374
MKT	1.4387	1.3833	1.4128	1.4007	1.4198	0.0269
HKT	1.4041	1.4428	1.3793	1.4111	1.4200	0.0308

A.6.2 Strong Wind Tests

The corresponding data from Fig. 5.132 - 5.137 are presented in Table A.43 - A.48 below.

Table A.43: Corrected drive force coefficients C_{F_M} [-] for the strong wind case, where LKT, MKT and HKT, stands for Light Kicker Trim, Medium Kicker Trim and Hard Kicker Trim, respectively.

Heading: 180°				
Sheet angle [°]	**60**	**70**	**80**	**90**
Heel angle: 0°		C_{F_M} [-]		
LKT	1.3285	1.3702	1.3789	1.3160
MKT	1.3303	1.3741	1.3808	1.3886
HKT	1.3213	1.3660	1.4071	1.3842

Table A.44: Corrected side force coefficients C_{F_S} [-] for the strong wind case, where LKT, MKT and HKT, stands for Light Kicker Trim, Medium Kicker Trim and Hard Kicker Trim, respectively.

Heading: 180°				
Sheet angle [°]	**60**	**70**	**80**	**90**
Heel angle: 0°		C_{F_S} [-]		
LKT	-0.4244	-0.1899	0.0512	0.2795
MKT	-0.4782	-0.2497	-0.0337	0.2146
HKT	-0.5001	-0.2972	-0.0647	0.1868

Table A.45: Corrected lift force coefficients C_{F_L} [-] for the strong wind case, where LKT, MKT and HKT, stands for Light Kicker Trim, Medium Kicker Trim and Hard Kicker Trim, respectively.

Heading: 180°				
Sheet angle [°]	**60**	**70**	**80**	**90**
Heel angle: 0°		C_{F_L} [-]		
LKT	-0.2202	-0.2404	-0.2403	-0.2251
MKT	-0.2173	-0.1989	-0.1911	-0.1877
HKT	-0.1954	-0.1788	-0.1734	-0.2208

Table A.46: Corrected pitch moment coefficients C_{M_P} [-] for the strong wind case, where LKT, MKT and HKT, stands for Light Kicker Trim, Medium Kicker Trim and Hard Kicker Trim, respectively.

Heading: 180°				
Sheet angle [°]	**60**	**70**	**80**	**90**
Heel angle: 0°		C_{M_P} [-]		
LKT	2.3736	2.4416	2.4625	2.3573
MKT	2.3362	2.4180	2.4266	2.4510
HKT	2.2862	2.3662	2.4359	2.4072

Table A.47: Corrected roll moment coefficients C_{M_R} [-] for the strong wind case, where LKT, MKT and HKT, stands for Light Kicker Trim, Medium Kicker Trim and Hard Kicker Trim, respectively.

Heading: 180°				
Sheet angle [°]	**60**	**70**	**80**	**90**
Heel angle: 0°		C_{M_R} [-]		
LKT	-0.7221	-0.2715	0.1893	0.6267
MKT	-0.8453	-0.4095	-0.0124	0.4604
HKT	-0.8936	-0.5143	-0.0846	0.3477

Table A.48: Corrected yaw moment coefficients C_{M_Y} [-] for the strong wind case, where LKT, MKT and HKT, stands for Light Kicker Trim, Medium Kicker Trim and Hard Kicker Trim, respectively.

Heading: 180°				
Sheet angle [°]	**60**	**70**	**80**	**90**
Heel angle: 0°	C_{M_Y} [-]			
LKT	0.1160	0.0761	0.0557	0.0575
MKT	0.1796	0.1219	0.0996	0.0971
HKT	0.2132	0.1673	0.1384	0.1301